THE OCCURRENCE, DISTRIBUTION AND ORIGIN OF HYDROCARBONS IN THE KHIBINY NEPHELINE SYENITE COMPLEX, KOLA PENINSULA, RUSSIA

BETTINA BEESKOW

A THESIS SUBMITTED IN PARTIAL FULFILMENT OF THE REQUIREMENTS OF KINGSTON UNIVERSITY FOR THE DEGREE OF DOCTOR OF PHILOSOPHY

JULY 2007

Abstract

The occurrence of hydrocarbon-bearing fluids in alkaline igneous rocks has been known for many years, but their origin is still controversial. The fluids may be of biogenic origin, derived from the host rocks, or the result of abiogenic processes. Three mechanisms for abiogenic production have been proposed: mantle derivation, late-magmatic C-O-H respeciation and post-magmatic Fischer-Tropsch generation. Here, new petrographic, microthermometric and laser Raman data, combined with data of carbon and bulk gas content and isotope signatures as well as permeability and porosity data of material from throughout the Khibiny intrusion are presented. These are discussed in the context of previously published work in order to characterise the occurrence and distribution of hydrocarbon-bearing fluids and to reassess the hypotheses for hydrocarbon generation for the Khibiny pluton.

Bulk gas data show a dominance of methane and only minor concentrations of higher hydrocarbons in whole-rock samples. On average, 12.8 cm^3 of hydrocarbons are released from one kg rock of the Khibiny pluton. Solid carbon is present at levels between 0.21 and 0.06 wt%. Both, methane and carbon contents are highest in the marginal areas suggesting a possible contribution from the host rocks. The fluid inclusion study shows that about 90 % of the inclusion population is methane-dominant and only 10 % water-dominant. The majority of the fluid inclusions are secondary and were trapped over a wide range of P-T conditions within subsequently healed microfractures. P-T entrapment conditions for primary fluid inclusions are around 600 MPa and 600°C. Melt inclusions often contain a methane-rich fluid phase. Isotope data for methane indicate a largely abiogenic origin, but the decrease of $\delta^{13}C$ towards the margin of the complex from − 5.4 ‰ to − 22.4 ‰ suggests addition of biogenic material derived from the host rocks. This is in agreement with the results of the fluid inclusion plane and microcrack study that indicates a high degree of fluid movement throughout the history of the pluton, up to the present day. Average palaeo and modern porosity estimates are 5.56 % and 4.80 %, respectively. Average palaeo and modern permeability values are 2.38 mD and 1.95 mD, respectively. Based on these porosity values the methane content in the Khibiny pluton is estimated at between 416 km^3 and 7649 km^3.

In summary, isotope data, the presence of primary CH_4-dominated fluid inclusions and melt inclusions, which also contain a methane-rich gas phase, indicate an abiogenic mantle origin of the hydrocarbons. There is little evidence for operation of a Fischer-Tropsch-type reaction in methane generation. An increase in carbon and methane content, together with decreasing $\delta^{13}C$ isotope values towards the pluton margin suggests that magmatically derived abiogenic hydrocarbons may have mixed with biogenic hydrocarbons derived from the surrounding country rocks.

Acknowledgements

Someone told me right at the beginning of the project "A PhD is not a sprint, it's a marathon!" Well, it turned out to be true and I am grateful that so many people cheered me on during this long run.

First and foremost I thank my supervisors Peter Treloar and Andy Rankin for their continuous support during the PhD program.

Many people were involved in the successful sampling I undertook in the Khibiny Mountains. I would like to thank Valentin Nivin for his hospitality and invaluable help with logistical questions. Also, I am grateful for the discussions and talks with Serafim Ikorski and the spontaneous friendship of Anaida Avedisyan who showed me a sample of daily life in Apatity. I thank Olaf for helping me sampling, carrying kilos of rocks and battling dense clouds of ravenous midges.

In the course of my analytical work I met many wonderful people who generously offered their help and support. I gratefully acknowledge the support of Frances Wall and Terry Williams who introduced me to microprobe analysis at the Natural History Museum in London and shared my interest in those strange Khibiny rocks. The microcrack analysis done during my visits in Nancy wouldn't have been possible without the help and support of Marc Lespinasse. I am also grateful to Torsten Vennemann and Jorge Spangenberg from the University Lausanne for their generous help with the isotope analyses. The many discussions in the laboratory deepened my understanding of the isotope system. Martin Ziemann at the University Potsdam deserves thank for his generous help, our discussions and his explanations about the intricacies of the laser Raman spectroscope.

Many people at Kingston University were in one way or another involved in the completion of this thesis. Thanks to Ian Gill for preparing the seemingly unending stream of samples, it has really stopped now, and for his perpetually humorous disposition and to Pam Murphy for the time she spent on the laser Raman spectroscope with me. I also wish to thank my postgraduate colleagues, especially Paul and Jon who helped me immensely by giving me encouragement and friendship.

Joanne Potter, despite somewhat different scientific opinions, gave friendship over the years, for which I thank her.

I would also like to thank Alan Parker and Jon Strong not only for proof reading articles and this thesis but also for being good friends beyond my time at Kingston University.

During my time in Surbiton James Trainer and my other friends from The Angel taught me a bit of the English way of life – from horse racing to karaoke. Thanks for that!

Most importantly, I thank my family for their continuing belief in me and my work and that I eventually succeed…

Contents

1 Introduction to the project 1

1.1 Introduction 1

1.2 Objective of the study 3

1.3 Approaching the problem 3

1.4 Research methodology 5

2 Mixed CH_4–CO_2 fluid inclusions in quartz from the South Wales Coalfield as suitable natural calibration standards for microthermometry and Raman spectroscopy 8

3 An introduction to existing hypotheses of hydrocarbon origin in igneous rocks 9

3.1 Abiogenic origin 11

3.1.1 Mantle origin 11

3.1.2 The respeciation of C-O-H fluids 15

3.1.3 Hydrocarbon generation via a Fischer-Tropsch-type reaction 18

3.2 Biogenic origin of hydrocarbons in igneous rocks 22

3.3 The discrimination of hydrocarbon sources or generation mechanisms 24

3.4 Summary 30

4 Geology and petrology of the Khibiny intrusion and surrounding areas.....31

4.1 Location of the Khibiny pluton and a brief historical review of its discovery 31

4.2 Geology of the Khibiny pluton 32

4.2.1 Geology of the surrounding host rocks.....37

4.2.2 Rock definitions 38

4.2.3 Fieldwork and hand-specimen description 40

4.3 Petrology and mineralogy of the samples used in this study 49

4.3.1 Methods 49

4.3.2 Petrographic description 52

4.3.3 Composition of the rock-forming minerals 68

4.4 Summary 74

5 Carbon occurrence in the Khibiny intrusion 76

5.1 Introduction 76

5.2 Literature review 76

5.2.1 Bitumen, organic matter and graphite in the Khibiny pluton 76

5.2.2 Carbonatites in the Khibiny pluton.....77

5.3 Solid carbon data of this study 78

5.3.1 Methods.....78

5.3.2 Results 80

5.3.3 Discussion 88

5.4 Summary.....92

6 The identification, characterisation and interpretation of fluid and solid inclusions in the Khibiny pluton 94

6.1 Introduction 94

6.2 A brief review of previous fluid inclusion studies on rocks from the Khibiny pluton 95

6.3 Methods 97

6.3.1 Sample preparation 97

6.3.2 Laser Raman Spectroscopy 98

6.3.3 Microthermometry 100

6.4 Description of fluid inclusions, their occurrence and distribution 100

6.4.1 Primary fluid inclusions 101

6.4.2 Secondary fluid inclusions 102

6.4.3 Compositional fluid inclusion types 104

6.5 Results of laser Raman analysis 108

6.6 Results of microthermometry 108

6.6.1 Microthermometric results with respect to rock type and fluid inclusion appearance 120

6.7 Fluid entrapment and evolution 125

6.7.1 Isochore projections 125

6.7.2 Interpretation of fluid inclusion observation and isochore projection 130

6.8 Melt inclusions 134

6.9 Summary 136

7 Bulk gas composition of the fluids trapped in the rocks of the Khibiny pluton 140

7.1 Introduction 140

7.2 A review of existing data 141

7.3 Methods 146

7.4 Results and Discussion 148

7.4.1 Bulk gas composition 148

7.4.2 The relevance of the Anderson-Schulz-Flory distribution for conclusions on hydrocarbon origin 153

7.4.3 The spatial distribution of gases within the Khibiny complex 160

7.5 Summary 165

8 The carbon and hydrogen isotopic composition of the fluids of the Khibiny pluton 167

8.1 Introduction 167

8.2 A review of previous isotope data published from the Khibiny pluton 169

8.3 Methodology 174

8.3.1 Sample preparation 174

8.3.2 Thermal decrepitation 174

8.3.3 Crushing of rock samples 177

8.3.4 Comparison of the methods 179

8.4 Results 184

8.5 Discussion 185

8.5.1 The origin of methane based on isotopic mass balance calculations 185

8.5.2 The δD versus $\delta^{13}C$ signature of methane from the Khibiny pluton 193

8.5.3 Isotope distribution of hydrocarbons as an indicator for abiogenic origin 195

8.6 Summary 198

9 Crack characteristic, density and orientation in the Khibiny pluton and the implication for fluid movement and storage.....200

9.1 Introduction 200

9.2 Aims and Objectives.....200

9.3 Definitions 201

9.3.1 Microcracks 201

9.3.2 Fluid inclusion planes.....202

9.3.3 Porosity and permeability in igneous rocks.....203

9.4 Methods 204

9.4.1 Sampling and sample preparation.....204

9.4.2 Acquisition of crack parameters 205

9.4.3 Quantification of porosity and permeability 208

9.4.4 Determination of crack orientation.....210

9.5 Results and discussion 212

9.5.1 Characteristics of MCs and FIPs 212

9.5.2 Porosity and permeability data and their implication 216

9.5.3 Differences with rock type 226

9.5.4 Orientation of FIPs 228

9.6 Conclusions 232

10 A reassessment of models for hydrocarbon generation in the Khibiny nepheline syenite complex, Kola Peninsula, Russia.....235

11 Conclusions 237

11.1 Aim of the study 237

11.2 Brief summary of data 238

11.3 Towards a new model for hydrocarbon generation in the Khibiny Mountains 240

11.4 The Khibiny pluton in the context of hydrocarbon occurrences in igneous rocks ...241

11.5 Economic potential and ecological significance.....242

11.6 Recommendation for further work 243

References 245

Appendices 273

A 1.0: List of abbreviations

A 4.1a: Sampling list

A 4.1b: Satellite image of sampling locations

A 4.2: Electron microprobe results of selected minerals

A 4.3: Laser Raman spectra of main minerals

A 6.1a: Microthermometric results of methane-dominant inclusions

A 6.1b: Microthermometric results of water-dominant inclusions

1 Introduction to the project

1.1 Introduction

Hydrocarbons are one of the world's key natural resources. They are currently the main source of energy and heat and research into their formation, distribution, migration, accumulation and alteration underpins much geological research.

More than a century of research has established that the bulk of the world's hydrocarbons result from decomposition of organic matter deposited in sedimentary basins (Hunt, 1995). It has been shown that some naturally occurring hydrocarbons may have an inorganic source. Although, by comparison with organic hydrocarbons, the quantities of these are insignificant, they have nevertheless, attracted great interest and have even been proposed as the main source of petroleum (e.g. Gold, 1979; Porfirev, 1974). Abiogenically derived hydrocarbons have been documented in metamorphic rocks as a product of respeciation of a C-O-H fluid and graphite (Holloway, 1984). Igneous rocks are an unusual environment to find hydrocarbon-rich fluids. Mostly igneous fluids are dominated by CO_2 and H_2O and therefore, hydrocarbons within igneous rocks are generally assumed to be of a secondary nature and to have migrated into the rock body (e.g. Parnell, 1988). However, the variety and widespread occurrence of those igneous rocks that do contain hydrocarbons suggests that the migration model may be an over-simplification. Hydrocarbons have been described from basic and ultrabasic rocks of mid-ocean ridge basalts and ophiolites, from alkaline rocks and from mantle xenoliths (e.g. Kelley, 1996; Abrajano *et al.*, 1990; Gerlach, 1980; Krot *et al.*, 1994) and several hypotheses for their origin or generation mechanism have been proposed. Most studies suggest that the abiogenic hydrocarbons are derived, as in

metamorphic rocks, through respeciation of a C-O-H fluid; are catalytically generated from CO_2 and H_2 by the low pressure-temperature Fischer-Tropsch-type reaction, or simply are derived directly from the mantle (Potter and Konnerup-Madsen, 2003 and references therein).

Many alkaline igneous rock complexes are significantly enriched in gaseous hydrocarbons although they may also contain dispersed bitumens in both liquid and solid forms. With respect to hydrocarbon origin and fixing the best studied alkaline complexes are the Khibiny and Lovozero peralkaline intrusions of the Kola Peninsula (NE Baltic shield, NW Russia), the Ilímaussaq complex of South Greenland and the Strange Lake complex in Canada. (e.g. Potter, 2000; Konnerup-Madsen, 2001; Salvi and Williams-Jones, 1997). The largest, and to date, best studied of these in terms of petrology, mineralogy and geochemistry is the Khibiny complex. This study focuses on its hydrocarbon reservoir with special respect to its origin, distribution and migration.

The methane-dominant hydrocarbons in the Khibiny complex occur in two main forms. As free gas they occupy open microcracks and fractures. As fluid inclusions they fill mineral cavities and healed microfractures. The high abundance of these fluids has been known for more than half a century (Petersilie, 1960; 1962; Petersilie *et al.*, 1961) but still their origin remains unclear. This is due to the variety of possible carbon sources involved in methane generation and the complexity of the system. Consequently a number of different hypotheses for the origin of methane in alkaline rocks have been proposed. Early research suggested derivation from a mantle fluid (Petersilie and Sørensen, 1970). More recently, the Fischer-Tropsch reaction, that involves an abiogenic, low temperature conversion of CO_2 and H_2O, catalysed by Fe-rich minerals, has been used to explain the high abundance of methane-rich fluids (Voitov, 1992; Potter, 2000).

1.2 Objective of the study

The study has three principal goals:

- to constrain the sources of the hydrocarbons and the conditions and mechanisms of their *origin and evolution;*
- to identify the *distribution* of hydrocarbons within the Khibiny complex and the parameters that influence it;
- to examine the *migration pathways* of the hydrocarbons.

In the light of existing and new data, a critical review and reassessment of existing theories should lead towards a better understanding of processes of hydrocarbon generation, storage and movement in the Khibiny pluton.

1.3 Approaching the problem

The origin, distribution and migration of hydrocarbons in the Khibiny complex is most likely constrained by spatial variations within the complex. Parameters that change with location and may thus influence hydrocarbon occurrence are considered to be:

- the *distance from host rocks* that may deliver material for hydrocarbon genesis or be the direct source of the hydrocarbons themselves;
- the individual *rock types* inasmuch as some mineral species are more suitable than others for the storage of hydrocarbons or to catalyse their generation through late or post magmatic reactions;
- the available *migration pathways* available to move hydrocarbons, or their precursors, through the complex; and
- the *tectonic settings* that encourage hydrocarbon movement and storage.

This study has therefore used samples from a variety of different locations in order to study the hydrocarbon fluids in the context of their local environment. To gain a

comprehensive data base, petrographic studies of minerals and mineral-fluid relationships were carried out in different rock types (Chapter 4) and the solid carbon contents were determined (Chapter 5). Fluid characteristics were defined through investigation of fluid inclusions (Chapter 6), bulk gas composition (Chapter 7) and stable hydrogen and carbon isotope signatures (Chapter 8). In addition, modern and palaeo migration pathways in the form of microcracks and fluid inclusion planes, respectively, were studied on selected samples using image-analysis techniques (Chapter 9).

Key to understanding the range of fluid inclusion chemistries in the Khibiny Complex is the requirement to constrain precisely the location of the solid-liquid-gas triple point in the methane system. This was done as part of this study through the use of large methane-rich inclusions from the South Wales coal-field. Laser Raman spectroscopy and microthermometry were both used to do this. As the data from South Wales enable a robust interpretation of the methane inclusions from the Khibiny fluid system the results are summarised in Chapter 2.

1.4 Research methodology

A variety of techniques have been used to understand how hydrocarbons are distributed, what their main chemical characteristics are and how they migrate through the rock system. For a better overview a short outline of the research methodology is given here.

Geological fieldwork (in co-operation with Kola Science Centre, Apatity, Russia)

Different rock types of the Khibiny complex were sampled during the Summer of 2003 field season. Oriented samples were obtained and their location recorded by GPS. This was important for the investigation of spatial gas distribution and to ascertain if gas content or gas chemistry within the Khibiny pluton is dependent on rock type or location. Orientation of sample material was necessary for examination of microcracks and fluid inclusion planes in the igneous rocks of the Khibiny complex. In this way, it is possible to deduce principal migration directions and whether cracks are related to tectonic events or not.

Petrological investigations (in co-operation with Natural History Museum, London, UK)

Standard petrographic techniques were used to estimate modal mineral compositions and to document relationships between mineral assemblages and bulk gas chemistry and content. Furthermore, the textural association between mineral assemblages and fluid inclusion population was investigated to constrain possible fluid-rock interactions. Detailed microprobe analyses were used to study general mineral compositions as well as the chemistry and geometry of overgrowth and alteration structures.

Determination of carbon content (in co-operation with Alfred-Wegener-Institute Potsdam, Germany)

In order to gain a comprehensive data set, it was necessary to determine whether all the organic carbon in the Khibiny is contained within the fluid phase or whether there are additional solid phases. Their distribution may indicate possible hydrocarbon generation mechanisms.

Fluid inclusion investigations

The study of fluid inclusions comprises a major part of this thesis. Initial microscopic observations were carried out in order to understand the occurrence and population density of fluid inclusions with regard to their host rocks and unusual petrographic features. The fluid composition was analysed using non-destructive laser Raman spectroscopy and, in combination with microthermometric results, data on pressure and temperature conditions of entrapment were obtained.

Bulk gas analysis (in co-operation with Kola Science Centre, Apatity, Russia and Exxon Mobil, Houston, USA)

The gas compositions of whole-rock samples were obtained in order to identify volatile species, not detected by the laser Raman technique, and to examine the molar proportions of all the detected gas components (methane and higher hydrocarbons). These data also contribute to the investigation of spatial gas distribution and their composition may indicate a biogenic or abiogenic gas origin.

Investigation of $\delta^{13}C$ and δD isotope composition (in co-operation with University of Lausanne, Switzerland)

Isotope data provide important constraints on hydrocarbon origin. However, these data are sparse, probably due to the lack of suitably established techniques for gas release

from igneous rocks coupled to appropriate gas separation and isotope detection systems. For this study, two extraction mechanisms (one mechanical and one thermal) were used to release gas from selected samples and to measure their stable hydrogen and carbon isotope signatures.

Examination of fluid migration in the Khibiny complex (in co-operation with University of Nancy, France)

A preliminary study of the orientation of microcracks and fluid inclusion planes was performed to obtain information on fluid migration mechanisms, porosity and permeability in the rocks of the Khibiny complex. These data were used to compare palaeo porosities and permeabilities with those of the present day and to model fluid migration histories.

A detailed description of the methods is given in the relevant chapters.

The thesis concludes with a critical reassessment of the existing hypotheses for hydrocarbon origin and generation (Chapter 10).

2 Mixed CH_4–CO_2 fluid inclusions in quartz from the South Wales Coalfield as suitable natural calibration standards for microthermometry and Raman spectroscopy

B. Beeskow, A.H. Rankin, P.J. Murphy and P.J. Treloar

Data based on Laser Raman spectroscopy and microthermometric techniques is an essential part of the thesis work. Therefore, an introductory study of methane-dominant fluid inclusions from South Wales was carried out and is presented here. The project was initiated by A.H. Rankin. During the course of this study A.H. Rankin provided training in fluid inclusion techniques and P.J. Murphy in laser Raman analysis. A.H. Rankin, P.J. Murphy and B. Beeskow interpreted the data. B. Beeskow wrote the first draft of the paper. P.J. Treloar and B. Beeskow wrote the final version for publication.

This work is published in Chemical Geology 223 (2005), page 3-15.

ELSEVIER

Chemical Geology 223 (2005) 3–15

CHEMICAL GEOLOGY
INCLUDING
ISOTOPE GEOSCIENCE

www.elsevier.com/locate/chemgeo

Mixed CH_4–CO_2 fluid inclusions in quartz from the South Wales Coalfield as suitable natural calibration standards for microthermometry and Raman spectroscopy

B. Beeskow *, A.H. Rankin, P.J. Murphy, P.J. Treloar

School of Earth Sciences and Geography Kingston University, Penrhyn Road, Kingston upon Thames, Surrey, KT1 2EE, UK

Accepted 16 May 2005

Abstract

Laser Raman and microthermometric analysis have been used independently to calculate the molar proportions of mixed CH_4–CO_2 fluid inclusions in quartz from the South Wales Coalfield, UK. The respective ratios of the mean values obtained are 84:16 and 85:15 mol%. Therefore, the fluid inclusions are suitable for independently checking the validity of LRM and microthermometric data, and for determining the instrumental efficiency coefficient ξ of Raman microprobes. Individual fluid inclusions show consistent and reproducible phase transitions on heating and cooling between room temperature and −196 °C. LRM tracking of these phase changes shows that on cooling CO_2 is strongly partitioned into a solid phase, thus purifying the residual CH_4 liquid down to −196 °C at which point it freezes. Reheating results in the melting of the CH_4 solid to form co-existing liquid+vapour+solid ($L+V+S$) CH_4 at the triple point of −182.5 (±1) °C. In these samples, this phase transition is exceptionally clear and reproducible making the inclusions suitable as a low temperature calibration standard for microthermometric studies. The Raman spectra for L, V and S methane are distinguishable, with a prominent peak at 2906 (±1) cm^{-1} for CH_4 (S) at −190 °C, compared with peak positions for CH_4 (V) and CH_4 (L) at −105 °C at 2917 and 2910 (±1) cm^{-1}, respectively. Similar patterns apply to the CO_2 spectra. With change of aggregation the peak position shifts by up to 7 wave numbers. These data show that the Raman peak positions in natural inclusions depend not only on temperature and pressure as previously reported, but also on the state of matter in which the component occurs: L, V or S.

Keywords: Fluid inclusions; Raman spectroscopy; Microthermometry; Methane triple point

1. Introduction

Microthermometry and laser Raman (LRM) spectroscopy are the two most widely used non-destructive methods of fluid inclusion analysis, particularly of the

* Corresponding author. Fax: +44 20 8547 7497.
E-mail address: B.Beeskow@kingston.ac.uk (B. Beeskow).

0009-2541/$ - see front matter © 2005 Elsevier B.V. All rights reserved.
doi:10.1016/j.chemgeo.2005.01.028

volatile components (e.g., Roedder, 1984; Van den Kerkhof, 1988).

Raman spectroscopy is essentially a qualitative method whereby certain Raman-active molecular species may be identified on the basis of their characteristic spectra (Burke, 2001). However, it is also possible to estimate the relative molar ratios of these species in fluid inclusions based on peak area ratios (e.g., Seitz et al., 1987; Dubessy et al., 1989; Chou et al., 1990; Thomas et al., 1990).

Microthermometry is an indirect method of volatile analysis based on measurements of the temperatures at which distinct phase changes, assigned to particular chemical species, take place. With reference to appropriate phase diagrams, it is possible to estimate molar proportions and volumes of binary mixtures of volatiles such as CO_2, N_2 and CH_4 in the inclusions (e.g., Thiery et al., 1994). Successful application of this approach depends on the degree of confidence in recognising these phase changes as well as the accuracy of the temperature measurements and phase diagrams used.

Calibration of heating and cooling stages is usually carried out using the melting points of pure chemical substances or, preferably, the known transition points in natural and synthetic fluid inclusions. For temperatures down to −100 °C, the melting point of pure hexane (−95 °C) or the triple point of CO_2 (−56.6 °C) are suitable (Shepherd et al., 1985) and, depending on the operating conditions, accuracies better than ±1 °C are often achievable. Where information on the PVTX properties of CH_4-bearing fluids is required it is necessary to undertake measurements well below these temperatures, but unfortunately suitable calibration material is lacking. The triple point of pure CH_4 at −182.5 °C (Kleinrahm and Wagner, 1986; Goldstein and Reynolds, 1994) in natural or synthetic inclusions would provide an ideal calibration point at very low temperatures. However, observation of this transition has seldom been reported in the literature (see for instance Hurai et al., 2002). This is due to a number of factors:

1) pure CH_4 inclusions are very rare,
2) the phase changes at the triple point may be difficult to recognise,
3) the temperature at the triple point is close to the lower limit of commercial stages (ca. −196 °C) and,
4) solid CH_4 does not always form, due to metastability and supercooling effects.

As part of a combined laser Raman and microthermometric study of fluid inclusions in large quartz crystals associated with Carboniferous coals from South Wales, UK we have routinely observed abundant, large CH_4-bearing fluid inclusions (with a minor CO_2 component), which readily freeze at around −190 °C. In this paper we demonstrate how it is possible to isolate the pure CH_4 component of the inclusions through heat-cool cycling. This enables the observation and accurate measurement of the CH_4 triple point at −182.5 °C. We discuss the use of these fluid inclusions as calibration standards for low temperature fluid inclusion microthermometry. A further aspect outlined here is their suitability for determining the instrumental efficiency coefficient ζ of Raman microprobes, which is necessary for calculations of molar proportions of fluid inclusion components (Pasteris et al., 1988). We also report on the identification of the various phase changes that take place on heating and cooling of these inclusions and the partitioning of CH_4 and CO_2 between these phases down to the triple point of pure methane.

2. Methods

A series of 0.1–0.2 mm thick double-polished fluid inclusion wafers were prepared from two quartz crystals. Some were cut parallel to the c-axis and others perpendicular to it. The overall size, shape and distribution of the fluid inclusions were determined using a standard petrographic microscope.

A Renishaw RM1000 laser Raman microprobe, equipped with an argon ion laser (514.5 nm) and thermoelectrically cooled CCD detector, was used to measure the Raman spectra of various phases developed in the fluid inclusions upon cooling and heating. Measurements were made in confocal mode by focussing the laser beam through the optical path of an Olympus microscope using lenses with magnifications of ×20 and ×50. A pure silicon standard (520 cm^{-1}) was used to calibrate the microprobe, and the stated peak positions are reproducible to within ±1 cm^{-1}. A pure, natural diamond standard was used to determine the accuracy of the spectra at higher wave-

length using the single peak at 1332 cm^{-1} and to check for any drift towards higher wavelengths (Chalmers and Griffiths, 2002).

Spectra were usually acquired over a 30 s period over the range from 1000 to 3000 cm^{-1}. A laser power of 100 mW was reduced to <1 mW on the sample.

Microthermometric analyses of fluid inclusions were carried out using a Linkham TH600 heating/freezing stage mounted on the Olympus microscope attached to the Laser Raman microprobe. For the present study, measurements were carried out on phase changes below room temperature only. The system was cooled rapidly down to about −195 °C to avoid metastable effects. Heating rates of 10 °C/min were used. These were reduced to 1 °C/min close to transition points in order to define precisely the temperatures on which phase changes occur. The same rates were used for heat-cool-cycling.

The stage was calibrated at regular intervals using a synthetic FLINCOR H_2O fluid inclusion with a known ice melting point at −0.2 °C, and a synthetic FLINCOR CO_2 standard showing a triple point value for pure CO_2 at −56.6 °C. The accuracy of the melting point of the FLINCOR standards was established by careful calibration of the stage using the known melting points of pure (specpure) organic liquids (Shepherd et al., 1985). All these measurements are reproducible to within ±0.2 °C.

3. Description of sample and fluid inclusion population at room temperature

The methane-rich fluid inclusions considered here are contained within large euhedral quartz crystals, up to 3 cm in size, which form in vugs and cavities within vertical fractures. These cross-cut a sequence of anthracitic coal, mudstone and sandstone from the lower benches of the Nant Helen open cast coal mine (UK National Grid Reference: SN827113) in Glamorgan, Wales, UK. The crystals studied were provided by Dr. N. Hollingworth (NERC) and are associated with minor millerite and calcite overgrowths.

The regional geological setting of the Nant Helen mine within the South Wales coalfield has been summarised by Alderton et al. (2004). The authors also report on the PVTX properties of hydrocarbon-bearing and associated fluid inclusions in fracture-fill and nodule quartz from a number of locations in this coalfield. They conclude that the quartz mostly formed at low temperature (100–200 °C) and shallow depths (<ca. 2.5 km) from fluids generated during burial and associated coalification.

The host quartz crystals for the inclusions considered here are exceptionally clear and the methane-rich inclusions are abundant and large. In this respect, and also in terms of estimated PVTX trapping conditions, they are similar to fluid inclusions reported in euhedral quartz crystals from other low temperature metamorphic environments associated with carbonaceous sediments (e.g., by Hurai et al., 2002; Kisch and Van den Kerkhof, 1991; Mullis, 1987). The fluid inclusions present in the Nant Helen quartz crystals are between 20 and 100 μm in size, although inclusions up to 200 μm also occur. Observations at room temperature allow two types of fluid inclusions to be distinguished.

Type 1 inclusions make up about 95% of the population. They are composed essentially of CH_4–CO_2 and the majority appears mono-phase at room temperature. These inclusions are mostly regularly distributed along healed microfractures or along planes parallel to the hexagonal crystal faces of the host quartz (Fig. 1a). They also occur in randomly distributed clusters (Fig. 1b). The regularly distributed fluid inclusions show both negative crystal shapes and elongate morphologies. The majority of the clustered inclusions typically exhibit irregular flat shapes, and are often connected by thin channels indicative of necking-down. At the margins of irregularly shaped inclusions, especially those that have necked down, a small rim of liquid water is sometimes observed. However, this phase is mostly not detectable by LRM spectroscopy.

Type 2 inclusions make up the remaining 5% of the inclusion population. They are two-phase aqueous fluid inclusions containing a NaCl (±$CaCl_2$) brine and a CH_4-rich vapour bubble, which occupies 10% to 20% of the total volume of the inclusion. They are only observed interspersed with clusters of *Type 1* inclusions.

The apparent co-evality of *Type 1* and *Type 2* might suggest heterogeneous entrapment of coexisting brine and immiscible bubbles of methane-rich vapour bubbles from a parent fluid. However, there is also a

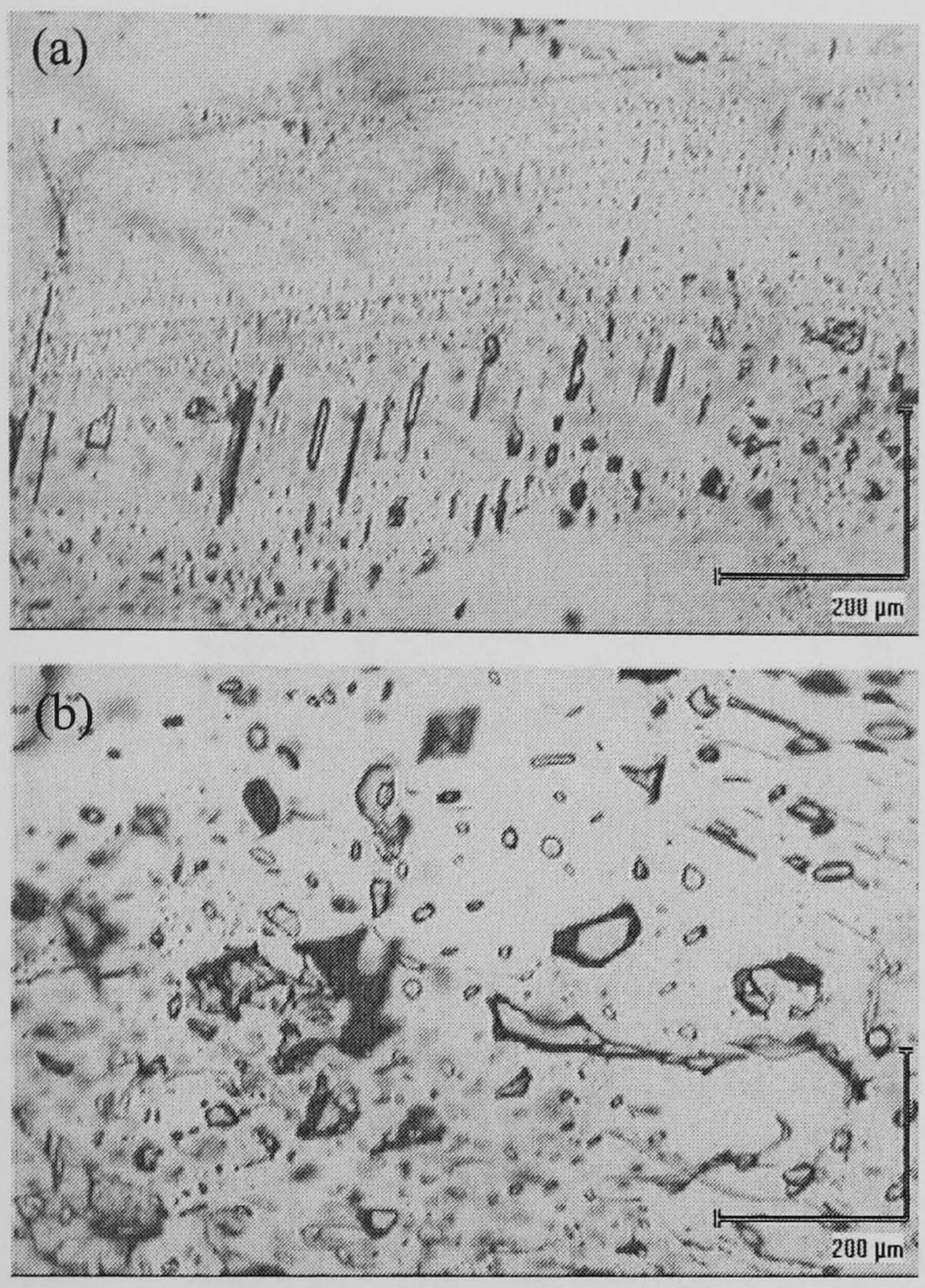

Fig. 1. Photomicrographs showing the distribution of mixed CH_4–CO_2 inclusions in quartz. (a) Along the hexagonal face of quartz, (b) as randomly distributed groups, showing some evidence for necking down.

suggestion of post-entrapment changes in *Type 1* inclusions involving water loss by leakage or necking down. This is inferred from the observation that some of the irregularly-shaped fluid inclusions contain water in bulges. Water is much more mobile than gases such as CO_2 and CH_4 due to the higher polarity of the water molecules and it is therefore, possible that under certain conditions the inclusions might preferentially lose water and become more enriched in CO_2 and CH_4 (Hall and Sterner, 1993; Bakker and Jansen, 1994). Such modifications might also be strain induced (Kerrich, 1976); a theory supported by the presence of microcracks within the crystal. However, water loss can also be initiated when the f_{H2O} gradient, i.e., f_{H2O} in the fluid inclusion, is greater than f_{H2O} in the intergranular fluid (Huizenga, 2001). In the samples studied, changes in fluid composition, and hence of the f_{H2O} gradient, is indicated by the presence of calcite overgrowths on the host quartz crystals.

We therefore assume that preferential water loss due to secondary processes is the most plausible explanation for the occurrence of discrete aqueous and essentially H_2O-free methane-rich inclusions observed in these samples.

4. Results

Detailed microthermometric and LRM analyses were carried out on some 200 *Type 1* inclusions as discussed below.

Microthermometric data for *Type 2* inclusions show salinities in the range of 5 to 30 wt.% and homogenisation temperatures from 20 to 120 °C. However, they are not considered further in the present paper as we wish to focus on the methane-rich inclusions.

4.1. LRM analyses at room temperature

In every inclusion analysed the only distinct peaks recognised were at 2914, 1387 and 1285 cm^{-1}. The first can be ascribed to CH_4 and the latter two to the presence of CO_2 (Burke, 2001). The detected CH_4

Fig. 2. Behaviour of CH_4–CO_2 inclusions on freezing (a) mono-phase inclusion at room temperature, (b) at −70 °C CH_4 a vapour bubble (V) appears, (c) at −100 °C a dendritic CO_2-solid (S_1) nucleates, (d) heat–cool cycling up to -80 °C was performed to develop a single solid CO_2 crystal, (e) further cooling leads to the expansion of vapour V and solid S_1, (f) at temperatures below −190 °C the remaining liquid L forms a second solid S_2, consisting of CH_4. Due to the sudden contraction of CH_4, when it converts from liquid to solid, the vapour "jolts" and releases tiny gas bubbles into S_2. (g) PT-diagram (modified from Thiery et al., 1994) showing the topology of the binary system CO_2–CH_4 and illustrating the path and phase transition of fluid inclusions during cooling and heating. Dashed lines and arrows show the path of fluid inclusions during cooling and heating and full lines mark the two-phase-assemblages for the pure end-members (dividing the field into G (gas), S (solid), and L (liquid) for pure CH_4 and pure CO_2. Grey squares mark the triple point of the pure end-members. The dotted line indicates the critical curve, which connects the critical points of the pure end-members (marked with a grey star). The thin full line marks the univariant SLG curve. See text for description of the heating and cooling path. Also shown is the pressure at homogenisation (P_h). Note, P and T axes are not to scale.

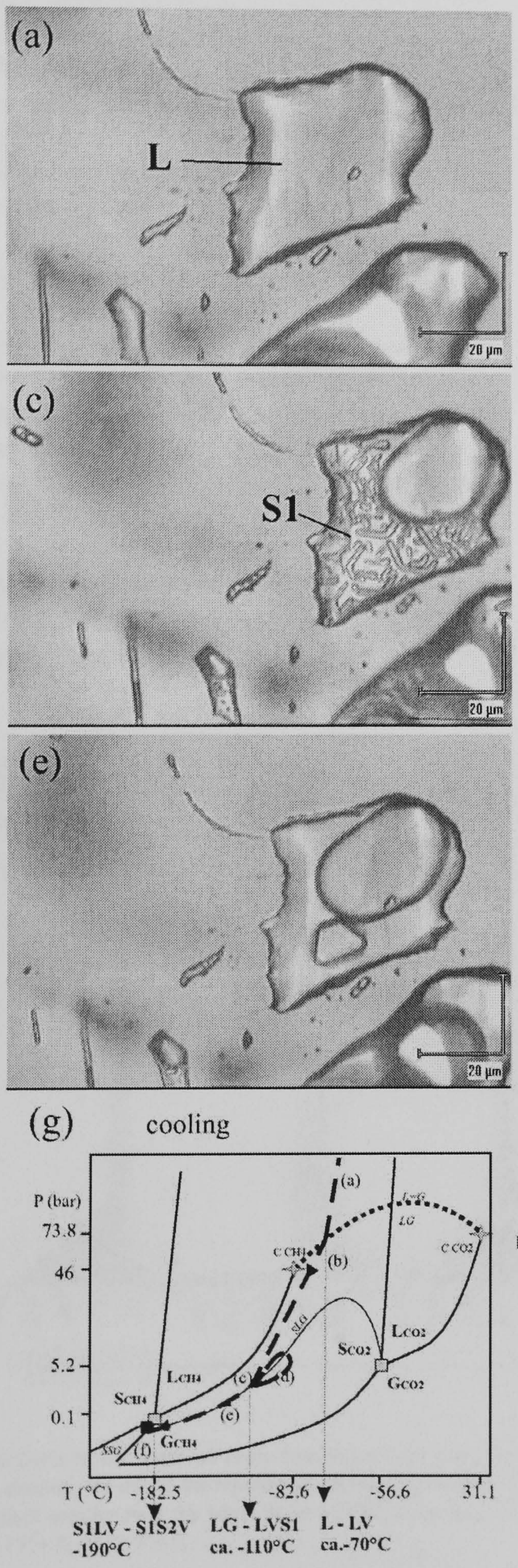
(a)
L
20 µm
(b)
V
20 µm
(c)
S1
20 µm
(d)
S1
20 µm
(e)
20 µm
(f)
V
S2
20 µm
(g)
cooling
heating
P (bar)
73.8
46
5.2
0.1
Ph = 58.2
T (°C)
-182.5
-82.6
-56.6
31.1
(a)
(b)
(c)
(d)
(e)
(f)
LG
C CH4
C CO2
LVG
SLG
SSG
LCH4
SCH4
GCH4
SCO2
LCO2
GCO2
S1LV - S1S2V
-190°C
LG - LVS1
ca. -110°C
L - LV
ca.-70°C
S1S2V - S1LV
-182. 5°C
S1LV - LV
-75°C
LV - L
-69.9°C

peak is at a relatively low wavelength compared with standard literature values (e.g., 2917 cm^{-1} reported in Burke, 2001). This is likely to be the result of high density and pressure within the fluid inclusions (Van den Kerkhof, 1988).

No other peaks were apparent, even in extended runs, lasting over 30 s, and in all instances we were unable to detect the broad band at around 3400 cm^{-1}, indicative of liquid water.

4.2. Microthermometry

The following description is based on observations during runs on some 80 fluid inclusions at temperatures between 20 and −195 °C, using the methods described by Shepherd et al. (1985). The phase transitions during heating and freezing were remarkably consistent for all inclusions. The sequence of phase transitions $S+L+V \rightarrow L+V \rightarrow L/V$ during heating corresponds to H_2 behaviour, as defined by Van den Kerkhof (1988). The solid (S_1 and S_2), liquid (L) and vapour (V) phases were identified by LRM analyses.

Upon rapid cooling the fluid separates into liquid (L) and vapour (V) at about −70 °C (Fig. 2b), and at approximately −110 °C a dendritic CO_2-rich solid phase (S_1) forms in the residual liquid (Fig. 2c). Heat-cool cycling was performed in order to grow a single S_1-crystal (Fig. 2d). Further cooling leads to growth of the vapour and solid phase (Fig. 2e), and at approximately −190 °C the remaining liquid forms a second solid phase (S_2) consisting of CH_4 (Fig. 2f) at the eutectic point of the CO_2–CH_4 system.

Heating leads to the initial melting of S_2 close to the reported triple point of pure CH_4 at −182.5 °C. On further heating S_1 (solid CO_2) melts at approximately −75 °C. Finally, at about −69.9 °C, homogenisation occurs usually to liquid, and rarely to vapour. The low temperature for the CO_2 melting point, compared to the triple point of pure CO_2 at −56.6 °C, is due to the presence of CH_4 (Dubessy et al., 1989). The phase behaviour during cooling and heating is shown in the schematic PT diagram for the binary CO_2–CH_4 system (Fig. 2g), modified from Thiery et al. (1994). The cooling path of the inclusions moves through the

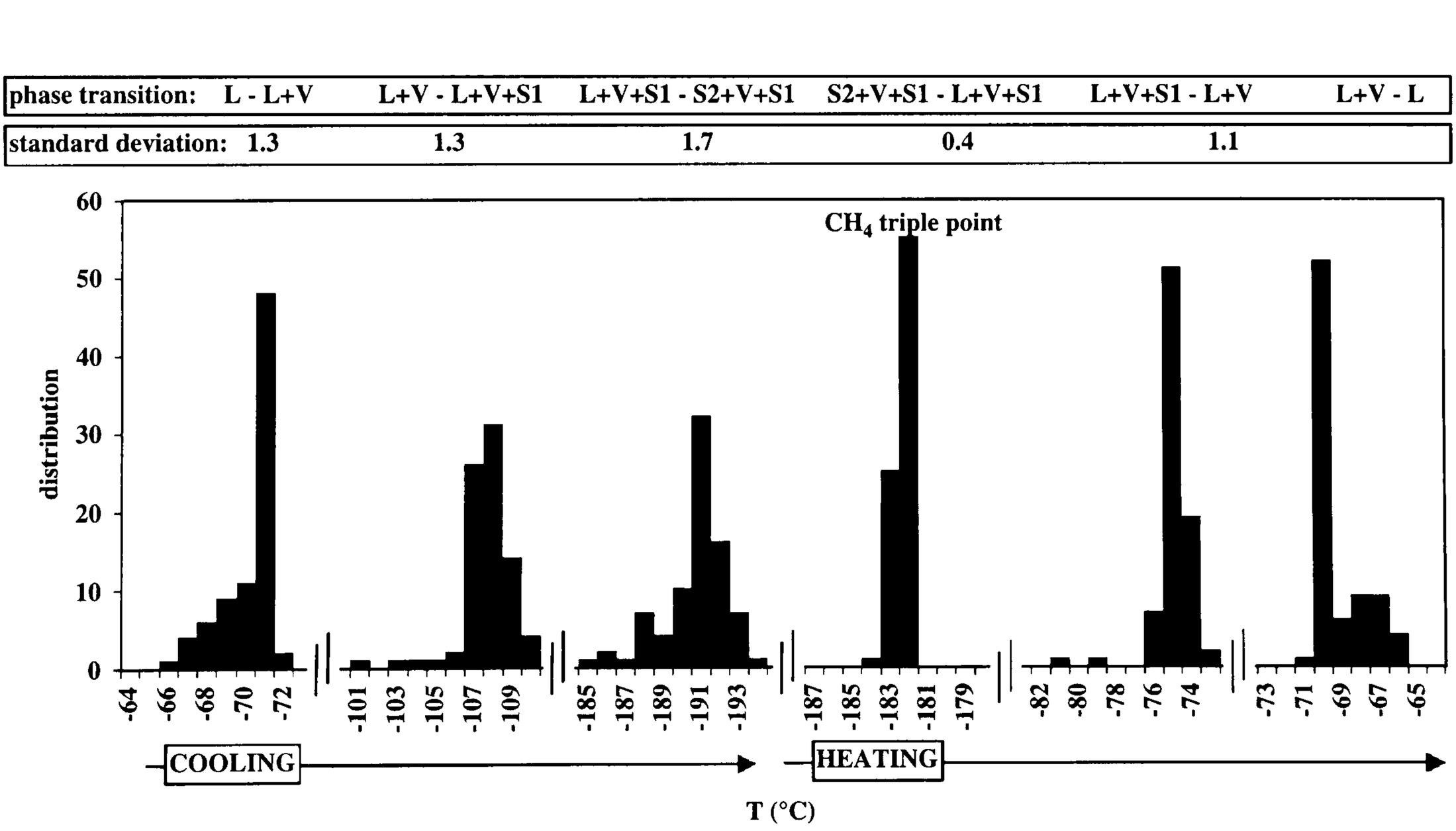

Fig. 3. Temperatures of the observed phase transitions during cooling and heating. The large temperature ranges of 10 °C, recorded for phase transitions on cooling, are due to the rapidity of the freezing process. The temperature variations for phase transitions during heating are about 5 °C, but are much smaller near the triple point of CH_4 at around −182 to −183 °C. Note the small standard deviation for the triple point transitions $S_2+V+S_1 \rightarrow L+V+S_1$.

critical curve and then enters the *LG* (liquid–vapour)-field where a vapour bubble nucleates. On reaching the *SLG* (solid–liquid–vapour)-line, solid CO_2 is formed. The loop shown on the diagram marks the heat-cool cycling (between −110 and ca. −85 °C), performed to obtain a single solid CO_2 crystal (S_1) during experimental runs. On cooling the inclusions further, the eutectic point is reached (at ca. −195 °C) at which point S_1, S_2, and V co-exist.

Upon heating, the inclusions pass the triple point of CH_4 which is very close or co-incident with the eutectic point of the binary CH_4–CO_2 system. From here the heating path continues along the univariant *SLG*-line with the co-existence of solid, liquid and vapour. This phase assemblage develops along the *SLG*-curve until the solid CO_2 disappears and the *LG*-field is entered. With the disappearance of the vapour bubble the heating path leaves the *LG*-field via the critical curve ($L=G$).

A summary of all the relevant microthermometric measurements, together with standard deviations for each of the recognised phase transitions is shown in Fig. 3. The phase transitions during cooling are, due to the rapidity of cooling process, only approximate values in a range of 10 °C. Each phase transition that occurs during heating takes place usually within a 5 °C temperature range. The S_2 phase change occurs over an extremely narrow temperature range ($\sigma=0.4$) between −183 to −182°C (excluding one outlying value at −184 °C).

5. Observation and interpretation of combined LRM and microthermometric analyses

5.1. Composition of fluid inclusions

Microthermometric results and LRM data can be used to obtain relative molar proportions of CH_4 and CO_2 in fluid inclusions, provided no other components are present in significant amounts.

To determine the relative molar proportions of the components based on LRM data the procedures described by Burke (2001) were used. The peak areas for CO_2 and CH_4 are proportional to the number of molecules present in the irradiated volume of the sample. Therefore, comparison of the relative peak areas of the species permits their relative proportions to be determined (Seitz et al., 1996). Molar fractions can be derived using the following simplified formula, based on the ratio method of Placzek (1934):

$$X_a = [A_a/(\sigma_a\zeta_a)]/\sum[A_i/(\sigma_i\zeta_i)],$$

X_a, A_a, σ_a and ζ_a represent the molar fraction, peak area, Raman cross-section and instrumental efficiency for species a, respectively. Index i represents the values for all species present in the inclusion and $\sum$ is their sum (Burke, 2001). For a two-component system, such as CH_4–CO_2, this relationship reduces to

$$X_{CO2} = [A_{CO2}/(\sigma_{CO2}\zeta_{CO2})]/[A_{CH4}/(\sigma_{CH4}\zeta_{CH4}) + A_{CO2}/(\sigma_{CO2}\zeta_{CO2})]$$

$$X_{CH4} = [A_{CH4}/(\sigma_{CH4}\zeta_{CH4})]/[A_{CH4}/(\sigma_{CH4}\zeta_{CH4}) + A_{CO2}/(\sigma_{CO2}\zeta_{CO2})].$$

To determine the peak area the GRAMS/32® software package was used which models an ideal value for a specific peak area using a maximum of 50 iterations. For CO_2 the peak areas of both peaks in the Fermi diad ($2\nu_2$ at about 1388 cm^{-1} and ν_1 at 1285 cm^{-1}) were used on the assumption that the sum of the peak areas remains constant even if the density changes (Dubessy et al., 1989). Raman scattering cross-sections σ for the appropriate wavelengths are 7.5, 1 and 1.5 for CH_4, CO_2 $2\nu_2$ peak, and CO_2 ν_1 peak, respectively (Burke, 2001). In theory, σ values are only applicable for low density fluids at 1 atm pressure. However, Dubessy et al. (1989) have shown that the internal field effect at higher densities is negligible. Therefore, we consider equal σ values for the calculation of molar proportions in solid liquid and vapour phase.

For our Raman microprobe the instrumental efficiency coefficient ζ is determined as 0.65 using artificial CO_2–N_2 gas mixtures provided by Van den Kerkhof and calculated as outlined in Van den Kerkhof and Kisch (1993).

To obtain mol% data, we normalized the values to the sum of X_{CH4} and X_{CO2} which is set to 100% and thus,

$$\text{mol\% } CH_4 = X_{CH4}/X_{CH4} + X_{CO2}$$

$$\text{mol\% } CO_2 = X_{CO2}/X_{CH4} + X_{CO2}$$

Following this method, we analysed some 80 fluid inclusions and calculated their composition in terms of molar proportions CH_4–CO_2. The average composition of all analysed fluid inclusions is 84 mol% CH_4 and hence 16 mol% CO_2. The majority of data fall within the range 78 to 88 mol% CH_4 as illustrated in Fig. 4a.

The compositions of the same fluid inclusions were also obtained using microthermometry. For this we determined homogenisation temperatures (T_h) and CO_2 melting temperatures (T_m). These data were plotted on the appropriate VX diagram (Fig. 4a) for the system CO_2–CH_4 (Thiery et al., 1994) to determine the relative mol% of CH_4 and CO_2 for the analysed inclusions. The estimated values for the inclusions range from 81 to 87 mol% with a mean composition of 85 mol% CH_4 and 15 mol% CO_2. The microthermometry data also indicate a molar volume of approximately 65 cm^3/mol for the fluid inclusions. As an example, data for a single fluid inclusion are shown in more detail. In the expanded diagram (Fig. 4b) the VX properties of the single phases (L and V)

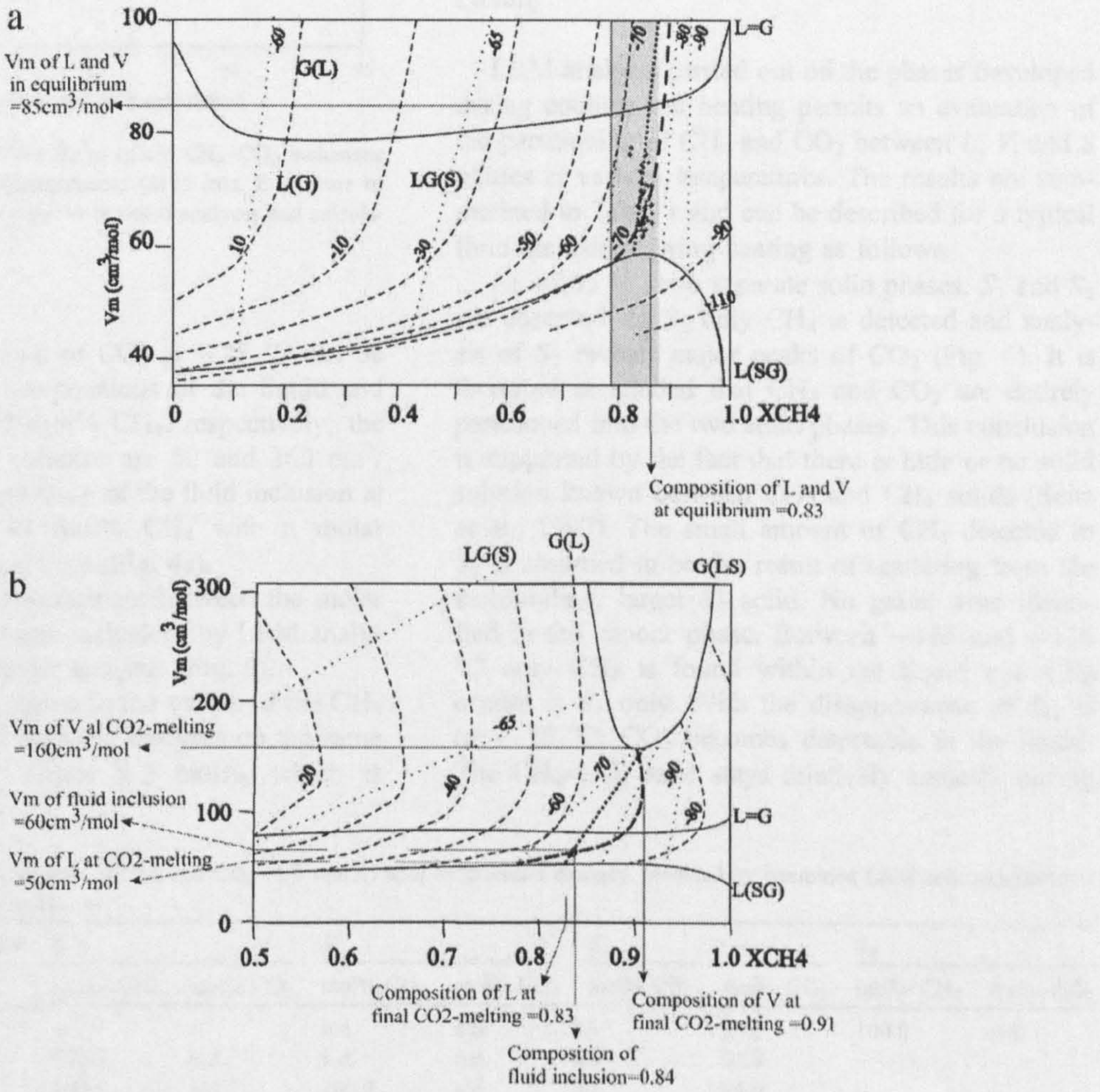

Fig. 4. (a) VX diagram for the CO_2–CH_4 system (modified from Thiery et al., 1994). Dotted lines and italic numbers indicate isotherms of melting temperature (disappearance of S_1). Dashed lines indicate isotherms of homogenisation temperature. The crosses show representative microthermometric results in the range of 81 to 87 mol%. The shaded, grey area marks the range of compositions calculated from the LRM peak areas of 78 to 88 mol%. (b) The expanded diagram with molar Volume (V_m) up to 300 cm^3/mol shows the properties of L and V at the final CO_2 melting for a single fluid inclusion. At the final melting point of CO_2 at −75 °C the compositions of the liquid and vapour are ca. 84 and 92 mol% CH_4, respectively.

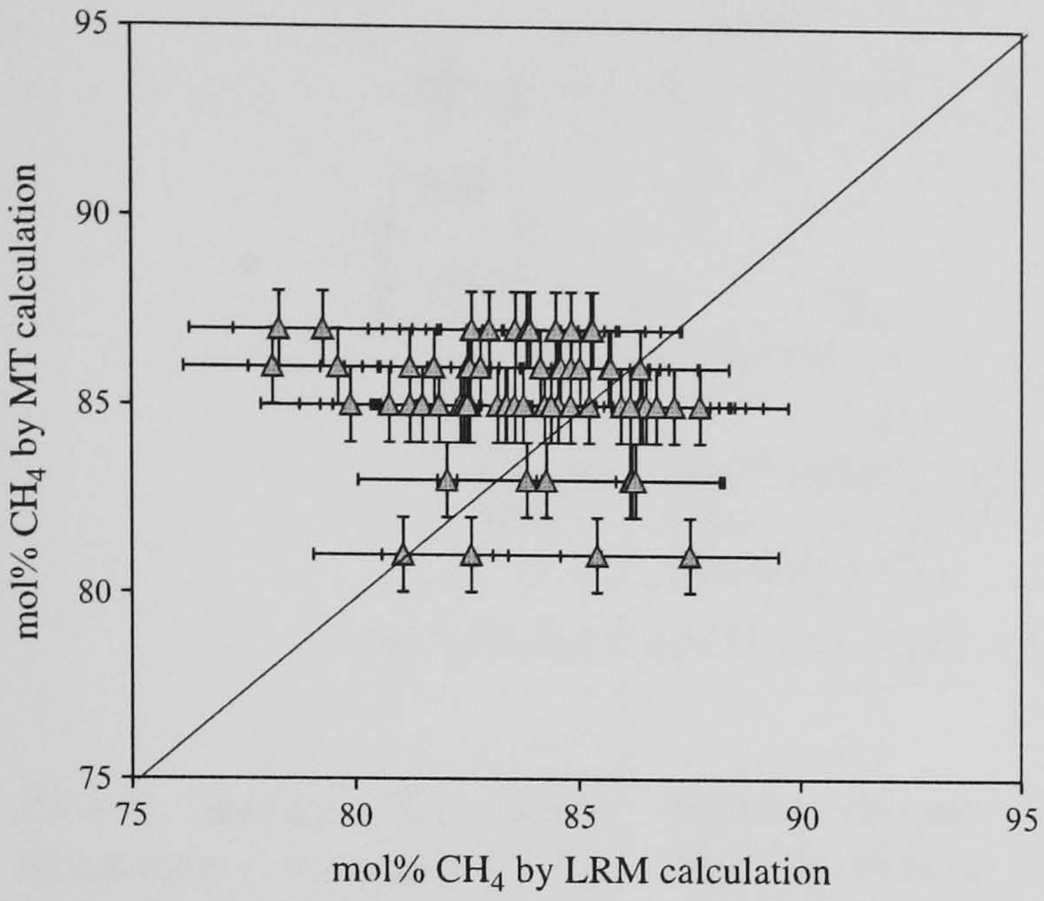

Fig. 5. Comparison of mol% CH_4 in mixed CH_4–CO_2 inclusions based on LRM and microthermometric (MT) data. Error bars of LRM analysis were obtained by 30 repeated analyses and calculations per inclusion.

at the final melting point of CO_2 at −75 °C can be estimated. Here, the compositions of the liquid and vapour are 84 and 92 mol% CH_4, respectively; the corresponding molar volumes are 50 and 160 cm^3/mol. The overall composition of the fluid inclusion at L/V equilibrium is 83 mol% CH_4 with a molar volume of about 85 cm^3/mol (Fig. 4a).

There is very good agreement between the molar ratios derived for the same inclusions by LRM analysis and microthermometric analysis (Fig. 5).

For the LRM data, errors in the values of the CH_4 mol%, based upon 30 replicate analyses on the same fluid inclusions, are within ±2 mol%, which is equivalent to a possible range in peak area ratios for CH_4:CO_2 of between 95.5:4.5 and 96.6:3.4.

Microthermometric data are reproducible to within less than ±1 mol% for repeated analyses on the same fluid inclusion. However, the high precision of microthermometry data may not apply to small inclusions (less than 10 μm) where observations of phase changes are usually less certain.

5.2. Observations of partitioning of CH_4 and CO_2 between liquid, vapour and solid during heat–cool cycling

LRM analysis carried out on the phases developed during cooling and heating permits an evaluation of the partitioning of CH_4 and CO_2 between L, V, and S phases at various temperatures. The results are summarized in Table 1 and can be described for a typical fluid inclusion during heating as follows.

At −195 °C, two separate solid phases, S_1 and S_2 are observed. In S_2 only CH_4 is detected and analysis of S_1 reveals major peaks of CO_2 (Fig. 6). It is therefore concluded that CH_4 and CO_2 are entirely partitioned into the two solid phases. This conclusion is supported by the fact that there is little or no solid solution known between CO_2 and CH_4 solids (Seitz et al., 1987). The small amount of CH_4 detected in S_1 is assumed to be the result of scattering from the surrounding, larger S_2 solid. No gases were identified in the vapour phase. Between −165 and −135 °C only CH_4 is found within the liquid and CO_2 occurs in S_1 only. With the disappearance of S_1, at ca. −75 °C, CO_2 becomes detectable in the liquid. The CH_4–CO_2 ratio stays relatively constant during

Table 1
Variation of the relative proportions of CH_4 and CO_2 (±2 mol%) with temperature changes, obtained by combined LRM and microthermometric analysis for a single inclusion

Temp. in °C	Phases present	L		V		S_1		S_2	
		mol% CH_4	mol% CO_2	mol% CH_4	mol% CO_2	mol% CH_4	mol% CO_2	mol% CH_4	mol% CO_2
−195	S_2+V+S_1	–	–	n.d.	n.d.	2.4	97.6	100.0	n.d.
−165	$L+V+S_1$	100.0	n.d.	n.d.	n.d.	3.0	97.0	–	–
−135	$L+V+S_1$	100.0	n.d.	100.0	n.d.	5.1	94.9	–	–
−105	$L+V+S_1$	92.5	7.5	100.0	n.d.			–	–
−75	$L+V$	84.5	15.5	100.0	–	–		–	–
−45	L	85.9	14.1	–	–	–		–	–
−15	L	85.0	15.0	–	–	–		–	–
25	L	86.3	13.7	–	–	–		–	–

Note, methane detected in S_1 is due to scattering from the surrounding liquid or solid methane.

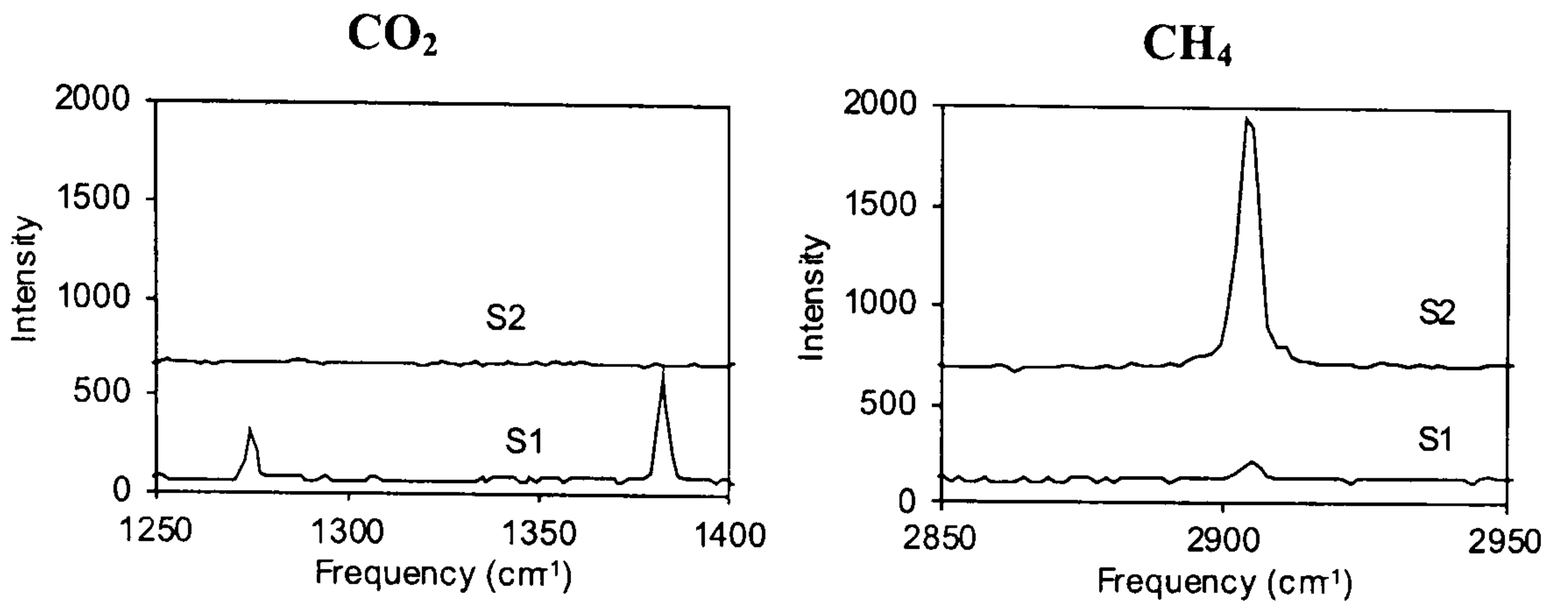

Fig. 6. Raman spectra of solid phases at approximately −195 °C. S_1=solid CO_2; S_2=solid CH_4.

further heating. The vapour bubble contains no detectable component up to −145 °C. Above this temperature it comprises virtually pure CH_4 until it vanishes at approximately −75 °C. No CO_2 was detected within the vapour. This preferential partitioning of CH_4 into vapour is due to its higher volatility compared to CO_2 (Seitz et al., 1987). Between −45 °C and room temperature the fluid inclusion comprises a homogeneous fluid, containing 86 mol% CH_4 and 14 mol% CO_2.

5.3. Variations in CH_4 and CO_2 Raman peak positions for different phases

The characteristics of the Raman peaks for CH_4 and CO_2 are dependent on the rate of change of their molecular properties during vibrational motion and therefore, changes in Raman peak positions are interpreted in terms of molecular interactions (Rosso and Bodnar, 1995). It has long been known that Raman peak frequencies decrease several wave numbers (up to 7 cm^{-1}) with increasing pressure or density (Van den Kerkhof, 1988). However, the shift of the Raman peaks described here are also caused by changes in the state of aggregation.

In the present study, the observed peak positions (in wave numbers) for *S*, *L*, and *V* show systematic variations. They are relatively low in the solid phase, intermediate in the liquid phase, and elevated within the vapour phase (Fig. 7). Systematic data for the shift in peak position are shown for one fluid inclusion as an example in Table 2.

During heating, the peak position of CH_4 in *L* increases continuously from 2907 to 2914 cm^{-1}. Solid CH_4 exhibits similar wave numbers to CH_4 in *L* at very low temperatures. CH_4 detected in the vapour shows much higher wave numbers compared to liquid and solid CH_4. It is first detectable at −145 °C with wave numbers of 2919 cm^{-1}. In the course of heating the peak position of *V* decreases by about 5 cm^{-1} down to 2914 cm^{-1} before the bubble disappears. CH_4 detected in the solid CO_2 phase (S_1) shows peak positions similar to these observed in *L* and S_2. Therefore it is most likely to be the result of scattering of the surrounding liquid or solid CH_4 rather than a component of S_1. The peak position of CO_2 shows

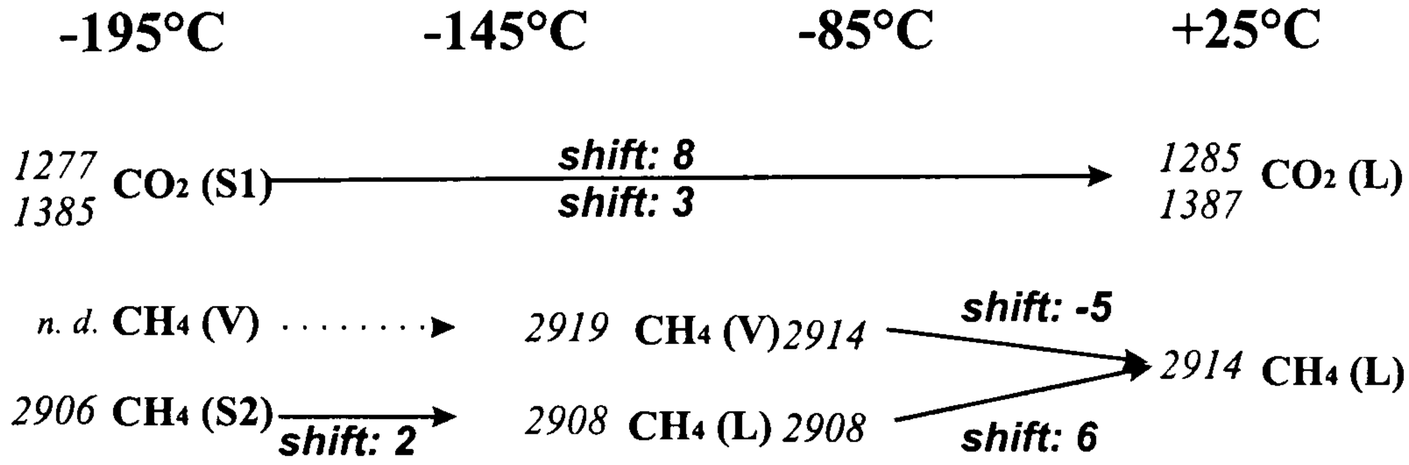

Fig. 7. Illustration of the shift in the Raman peak position with increasing temperature and change in state of aggregation; liquid (*L*), vapour (*V*) and solid (*S*) for a single fluid inclusion. For relevant data, see Table 2.

Table 2
Variation in peak position of CO_2 and CH_4 during heating in liquid (L), vapour (V) and solid (S) for a single fluid inclusion

Temp. in °C	Phases present	$CO_{2_{1275}}$ in S_1	$CO_{2_{1385}}$ in S_1	CH_4 in S_1	$CO_{2_{1275}}$ in L	$CO_{2_{1385}}$ in L	CH_4 in S_2/L	CO_2 in V
−195	S_2+S_1+V	1277	1385	2906	n.d.	n.d.	2906	
−185	S_2+S_1+V	1277	1385	2906	n.d.	n.d.	2906	
−175	$L+S_1+V$	1277	1386	2907	n.d.	n.d.	2907	
−165	$L+S_1+V$	1276	1385	2907	n.d.	n.d.	2908	
−155	$L+S_1+V$	1277	1385	2908	n.d.	n.d.	2908	
−145	$L+S_1+V$	1277	1385	2908	n.d.	n.d.	2908	2919
−135	$L+S_1+V$	1277	1385	2909	n.d.	n.d.	2909	2918
−125	$L+S_1+V$	1277	1385	2909	n.d.	n.d.	2909	2918
−115	$L+S_1+V$	1277	1385	2910	n.d.	n.d.	2909	2917
−105	$L+S_1+V$	1278	1385	2910	n.d.	n.d.	2910	2917
−95	$L+S_1+V$	1278	1385	2911	n.d.	n.d.	2911	2916
−85	$L+S_1+V$	1278	1385	2911	n.d.	n.d.	2911	2914
−75	$L+V$	–	–	–	n.d.	1386	2912	2914
−65	L	–	–	–	1282	1386	2913	–
−55	L	–	–	–	1283	1387	2913	–
−45	L	–	–	–	1284	1386	2913	–
−35	L	–	–	–	1285	1387	2913	–
−25	L	–	–	–	1284	1387	2913	–
−15	L	–	–	–	1285	1387	2913	–
−5	L	–	–	–	1284	1387	2914	–
5	L	–	–	–	1284	1388	2914	–
15	L	–	–	–	1284	1386	2914	–
25	L	–	–	–	1285	1387	2914	–

The data given are exemplarily for one fluid inclusion.

only minor shifts in peak position during heating, provided there is no change in the state of aggregation. The peaks are located relatively constant at about 1277 and 1385 cm^{-1}. With the conversion from S_1 to L an immediate increase (surge) in peak position by 8 and 3 cm^{-1}, respectively occurs.

5.4. Determination of the instrumental efficiency coefficient

In general, the intensity of Raman signals is influenced by several optical and physical parameters. For the accurate interpretation of Raman data, in terms of relative mol proportions of components in fluid inclusions, it is necessary to use a reliable value for the instrumental efficiency coefficient ζ. Here, we have identified a simple and reliable standard material for determining the instrumental efficiency for an individual Raman microprobe. The compositions of fluid inclusions can be determined independently by microthermometry and Raman analysis. When there is disagreement between the two data sets an instrumental efficiency coefficient is needed as described in Van den Kerkhof and Kisch (1993). The following equation enables this to be determined:

$$\zeta = \left(1 - X^*_{CH4}\right)X_{CH4}/(1 - X_{CH4})X^*_{CH4},$$

where X_{CH4} indicates the mol fraction CH_4 based on microthermometric results and X^*_{CH4} represents values obtained by LRM.

5.5. CH_4 as a potential low temperature calibration standard

As is evident from the frequency histogram (Fig. 3), the phase transition $S_2+V+S_1 \rightarrow L+V+S_1$ occurs over an extremely small temperature interval. Repeated heat–cool experiments show a reproducibility of the phase transition within ± 1 °C (30 repetitions per inclusion). The transition from S_2 to L (solid to liquid CH_4) is remarkably clear and easy to observe. A faint meniscus occurs and the sudden release of the vapour bubble, from a constricted shape within the solid to a well-rounded shape in the liquid, is a further indicator of this transition (Fig. 8).

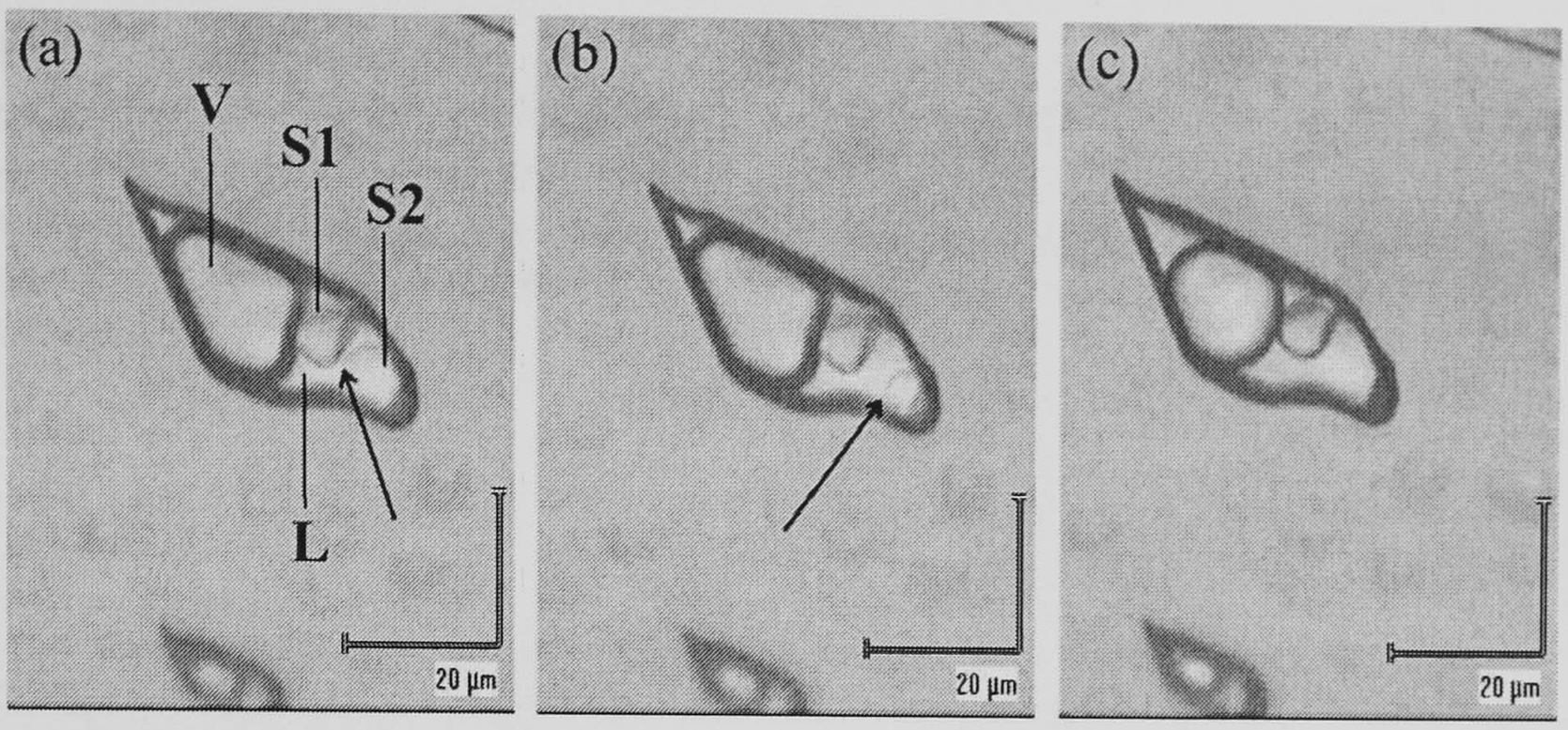

Fig. 8. Observation of the triple point of CH_4 at −182.5 °C on slight heating. (a) Note the small triangular single crystal of solid CO_2 (S_1) and the large deformed vapour bubble (V). A faint "meniscus" (arrowed) separates CH_4 solid (S_2) from CH_4 liquid (L) (b) as above, with continued melting of CH_4 solid (c) final melting of CH_4 solid results in the return of the large CH_4 vapour bubble to its original shape.

Due to the large size of the inclusions the distinct phase transition is readily observable. These samples thus make reliable and suitable calibration standards for low temperature microthermometric analyses.

6. Conclusions

This study focuses on coupled Raman microprobe spectrometry and microthermometry of individual mono-phase fluid inclusions in quartz crystals from the South Wales coalfield, UK. LRM analyses have revealed the presence of CH_4 and CO_2. Microthermometry shows a sequence of phase transitions that characterise the inclusions as H_2-type, according to the classification of Van den Kerkhof (1988), which is typical for CH_4–CO_2 mixed inclusions. During cooling, the following phase transitions were observed: $L/V \rightarrow L+V \rightarrow S_1+L+V \rightarrow S_1+S_2+V$, and during heating: $S_1+S_2+V \rightarrow S_1+L+V \rightarrow L+V \rightarrow L/V$.

In conjunction with peak area calculations, LRM analyses permit calculation of the relative chemical composition of the fluid. The data document an average composition of 86 mol% CH_4 and 14 mol% CO_2 (±2 mol%). Likewise, microthermometric results were used to derive the chemical composition of fluid inclusions and yield similar ratios: 85 mol% CH_4 and 15 mol% CO_2 (±1 mol%) Thus, either method can be used independently to define CH_4 : CO_2 ratios and to confirm the values derived from the other method. Due to their well-defined composition, the fluid inclusions serve as ideal standards for determining the instrumental efficiency coefficient of Raman microprobes. The data also legitimise the use of LRM-based results of fluid composition as opposed to the more conventional microthermometric-based estimates. This is of particular help when small fluid inclusions are being investigated and where phase transitions during heating and freezing are difficult to and observe.

When combined, LRM and microthermometry can be used to analyse separate phases in fluid inclusions and hence, to predict shifts in the Raman peak position when the state of aggregate of the phase changes. Generally, the wave number decreases from $V \rightarrow L \rightarrow S$.

The identification of individual phases provides a means towards a better understanding of the processes taking place during heating-freezing. Here, it is used to document the purification of liquid and vapour CH_4 by extraction of CO_2 entirely into a separate solid phase (S_1). The partitioning causes the formation of a solid pure CH_4 (S_2) at −195 °C. Therefore, the rare observation of the triple point of CH_4 during heating at −182.5 °C is possible. The fact that the phase transition is exceptionally clear and reproducible makes these inclusions ideal as a low temperature calibration standard for heating-freezing studies.

Acknowledgements

We thank Neville Hollingworth (NERC, UK) for providing sample material. BB gratefully acknowl-

edges the financial support provided by Kingston University during the tenure of a Ph.D. studentship. We are also grateful to Larry Diamond and Alfons Van den Kerkhof for their constructive comments in reviewing the manuscript and to Csaba Szabo for his helpful editorial comments.

References

Alderton, D.H.M., Oxtoby, N., Brice, H., Grassineau, N., Bevins, R.E., 2004. The Link Between Fluids and Rank Variation in the South Wales Coalfield: Evidence from Fluid Inclusions and Stable Isotopes, Geofluids, vol. 4. Blackwell Publishing Ltd., pp. 221–236.

Bakker, R.J., Jansen, J.B.H., 1994. A mechanism for preferential H_2O leakage from fluid inclusions in quartz, based on TEM observations. Contrib. Mineral. Petrol. 116, 7–16.

Burke, E.A.J., 2001. Raman microspectometry of fluid inclusions. Lithos 55, 139–158.

Chalmers, J.M., Griffiths, P.R., 2002. Handbook of vibrational spectroscopy. Applications in Industry, Materials and the Physical Science, vol. 4. John Wiley and Sons Ltd., Chichester, pp. 2594–2598.

Chou, I.-M., Pasteris, J.D., Seitz, J.C., 1990. High-density volatiles in the system C–O–H–N for the calibration of an laser Raman microprobe. Geochim. Cosmochim. Acta 54, 535–543.

Dubessy, J., Poty, B., Ramboz, C., 1989. Advances in C–O–H–N–S fluid geochemistry based on micro-Raman spectrometric analysis of fluid inclusions. Eur. J. Mineral. 1, 517–534.

Goldstein, R., Reynolds, T.J., 1994. Systematics of fluid inclusions in diagenetic minerals. SEPM Short Course 31 (199 pp.).

Hall, D.L., Sterner, S.M., 1993. Preferential water loss from synthetic fluid inclusions. Contrib. Mineral. Petrol. 114, 489–500.

Huizenga, J.-M., 2001. Thermodynamic modelling of C–O–H fluids. Lithos 55, 101–114.

Hurai, V., Kihle, J., Kotulová, J., Marko, F., Swierczewska, A., 2002. Origin of methane in quartz crystals from the Tertiary accretionary wedge and fore-arc basin of the western Carpathians. Appl. Geochem. 17, 1259–1271.

Kerrich, R., 1976. Some effects of tectonic recrystallisation on fluid inclusions in vein quartz. Contrib. Mineral. Petrol. 59, 195–202.

Kisch, H.H., Van den Kerkhof, A.M., 1991. CH_4-rich inclusions from quartz veins in the Valley-and-Ridge province and the anthracite fields of the Pennsylvania Appalachians. Am. Mineral. 76, 230–240.

Kleinrahm, R., Wagner, W., 1986. Measurement and correlation of the equilibrium liquid and vapour densities and the vapour pressure along the coexistence curve of methane. J. Chem. Thermodyn. 18, 739–760.

Mullis, J., 1987. Fluid inclusion studies in very low grade metamorphism. In: Frey, M. (Ed.), Low Temperature Metamorphism. Blackie, Glasgow, pp. 162–199.

Pasteris, J.D., Wopenka, B., Seitz, J.C., 1988. Practical aspects of quantitative laser Raman microprobe spectroscopy for the study of fluid inclusions. Geochim. Cosmochim. Acta 52, 979–988.

Placzek, G., 1934. Die Rayleigh und Raman Streuung. In: Marx, E. (Ed.), Handbuch der Radiologie. Akademische Verlagsgesellschaft, pp. 209–219.

Roedder, E., 1984. Fluid Inclusions. Reviews in Mineralogy, vol. 12. Mineralogical Society of America.

Rosso, K.M., Bodnar, R.J., 1995. Microthermometric and Raman spectroscopic detection limits of CO_2 in fluid inclusions and the spectroscopic characterization of CO_2. Geochim. Cosmochim. Acta 59 (19), 3961–3975.

Seitz, J.C., Pasteris, J.D., Wopenka, B., 1987. Characterization of CO_2–CH_4–H_2O fluid inclusions by microthermometry and laser Raman microprobe spectroscopy: inferences for clathrate and fluid equilibria. Geochim. Cosmochim. Acta 51, 1651–1664.

Seitz, J.C., Pasteris, J.D., Chou, I.-M., 1996. Raman spectroscopic characterization of gas mixtures: II. Quantitative composition and pressure determination of the CO_2–CH_4 system. Am. J. Sci. 296, 577–600.

Shepherd, T.J., Rankin, A.H., Alderton, D.H.M., 1985. A Practical Guide to Fluid Inclusion Studies. Blackie, London.

Thiery, R., Van den Kerkhof, A.M., Dubessy, J., 1994. VX properties of CH_4–CO_2 and CO_2–N_2 fluid inclusions modelling for $T<31$ °C and $P<400$ bar. Eur. J. Mineral. 6, 753–771.

Thomas, A.V., Pasteris, J.D., Bray, C.J., Spooner, E.T.C., 1990. H_2O–CH_4–NaCl–CO_2 inclusions from the footwall contact of the Tanco granitic pegmatite: estimates of internal pressure and composition from microthermometry, laser Raman spectroscopy, and gas chromatography. Geochim. Cosmochim. Acta 54, 559–573.

Van den Kerkhof, A.M., 1988. The system CO_2–CH_4–N_2 in fluid inclusions: theoretical modelling and geological applications. Ph.D. Thesis, Vrije Universiteit Amsterdam, The Netherlands.

Van den Kerkhof, A.M., Kisch, H.J., 1993. CH_4-rich inclusions from quartz veins in the Valley-and-Ridge province and the anthracite fields of the Pennsylvania Appalachians — reply. Am. Mineral. 8, 220–224.

3 An introduction to existing hypotheses of hydrocarbon origin in igneous rocks

Despite much study, the origin of hydrocarbon gases in igneous rocks is still unclear.

A simple flow chart (Fig. 3.1) illustrates how the principal hypotheses for hydrocarbon origin in igneous rocks can be divided into biogenic and abiogenic models.

Due to the geological settings of igneous rocks it is clear that biogenic hydrocarbons can be incorporated into them from the surrounding organic-rich host rocks. This incorporation can be due to either interaction between magma and basement fluids during emplacement or movement of meteoric or basement fluids through fault systems in the cooled pluton.

A number of workers have discussed the likelihood of hydrocarbon origin through abiogenic processes. There are three main models for abiogenic hydrocarbon generation in igneous rocks: a direct mantle origin; the respeciation of a C-O-H- magmatic fluid and generation at low temperature and pressure conditions by fluid-rock interaction.

In theory, it should be possible to distinguish biogenic from abiogenic hydrocarbon on the basis of the isotopic and compositional characteristics of the fluid and the geological environment in which it occurs. However, as differences in chemical and isotopic signatures are often small, few studies have been able to define unambiguously the mechanism of hydrocarbon generation. As it is possible that both abiogenic and biogenic hydrocarbons may exist in the same pluton, there is ample scope for confusion. A number of different hypotheses for hydrocarbon origin are discussed in the following pages together with some important case studies.

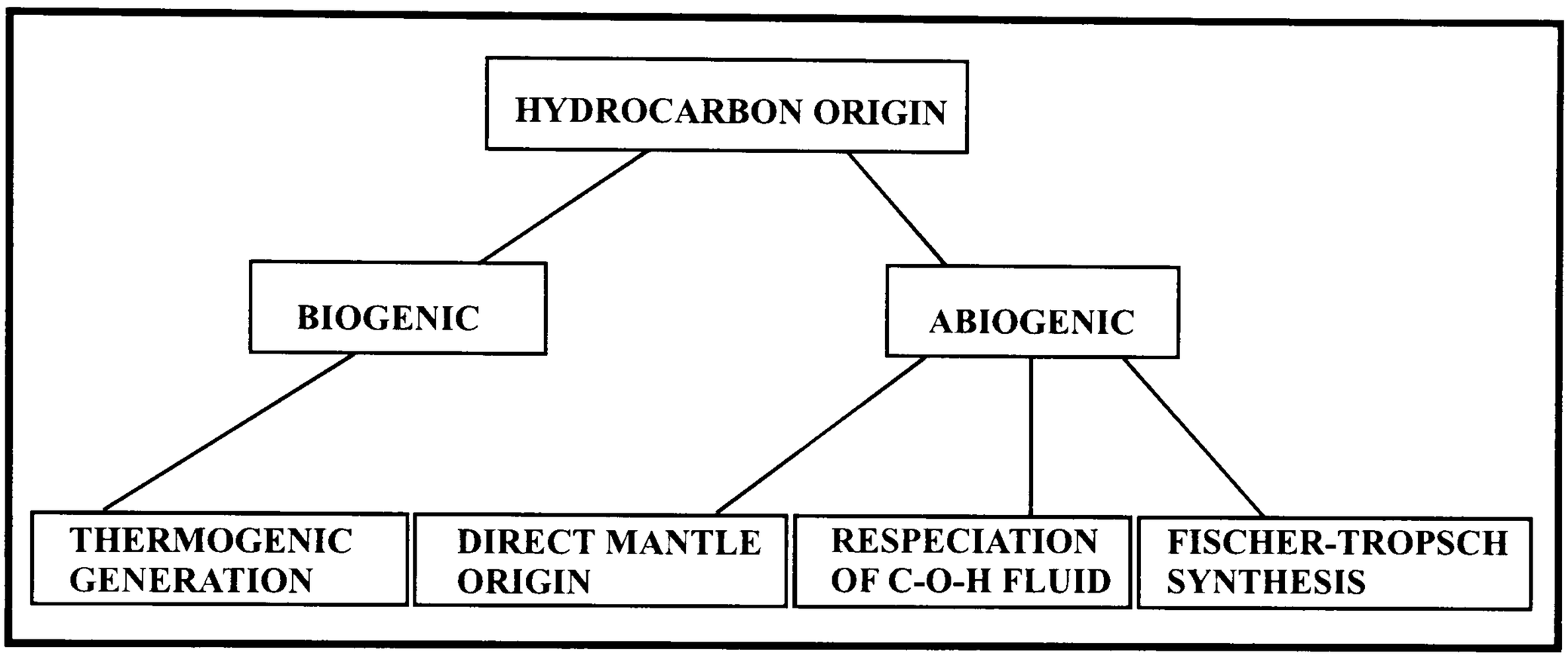

Figure 3.1: Schematic illustration of possible hydrocarbon origins in igneous rocks.

3.1 Abiogenic origin

The existence of hydrocarbons of abiogenic origin has received considerable attention since the Russian geologist Kudryavtsev (1951) first enunciated the theory of deep, abiotic petroleum origins. The most prominent western supporter of abiogenic methane production is Thomas Gold. He proposed the "mantle methane hypothesis" and rejected the largely biogenic origin of oil and gas from the decomposed remains of buried animal and plant material, a theory favoured by most geochemists (Gold, 1979). In general, the existence of abiogenic methane and short-chained hydrocarbons is widely accepted to occur in a variety of metamorphic and igneous settings. They have been shown to be present along the world's mid-ocean ridges (e.g. Welhan and Craig, 1983; Charlou *et al.*, 1998; Frueh-Green, 2004), in the Canadian and Fennoscandian Shield (Sherwood-Lollar *et al.*, 1993a), and in alkaline intrusions (e.g. Konnerup-Madsen *et al.*, 1985; Ikorski, 1991; Salvi and Williams-Jones, 1997; Markl, 2001; Potter and Konnerup-Madsen, 2003). Different hypothesis have been proposed for their generation and origin. The three most important theories with regard to alkaline igneous rocks are mantle origin, C-O-H-respeciation and low P-T-fluid rock interaction.

3.1.1 Mantle origin

The potential for abiogenic hydrocarbon reservoir outgassing from the primeval mantle was argued by Gold (1979). He suggested that a large homogenous mantle source explains the very uniform $\delta^{13}C$ signature (-25 ‰ to –28 ‰) found within igneous rocks. Similar observations were made by Sugisaki and Mimura (1994). They assumed three possible origins for mantle hydrocarbons: (a) inorganic synthesis by Fischer-Tropsch-type reactions in the mantle (b) delivery by meteorites to the early earth or (c) recycling

through subduction. Magma, intrusive into the crust, might be a carrier of hydrocarbons which are consequently stored in igneous rock bodies after cooling.

To prove his theory of mantle methane, Gold convinced the Swedish Government to study the region of a giant meteoritic impact crater, the 360 Ma old "Siljan Ring" in Central Sweden (Fig. 3.2). The impact left a circular structure, about 45 km in diameter, and is assumed to have fractured the rock to great depths. It was considered therefore to be a favourable location for finding upwelling mantle hydrocarbons. However, the project yielded only 80 barrels of oil with doubtful provenance (Glasby, 2006). Within the Gravberg 1 well, dolerite sills were found to intrude the granitic host rock (Laier, 1988). Within the granite, gases are poor in methane whereas gases in the dolerite are abundant and rich in methane (200-1000 ppm) (Castano, 1988). The gases are compositionally and isotopically similar to hydrocarbons of abiogenic origin (Jeffrey and Kaplan, 1988) and could therefore be of magmatic origin or result from migration from a deep source. However, a low-temperature Fischer-Tropsch reaction has also been suggested as a possible generation mechanism (Jeffrey and Kaplan, 1988). Smith (1996) studied methane-bearing fluid inclusions which are particularly abundant in the mafic sills. However, he also found them in almost all granite samples below 1500 m depth. The upper boundary of the methane-bearing inclusions is a dolerite sill, which suggests that it may have acted as a seal to fluid migration. Samples below about 4200 m depth were found to be particularly rich in methane. This suggests considerable mobility for the methane-rich gas phase.

Other evidence, experimental and observable, also suggests a possible mantle origin for hydrocarbons in igneous rock. Scott *et al.* (2004) showed that methane may form inorganically at mantle conditions of >30 kbar and >1200°K from carbonate species, such as $FeCO_3$ or $MgCO_3$, in the presence of H_2O at oxygen fugacities buffered by iron-

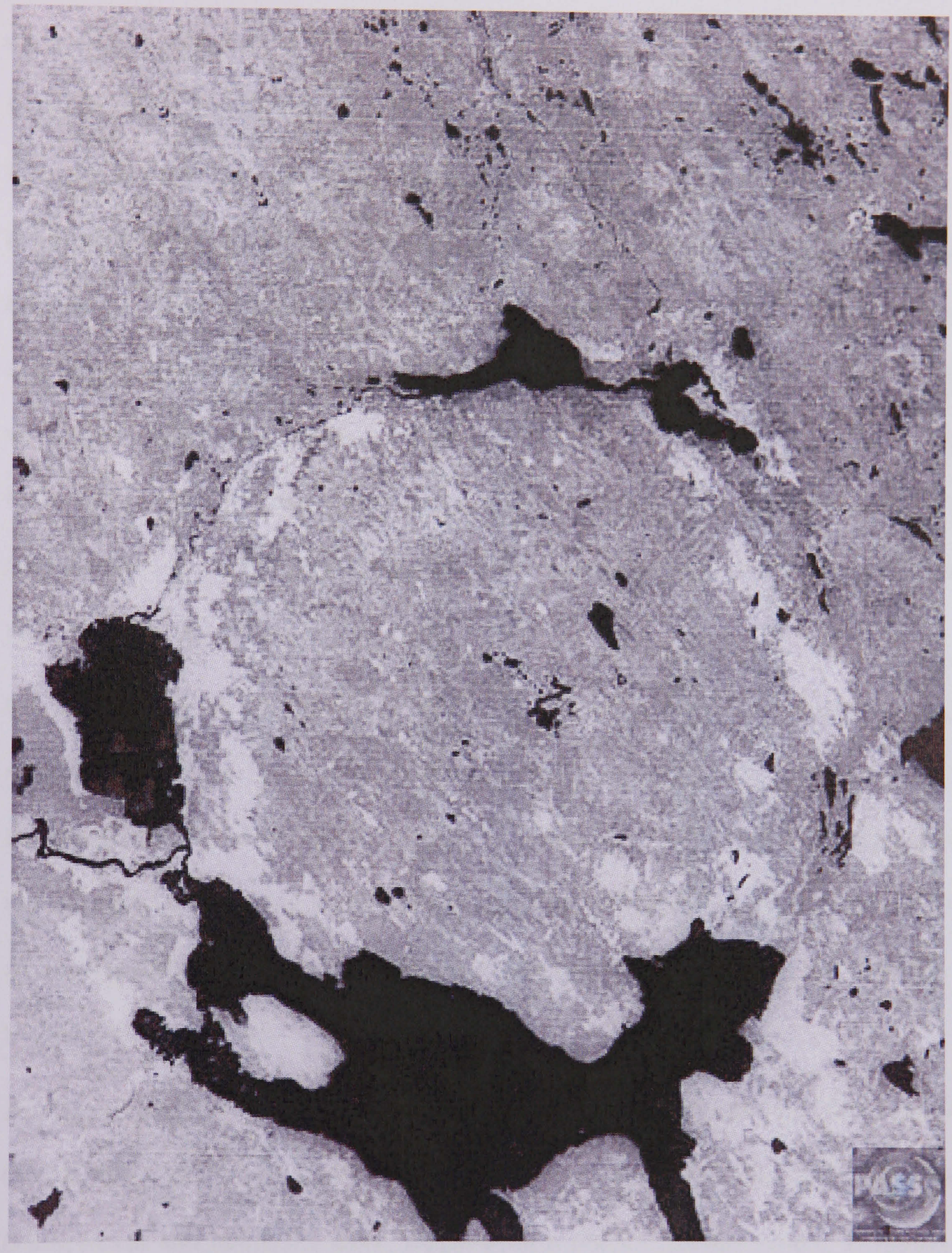

Figure 3.2: Satellite image of the Siljan crater in Central Sweden (http://www.astrosurf.com/lombry/Documents/impact-siljan.jpg).

bearing phases near the wustite-magnetite f_{O2} buffer. Experimental data suggest that such conditions may be widespread in the mantle and that methane at pressures of up to 1 GPa could be the dominant C-bearing fluid phase under reducing conditions in the mantle (Kenney *et al.*, 2002). Ryabchikov *et al.* (1981) documented very low oxygen fugacities for rocks of mantle origin: olivines from tholeiite basalts and titanium garnets from alkali rocks. Strongly reduced conditions, compared with the crust (QFM), are also believed by Pasteris (1987) to exist in portions of the upper mantle and several studies by, amongst others, Ryabchikov *et al.* (1981), Eggler and Baker (1982) and Olafsson and Eggler (1983) imply that fO_2 variations in the mantle would permit different fluid speciation in different regions or materials in the upper mantle. Hydrocarbons traced back to their mantle source have also been found in garnets from the Mir kimberlite pipe (Krot *et al.*, 1994). These data all suggest methane to be a primary gas phase in upper mantle rocks.

On the basis of $\delta^{13}C$ values of -3.2 ‰ to -12.8 ‰, Petersilie (1962) suggested a magmatic origin for hydrocarbons in the alkaline rocks of the Khibiny pluton. He interpreted the ^{13}C data, similar to that in diamonds, carbonatites and CO_2 of deep-seated origin, as implying a juvenile carbon source (Petersilie and Sørensen, 1970). As an incompatible compound, primary mantle CH_4 could easily be incorporated into mantle derived magmas.

Another example of probably mantle hydrocarbons was reported by Abrajano *et al.* (1988). They found isotopically anomalous methane-rich gas in the Zambales Ophiolite (Philippines) and inferred a direct origin from a reduced mantle source. However, the authors considered a hydrocarbon generation during low-temperature reduction of water and CO_2 during serpentinisation of the ophiolite to be an equally valid model.

Markl *et al.* (2001) presented new phase compositional data for the Ilímaussaq complex in order to evaluate the importance of various physico-chemical parameters during the

formation of agpaitic melts. They showed that the earliest augite syenite melt at Ilímaussaq was reduced (QFM –2) and contained methane as a stable fluid phase. This explains the presence of methane-dominated fluid inclusions in early augite syenites and later agpaitic rocks in the Ilímaussaq complex. Water-dominated fluid inclusions were found in the oxidised mineralogy that developed at late stages of magma evolution (Markl, 2005). In fact, the reduced redox-conditions are, according to Markl (2005), one of the fundamental requirements for the development of the special mineralogy of agpaitic rocks. Based on mineralogical observation, he also questions the hitherto established model of late magmatic fluid respeciation in the Ilímaussaq complex (Konnerup-Madsen *et al.*, 1979).

3.1.2 The respeciation of C-O-H fluids

The preferred explanation for the presence of abiogenic hydrocarbons in many metamorphic and igneous rocks is that they were derived from a C-O-H-fluid which exsolved from the magma and evolved by cooling along a relatively reduced QFM rock buffered redox path (Gerlach, 1980, Konnerup- Madsen *et al.*, 1985; Kogarko *et al.*, 1987; Cesare, 1995; Nivin *et al.*, 1995; Andersen and Burke, 1996).

Magmatic fluids are generally described by the three components carbon, oxygen and hydrogen and the resulting fluid species in this system are H_2O, CO_2, CH_4, CO, H_2 and O_2 (Huizenga, 2001). In the presence of graphite, four independent chemical equilibria describe the relationship of the main volatile species:

$$CO + ½O_2 \leftrightarrow CO_2 \qquad \text{(R3.1)}$$

$$H_2 + ½O_2 \leftrightarrow H_2O \qquad \text{(R 3.2)}$$

$$CH_4 + 2O_2 \leftrightarrow CO_2 + 2H_2O \qquad \text{(R 3.3)}$$

$$C + O_2 \leftrightarrow CO_2 \qquad \text{(R 3.4)}$$

The C-O-H system can be illustrated by a ternary isothermal and isobaric phase diagram (Fig. 3.3). The diagram can be subdivided into a two-phase field, where graphite and a C-O-H fluid coexist, and a single-phase field, where only a carbon undersaturated fluid occurs. Pressure, temperature, oxygen fugacity and graphite activity strongly influence the speciation of the fluid and changes cause changes in fluid composition. Figure 3.4 shows schematically the C-O-H phase relationship at 600°C and 2 kbar and the development of the fluid composition with subsequently decreasing fO_2 condition. Depending on the initial composition, the fluid re-equilibrates with or without associated graphite precipitation and forms a CH_4-rich fluid (Konnerup-Madsen, 2001). A fluid of composition "a" changes its initial composition above the graphite saturation curve, with associated graphite precipitation, and develops to an essentially H_2O-CH_4 fluid. The more H_2O-rich fluid "b" evolves away from the oxygen apex only, until reaching point "b'" without graphite precipitation. Here, the final fluid consists of H_2-H_2O-CH_4.

This model was applied to the peralkaline Ilímaussaq complex by Konnerup-Madsen (2001). He assumed the respeciation of an initial CO_2-H_2O-rich fluid below 500°C during the final solidification stage in the agpaitic melt. The low oxygen fugacity of QFM -2 indicated that fluid buffering caused the change in bulk fluid composition from an initial CO_2-H_2O-rich fluid to CH_4-rich composition. The final oxygen fugacity was reached, according to the reaction:

$$CO_2 + 2H_2O \rightarrow CH_4 + 2O_2. \qquad \text{(R 3.5)}$$

Chlorides were very abundant in the Ilímaussaq magma (Larsen and Sørensen, 1987) and the high salinity of the exsolved fluid probably enhanced fluid immiscibility. The initial fluid is therefore thought to have developed not only a CH_4-rich phase but also aqueous brine. The compositional changes of the hydrocarbon and aqueous fluid during buffering are shown in Figure 3.5.

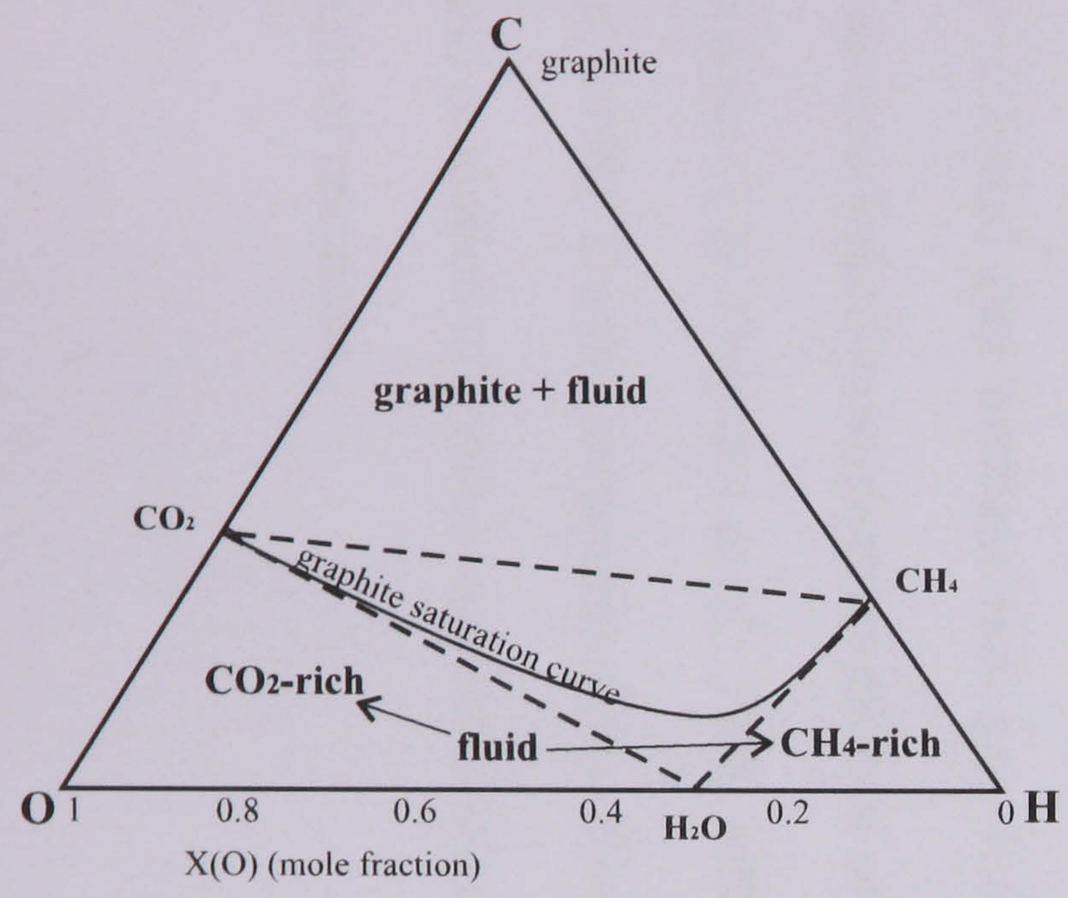

Figure 3.3: An isobaric and isothermal ternary C-O-H plot at 2 kbar and 600°C illustrating the different phases and compositions possible. The grey shaded area marks the range where only fluid occurs. Above the graphite saturation curve an additional solid phase appears in the form of graphite.

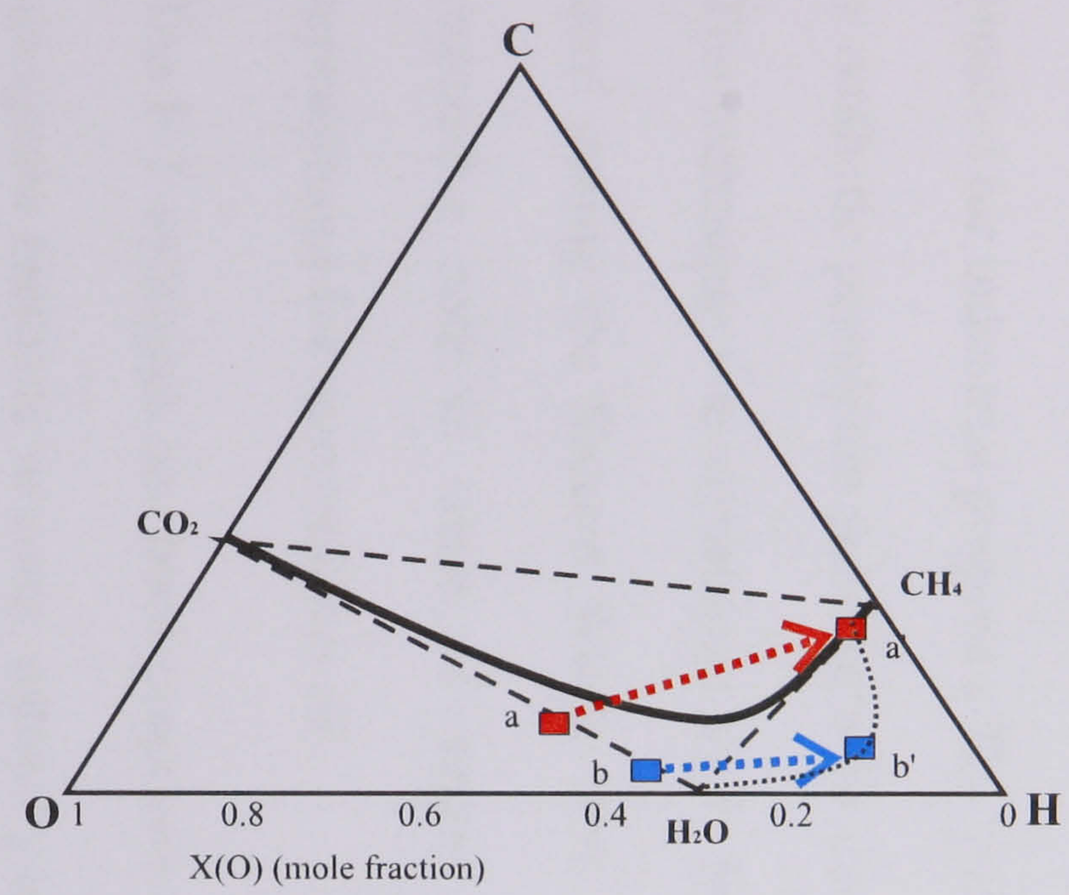

Figure 3.4: An isobaric and isothermal ternary C-O-H diagrams at 2 kbar and 600°C shows schematically the development of C-O-H fluids with decreasing oxygen fugacity, from QFM to QFM-2 (modified from Konnerup-Madsen, 2001).
An initial fluid "a" changes its composition from CO_2-rich to CH_4-rich with crossing the graphite saturation curve. On crossing the bold line, graphite precipitates. If the initial fluid composition is "b", a CH_4 rich fluid develops without graphite precipitation. The final compositions are marked with "a'" and "b'", respectively.

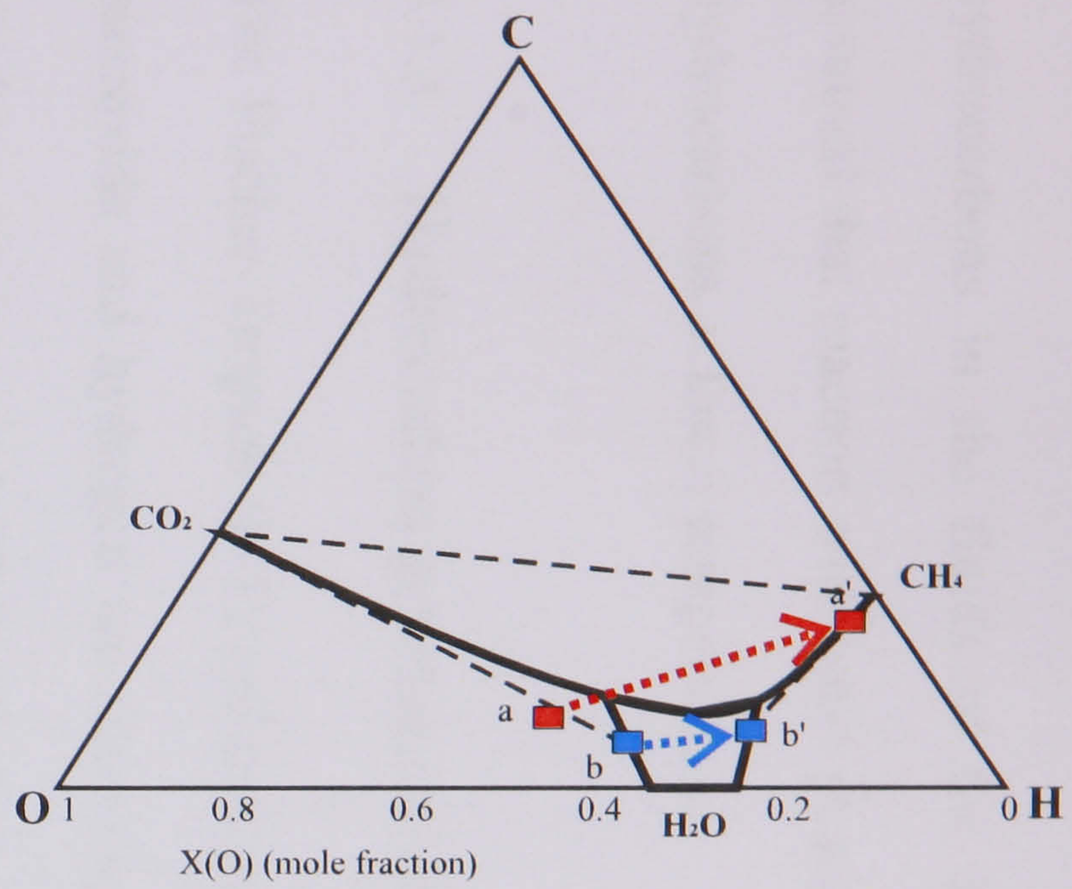

Figure 3.5: The schematic fluid evolution of an immiscible fluid (modified from Konnerup-Madsen, 2001). The initially exsolved bulk fluid "a" develops towards "a'" with subsequent graphite precipitation. The aqueous fluid has an initial composition of "b" and follows the path towards "b'".

The respeciation-model, however, does not explain the occurrence of higher hydrocarbons in the fluids of the Ilímaussaq complex. Konnerup-Madsen (2001) assumed that reaction with solid phases catalysed the formation of some of the higher hydrocarbons at lower temperatures.

3.1.3 Hydrocarbon generation via a Fischer-Tropsch-type reaction

The Fischer-Tropsch (F-T) reaction is a catalyzed chemical reaction in which carbon monoxide and hydrogen are converted into hydrocarbons of various forms. Typical catalysts are iron and cobalt (Anderson, 1984). This process has long been known and studied for industrial purposes. The principal function of the process is the production of a synthetic petroleum substitute for use as synthetic lubrication oil or as fuel (Fig. 3.6). The technique was developed by F. Fischer and H. Tropsch in the 1920s, and mainly used during the Second World War. However, the fuel obtained by this process is expensive both in terms of money and energy and therefore is not a practical replacement for conventional oil.

The F-T synthesis has been proposed to be a driving mechanism for the generation of abiogenic methane in some natural geological environments. For instance, it is largely established that methane-rich gas, found in the oceanic crust, is the product of F-T reaction linked to serpentinisation of olivine in peridotites and dunites at the Mid Ocean Ridges (e.g. Abrajano *et al.*, 1988, 1990; Berndt *et al.*, 1996; Kelley, 1996; Charlou *et al*, 1998). During serpentinisation, H_2-rich fluids are produced due to H_2O dissociation and oxidation of ferrous ions (Sherwood-Lollar *et al.*, 1993a) according to the following pair of reactions.

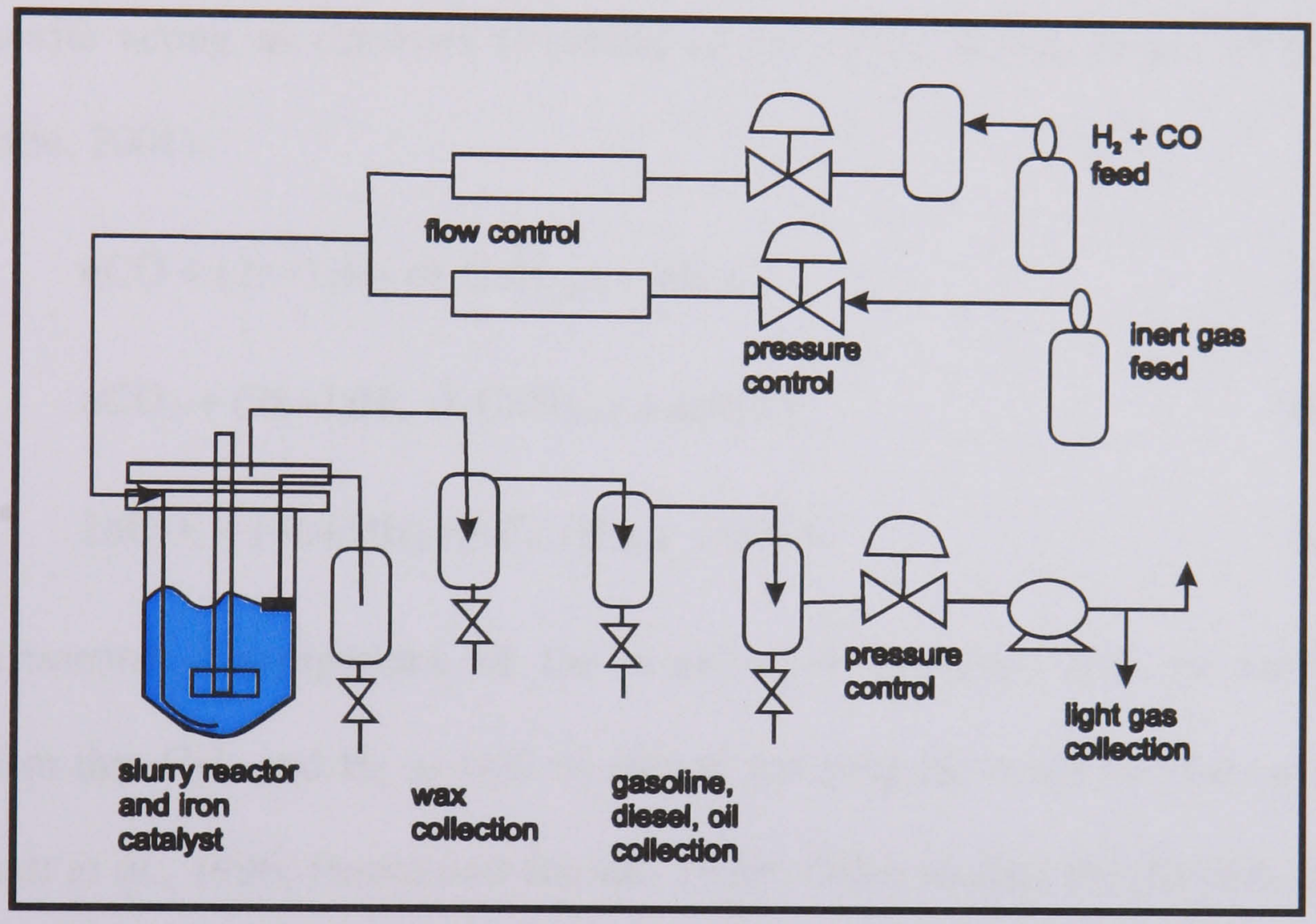

Figure 3.6: Schematic illustration of a Fischer Tropsch unit (modified after Mike Zarochak (http://www.netl.doe.gov/onsite_research/Facilities/1L.html)

$$5Mg_2SiO_4+Fe_2SiO_4+9H_2O \rightarrow 3\ Mg_3Si_2O_5(OH)_4+Mg(OH)_2+ 2Fe(OH)_2$$

Forsterite fayalite → serpentine brucite

$$3Fe(OH)_2 \rightarrow Fe_2O_4 + H_2 + 2H_2O$$

Magnetite (R 3.6)

The H_2 produced is then consumed in the formation of methane and higher hydrocarbons through disequilibrium reactions with CO or CO_2 with FeNi alloys and magnetite acting as catalysts (Yoshida *et al.*, 1993; Berndt *et al.*, 1996; Holm and Charlou, 2001):

$$nCO + (2n+1)H_2 \rightarrow CnH_{2n+2} + nH_2O \quad \text{(R 3.7)}$$

$$nCO_2 + (3n+1)H_2 \rightarrow CnH_{2n+2} + 2nH_2O \quad \text{(R 3.8)}$$

$$2nCO_2 + (3n+4)H_2 \rightarrow C_{n+1}H_{2n+4} + 4nH_2O \quad \text{(R 3.9)}$$

Experimental investigations of the reaction of seawater with ultramafic minerals confirm that CH_4 and H_2 as well as ethane and propane occur as reaction by-products (Berndt *et al.*, 1996; Horita and Berndt, 1999). Other studies (McCollom and Seewald, 2001), however, show that CH_4 and higher hydrocarbons may also be derived from a reduced carbon source present in the minerals themselves rather than from reduction of CO_2 in the fluid. Therefore, although an inferred link between serpentinisation and CH_4 generation via F-T reaction is shown by several studies, a mantle origin of methane or generation during respeciation of a magmatic C-O-H fluid cannot always be excluded (e.g. Abrajano *et al.*, 1988; Früh-Green *et al.*, 2004) as an alternative methane source in these environments.

Salvi and Williams-Jones (1997) were able to determine the concentrations of alkanes up to C_6 for inclusions in the peralkaline Strange Lake granite (Canada) and concluded that those for C_2 to C_6 alkanes are far too high to be explained by a simple respeciation

model. They point out that the proportions of the alkanes relative to methane are remarkably similar to those resulting from F-T synthesis and suggest a natural F-T synthesis occurring as a result of the reaction of orthomagmatic CO or CO_2 with H_2 generated during alteration of arfvedsonite to aegirine (Salvi and Williams-Jones, 2006):

$$3\ Na_3Fe_5Si_8O_{22}(OH)_2 + 2\ H_2O \rightarrow\ 9\ NaFeSi_2O_6 + 2\ Fe_3O_4 + 6\ SiO_2 + 2\ H_2.$$

arfvedsonite aegirine magnetite quartz (R 3.10)

Magnetite, which is a product of the alteration, is inferred to be the catalyst. This model of associated mineral alteration and hydrocarbon generation via F-T reaction has been extended to the Khibiny and Lovozero alkaline complexes of the Kola Peninsula by Potter *et al.* (1998, 1999, 2004).

Sherwood-Lollar *et al.* (1993a) investigated hydrocarbon gases at several locations in the Fennoscandian and Canadian Shields. Based on carbon, hydrogen and helium isotopic data, they proposed an abiogenic, non-mantle origin for most of the gases found. Since graphite is a common mineral phase in both Shields it is assumed to be the most reasonable carbon source for methane production. At a number of sites the gas could be interpreted as the product of regional-scale mixing between bacterial gas and abiogenic endmembers, but the authors favour a scenario whereby the isotopic distinction of the CH_4 gases in the Shields are due to variable isotopic compositions of the available carbon sources. They conclude that the F-T reaction at low temperatures, in conjunction with hydration of ultramafic rocks and serpentinisation reactions, are the key processes for inorganic CH_4 production. It is worth noting, that Sherwood-Lollar *et al.* (1993b) conclude that the gas in half of the investigated samples from the Canadian and Fennoscandian Shield rocks is of bacterial origin.

The F-T reaction has also been suggested to explain the presence of abiogenic hydrocarbons in extraterrestrial bodies (Lancet and Anders, 1970; Zolotov and Shock, 1999) and has even been proposed as the mechanism by which life originated (e.g. McCollom *et al.*, 1999).

3.2 Biogenic origin of hydrocarbons in igneous rocks

From a petroleum exploration standpoint, the quantity of hydrocarbons formed by the inorganic processes discussed above is negligible. Economically valuable hydrocarbon accumulations are largely formed from organic matter. This material, consisting of dead plants and animals, is deposited over time, and further sediment accumulations bury and compress it (Hunt, 1995). At temperatures of up to 50°C diagenesis starts with the biological, chemical and physical alteration of the organic matter and the formation of kerogen. Deeper burial, along with increasing temperature and pressure, leads to the thermal decomposition of kerogen to form bitumen, oil and methane gas. This process is called catagenesis and occurs between 50°C and 200°C. In the metagenesis zone, at temperatures of 200°C to 250°C, methane formation continues and the remaining organic matter converts to graphite. The end of this phase coincides approximately with the beginning of metamorphism.

Natural gas, the gaseous hydrocarbon phase of petroleum, is more widely distributed than oil because it migrates more easily and is generated from source rocks which are more widely distributed than those for oil (Hunt, 1995). The origin of hydrocarbon gases can be either bacterial (methanogenic bacteria) or thermogenic (from coal, kerogen and oil). Bacterial methane is formed by microbial fermentation or CO_2 reduction, whereby the latter is the dominant process. Although Sherwood-Lollar *et al.* (1993b) found evidence for active bacterial communities in deep hydrogeological environments in the Canadian and Fennoscandian Shields, it is largely confirmed that

bacterial methane generation usually ceases at temperatures above 70°C as bacterial populations decrease and nutrients for metabolism become less available (Hunt, 1995). At higher temperatures only thermogenic methane may form. With increasing temperature the amount of condensable liquid in the gas decreases and the gas develops from so-called wet-thermogenic (methane and larger amounts of higher hydrocarbons) to dry-thermogenic (methane-dominant) species. Igneous activity may cause maturation of organic matter to form dry thermogenic gas. As the country rocks to a pluton become subjected to high-temperature alteration (Schutter, 2003 and references therein) the formation of dry thermogenic gas and pyrobitumen from oil or kerogen can occur.

Biogenic hydrocarbons cannot originate directly from igneous rocks, but can migrate from the source rocks into igneous rocks along fractures, faults and joints. This process is mainly temperature and pressure driven. Migration in solution or by diffusion can be important for the transport of large volumes of gas (Hunt, 1995). Late magmatic or hydrothermal fluids may therefore cause a leaching of hydrocarbons from the source rocks (Welhan and Lupton, 1987) and deposition in the igneous rock body.

Alternatively, organic-rich material may also become assimilated and recycled into the magmatic system during its passage through sedimentary source rocks (Des Marais *et al.*, 1981; Darling, 1998). A combination of both mechanisms can be envisaged.

The extent of hydrocarbon accumulation in igneous rocks largely depends on the porosity of the rocks. In fact, some volcanic igneous rocks contain economically valuable amounts of petroleum (e.g. Chen *et al.*, 1999; Luo *et al*, 1999). Plutonic rocks, however, are not considered as appropriate reservoir rocks.

3.3 The discrimination of hydrocarbon sources or generation mechanisms

The discrimination of abiogenic versus biogenic sources of CH_4 in the terrestrial subsurface is still controversial (Gold, 1979, Kenney *et al.*, 2002, Sherwood-Lollar *et al.*, 2006).

Carbon isotope ratios of methane have been the most common method used to classify natural gases (e.g. Galimov, 1973; Whiticar, 1996). In conjunction with hydrogen isotope ratios of methane (Fig. 3.7) these data can characterise different sources (Schoell, 1988; Whiticar, 1999). The higher hydrocarbons provide additional information that can be used to detect multiple sources, mixtures or alteration effects. A carbon isotopic trend where isotopic ^{13}C ratios become increasingly depleted with increasing molecular weight for methane-ethane-propane-butane is indicative of an abiogenic gas source. In contrast, an isotopic enrichment with decreasing molecular weight indicates a biogenic gas origin (Fig. 3.8). However, the "carbon isotopic reversal trend" alone is not sufficient to support an abiogenic origin (Horita and Berndt, 1999).

An inverse correlation between ^{13}C depletion and ^{2}H enrichment between CH_4 and ethane has found to be indicative of crustal abiogenic origin through water-rock interactions (Fig. 3.9; Sherwood-Lollar *et al.*, 1993b, 2002, 2006; Lippmann *et al.*, 2003). Based on a hypothesis of Des Marais *et al.* (1981), this pattern is thought to be caused by the synthesis of higher hydrocarbons from CH_4 during polymerisation. Here, $^{12}CH_4$ reacts faster than $^{13}CH_4$ to form chains so that ^{12}C is likely to be incorporated in larger chains, whereas ^{1}H will be preferentially eliminated during polymerisation due to the weaker ^{12}C-^{1}H bond in contrast to ^{12}C-^{2}H bond (Sherwood-Lollar *et al.*, 2002). In contrast, the isotopic pattern of biogenic gas produced by thermal cracking of high

molecular weight organic precursors is marked by increasing ^{13}C and ^{2}H isotopes with increasing molecular weight from C_1 to C_4 chains (Schoell, 1988).

A criterion used to confirm that gases are the product of abiogenic formation by Fischer-Tropsch reaction (e.g. Potter and Konnerup-Madsen, 2003) is the Anderson-Schulz-Flory (ASF) distribution. In the ASF model, the formation of hydrocarbon chains is assumed as a stepwise polymerisation procedure, and the chain growth probability to be independent of carbon number. The methodology is a thermodynamic approach where a constant probability of chain growth follows an exponential function (Vessia, 2005; Fig. 3.10). However, significant deviations from the ideal ASF distribution have been observed in many studies (Jun, 2004). This is due to the dependency of chain growth probability from pressure, temperature, initial gas composition and catalyst type (Pichler *et al.*, 1967; Vessia, 2005).

Mantle derived abiogenic fluids are typically identified based on a $\delta^{13}C$ value for CH_4 more enriched than -25 ‰. A further common test used to measure the contribution of fluids of mantle origin employs the isotopic ratio of helium nuclei, $^{3}He/^{4}He$, where a ratio indicative of mantle derived helium is $R/Ra > 0.1$ (Jenden *et al.*, 1993).

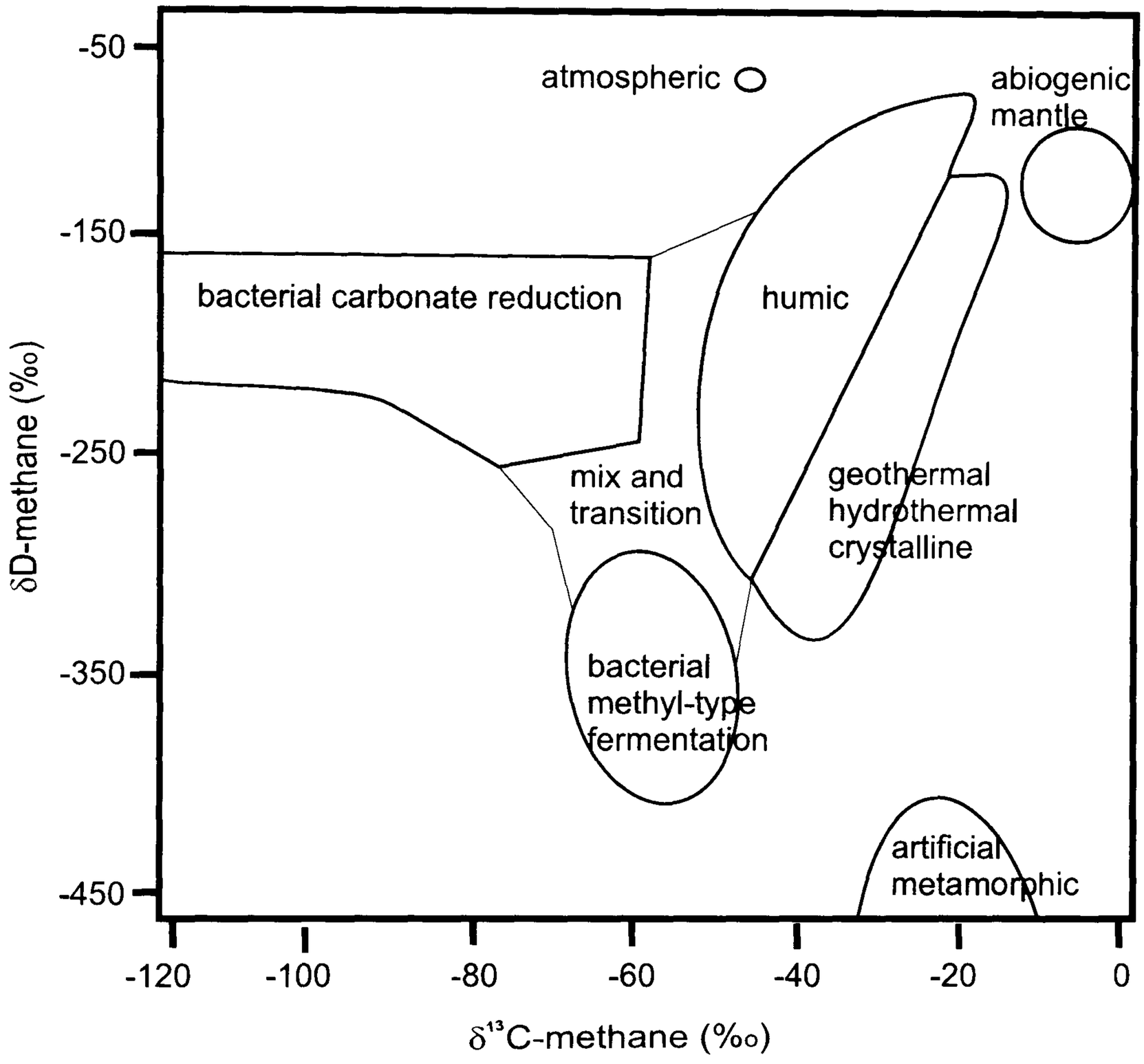

Figure 3.7. Simplified diagram showing the combination of carbon and hydrogen isotope ratios of methane, relative to PDB and VSMOW respectively, to characterise various sources (after Whiticar, 1996).

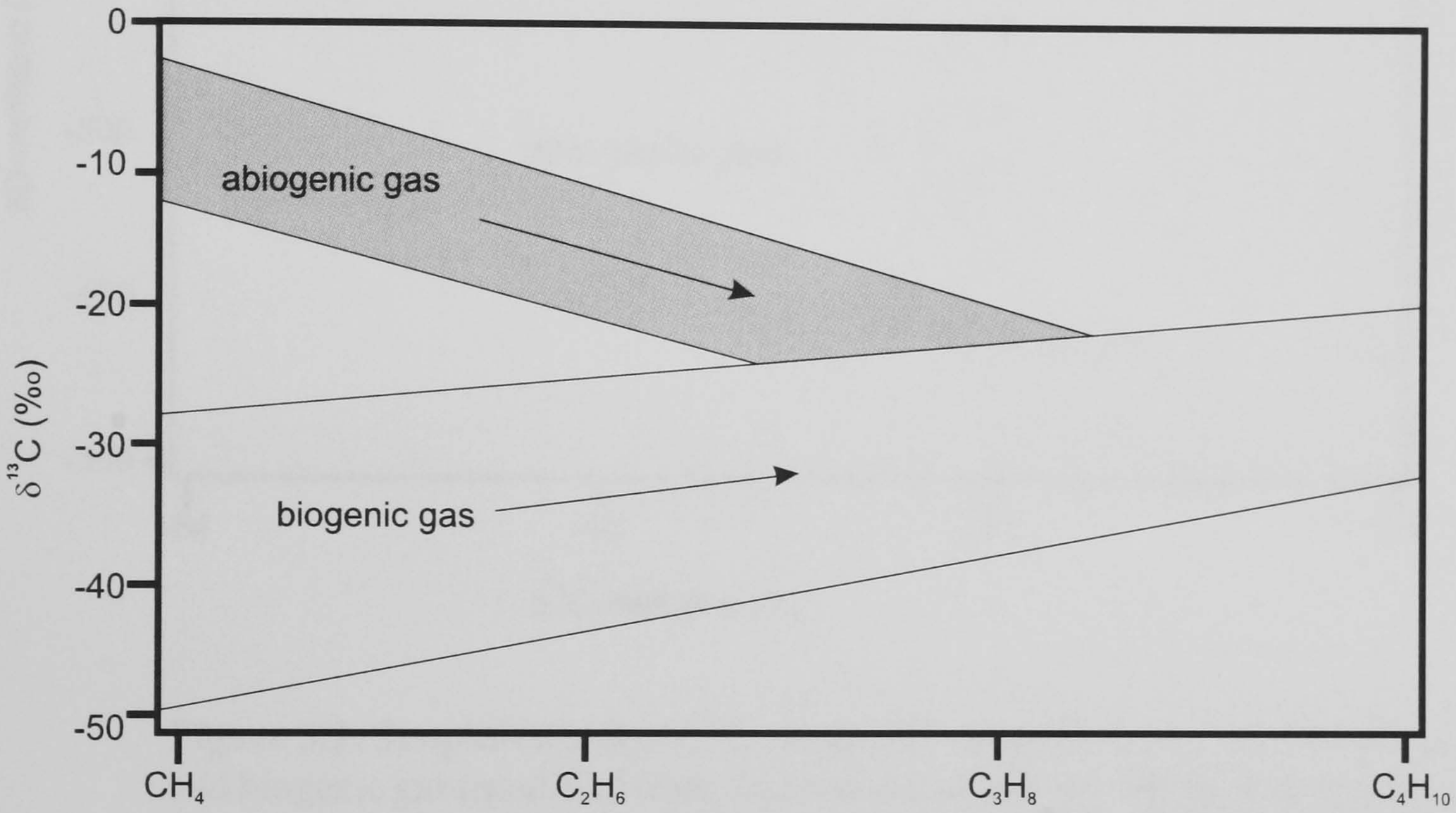

Figure 3.8: A simplified plot showing the distribution of $\delta^{13}C$ values with increasing carbon number for abiogenic and biogenic gases (modified from Potter and Konnerup-Madsen, 2003).

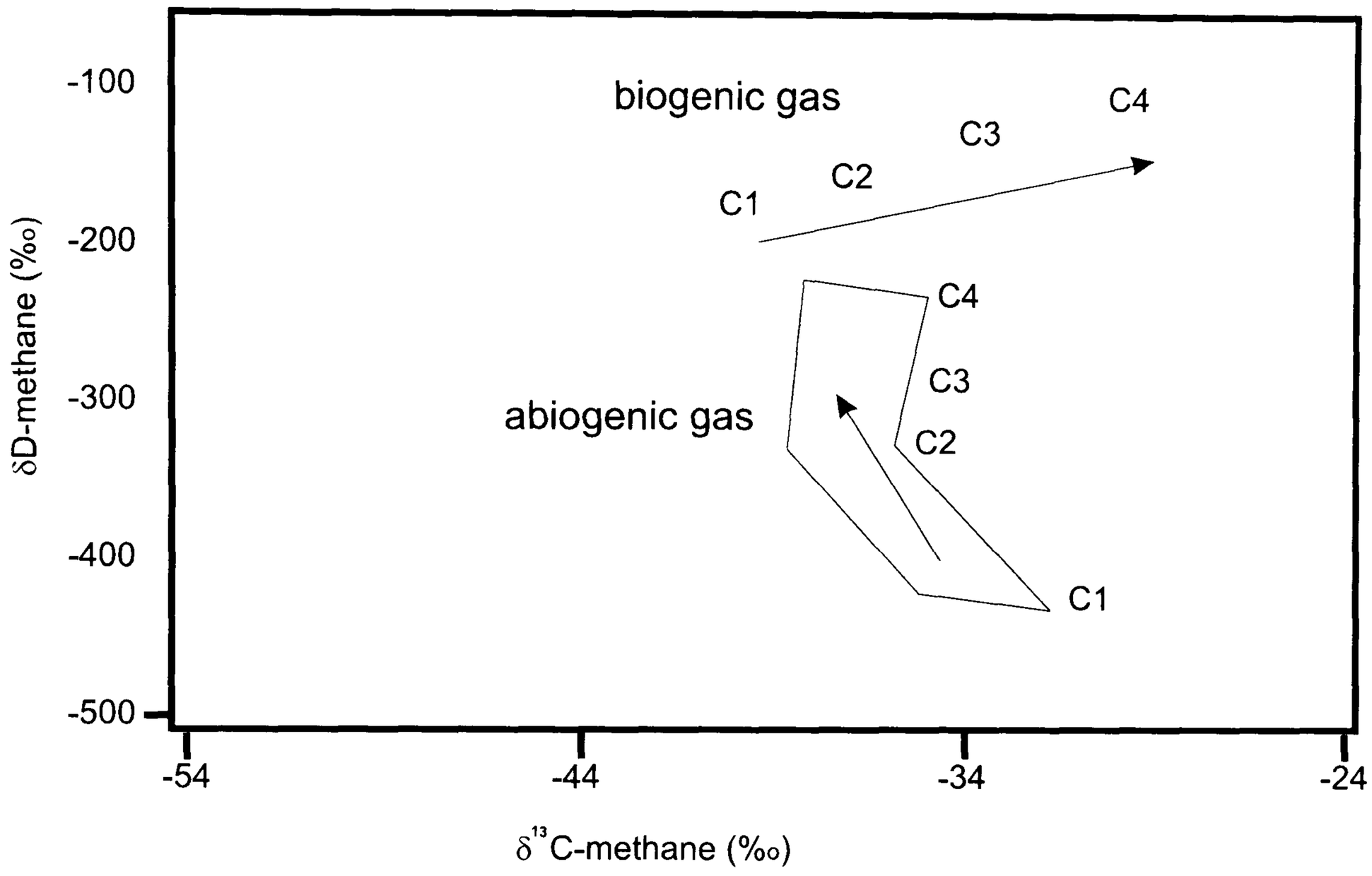

Figure 3.9: Simplified plot of $\delta^{13}C$ versus $\delta^{2}H$ values for C_1-C_4 for abiogenic and biogenic gas (modified from Sherwood-Lollar *et al.*, 2002). It shows the characteristic ^{12}C depletion and ^{2}H enrichment for abiogenic gas. In contrast, the pattern for thermogenic gas reservoirs shows a positive correlation of $\delta^{13}C$ and $\delta^{2}H$ values.

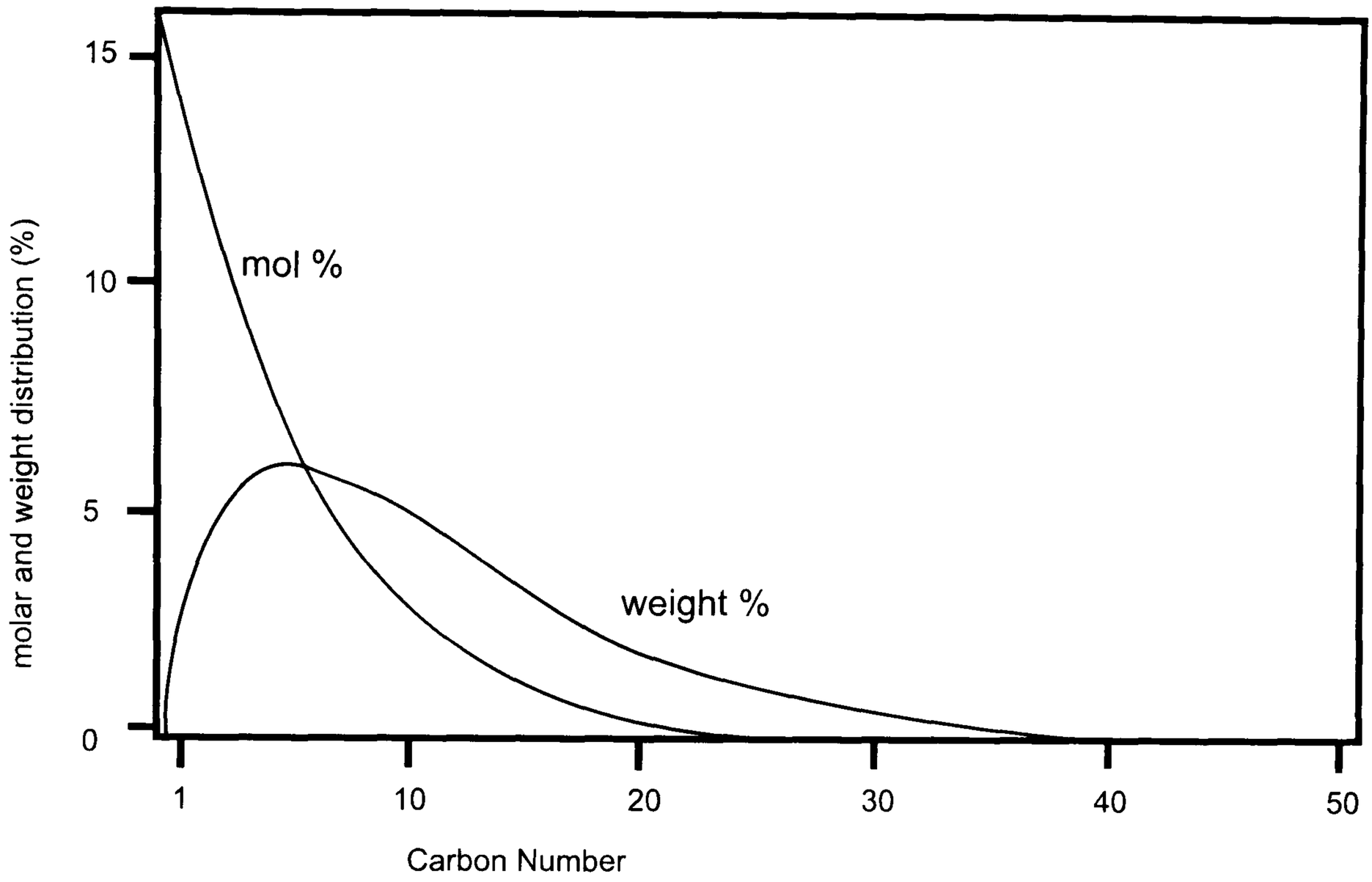

Figure 3.10: A typical synthetic Anderson-Schulz-Flory distribution (modified from Vessia, 2005).

3.4 Summary

Hydrocarbons in igneous rocks can be abiogenic or biogenic in origin.

Three models exist for their abiogenic origin:

- Direct mantle origin;
- Respeciation from a magmatic C-O-H fluid;
- Generation at low P-T via fluid rock interaction such as Fischer-Tropsch reaction.

Biogenic hydrocarbon can only be incorporated into an igneous rock body by secondary mechanisms:

- Assimilation of organic-rich material during emplacement;
- Migration from an organic-rich host rock.

The identification of the hydrocarbon source is difficult. The main tool to classify fluid sources and generation mechanisms is the combination of carbon and hydrogen isotope ratios. In addition, the general geochemistry of the fluids, textural observations and geological settings can be applied to narrow the interpretation. However, despite modern analytical techniques, there often remain ambiguities as to which mechanisms lead to hydrocarbon accumulation in igneous rocks. This is especially due to the fact that the discrimination of abiogenic as opposed to biogenic sources of hydrocarbons is still not robust. The combination of different generation mechanisms or mixing of fluids of different origin is often probable and will cause an imprecise isotopic and chemical signature in terms of fluid origin or generation mechanism.

4 Geology and petrology of the Khibiny intrusion and surrounding areas

4.1 Location of the Khibiny pluton and a brief historical review of its discovery

The Khibiny Mountains are located in the centre of the Kola Peninsula. They are over 1000 m high and surrounded by hilly plains and the lakes Imandra and Umbozero. The highest peaks of up to 1200 m are found in the western area of the massif. Khibiny's vegetation consists of thick pine, fir and birch woods in the foothills. This changes uphill into forest tundra and tundra and, on the flat Khibiny tops, into arctic stone desert. Due to its location above the Arctic Circle, there is 24 hours day light during the short summer period between late June and September, whereas from mid-December till early January the sun does not rise.

The first expedition to the remote area of the Khibiny tundra was conducted in 1887 by the Finish geologist W. Ramsey. He discovered and exploited the mineral resources of the Khibiny Mountains together with V. Hackman and A. Petrelius. In 1916 the first railway line was driven into Khibiny and A.E. Fersman started to assess the economical potential of the area. Apatite, the raw material in the production of phosphate fertilizer and explosives, was discovered in 1921 and has been mined since 1926. With the establishment of the "Apatit Trust" in 1929 the largely uninhabited land began to attract settlements and towns. The town of Kirovsk, south of Khibiny, became the centre of the new mining industry. In the 1960s the population was increased to 40,000 and settlements and villages developed. The group of villages was called "New Town" until it was united in 1966 and named Apatity. Meanwhile the mining industry was

expanding as the apatite deposit turned out to be the largest in the world. Maximum ore extraction was reached in 1985 with 54 million tons (Kamenev, 1987). On average the ore contains 16 % P_2O_5. Today, six mines are working; all located in the south of the Khibiny pluton, along the mountain ranges of Kukisvumchorr, Yuksporr, and Rasvumchorr where an apatite ore lens of 3 km length and 0.2 km width occurs.

Besides the economically valuable mines and metallurgic plants, scientific centres have been developed. In 1932 the station "Tietta" (saami for science) was built as a base for multiple expeditions to the Khibiny Mountains. An Alpine Botanical Garden was also established. In 1951, the Geological Research Institute was opened in Apatity. Different scientific disciplines, covering environmental and economical problems in the Arctic and Subarctic, are still concentrated here. Researchers have discovered more than 350 mineral types in the Khibiny complex. The most renowned are, apart from apatite, titanite, eudialyte and astrophyllite.

4.2 Geology of the Khibiny pluton

Intracontinental magmatism in the north-eastern Fennoscandian Shield occurred at the end of the Devonian between 380 - 360 Ma (Kramm *et al.*, 1993). Along with minor carbonatite intrusions, dyke swarms, pipes and extrusives, 24 alkaline intrusions were emplaced into the Precambrian basement (Dudkin and Mitrofanov, 1994). Amongst them are the giant agpaitic centres of Khibiny and Lovozero (Fig. 4.1). Their location, near a triple junction, suggests that these plutons formed during the initial stage of continental rifting that did not go to completion. Other intrusions are also controlled by fault zones, such as the Kovdor, Afrikanda, Kurga, Kontozero and Ivanovka intrusions (Arzamastsev *et al.*, 2000). All belong to the so-called Kola-Alkaline-Province that covers an area of about 100,000 km² (Kramm and Kogarko, 1994).

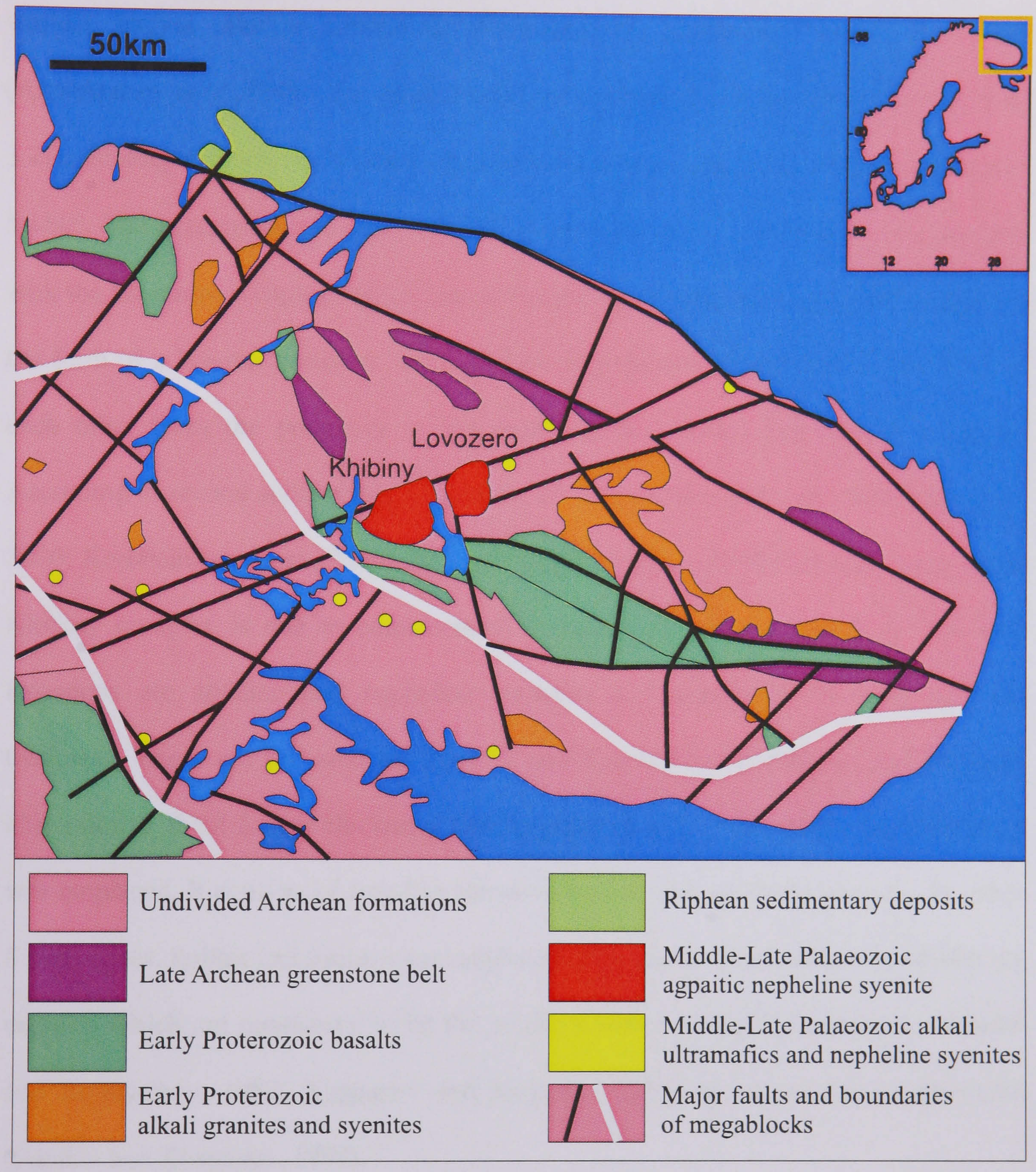

Figure 4.1: A simplified geological map of the Kola Peninsula based on Sheglov *et al.* (1993).

The Khibiny massif is located in the central part of the Kola Peninsula between 67°35´N/33°15´E and 67°55´N/34°20´E. It covers an area of 1327 km² and is one of the world's largest alkaline intrusions. According to geophysical data and drilling (Arzamastsev *et al.*, 2000), the outer contacts of the massif are subvertical to a depth of 3 km. At deeper levels the western and southern contacts plunge inward at an angle of 50-60°. The eastern contact dips outwards at an angle of 80° indicating a possible link with the Lovozero complex. The pluton is horseshoe-shaped, opening to the east. It has the form of a layered intrusion, composed of eight main rock formations that succeed each other from the periphery to the centre in the eastern part of the intrusion. According to several authors (e.g. Galakhov, 1975; Kogarko, 1995; Arzamastesev *et al.*, 2000; Korobeinikov *et al.*, 2000) the ring-shaped layering of different rock types in the Khibiny complex is due to emplacement in successive phases (Fig. 4.2). The first intrusions are alkaline and nepheline trachytes and porphyries of about 0.3 km thickness. These are followed by phase 2 and 3 intrusions of massive and trachytic khibinites of about 5.5 km thickness. During phase 4, a 2 - 3 km thick rischorrite body was emplaced. It consists of ring-like intrusive bodies with poikilitic textures. In phase 5 melteigites, ijolites and urtites were emplaced. This phase also includes the apatite ore deposits which are considered to be the result of either crystal fractionation (Kogarko and Romanchev, 1982; Khapayev and Kogarko, 1987) or convective accumulation (Frenkel and Khapayev, 1990).

Phases 6 and 7 comprise the heterogeneous emplacement of nepheline syenites and foyaites before, during phase 8, carbonatite emplacement ended the magmatic layered sequence. Many radial dykes of tinguaite, alkaline trachyte, monchiquite and damkjernite crosscut the ring-like structure and are considered to have been emplaced before the carbonatite stock. Recently, alkaline syenites (pulaskites) have been described within the foyaites (Korobeinikov *et al.*, 2000).

	phase	rocks	rock-forming minerals	accessories
	1	alkaline and nepheline trachytes and nepheline porphyries	nepheline, K-fsp, aegirine-augite	titanite, apatite, biotite
	2	massive khibinite	microcline, nepheline, aegirine, arfvedsonite	eudialyte, titanite, lamprophyllite
	3	trachytic khibinite	microcline, nepheline, aegirine, arfvedsonite	eudialyte, titanite, lamprophyllite
	4	rischorrite	microcline, orthoclase, nepheline, aegirine, aegirine-augite, arfvedsonite, biotite	eudialyte, titanite, astrophyllite, lamprophyllite, apatite
	5	melteigite, ijolite and urtite	nepheline, aegirine-augite	apatite, titanite, titanomagnetite
	6	aegirine-nepheline syenite	microcline, nepheline, aegirine-augite, arfvedsonite, biotite	eucolite, titanite, astrophyllite
	7	foyaite	microcline, nepheline, aegirine-augite, arfvedsonite, biotite	eucolite, titanite, astrophyllite
	8	carbonatites	calcite, aegirine, biotite	apatite

Figure 4.2: Map shows the different sequences of intrusive stages of the Khibiny pluton according to Kogarko (1995).

Generally, the genesis of agpaitic rocks is explained by prolonged fractional crystallisation of alkali basaltic or nephelinitic mantle-derived magmas (Larsen and Sørensen, 1987; Kramm and Kogarko, 1994). Experimental results have demonstrated, that agpaitic rocks have an unusually long crystallisation interval, down to <400°C (Marks and Markl, 2003). The long crystallisation time is mainly explained by retention of volatiles and alkali metals in the melt. Therefore a continuous transition from peralkaline, volatile-rich silicate melts to hydrothermal Na-oversaturated solutions is predicted (Sørensen, 1997).

Kramm and Kogarko (1994) concluded, based on Nd-Sr isotope data, that the magma source was a mixture of two end-members: a depleted upper mantle and an enriched source which is equal to Bulk Earth composition. Crustal material is assumed not to be involved in the genesis of the alkaline magmas of the Khibiny pluton.

The Khibiny and Lovozero pluton are separated by a 5 km wide zone of Precambrian rocks. They both consist predominantly of agpaitic nepheline syenite and have often been considered to have the same magma source. However, the massifs differ notably in their internal structure. Rock units in the Lovozero complex have subhorizontal dips, show traces of layering and a shallow intrusive contact against the host rock. The Khibiny massif is a concentrically zoned poly-phase intrusion with steeply dipping contacts with the host rocks. Shablinsky (1963) assumed that the Lovozero sheet-like intrusion was underlain by a concentrically zoned intrusion similar to the Khibiny massif. However, Arzamastsev *et al.* (2000) stated that no common magma conduits within the uppermost crustal levels have been found during geophysical investigations and three-dimensional modelling. Therefore the link between the two complexes is still unproven.

4.2.1 Geology of the surrounding host rocks

It is possible that the hydrocarbons in the Khibiny pluton might have been derived from the surrounding host rocks and thus have a biogenic origin. Organic material could have been incorporated into the pluton either via convective fluid flow during emplacement or during subsequent percolation of meteoric waters and/or host rock related fluids along fracture systems. Due to the conical shape of the Khibiny pluton (Arzamastsev *et al.*, 2000) it is possible that organic-rich cold fluids have flowed upwards from the underlying host rocks into the fractured and marginal sequences of the Khibiny pluton. The primary structures that could have served as pathways for a fluid flux into the pluton are joints, formed due to internal stresses related to cooling and crystallisation of the magma (Petford, 2003). Secondary fractures caused by weathering and tectonic events could also have acted as fluid pathways.

The host rocks into which the Khibiny Complex was emplaced are Archaean granite gneisses and Proterozoic volcanic-sedimentary rocks (Sørensen, 1970; Kogarko *et al.*, 1995). In the north and south-east the pluton is intrusive into Archaean gneisses and in the south and west into the Early Proterozoic Imandra-Varzuga greenstone belt. The greenstone belt is comprised of an alternating sequence of sedimentary and extrusive volcanic rocks represented by mafic and silicic schists, quartzites, carbonaceous and graphitic schists and metamorphosed limestone and dolomites. Petersilie (1962) described bitumens and low methane contents from some of the schists in the greenstone belt. It is thus likely that the carbonate and graphitic schists contained primary organic material some of which could have been incorporated into the pluton either during convective fluid-flow during emplacement or during subsequent percolation of meteoric waters along fracture systems. The origin of hydrocarbons could, therefore, be explained by involvement of organic matter from the sedimentary rocks.

That the Imandra-Varzuga greenstone belt is likely to have held biogenic carbon in its sedimentary successions is also indicated by the presence of mature organic material in rocks of the same age from the nearby Lake Onega area (Karelia, NW Russia). Dated at 2 Ga, this constitutes one of the most remarkable accumulations of organic carbon from the Palaeoproterozoic. The material occurs in the form of shungite, which is a black, non-crystalline, semi-metallic material that contains >98 % carbon (Melezhik *et al.*, 2004). It has been deposited in a 1000 m thick sedimentary volcanic succession. The total carbon reserve is estimated to exceed 25 x 10^{10} t and is assumed to have been accumulated within a volcanic continental rift setting, developed on the rifted eastern margin of the Archaean Baltic shield. That no shungite has been found from the Khibiny area might be due to erosion of a less voluminous sequence.

4.2.2 Rock definitions

The Khibiny pluton is for the most part an ultrabasic agpaitic intrusion. The term ultrabasic indicates that the rocks are silica undersaturated and contain less than 45 % SiO_2. The agpaicity of the rocks is defined by the molecular ratio $(Na_2O+K_2O)/Al_2O_3 < 1$.

In general, the Khibiny massif consists of a variety of nepheline syenites (khibinite, rischorrite, lujavrite and foyaite), foidolites (ijolite and urtite) and minor alkali syenite (pulaskite) plus a small carbonatite stock. The unusual names of the rocks are mostly historical and relate to arbitrary textural criteria and moderate chemical variations. The rock definitions are based on the recommendation of the IUGS (International Union of Geological Science) subcommision on the systematic of igneous rocks by Le Maitre (2002) and are given in Table 4.1.

Nepheline syenites (QAPF 11)	
Khibinite	eudialyte bearing nepheline syenite with aegirine, alkali amphibole, accessories containing Ti and Zr
Rischorrite	variety of biotite bearing nepheline syenite in which the nepheline crystals are poikilitically enclosed in microcline perthite, aegirine-augite, apatite, opaques often abundant.
Lujavrite	melanocratic agpaitic variety of nepheline syenite rich in eudialyte, arfvedsonite, aegirine with perthitic alkali feldspar or separate microcline and albite. A pronounced igneous lamination is characteristic as is the abundance in minerals rich in incompatible elements such as REE, U, Th, Li.
Foyaite	hypersolvus nepheline syenite, with trachytic texture caused by platy alkali feldspar crystals.
Foidolites (QAPF 15)	
Ijolite	plutonic rock consisting of pyroxene with 30-70% nepheline.
Urtite	plutonic rock consisting of >70% nepheline with some aegirine-augite, no feldspar, modally as a leucocratic variety of foidite.
Alkali syenite (QAPF 7)	
Pulaskite	variety of nepheline bearing alkali feldspar containing alkali feldspar and varying amounts of sodic pyroxene, amphibole, fayalite, biotite and minor nepheline
Carbonatite	
Carbonatite	collective term for an igneous rock in which the modal amount of primary carbonate minerals >50% is

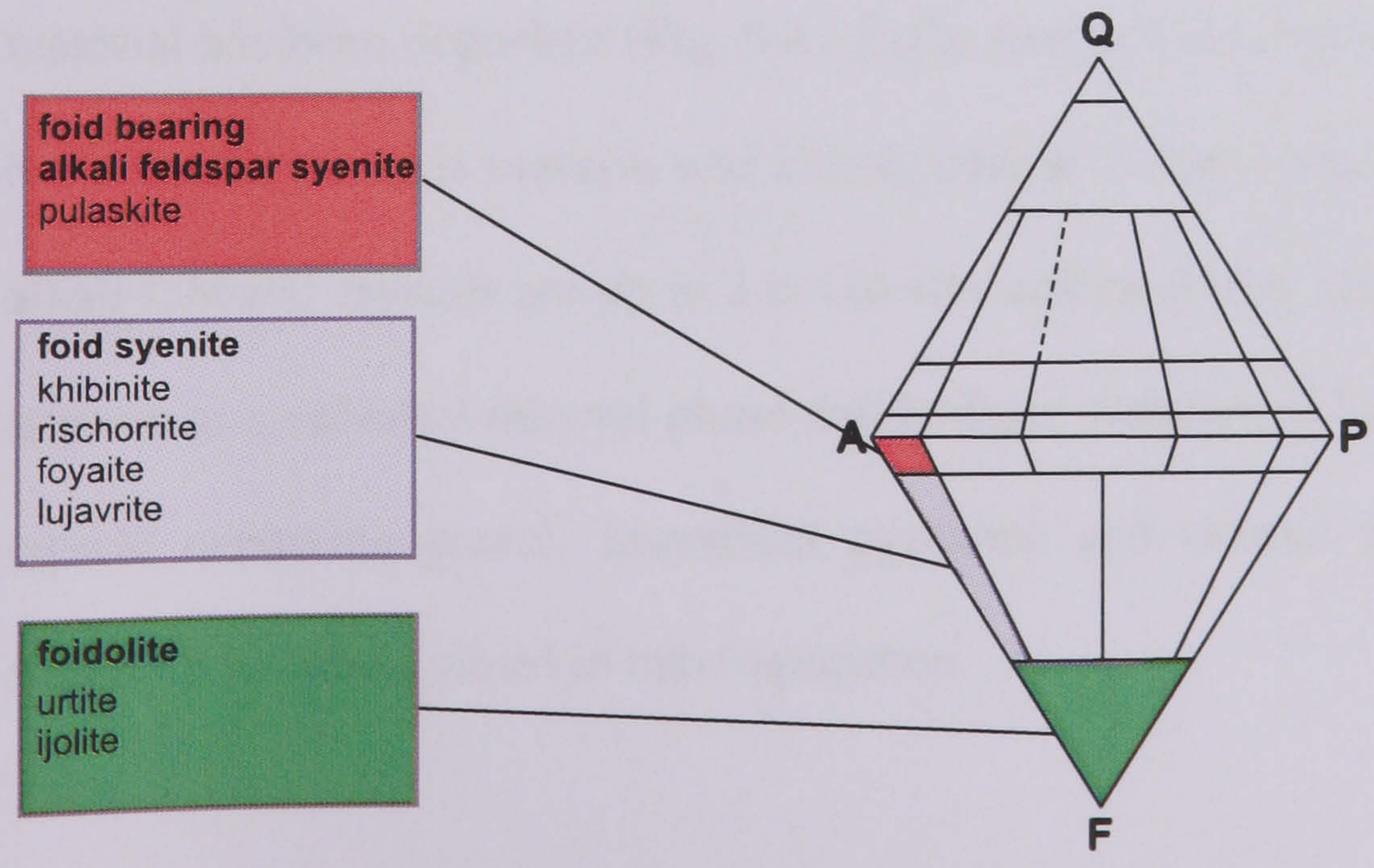

Table 4.1: The definition of rock types found in the Khibiny pluton based on the recommendations of the IUGS (International Union of Geological Science) subcommision on the systematic of igneous rocks by Le Maitre (2002).

4.2.3 Fieldwork and hand-specimen description

Fieldwork and sampling in different rock sequences of the Khibiny Mountains was carried out in summer 2003 (Fig. 4.3; Appendix A4.1) with the aim of investigating fluid inclusion characteristics in diverse areas of the complex in order to ascertain the spatial distribution of methane and possible interacting parameters. The sampling was focused around a fault zone to examine if microcracks and fluid inclusion planes, as the main carrier of free and occluded gas, are related to tectonic structures. Most samples were taken along traverses as oriented surface samples. The distance between sampling locations along a traverse varied between 50 m and 700 m, depending on outcrop abundance and the length of traverses.

Massive khibinite (traverse L1)

In the easternmost part of the Khibiny pluton, a traverse within massive khibinite was sampled. The traverse followed a mountain ridge and was cut by a valley where, according to published maps (e.g. Kogarko, 1995), the fault lies. The sampling was performed at altitudes between the mountain top and the zone where eroded gravel material has been deposited (Fig. 4.4). Eight samples were obtained along the 5 km long traverse. Khibinite is massive and mostly coarse to very coarse grained. Nepheline and alkali feldspar crystals are up to 3 cm in size and randomly distributed. Nepheline often appears as a euhedral mineral phase and feldspar weathering largely causes formation of typical nepheline gravel. Interstitial pyroxene and titanite have been identified. No eudialyte was recognized in hand-specimen.

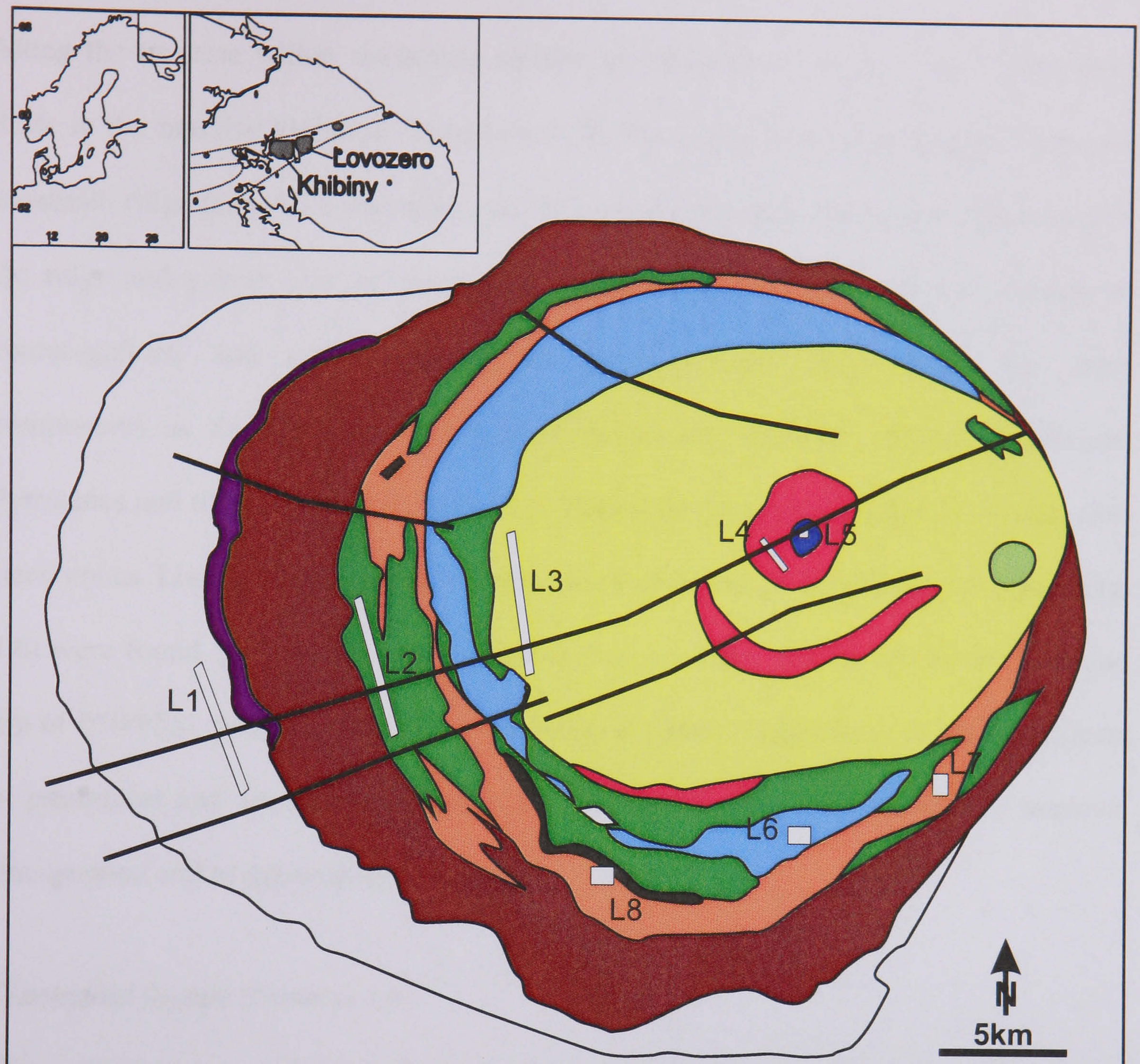

Figure 4.3: A geological map of Khibiny based on Kogarko (1995) and Korobeinikov *et al*. (2000). Also shown are major faults and sample locations and traverses along which samples were collected.

Rischorrite (traverse L2)

Along the traverse within rischorrite similar morphological features were observed to those in the massive khibinite. Sampling of 16 hand-specimens was performed along a mountain ridge (Fig. 4.5), depending on the outcrop situation, either between the top of the ridge and gravel zone or directly on top of the ridge. The rocks are medium- to coarse-grained and contain, based on hand-specimen observations, the same components as the khibinite. The main minerals are nepheline and alkali feldspar. Pyroxenes and titanites occur in interstices. Eudialyte occur as aggregates in centimetre-sized zones. Locally, foliated rock varieties were observed. Several tinguaite dykes (Fig. 4.6) were found, particularly south of the fault zone. They all have the same strike and dip of 050/85S, radial relative to the ring-shaped pluton. Tinguaites are the equivalents of phonolites and are very common in the Khibiny pluton. They are usually massive, fine-grained and of greenish-grey colour.

Trachytoid foyaite (traverse L3)

The overall texture of these rocks is similar to that described above. However, they are lighter in colour and nepheline is not as common as in the khibinites (Fig. 4.7). Pyroxene, titanite and biotite are the main mafic components. In the southern part of the traverse pegmatoid structures and coarsely orientated mineral assemblages were observed. In the northern part of the traverse some small felsic veins and a tinguaite dyke of about 5 m width with a marginal pegmatoid zone were observed.

Altogether 21 samples were obtained from this rock unit and seven representative samples used for this study.

Figure 4.4: Field photo of a mountain ridge in massive khibinite (traverse L1). Sampling was performed in the upper part where the outcrop situation was best .

Figure 4.5: Field photo of a mountain ridge in rischorrite with typical notches. The lower part of the ridge is covered with gravel. Sampling was performed on top of, or along, the upper part of the flanks (traverse L2).

Figure 4.6: Field photo of tinguaite dyke with greenish colour on the top of the rischorrite mountain ridge (traverse L2). The dyke is massive, about 50 cm wide and strikes E-W.

Figure 4.7: Field photo of the foyaite formation (traverse L3) near Lake Akademitcheskiy.

Massive foyaite (traverse L4)

Within this rock unit sampling of only five hand-specimens was possible. They are all from north of the fault zone where few irregular outcrops were found. The samples comprise a very coarse grained mineral assemblage of nepheline, alkali feldspar and pyroxene. Titanite, eudialyte and astrophyllite were identified as accessory minerals. Some outcrops exhibited an irregular mineral pattern and others a weak subhorizontal mineral foliation.

Alkaline syenite (traverse L5)

Outcrops of this rock unit were only found along a small gorge. Five relatively fresh samples were obtained from this location. Alkali feldspar was the overall dominant mineral and appeared as up to 2 cm large euhedral crystals in irregular patterns. Minor minerals, found in hand-specimens, are pyroxene and amphibole. Nepheline is rare.

Lujavrite (location L6)

Eight samples of lujavrite were collected from the southern area of the Khibiny pluton. The rocks appear massive and relatively light coloured. They contain occasional lens-shaped dark coloured xenolithic inclusions of unknown origin (Fig. 4.8). A 7 m wide shear zone, striking and dipping 040/80E, with sub parallel aligned aggregates of golden-brown astrophyllite and orientated mineral pattern, was observed.

Ijolite (location L7)

In the Yurkpach open pit (Fig. 4.9) 14 samples were obtained from the upper level of the mine. The rocks are massive and dark coloured. The dominant mineral species are nepheline and pyroxene with a ratio of about 1:1. Nepheline is medium- to coarse-grained, approximately equigranular and subhedral with diameters of up to 0.5 cm. The pyroxenes surround the nephelines and are approximately 0.2 cm in size.

Figure 4.8: Field photo of lujavrite (location L6) containig a xenolith lens of unknown origin (pers. comm. A. Spaschenka)

Figure. 4.9: Field photo of the Yurkpach open pit (location L7). Sampling was performed in the ijolite rock sequences in the upper part of the mine.

Apatite nepheline ore (location L8)

More than 30 samples of apatite nepheline ore and urtite were obtained in the Yuksporr underground mine (Fig. 4.10). The apatite ore appears in banded, lensed and blocky varieties (Fig. 4.11). Large brecciated zones (Balaganskaya and Pripachkin, 1994) were observed and sampled. The apatite minerals have a distinct light grey-greenish colour. They have grain sizes from fine-crystalline to large 0.5 cm crystals. The apatite layers are intertwined or alternate with darker nepheline minerals of similar grain size. Titanite is an abundant accessory phase. The apatite nepheline ore body is located within urtite, a massive, dark coloured rock. It contains euhedral 0.5 cm sized nepheline crystals set in a fine-crystalline pyroxene-rich matrix. Urtite is similar to ijolite in appearance but nepheline is the dominant mineral phase.

Samples from the underground mine are largely omitted in this study. Previous fluid inclusion studies concentrated mostly on these rock units as they contain large amounts of fluid inclusions and the rocks are easy to access. The aim of this study, however, is to assess the fluid inclusion distribution and characteristics throughout the Khibiny pluton. Therefore, the well studied and restricted apatite deposits are excluded here.

Figure 4.10: Field photo of the Yuksporr underground mine (location L8).

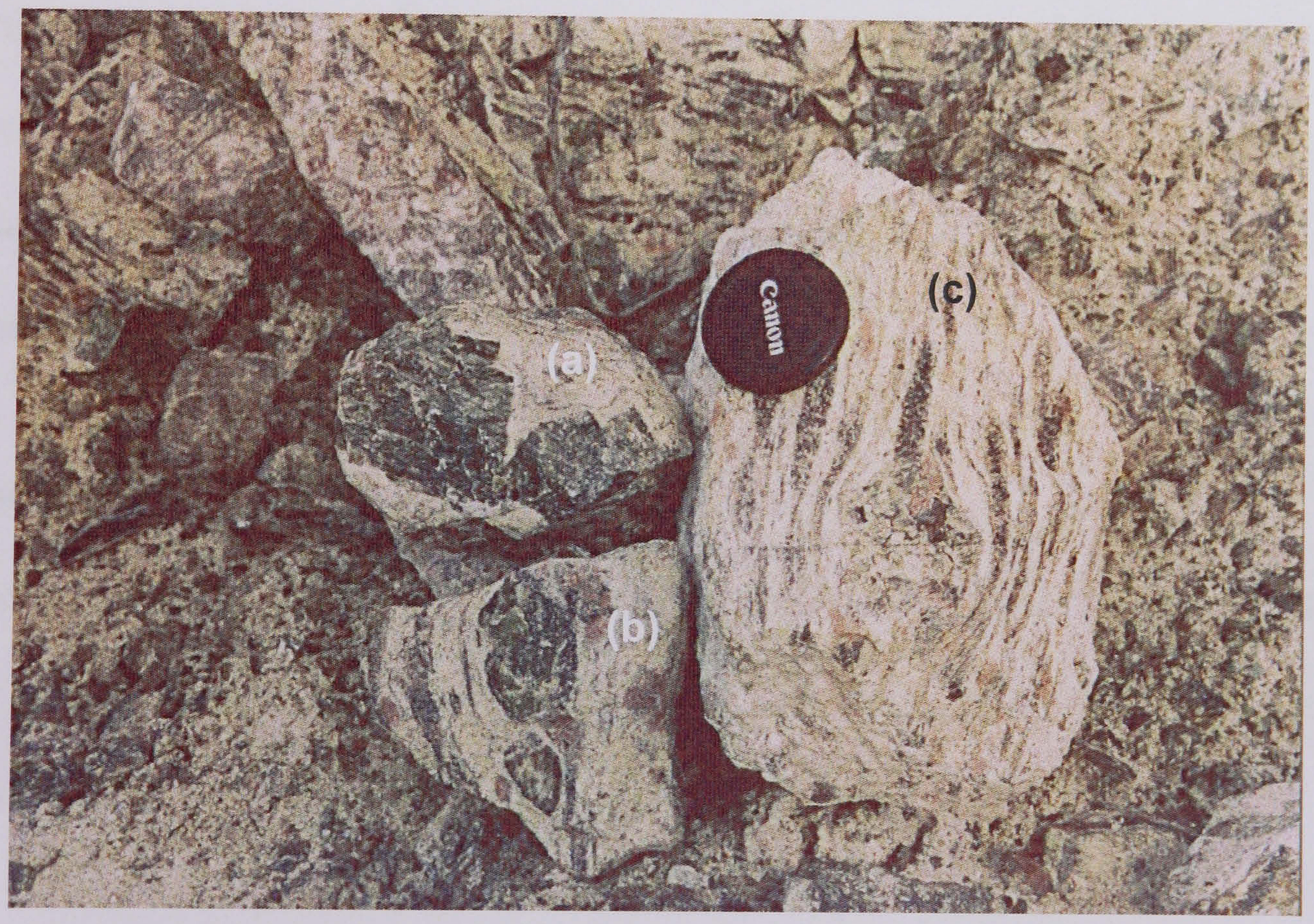

Figure 4.11: Field photo of typical appearance of apatite-nepheline-ore mined in the Yuksporr mine. (a) blocky structure, (b) lens shaped structure and (c) banded ore.

4.3 Petrology and mineralogy of the samples used in this study

This section focuses on the occurrence, textural relationship and composition of the minerals in the different rock types of the Khibiny pluton. A summary of modal composition (based on hand-specimen data) together with the observed minerals is listed in Table 4.2. Typical mineral occurrences and mineral assemblages are shown in photomicrographs (Fig. 4.12). Representative mineral compositions, obtained by microprobe analysis and laser Raman spectroscopy, are listed in Appendices A4.2 and A4.3.

4.3.1 Methods

Polished thin sections (30 μm) were prepared for petrographical investigation and microprobe analysis. Double polished thick sections (100 μm), which were primarily prepared for fluid inclusion studies, were additionally used to perform qualitative laser Raman analyses of the main minerals.

Microscopy

A conventional petrographic microscope was used to investigate the main minerals and their textual relationships. Magnifications of up to x100 were employed to obtain important textural data.

Microprobe Analysis

Major-element mineral compositions were determined using an Oxford Instruments ISIS Energy Dispersive System (EDS) mounted on a JEOL 630 scanning electron microprobe (SEM) at Kingston University, and a Cameca SX50 Wavelength

		modal macroscopic estimates			minor phases													
		nepheline	alkali feldspar	mafic minerals	aegirine/augite	aenigmatite	albite	amphibole	analcite	astrophyllite	biotite	cancrinite	eudialyte	lorenzenite	natrolite	opaques	titanite	serizited nepheline
khibinite	Kh-03-1	80	15	5	x	x		x						x			x	
	Kh-03-2	30	50	20	x													
	Kh-03-3	40	40	20	x	x								x		x	x	
	Kh-03-4	50	40	10	x									x		x	x	
	Kh-03-5	30	50	20	x	x		x			x	x				x	x	
	Kh-03-6	60	20	20	x			x	x	x				x		x	x	
	Kh-03-7	20	70	10	x		x	x							x		x	
	Kh-03-8	40	40	20	x	x	x	x				x			x	x	x	
rischorrite	Kh-03-9	30	50	20	x	x		x			x					x	x	
	Kh-03-10	45	45	10	x	x		x			x	x			x	x	x	
	Kh-03-11	45	45	10	x	x		x								x	x	
	Kh-03-13	30	30	40	x	x		x					x				x	
	Kh-03-14	30	60	10	x	x		x	x					x		x	x	
	Kh-03-42	95	0	5	x				x			x					x	
	Kh-03-43	40	30	30	x			x	x							x	x	
	Kh-03-44	25	25	10	x	x		x		x		x		x	x	x	x	
	Kh-03-45	30	65	5	x	x			x		x		x	x		x	x	
	Kh-03-46	20	75	5	x			x	x		x	x			x		x	
	Kh-03-50	20	75	5	x	x					x	x				x	x	
trachytoid foyaite	Kh-03-35	40	50	10	x		x	x			x	x				x	x	
	Kh-03-36	30	65	5	x		x	x			x	x				x	x	
	Kh-03-37	30	60	10	x		x	x	x		x	x				x	x	x
	Kh-03-38a	25	60	15	x		x	x			x					x	x	x
	Kh-03-38b	10	70	20	x			x			x						x	x
	Kh-03-38c	20	65	15	x			x			x					x	x	x
	Kh-03-39	40	50	10	x		x	x					x	x			x	x
	Kh-03-40	20	75	5	x	x		x			x						x	
	Kh-03-41	45	50	5	x			x			x					x	x	x
massive foyaite	Kh-03-51	25	60	15	x												x	x
	Kh-03-52	10	70	20	x				x			x					x	
	Kh-03-53	15	70	15	x			x			x					x	x	
	Kh-03-54	30	60	10	x			x	x		x	x		x		x	x	
	Kh-03-55	20	70	10														

Table 4.2: Estimates of modal composition and the observed minerals of rocks studied during the research. Modal macroscopic estimates are based on hand specimen observations and confirmed by optical microscopy. Minor phases have been identified using optical microscopy.

		modal macroscopic estimates			minor phases													
		nepheline	alkali feldspar	mafic minerals	aegirine/augite	aenigmatite	albite	amphibole	analcite	astrophyllite	biotite	cancrinite	eudialyte	lorenzenite	natrolite	opaques	titanite	serizited nepheline
alkaline syenite	Kh-03-57	10	80	10	x							x						x
	Kh-03-58	10	85	5	x													
	Kh-03-59	5	80	15	x													
	Kh-03-60	5	90	5				x	x		x	x					x	
lujavrite	Kh-03-17	40	30	30	x					x	x							
	Kh-03-18	50	30	20	x					x	x							
	Kh-03-19	50	20	30	x					x	x							
	Kh-03-20	40	40	20	x			x		x	x							
	Kh-03-21	40	40	20	x			x		x	x							
	Kh-03-22	40	40	20	x			x	x		x							
ijolite	Kh-03-61	45	5	50	x	x			x	x	x						x	x
	Kh-03-62	40	10	50	x	x				x	x	x				x	x	x
	Kh-03-63	30	20	50	x	x				x	x	x				x	x	x
	Kh-03-64	35	15	50	x	x				x	x	x				x	x	x
	Kh-03-65	40	0	60	x				x		x					x	x	x
	Kh-03-66	60		40	x			x	x		x	x		x				x
	Kh-03-74	60	20	20	x			x			x	x				x		x

Table 4.2 continued: Estimates of modal composition and the observed minerals of rocks studied during the research. Modal macroscopic estimates are based on hand specimen observations and confirmed by optical microscopy. Minor phases have been identified using optical microscopy.

Dispersive microprobe at the Natural History Museum, London. EDS microanalysis was carried out with an accelerating voltage of 15 keV. Calibrations were performed regularly through use of a Cobalt standard and internal standard material.

Laser Raman Spectroscopy

The main minerals have also been confirmed by laser Raman spectroscopy. This is an easy to apply method for several minerals if only qualitative data are required. It is also sensible in conjunction with fluid inclusion analysis to obtain the necessary information on host minerals and their background signal.

4.3.2 Petrographic description

Khibinite

These felsic rocks are holocrystalline, coarse grained and have equigranular textures. Their modal composition comprises various proportions of nepheline and alkali feldspar and 5 - 20 % mafic minerals.

The majority of nepheline crystals have euhedral to subhedral shape and are up to 2 cm in size. Nepheline appears either in large separate clusters (Fig. 4.12a), or intergrown with alkali feldspar. Euhedral inclusions of nepheline are occasionally present within feldspar (Fig. 4.12h). Nepheline frequently contains inclusions (Fig. 4.12g) of colourless needles of aegirine or amphibole, astrophyllite in bundles, stubby prism of apatite and fluid inclusions. They are from about 1 mm to 1 cm in size. In some minerals an alignment of mineral inclusions and fluid inclusions is present. Some nepheline crystals show zoning caused by temporary accumulation of larger amounts of mineral and fluid inclusions. The majority of fluid inclusions, however, appear in microcracks or in separate clusters. Nepheline grain boundaries are often filled with secondary minerals such as cancrinite (Fig. 4.12v) and natrolite (Fig. 4.12t and u).

Alkali feldspar appears mostly as perthite and microperthite with stringy and lensoid shapes (Fig. 4.12d and e). They occur as subhedral, elongated crystal laths, up to 3 cm long. Short-prismatic or needle-shaped inclusions of about 10 µm to 1 mm sized apatite, pyroxene and amphiboles occur along boundaries between K-rich and Na-rich zones together with small (<10 µm) fluid inclusions. A second generation of lamellar, non-perthitic feldspar is present in small amounts, mostly along grain boundaries of perthite (Fig 4.12f). These are clear and inclusion-free and probably belong to a later stage of crystallisation.

The remaining 5 - 10 % of the rock matrix is made up by titanite, aegirine and aegirine-augite, arfvedsonite, aenigmatite, biotite and opaque minerals. They occur as distinct clusters of phenocrysts within the nepheline-feldspar groundmass and in interstices. Titanite and aegirine are also found as euhedral microlith among nepheline and alkali feldspars. Pyroxenes commonly show elongated, euhedral, stubby prismatic shapes and green colour of aegirine (Fig. 4.12n). Amphiboles typically occur in intergranular spaces (Fig. 4.12b) between nepheline crystals. A strongly blue-brown pleochroism is indicative of arfvedsonite. Other mafic minerals are subrounded opaque magnetite and titano-magnetite, euhedral to subhedral titanite and platy lorenzenite. They often occupy intergranular spaces where they develop micro-mineral assemblages.

Rischorrite

Rischorrite is a felsic rock with a holocrystalline texture. The samples consist of 80 – 95 % perthitic alkali feldspar and nepheline. Both minerals occur in about the same proportions. The remaining 5 - 20 % comprises mafic minerals. The overall appearance and the mafic mineral assemblages are similar to that of khibinite.

Some samples show exceptional features. Sample Kh-03-42 is dominated by nepheline with about 95 % and only few mafic minerals are apparent. Cancrinite were found

within nepheline or at its margins. Nepheline occurs as centimetre-sized megacrysts. It is often altered to sericite (Fig. 4.12c) and frequently cut by cracks and zones along where aegirine needles and fluid inclusions are concentrated. Sample Kh-03-44 contains about 25 % cancrinite which is present in clusters with an extension of several mm up to 1 cm in size. The crystals occur in association with either nepheline or opaques. This sample also contains very high amounts of methane (c. 100 cm^3/kg). This is somewhat contradictory with the observation that cancrinite usually contains carbon in its oxidised form as CO_3 and no reports of CH_4 trapped in its framework are found in the literature.

The typical mafic minerals in all rischorrite samples are aegirine, aenigmatite, arfvedsonite, titanite and biotite. They mostly occur as assemblages in intergranular spaces (Fig. 4.12s). Aenigmatite is often surrounded by a rim of lorenzenite and aegirine (Fig. 4.12p). Aegirine is also present as small mm-sized mineral needles throughout nepheline and alkali feldspar crystals.

Trachytoid foyaite

This is a holocrystalline rock with a modal content of 10 - 45 % nepheline, 50 - 75 % alkali feldspar and 5 - 20 % mafic minerals. Nepheline and alkali feldspar are present in slightly separated clusters and are not as homogeneously distributed as in rischorrite and khibinite. Albite occurs interstitially between perthite laths (Fig. 4.12f).

Nepheline crystals occur in clusters, in intergranular spaces between perthite laths or as groups of large subhedral-euhedral minerals. They are rich in fluid inclusions; some of which are related to nepheline growth zones.

The dominant mafic mineral is the green, elongated and often euhedral aegirine. Minor biotites with altered margins are present. Together with amphibole, they fill interstices between nepheline and alkali feldspar. Agglomerates of subhedral titanite are abundant

and eudialyte (Fig. 4.12j), strongly cracked and with irregular margins, occurs in some samples. Amphibole occurs both, interstitially and as euhedral phenocrysts (Fig. 4.12o).

Massive foyaite

These rocks comprise various proportions of alkali feldspar and nepheline together with about 10 % mafic components. They are felsic and have a granitic texture. Sample Kh-03-51 contains highly altered nepheline with sericitisation (Fig. 4.12c) along grain boundaries and microcracks. Nepheline is also partly altered to cancrinite which appears along grain boundaries (Fig. 4.12v). Alkali feldspar generally appears as laths of strongly perthitic twins (Fig. 4.12f). The average grain size of the crystals is 0.5 cm but the larger ones are up to 1 cm in size. Discrete grains of albite are occasionally present along their grain boundaries. This is assumed to be the product of perthite exsolution and diffusion of the albite component (Deer *et al.*, 1992). Mafic minerals are titanite, pyroxene, amphibole biotite, magnetite and titano-magnetite. Titanite occurs as an intergranular phase or embedded in alkali feldspar mostly as euhedral to subhedral crystals (Fig. 4.12l). Pyroxenes, amphiboles biotite and opaques are mostly present as anhedral interstitial filling (Fig. 4.12s). Analcite is present occasionally as separate grains up to 3 mm in size.

Alkaline syenite

This is a leucocratic, coarse grained rock. Its major minerals are alkali feldspar (80 – 90 %) and nepheline (5 -10 %) with average grain sizes of 0.5 cm. Nepheline often shows a euhedral shape, whereas feldspar perthites are subhedral to anhedral. Both, perthites and nephelines are strongly cracked and contain abundant fluid and mineral inclusions. The typical mafic minerals are biotite, pyroxene, amphibole and titanite which often occur as assemblage in separate clusters (Fig. 4.12s) or as euhedral

phenocrysts (Fig. 4.12l). Biotite is the dominant mafic mineral and forms crystals of up to 0.5 cm in size.

Lujavrite

The lujavrites are greyish, medium to coarse grained felsic rocks. They are composed of 40 - 50 % subhedral nepheline and about 30 % alkali feldspar, both with an average size of 0.5 cm. Nepheline is distinctly euhedral or subhedral and mostly smaller than the feldspar. It is clear and free of inclusions. The alkali feldspars occur typically as perthites that occupy patchy areas and are penetrated by small mm-sized mafic crystals. The majority of the mafic minerals are euhedral, prismatic to acicular aegirine, fibrous golden-brown astrophyllite and platy biotites. They are up to 1 cm in size and occur as isolated grains or aggregates (Fig. 4.12i and 4.12x). Arfvedsonite is present as anhedral plates with inclusions of euhedral aegirine. Albite occurs both interstitially and along grain boundaries of alkali feldspar and has irregular crystal shapes. Other accessory minerals are analcite, natrolite and cancrinite. Analcites occur as rounded crystals mostly next to nepheline. Natrolite and cancrinite fill intergranular spaces and exhibit an irregular shape.

Ijolite

This is a medium grained rock composed of nepheline and aegirine in approximately similar proportions. Alkali feldspar is observed only as an accessory phase. Nepheline is euhedral to subhedral and occurs as distinct crystals or separate crystal groups surrounded by areas of mafic minerals. It appears to be larger than the mafic minerals with grain sizes of about 0.5 cm. Nepheline hosts large amounts of primary fluid inclusions and mineral inclusions. The nepheline crystals are penetrated by microcracks where also mineral and fluid inclusions accumulated. The pyroxene crystals show the dark green colour of aegirine and are often aligned. They have a subhedral shape and

are about 0.2 cm in size. Occasionally they reach up to 0.5 cm in size. The pyroxenes often occur in association with biotite. Other accessories are titanite, magnetite and lorenzenite. The mineral association of opaques, surrounded by titanite, and associated with pyroxenes, amphiboles and biotite is also present (Fig. 4.12r). Cancrinite occurs as a vein filling (Fig. 4.12w).

Mineral assemblages and typical mineral occurrence and their relation to fluid inclusions

Previous studies by Salvi and Williams-Jones (1997) and Potter (2000) both indicated a likely relationship between the generation of methane-rich fluid inclusions and the alteration of mafic minerals.

Their studies describe the following alteration reactions that might generate hydrocarbon gas via a Fischer-Tropsch-type reaction (see also Chapter 3):

1. hydration of Na/K silicates;
2. replacement of titano-magnetite and nepheline by magnetite, biotite, aegirine, natrolite and pectolite;
3. replacement of arfvedsonite by aegirine.

The petrography of the rocks from the Khibiny pluton reported here confirms the presence of the minerals and mineral assemblages mentioned above:

1. Hydrated Na/K silicates are frequent and are likely to be associated with alteration processes (Figs. 4.12t-w).
2. Mineral associations involving aegirine, arfvedsonite, biotite and magnetite and titano-magnetite are numerous. In most rock types the following mineral textures are observed:

- magnetite and titano-magnetite surrounded by a corona of titanite
- a core of magnetite surrounded by aegirine-augite and titanite

- the association of titanite, aenigmatite and opaques
- titano-magnetite minerals with a rim of titanite, itself rimmed by lorenzenite and aegirine (Fig. 4.12r)
- the mineral assemblage of titanite, aenigmatite, aegirine, surrounded by nepheline (Fig. 4.13)
- the mineral assemblage of aegirine, biotite, titanite and aenigmatite surrounded by nepheline (Fig. 4.14)
- aenigmatite with rims of aegirine-augite, lorenzenite and K-feldspar (Fig. 4.15)
- aegirine-augite intergrown with amphibole
- large inter-granular areas between nepheline filled with clusters comprising groups of biotite, titanite, opaques, arfvedsonite, aegirine augite as relatively equigranular intergrowths (Fig. 4.12s)

3. The mineral association of arfvedsonite and aegirine is frequent. Evidence for replacement of arfvedsonite by aegirine, however, was not found. The analysed amphiboles often show a zonation (Fig. 4.12m) that indicates a change in the chemical composition of the mineral. The composition of the core is calcic-sodic and towards the rim it changes to alkaline amphibole (Figs. 4.16 and 4.17). Often a small rim of Na-feldspar surrounds the amphibole. This probably indicates that the magma composition changed and became more sodium-rich during crystallisation.

The petrographic investigation of mineral assemblages documents either late stage alteration or replacement or are the result of changes in magma chemistry during cooling. Evidence for simultaneous hydrocarbon generation via a Fischer-Tropsch-type reaction, however, was not found. The surrounding cracks might well be the result of alteration and expansion of the mafic minerals, but there is no evidence of that the fluid inclusions trapped therein are the product of any alteration reaction. The fluid inclusion

population is neither exceptionally high nearby altered mineral assemblages nor is their composition different to that found elsewhere in the rocks. Mafic minerals and hydrated Na/K silicates are mostly fluid inclusion free. Fluid inclusions occur mainly as secondary inclusions along microcracks in nepheline. It is therefore likely that fluid inclusions, even if in close proximity to altered minerals, are the result of fluid migration and secondary entrapment, as is common everywhere in the complex.

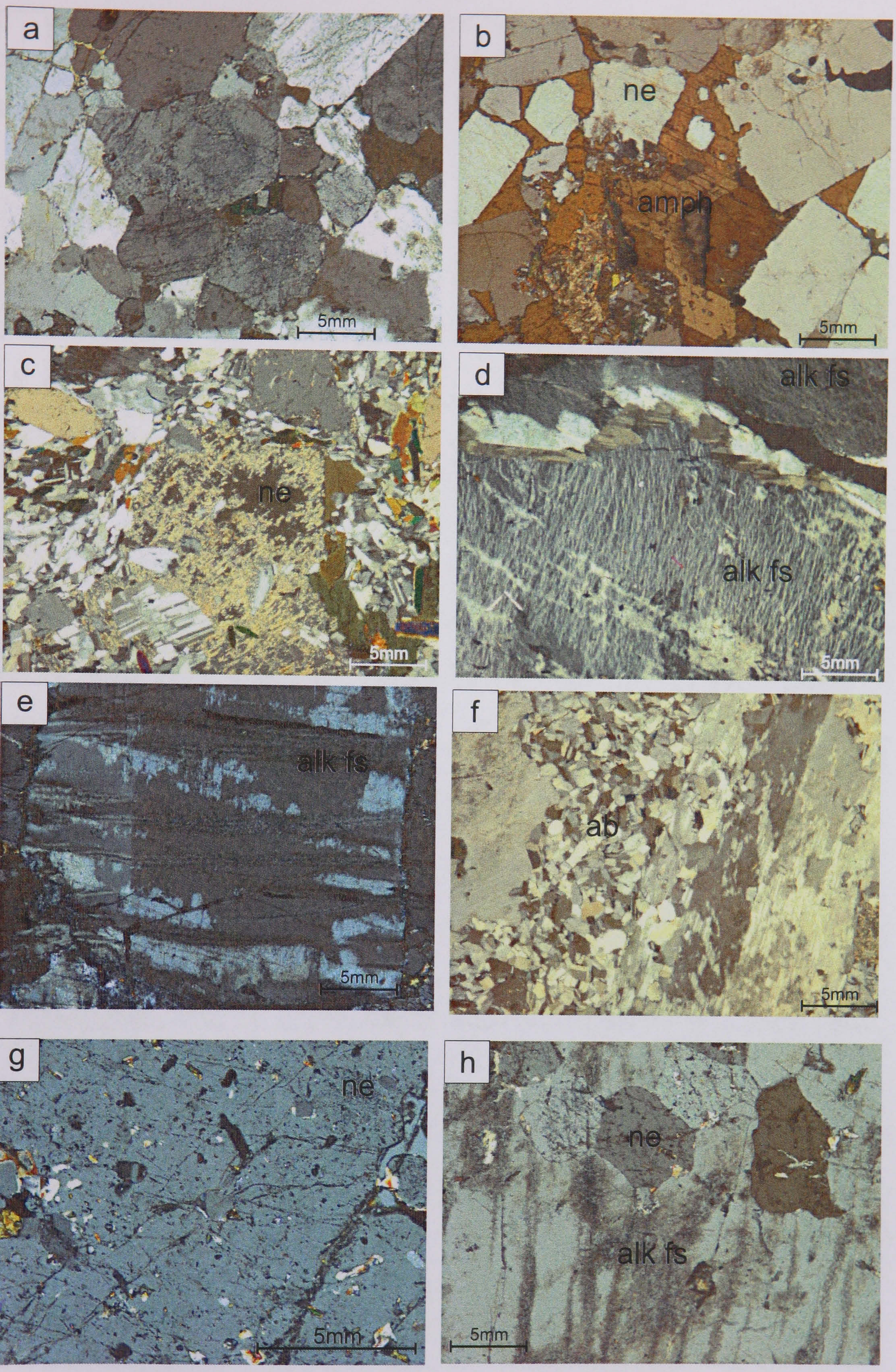

Figure 4.12: Photomicrographs (xpl) of the main minerals and mineral assemblages in Khibiny. (a) Kh-03-11 (rischorrite), typical assemblage of nepheline (ne) in clusters. (b) Kh-03-9 (rischorrite), euhedral nepheline with mainly amphibole (amph) as interstitial filling. (c) Kh-03-38 (trachytoid foyaite), altered nepheline. (d) Kh-03-5 (khibinite), stringy perthite of alkali feldspar (alk fs). (e) Kh-03-3 (khibinite), alkali feldspar as typical replacement perthite (Deer *et al.*, 1992). (f) Kh-03-38 (trachytoid foyaite), twinned alkali feldspar (perthite) with small albite (ab) minerals along the grain boundary. (g) Kh-03-8 (khibinite), mineral inclusions in nepheline. (h) Kh-03-10 (rischorrite) nepheline inclusions in perthite.

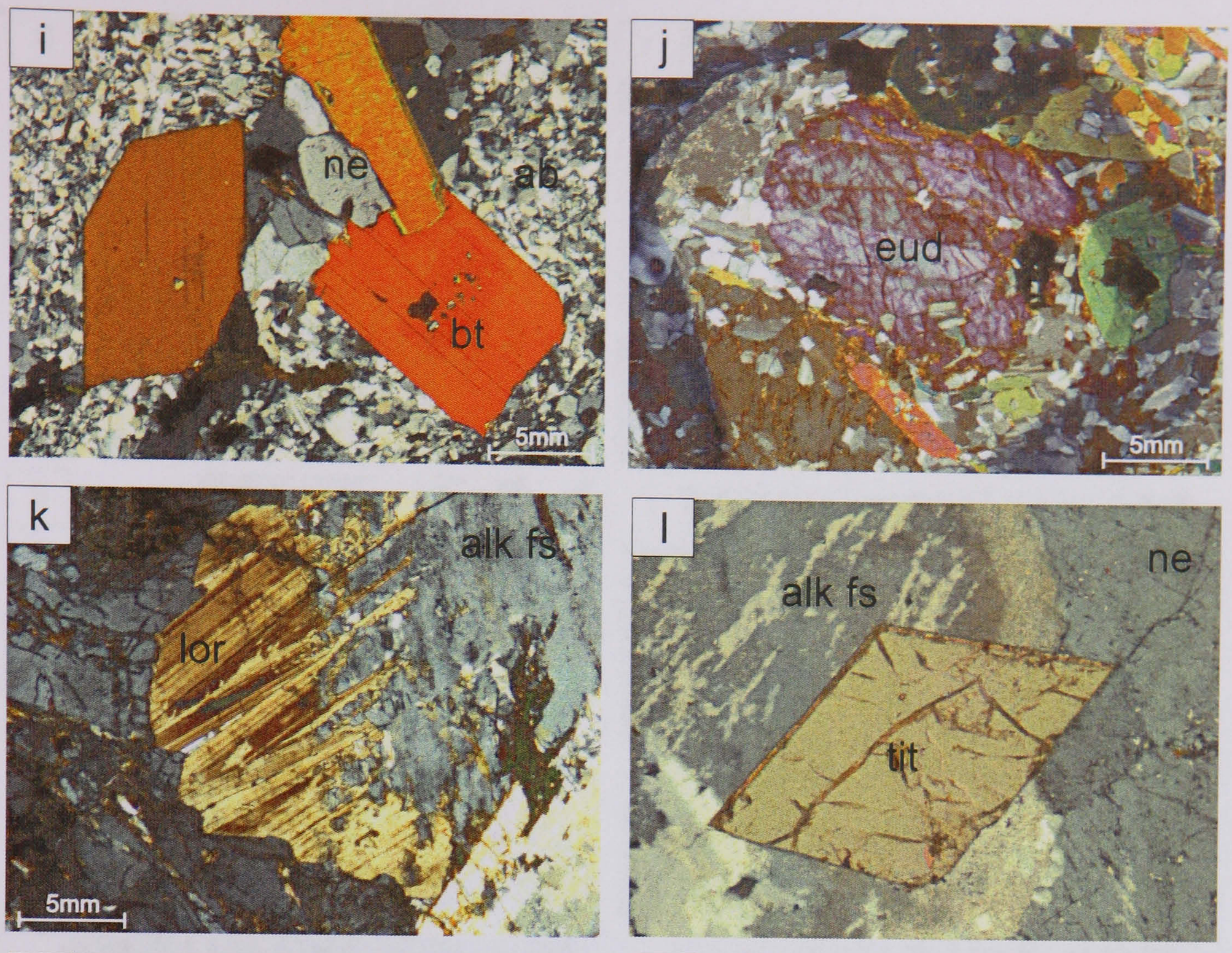

Figure 4.12 continued: (i) Kh-03-20 (lujavrite), large euhedral biotite (bt) minerals next to nepheline (centre) and surrounded by albite. (j) Kh-03-39 (trachytoid foyaite), slightly altered eudialyte (eud). (k) Kh-03-1 (khibinite), lorenzerite (lor). (l) Kh-03-56 (alkaline syenite), euhedral titanite (tit) surrounded by alkali feldspar.(m) Kh-3, apatite (ap) mineralisation (right) and altered nepheline (left). (n) Kh-03-2 (khibinite), accumulation of aegirine (aeg) needles in nepheline. (o) Kh-03-40 (trachytoid foyaite), zoned euhedral amphibole in patchy perthite. (p) Kh-03-10 (rischorrite), aenigmatite (aenig) surrounded by a rim of lorenzerite and aegirine needles.

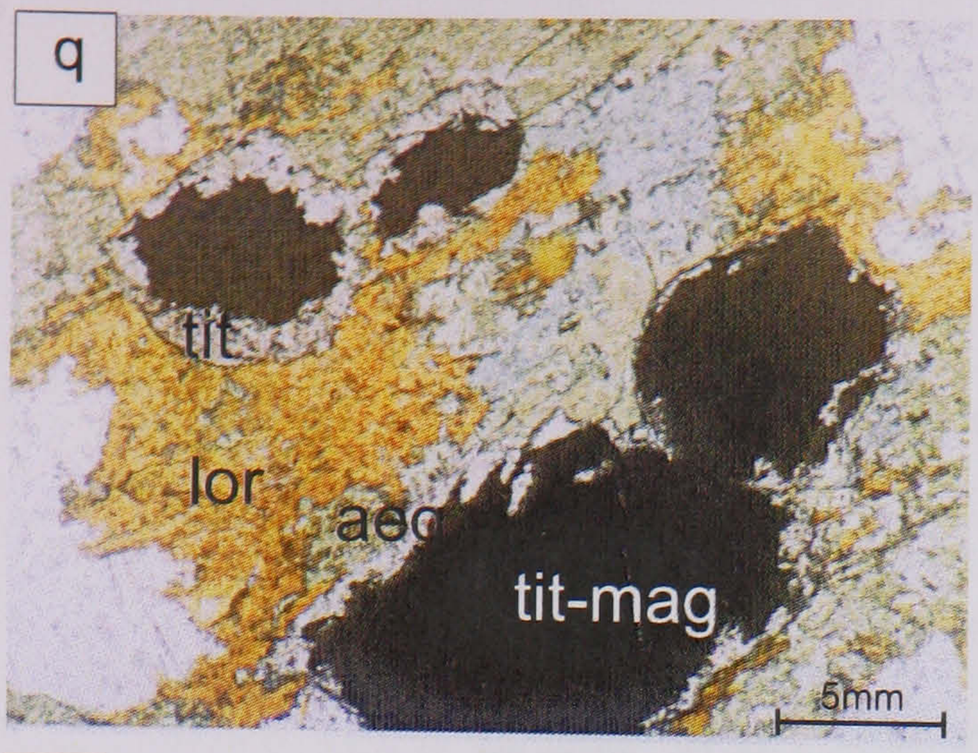

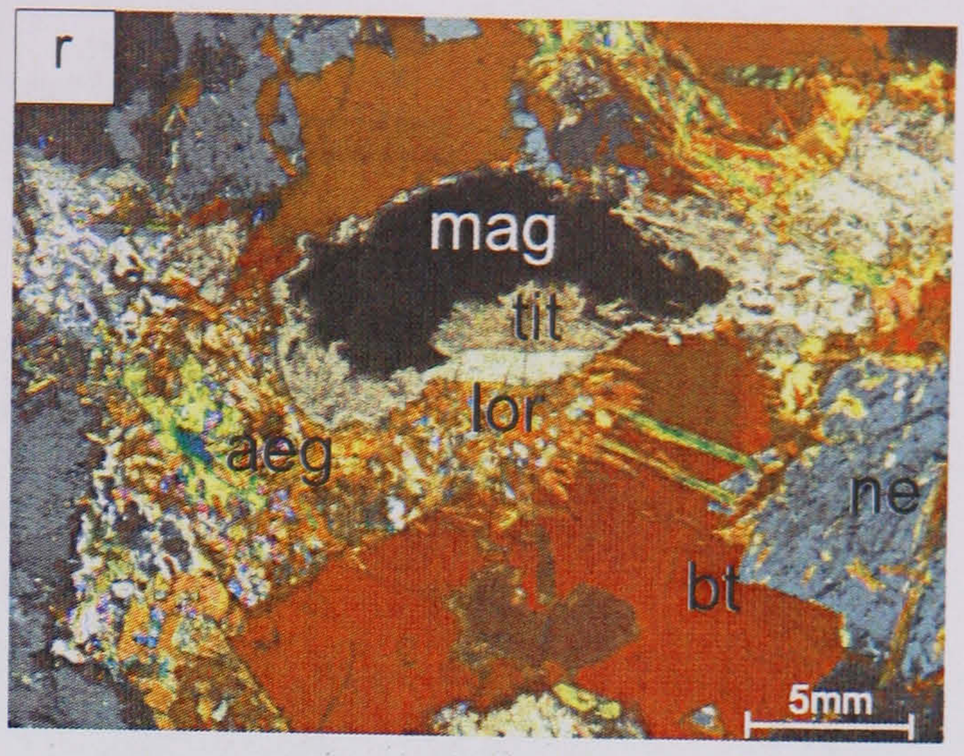

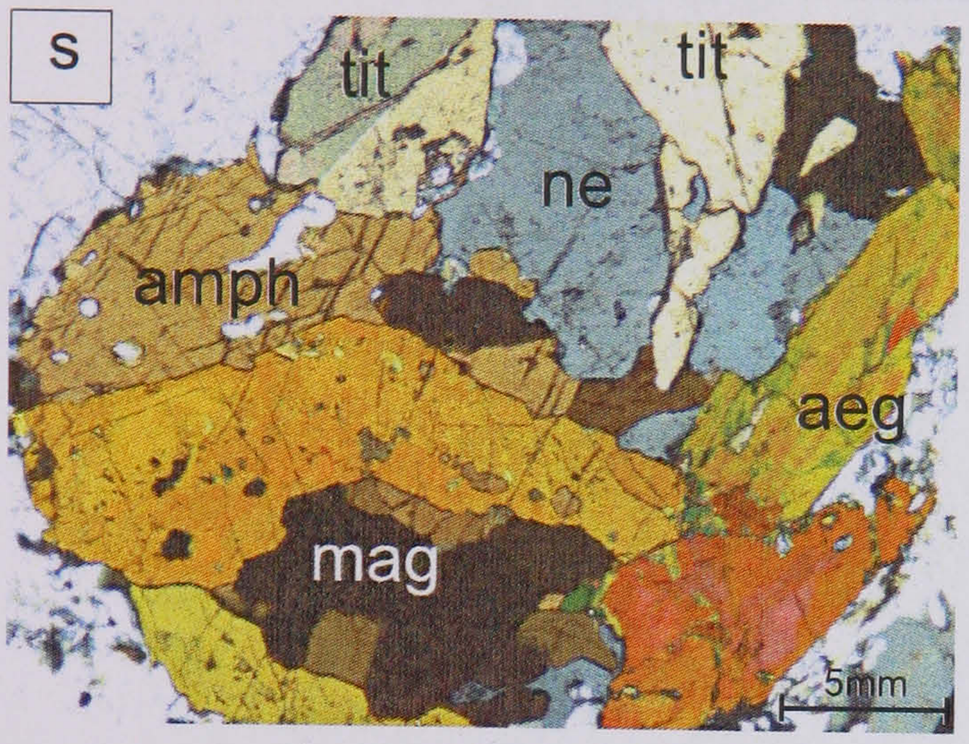

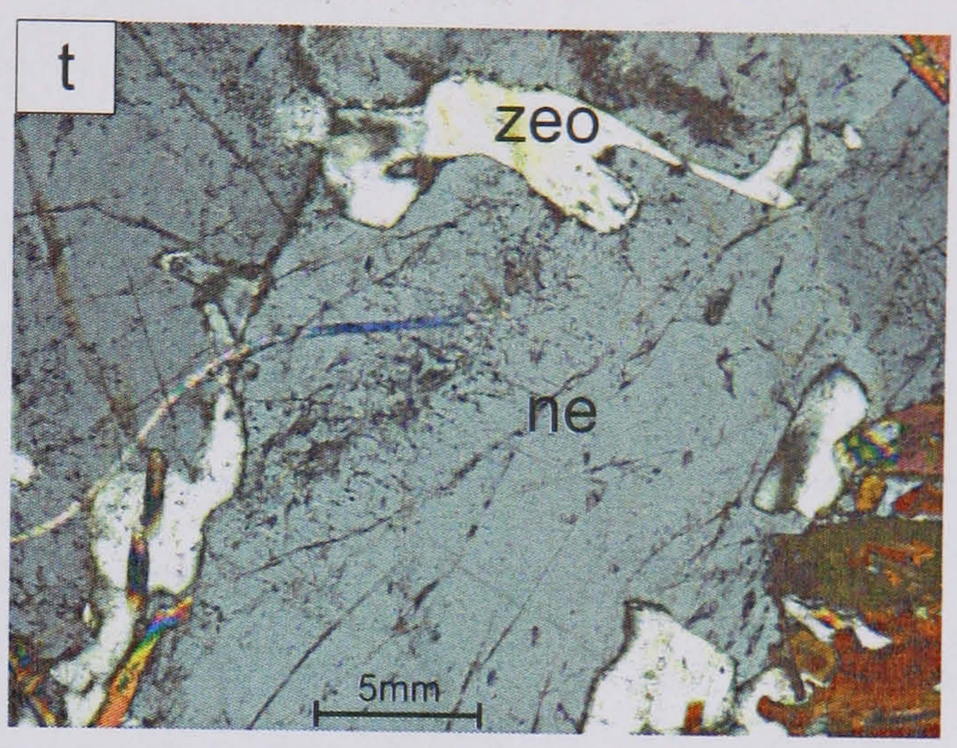

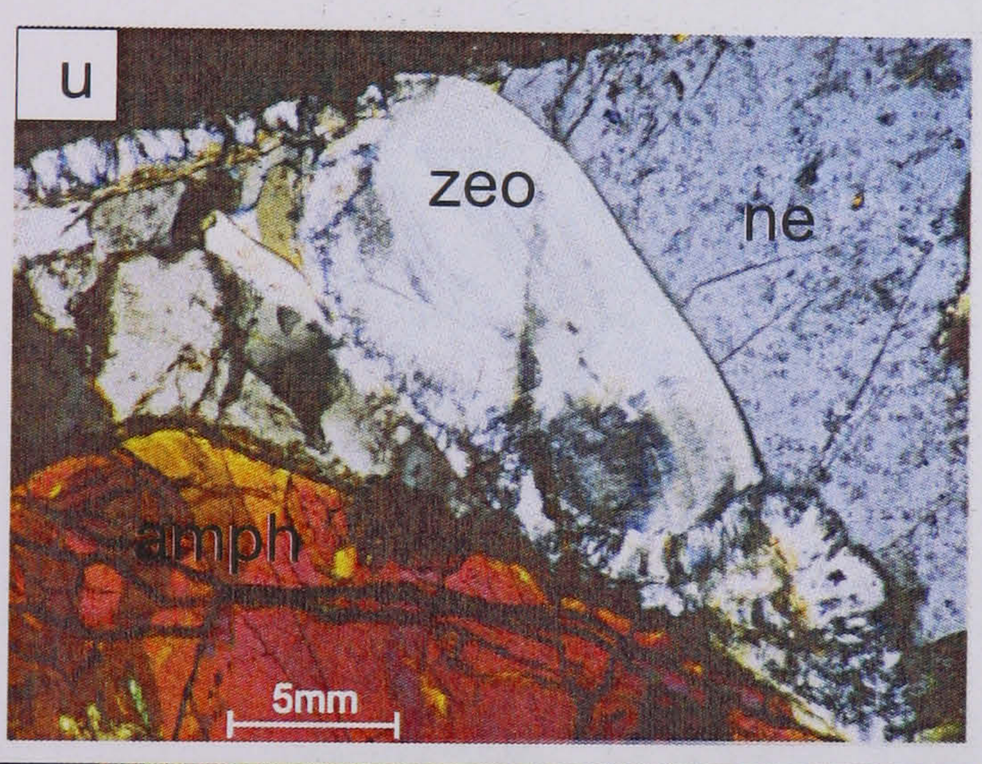

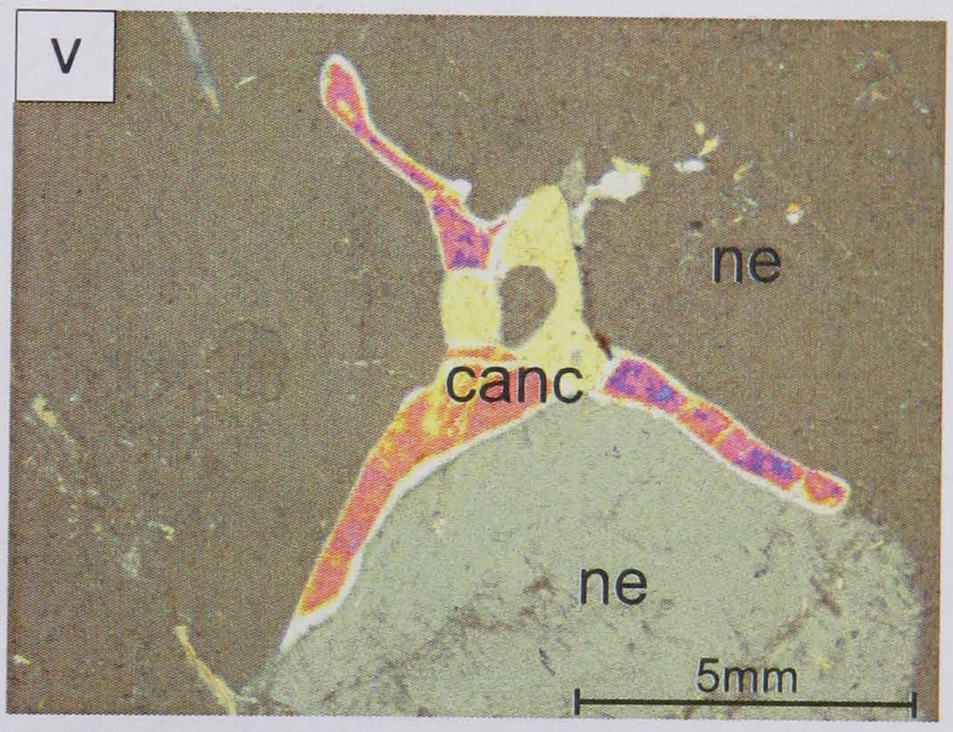

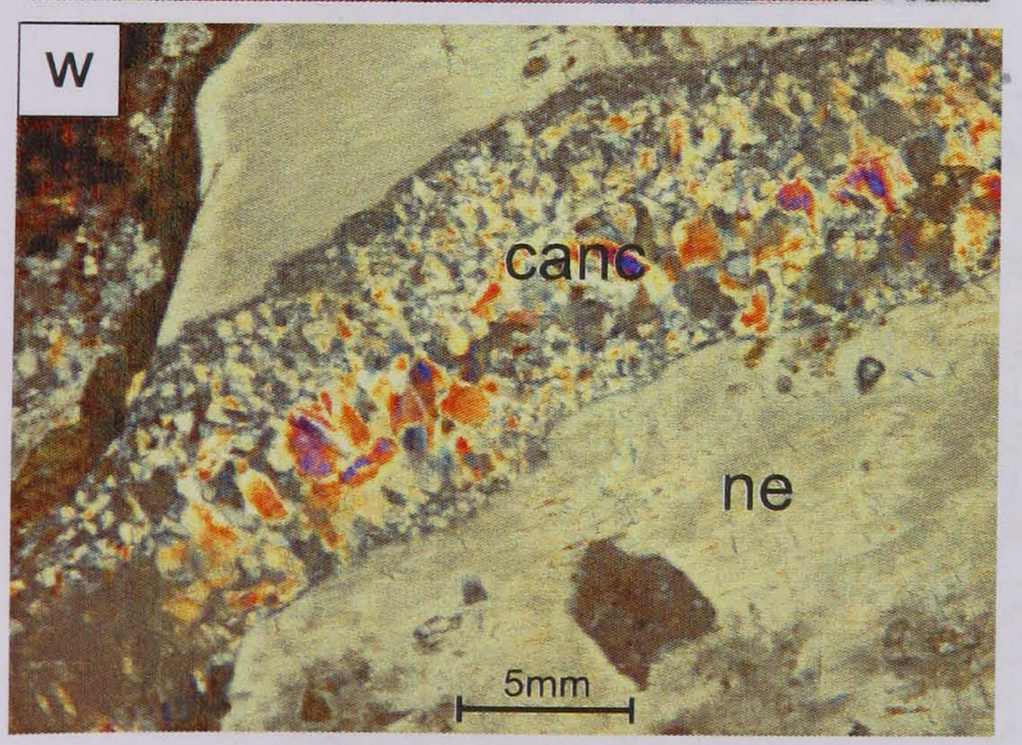

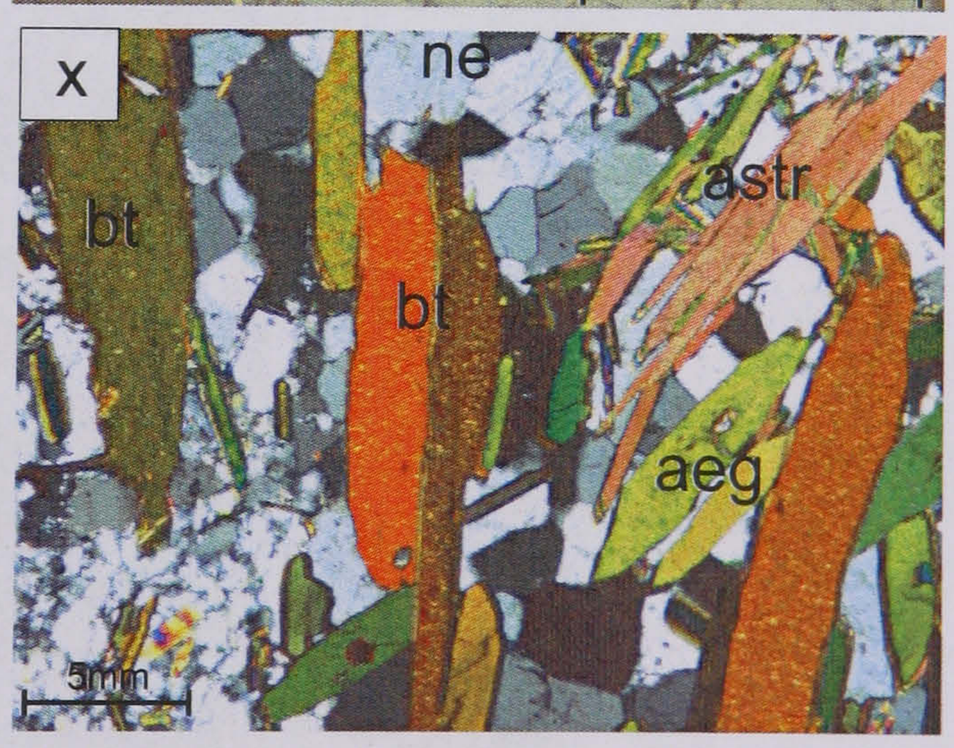

Figure 4.12 continued: (q) Kh-03-10 (rischorrite), titano-magnetite (tit-mag) surrounded by titanite, lorenzenite and aegirine needles. (r) Kh-03-62 (ijolite), magnetite (mag) rimmed by titanite, aegirine and biotite. (s) Kh-03-53 (massive foyaite), typical mineral assemblage of magnetite, amphibole, aegirine, and titanite. (t) Kh-03-1 (khibinite), zeolite (zeo) along nepheline grain boundaries. (u) Kh-03-6 (khibinite), zeolite accumulation next to amphibole. (v) Kh-03-52 (massive foyaite), cancrinite (canc) along nepheline rims. (w) Kh-03-74 (ijolite), cancrinite vein filling. (x) Kh-03-17 (lujavrite) biotite, aegirine and astrophyllite (astr) needles in a matrix of nepheline.

Kh-03-2	titanite	aenigmatite	aegirine	nepheline	K-feldspar
SiO_2	30.06	40.67	51.70	47.24	63.70
TiO_2	39.69	9.91	1.32	0.02	0.00
Al_2O_3	0.13	0.47	1.10	33.06	18.70
Fe_2O_3	0.35	3.20	26.70	0.00	0.24
FeO	0.00	33.66	3.42	1.35	0.00
MnO	0.08	3.53	0.36	0.02	0.00
MgO	0.00	1.17	0.63	0.02	0.00
CaO	25.24	0.29	2.67	0.06	0.00
Na_2O	1.54	7.49	12.28	16.27	1.24
K_2O	0.00	0.00	0.01	2.00	15.50
TOTAL	**97.08**	**100.39**	**100.18**	**100.04**	**99.38**
Si	0.671	5.813	2.106	4.413	2.963
Ti	0.999	1.065	0.061	0.002	0.000
Al	0.003	0.079	0.053	3.640	1.025
Fe^{3+}	0.006	0.000	0.818	0.000	0.008
Fe^{2+}	0.000	4.366	0.116	0.105	0.000
Mn	0.001	0.427	0.012	0.002	0.000
Mg	0.000	0.249	0.038	0.003	0.000
Ca	0.603	0.045	0.117	0.006	0.000
Na	0.067	2.075	0.970	2.946	0.112
K	0.000	0.000	0.001	0.238	0.919
TOTAL	**2.351**	**14.120**	**4.291**	**11.355**	**5.028**
O	**4.000**	**20.000**	**6.000**	**16.000**	**8.000**

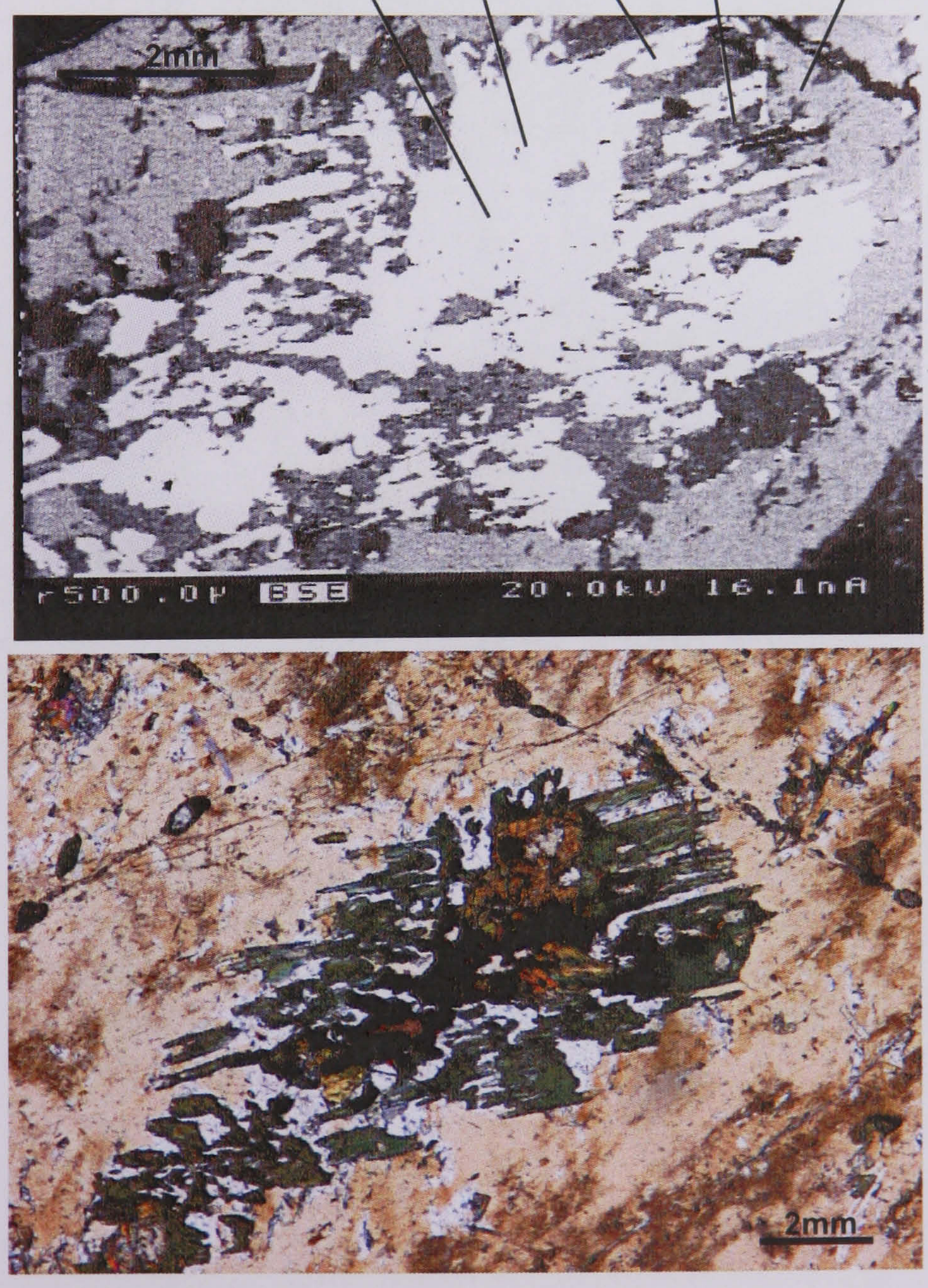

Figure 4.13: SEM analyses, BSE (backscattered electron) image and photomicrograph of titanite, aenigmatite, aegirine, surrounded by nepheline and K-feldspar in sample Kh-03-2.

Kh-03-58	nepheline	aegirine	biotite	aenigmatite	titanite
SiO_2	44.24	51.79	34.91	39.38	29.85
TiO_2	0.02	0.63	3.52	9.72	34.82
Al_2O_3	31.87	1.14	9.87	1.27	0.50
Fe_2O_3	0.00	22.39	9.20	0.00	2.19
FeO	0.70	5.21	20.20	37.70	0.00
MnO	0.00	0.87	2.31	3.42	0.13
MgO	0.00	1.59	5.44	0.99	0.03
CaO	0.01	6.78	0.04	0.23	25.66
Na_2O	16.60	9.81	9.03	0.00	0.71
K_2O	6.13	0.01	0.31	7.59	0.00
BaO	0.00	0.03	0.00	0.00	0.27
TOTAL	**99.57**	**100.26**	**94.82**	**100.28**	**96.37**
Si	4.278	2.096	5.672	5.766	0.703
Ti	0.002	0.029	0.430	1.070	0.926
Al	3.632	0.054	1.891	0.219	0.014
Fe^{3+}	0.000	0.682	0.000	0.000	0.039
Fe^{2+}	0.056	0.176	3.864	4.617	0.000
Mn	0.000	0.030	0.317	0.424	0.003
Mg	0.000	0.096	1.317	0.215	0.001
Ca	0.001	0.294	0.006	0.036	0.648
Na	3.112	0.770	2.844	0.001	0.032
K	0.756	0.001	0.065	1.417	0.000
Ba	0.000	0.001	0.000	0.000	0.005
TOTAL	**11.839**	**4.241**	**16.407**	**13.764**	**2.395**
O	**16.000**	**6.000**	**22.000**	**20.000**	**4.000**

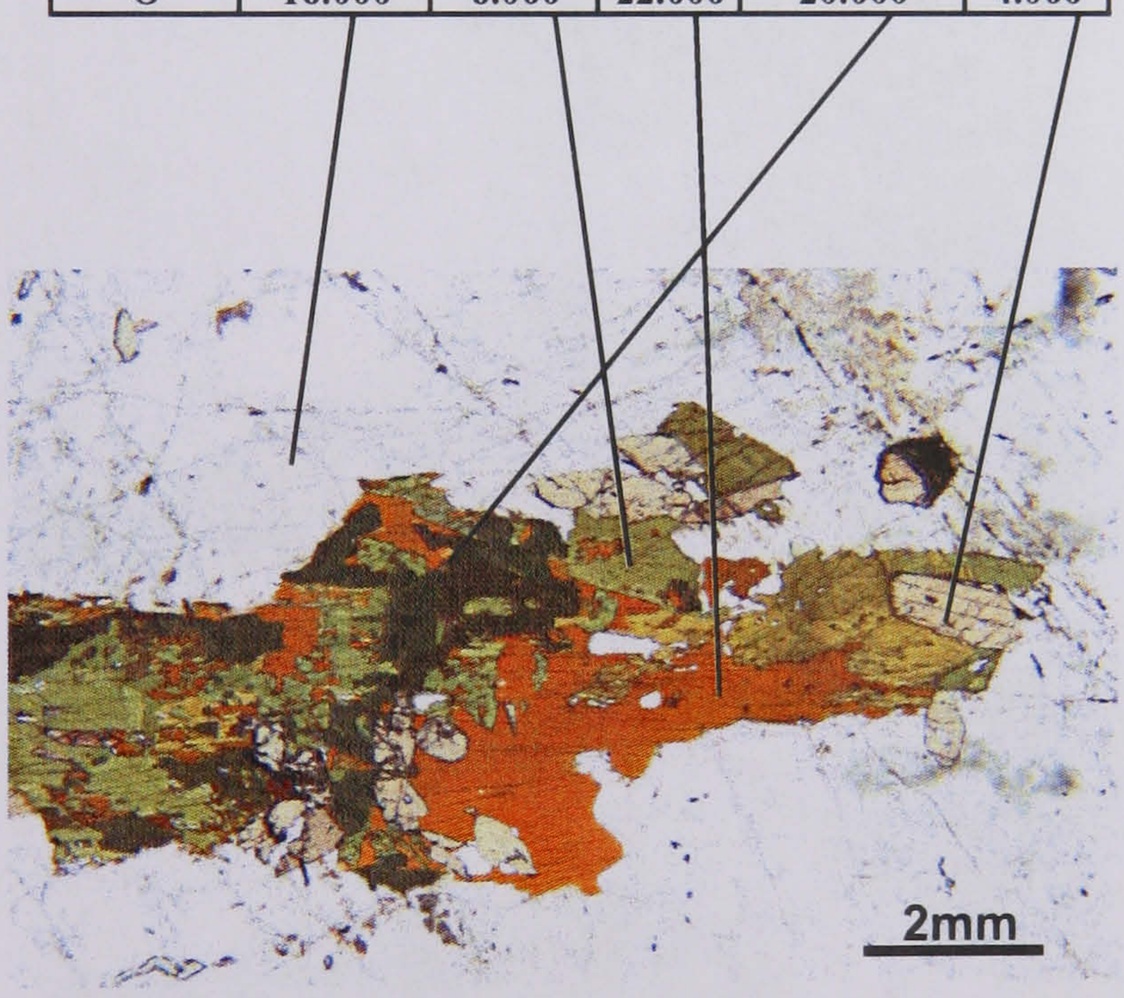

Fig. 4.14: SEM analyses and photomicrograph of a typical mineral assemblage in alkaline syenite (Kh-03-58). The assemblage comprises aegirine, biotite, aenigmatite and titanite surrounded by nepheline.

Kh-03-9	aenigmatite	aegirine	lorenzerite	nepheline	K-feldspar
SiO_2	41.16	51.53	35.09	41.18	64.02
TiO_2	9.69	1.48	46.45	0.01	0.03
Al_2O_3	0.42	1.00	0.06	33.72	17.71
Fe_2O_3	0.00	22.91	0.88	0.00	0.56
FeO	36.48	0.61	0.00	0.75	0.00
MnO	2.67	1.92	0.08	0.00	0.02
MgO	1.49	7.82	0.00	0.01	0.00
CaO	0.07	0.79	0.08	0.00	0.00
Na_2O	7.52	7.53	18.15	16.59	0.41
K_2O	0.02	4.05	0.00	8.13	16.68
TOTAL	**99.52**	**99.64**	**100.79**	**100.38**	**99.43**
Si	5.588	2.062	2.069	4.019	2.996
Ti	1.484	0.067	2.060	0.001	0.001
Al	0.067	0.047	0.004	3.878	0.977
Fe^{3+}	0.000	0.690	0.043	0.000	0.020
Fe^{2+}	4.458	0.021	0.000	0.061	0.000
Mn	0.307	0.065	0.004	0.000	0.001
Mg	0.302	0.466	0.000	0.001	0.000
Ca	0.010	0.034	0.005	0.000	0.000
Na	1.979	0.584	0.001	3.140	0.037
K	0.003	0.207	1.365	1.012	0.996
TOTAL	**14.197**	**4.243**	**5.552**	**12.112**	**5.028**
O	**20.000**	**6.000**	**9.000**	**16.000**	**8.000**

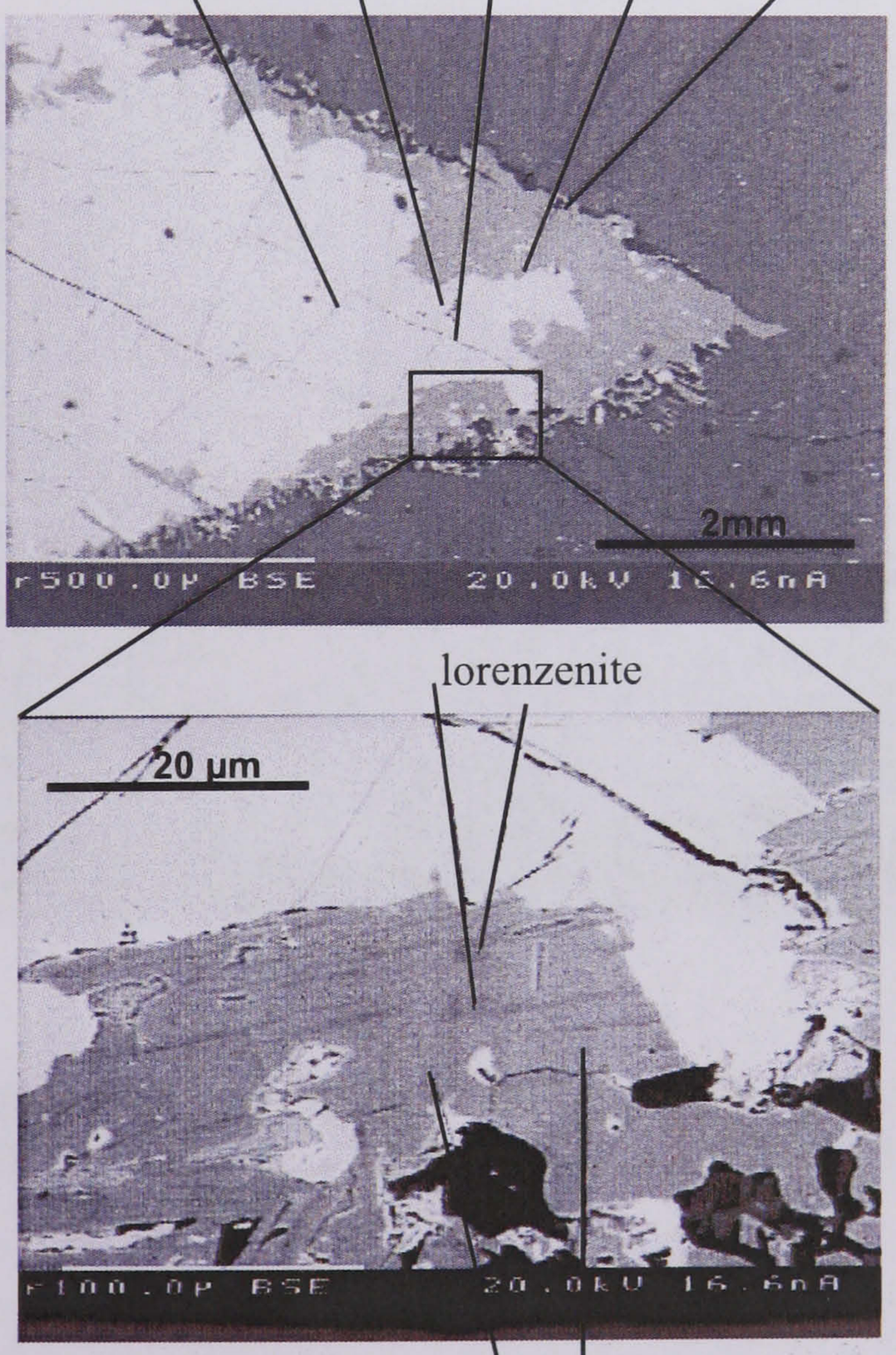

Figure 4.15: SEM images and analyses of aenigmatite which is surrounded by a rim of aegirine and lorenzenite. A small rim of K-feldspar is located between nepheline host mineral and mafic minerals.

Kh-03-9	K-arfvedsonite	K-arfvedsonite	K-arfvedsonite	K-arfvedsonite	K-richterite	K-richterite	K-richterite	K-richterite	Ti-K-richterite	Ti-K-arfvedsonite
SiO_2	50.76	51.12	50.71	50.27	50.77	50.81	51.14	50.90	50.18	50.63
TiO_2	1.52	1.65	1.65	1.84	2.14	2.10	2.20	2.20	2.38	2.45
Al_2O_3	1.12	1.02	1.01	1.26	1.82	1.90	1.83	1.98	2.11	0.99
Fe_2O_3	1.61	2.51	1.05	1.10	0.00	0.00	0.14	0.21	0.30	1.31
FeO	20.48	20.12	21.96	21.63	13.30	13.26	13.34	13.45	15.32	21.81
MnO	1.03	1.00	1.01	1.09	0.62	0.63	0.59	0.66	0.80	1.11
MgO	7.47	7.47	6.82	6.86	13.89	13.78	14.10	13.88	12.35	6.82
CaO	1.37	1.34	1.48	1.76	6.03	6.07	6.11	5.97	5.34	1.59
Na_2O	7.36	7.32	7.44	7.07	5.18	5.01	5.20	5.34	5.68	7.09
K_2O	3.94	3.73	3.69	3.85	3.14	3.12	3.09	3.09	3.21	3.87
TOTAL	**98.59**	**99.24**	**98.75**	**98.65**	**98.90**	**98.68**	**99.76**	**99.71**	**99.70**	**99.61**
Si	7.896	7.887	7.912	7.854	7.592	7.606	7.578	7.558	7.534	7.838
Ti	0.205	0.185	0.186	0.232	0.321	0.335	0.320	0.347	0.373	0.181
Al	0.178	0.191	0.194	0.216	0.241	0.236	0.245	0.246	0.269	0.285
Fe^{3+}	0.189	0.291	0.124	0.129	0.000	0.000	0.015	0.023	0.034	0.153
Fe^{2+}	2.664	2.596	2.866	2.827	1.663	1.660	1.653	1.671	1.923	2.824
Mn	0.136	0.131	0.133	0.144	0.079	0.080	0.074	0.083	0.102	0.146
Mg	1.732	1.718	1.586	1.598	3.096	3.075	3.115	3.073	2.764	1.574
Ca	0.228	0.221	0.247	0.295	0.966	0.973	0.970	0.950	0.859	0.264
Na	2.220	2.190	2.251	2.142	1.502	1.454	1.494	1.537	1.654	2.128
K	0.782	0.734	0.734	0.767	0.599	0.596	0.584	0.585	0.615	0.764
TOTAL	**16.230**	**16.145**	**16.232**	**16.204**	**16.058**	**16.015**	**16.048**	**16.073**	**16.127**	**16.156**
O	**23.000**	**23.000**	**23.000**	**23.000**	**23.000**	**23.000**	**23.000**	**23.000**	**23.000**	**23.000**

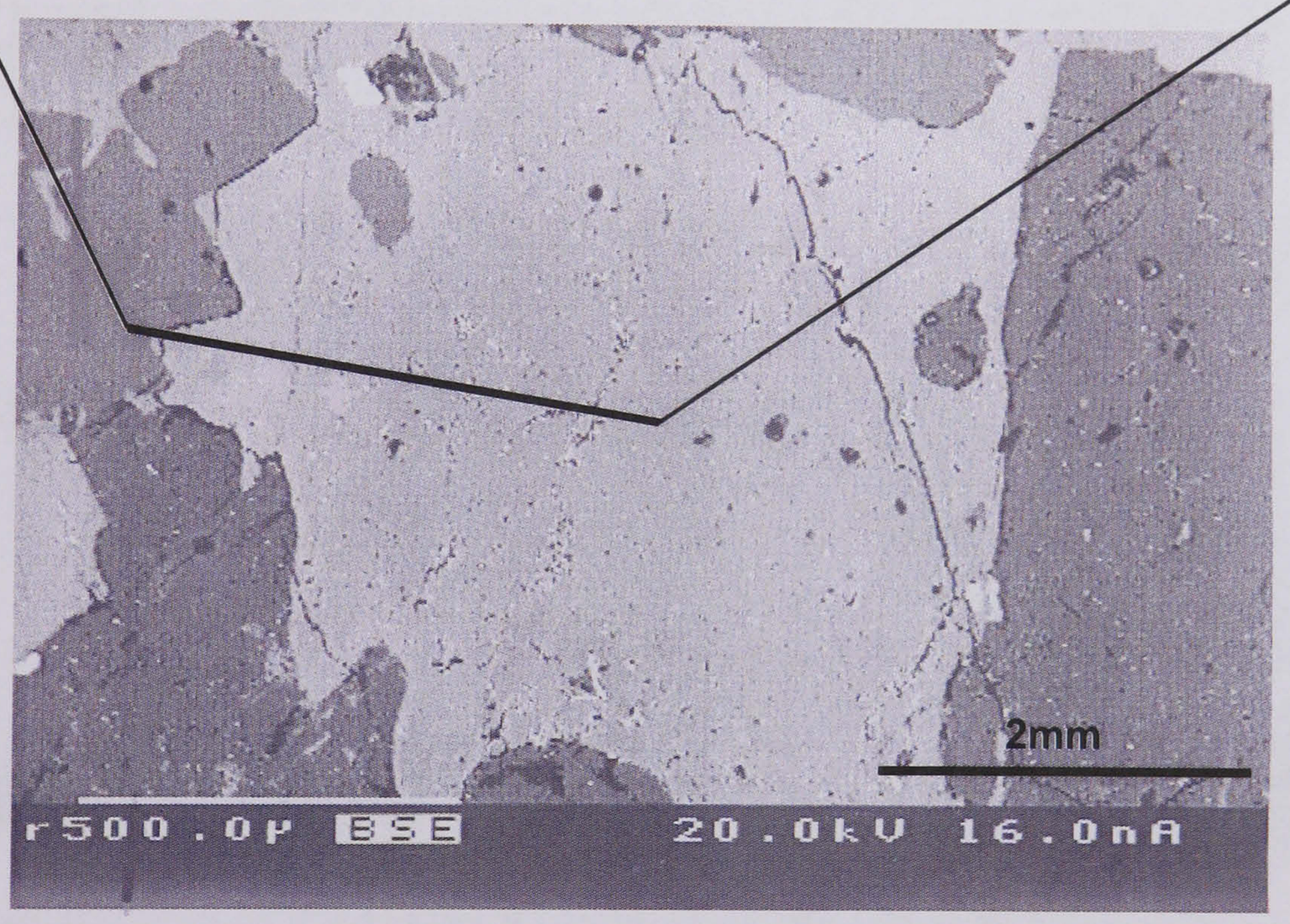

Figure 4.16: Change in amphibole composition from richterite in the core to arfvedsonite at the rim. (sample Kh-03-9).

Kh-03-2	K-Mg-kataphorite	K-Mg-kataphorite	K-Mg-kataphorite	Ca-Mg-arfvedsonite	Na-feldspar	Na-feldspar	K-feldspar	K-feldspar
SiO_2	49.68	49.91	49.99	51.43	69.50	63.75	63.91	65.82
TiO_2	1.91	1.78	2.10	1.74	0.00	0.00	0.06	0.04
Al_2O_3	3.75	3.56	3.88	2.33	18.94	20.75	17.47	18.71
Fe_2O_3	1.47	1.07	1.76	1.38	0.35	0.24	0.50	0.49
FeO	11.91	12.25	11.73	14.25	0.00	0.00	0.00	0.00
MnO	1.00	0.96	0.95	1.23	0.03	0.01	0.02	0.00
MgO	14.01	13.91	13.60	12.10	0.00	0.00	0.00	0.00
CaO	6.89	6.76	5.61	4.16	0.01	0.02	0.00	0.00
Na_2O	5.82	5.85	6.59	7.46	11.97	11.94	0.98	5.70
K_2O	1.59	1.66	1.63	1.57	0.10	0.72	15.63	11.29
BaO	0.08	0.01	0.03	0.00	0.04	0.03	0.26	0.19
TOTAL	**100.15**	**99.75**	**99.91**	**99.67**	**101.10**	**97.53**	**98.93**	**102.44**
Si	7.311	7.370	7.355	7.639	3.013	2.890	3.003	2.958
Ti	0.650	0.620	0.673	0.408	0.000	0.000	0.003	0.002
Al	0.211	0.198	0.232	0.194	0.968	1.109	0.967	0.991
Fe^{3+}	0.163	0.118	0.195	0.154	0.011	0.008	0.018	0.017
Fe^{2+}	1.466	1.513	1.444	1.770	0.000	0.000	0.000	0.000
Mn	0.125	0.120	0.118	0.155	0.001	0.000	0.001	0.000
Mg	3.074	3.062	2.983	2.679	0.000	0.000	0.000	0.000
Ca	1.086	1.069	0.884	0.662	0.001	0.001	0.000	0.000
Na	1.661	1.675	1.880	2.149	1.006	1.050	0.089	0.496
K	0.299	0.313	0.306	0.298	0.006	0.042	0.937	0.647
Ba	0.005	0.001	0.002	0.000	0.001	0.001	0.010	0.007
TOTAL	**16.050**	**16.058**	**16.072**	**16.108**	**5.011**	**5.103**	**5.029**	**5.121**
O	**23.000**	**23.000**	**23.000**	**23.000**	**8.000**	**8.000**	**8.000**	**8.000**

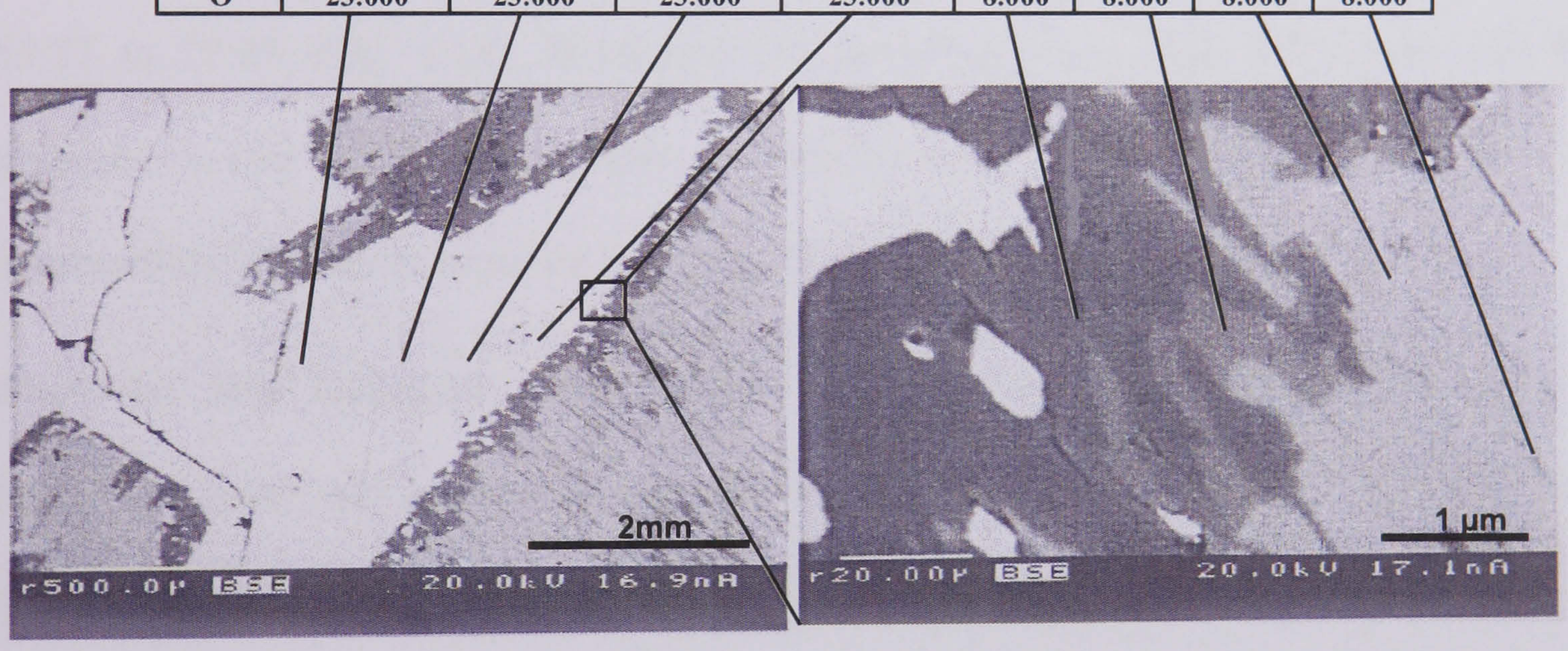

Figure 4.17: SEM analyses of amphibole in khibinite documenting the change in composition from kataphorite in the core to arfvedsonite in the rim. It is surrounded by Na-feldspar rim in K-feldspar (sample Kh-03-2).

4.3.3 Composition of the rock-forming minerals

The chemical composition of the main rock-forming minerals is similar across all the rock types and is therefore not discussed by rock type. Representative microprobe results are presented in Appendix A4.2. The calculation of Fe^{2+}/Fe^{3+} ratios is based on Droop (1987). Additionally, major minerals were confirmed using laser Raman spectroscopy. The specific spectra are shown in Appendix A4.3.

Felsic minerals

Nepheline and alkali feldspar are the most abundant felsic minerals in the Khibiny rocks.

Nepheline show little chemical variation with rock type. The Na:K ratio ranges from 63:37 to 77:23 (Fig. 4.18). Nepheline in rischorrite has a high K:Na ratio and in khibinite a low K/Na ratio. Those in foyaite, lujavrite and alkali syenite have a intermediate Na:K ratio between these two (between 70:30 and 75:25).

Alteration and secondary mineralisation is apparent in nepheline. Cancrinite is frequently found along grain boundaries but also within the minerals. Zeolites have been precipitated as secondary minerals in veins (Fig. 4.12w).

Alkali feldspar is typically perthitic with separate potassium- and sodium-rich endmembers. There is rarely any solid solution. The albite component is essentially potassium-free whereas orthoclase often contains minor sodium (Fig. 4.19). Discrete grains of albite are present, especially in trachytoid foyaite. They are smaller in size than the perthite laths and tend to occupy marginal areas of the perthitic phases. This phenomenon may be due to perthite exsolution accompanied by diffusion of the albite component to the crystal boundaries (Deer *et al.*, 1992).

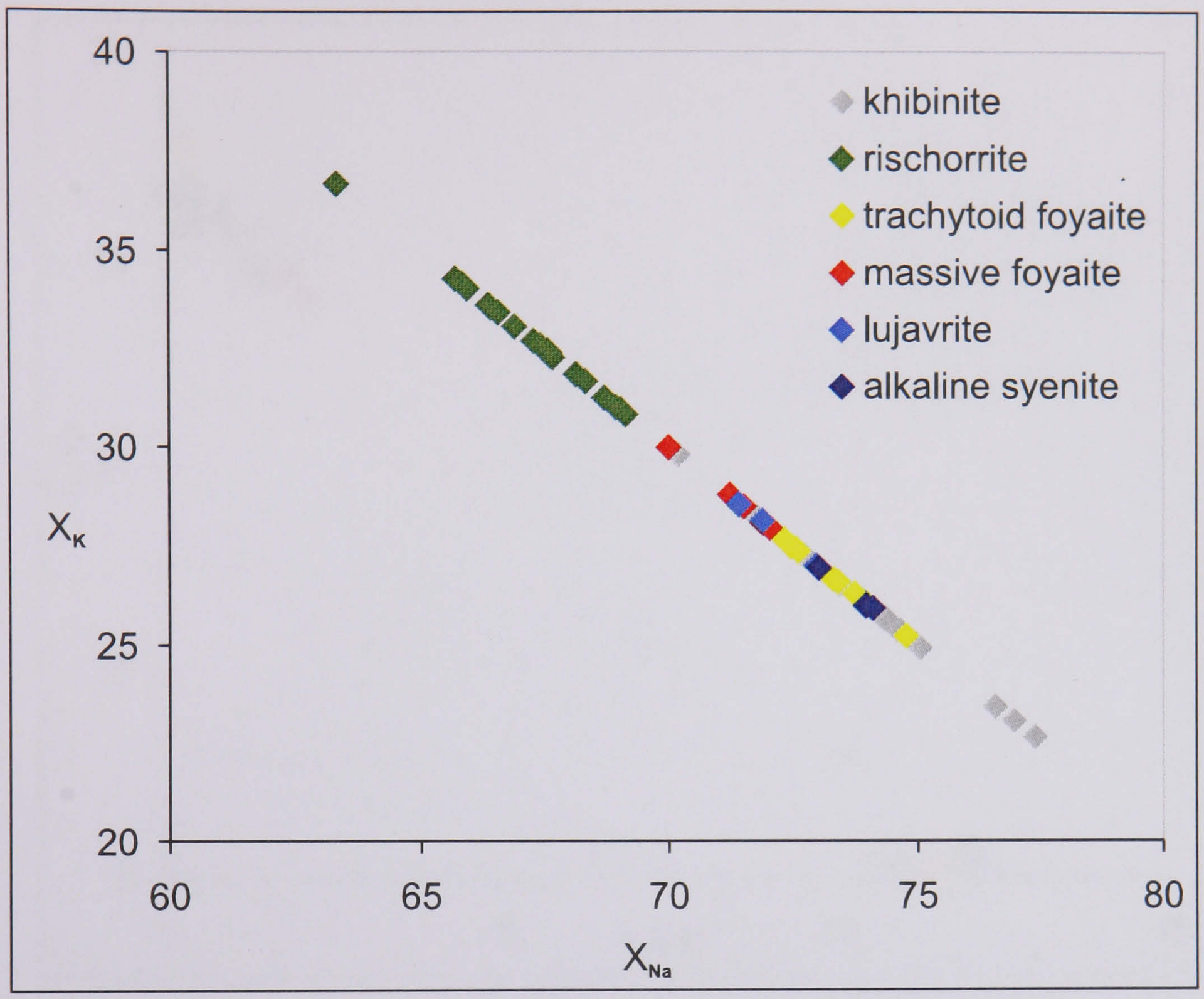

Figure 4.18: Plot of X_{Na} versus X_K in nepheline in different rock types of the Khibiny pluton.

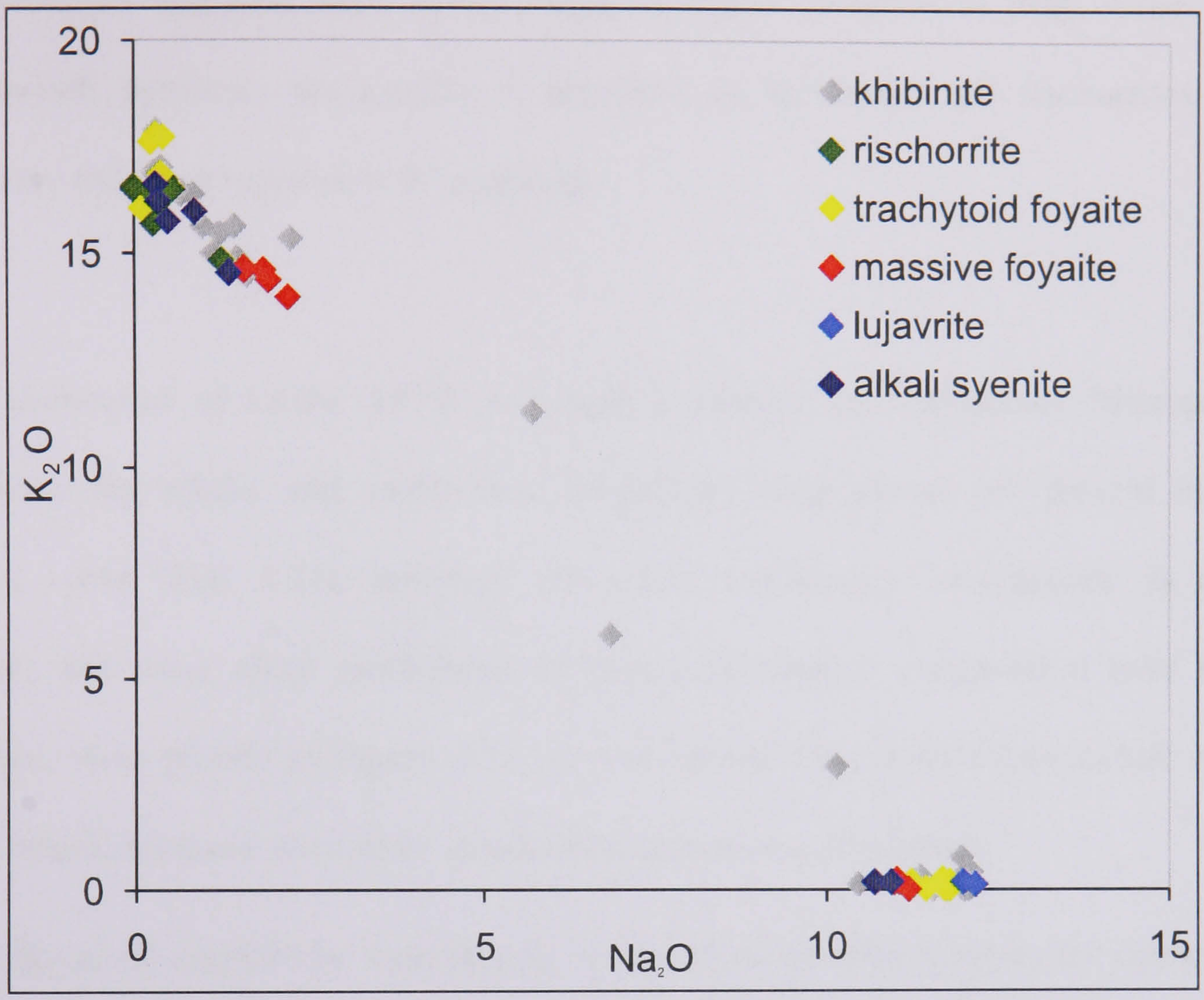

Figure 4.19: Plot of Na_2O versus K_2O in alkali feldspar from in different rock types of the Khibiny pluton.

Mafic minerals

Clinopyroxenes are the most common mafic phases in all the rock types investigated. The pyroxenes analysed have mainly aegirine augite composition (Fig. 4.20). The titanium-rich pyroxene aenigmatite is abundant in khibinites and rischorrites and commonly observed together with nepheline.

The classification of Leake (1978) was used to classify the amphiboles. Microprobe data show that alkalic and sodic-calcic amphibole compositions are present in the Khibiny rocks (Fig. 4.21). Amongst the alkali amphiboles, arfvedsonite is most common, but some alkali amphiboles of ferro-eckermannite composition have been identified. Also plotted in Figure 4.21 are microprobe data from Yakovenchuk *et al.* (2001) which, with one exception, are all of arfvedsonite composition.

The sodic-calcic amphiboles represent the intermediate position between the calcic and alkali amphiboles. Of the sodic-calcic amphiboles, katoporite is identified in khibinite rocks. The amphiboles analysed in rischorrite rocks show a wide variety of compositions from contains ferro-richterite to magnesio-taramite. Both alkali and sodic-calcic amphibole compositions occur often in the same mineral. A detailed study of individual crystals show that the amphibole composition changes from core to rim. In many cases amphiboles are zoned with sodic-calcic composition in the core and alkali composition in the rim (Fig. 4.16 and 4.17). This suggests that the magma composition changed during amphibole crystallisation; Mg, Ca depletion coincided with Na, K enrichment.

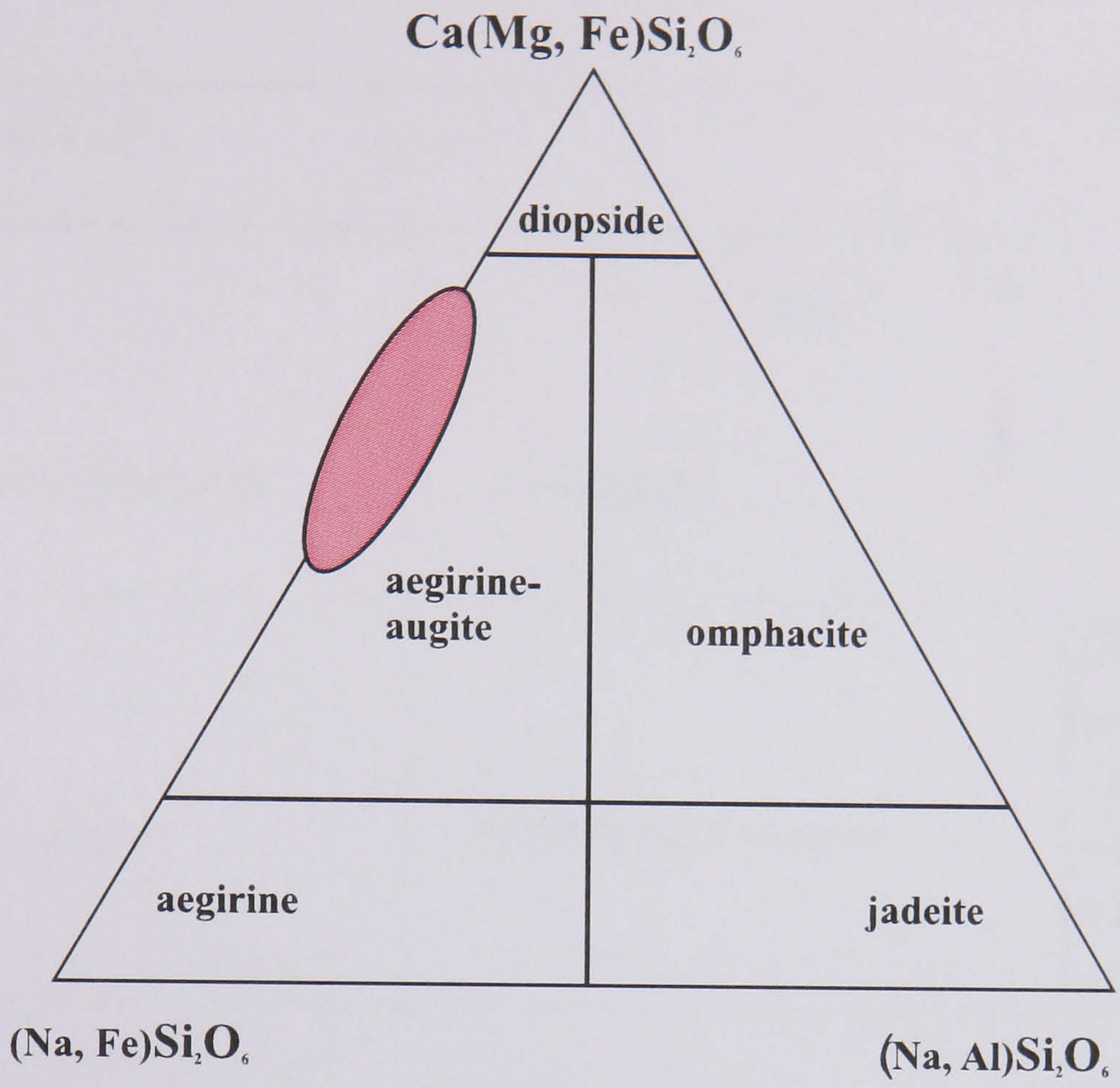

Figure 4.20: Triangular plot showing the compositional range of pyroxenes in the analysed samples of the Khibiny complex.

Alkali amphibole

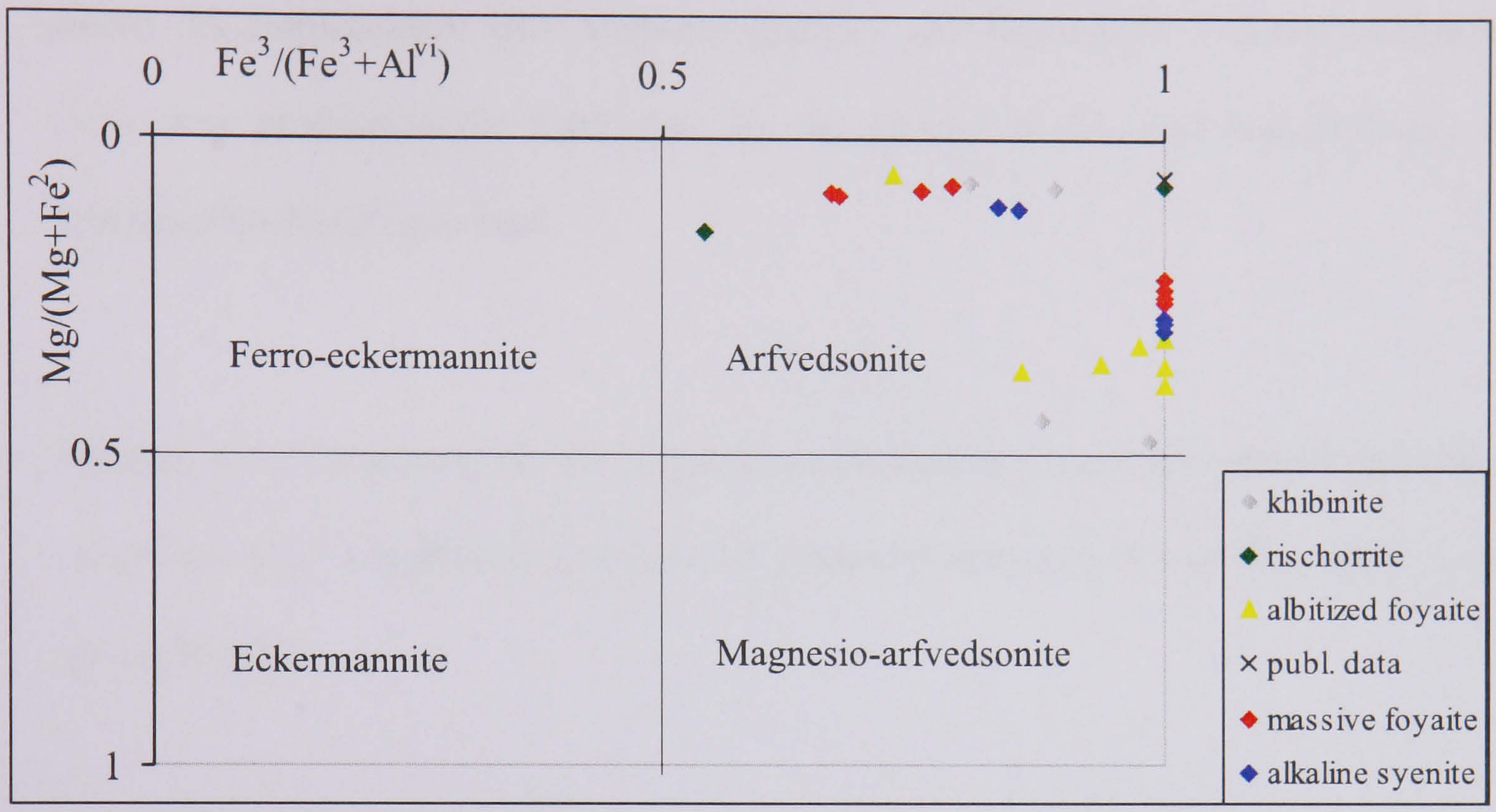

Sodic-calcic amphibole

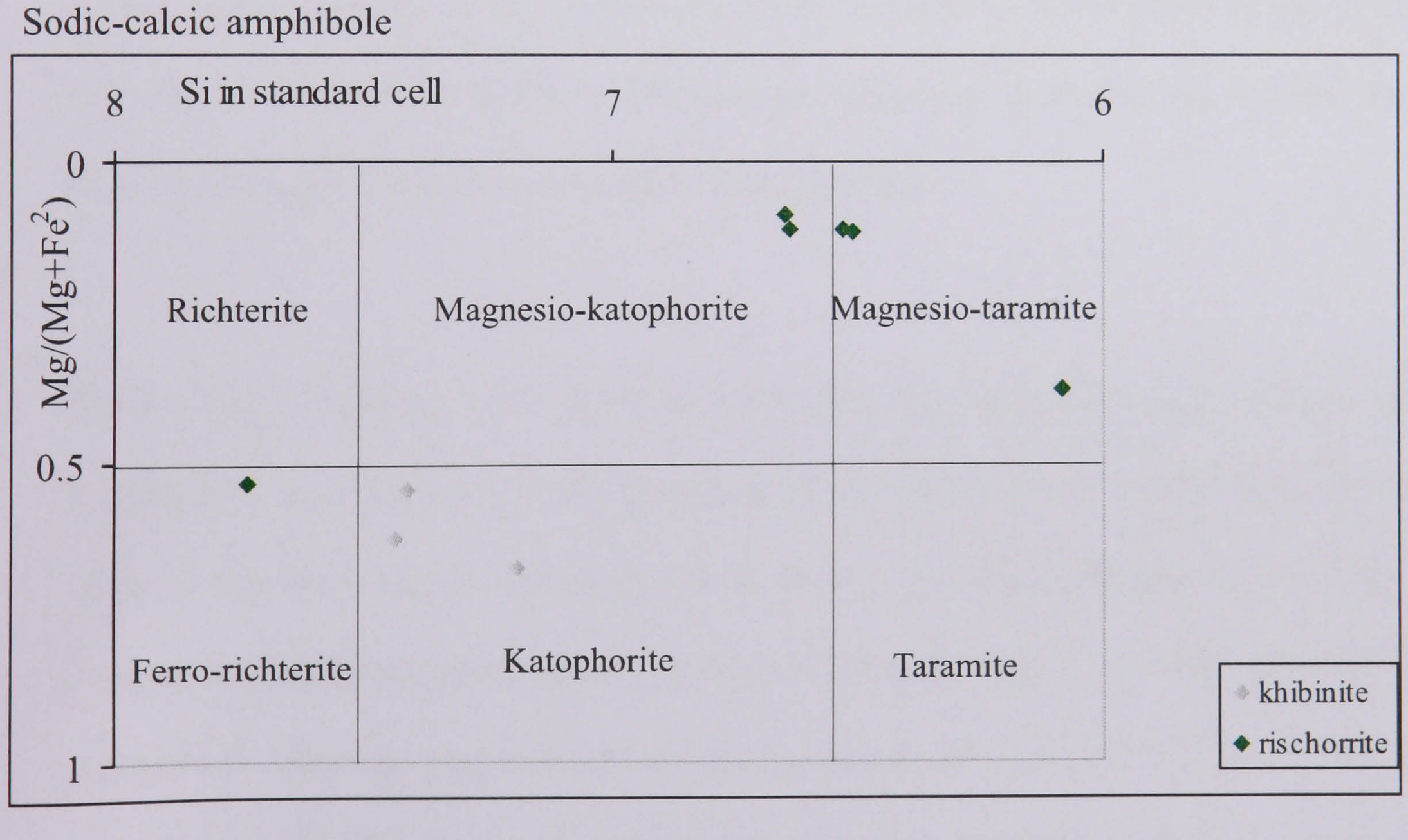

Figure 4.21: Amphibole compositions for different rock types plotted according to the scheme of Leake (1978). Published data are from Yakovenchuk *et al.* (2001).

4.4 Summary

The largest alkaline intrusion of the Kola Alkaline Province is the Devonian Khibiny pluton. Its emplacement into Archaean gneisses and Proterozoic volcano-sedimentary rocks was predominantly controlled by the rifting of the Kontozero-Khibiny and Kandalashka-Kontozero fault.

The pluton was emplaced in several phases and exhibits a horseshoe-shaped structure. It comprises mainly nepheline syenites and minor occurrences of foidolite, alkali syenite and carbonatite.

Typical felsic minerals in all investigated rocks are nepheline and alkali feldspar. The main mafic minerals are aegirine, arfvedsonite, aenigmatite, titanite and biotite. They often occur together interlocked as mineral assemblages.

The previously reported association between alteration and replacement reactions and hydrocarbon generation could not be proved on the basis of the samples studied here. Textural data show that the development of mafic mineral assemblages is the result of changes in magma chemistry during cooling and the product of late-stage alteration or replacement reactions. Hydrocarbon generation during these stages, however, could not be confirmed. Cracks, cleavages and intercrystal spaces of mafic minerals and hydrated Na/K silicates, were mostly fluid inclusion free and there is also no notably higher fluid inclusion concentration in the surrounding areas. Primary fluid inclusions occur mainly in nepheline whereas secondary fluid inclusions occur in microcracks that penetrate through nepheline and alkali feldspar. Although alteration processes cannot be excluded

as a mechanism for hydrocarbon generation, this study finds no clear petrographical evidence for it. This is discussed in more detail in Chapter 10.

5 Carbon occurrence in the Khibiny intrusion

5.1 Introduction

Carbon is present within the Khibiny alkaline complex not just in the form of hydrocarbon gases, but also as dispersed bitumens, solid organic matter, graphite and carbonatite (Nivin *et al.*, 2005). The characteristics of hydrocarbon gases are described elsewhere in this thesis. In this chapter data are summarised that pertain to the origin of the solid organic matter in the Khibiny complex. This includes a literature review on solid carbon data from the Khibiny complex and the presentation of a preliminary data set of carbon contents from Khibiny rocks. These data possibly indicate a relationship between carbon and hydrocarbon occurrence and help in developing a model for hydrocarbon generation in the alkaline igneous rocks of the Khibiny pluton.

5.2 Literature review

5.2.1 Bitumen, organic matter and graphite in the Khibiny pluton

Bituminous matter and organic carbon are present in all intrusive rocks of the Kola Peninsula (Petersilie, 1964). Nivin *et al.* (2005) published the following data on carbon content for the Khibiny complex. The total content of reduced carbon in the rocks averages 0.04 wt% but concentrations as high as 0.1 wt% are present in hydrated ijolite-urtites. Minerals in pegmatites and hydrothermal veins contain up to 2.1 wt% carbon.

Carbon in the form of dispersed bitumens has been found in concentrations between 0.0001 and 0.001 wt% by Pripachkin *et al.*, (1985) and Sokolov and Chukanov (unpublished). According to Petersilie (1964) their compositions do not differ from the

disseminated bitumens of sedimentary rocks in petroleum- and gas-bearing provinces. They contain paraffins, naphtalenes and aromatic hydrocarbons and are therefore regarded as bitumens of naphtoid type (Petersilie and Sørensen, 1970). This indicates that their cycle of formation probably spanned the temperature range of 100 to 600°C, from the thermally stable oxygen compounds to the least stable paraffinic hydrocarbons. Petersilie (1962) described the dispersed bitumens as being relatively evenly distributed but that rocks that contain larger amounts of gas are also rich in bitumens. He therefore concluded a definite relationship between hydrocarbon gases and bituminous matter.

Electron fraction studies and spectroscopic studies of bitumens from the igneous complexes of the Kola Peninsula reveal that they contain esters of carboxylic acids and other organic substances, that indicate two possible origins for them (Petersilie, 1962). They were either introduced by distillation of organic matter from the sedimentary rocks of the Imandra-Varzuga series or formed during emplacement of alkaline melts. Petersilie (1962) suggested that they are most likely to be formed syngenetically along with the hydrocarbon gases and the host minerals.

Pure graphite has been described by Nivin *et al.* (2005) as occurring as dispersed matter or as large radial aggregates in albitised nepheline syenites, pegmatites and hydrothermal veins. There is no information on their possible origin in the literature.

5.2.2 Carbonatites in the Khibiny pluton

The carbonatite stock that crops out in the eastern part of the complex is about 1 km in diameter and extends to a depth of >1600 m. It is cut by several dykes and veins (Nivin *et al.*, 2005). The carbonatite contains calcite in association with albite, biotite and aegirine. Detailed information can be found in Dudkin (2001). Geochemical and isotopic data suggest a synchronous extraction of the parental carbonatite and nepheline syenite magmas but different mantle sources (Kramm and Kogarko, 1994). The rocks

also show some degree of crustal contamination (Zaitsev *et al.*, 1997). Fluid inclusions in the carbonatite are rich in CO_2 and H_2O (Potter, 2000).

5.3 Solid carbon data of this study

5.3.1 Methods

Three methods have been employed to characterise the solid carbon content in rock samples of the Khibiny pluton:

- total, organic and carbonate carbon content were analysed by elemental analysis using a Vario EL III instrument (CHNOS-Elementaranalysator);
- total carbon were thermogravimetically analysed using a Mettler TG analyser;
- identification of carbon in the form of graphite was done by laser Raman spectroscopy.

Elemental carbon analysis

The CHNOS-Elementaranalysator Vario EL III (Fa. Elementar) at the Alfred-Wegener-Institute in Potsdam was used to determine the partial content of carbon in powdered rock samples. A nominal of 5 mg sample material was placed into a tin capsule; the capsule was closed by folding and then injected into a combustion chamber. At 1300°C the sample was evaporated in an oxygen-rich environment by catalytic tube combustion. Using a He-carrier gas, the oxidized gas mixture was transported through the system to separate different oxidised gas species. C was separated and measured in the form of CO_2 by a thermal conductivity detector cell.

The organic carbon content was measured by the same technique but previous removal of carbonate. For this purpose, the sample was placed into a silver capsule, moistened

with concentrated ethanol and spiked with hydrochloric acid (HCl, 10 %). This caused the removal of all carbonate in the sample by the reaction:

$$X\,CO_3 + 2\,HCl \rightarrow CO_2 + H_2O + X^{2+} + 2\,Cl^- \qquad \text{(R 5.1)}$$

which was visible through the CO_2 gas release (gas bubbles). Spiking with HCl was continued until gas release ceased. Samples were then placed onto a heating plate for 12 hours to dry at about 70°C and after closing of the capsules analysed. The calculated difference of total and organic carbon content results in carbonic carbon content. Standard reference material and internal laboratory standards were analysed using the same preparation procedure as the investigated samples and the absolute error was estimated to be less than 10 %.

Thermogravimetry

The loss of *in situ* moisture (typically up to 200°C) and volatile organic matter (up to 600°C) was measured thermo-gravimetrically. Measurements were performed in a Mettler TG analyser in the School of Pharmacy and Chemistry at Kingston University. Powdered samples of approximately 20 mg weight were dried at 110°C to remove adhesive water that might distort the results. The sample was then placed onto a scale and heated at a rate of 20°C per minute to 700°C in a closed system. The resulting weight loss of the sample was simultaneously detected and plotted against temperature.

Laser Raman spectroscopy

Solid carbon in the form of graphite was also detected in fluid inclusion wafers using the laser Raman microprobe. A detailed description of the method can be found in Chapter 6.

5.3.2 Results

Carbon content analysed by elemental analyses

Results of elemental carbon analyses from a number of rock samples are shown in Table 5.1. and illustrated in Fig. 5.1. Values of total carbon content range from 0.209 wt% to 0.058 wt% and their average is 0.113 wt%. These are similar to values obtained for organic carbon which ranges from 0.205 to 0.064 wt%. The content of carbonate carbon, calculated as the difference between total and organic carbon, is therefore in the range from 0.026 to 0.003 wt%. These results show that most of the solid carbon in the rocks is contained as organic material in the form of bitumen and solid organic matter or as graphite.

There are very few data available in the literature on carbon contents in the Khibiny alkaline complex. Petersilie (1962) quotes an organic carbon content of 0.14 wt%. This value is in good agreement with the data produced by this study.

		content in wt%						
sample	rock type	C total (1)	C total (2)	average C total	Corg (1)	Corg (2)	average C org	average C carb
Kh-03-4	khibinite	0.110	0.111	0.111	b.d.	b.d.	b.d.	b.d.
Kh-03-5	khibinite	0.228	0.189	0.209	0.205	0.205	0.205	0.004
Kh-03-14	rischorrite	0.093	0.096	0.095	b.d.	b.d.	b.d.	b.d.
Kh-03-48	rischorrite	0.135	0.121	0.128	0.085	0.121	0.103	0.025
Kh-03-23	lujavrite	0.107	0.100	0.104	0.069	0.087	0.078	0.026
Kh-03-36	trachytoid foyaite	0.109	0.126	0.118	0.102	0.095	0.099	0.019
Kh-03-53	massive foyaite	0.139	0.136	0.138	0.131	0.139	0.135	0.003
Kh-03-54	massive foyaite	0.088	0.083	0.086	b.d.	b.d.	b.d.	b.d.
Kh-03-56	alkaline syenite	0.081	0.075	0.078	0.072	0.062	0.067	0.011
Kh-03-60	alkaline syenite	0.075	0.071	0.073	0.068	0.059	0.064	0.009
Kh-03-67	ijolite	0.055	0.060	0.058	b.d.	b.d.	b.d.	b.d.
Kh-03-U7	apatite-nepheline ore	0.169	0.149	0.159	0.122	0.156	0.139	0.020

Table 5.1: Content of total carbon (C total), organic carbon (C org) and carbonate carbon (C carb) in wt% in selected samples from the Khibiny pluton. All analyses were repeated (indicated with 1 and 2) and the average values determined. The carbonate carbon is calculated as the difference between total carbon and organic carbon. b.d.=below detection limit (less than 0.100 wt%).

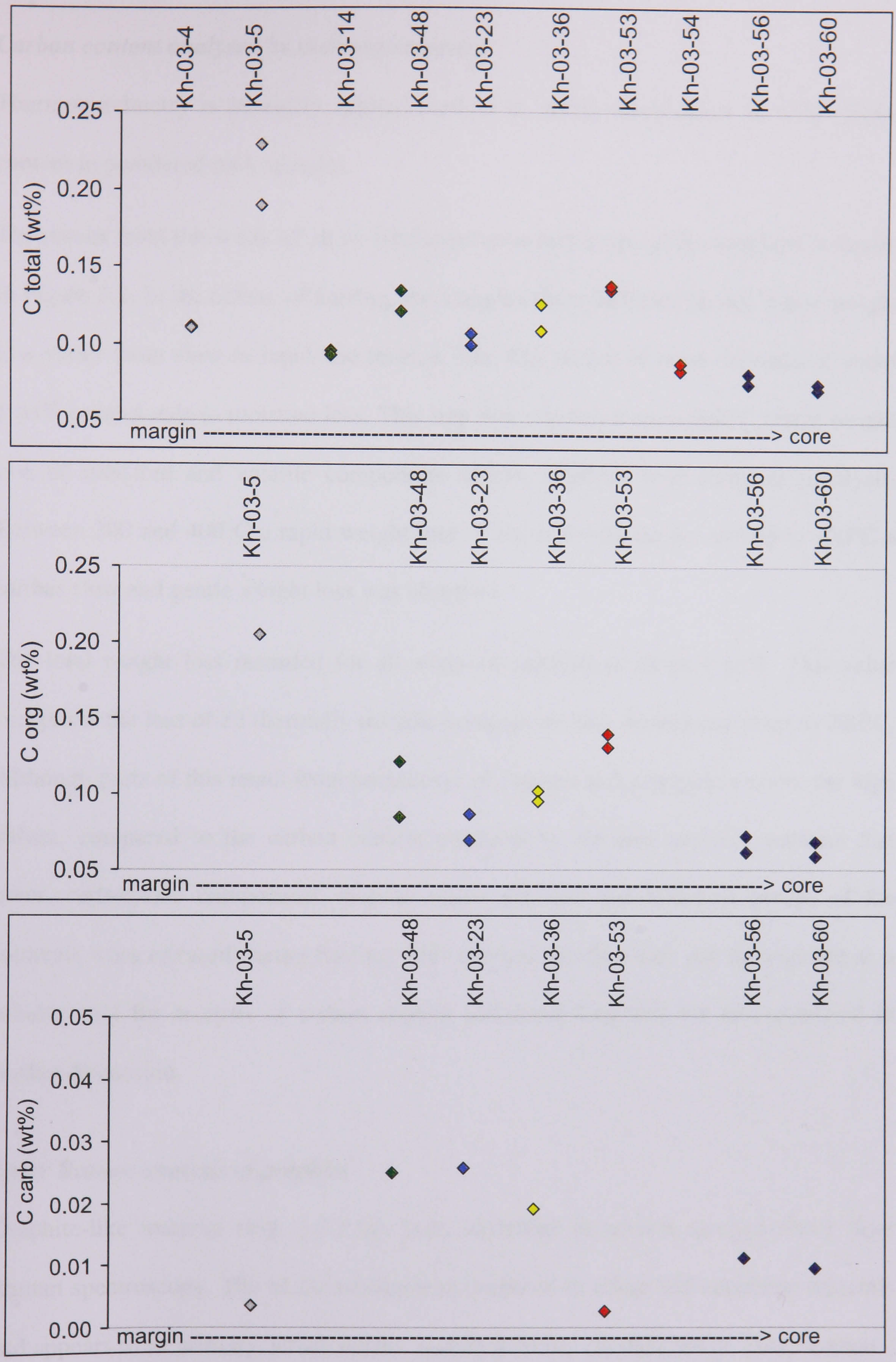

Figure 5.1: Content of total carbon, organic carbon and carbonate carbon in selected samples of the Khibiny complex. Different rock types are indicated by colour (grey - khibinite; green - rischorrite; blue - lujavrite; yellow - trachytoid foyaite; red - massive foyaite; dark blue - alkaline syenite) and arranged from margin to core.

Carbon content analysed by thermogravimetry

Thermogravimetry is an easily applied method to obtain information on total carbon content in powdered rock samples.

The results from this study all show similar patterns and a typical thermograph is shown in Figure 5.2. In the course of heating, the samples show different phases where weight loss varies from slow to rapid and reverse. The first period of mass decrease of about 1 wt% corresponds to moisture loss. This step was registered up to 200°C where weight loss of moisture and volatile components almost overlaps with incipient pyrolysis. Between 200 and 400°C a rapid weight loss of about 1 wt% occurs and up to 700°C a further slow and gentle weight loss was observed.

The total weight loss recorded for all analysed samples is about 4 wt%. This value comprises the loss of all thermally instable components that decompose at up to 700°C. Although parts of this result from breakdown of organic and inorganic carbon, the high values, compared to the carbon content obtained by element analysis, indicate that other, carbon-free components such as water, fluorine and hydroxyl groups of the minerals were released during heating. This method can therefore not be regarded as a reliable tool for analysis of carbon content and these data will not be considered in further discussion.

Laser Raman analysis of graphite

Graphite-like material (Fig. 5.3.) has been identified in several samples using laser Raman spectroscopy. The black substance is occluded in albite and nepheline minerals and appears to be primary, which means, included during crystal growth. Small carbon

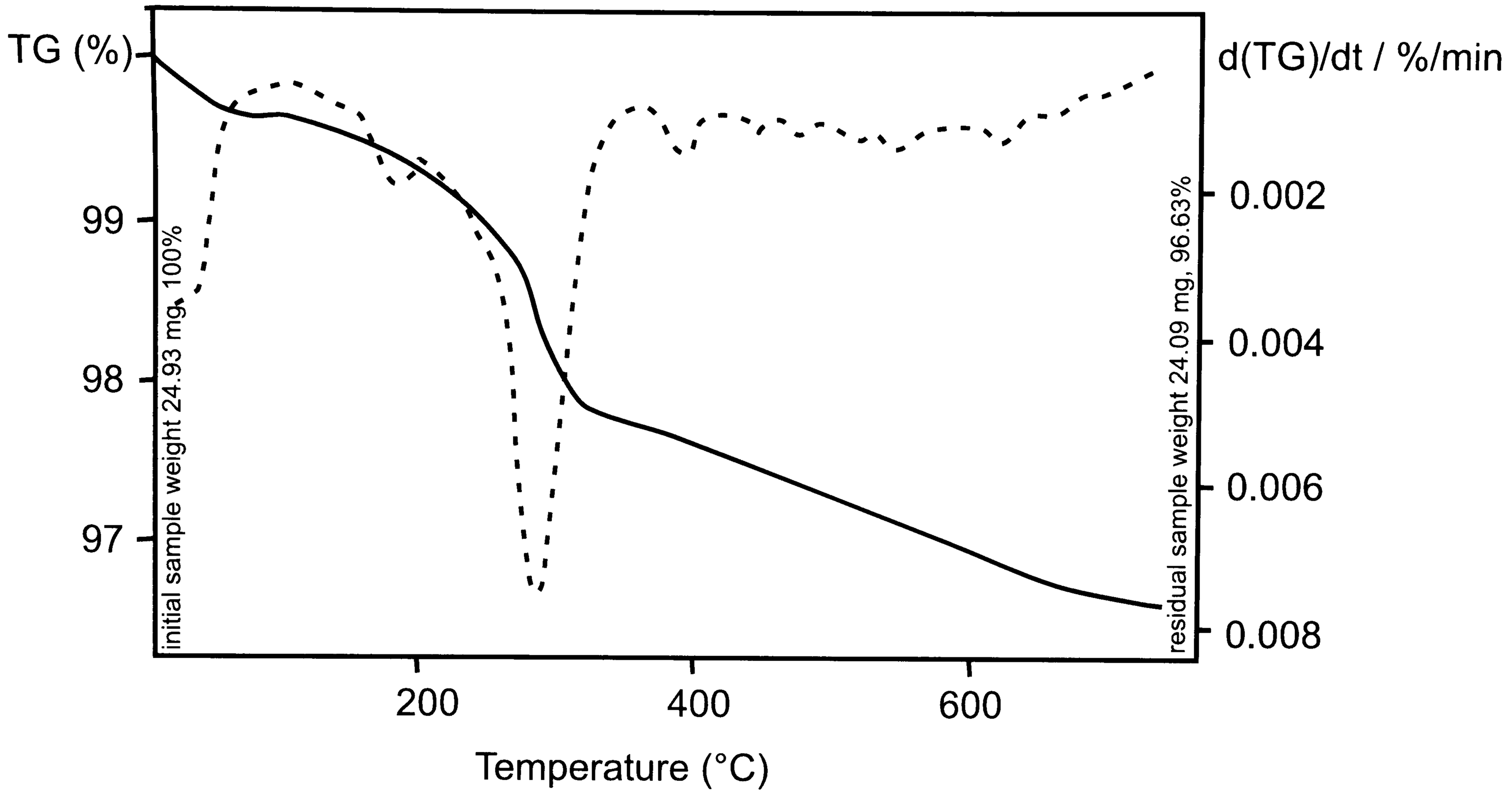

Figure 5.2: Record of a typical thermograph (TG) that plots sample weight loss in % versus temperature. The initial weight of the sample at room temperature was 24,93 mg (100 %). At the end of the experiment, at 700°C, 24.09 mg (96.63 %) sample remained. The weight loss gradient is best illustrated using its change with time in form of the first derivate d(TG)/dt drawn as dashed line. It highlights the strong weight loss below 100°C and at about 300°C.

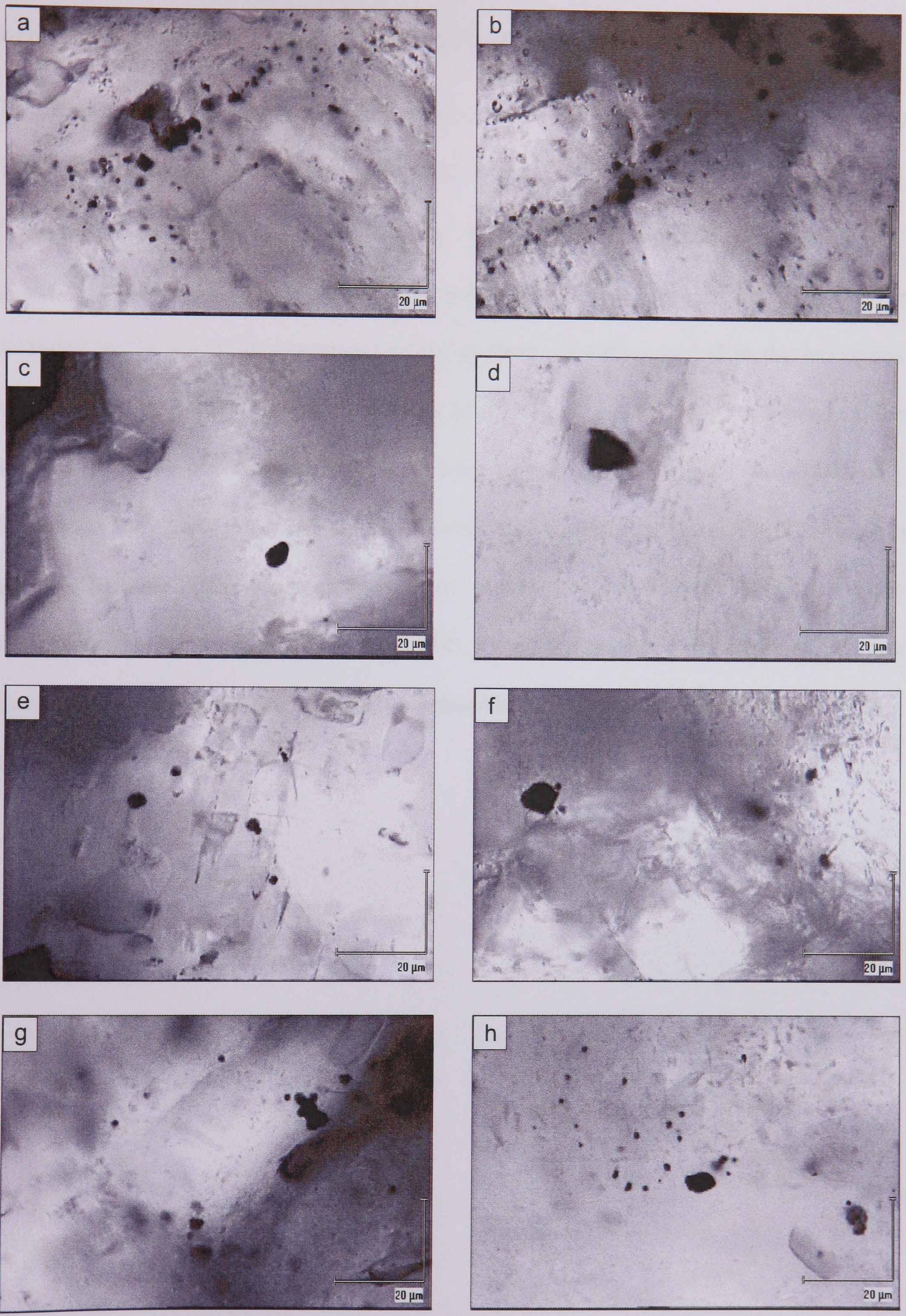

Figure 5.3: Graphite occurrence in the Khibiny pluton. Image a and b show secondary trapped graphite along filled veins in sample Kh-03-50. Graphite is also found as individual aggregation, shown in images c (Kh-03-40), d (Kh-03-46), e and f (both Kh-03-44) or as dispersed accretions within minerals, exemplarily shown in images g and h of sample Kh-03-35. The association to fluid inclusions is often (as seen in b and d), but not always apparent.

particles were also found along healed microcracks. These are of secondary nature and were emplaced after crystallisation and cooling of the Khibiny pluton.

The Raman spectral profiles show bands typical for graphite crystals at or near 1356 cm^{-1}, 1585 cm^{-1}, 2448 cm^{-1}, 2711 cm^{-1}, 2963 cm^{-1}, 3248 cm^{-1} and 4303 cm^{-1} (Fig. 5.4). The peaks at 1585 cm^{-1} and 1350 cm^{-1} are commonly designated as the G and D1 peaks, respectively. The G mode, which is described in the literature at 1582 cm^{-1}, is assigned to "in plane" displacement of the carbons strongly coupled in the hexagonal sheets of the graphite structure (Jawhari *et al.*, 1995). When disorder is introduced into the entire graphite structure, additional lines appear at 1357, 2450 and 3250 cm^{-1} (Guedes, 2005; Jawhari *et al.*, 1995; Pasteris and Wopenka, 1991). The S1 mode at about 2700 cm^{-1} has been attributed to overtone or scattering related to three dimensional ordering (Lespade *et al.*, 1984). The broad Raman peak detected in some samples at about 4300 cm^{-1} is not described in the literature and its cause remains unknown.

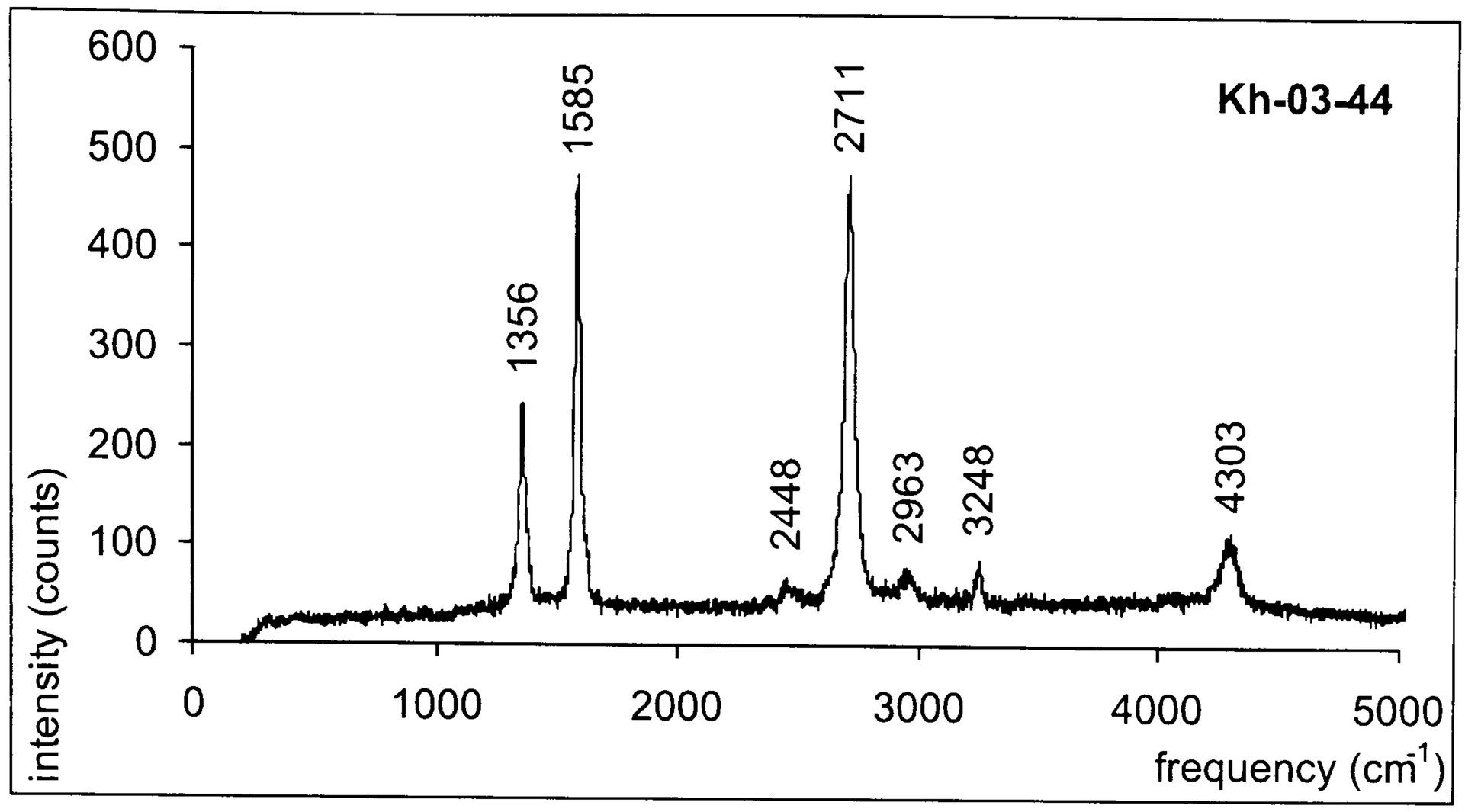

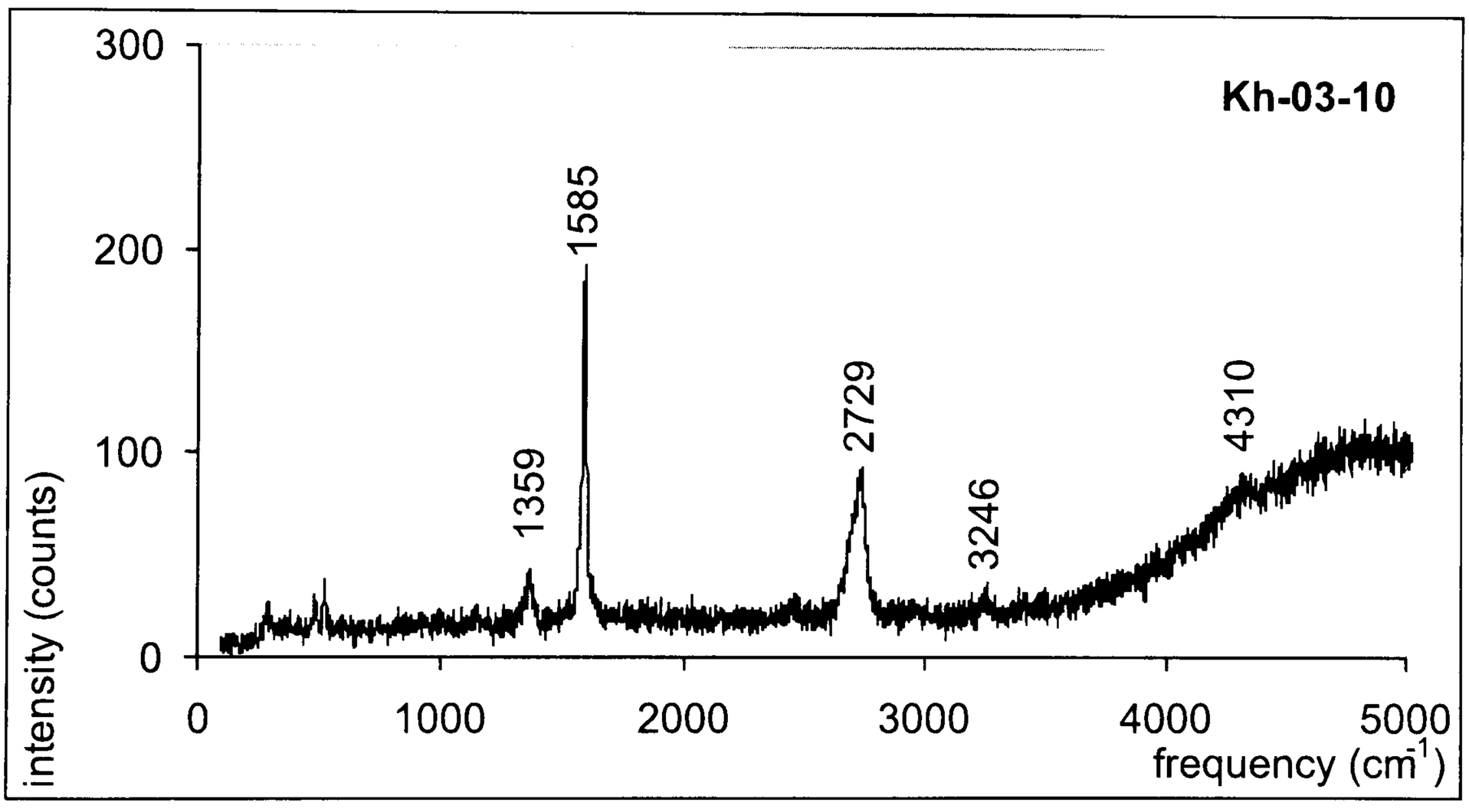

Figure 5.4: Typical graphite spectra obtained by laser Raman spectroscopy. See text for description.

5.3.3 Discussion

Spatial distribution of solid carbon

The spatial distribution of total carbon from margin to core is inhomogeneous but shows a slight tendency to decreasing values towards the core (Fig. 5.5). This pattern is similar to that observed for the hydrocarbon gas content in the Khibiny pluton (Chapter 7) and confirms the relationship between solid carbon and gaseous hydrocarbon occurrence reported by Petersilie (1962). There are two possible explanations for it:

1. The distribution implies influence from host rock-originated organic matter, which, in the course of magma emplacement, was thermogenically transformed to bitumen or kerogen and methane (Hunt, 1995) and incorporated into the magma body.

2. The solid carbon is a product of respeciation of gaseous hydrocarbon in a late- or post-magmatic state that caused precipitation of solid carbon. A high concentration of gaseous hydrocarbons should be accompanied by abundant precipitated solid carbon.

Graphite origin

Graphitisation of organic matter is a function of temperature and pressure. Well-ordered graphite develops in nature from about 350 to 700°C at 0.2 to 0.6 GPa (Tagari and Oba, 1986). This might be prevailed during pluton emplacement where host-rock material was heated and partly incorporated into the plutonic material. This explanation is consistent with the spatial distribution of total carbon as shown in Fig. 5.5.

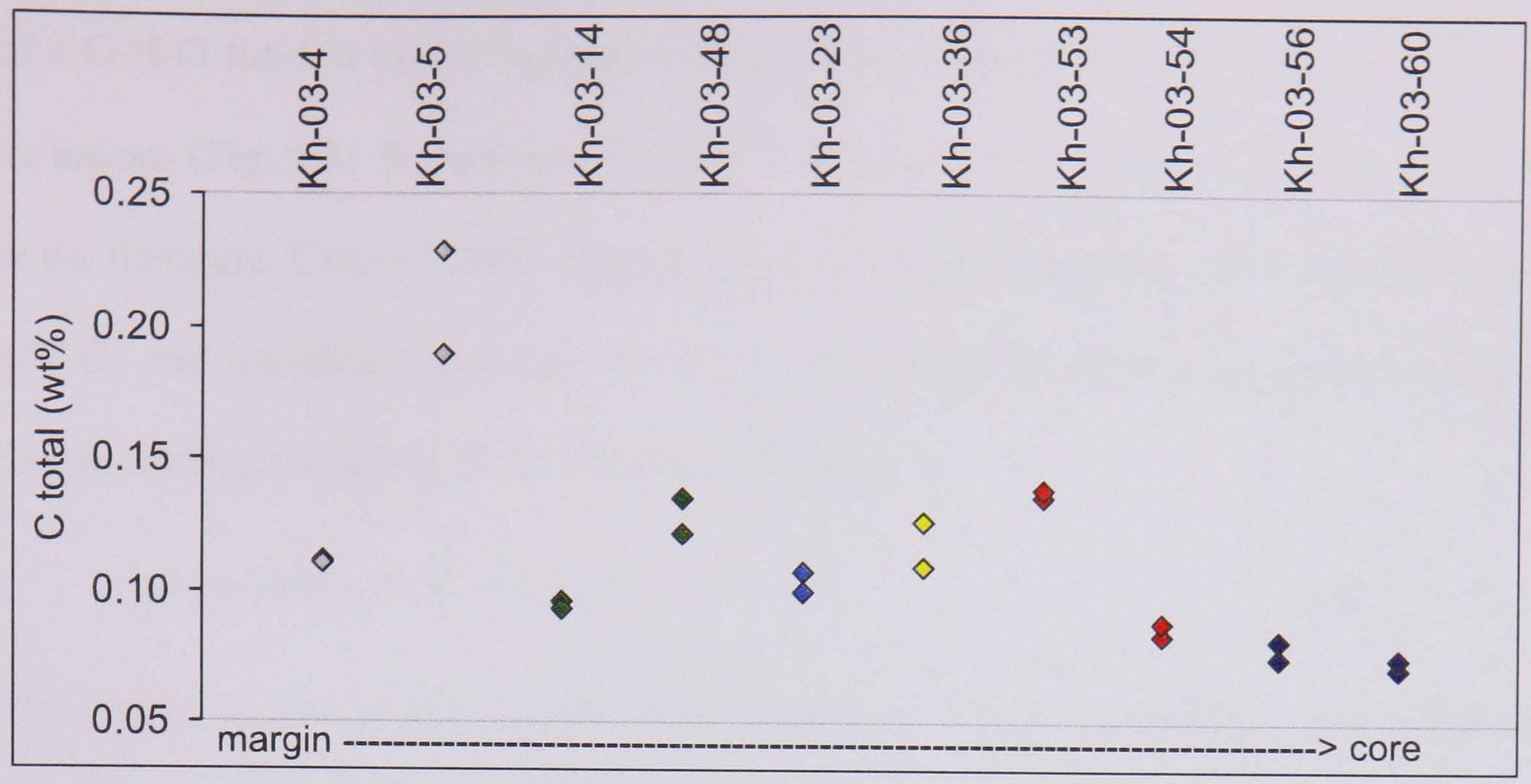

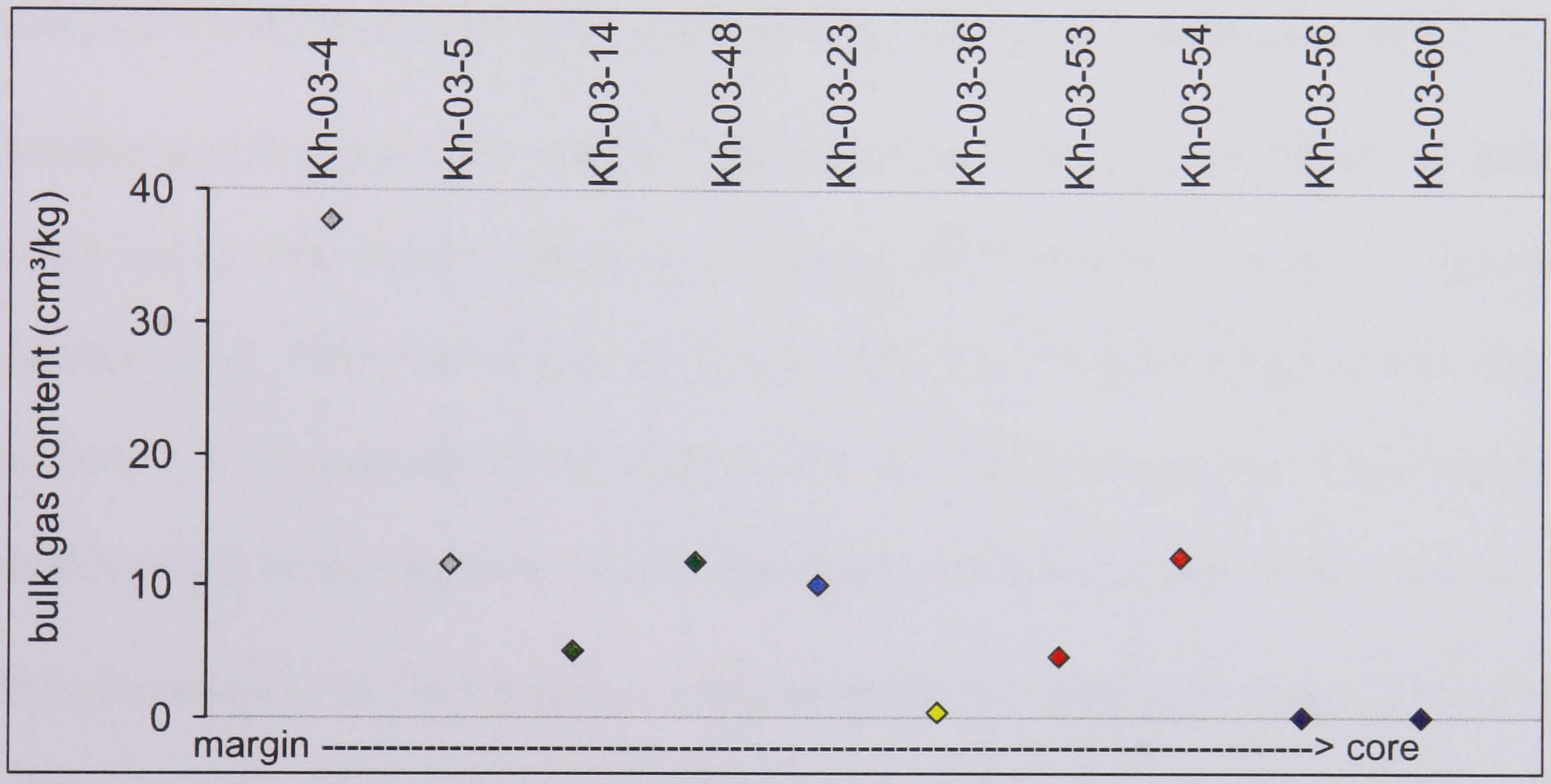

Figure 5.5: Comparison of total carbon content and bulk gas content on selected samples. Both data sets show the similar trend of decreasing values from margin to core. Different rock types are indicated by colour (grey - khibinite; green - rischorrite; blue - lujavrite; yellow - trachytoid foyaite; red - massive foyaite; dark blue - alkaline syenite) and arranged from margin to core.

However, another possibility for graphite generation is the post-entrapment respeciation of a C-H-O fluid, a theory supported by graphite occurrence in association with fluid inclusions (Fig. 5.3). Several mechanisms of compositional change have been discussed in the literature. Cesare (1995) suggested that if a fluid inclusion contains small amounts of CO_2 and significant amounts of CH_4 it will re-equilibrate and precipitate graphite during cooling according to the following reaction:

$$CO_2 + CH_4 \rightarrow 2C + 2\ H_2O \qquad \text{(R 5.2)}$$

This closed system change requires high activation energy (Ziegenbein and Johannes, 1980) and results in the evolution of graphite-bearing CH_4-H_2O fluid inclusions.

Another potential trigger of graphite precipitation is water leakage (Huizenga, 2001) which can be strain induced (Bakker and Jansen, 1994) or initiated by an f_{H2O} gradient (Sterner *et al.*, 1995). Assuming a CO_2-CH_4-H_2O fluid, water leakage would trigger reaction 5.2, because one of the starting materials (H_2O) is removed. The remaining fluid becomes increasingly rich in CH_4 (Huizenga, 2001) and graphite will precipitate.

Fluid inclusions may also behave as open system with respect to hydrogen (Hall *et al.*, 1991). In high density fluids, graphite and water will be formed according to the reaction:

$$CO_2 + 2\ H_2 \rightarrow C + 2\ H_2O. \qquad \text{(R 5.3)}$$

In the course of this study, fluid inclusion compositions and bulk gas compositions have generally been found to be CO_2-free. This could mean that reaction 5.3 may have caused total CO_2 removal. However, graphite occurrence is not sufficiently widespread and abundant to support this theory.

Therefore, simple hydrogen diffusion out of CH_4-dominant inclusions, as shown in experiments of Morgan *et al.* (1993):

$$CH_4 \rightarrow C + 2\ H_2 \qquad \text{(R 5.4)}$$

is the most likely respeciation-reaction to cause graphite precipitation in the Khibiny pluton.

5.4 Summary

It is already known from the literature that carbon-bearing species, other than gaseous hydrocarbons, occur in the Khibiny pluton. These are the carbonatite stock in the core of the pluton and dispersed organic matter such as bitumen and graphite in the entire rock formation. This study confirms the occurrence of solid carbon in rocks other than carbonates.

Elemental analyses were performed to obtain the total carbon contents in different rock types of the Khibiny pluton which range from 0.209 to 0.058 wt%. The largest part is organic carbon (0.205 to 0.064 wt%) with only a small proportion (0.026 to 0.003 wt%) contributed from carbonates.

The thermogravimetric results confirm the occurrence of solid carbon. However, the results are not in agreement with the elemental analyses. The deviation may be due to the evaporation of other volatile species in the sample and the method is therefore regarded as unsuitable for the analyses of carbon content in the studied samples.

Laser Raman studies identify graphite as fine dispersed species within mineral grains and along filled microcracks.

The spatial distribution of solid carbon is inhomogeneous, with higher concentrations in the marginal area and decreasing values towards the core. This is in compliance with the spatial distribution of gaseous hydrocarbons.

Based on these data, the origin of solid carbon can be explained in two ways:

1. Organic matter, contained in the host rock, has been thermogenically transformed in the course of magma emplacement. The products of this transformation are kerogen-like substances and methane which became introduced into the magma body. This would also explain the higher concentration of both solid carbon and gaseous hydrocarbons in the marginal area.

2. Solid carbon is the product of late- or post-magmatic respeciation of gaseous hydrocarbons that lead to precipitation of solid material. This is most likely to be caused by hydrogen leakage.

6 The identification, characterisation and interpretation of fluid and solid inclusions in the Khibiny pluton

6.1 Introduction

Fluid inclusions are fluid-filled vacuoles sealed within minerals (Roedder, 1984; Goldstein and Reynolds, 1994). They consist mostly of water (or brine), CO_2, CH_4, N_2 and can store information about ancient temperatures, pressures, and fluid compositions in a variety of geological environments.

The presence of fluid inclusions has been noticed and described since antiquity, but modern scientific studies and the applications to geology did not seriously begun until the work of Sorby (1858). He concluded that bubbles in fluid inclusions were caused by thermal contraction and that re-heating would cause the disappearance of the bubble, as the liquid expands to fill the cavity. The recorded temperature could then serve as an estimate for the temperature of mineral formation. In petrology textbooks from the end of the 19th century there have been many descriptions of fluid inclusions (e.g. Zirkel, 1873). However, they found little application during these early times due to the controversy between "magmatists" and "solidists" (Van den Kerkhof, 1988).

In the middle of the 20th century fluids became an increasingly important research area in petrology and ore exploration (e.g. Ermakov, 1966). Accompanying the development and improvement of equipment for the analysis of fluid inclusions, a renewed interest for fluid inclusions was aroused. Early fluid inclusion research has been performed notably in the former Soviet Union (e.g. Lemmlein, 1929; Ermakov, 1944), Germany

(Correns, 1953; 1954) and France (e.g. Deicha, 1950). In the United States Edwin Roedder has been instrumental in taking a major leadership role in fluid inclusion research bringing together fluid inclusion studies from diverse backgrounds for the last half of the 20th century (e.g. Roedder, 1972, 1984).

The combined microscope heating-freezing-stage allows the observation of phase transitions at various controlled temperatures and the resulting data can be used to estimate fluid density and mineral-forming conditions (e.g. Touret, 2001). Microthermometry is therefore one of the most important methods for fluid inclusion studies in the 20th century. Since the early 1980s laser Raman spectroscopy has been successfully applied to fluid inclusion analyses (e.g. Rosasco and Roedder, 1975 and 1979) and its non-destructive character soon made it an essential instrument in fluid inclusion studies.

A more comprehensive review of the early history of fluid inclusion studies can be found in Roedder (1972). Nowadays, fluid inclusion studies are an important branch of petrology and the obtained data cover a wide field of applications (e.g. Fu *et. al.*, 2002; Santosh et. al., 2006; Stasiuk *et. al.*, 2006)

6.2 A brief review of previous fluid inclusion studies on rocks from the Khibiny pluton

It has been known from the Russian scientific literature for more than five decades, that large amounts of methane-rich fluids are trapped as inclusions within the minerals of the Khibiny pluton. Early investigations, however, have been mostly limited to descriptions of fluid inclusion population, their bulk composition and general characteristics (e.g. Ikorsky, 1965; Zakrzhevskaya, 1972; Kogarko. and Romanchev, 1982). This is probably due to the lack of suitable instrumentation for detailed single fluid inclusion

analyses. The gas compositions previously reported were mostly determined by bulk gas analysis using destructive methods (crushing of a small proportion of the rock sample, followed by gas chromatography). Non-destructive methods such as microthermometry and laser Raman spectroscopy were not applied to these fluid inclusions until Potter (2000). The results of Potters study can be summarized as follows:

In the Khibiny complex five compositional fluid inclusion types were distinguished:

1. CH_4-rich fluid inclusions (most abundant)
2. CH_4-H_2O-mixed fluid inclusions (rare)
3. H_2O-dominant fluid inclusions (fairly abundant)
4. CO_2-dominant fluid inclusions (only found in one carbonatite sample)
5. CO_2-H_2O-mixed fluid inclusions (only found in one carbonatite sample)

According to Potter (2000), the fluid inclusions are closely associated with magnetite, forming trails extending out from the magnetite crystals into the nepheline hosts. They are also associated with secondary hydrous minerals such as biotite reaction rims around magnetite, natrolite, cancrinite and analcite. All of the fluid inclusions are thought to be secondary in origin. Based on isochore constructions they are assumed to be trapped at the CH_4-H_2O solvus at around 350°C, below 2 kbar (Potter, 2000).

In the present study, similar techniques have been applied to analyse a new, comprehensive set of fluid inclusion samples from the common rock types of the Khibiny pluton. The above results of Potter (2000) are only partly confirmed. Hence some of the conclusions drawn differ from those presented by Potter (2000)

6.3 Methods

6.3.1 Sample preparation

For the fluid inclusion studies reported here, doubly polished wafers of c. 100 µm thicknesses were prepared according the following procedure (pers. comm. I. Gill). Representative areas of the samples were cut with a diamond-bladed trimming saw and air-dried before placed into 25 mm diameter sized plastic moulds and embedded in an epoxy resin. After about 24 hours, the resin was cured and the embedded blocks were removed from the moulds and mounted onto specimen holders that fit a Struerers Abramin pressure polisher/grinder. Here, the blocks were ground on silicon carbide with a grit size of 15 µm until flat. This was followed by cleaning the samples in an ultrasonic bath and rinsing with tap water. The final polishing was done using a PSU Kemet cloth drenched in slurry of tin oxide ("Superlite") and water on the Abramin polisher for about 4 minutes at a pressure of 200 N. The specimens were periodically checked under a reflected light microscope until the required finish was obtained.

After cleaning in an ultrasonic bath, rinsing with water and 24 hours air drying, the polished face of the samples were bond to glass slides with "Loctite" (superglue) and dried for 2 hours. To obtain wafers of about 400 µm thickness, excess material was cut off on a CS-10 cut off saw. The wafers were then cleaned with isopropanol and lapped down to 150 µm using a Logitech LP30 machine. For the final polishing the samples were cleaned again with isopropanol and treated on the Abramin polisher as described above. Afterwards, the samples were placed into petri-dishes and covered with acetonitrile that dissolved the "Loctite" between wafer and glass slide. The sample slices were cleaned from remaining impurities with acetonitrile and a small artist's brush before ready to use on the heating- freezing stage and laser Raman microprobe.

For the present study, the largest fluid inclusions (10-20 μm) were chosen, in order to optimise observations of phase transitions and hence estimate fluid compositions. It has to be noted, that there may be some bias in this approach in that the lager inclusions may not be truly representative of the entire fluid inclusion population (Fig. 6.1). However, the results obtained here are in good agreement with bulk gas analyses (Chapter 7) and it is therefore assumed that the investigated large fluid inclusions are characteristic and representative of the overall fluid inclusion population in the samples studied.

6.3.2 Laser Raman Spectroscopy

A confocal, multichannel Renishaw laser Raman microprobe RM 1000 with a 514 nm argon laser and thermoelectrically cooled CCD detector system was used to determine the composition of fluid inclusions. The system was attached to an Olympus microscope with lens magnification of up to x100, enabling analysis of areas < 4 μm^2. To check or, if necessary, correct any drift of the instrument, a silicon standard and a diamond standard with peak positions at 521 cm^{-1} and 1331 cm^{-1}, respectively were used for regular calibration. The peak positions obtained were reproducible to within ±1 cm^{-1}.

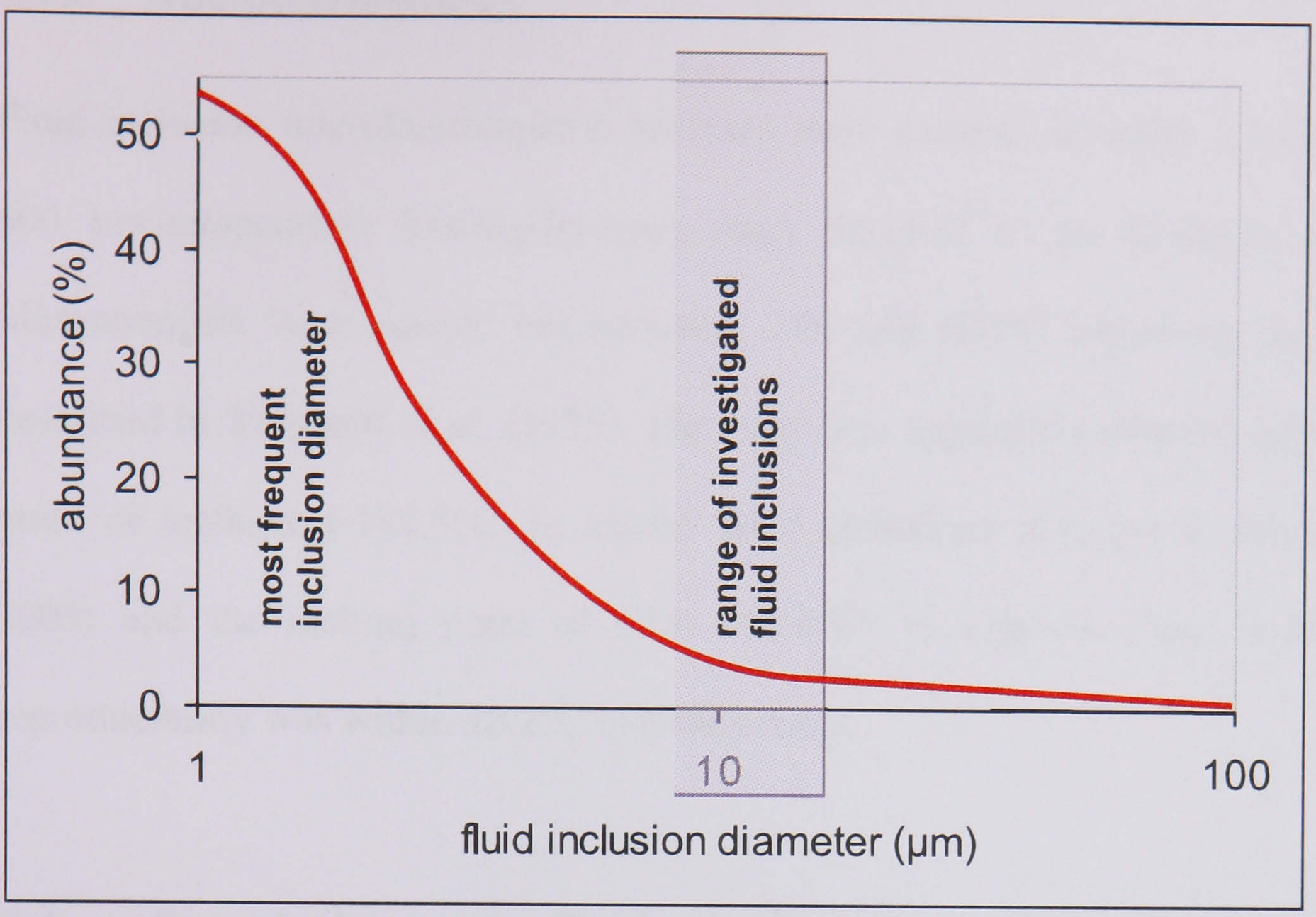

Figure 6.1: Schematic chart showing the frequency distribution of fluid inclusions versus diameter. The investigated fluid inclusions have diameters between 10 µm and 20 µm.

6.3.3 Microthermometry

Fluid inclusion microthermometric analyses were carried out using a Linkam THMS 600 low-temperature heating-freezing stage attached to an Olympus microscope. Measurements were carried out between -196 and 600°C following the procedures described in Shepherd *et al.* (1985). The stage was regularly calibrated using the triple point of methane (-182.5°C) in natural fluid inclusions (Chapter 2; Beeskow *et al.*, 2005) and the melting point of CO_2 (-56.6°C) in synthetic fluid inclusions. The reproducibility was within ±0.2°C over this range.

6.4 Description of fluid inclusions, their occurrence and distribution

The present investigation reveals the presence of both, primary and secondary fluid inclusions in the Khibiny rocks. The term "primary" indicates entrapment of fluid during time of mineral crystallisation (Roedder, 1984). The primary inclusions therefore contain any phase present at the time of crystal growth. Secondary fluid inclusions were incorporated later (after primary crystal growth has either ceased or interrupted) and usually contain phases that enter crystals along fractures. They are trapped as the fractures heal and are present now in so-called fluid inclusion planes (FIPs).

The majority of fluid inclusions in the samples of the Khibiny pluton are hosted in nepheline, alkali feldspar and eudialyte. They are best observed in nepheline due to the clarity of the mineral and the fact that the contained fluid inclusions are large compared to their presence in other minerals. In alkali feldspar, the inclusions are relatively small (< 5-10 μm) and mostly aligned parallel to the cleavage plane or alteration zones of the mineral. The mafic minerals aegirine and arfvedsonite rarely contain any fluid

inclusions. Only a few sporadic fluid inclusions with primary characteristics have been identified in these minerals. Cleavage planes and microcracks of pyroxenes and amphiboles appear devoid of fluid inclusions.

6.4.1 Primary fluid inclusions

Based on textural observations, three different forms of primary fluid inclusions could be distinguished in the Khibiny rocks.

1. Small fluid inclusions are found in arrays parallel to growth zones in nepheline (Fig. 6.2a). This is a typical criterion for fluid entrapment during crystallisation of the mineral and the inclusions are therefore regarded as being primary (Roedder, 1984). They are well rounded with diameters of up to 5 μm. Due to their small sizes, their compositions could not be determined.

2. Larger primary fluid inclusions, between 10 and 20 μm in diameter, are found in isolation or in small isolated clusters, mainly in nepheline. They show no relationship to microfractures and are therefore likely to be primary in origin. At room temperature these inclusion appear either mono-phase (CH_4-rich) or two-phase (L+V); the latter being sub-divided into CH_4-H_2O and H_2O-rich types (Fig. 6.2b). These inclusions show a wide variety of shapes. Usually they are rounded to sub-rounded but irregular shapes are also common, often with signs of necking down (Fig. 6.5). Hereafter, these primary types are referred to as "cluster-inclusions" and "single-inclusions".

3. Another group of proposed primary fluid inclusions are attached to small aegirine needles in nepheline (Fig. 6.2c and d). As observed at room temperature, they are mono-phase CH_4-dominated inclusions or two-phase (L+V) H_2O-CH_4 mixed inclusions with diameters in the range of 5 to 10 μm. As there is no association between fluid inclusions and microcracks, these are regarded to be primary in

origin, entrapped, together with aegirine, during nepheline crystallisation. A similar association has been noted in the Ilímaussaq complex where fluid inclusions are also considered to be primary in origin (Konnerup-Madsen et al., 1979; Krumrei and Markl, 2005).

6.4.2 Secondary fluid inclusions

The majority (approximately 90 %) of fluid inclusions observed in this study appears to be secondary in nature. The generally-accepted formation mechanism involves the fracturing of the rock after crystallisation through thermal or mechanical stress (Roedder, 1984). The resulting cracks are then used as fluid pathways until they are closed by these later fluids. During this process, so-called "secondary" fluid inclusions are entrapped within characteristically linear formed fluid inclusion planes (FIPs). In the observed samples these planes are especially abundant in nepheline and alkali feldspar minerals.

Similar to primary fluid inclusions, FIPs are best to observe in the clear nepheline crystals (Fig. 6.2e to g). Small FIPs start and terminate within mineral grains and larger ones cross-cut several mineral grains. They are either randomly orientated or aligned sub-parallel to each other. Fluid inclusions in FIPs vary in size between 5 and 20 µm and have a well rounded or elongated or even tabular shape.

In alkali feldspars, fluid inclusions are often concentrated in zones of albitisation that follow cleavage planes and microfractures (Fig. 6.2h). Here, migrating fluids lead to ion exchange in feldspar, accompanied by precipitation of micro-minerals and fluid entrapment. The fluid inclusions are usually very small with average diameters of 2-5 µm.

The high abundance of FIPs indicates a high level of post-magmatic fluid movement. A detailed description and interpretation of FIPs will follow in Chapter 9.

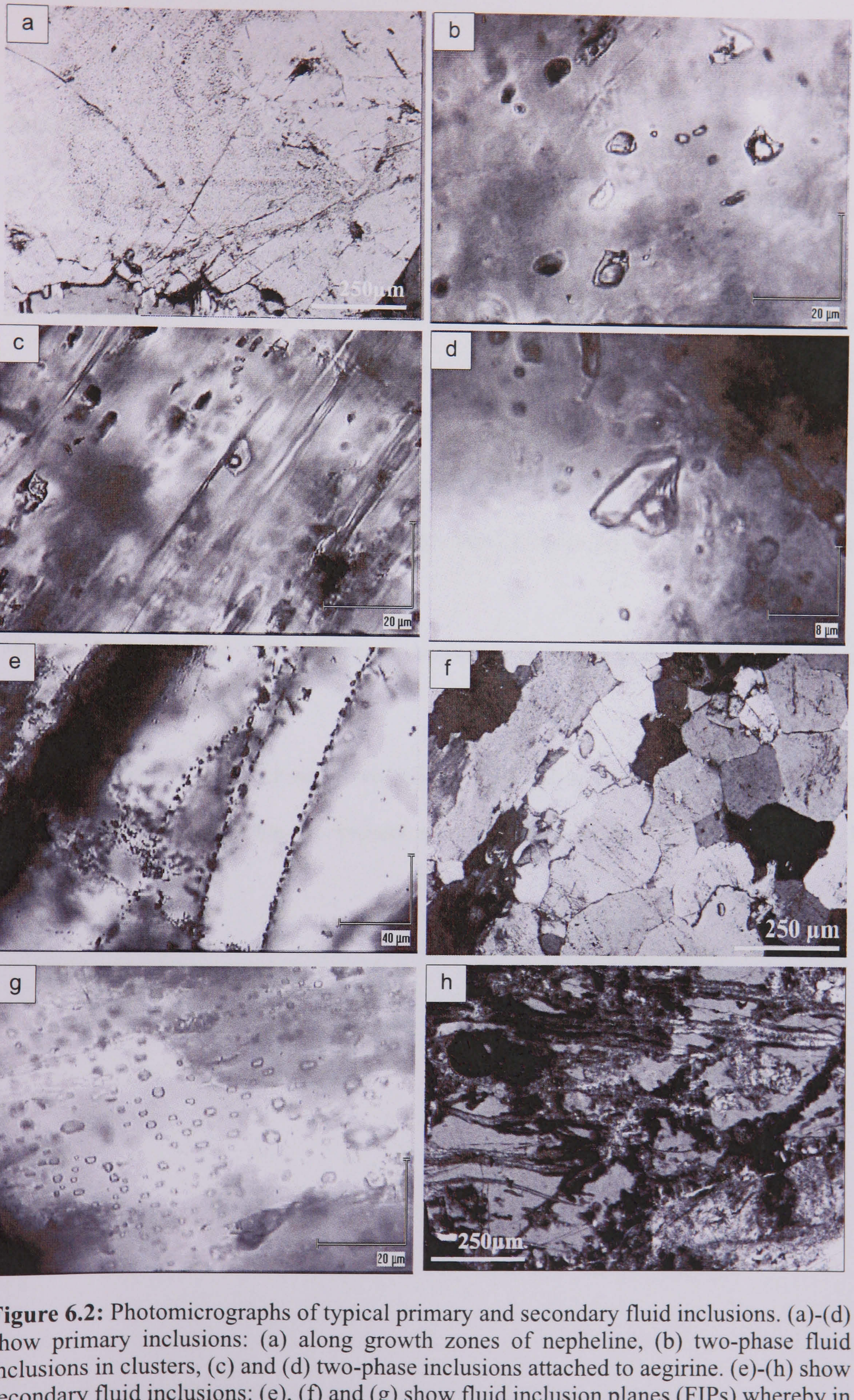

Figure 6.2: Photomicrographs of typical primary and secondary fluid inclusions. (a)-(d) show primary inclusions: (a) along growth zones of nepheline, (b) two-phase fluid inclusions in clusters, (c) and (d) two-phase inclusions attached to aegirine. (e)-(h) show secondary fluid inclusions: (e), (f) and (g) show fluid inclusion planes (FIPs) whereby in (g) the plane is very shallow to the thin section surface. (h) shows alteration zones in feldspar with subsequent fluid inclusion entrapment.

6.4.3 Compositional fluid inclusion types

This study reveals two different compositional fluid inclusion types.

1. The vast majority of fluid inclusions (c. 90 %) are *methane-dominant* and appear mono-phase at room temperature (Fig. 6.3).

2. The remaining c. 10 % of the fluid inclusion population is *water-dominant* and consists of two phases; a mostly methane-rich vapour bubble and liquid water (Fig. 6.4). The ratio of liquid to vapour, estimated using the chart of Roedder (1972), is variable from 20:80 to 80:20. The majority of inclusions contain about 50 vol% gas. Raman-inactive daughter minerals were present occasionally in two-phase inclusions.

Methane-dominant and water-dominant compositions were found in both, primary and secondary fluid inclusions.

There is evidence for necking down whereby two-phase CH_4-H_2O fluid inclusions separate into two mono-phase inclusions, one of them water-rich and one methane-rich (Fig 6.5).

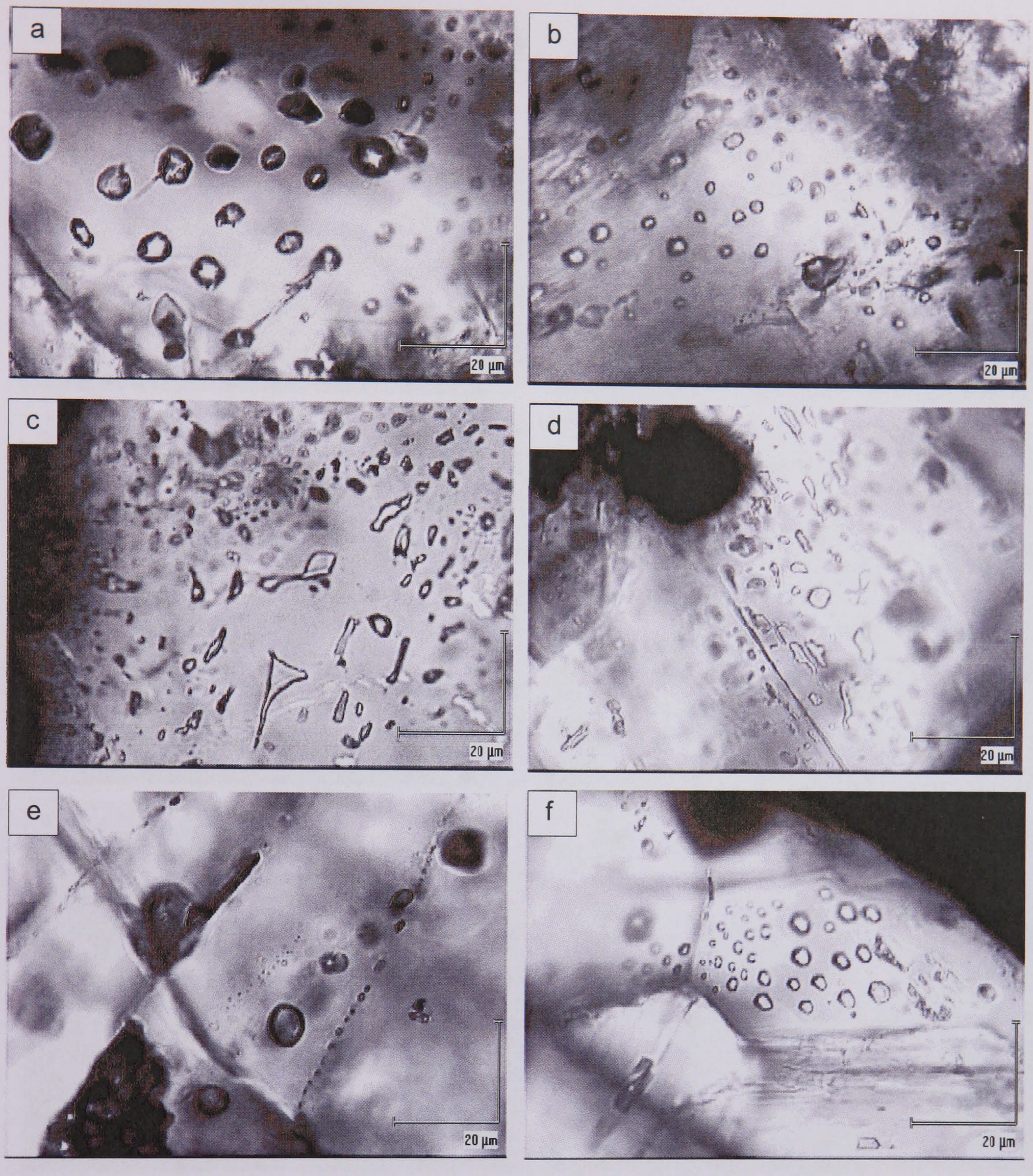

Figure 6.3: Photomicrographs of mono-phase methane-dominant fluid inclusions in nepheline. (a)-(d) shows the occurrence in clusters. In (c) and (d) signs of necking down are visible. (e) shows methane-dominant inclusions of different sizes that follow FIPs and (f) fluid inclusions with negative crystal shape.

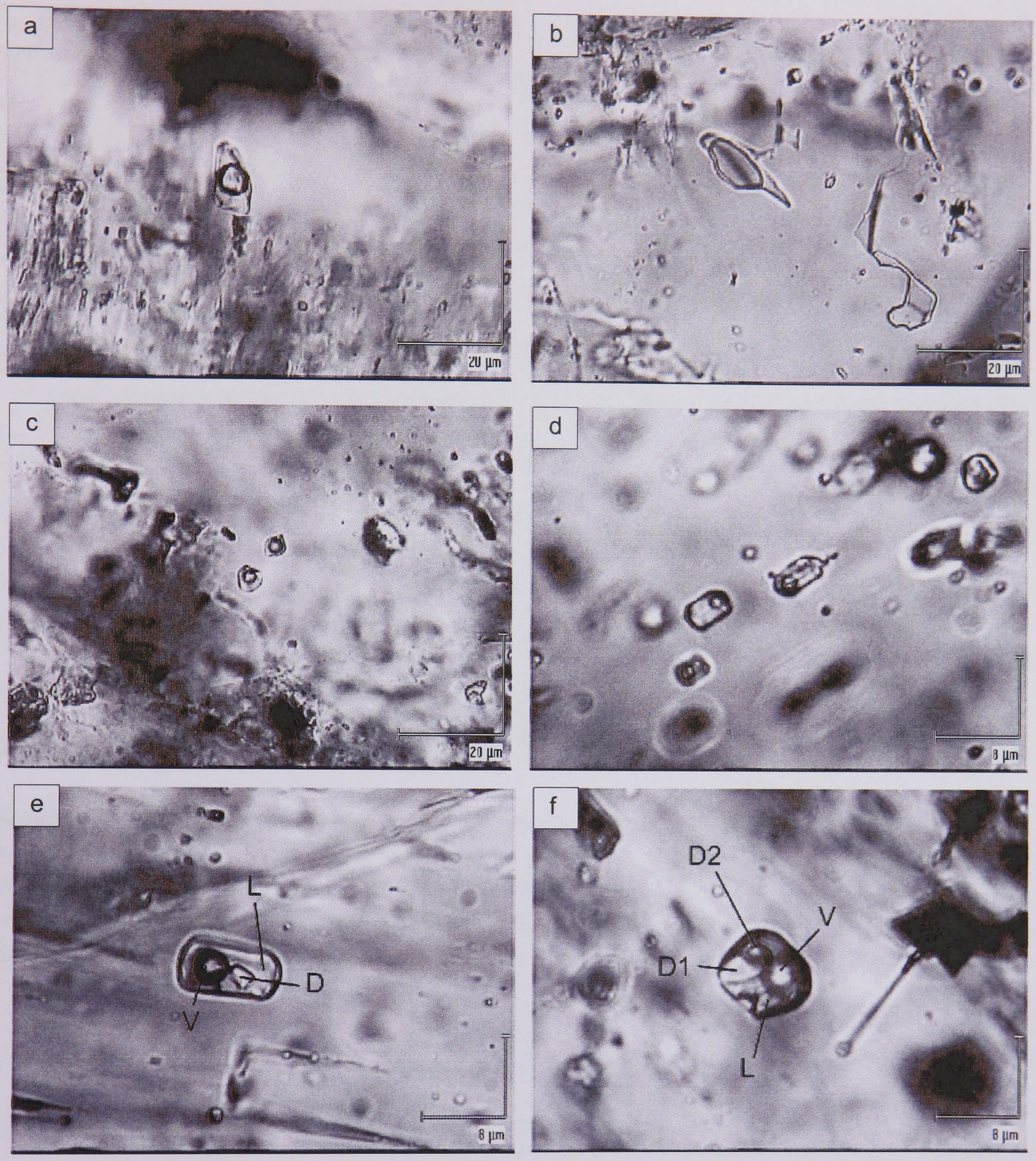

Figure 6.4: Photomicrographs of water-dominant fluid inclusions. They contain water in the liquid phase and methane in the gas bubble. The photomicrographs show also the different degree of filling (size of the gas bubble). (a) shows a primary, "single inclusion". (b) shows inclusions that indicate signs of necking down. (c) and (d) show inclusions in clusters. (e) and (f) show inclusions that also contain one and two Raman inactive daughter minerals.

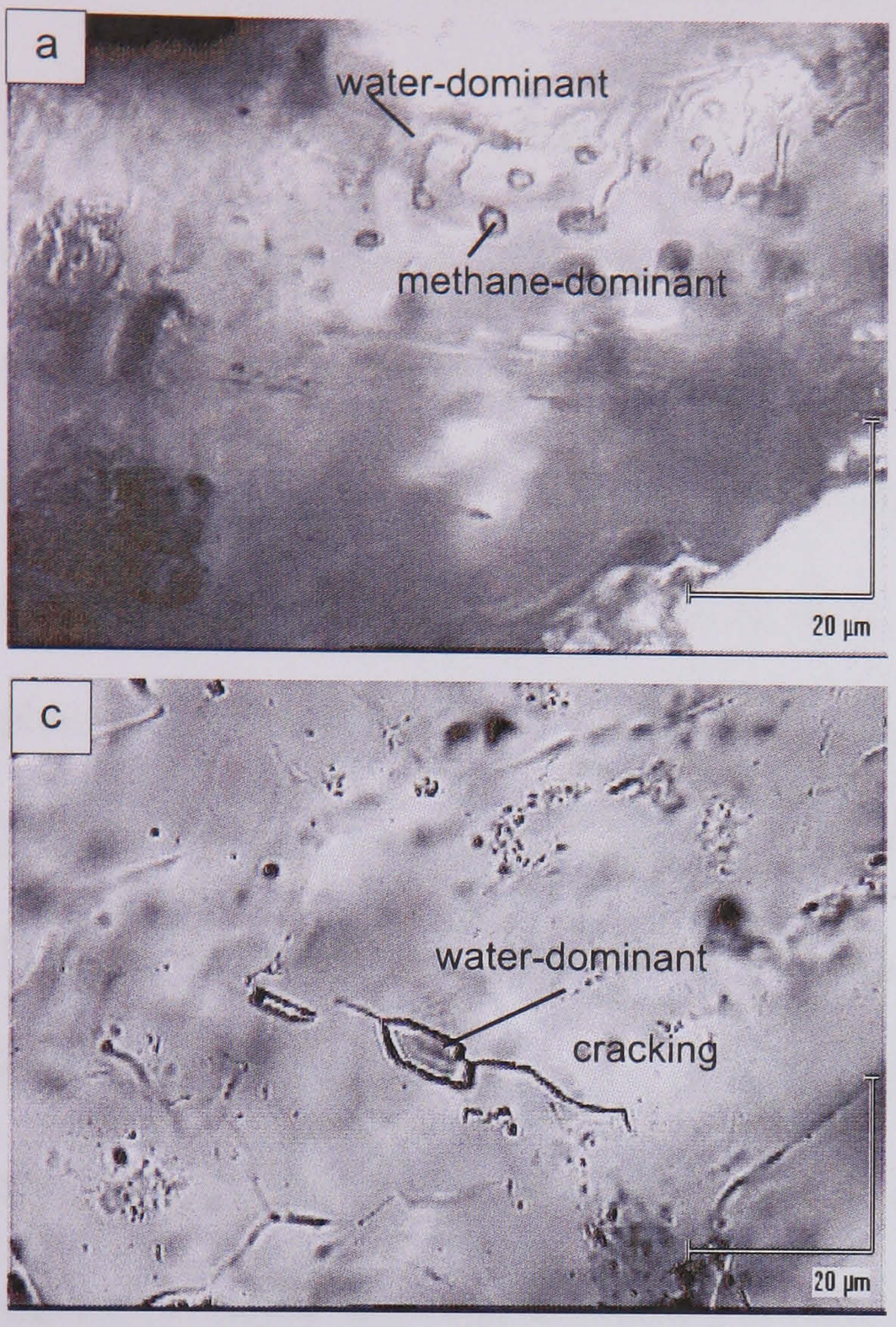

Figure 6.5: Photomicrographs showing examples for post-entrapment changes to fluid inclusions. (a) and (b) shows necking of two phase inclusions whereby two mono-phase inclusions developed, one is methane-, the other water-dominant. (c) shows cracking which causes leaking of fluid and hence changes in fluid density. (d) shows necked down fluid inclusions with different degree of filling.

6.5 Results of laser Raman analysis

The majority of mono-phase fluid inclusions analysed by laser Raman spectroscopy shows a typical single methane peak at between 2911 and 2915 cm^{-1} (Burke, 2001; Fig. 6.6a). Ethane and propane have been identified in low concentrations as additional components with peak positions at 2954 and 2890 cm^{-1}, respectively (Fig. 6.6b). In two-phase inclusions a broad water peak at c. 3400 cm^{-1} has been recorded in the liquid phase. Gaseous bubbles in two-phase inclusions produced methane peaks (Fig. 6.6c). No free hydrogen has been detected in the fluid inclusions as reported by Potter (2000). Fluorescence, produced by the host minerals or higher hydrocarbons in the fluid inclusions, caused a broad shoulder at higher wavelengths and may have swamped the hydrogen signal (Fig. 6.6d). Feldspar in particular interferes strongly with the Raman signal, probably as a result of its REE content (Burruss, 1992).

6.6 Results of microthermometry

A summary of microthermometric data is given in Table 6.1 and the entire data set is available in Appendix 6.1A. The typical microthermometric behaviour for the fluid inclusions found in the Khibiny rocks is schematically summarized in Fig. 6.7.

Methane-dominant fluid inclusions

The methane-dominant, mono-phase fluid inclusions display H1 behaviour as defined by Van den Kerkhof (1988). This means, that homogenisation is the only phase transition that takes place in the course of heating (Fig. 6.7A and Fig. 6.8).

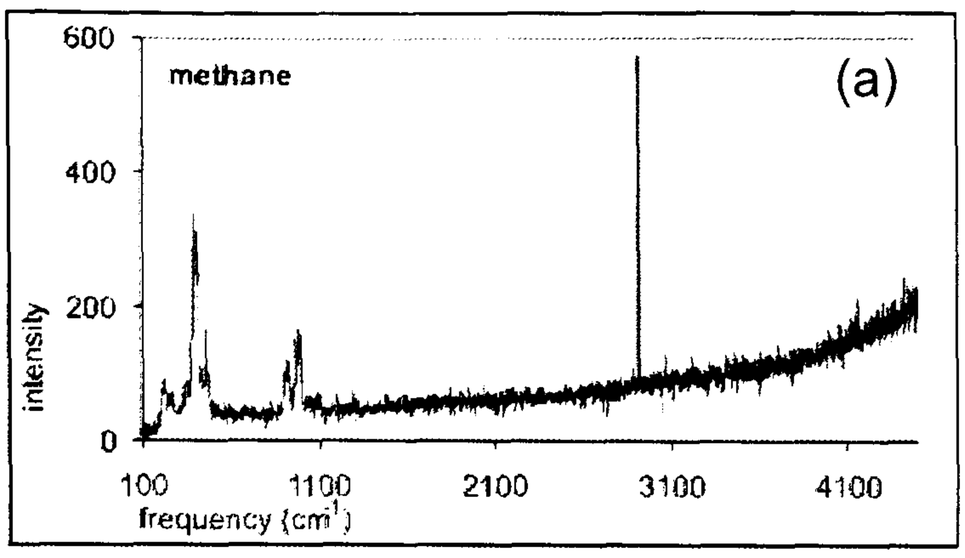

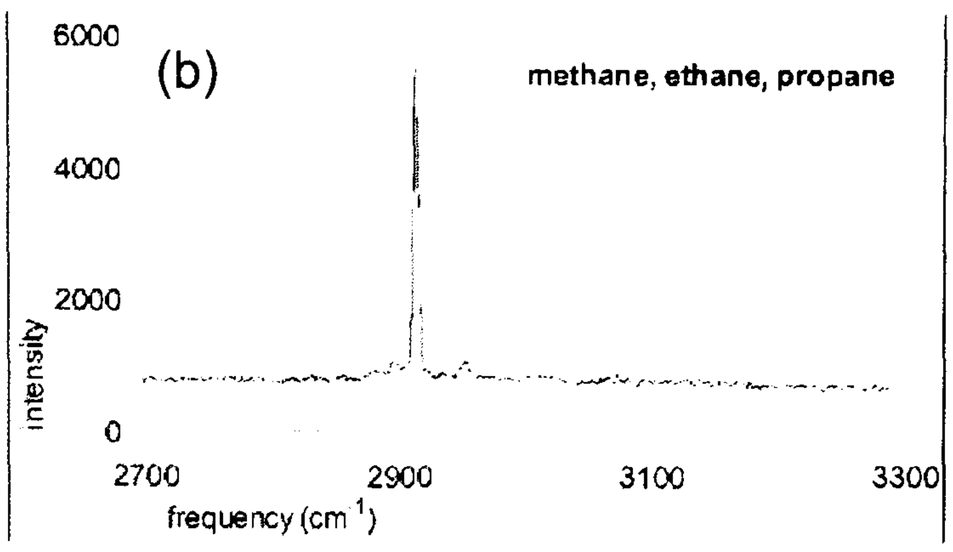

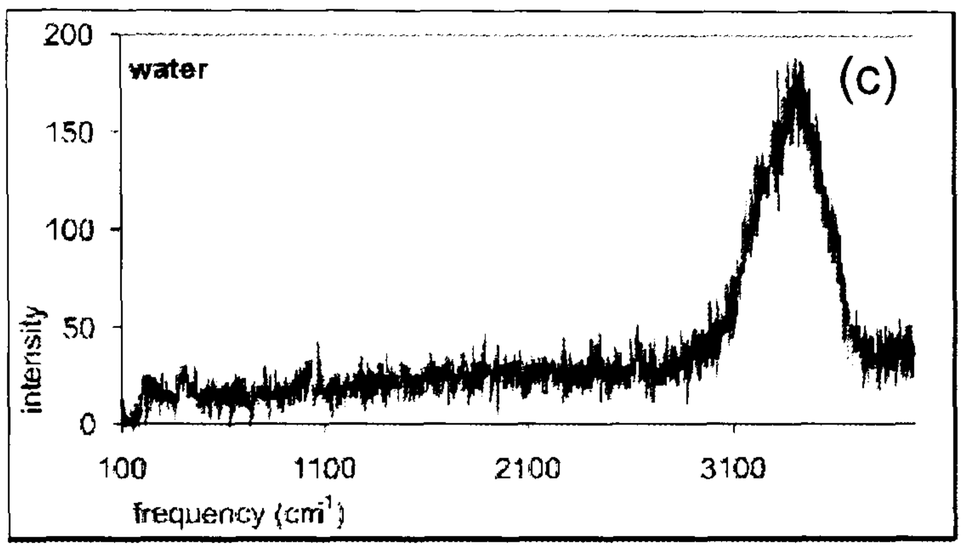

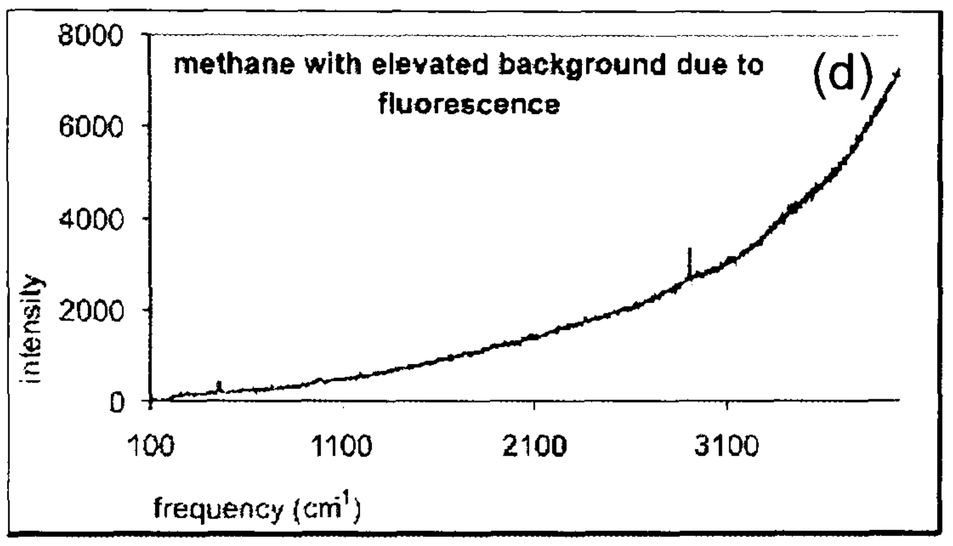

Figure 6.6: Typical laser Raman spectra found in fluid inclusions of the Khibiny pluton. (a) shows a well pronounced methane peak at 2915 cm^{-1}. The peaks at lower frequencies are attributed to scattering from the host mineral. (b) shows the small peaks of propane at 2894 cm^{-1} and ethane at 2949 cm^{-1} next to the large dominant methane peak at 2914 cm^{-1}. (c) shows the broad peak of water around 3430 cm^{-1} and (d) the often observed elevated background due to fluorescence. Also a small methane peak is visible at 2915 cm^{-1}.

	inclusion type (N)	T homogenisation	T first ice melting	approx. T HH melting	approx. T last ice melting
methane-dominant fluid inclusions (562)	single (34)	MIN = -89.9 MAX = -74			
	clusters (292)	MIN = -98.2 MAX = -64.3			
	FIPs (236)	MIN = -98.9 MAX = -62.5			
water-dominant fluid inclusions (89)	single (7)	MIN = 452 MAX = >500	MIN = -56 MAX = -50	MIN = -33 MAX = -22	MIN = -9 MAX = -2.2
	clusters (78)	MIN = 255 MAX = >500	MIN = -58 MAX = -40	MIN = -39 MAX = -20	MIN = -16.7 MAX = -1.5
	FIPs (4)	MIN = 330 MAX = >500	MIN = -56 MAX = -50	MIN = -35 MAX = -24	MIN = -8 MAX = -3.3

Table 6.1: Summary of microthermometric results of methane and water-dominant inclusions in the samples from the Khibiny pluton investigated in this study.

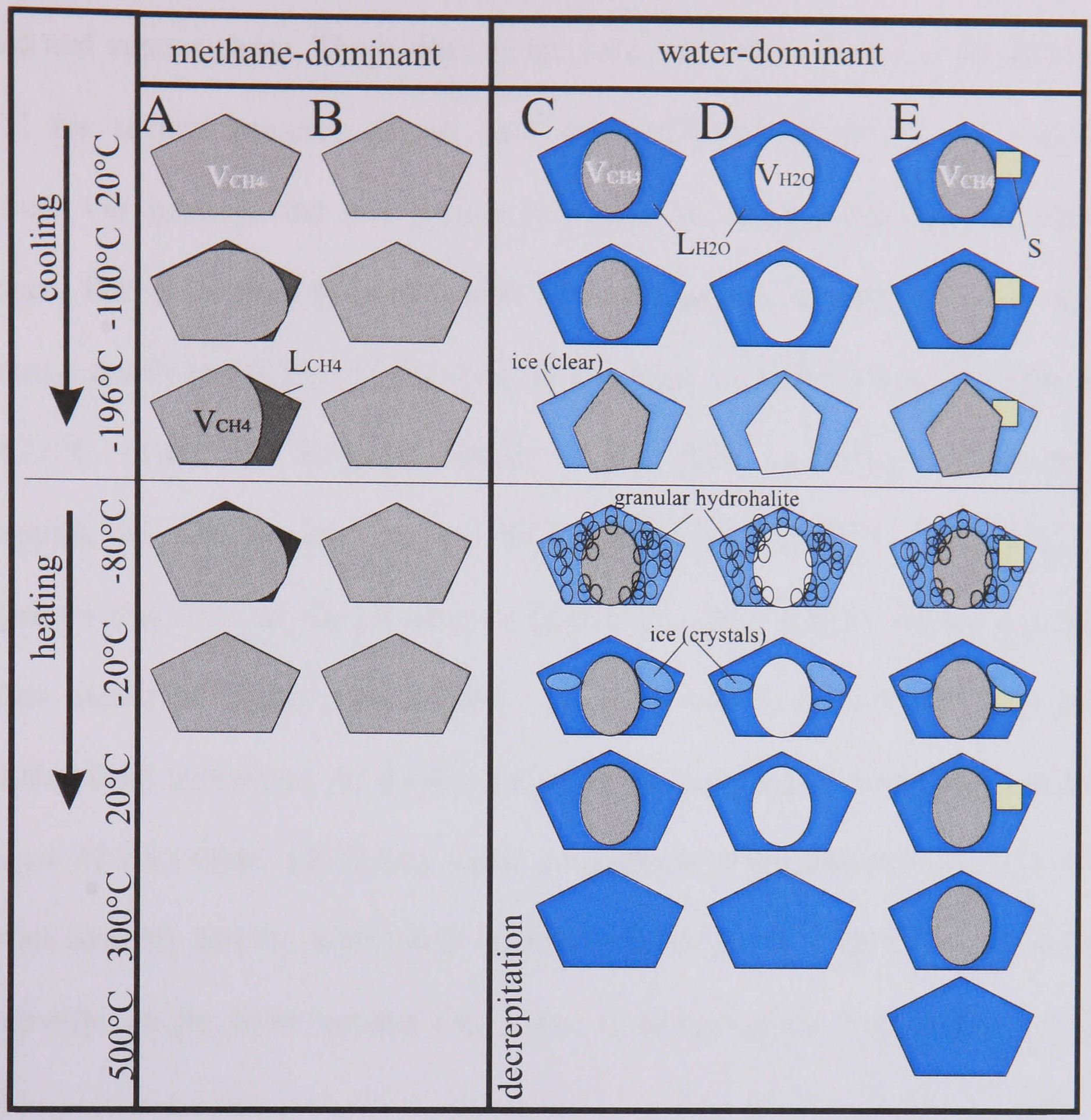

Figure 6.7: Typical sequences of fluid inclusion behaviour during microthermometric runs. (A) Mono-phase methane-dominant inclusions separate into two phases (L+V) on cooling. During heating homogenisation in a range of -100°C to -65°C occurs. (B) Many mono-phase methane-dominant inclusions are unresponsive on cooling and heating. (C) In two-phase aqueous inclusions, the aqueous phase freezes and the gas bubble become distorted. First, hydrohalite becomes visible during heating, with its typical fine granular texture. On further heating hydrohalite disappears and large ice crystals develop. Final ice melting occurs in a range up to about 0°C. Homogenisation occurs in a wide range, between 300°C and 500°C. However, many inclusions decrepitate before homogenisation. (D) Two-phase water-rich inclusions in which no methane was detected behave similar to that of (C) and it is likely that methane exists in very small amounts. (E) Rarely L+V+S inclusion occur. The cool-heat behaviour is similar to (C). On heating, the solid phase (daughter mineral) dissolves in a range of 179°C to 265°C, before final homogenisation or decrepitation occurs.

During cooling down to about -190°C the mono-phase fluid inclusions separate to form a liquid and vapour phase. The inclusions are very reluctant to freeze, even when held at -190°C for several minutes. In no case was solidification of the fluid inclusions observed. On heating, the two phases homogenise mostly critically by fading of meniscus. The majority of fluid inclusions homogenise between -80°C and -84°C which indicates a nearly pure CH_4 composition, as it is close to methane's critical temperature of -82.6°C (Van den Kerkhof, 1988). Some fluid inclusions, however, show homogenisation temperatures up to -65°C and down to -98°C (Fig. 6.9). These divergences may indicate the presence of impurities. Laser Raman studies and bulk gas analyses identified higher hydrocarbons as additional components in the methane-dominated fluid inclusions. As these components have higher critical temperatures (e.g. $T_{c(C2H6)}$ = 32.2°C; Olds, 1953) they cause an increase in homogenisation temperatures. Volatiles such N_2 and H_2, with lower critical temperature of -146.95°C and -239.95°C, respectively, might have caused the lower homogenisation temperature (Dubessy, 1994).

Post-entrapment changes, such as leakage and necking down have been frequently noted amongst the fluid inclusion populations. This affects fluid density and composition and may also cause the spread of the recorded homogenisation temperatures. Low homogenisation temperature indicates high entrapment pressure and high homogenisation temperature indicates the entrapment at low pressure (Van den Kerkhof, 1988).

Many mono-phase methane-dominant inclusions are unresponsive during cooling and heating. That means they do not separate on cooling and hence no homogenisation

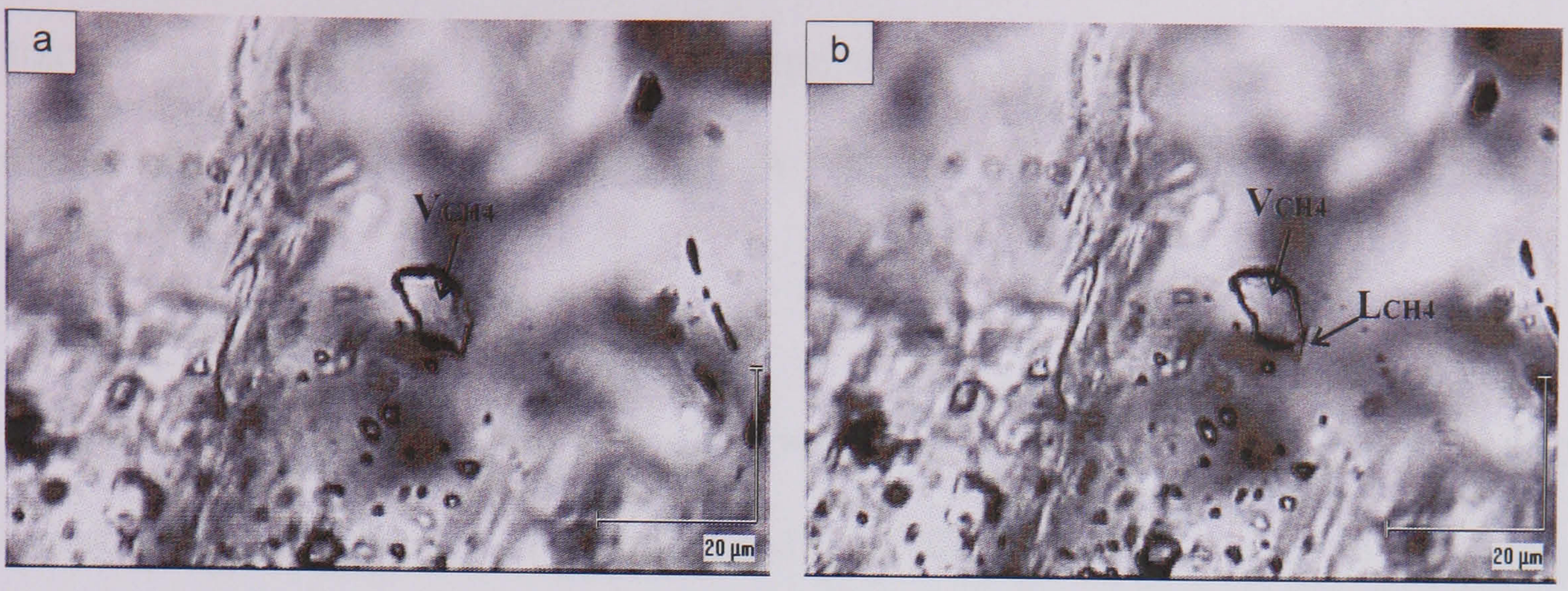

Figure 6.8: Photomicrographs of a methane-dominant fluid inclusion that shows the typical behaviour on cooling: the separation into a large vapour phase and a small liquid rim. Homogenisation occurs usually critical or to vapour. (a) shows the inclusion at room temperature and (b) at about -100°C.

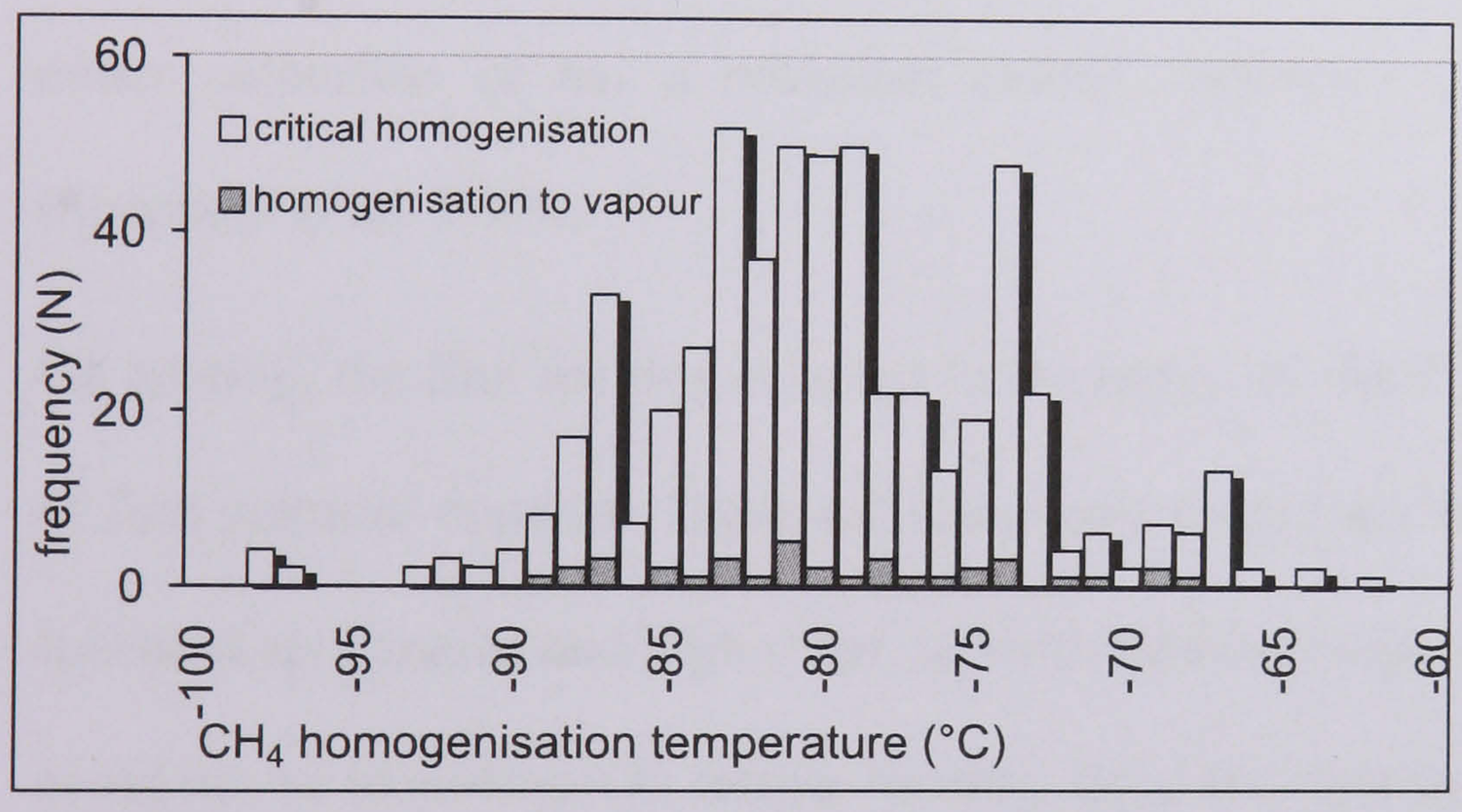

Figure 6.9: Frequency histogram showing the range of homogenisation temperatures of all analysed methane-dominant inclusions. The majority homogenise critically around the pure CH_4 critical point at -82.6°C. Only minor proportions homogenise to vapour as shown by dark grey bars.

temperature data could be obtained (Fig. 6.8B). This might be just due to their small size that precludes observation of phase separations and homogenisations or it could be due to metastability effects (Roedder, 1984).

Water-dominant fluid inclusions

A typical microthermometric run of two-phase (L+V) fluid inclusions up to room temperature is illustrated in Figs. 6.8C and 6.10. The temperatures of first ice melting, hydrohalite melting, last ice melting and homogenisation are documented in histograms (Fig. 6.11b and c).

On cooling to below -100°C sudden freezing of the aqueous phase occurs. This is occasionally visible by the distortion of the vapour bubble. At this point, ice, hydrohalite ($NaCl\ .2H_2O$) and possibly antarcticite ($CaCl_2\ .6H_2O$) coexist. The solid is either colourless or has a brownish colour, indicative of the appearance of $CaCl_2$ (Shepherd *et al.* 1985).

On heating, the first melting is noted in the range of -58°C to -40°C by the appearance of fine granular crystals. These are assumed to represent hydrohalite, because of their speckled appearance and high relief, as described in Shepherd *et al.* (1985). Antarcticite could not be identified. On further heating, large ice crystals develop and the fine grains of hydrohalite disappear between -39 and -18°C. Final ice melting occurs in the range of -17°C to -1.5°C. Although methane was detected by laser Raman spectroscopy, no clathrate development was observed. The homogenisation of vapour and liquid phases occurs over a wide temperature range, between 290°C and >500°C. Many inclusions, however, decrepitate before homogenisation or become invisible due to degradation and cracking of the nepheline host mineral (Fig. 6.12).

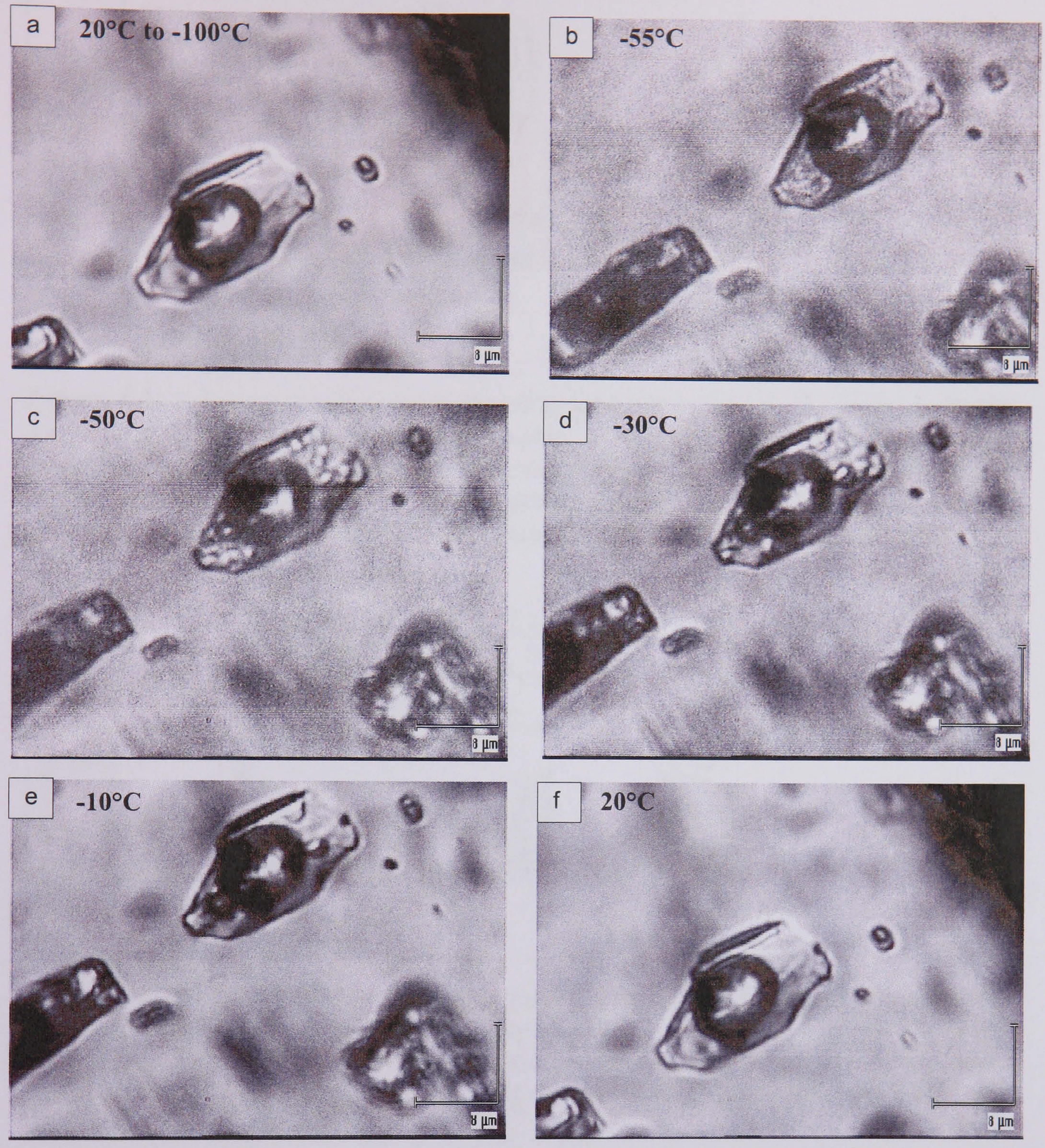

Figure 6.10: Photomicrographs of the heating-freezing behaviour of a two-phase (V+L) water-dominant inclusion. (a) The fluid inclusion at room temperature. On cooling down no changes are visible. (b) On heating, the first melting is visible when granular hydrohalite appears. (c and d) In the course of heating, large ice crystals develop and hydrohalite disappears. (e) Only few crystals remain before final ice melting (f). The fluid inclusion decrepitated on heating, therefore, final homogenisation cannot be shown. The images (b), (c) and (d) are slightly blurred due to ice growth on the lens.

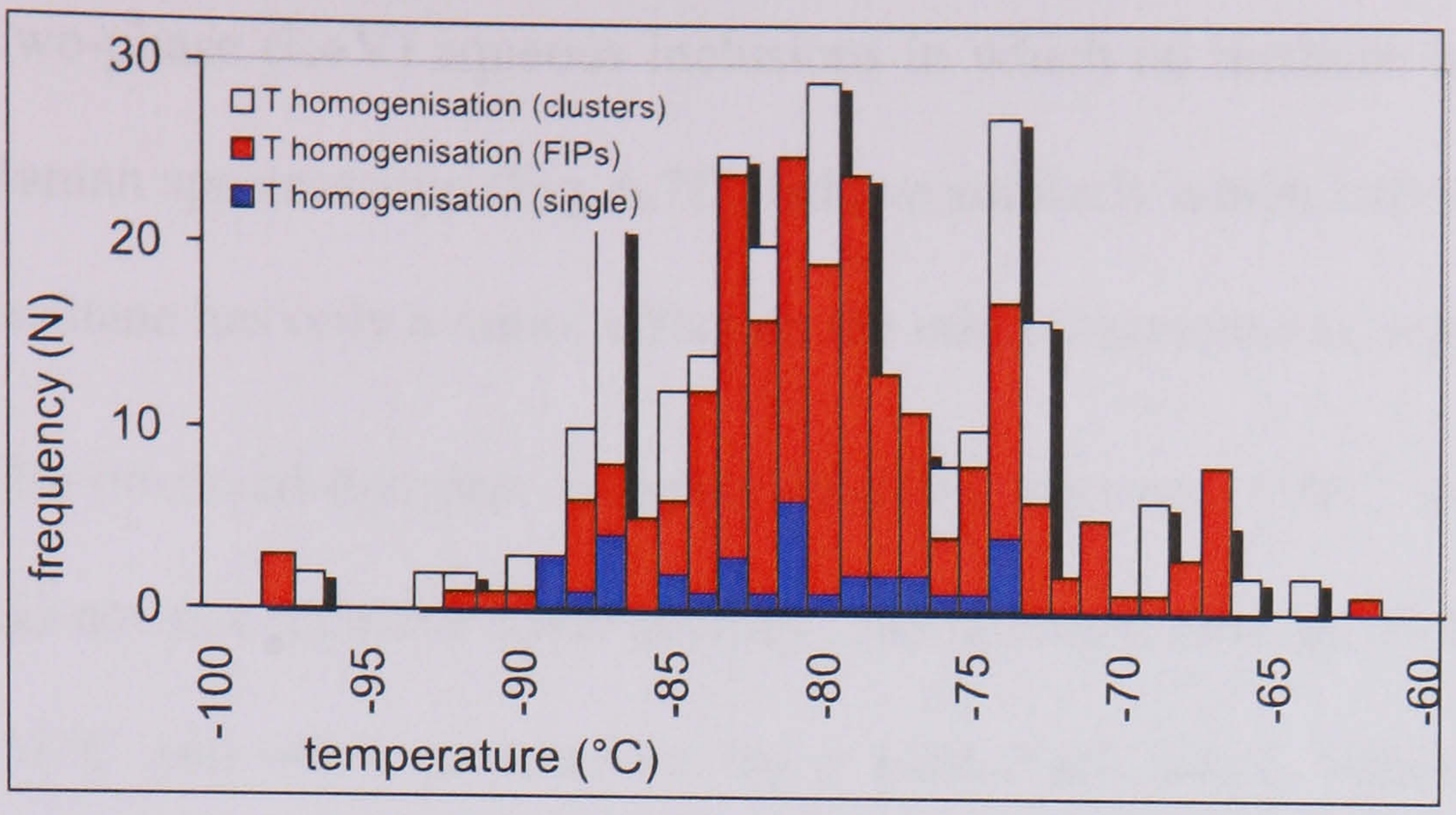

Figure 6.11a: Frequency histogram showing the differences of CH_4 homogenisation temperatures in different entrapment mode; in clusters, FIPs or as single fluid inclusions. It shows, that most fluid inclusion investigated appear in clusters. Many appear also in FIPs and only few separate, single fluid inclusions have been investigated. All have relatively similar ranges of homogenisation temperatures.

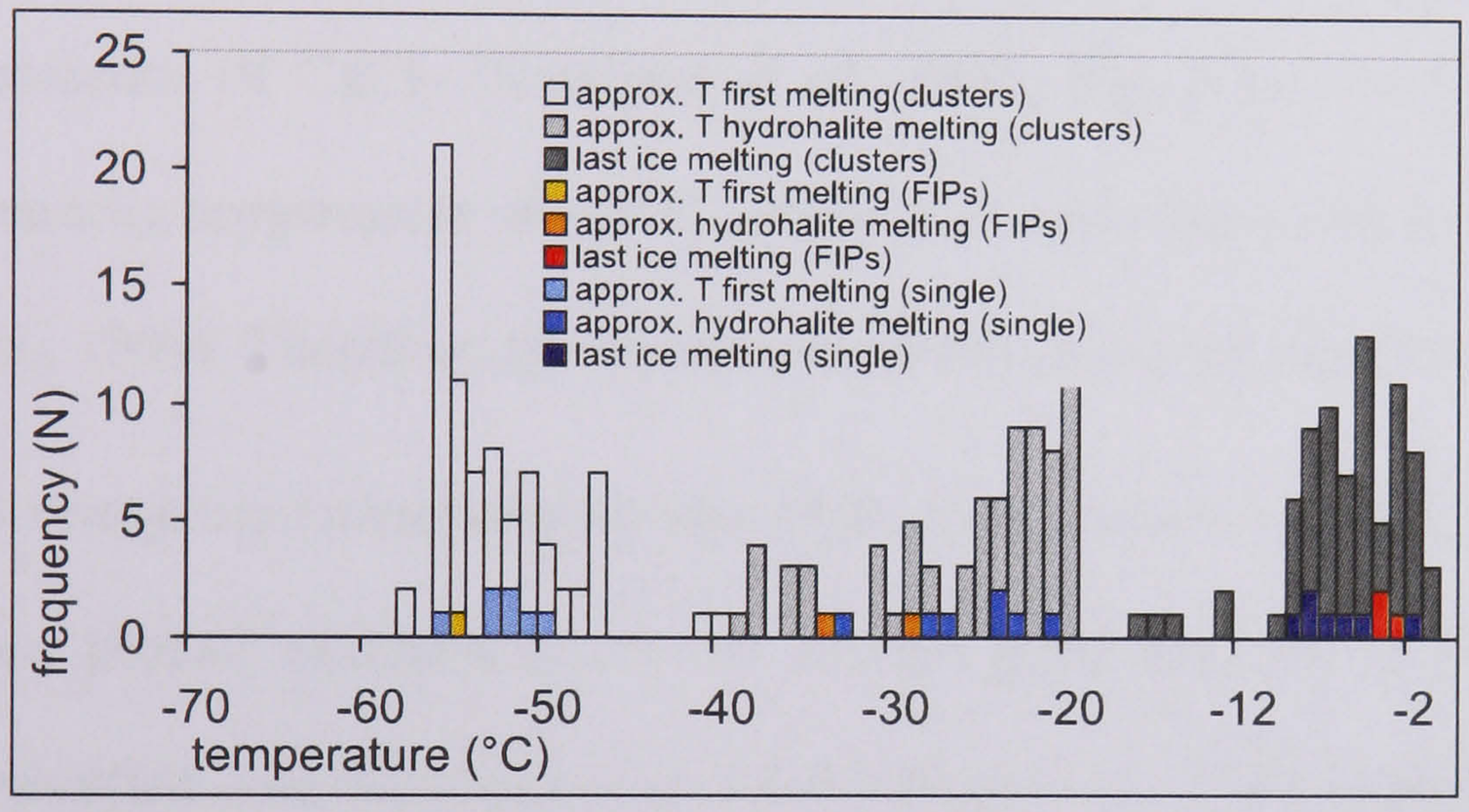

Figure 6.11b: Frequency histogram showing the range of first ice melting, hydrohalite melting and final ice melting temperatures of aqueous incluisons in clusters, FIPs and as single inclusions. Only six fluid inclusions in FIPs and six separate single fluid incluisons have been investigated as they are very rare. There are no significant differences between them.

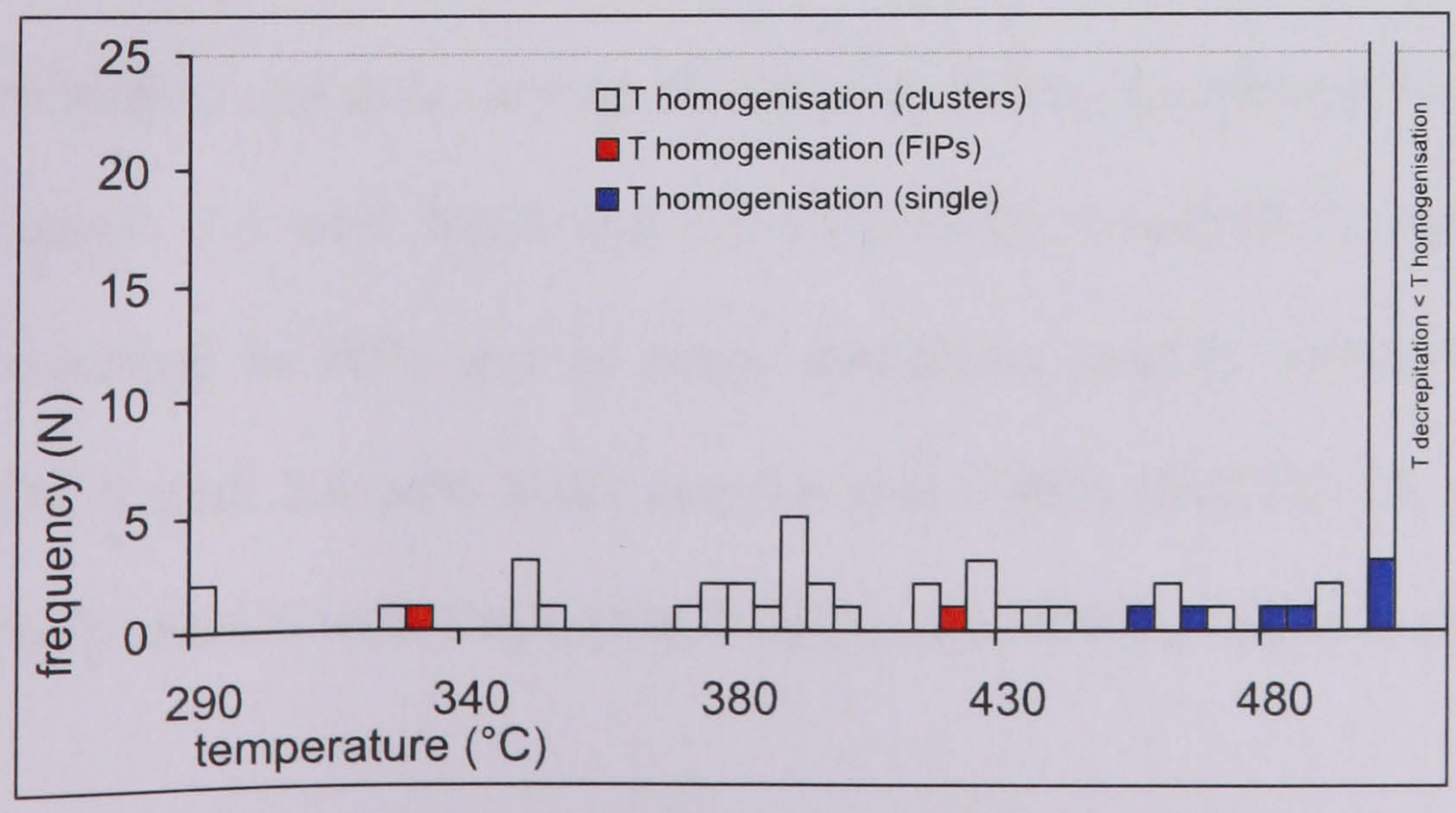

Figure 6.11c: Frequency histogram showing the range of homogenisation temperatures of aqueous incluisons in clusters, FIPs and as single inclusions. Most fluid inclusions homogenise above 500°C where no observation could be made due to either decrepitation or degradation of the host mineral.

Two-phase (L+V) aqueous inclusions in which no methane has been detected by laser Raman spectroscopy (Fig. 6.7D) behave similarly which indicates that the occurrence of methane has only a minor effect on the microthermometric results (Hanor, 1980).

The observed daughter minerals dissolved between 179°C and 265°C (Fig. 6.7E) and did not re-crystallise upon cooling. The recorded first ice melting temperature between -58°C and -40°C is too low for a pure NaCl brine, which should be equal to the H_2O-NaCl eutectic temperature of -21.8°C (±1°C) (Bodnar and Vityk, 1994). The tendency towards lower values is diagnostic for additional salts in solution. The frequently observed brownish colour of the solid ice phase on cooling suggests the presence of $CaCl_2$ (Shepherd *et al.*, 1985, Fig. 6.13). A NaCl-$CaCl_2$ solution has a eutectic temperature of -55°C, which is in agreement with the observed data (Oakes *et al.*, 1990). Therefore, the aqueous fluid inclusions are regarded as $CaCl_2$-NaCl-bearing.

Average microthermometry data of the three inclusion groups (single, FIPs and clusters) are plotted exemplarily on the ternary phase diagram H_2O-NaCl-$CaCl_2$ (Fig. 6.14; modified after Shepherd *et al.* 1985; Oakes *et al.*, 1990; Goldstein and Reynolds, 1994). By using temperature of hydrohalite melting and final ice melting, the weight-ratios are graphically estimated by extrapolation of the tie line between melting temperatures and the H_2O apex. The results show a wide range of salt concentrations in the fluid inclusions and also varying NaCl:$CaCl_2$ ratios. On average, brine of "cluster-inclusions" contain 5.4 wt% NaCl and 3.6 wt% $CaCl_2$ (NaCl:$CaCl_2$ ratio 60:40), whereas these occurring in FIPs and as single inclusions contain somewhat higher proportions of $CaCl_2$ with 2.4 wt% NaCl and 6.6 wt% $CaCl_2$ (NaCl:$CaCl_2$ ratio 30:70) and 4.4 wt% NaCl and 6.6 wt% $CaCl_2$ (NaCl:$CaCl_2$ ratio 40:60), respectively.

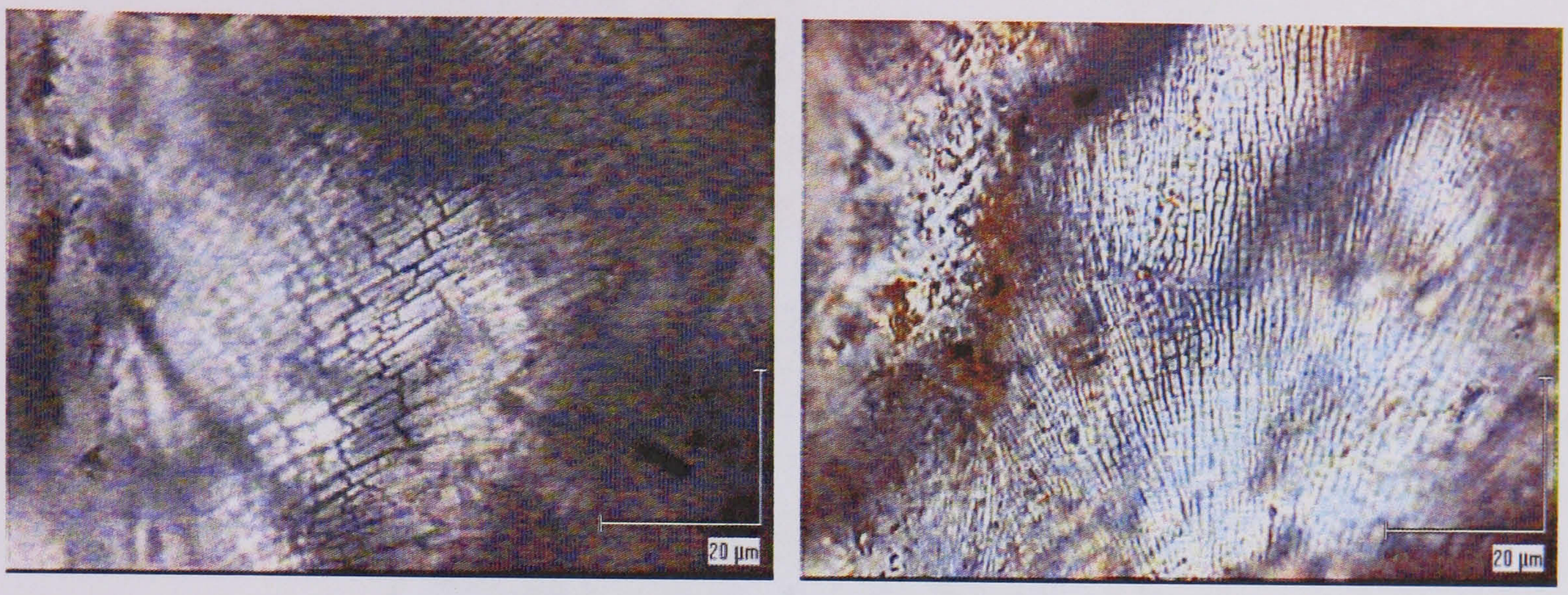

Figure 6.12: Photomicrographs showing the degradation of the nepheline host mineral during microthermometry. It mostly starts around 400-500°C. The observation of final homogenisation of two-phase aqueous inclusions is therefore often impossible.

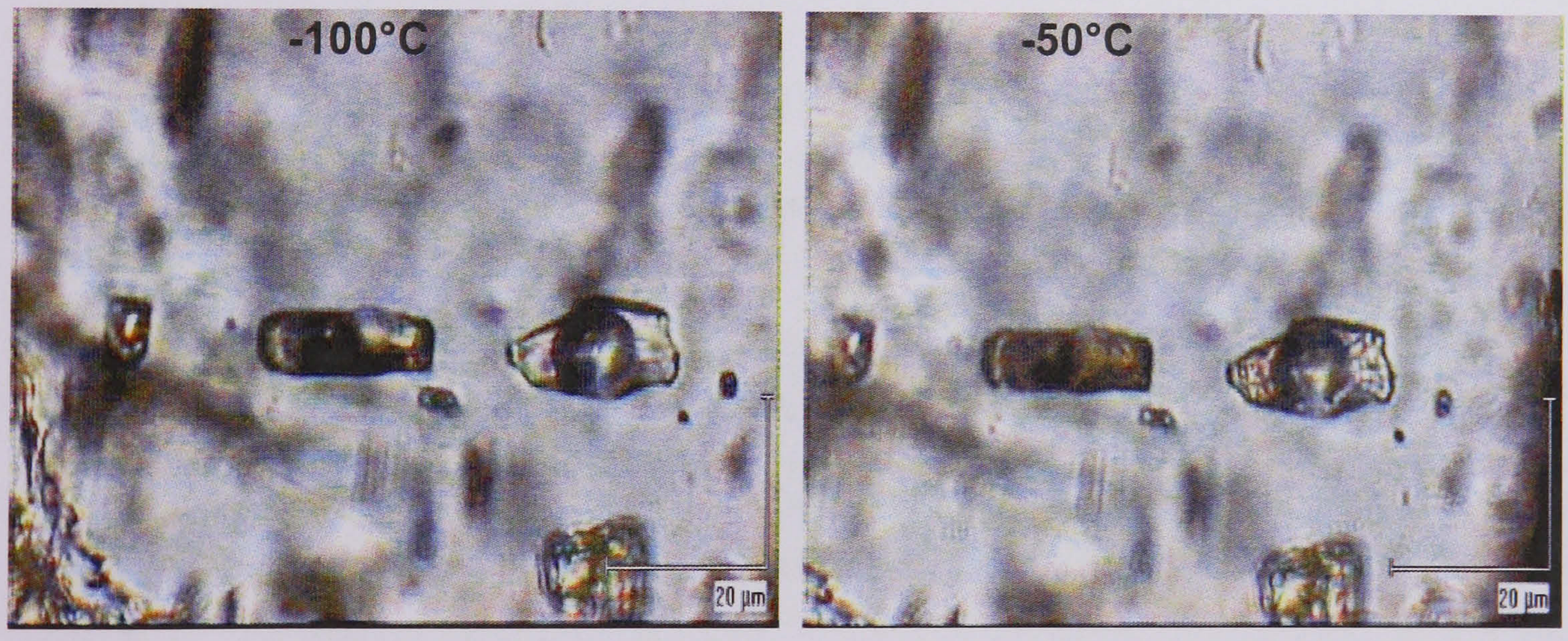

Figure6.13: Typical pale brown and speckled appearance that occurs in the initial phase of heating of a $CaCl_2$ containing aqueous fluid inclusion.

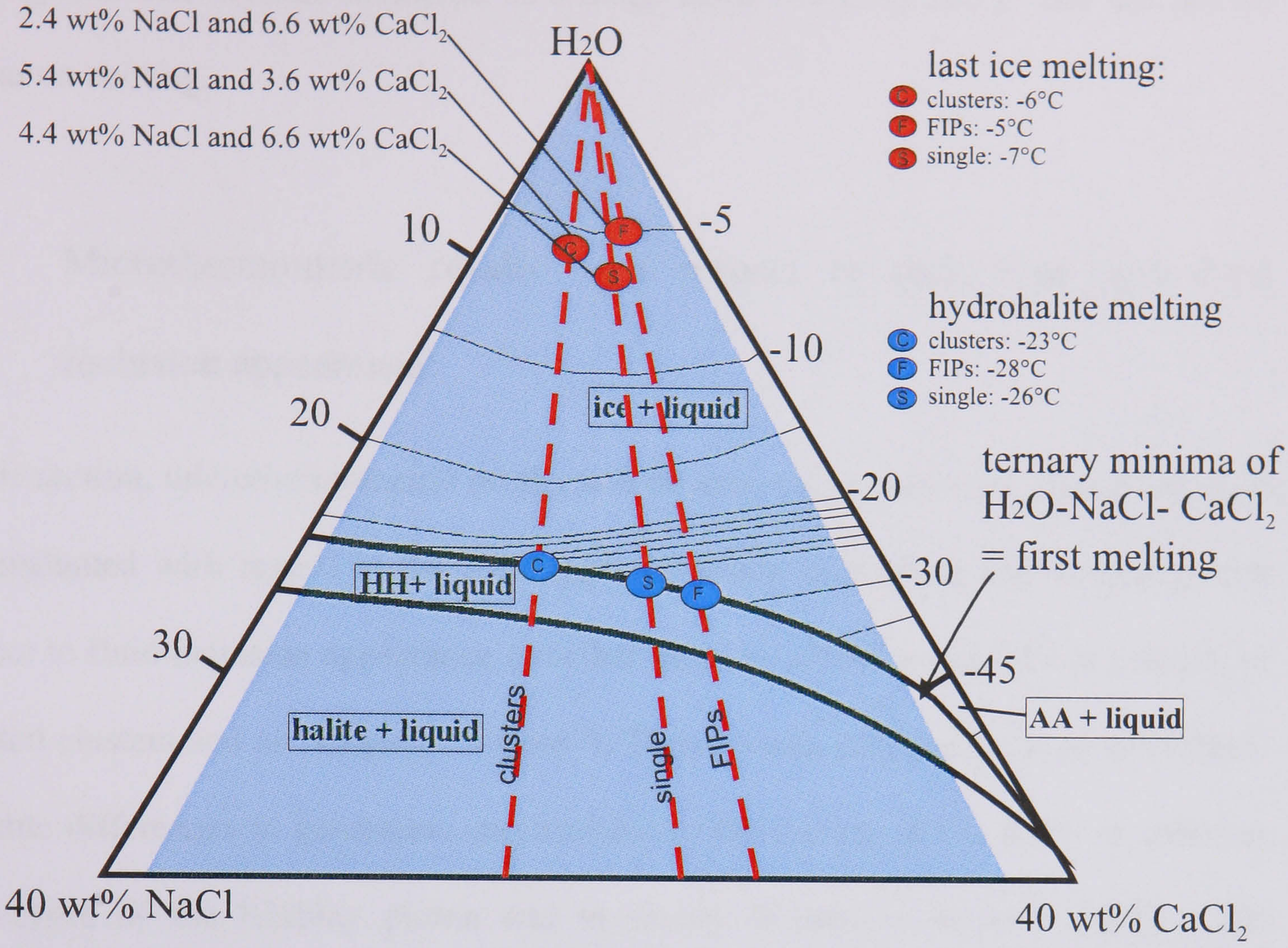

Figure 6.14: Ternary diagram of the H_2O-NaCl-$CaCl_2$ system. Phase boundaries and isotherms are modified from Shepherd *et al.* (1985) and Oakes *et al.* (1989). The black arrow shows the ternary minima where melting of the solid antarcticite (AA) occurs (not observed). The melting path of the inclusions follows then the isopleth dividing hydrohalite (HH) + liquid field and ice + liquid field. On heating the fluid composition changes along the phase boundary until all HH is liquid (indicated by the blue dots). Then it follows the tie-line towards the H_2O-apex until all ice is molten (indicated by the red dots). Here, the composition of the brine can be graphically estimated. Exemplarily, the average composition of inclusions in clusters, FIPs and "single-inclusions" is shown. The wide range of microthermometric results of water-dominant inclusions is shown by the blue covered area.

Only four daughter-mineral-bearing inclusions were microthermometrically investigated. The crystals dissolved in a range from 179°C to 265°C and did not re-appear on cooling.

6.6.1 Microthermometric results with respect to rock type and fluid inclusion appearance

In this section, microthermometric results will be assessed in two ways. Firstly, the data are evaluated with regard to the rock types in which they occur and secondly with respect to fluid inclusion appearance (whether they are secondary in FIPs or primary in isolated clusters and as "single inclusions"). These results can then be used to evaluate possible differences in generation mechanisms or the history of the fluids in different rock types of the Khibiny pluton and to assess differences between primary and secondary fluid inclusions.

Methane-dominant fluid inclusions

As stated above, methane-dominant fluid inclusions homogenise between -62°C and -99°C. Only small differences appear in the T_h-histograms, when separated by rock type (Fig. 6.15). A maximum with T_h = -74°C tends to be more dominant in the rocks from the inner complex (foyaites, alkaline syenite, ijolite, lujavrite) whereas the inclusions in the outer two rock formations (khibinite and rischorrite) show their T_h-maximum at -83°C. This observation indicates differences in either fluid composition (see Section 6.6.1) or entrapment conditions. The trapped fluids near the core of the complex may either contain a larger proportion of higher hydrocarbons whereas fluids from the outer rock sequences have relatively pure methane compositions or fluids from the outer rock sequences contain more impurities of H_2 or N_2 than these of the inner rock sequences.

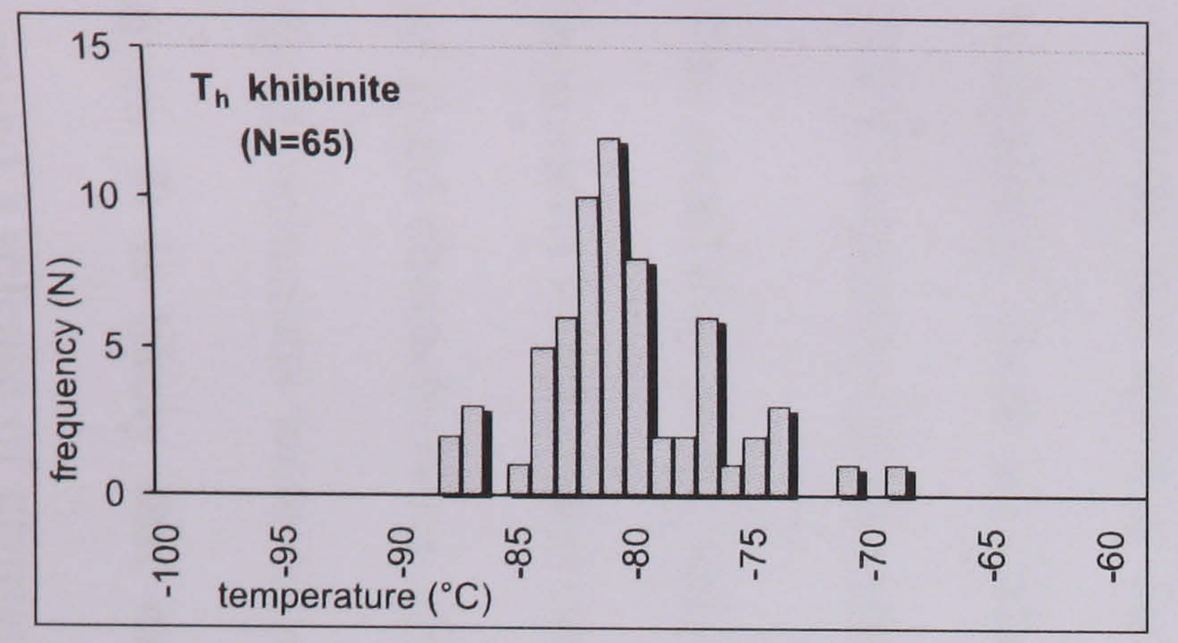

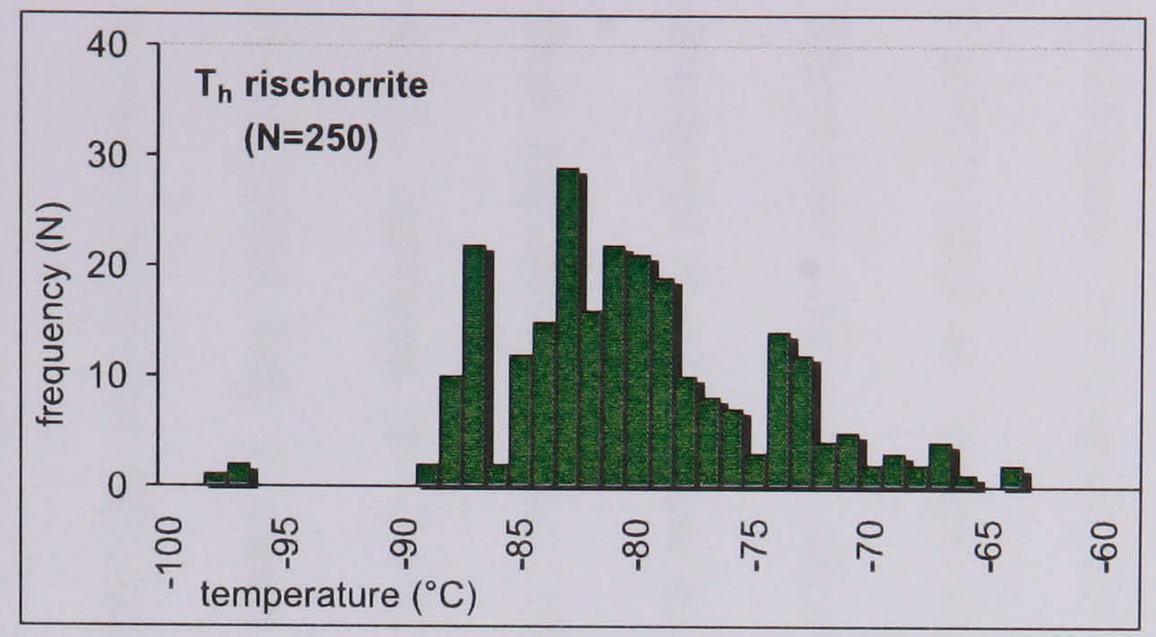

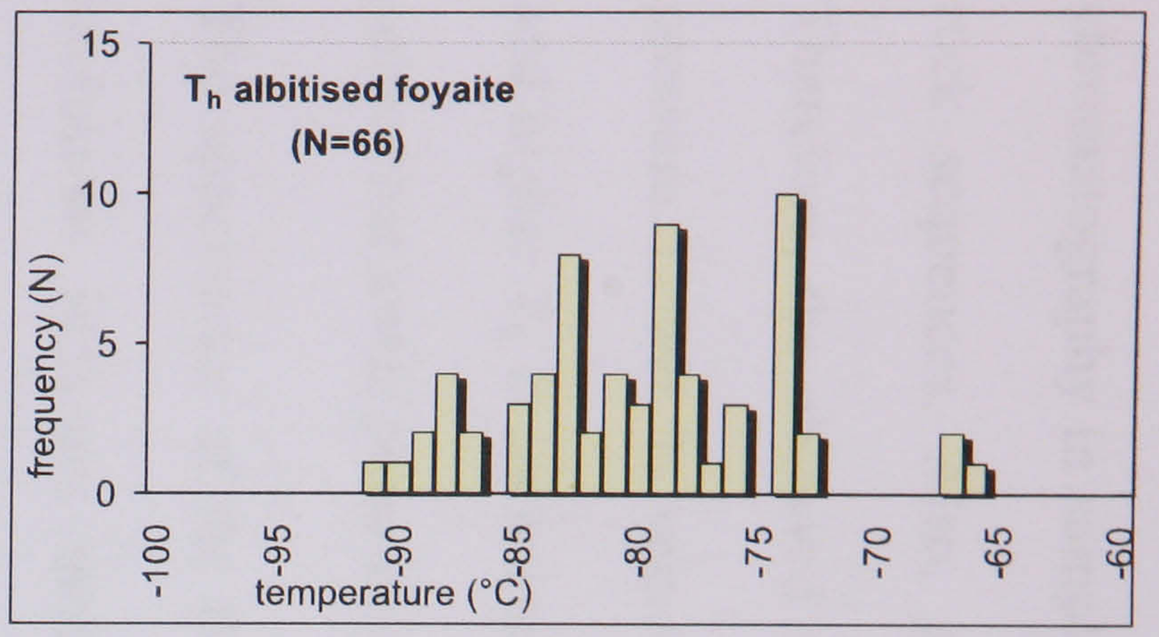

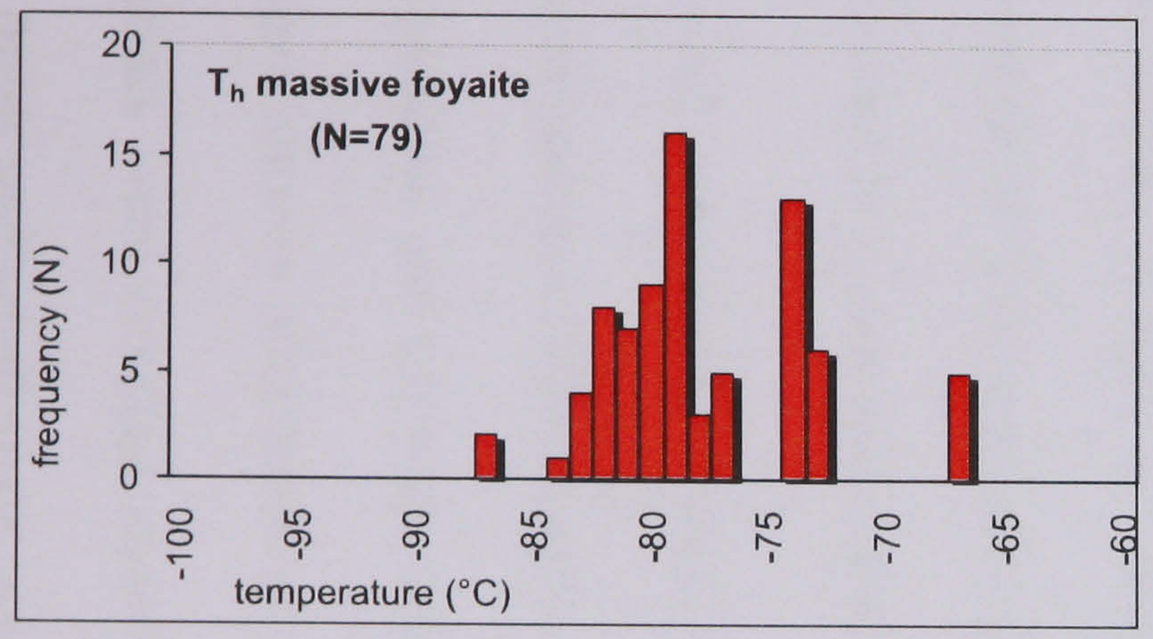

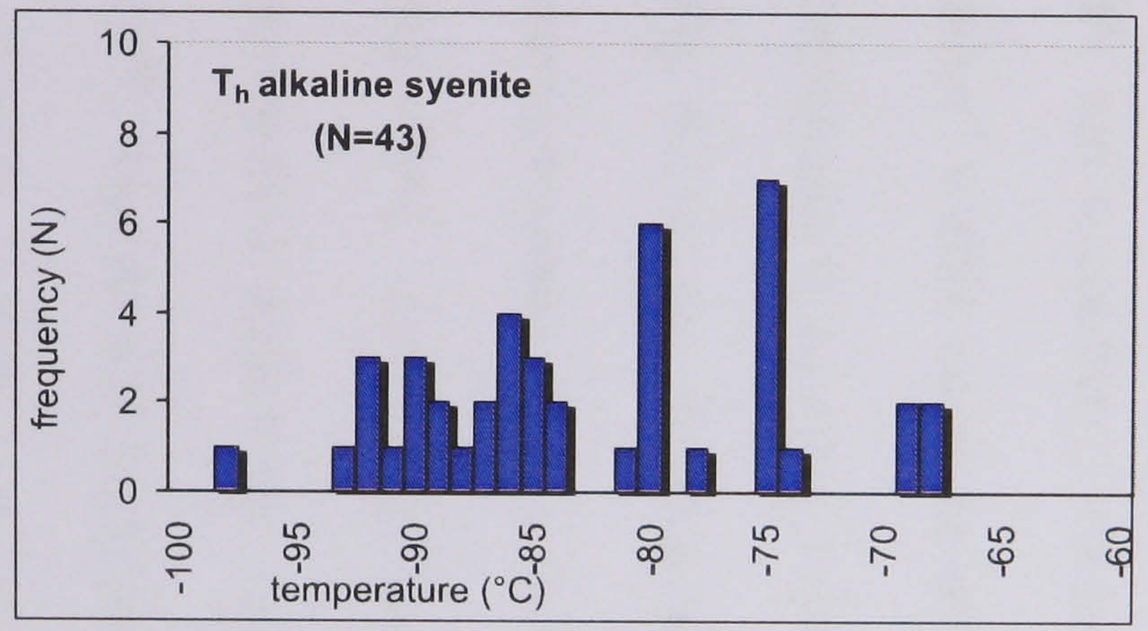

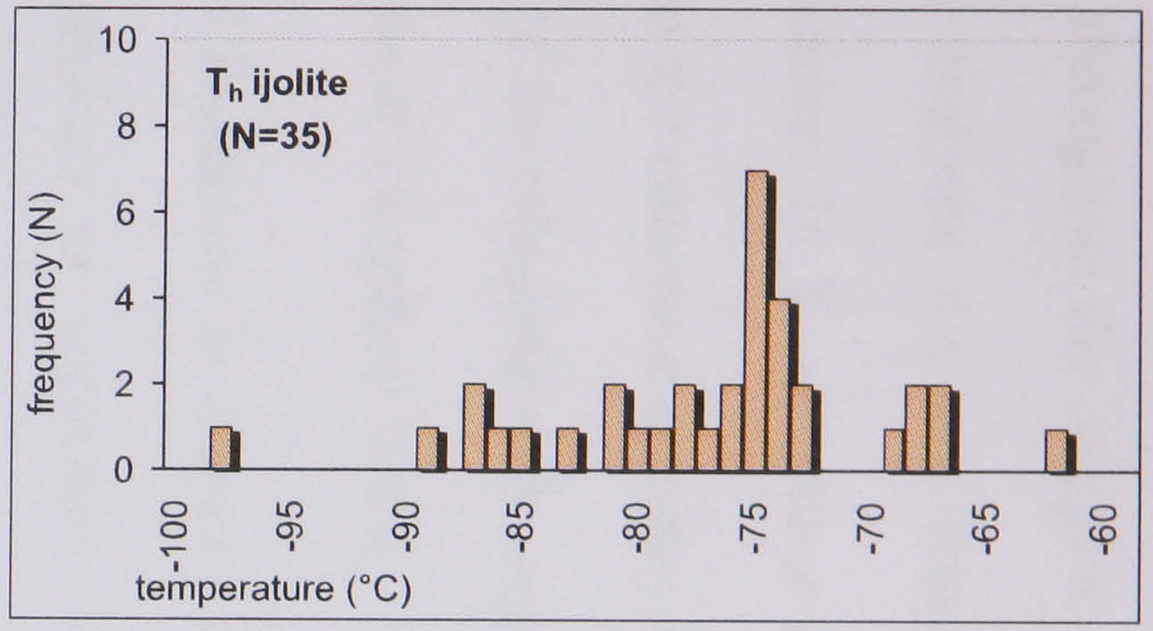

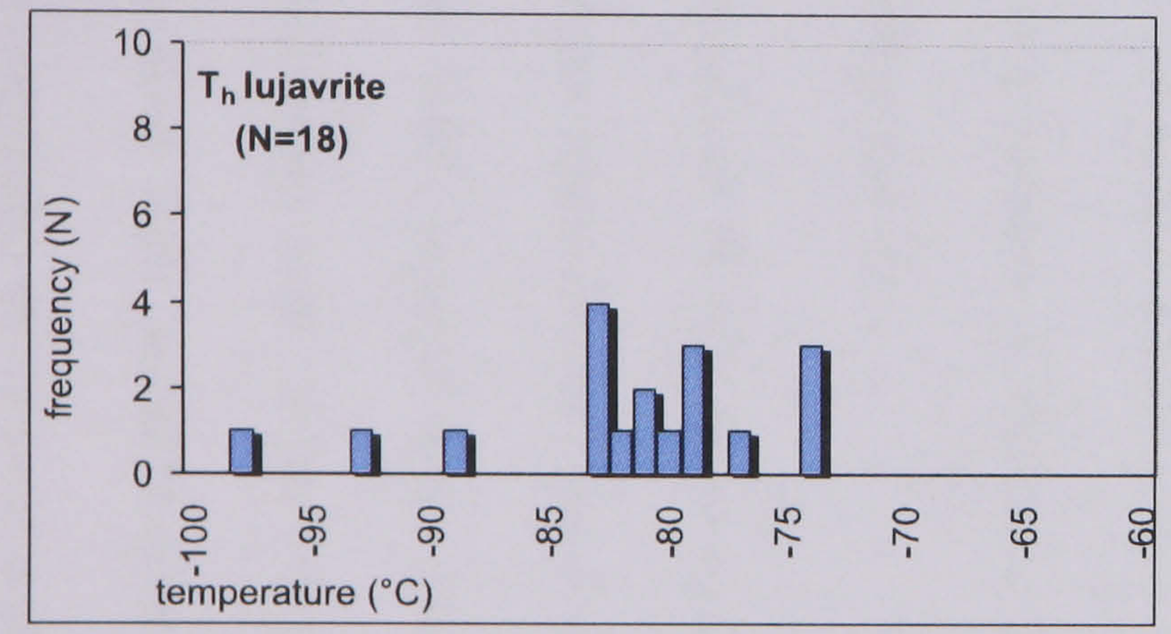

Figure 6.15: Frequency histograms of homogenisation temperatures (T_h) of methane-dominant fluid inclusions in different rock types of the Khibiny pluton. The majority homogenise around the critical temperature of methane at -82.6°C. The frequency maximum shifts to somewhat higher values in inclusions from rocks of the inner part of the Khibiny complex (foyaites, alkaline syenite and ijolite).

However, higher hydrocarbons (ethane and propane) were detected by gas chromatography in samples throughout the complex and are not restricted to the inner rock sequences. Also, gas analyses did not reveal other impurities (Chapter 7). Therefore, the observed variations in T_h are rather the result of different entrapment pressure. Lower T_h values in the core-near samples indicate high entrapment pressure and higher T_h in inclusions of the marginal rock sequences indicates the entrapment at somewhat lower pressure (Van den Kerkhof, 1988).

The appearance of the fluid inclusions in clusters, FIPs and as separate single fluid inclusions indicates their primary or secondary origin. It is assumed, that fluid inclusions entrapped in FIPs are secondary, whereas the majority of inclusions in clusters and as "single-inclusion" within minerals are believed to be of primary origin. Therefore, different microthermometric results should be expected. For the methane-dominant fluid inclusions (Fig. 6.11a) no strong differences are apparent in relation to their appearance. The "cluster-inclusions" show a wide spread of data and two, nearly equal, maxima at -74°C and -80°C. Inclusions that occur in FIPs show a similar distribution but a more pronounced maximum around the critical temperature of methane between -82 and -83°C. The second maximum at -74°C is less dominant. This indicates that most of the inclusions in FIPs are relatively pure methane. The "single-inclusions" show a smaller range of homogenisation temperatures of between -89 and -74°C which indicate smaller density variations and fewer impurities.

The similarity in T_h values and comparable Raman results of primary and secondary inclusions implies that both inclusions contain fluids of the same origin. The similarity of fluid characteristics (composition and pressure of the fluid) suggests that secondary fluid inclusions were entrapped shortly after primary inclusions and not far away from them. It is likely that minerals were cracked shortly after their solidification. This caused a release of primary fluids and small-scale, post-magmatic movement with fluid

entrapment in FIPs near by. Thereby, neither pressure nor composition of the fluids would have changed significantly.

Water-dominant fluid inclusions

The temperature range for first ice melting, hydrohalite melting and last ice melting appears to be similar for all inclusion types (Fig. 6.11b and c).

Although a large number of fluid inclusions decrepitate, or their host minerals degrade before homogenisation, some differences of T_h are noticeable (Fig. 6.11c). The fluid inclusions in FIPs and "cluster-inclusions" show a wide spread of homogenisation temperatures, whereby the majority of fluid inclusion homogenise between 375°C and 440°C. Despite the scarcity of data for single inclusions, the trend to higher homogenisation temperatures, >455°C is visible.

The comparisons of T_h values with respect to rock type show no significant differences (Fig. 6.16). The widest range of T_h is found in samples of khibinite and albitised foyaite, from 290°C to >500°C. Most inclusions show homogenisation above 380°C and a large number of inclusions even decrepitate before homogenisation. Also, due to the scarcity of data, a conclusion regarding fluid inclusion behaviour with respect to rock type can not be drawn.

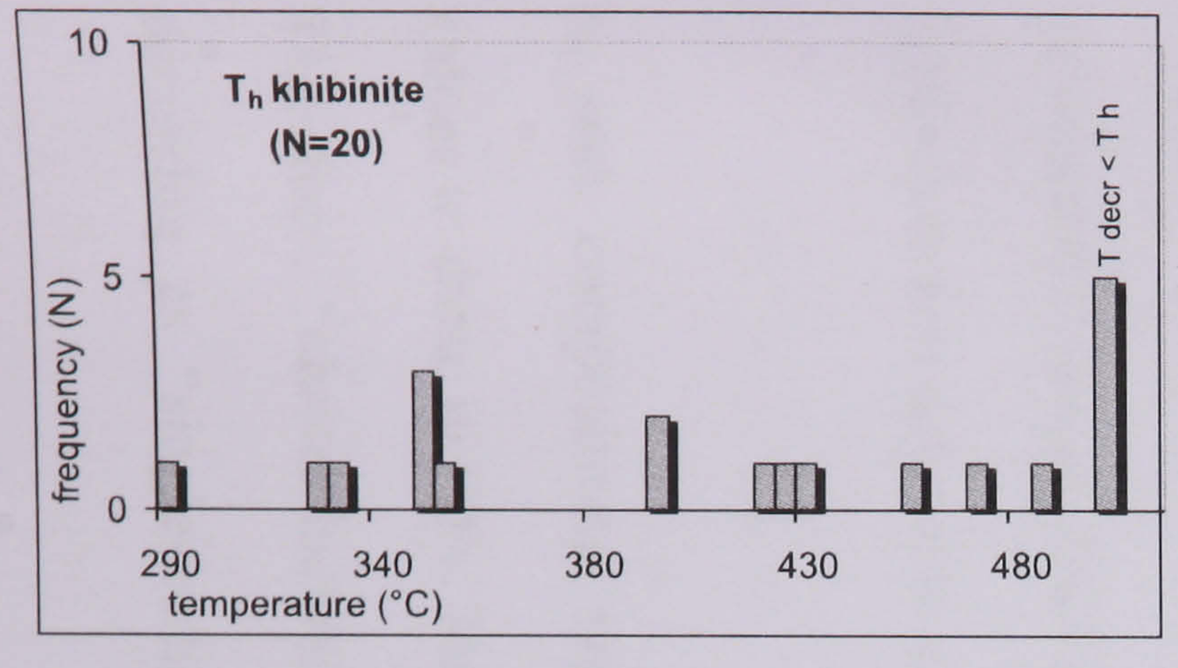

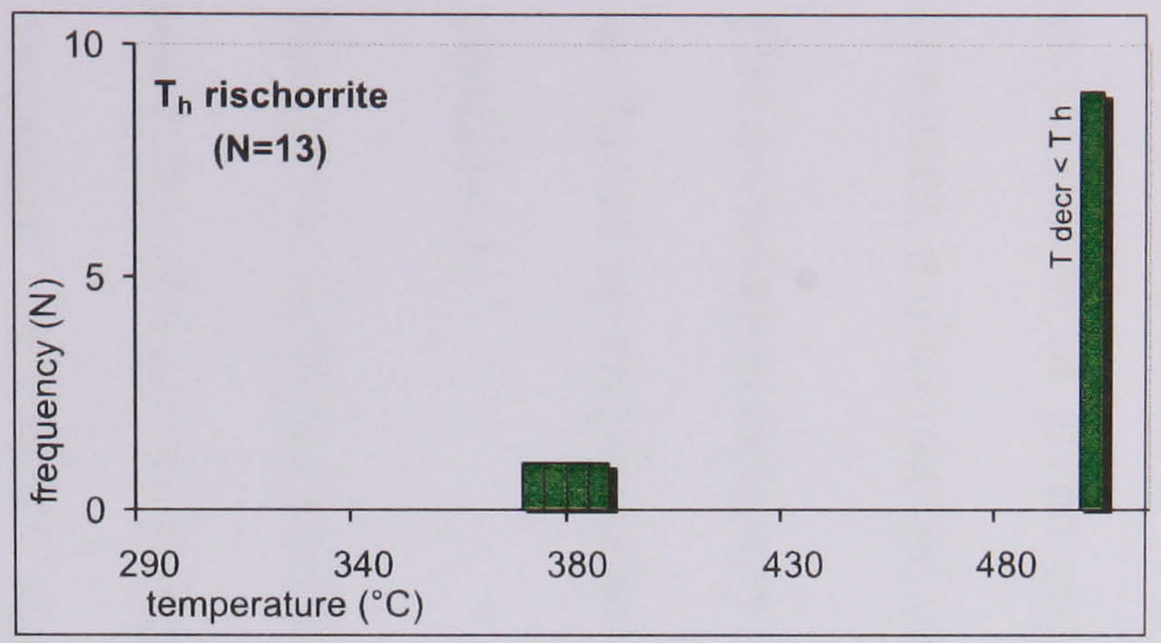

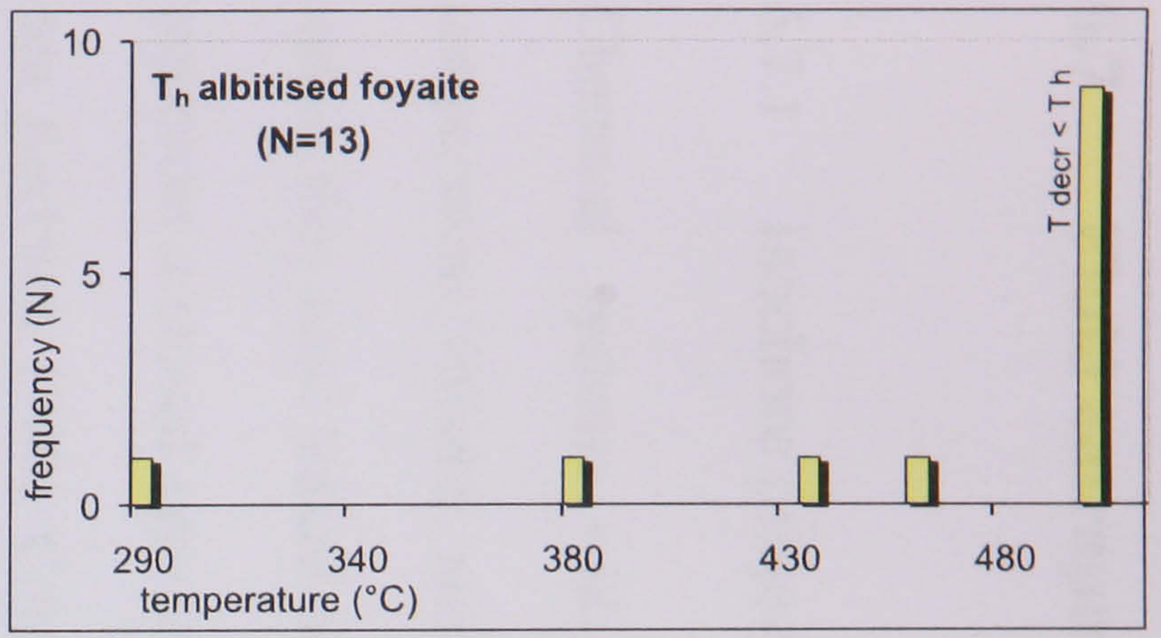

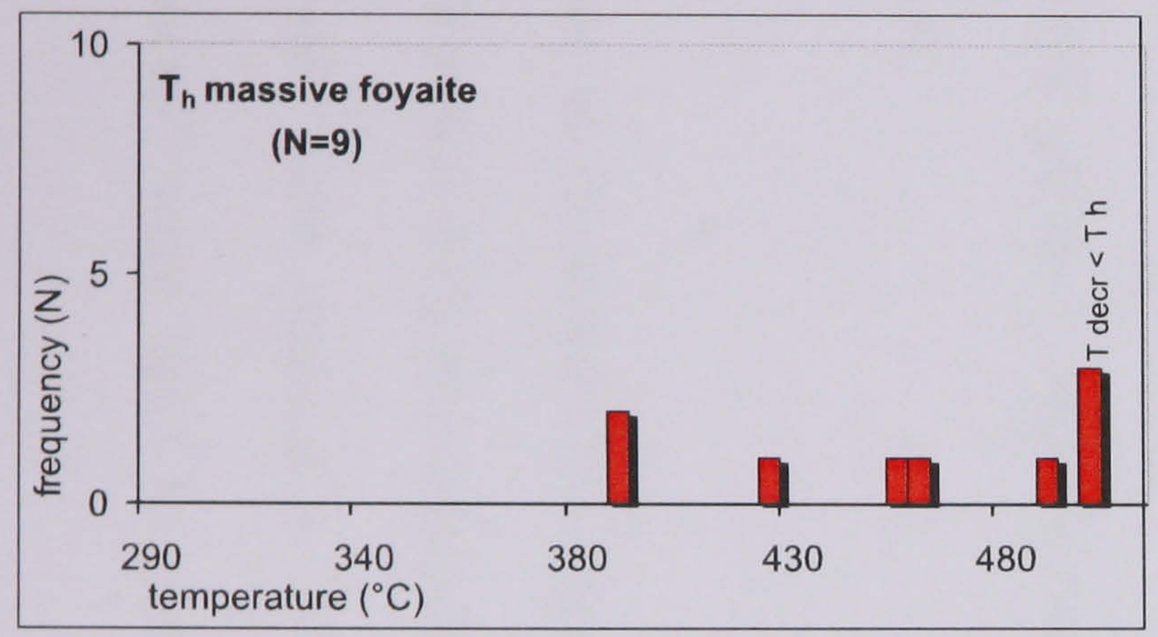

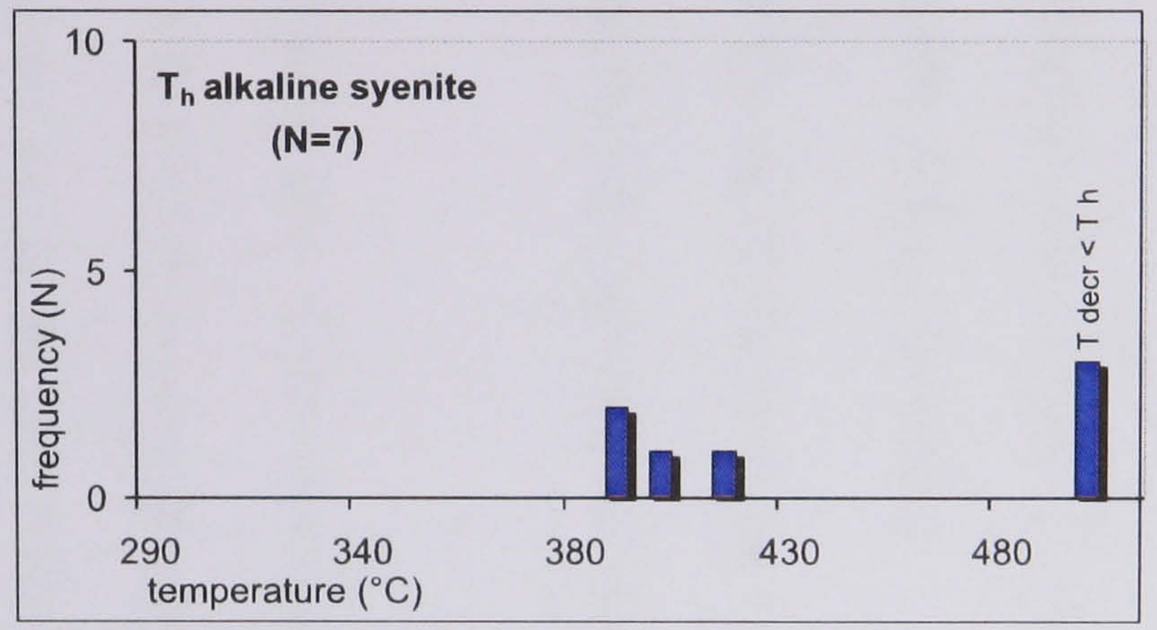

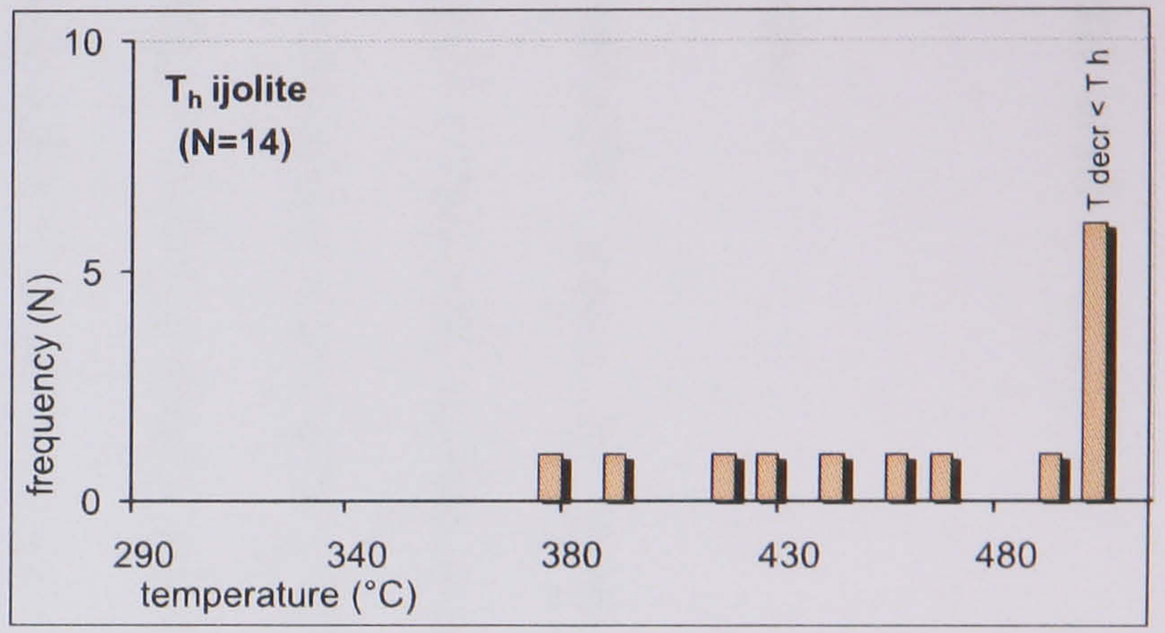

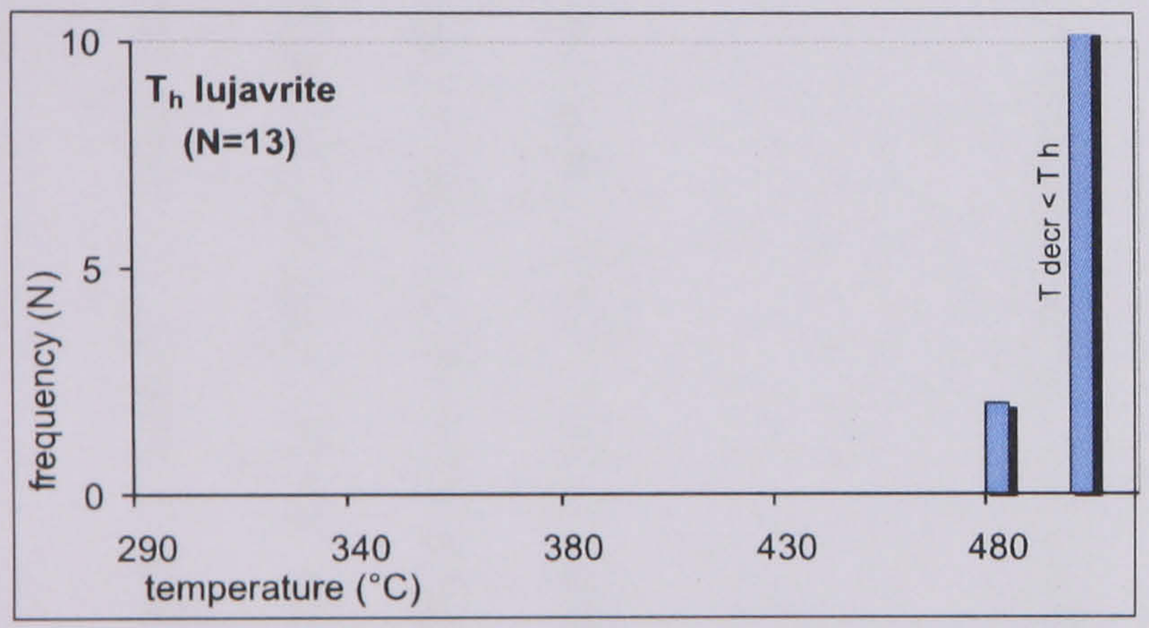

Figure 6.16: Frequency histograms of homogenisation temperatures (T_h) of aqueous fluid inclusions in different rock types of the Khibiny pluton. For many inclusions homogenisation could not be observed during heating >500°C. Above this temperature no data could be obtained as the host minerals degrade and the fluid inclusions decrepitate. Homogenisation appears to be independent on rock type mostly above c. 380°C. Only in samples of khibinite and albitised foyaite some inclusions homogenise below this temperature.

6.7 Fluid entrapment and evolution

6.7.1 Isochore projections

Chemical systems with variable states of matter are determined by pressure, temperature, volume, mass and composition. For isochore projections, fluid inclusions, unless they have leaked or experience non-elastic stretching, are generally considered to represent a closed system where volume, mass and composition remain constant (Van den Kerkhof, 1988). Consequently, temperature and pressure are the only variables in an inclusion of given composition that change. If volume and mass are assumed to be constant, it also implies constant density (d=m/V).

The correlation between PVTX for fluids is given by equations of state (EoSs). These are based on empirically-determined experimental data and used to extrapolate physical conditions.

Based on fluid inclusion data of this study entrapment conditions of fluid inclusions were determined by using EoSs for isochore projections. For this purpose the computer programs "FLUIDS", designed by R. Bakker (download at http://www.unileoben.ac.at/~buero62/minpet/ Bakker/Programs/ Computer.html; Bakker, 2003) for analyses of fluid inclusion data were used.

In both compositional types of inclusions the "cluster-inclusions" show similar T_h values to those in FIPs. This makes their possible primary origin somewhat ambiguous. Therefore, "cluster-inclusions" were omitted in PVTX modelling. Fluid inclusions occurring as "single-inclusions" were used to obtain data on primary entrapment

condition and fluid inclusions in FIPs for calculation of secondary entrapment conditions.

Methane-dominant fluid inclusions

For methane-dominant fluid inclusions the EoS of Peng & Robinson (1976), applicable for any gas mixture, is employed in the BULK program by Bakker (2003). Exemplarily, the calculated isochore for pure methane inclusions is shown in Figure 6.17a. The isochore for this type of inclusion is very shallow with pressures between 25 and 100 MPa in the temperature range from 100°C to 1000°C. For the methane-dominant inclusions of this study an average methane-ethane ratio of 0.95/0.05 is known from bulk gas analysis (Chapter 7) and also implied by laser Raman studies. If the ethane component is considered in the isochore calculation, the isochore slope increases slightly as well as the internal pressure to 80 MPa at 100°C and 275 MPa at 1000°C.

It is known from the literature, that with decreasing mol% CH_4 and increasing mol% of higher hydrocarbons the slope of the isochores would somewhat increase, as the fluid becomes less compressible (Burruss, 1992). However, the small amounts of propane and butane, occasionally detected in the fluid inclusions, are not considered for isochore projection, as their effect is judged to be negligible.

The methane-dominant fluid inclusions were probably trapped by the growth of a mineral that precipitates from an aqueous phase and it is likely that an aqueous liquid phase wets the inclusion wall. Therefore, the calculations are repeated introducing an aqueous phase (1 %) which is assumed to have brine composition similar to that of the average water-dominant "single-inclusion". For the calculation of the of the aqueous phase behaviour a combination of EoSs for the system NaCl-KCl-$CaCl_2$-$MgCl_2$ (Bakker, 1999) is used. The projected isochors show a somewhat steeper slope compared to that of pure gaseous inclusions (Fig. 6.17a).

Isochores for primary (single) and secondary (these in FIPs) inclusions of this study are very similar (Fig. 6.17b). The differences are basically controlled by varying T_h values. The isochore-range for primary inclusions is embraced by that of isochores from inclusions in FIPs.

Water-dominant fluid inclusions

The isochores of water-dominant inclusions are constructed in a similar way to these for methane-dominant inclusions, using bulk compositions calculated from microthermometric data in the BULK program (Bakker, 2003). For the methane-rich vapour phase a composition similar to that of the average methane-dominant primary inclusions is assumed (methane:ethane ratio of 0.95:0.05). In the calculation, the average NaCl:$CaCl_2$ ratio of 60:40 for single inclusions and 30:70 for inclusions in FIPs are used based on the graphical estimates (see Fig. 6.14). The upper and lower limits of isochore projection are set by the different homogenisation temperatures. The average degree of filling (size of the gas bubble at room temperature) of 50 % is used in the calculation. This is visually estimated using the chart of gas volumes in inclusions by Roedder (1972).

The isochoric P-T-paths for entrapment conditions of aqueous fluid inclusions are calculated using the EoS proposed by Bowers & Helgeson (1983) and modified by Bakker (1999). To illustrate the changes of isochore positions depending on fluid compositions, isochores of a pure H_2O inclusion, a H_2O-NaCl, H_2O-NaCl-$CaCl_2$ and H_2O-NaCl-$CaCl_2$-CH_4 mixed inclusion are shown in Fig. 6.17c. Compared to a pure H_2O inclusion, salt causes a steepening of the isochore. The differences between H_2O-NaCl and H_2O-NaCl-$CaCl_2$ mixed brines, however, are fairly small. The addition of methane causes a shift of the isochore position to lower pressure that corresponds with high temperature.

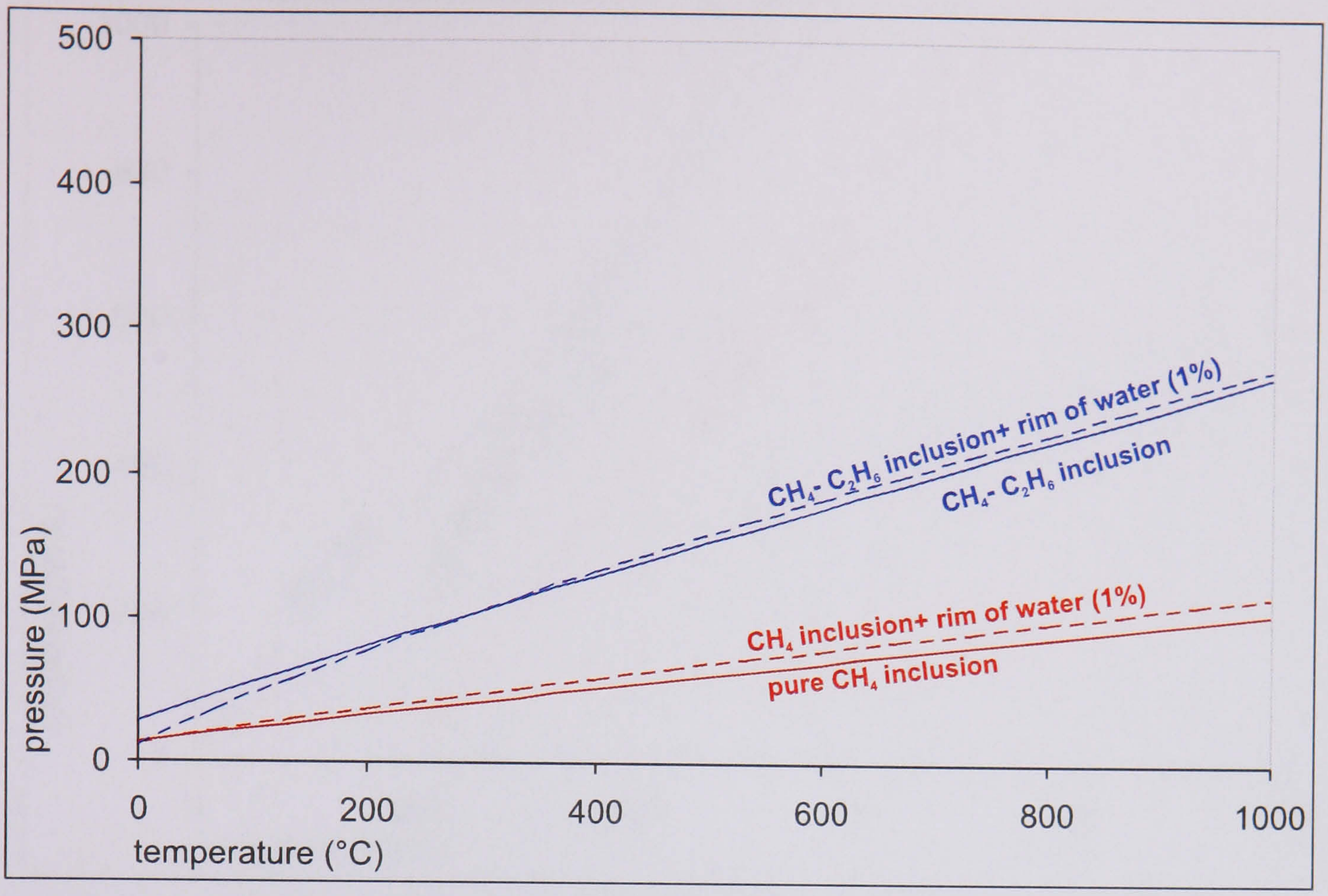

Figure 6.17a: Isochoric projection constructed for different gas compositions with and without a rim of water. Pure methane isochores are very shallow. The addition of 5% ethane causes an increase in isochore slope. A small rim of water does not change the isochoric projection considerably.

Figure 6.17b: Minimum and maximum isochoric projections constructed for primary (yellow) and secondary (blue) methane-dominant inclusions of the Khibiny pluton. Homogenisation temperatures are shown on the right.

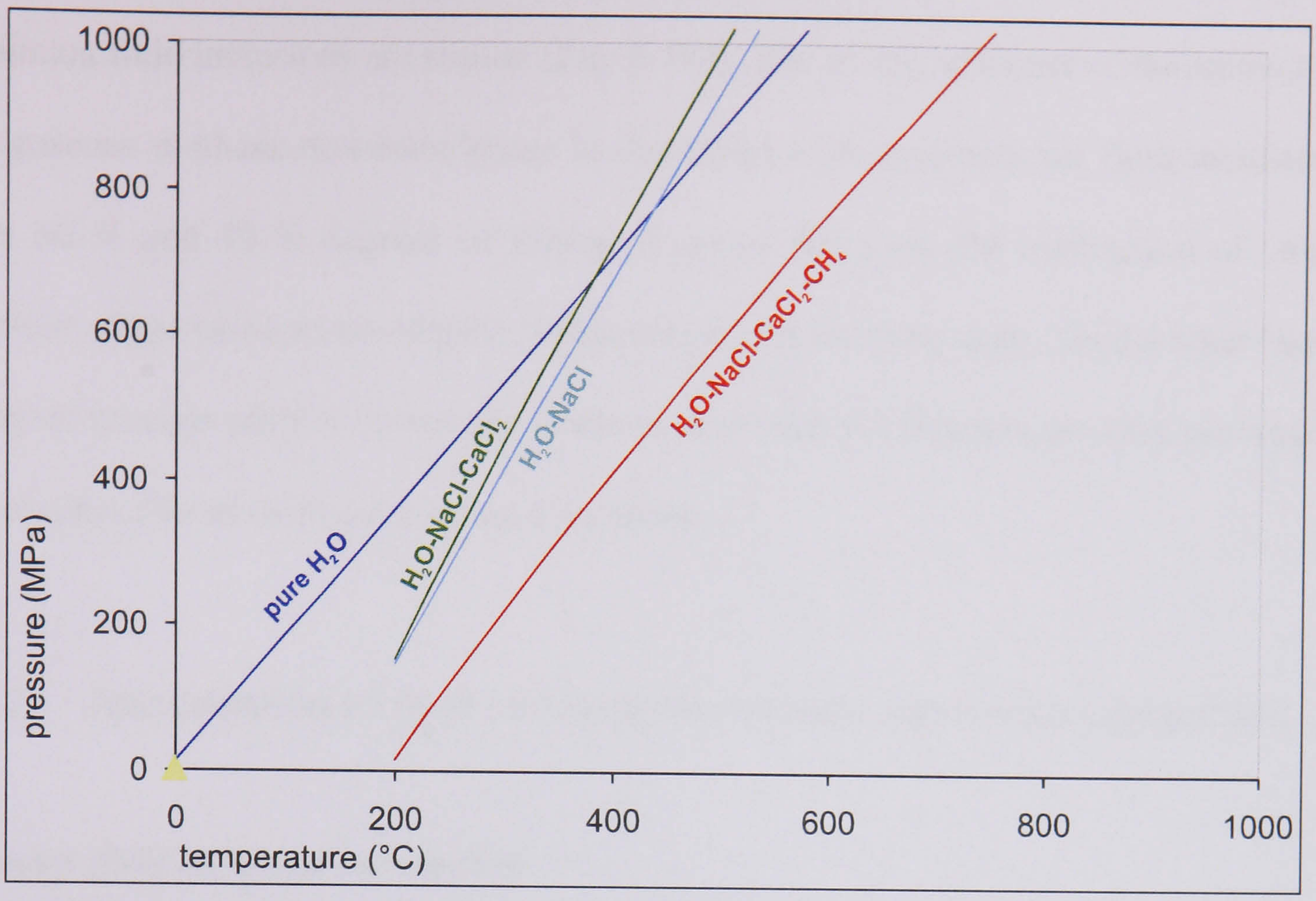

Figure 6.17c: Isochoric projection for different types of water-dominant inclusions. Generally, the isochores are steeper than that of methane-dominant inclusions. The addition of salt causes an further increase in isochore slope. The occurrence of methane in water-dominant inclusions causes a shift of isochore position towards higher temperatures.

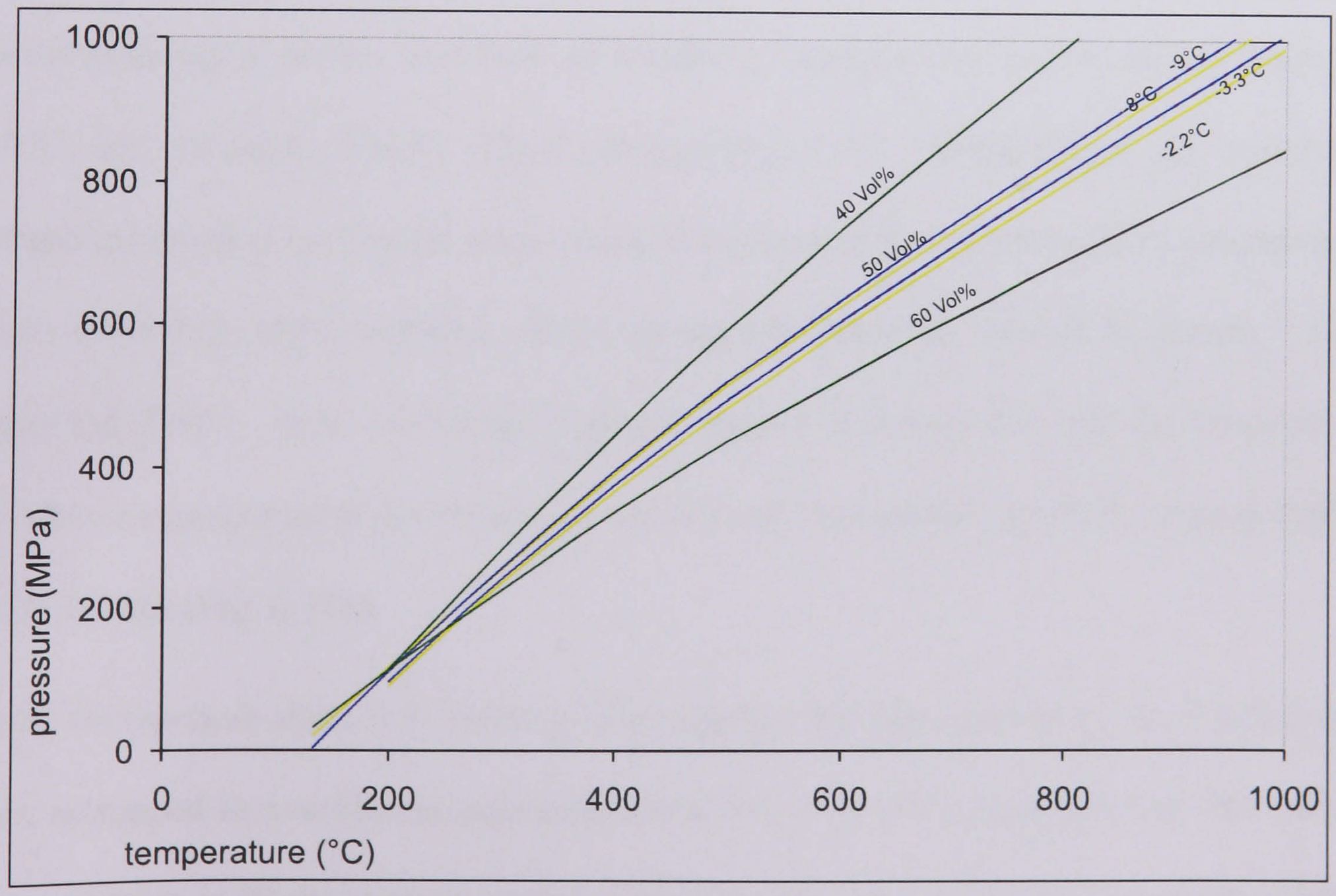

Figure 6.17d: Minimum and maximum isochoric projections constructed for primary (yellow) and secondary (blue) water-dominant fluid inclusions of the Khibiny pluton. Temperatures of final ice melting are shown. Degrees of filling (gas bubble) of 50 vol% were used for isochore calculations. Isochor projections for inclusions with 40 and 60 vol% degree of filling are shown to illustrate the strong influence of this parameter.

As for methane-dominant inclusions, the isochores of primary and secondary water-dominant fluid inclusions are similar (Fig. 6.17d). The strong influence of the amount of the gaseous methane-dominant phase is illustrated with isochores for fluid inclusions with 60 % and 40 % degrees of filling. It shows that even the subtraction of small portions of gas cause a considerable steepening of the isochore slope. On the other hand, a higher gaseous portion lowers the isochore slope and the isochore position eventually approaches that of methane-dominant inclusions.

6.7.2 Interpretation of fluid inclusion observation and isochore projection

Primary fluid inclusion entrapment

Entrapment conditions of primary fluid inclusions can be estimated using inclusions which were certainly trapped during crystal growth, assuming that they did not suffer any changes in composition, pressure and density at a later stage.

Microthermometry shows that homogenisation of aqueous inclusions mostly starts at 450°C and exceeds 500°C. These temperatures are representative of minimum entrapment conditions. For the upper limit of primary inclusion entrapment, temperature values around the H_2O-saturated solidus for agpaitic nepheline syenite (Sørensen, 1970; Edgar and Parker, 1974) are likely. The intersection of the solidus with the isochore of the water-dominant inclusions encloses the relevant entrapment envelope around 600°C and 600 MPa (Fig. 6.17e).

Based on isochore data, it is inferred that primary methane-dominant fluid inclusions were entrapped in a similar temperature range but at lower pressure (below 200 MPa), as entrapment is likely to have occurred near the solidus of the H_2O-saturated solidus for agpaitic nepheline syenite (Sørensen, 1970; Edgar and Parker, 1974).

The P-T conditions of primary fluid inclusion entrapment above the CH_4-H_2O-solvus (Zhang and Frantz, 1992) indicate that a homogeneous fluid was present at the time of trapping. The following two possibilities may explain the occurrence of two compositionally distinct primary fluid inclusion populations.

1. Two fluids, one aqueous and another methane-dominant existed successively. First, a water-dominant fluid (with methane dissolved in it) was present in the magma and secondly, at approximately hydrostatic P-T conditions, a methane-dominant fluid existed. The relicts of the initially water-dominant fluid are found as primary inclusions, entrapped at high P-T conditions. In the course of magma cooling the aqueous fraction of the fluid was preferentially incorporated into hydrous mineral phases during crystallisation. This produced a virtually water-free, methane-dominant fluid which was trapped shortly afterwards. It is also possible that fluids from the host rocks intruded into the hot ascending pluton. This would explain the hydrostatic P-T conditions of primary methane-entrapment.

2. Another possibility is that all primary inclusions were trapped from the same homogenous, CH_4-H_2O-mixed fluid. In this case, the observation of apparently two fluid generations, one methane-dominant and another one water-dominant, would be due to post-entrapment changes. Water-dominant inclusions might represent the fluid at the time of entrapment whereas methane-dominant inclusions would be the result of preferential water loss during leakage or diffusion. Necking down might also have changed the initial fluid inclusions and produced two or more inclusions with varying portions of methane and water.

Secondary fluid inclusion entrapment

The differences between isochores of primary and secondary fluid inclusions of both, water- and methane-dominant species are small. This indicates relatively similar compositions and entrapment conditions of primary and secondary inclusions. Cracking and healing presumably started immediately after mineral crystallisation.

Generally, for the entrapment of secondary fluid inclusions, a wide range of entrapment conditions is likely (Fig. 6.17f) as fluid movement, entrapment and release started shortly after mineral crystallisation and continued repeatedly. An aqueous fluid with dissolved gas can be trapped under any P-T conditions below the nepheline syenite solidus and above the CH_4-H_2O-solvus. The recorded homogenisation temperatures above 350°C of two-phase water-rich inclusions support this view. In a low-temperature two-phase system below the CH_4-H_2O-solvus (Zhang and Frantz, 1992), CH_4-H_2O fluids are immiscible and entrapment with variable liquid to vapour ratios is likely. The variability in liquid to vapour ratios, however, could also result from necking down. The majority of secondary inclusions are found to be methane-dominant with no visible water phase. They might be trapped from the heterogeneous fluid in which they occur as isolated droplets in the water phase. This is expected when the bulk of the growth of the host crystal occurs from a water solution that contains dispersed bubbles (Roedder and Bodnar, 1980). Another possibility for the dominant entrapment of only methane-dominant inclusions is the general absence of large portions of the aqueous phase in the post-magmatic fluid history.

The brine in secondary water-dominant inclusions has lower Na:Ca ratio (contains more Ca^{2+} than Na^{+}) than that in primary inclusions. This implies that sodium was incorporated into the crystal lattice of primary host minerals (e.g. nepheline) and crack fillings, and left behind somewhat Na-depleted brines.

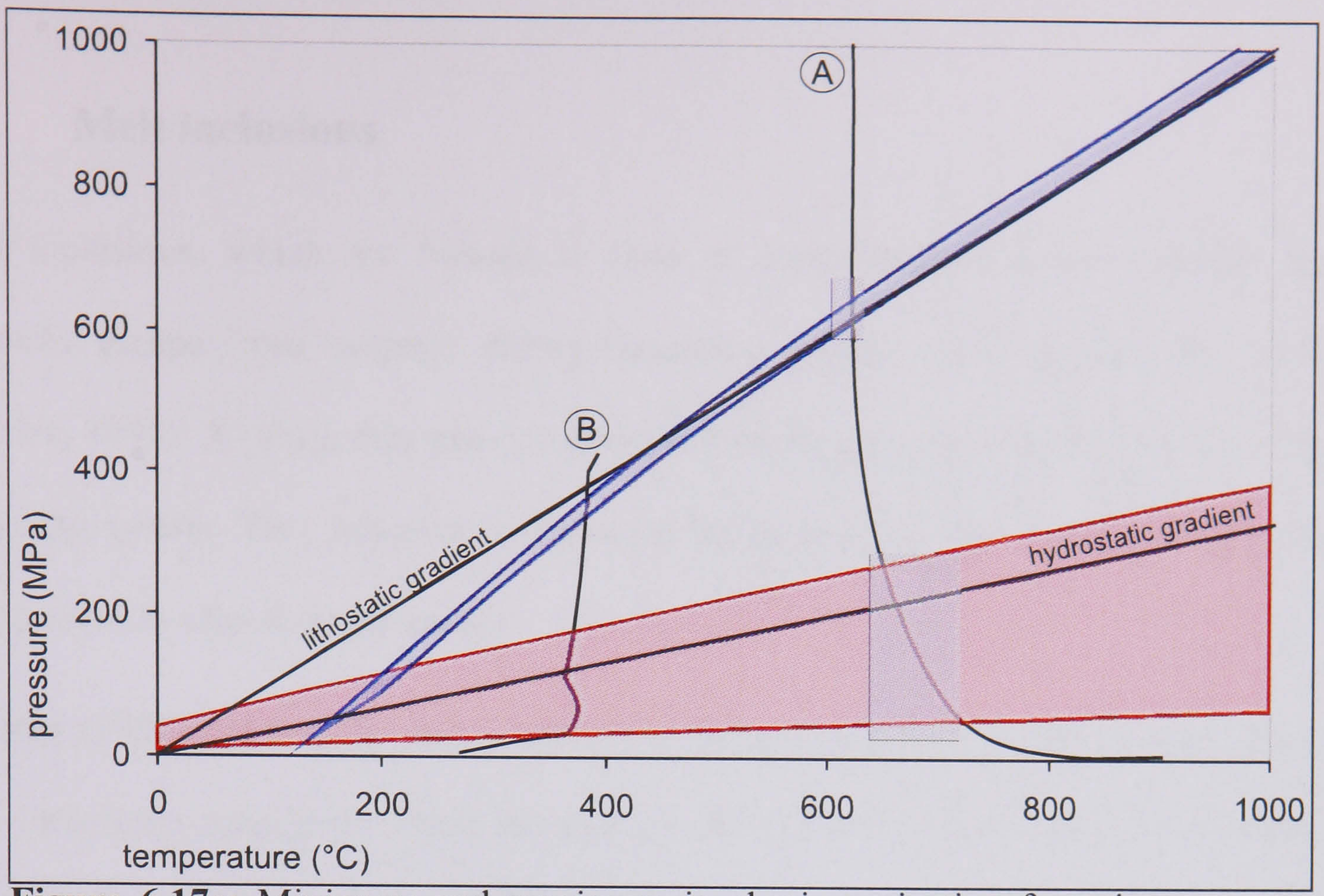

Figure 6.17e: Minimum and maximum isochoric projection for primary water-dominant (blue) and primary methane-dominant (red) inclusions of the Khibiny pluton. Also shown is the water-saturated nepheline syenite solidus (A) from Sørensen (1970) and the CH_4-H_2O solvus (B) from Zhang and Frantz (1992). The shaded boxes represent possible P-T envelopes for trapping of primary water- and methane-dominant inclusions. Also shown are the typical lithostatic gradient of 30 MPa/km and the hydrostatic gradient of 10 MPa/km.

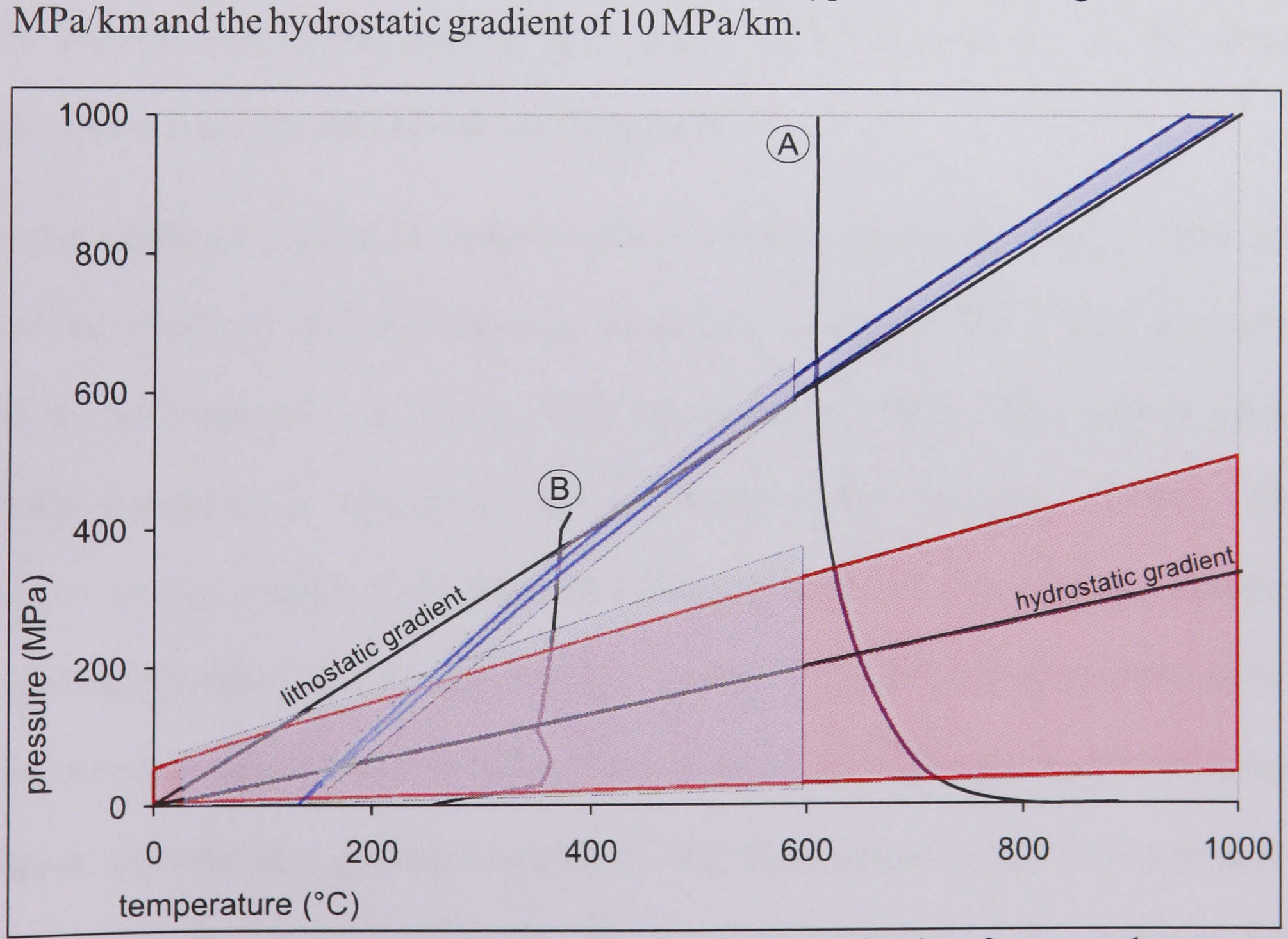

Figure 6.17f: Minimum and maximum isochoric projection for secondary water-dominant (blue) and secondary methane-dominant (red) inclusions of the Khibiny pluton. Also shown is the water-saturated nepheline syenite solidus (A) from Sørensen (1970) and the CH_4-H_2O solvus (B) from Zhang and Frantz (1992). The shaded boxes represent possible P-T envelopes for trapping of secondary water- and methane-dominant inclusions. Also shown are the typical lithostatic gradient of 30 MPa/km and the hydrostatic gradient of 10 MPa/km.

6.8 Melt inclusions

Melt inclusions, which are formed at time of crystallisation, retain volatiles that normally escape from magmas during degassing (Sorby, 1858; Lowenstern, 1995; Sobolev, 1996). As such, they provide direct information on the volatile contents of the magmatic system. This, however, is based on the assumption that inclusions behave as closed systems after their formation.

Roedder (1984) and Sobolev and Kostyuk (1975) list a variety of mechanisms by which melt inclusions may form. These include: (a) the skeletal growth due to non-uniform supply of nutrients to the crystal face or undercooling (lowering of the temperature of a liquid beyond the freezing temperature and still maintaining a liquid form); (b) the formation of re-entrants in the crystal during resorption events, followed by subsequent crystal growth; and (c) the wetting by a separate immiscible phase (e.g. a vapour bubble) that creates irregularities in crystal growth.

Solid inclusions are present in samples from the Khibiny pluton (Fig. 6.18). These are interpreted as silicate melt inclusions in comparison to descriptions of melt inclusions found in the literature (e.g. Sorby, 1858 and Roedder, 1984). They appear glassy (optically isotropic) or crystalline, and are found within nepheline minerals. The inclusions contain variable proportions of arfvedsonite, titanite, aegirine and nepheline as determined by laser Raman spectroscopy together with unidentified, Raman-inactive phases. Some of them contain an up to 5 μm methane-dominant gas phase (confirmed by Raman spectroscopy), present as a bubble. Microthermometric observations were not possible due to the strong degradation, cracking and darkening of the nepheline host mineral at temperatures above 500°C. However, the qualitative detection of methane in melt inclusions is strong evidence in support of its primary, magmatic origin.

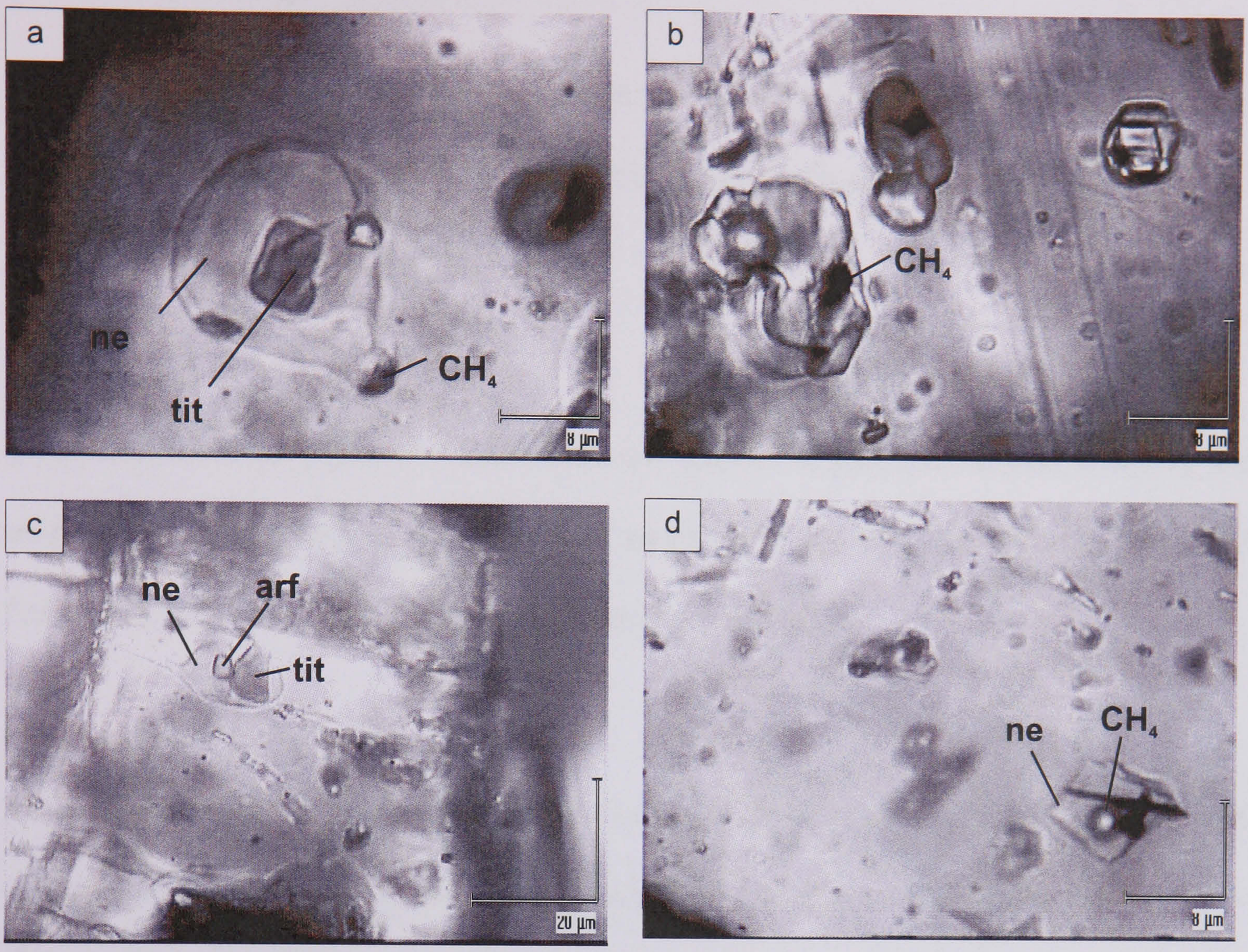

Figure 6.18: Photomicrographs of melt inclusions in rischorrite. The labelled crystalline components titanite (tit), arfvedsonite (arf), aegirine (aeg), nepheline (ne) and methane were identified by laser Raman spectroscopy. All other phases are unknown. Note, the inclusions are hosted in nepheline and the detected nepheline within the inclusion might be just the result of scattering from the host mineral. The melt inclusions shown in (a), (b) and (d) contain a small methane bubble.

6.9 Summary

Primary fluid inclusions occur in clusters, as individual "single-inclusions", and attached to aegirine micro crystals. Secondary fluid inclusions are most common and occur within fluid inclusion planes.

Two compositional types of fluid inclusions can be distinguished. The majority are mono-phase and methane-dominant; only about 10 % are two-phase (V+L) CH_4-H_2O fluid inclusions. The latter rarely include daughter minerals.

Laser Raman spectroscopy indicates methane with smaller amounts of ethane and propane in the methane-dominant inclusions. The two-phase aqueous inclusions show the typical broad peak of water associated with the liquid phase and the sharp peak for methane in the gas bubbles. The daughter minerals are Raman-inactive.

Microthermometric studies of methane-dominant fluid inclusions reveal homogenisation temperatures between -99°C and -62°C (distribution maximum of -84°C), with mostly critical homogenisation. This indicates a wide range of entrapment conditions. Homogenisation above the critical temperature of pure methane is in accord with the presence of higher hydrocarbons; homogenisation below the critical temperature might be due to other impurities. Also, density differences could cause the spread of T_h values. There are no significant differences in heating-freezing behaviour of primary and secondary fluid inclusions.

Based on temperatures of first ice melting, hydrohalite melting, last ice melting and total homogenisation the aqueous inclusions are found to contain variable amounts of NaCl and $CaCl_2$. Homogenisation occurs over a wide temperature range from 290°C to >500°C. Primary fluid inclusions have somewhat higher homogenisation temperatures (490°C) and a higher Na:Ca ratio than secondary inclusions.

The aqueous phase of the fluid is involved in magmatic and post-magmatic fluid-rock interactions, which causes ion exchange and incorporation of water in secondary crystal growth. This explains the different concentrations of NaCl and $CaCl_2$ in the brine in fluid inclusions.

The relatively similar behaviour of secondary and primary fluid inclusions of both compositional types on heating and freezing implies continuous fluid entrapment from magma crystallisation until present.

There are no significant differences in the microthermometric data between different rock types in the Khibiny complex. This indicates a similar fluid was present throughout the different stages of pluton formation.

PVTX modelling suggests two possibilities for the generation of primary fluid inclusions. Primary fluid entrapment is assumed to have occurred in the region of the solidus of a H_2O-saturated agpaitic nepheline syenite. This is above the CH_4-H_2O-solvus and therefore a homogenous, supercritical fluid must have existed at time of entrapment. This makes the existence of two different types of primary inclusions somewhat contradictory. The homogenous fluid might have changed its composition from water-dominant to methane-dominant in the course of magma crystallisation or

methane-dominant inclusions could have undergone post-magmatic changes, such as water-leakage. For water-dominant inclusions, the intersection of the projected isochore and the nepheline syenite solidus present the limits for the entrapment envelope around 600 MPa and 600°C. The adjacent lithostatic gradient supports this conclusion. The intersection of isochores for methane-dominant inclusions with the solidus of nepheline syenite occurs at a similar temperature range but lower pressure indicating hydrostatic conditions. This might be due to either post-entrapment changes such as water loss that also caused a density decrease in the inclusions and hence a too low pressure calculations for the isochore projections or a change of fluid composition, for instance by the introduction of methane-rich fluids from the host rock. The latter assumption is in agreement with the hydrostatic P-T conditions calculated for primary methane-entrapment.

Post-crystallisation fluid migration within the pluton, resulted in the formation of secondary fluid inclusions trapped along FIPs over a wide range of P-T conditions from an miscible (above CH_4-H_2O solvus) or immiscible (below CH_4-H_2O solvus) fluid. This process probably started shortly after crystallisation and might still be ongoing. It is therefore impossible to state a definite P-T envelope for secondary fluid entrapment.

Various secondary effects on the fluid inclusions since trapping are a serious handicap to accurate geobarometry. Textural observations indicate post-entrapment changes of the inclusions, especially a loss of the aqueous phase which probably became incorporated in primary minerals during their growth and alteration but also in minerals precipitated at a later stage in microcracks and fractures. There is also evidence that necking down occurred but it is not clear to what extend. The conclusions drawn here

from microthermometric results and isochore projection can therefore only be regarded as a suggestion for a possible fluid history.

Silicate melt inclusions have been observed in nepheline. They often contain a methane-dominant fluid phase which supports the hypothesis of the existence of an orthomagmatic hydrocarbon-rich fluid.

7 Bulk gas composition of the fluids trapped in the rocks of the Khibiny pluton

7.1 Introduction

Bulk gas analyses of whole-rock samples were performed to obtain a comprehensive data set on gas compositions and to corroborate the assumption that fluid inclusion compositions are representative of the composition of the main gas in the Khibiny pluton. The qualitative composition of the major volatiles stored in fluid inclusions of the Khibiny pluton was ascertained by Laser Raman spectroscopy and microthermometry (Chapter 6). The inclusions contain mainly methane but smaller proportions of ethane, propane and water were also detected. Bulk gas analysis, using gas chromatography (GC) and gas chromatography-mass spectrometry (GC-MS) techniques allows determining of gaseous species not only in fluid inclusions but also in pore space and along microcracks and grain boundaries. Furthermore, trace volatiles, which may not be detected using laser Raman spectroscopy, can also be determined.

The key objectives of the bulk gas study are:

- to identify the bulk gas compositions of rocks within the Khibiny pluton as an aid to determine their origin;
- to investigate and discuss any spatial variations in gas distribution within the Khibiny complex in terms of volume and composition;
- to compare the results of different analytical techniques used and to identify variations between them and the possible reasons for these.

7.2 A review of existing data

Since the discovery of large amounts of gas in the Khibiny pluton, bulk gas analyses data have been reported in a number of publications as summarised in Table 7.1.

According to the data of Petersilie *et al.* (1961), Petersilie (1962), Petersilie and Sørensen (1970), Kogarko *et al.* (1987) and Ikorsky *et al.* (1992) the main components of the gases in the alkaline rocks of the Khibiny pluton are CH_4 and H_2 which these authors suggested were of abiogenic origin. Other gases, occasionally detected in smaller proportions were N_2, CO_2, CO, He, O_2 and Ar.

The most recent study of bulk gas compositions is provided by Potter (2000), with a selection of these results published in Potter and Konnerup-Madsen (2003). These authors concluded that the hydrocarbon gases are the result of post-magmatic Fischer-Tropsch reaction (see Chapter 3 for details).

Voitov (1992) published data on the composition of free flowing "gas jets" in underground workings. They were mainly located in mines and railroad tunnels and associated with tectonically weakened zones with strong jointing and also with zones where lateral pressure deforms the rock. The gas showed a mixture of mainly H_2, N_2 and hydrocarbons in varying proportions. Voitov (1992) excluded atmospheric contamination in his analyses on the basis that the oxygen content was less than 1 vol% and he attributed nitrogen as a primary component of the original gas jet. The varying gas compositions reported were assumed to be related to geodynamic activities (seismic and acoustic emissions). According to Voitov (1992), these disrupted the subvertical gas flow from, presumably, several magma chambers and gas reservoirs in which hydrocarbon generation was considered as an ongoing process. Depending on the intensity and location of seismic and acoustic emissions, gases from varying reservoirs

published by	location	sample description	He	H_2	CH_4	hhc	C_2H_6	C_3-C_5	C_3H_8	C_4H_{10}	C_5H_{12}	CO	CO_2	N_2
Petersilie et al., 1961		rischorrite	-	1.25	12.59	-	1.02	-	0.25	0.114	-	1.96	0.39	3.4
		ijolite	-	0.68	24.50	-	0.95	-	0.019	0.079	0.013	2.31	0.23	5.0
		altered ijolite	-	2.25	0.44	-	0	-	0	0	-	3.50	15.5	-
Petersilie, 1962		ne syenite	-	1.5	168.7	-	1.91	-	0.4	0.1	-	4.05	0	0
Petersilie and Sorensen, 1970		khibinite	-	0.63	51.86	-	1.59	-	0.08	0.001	-	0	0.02	0.02
		khibinite	-	0.48	42.38	-	1.4	-	0.07	0.001	-	0	0.01	0.02
		urtite	-	0.59	49.20	-	0.98	-	0.02	0.014	-	0	0	0.04
		rischorrite	-	0.47	10.54	-	0.42	-	0.02	0.001	-	0.23	0.02	-
		foyaite	-	0.62	10.64	-	0.19	-	0.02	0	-	0	0.04	-
Kogarko et al., 1987		khibinite	-	1.77	99.14	2.150	-	-	-	-	-	1.32	0.19	4.59
		ijolite-urtite	-	3.45	89.70	2.530	-	-	-	-	-	4.13	0.19	-
Ikorsky et al., 1992; Tab.22	Rasvumchorr mine	295 P 232	0.002	0.86	8.88	-	0.630	-	0.058	0.013	0.002	0	0	-
	Yusporr mine	16 Y 110	0.005	0.31	2.51	-	0.122	-	0.01	0.003	0	0	0	-
	Kukisvumchorr mine	152 K 104	0.001	0.19	0.61	-	0.044	-	0.013	0.003	0.001	0	0	-
Potter, 2000		urtite	-	1.67	107.76	-	0	-	-	-	-	-	0	3.45
		ijolite	-	2.06	40.50	-	1.48	-	-	-	-	-	0	1.11
		rischorrite	-	2.00	18.10	-	0.90	-	-	-	-	-	0	1.30
		foyaite	-	0.81	0.05	-	0	-	-	-	-	-	0.84	1.26
		carbonatite	-	4.29	0.35	-	0.25	-	-	-	-	-	1.25	0.64
Voitov, 1991	Yusporr mine	free gas	0	13.90	79.5	1.900	-	-	-	-	-	-	-	4.30
	Yusporr mine	free gas	0.690	2.4	24.06	0.650	-	-	-	-	-	-	1.90	70.30
	Yusporr mine	free gas	0.087	2.88	56	2.170	-	-	-	-	-	-	2.88	35.98
	Kukisvumchorr mine	free gas	0.150	1.68	42.09	3.780	-	-	-	-	-	-	-	52.31
	Rasvumchorr mine	free gas	0.540	1.4	91.59	4.680	-	-	-	-	-	-	-	1.58
	Rasvumchorr mine	free gas	0.153	10.04	57.94	4.610	-	-	-	-	-	-	-	57.94
Nivin et al., 2005	Eveslogchorr	free gas	0.010	0.45	2.450	-	0.290	0.380	-	-	-	-	0.150	80.6
	Apatitovyi Tsirk	free gas	0.001	0.00	0.085	-	0.025	0.003	-	-	-	-	0.011	78.0
	Apatitovyi Tsirk	free gas	0.046	0.41	5.110	-	0.410	0.029	-	-	-	-	0	74.2
	Apatitovyi Tsirk	free gas	0.039	3.90	28.250	-	1.899	0.131	-	-	-	-	0	53.0
	Apatitovyi Tsirk	free gas	0.640	17.90	64.650	-	3.640	0.237	-	-	-	-	0	8.9
	Yusporr mine	free gas	0.001	0.80	0.120	-	0.076	0.001	-	-	-	-	0.120	78.3
	Kukisvumchorr mine	free gas	0.190	4.70	7.700	-	0.931	0.063	-	-	-	-	0	67.7
	Snezhnyi Tsirk	free gas	0.028	5.05	0.150	-	0.000	0	-	-	-	-	0	73.9
	av. composition of airless mixture	free gas	0.800	20.00	74.000	-	5.000	-	-	-	-	-	-	-
	av. composition of airless mixture	occluded gas	0.050	4.00	93.000	-	2.700	-	-	-	-	-	-	-

Table 7.1: Published results of bulk gas analyses from rocks of the Khibiny pluton (hhc - higher hydrocarbons)

(with different gas compositions) were released resulting in inhomogeneous gas jet compositions.

Nivin *et al.* (2005) also published data on free gas-air mixtures from boreholes within the Central Arch zone of the Khibiny pluton where they observed the highest gas flows. The main component of the gas phase was CH_4. Small amounts of H_2 and higher hydrocarbons, together with minor components such as He and CO_2, also occurred. The volume of occluded gas (trapped in inclusions) varied from <0.1 to 150 ml/kg rock and for free gas (occurring in fractures and microcracks), gas discharge rates within single shot-holes with a depth of 2 m and 4 cm diameter of up to 5 l/min were measured (Nivin *et al.*, 2001). Occluded gas and free gas were found to contain the same components but in different proportions.

All previous studies of gases from the Khibiny pluton show generally similar bulk compositions with a dominance of methane and strongly decreasing volumes of other detectable higher hydrocarbons up to butane.

Similar hydrocarbon-rich gases have also been found in the peralkaline rocks of Lovozero, Ilímaussaq and the Strange Lake complexes (Tab. 7.2).

According to Potter (2000), the gas composition of the Lovozero pluton is dominated by CH_4, similar to that of the nearby Khibiny pluton. The highest gas concentrations were found in foyaite and lujavrite. Higher hydrocarbons and other gases such as He and N_2 were detected in lower concentrations (Potter *et al.*, 2004). The authors assumed that N_2 was the result of atmospheric contamination, and suggested an abiogenic origin for the hydrocarbon gases via sub-solidus Fischer-Tropsch-type reactions.

In the Ilímaussaq complex (South Greenland) methane is predominant in all analysed rock specimens (Konnerup-Madsen and Rose Hansen, 1982). The amount of the C_2-C_5 species is relatively high and that of hydrogen fairly low. Also, the content of CO_2 and

CO is insignificant. The highest gas content was found in the coarsest grained samples by Petersilie and Sørensen (1970). They also found a relatively high content of He as being a characteristic feature of the gas compositions. Due to their occurrence in "mineral cavities" [presumably primary fluid inclusions], a non-biogenic origin for these gases was assumed (Petersilie and Sørensen, 1970). Furthermore, as the Ilímaussaq rocks are intruded into strongly granitized Precambrian rocks (Sørensen, 1965), it was thought highly unlikely that biogenic hydrocarbons had migrated from the adjacent host rocks (Konnerup-Madsen and Rose Hansen, 1982). The authors suggest an inorganic derivation for hydrocarbons from a pre-existing CO_2-dominant gas during crystallisation and cooling of the rocks (Petersilie and Sørensen, 1970; Konnerup-Madsen *et al.*, 1979, 1985, 1988). However, more recent studies by Schwinn (1999), Sommer (1999), Markl *et al.* (2001), Krumrei and Markl (2005) and Markl (2005) suggest that methane may have originated directly from the magma and that no late-stage respeciation took place.

Another example of CH_4-rich fluid associated with alkaline intrusives is the Strange Lake complex of Canada studied by Salvi and Williams-Jones (1996, 1997, 2006). The authors identified a carbonic fluid which coexisted with an immiscible brine of presumably magmatic origin containing CH_4, H_2, C_2H_6, CO_2, N_2 and higher hydrocarbons up to C_6. A post-magmatic generation from orthomagmatic CO_2 and CO fluid via Fischer-Tropsch reaction was proposed to explain the origin of the hydrocarbons.

published by	location	sample description	He	H_2	CH_4	hhc	C_2H_6	C_3H_8	C_4H_{10}	C_5H_{12}	CO	CO_2	N_2
Petersilie, 1964	Lovozero	-	-	2.01	14.50	-	0.68	0.46	0.02	-	0.78	0.04	-
Petersilie and Sorensen, 1970		syenite	0.006	2.10	12.21	-	0.63	0.13	0.009	-	0.23	0.05	-
		urtite	-	1.31	16.40	-	1.06	0.59		-	-	0.08	-
		foyaite	-	1.40	30.35	-	0.92	0.43	0.080	-	-	0.04	-
Potter et al., 2004	Lovozero	eudialyte in lujavrite	0.001	1.22	20.72	-	0.68	-	-	-	-	0	1.15
		loparite in juvite	0.041	2.12	5.13	-	0.36	-	-	-	-	0	0.53
		lujavrite	0.002	0.51	4.82	-	0.51	-	-	-	-	0	0.23
		lujavrite	0.029	1.97	2.91	-	0.36	-	-	-	-	0	0.32
		foyaite	0.002	1.10	23.78	-	0.51	-	-	-	-	0	1.20
		urtite	0.006	7.84	17.71	-	1.92	-	-	-	-	0	0.76
Nivin et al., 2001	Lovozero	free gas	2.00	35	60	-	3.2	-	-	-	-		-
		occluded gas	0.07	20	76	-	5.0	-	-	-	-		-
Kogarko et al., 1987	Lovozero	nepheline syenite	-	2.011	14.571	1.159	-	-	-	-	0.779	0.028	-
		balsic alkali effusive	-	4.370	0.570	0.008	-	-	-	-	1.720	0.020	-
Petersilie and Sorensen, 1970	Ilimausaq	augite in syenite	0.123	1.920	12.760	-	0.382	0.036	0.013	-	0	0.008	-
		naujaite	1.184	3.029	48.590	-	5.954	1.049	0.261	-	0	0.024	-
		sodalite in foyaite	0.009	0.730	4.080	-	0.424	0.077	0.009	-	0.397	0.004	-
		arfvedsonite in lujavite	0.149	2.780	0.990	-	0.128	0.008	0.001	-	0	0.006	-
		olivine gabbro	0.042	2.539	0.145	-	0.001	0.002	0.000	-	0	0	-
Konnerup-Madsen and Rose-Hansen, 1982	Ilimausaq	average in sodalite and ne	0.2	8.3	73.4	-	8.600	1.3	0.6	0.15	-	1.2	6.0
		average in arfvedsonite	1.5	18.8	66.3	-	6.200	0.8	0.4	0.04	-	0.7	5.1
Salvi and Wiliams-Jones, 1997	Strange Lake	fresh pegmatite	-	19.09	68.66	-	5.78	1.04	0.35	0.12	-	3.76	1.92
		altered pegmatite	-	19.23	36.70	-	3.58	0.49	0.20	0.07	-	48.35	6.27
Prinzhofer and Huc, 1995	Angola	thermognic gas	-	-	86.34	-	6.05	3.04	1.68	0.79	-	1.04	1.06
		thermognic gas	-	-	79.87	-	9.82	4.85	2.34	0.84	-	0.20	2.08
		thermognic gas	-	-	31.20	-	15.97	23.82	15.55	6.08	-	0.00	7.38
	North Sea	thermognic gas	-	-	41.45	-	17.76	21.25	15.20	3.84	-	0.12	0.38
		thermognic gas	-	-	95.16	-	2.86	1.40	0.40	0.09	-	0.09	0.00
		thermognic gas	-	-	73.96	-	13.95	5.83	1.62	0.40	-	3.33	0.91
Pironon, 2005	N-America	dry gas	-	-	94.448	-	1.441	0.340	0.170	0.080	-		

Table 7.2: Published results of bulk gas analyses from other peralkaline rock complexes (Lovozero, Ilimausaq and Strange Lake complex). For comparison, the bulk gas composition of some biogenic gas samples from Angola, North Sea and North America are shown (hhc - higher hydrocarbons).

7.3 Methods

In the present study the bulk gas compositions in different rock types of the Khibiny complex were analysed using gas chromatography at the Kola Science Centre in Apatity (Russia). In addition, selected samples were analysed using gas chromatography-mass spectrometry techniques at the Exxon Mobil Research Laboratories in Houston (USA).

The Kola Science Centre has many years of experience and practice in the preparation and analysis of gases contained in the alkaline rocks of the Kola Peninsula. The following procedure has been applied to the samples (Ikorski, 1999; pers. comm. S.V. Ikorsky, 2006):

Approximately 30-40 g of fresh rock sample was selected and crushed carefully by hand and sieved. An aliquot of 1 g of the 0.25-0.63 mm grain size fraction was used for analysis.

The sample was loaded into a vibrochamber [ball mill] together with three 5 mm diameter stainless steel balls. To clean the system from atmospheric contamination, the chamber was closed, placed onto the vibrator stage and connected to a continuous helium flow for 20 min. Then, the helium flow was stopped and the sample crushed for 20 minutes. The vibration frequency was set at 100 oscillations per second. This high vibration frequency ensured homogenous grinding. After finishing crushing, the helium carrier-gas was directed through the vibrochamber and the extracted gas transported into the gas chromatograph. The content of each component of extracted gas separated by the gas-chromatograph column was calculated by chromatogram-peak-estimation. The concentration of each component is proportional to the height of their specific chromatogram peak multiplied by its analytical sensitivity and divided by sample

weight. Chromatograph calibration was carried out regularly, using certified gas standards. The accuracy is mostly >95 %. The reproducibility of the gas analyses were tested by repeated analyses of internal standard material. The resulting precision ranges from 96 % and 94 %.

The active sample surface increases considerably during sample crushing resulting in a marked increase in contact between the sample surface and extracted gas. H_2O and CO_2 especially have a high affinity to sample surfaces and are strongly adsorbed onto freshly exposed material during this process (pers. comm.. S.V. Ikorsky). Therefore, these components were not analysed by the above method. Non-polar gases such as CH_4 and higher hydrocarbons, however, show only a small tendency to adsorb onto sample surfaces (Nelson, 2003). The recorded concentrations can thus be regarded as reasonable estimates of the true hydrocarbon composition.

At Exxon Mobil a similar extraction technique was used (pers. comm. M. Pottdorf). About 5 g sample material with grain sizes between 1 and 2 mm was placed in a ball mill and crushed at 105°C. Then, a representative aliquot of the liberated gas was injected into the gas chromatograph through a fixed volume sample loop whereby helium served as transport gas. Measurements were carried out on the coupled mass spectrometer.

7.4 Results and Discussion

7.4.1 Bulk gas composition

Results from the Kola Science Centre are shown in Table 7.3. The samples from different rock types contain a wide variety of gas volumes from 0.01 to 102.19 cm^3/kg. On average 12.8 cm^3/kg hydrocarbon gases were detected. A strong dominance of methane is characteristic in all samples. The highest concentration (98.5 cm^3/kg) was detected in rischorrite sample Kh-03-44. Higher hydrocarbons (ethane, propane and butane) were generally detected in smaller concentrations. In total, their concentration ranges from 0 to 3.7 cm^3/kg. The components of n-butane and i-butane were detected separately with n-butane occurring in higher concentration. Very small concentrations of higher hydrocarbons with double C-bonds, namely ethene, propene, α- and β-butene were also detected.

Hydrocarbons and other gaseous components contained in the Khibiny rocks were detected in selected samples at Exxon Mobil in Houston. The results on hydrocarbon content and distribution data are comparable with those measured at the Kola Science Centre (Table 7.4). The main components of the gas phase are methane with smaller proportions of higher hydrocarbons, up to pentane. CO_2 occurs in only one sample and N_2 was found in ijolite, rischorrite and massive foyaite. In the latter, an unusually high N_2 content was detected (9.37 mol%) which might be due to atmospheric contamination or could be a product of the breakdown of NH_4^+ in a hydrated mineral structures (Potter, 2000). The gases were also analysed for hexane, oxygen and H_2S but none of these components were identified.

For sample Kh-03-44, analyses were performed repeatedly using material of different grain size (Table 7.5). The detected gas compositions are similar indicating that grain size differences in the investigated range (between 1 and 4 mm) have a minor influence on the bulk gas data.

rock type	sample	total gas content	CH_4	C_2H_4	C_2H_6	C_3H_6	C_3H_8	i-C_4H_{10}	α-C_4H_8	n-C_4H_{10}	Σß-C_4H_8	CH_4	ΣC_2	ΣC_3
		cm³/kg	cm³/kg	cm³/kg	cm³/kg	cm³/kg	cm³/kg	cm³/kg	cm³/kg	cm³/kg	cm³/kg	mol%	mol%	mol%
khibinite	**Kh-03-1**	17.93	17.10	-	0.73	-	0.075	0.006	-	0.015	0.001	95.39	4.07	0.42
khibinite	**Kh-03-2**	14.17	13.80	-	0.34	-	0.024	0.002	-	0.0049	0.00029	97.38	2.40	0.17
khibinite	**Kh-03-3**	22.95	22.50	-	0.40	0.0039	0.035	0.0033	-	0.0069	0.0008	98.04	1.74	0.17
khibinite	**Kh-03-4**	37.60	36.20	-	1.20	0.0068	0.15	0.012	0.0002	0.028	0.0017	96.28	3.19	0.42
khibinite	**Kh-03-5**	11.63	10.90	-	0.65	0.0013	0.06	0.0043	-	0.013	0.00082	93.73	5.59	0.53
khibinite	**Kh-03-6**	18.34	17.70	-	0.57	0.002	0.056	0.0042	-	0.0088	0.00058	96.50	3.11	0.32
khibinite	**Kh-03-7**	12.88	12.10	-	0.73	-	0.042	0.0024	-	0.01	0.00052	93.91	5.67	0.33
khibinite	**Kh-03-8**	12.21	11.70	-	0.46	0.00098	0.038	0.0031	-	0.0087	0.00041	95.81	3.77	0.32
rischorrite	**Kh-03-9**	7.07	5.97	-	0.95	0.0017	0.11	0.00840	-	0.025	0.0019	84.48	13.44	1.58
rischorrite	**Kh-03-10**	33.58	32.40	-	1.07	0.0049	0.079	0.00630	-	0.017	0.0014	96.49	3.19	0.25
rischorrite	**Kh-03-11**	11.51	11.30	-	0.19	0.00073	0.012	0.00072	-	0.0026	-	98.21	1.65	0.11
rischorrite	**Kh-03-13**	14.57	13.90	-	0.58	0.0011	0.064	0.006	-	0.015	0.00076	95.42	3.98	0.45
rischorrite	**Kh-03-14**	5.09	4.98	-	0.10	0.0011	0.005	0.00026	0.00019	0.0012	-	97.88	1.97	0.12
rischorrite	**Kh-03-42**	30.85	30.40	-	0.42	0.0012	0.026	0.0016	-	0.005	0.00044	98.53	1.36	0.09
rischorrite	**Kh-03-43**	5.51	5.40	-	0.10	0.00043	0.0062	0.00043	-	0.001	-	98.04	1.82	0.12
rischorrite	**Kh-03-44**	102.19	98.50	-	3.30	-	0.28	0.029	0.0015	0.078	0.0054	96.39	3.23	0.27
rischorrite	**Kh-03-45**	0.05	0.04	-	0.002	0.001	0.0004	-	-	-	-	92.83	4.22	2.95
rischorrite	**Kh-03-46**	16.72	16.10	-	0.570	0.0018	0.035	0.0025	-	0.0095	0.0004	96.30	3.41	0.22
rischorrite	**Kh-03-48**	11.88	11.50	-	0.35	0.0015	0.024	0.0014	-	0.0042	0.00032	96.79	2.95	0.21
rischorrite	**Kh-03-49**	1.12	1.10	-	0.018	0.0019	0.0011	0.00002	0.00031	0.00028	-	98.07	1.60	0.27
rischorrite	**Kh-03-50**	0.05	0.04	-	0.001	0.001	0.00029	-	-	-	-	95.16	2.05	2.79
trachytoid foyaite	**Kh-03-35**	4.31	4.22	-	0.081	0.0017	0.0057	0.0005	0.00017	0.0014	-	97.90	1.88	0.17
trachytoid foyaite	**Kh-03-36**	0.35	0.34	-	0.0057	0.001	0.00057	0.000031	-	-	-	97.90	1.64	0.45
trachytoid foyaite	**Kh-03-37**	5.23	5.10	-	0.12	0.0036	0.0071	0.00029	0.00005	0.001	-	97.48	2.29	0.20
trachytoid foyaite	**Kh-03-38**	2.83	2.77	-	0.057	-	0.0033	0.00015	-	0.0004	-	97.85	2.01	0.12
trachytoid foyaite	**Kh-03-39**	1.33	1.30	-	0.026	0.00018	0.0017	0.000074	-	0.0002	-	97.88	1.96	0.14
trachytoid foyaite	**Kh-03-40**	0.12	0.12	-	0.0012	0.00056	0.00022	-	-	-	-	98.38	0.98	0.64
trachytoid foyaite	**Kh-03-41**	2.98	2.87	-	0.093	0.0032	0.0075	0.00041	0.00016	0.0012	0.00014	96.45	3.13	0.36

Table 7.3: Results of bulk gas analyses from this study. The data were produced at the Kola Science Centre in Apatity. They are given in cm³/kg and mol% and sorted by rock type.

rock type	sample		CH_4	C_2H_4	C_2H_6	C_3H_6	C_3H_8	i-C_4H_{10}	α-C_4H_8	n-C_4H_{10}	Σß-C_4H_8	CH_4	ΣC_2	ΣC_3
			cm^3/kg	cm^3/kg	cm^3/kg	cm^3/kg	cm^3/kg	cm^3/kg	cm^3/kg	cm^3/kg	cm^3/kg	mol%	mol%	mol%
massive foyaite	**Kh-03-51**	0.01	0.01	0.0002	0.0005	0.0012	0.00029	-	-	-	-	82.75	5.72	11.52
massive foyaite	**Kh-03-52**	8.61	8.46	-	0.14	0.0018	0.0076	0.00037	0.00053	0.0019	0.00012	98.23	1.63	0.11
massive foyaite	**Kh-03-53**	4.69	4.60	-	0.083	0.00085	0.0036	0.0002	0.00015	0.0007	0.00012	98.11	1.77	0.09
massive foyaite	**Kh-03-54**	12.26	11.90	-	0.33	0.0015	0.025	0.00160	0.00014	0.0042	0.00014	97.04	2.69	0.22
massive foyaite	**Kh-03-55**	1.46	1.44	-	0.017	0.0024	0.0016	0.0002	0.00023	0.0005	-	98.50	1.16	0.27
alkaline syenite	**Kh-03-56**	0.02	0.02	-	0.0012	0.00088	-	-	-	-	-	87.82	7.03	5.15
alkaline syenite	**Kh-03-57**	0.01	0.01	-	-	-	-	-	-	-	-	100	-	-
alkaline syenite	**Kh-03-58**	0.02	0.02	0.0004	0.0016	0.0014	0.00035	-	-	-	-	79.87	10.81	9.32
alkaline syenite	**Kh-03-59**	0.02	0.01	0.0004	0.0019	0.0021	0.00055	-	-	-	-	72.30	12.96	14.74
alkaline syenite	**Kh-03-60**	0.02	0.02	0.0003	0.0016	0.0011	0.00036	-	-	-	-	83.62	9.20	7.18
ijolite	**Kh-03-61**	22.14	21.20	-	0.86	-	0.066	0.0059	0.00016	0.011	0.00071	95.74	3.88	0.30
ijolite	**Kh-03-62**	6.38	5.99	-	0.36	-	0.023	0.0028	0.00011	0.0054	0.00025	93.86	5.64	0.36
ijolite	**Kh-03-63**	39.99	38.20	-	1.48	-	0.23	0.026	0.00008	0.048	0.0046	95.53	3.70	0.58
ijolite	**Kh-03-64**	31.53	29.90	-	1.38	-	0.18	0.023	-	0.04	0.004	94.84	4.38	0.57
ijolite	**Kh-03-65**	51.92	50.10	-	1.64	-	0.12	0.015	0.00078	0.037	0.0025	96.50	3.16	0.23
ijolite	**Kh-03-66**	46.09	43.80	-	2.03	-	0.18	0.026	0.00092	0.045	0.0053	95.04	4.40	0.39
ijolite	**Kh-03-67**	42.41	40.20	-	1.96	-	0.18	0.023	0.00023	0.042	0.0035	94.79	4.62	0.42
ijolite	**Kh-03-68**	21.51	20.60	-	0.81	-	0.079	0.0071	-	0.014	0.00071	95.77	3.77	0.37
ijolite	**Kh-03-69**	13.81	13.30	-	0.45	-	0.043	0.0037	-	0.011	0.00038	96.32	3.26	0.31
ijolite	**Kh-03-70**	0.03	0.03	-	0.0004	-	-	-	-	-	-	98.98	1.02	-
ijolite	**Kh-03-71**	4.36	4.18	-	0.16	0.00055	0.016	0.0014	0.00016	0.003	0.0002	95.84	3.67	0.38
ijolite	**Kh-03-72**	2.28	2.20	-	0.075	-	0.0057	0.00026	-	0.00072	-	96.42	3.29	0.25
ijolite	**Kh-03-73**	1.91	1.85	-	0.06	0.00073	0.0026	0.00017	-	0.00044	-	96.66	3.13	0.17
ijolite	**Kh-03-74**	4.62	4.46	-	0.15	0.00055	0.0095	0.00072	0.00026	0.003	0.0001	96.45	3.24	0.22
lujavrite	**Kh-03-17**	0.98	0.94	-	0.04	-	0.0024	0.000103	-	0.00032	-	95.64	4.07	0.24
lujavrite	**Kh-03-18**	1.10	1.05	-	0.043	0.00067	0.003	0.00017	-	0.00042	-	95.69	3.92	0.33
lujavrite	**Kh-03-19**	2.72	2.59	-	0.12	-	0.0068	0.00031	-	0.00095	-	95.29	4.41	0.25
lujavrite	**Kh-03-20**	3.72	3.58	-	0.13	-	0.0056	0.00028	-	0.0011	-	96.31	3.50	0.15
lujavrite	**Kh-03-21**	2.88	2.83	-	0.046	-	0.0013	-	-	0.00019	-	98.35	1.60	0.05
lujavrite	**Kh-03-22**	10.02	9.85	-	0.16	-	0.0068	0.00037	-	0.0015	-	98.32	1.60	0.07

Table 7.3 continued: Results of bulk gas analyses from this study. The data were produced at the Kola Science Centre in Apatity. They are given in cm^3/kg and mol% and sorted by rock type.

	Houston	Apatity	Houston	Apatity	Houston	Apatity	Houston	Apatity	Houston	Apatity
	Kh-03-22		Kh-03-54		Kh-03-44		Kh-03-67		Kh-03-4	
CH_4	98.225	98.316	88.094	97.043	94.171	96.385	94.994	94.792	97.206	96.280
C_2H_6	1.775	1.597	2.537	2.691	3.143	3.229	4.033	4.622	2.467	3.192
C_3H_8	0.000	0.068	0.000	0.216	0.270	0.274	0.446	0.424	0.261	0.417
C_4H_{10}	0.000	0.019	0.000	0.050	0.082	0.111	0.159	0.162	0.066	0.111
C_5H_{12}	0.000	-	0.000	-	0.000	-	0.034		0.000	-
N_2	0.000	-	9.369	-	1.928	-	0.334		0.000	-
CO_2	0.000	-	0.000	-	0.406	-	0.000		0.000	-

Table 7.4: Comparison of the results of bulk gas analyses (in mol%) of selected samples analysed in both, the Kola Science Centre in Apatity and Exxon Mobil in Houston.

	1-2mm	2-2.8mm	2.8-4mm
	Kh-03-44		
CH_4	94.744	94.171	91.966
C_2H_6	2.994	3.143	3.753
C_3H_8	0.276	0.270	0.563
C_4H_{10}	0.071	0.082	0.169
C_5H_{12}	0.000	0.000	0.000
N_2	1.278	1.928	1.907
CO_2	0.636	0.406	1.641

Table 7.5: Comparison of bulk gas composition (in mol%) of a rock sample using different grain sizes for crushing. The analyses were performed at Exxon Mobil.

7.4.2 The relevance of the Anderson-Schulz-Flory distribution for conclusions on hydrocarbon origin

In previous works (e.g. Szatmari, 1989; Salvi and Williams-Jones, 1997; Potter and Konnerup-Madsen, 2003) the logarithmic linear trend of hydrocarbon concentrations up to C_5 has been used as an indicator of gas origin (see also Chapter 3). A decrease in hydrocarbon concentration from 10^1 to 10^{-2} with increasing carbon number, the so-called Anderson-Schulz-Flory (ASF) distribution, is assumed to indicate an abiogenic origin. A shallow trend, however, with constant or only slightly decreasing hydrocarbon concentrations with increasing carbon number, is assumed to be indicative of biogenic gas.

In Figure 7.1 bulk gas data from the present study are plotted as log-normalised concentrations (mol%) and compared to published results of bulk gas data of other peralkaline rock complexes and to gases of undoubted biogenic origin.

Gases in khibinite, ijolite and lujavrite show a log-linear decrease in concentration from C_1 to C_4 concentrations. However, rischorrite, trachytoid and massive foyaite as well as alkaline syenites contain gases with similar concentrations of C_2 and C_3 components or even higher C_3 concentrations than C_2. The high C_3 concentration is mostly followed by low C_4 concentration, often below detection limit. This fluctuation can be interpreted differently depending on the generation mechanism responsible for the hydrocarbon gas. In case of an abiogenic origin, it might indicate that no further polymerisation towards higher hydrocarbons has occurred and therefore the C_3 concentration remains relatively high. On the other hand, assuming a biogenic origin, it could indicate a strong decomposition of C_4 or C_3 hydrocarbons that lead to higher concentration of the next lower (C_3 or C_2) hydrocarbon. The varying gas compositions could also be caused by

fractionation processes during fluid migration *in situ* or during chromatographic gas separation in the laboratory.

The hydrocarbon distributions in gases of other alkaline complexes are similar to those in the gases of the Khibiny complex with generally decreasing concentrations from C_1 to C_5. In some samples of the Lovozero and Ilímaussaq complex there also exists an increasing or constant C_3 concentration compared to C_2. Only the gas distribution of the two samples from the peralkaline granite at Strange Lake show a regular and smooth log-linear decrease of concentration with increasing C-number.

Figure 7.1 also shows examples of the C_1-C_5 distributions of biogenic hydrocarbon gases. Such gases exhibit a fairly similar pattern compared to those found in gases from peralkaline complexes. Only two samples of immature hydrocarbon gases dissolved in oil (Prinzhofer and Huc, 1995) show the expected C_1-C_5 distribution of biogenic gas: a very shallow hydrocarbon distribution with a relatively low methane content compared to higher hydrocarbons. All other biogenic gas samples show similar carbon distribution patterns to those from the intrusive alkaline complexes. A typical ASF distribution with decreasing hydrocarbon concentration with increasing carbon number is observed for dry gas, which is the dominant *biogenic* gas phase at depth > 5.5 km (Hunt, 1995). This clearly demonstrates that the ASF distribution is questionable proof for abiogenic origin of hydrocarbon gas.

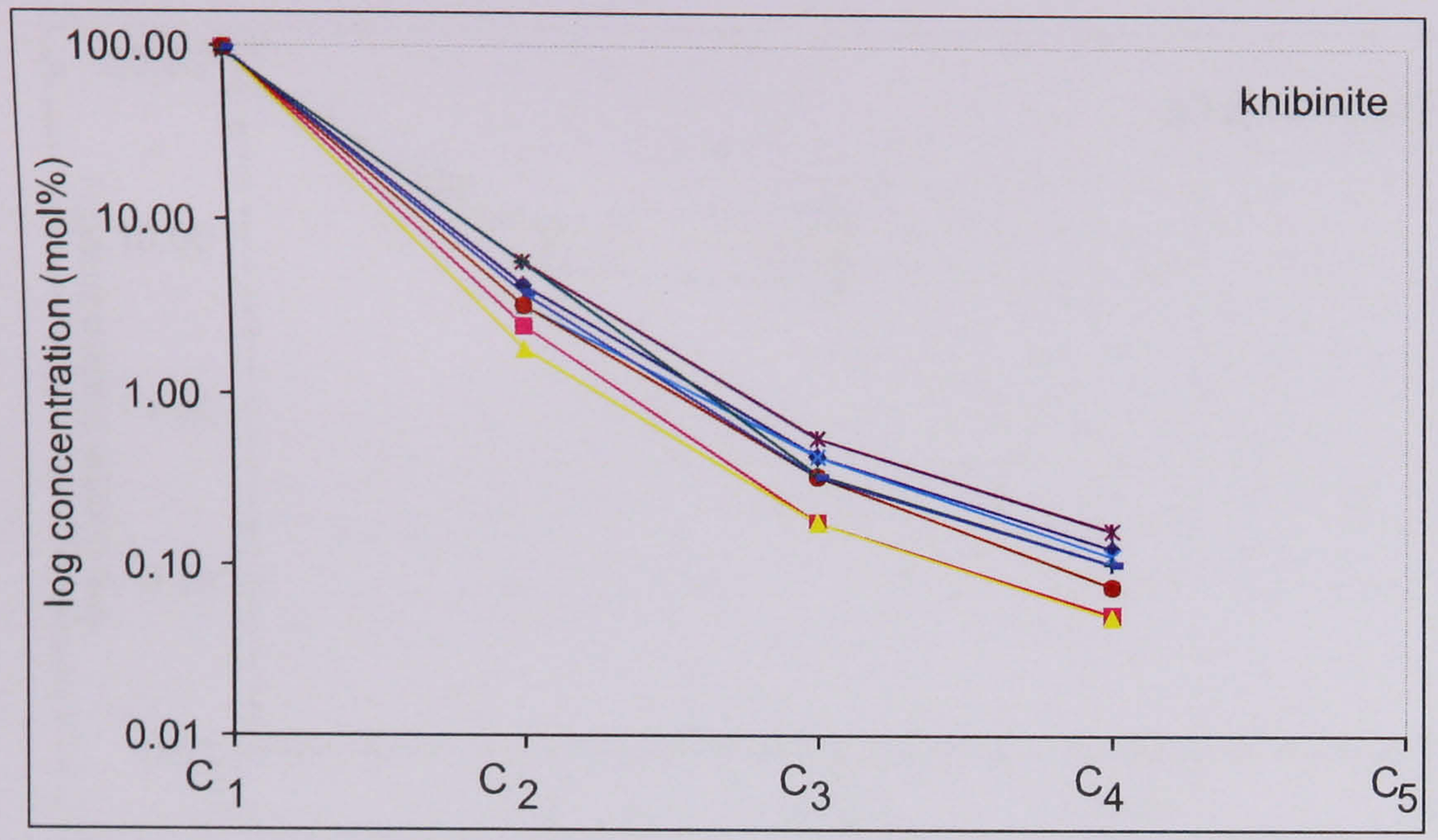

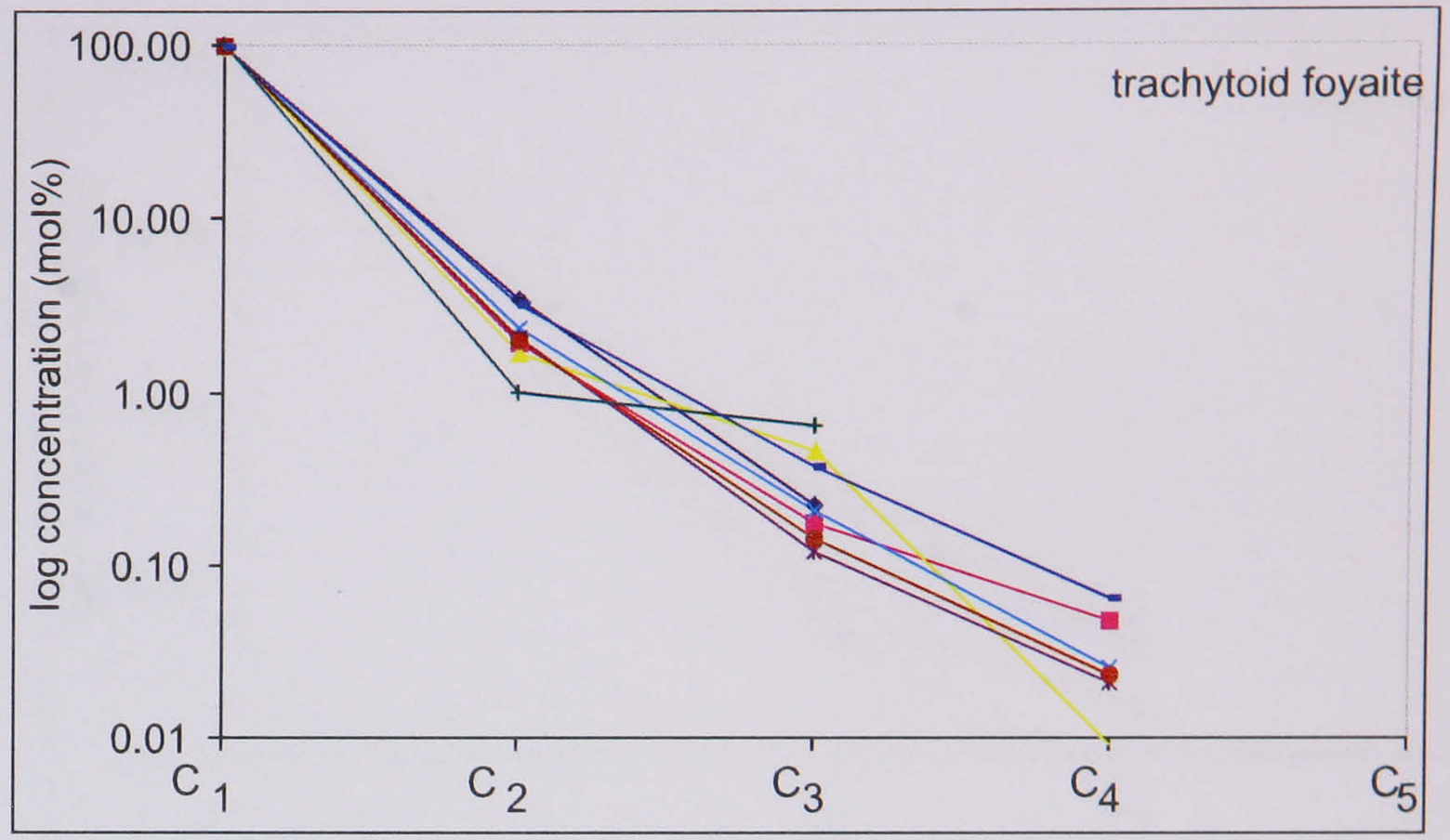

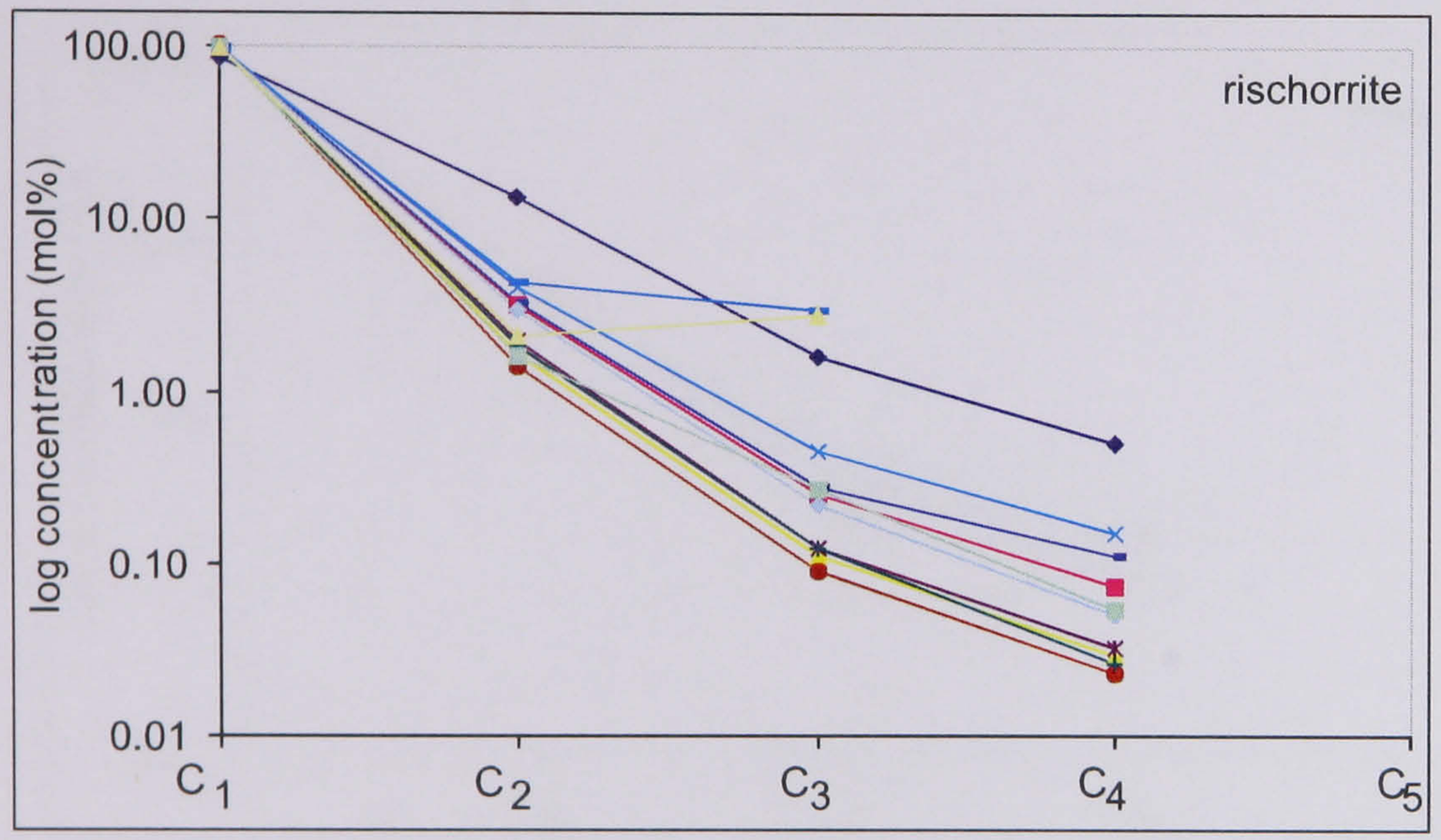

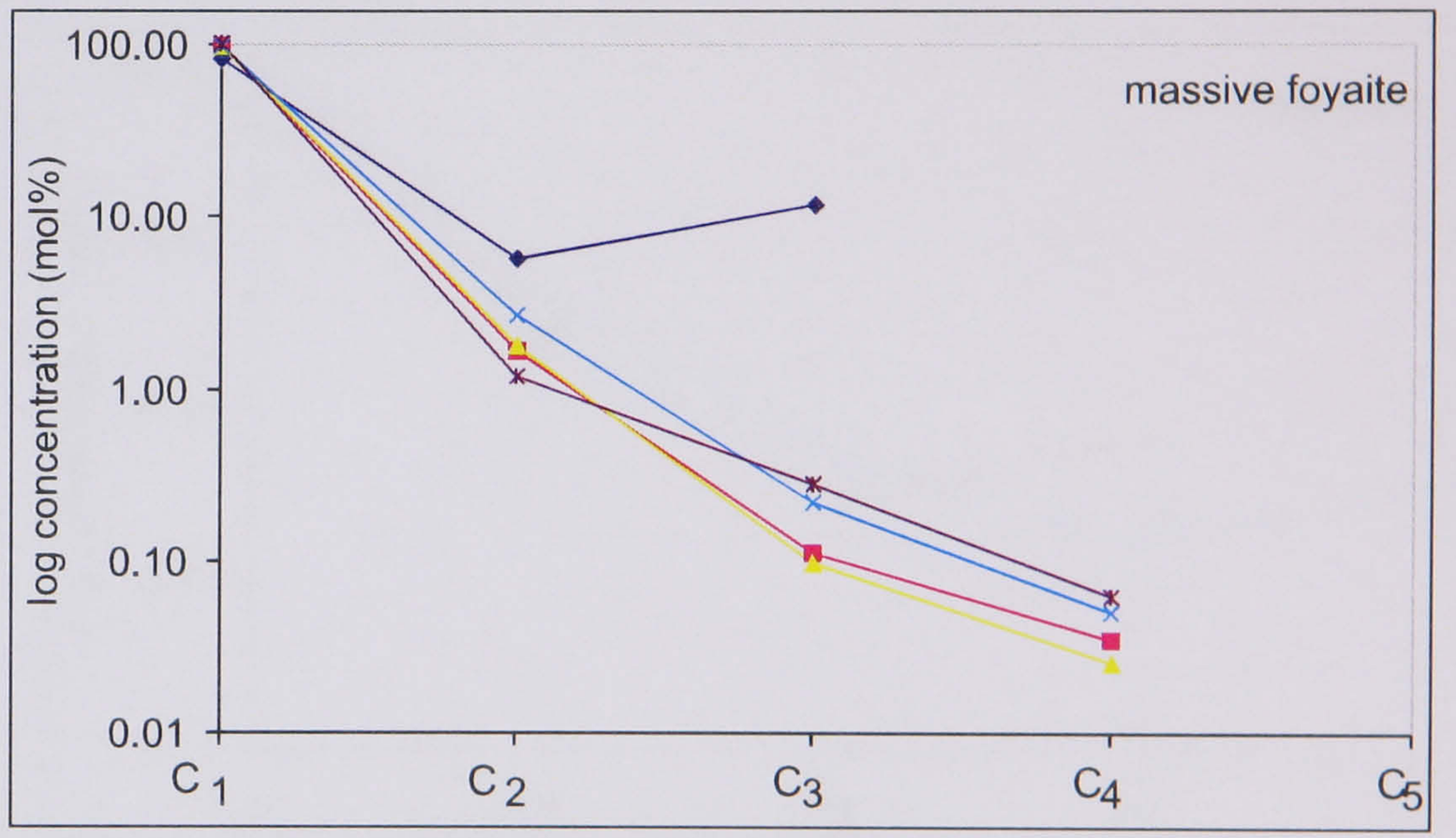

Figure 7.1: Log normalised abundance (in mol%) of methane and higher hydrocarbons in the gas phase of the different rock types of the Khibiny complex (see Table 7.3 for data).

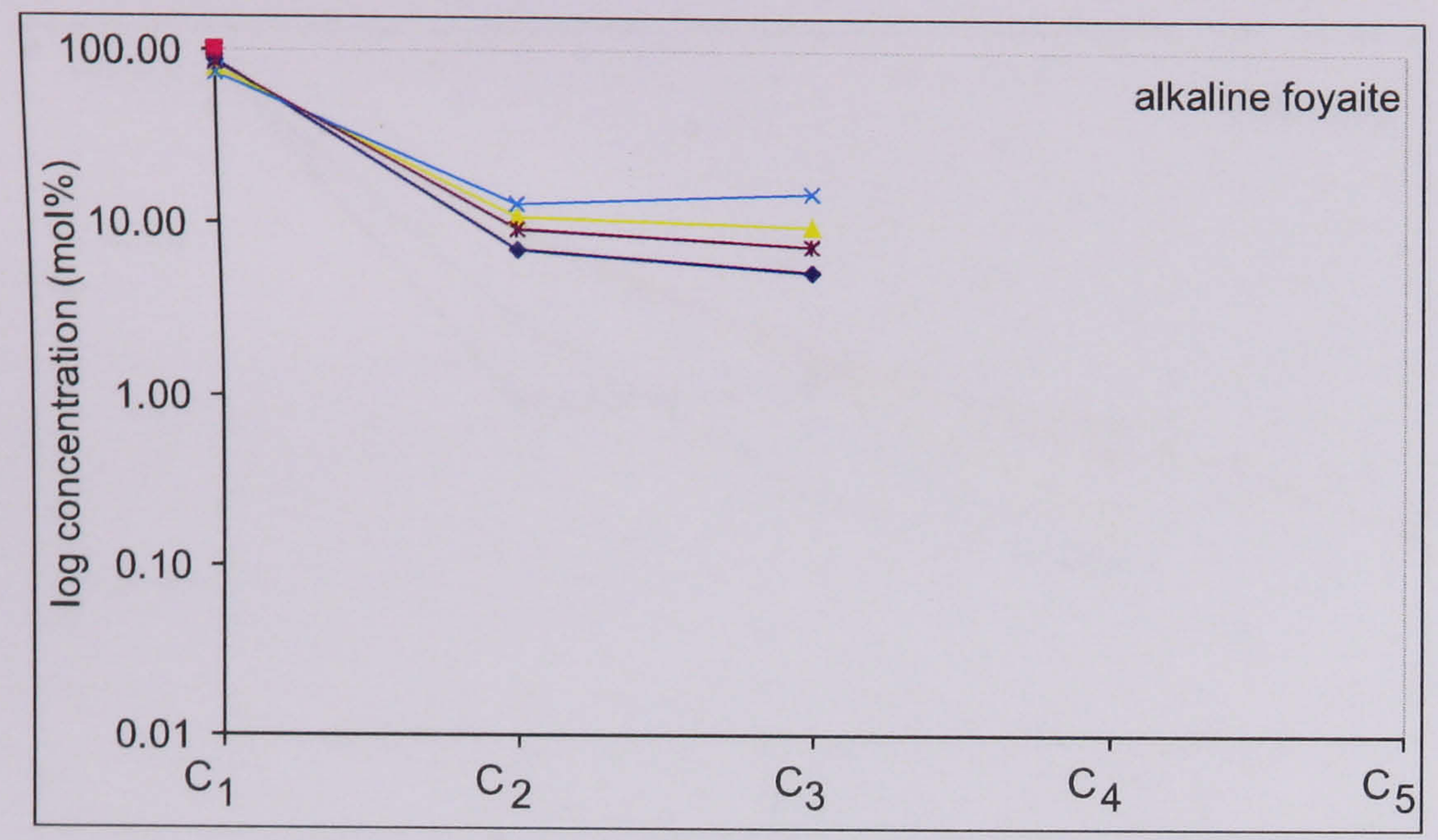

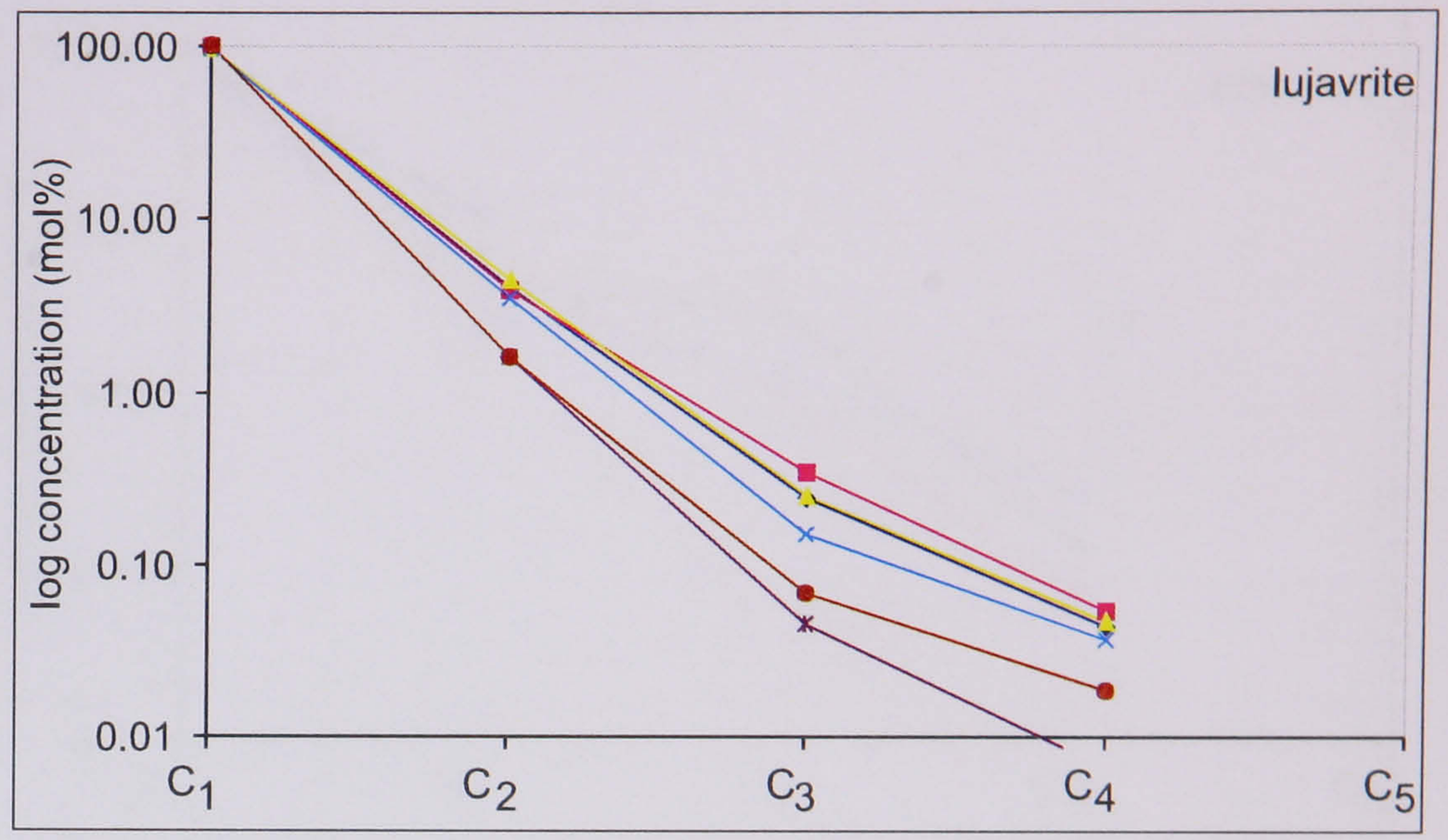

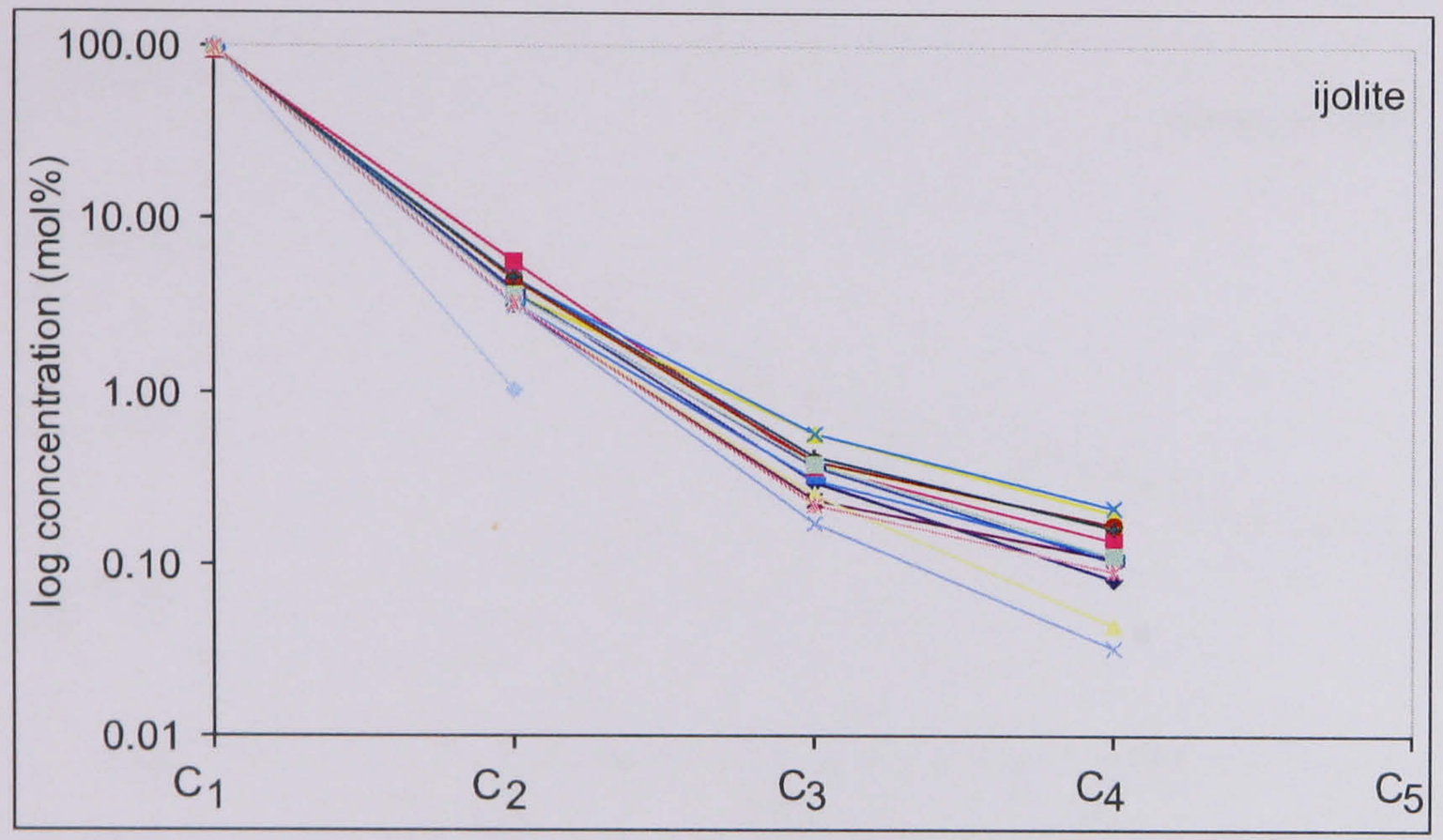

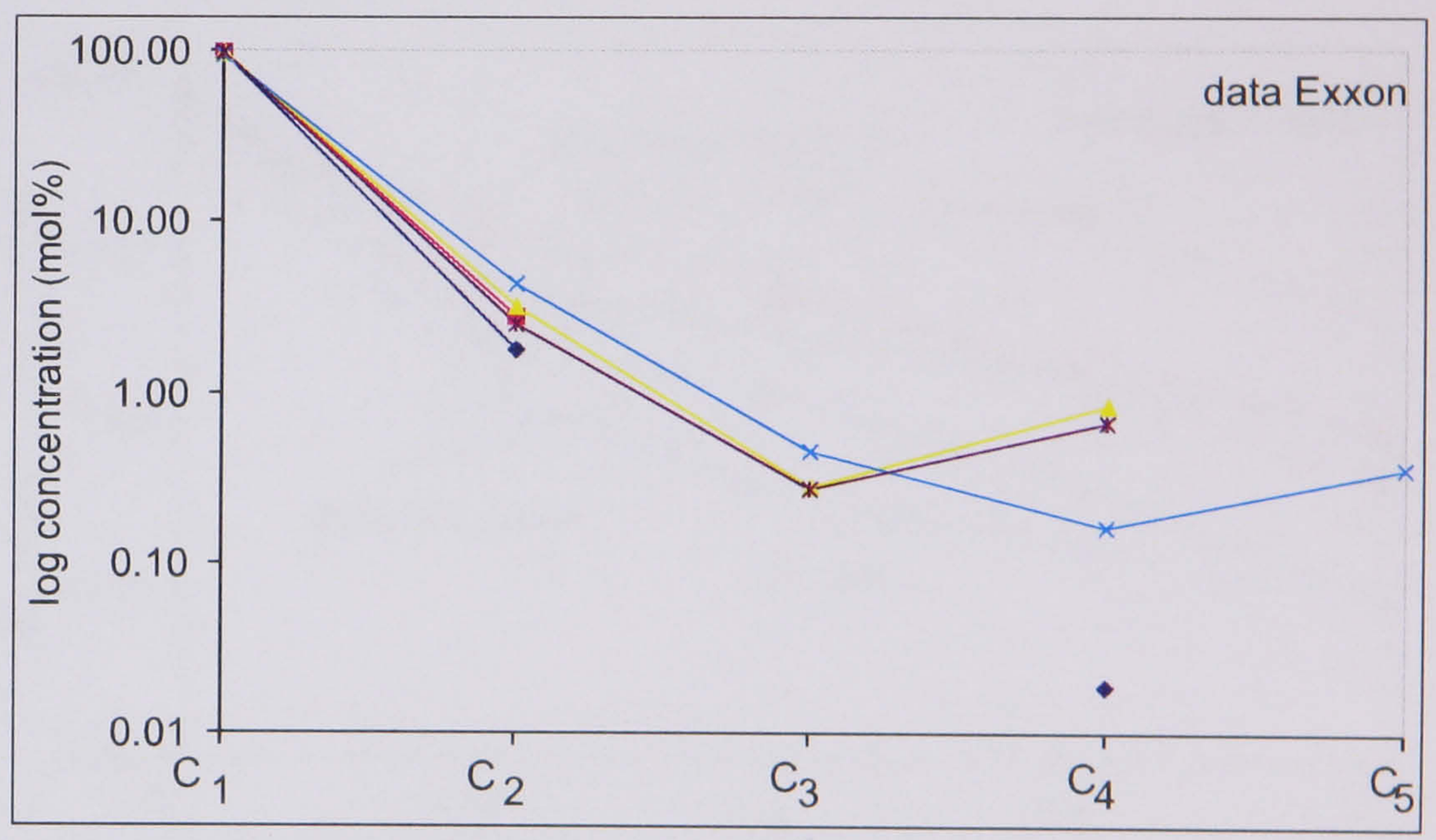

Figure 7.1 continued: Log normalised abundance (in mol%) of methane and higher hydrocarbons in the gas phase of the different rock types of the Khibiny complex (see Table 7.3 for data). The last chart shows the values produced at the Exxon Mobil laboratory (see Tab. 7.4 for data).

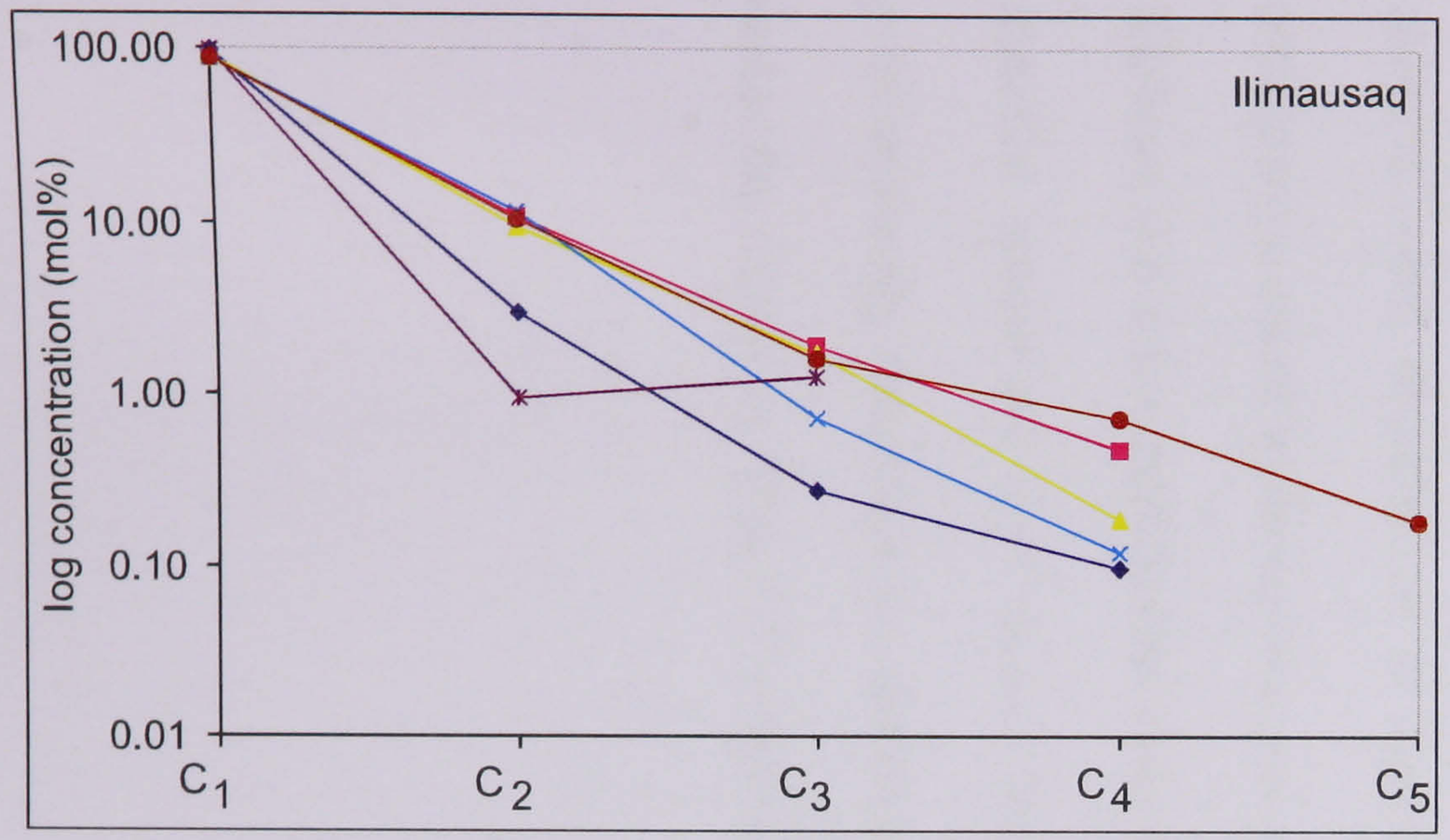

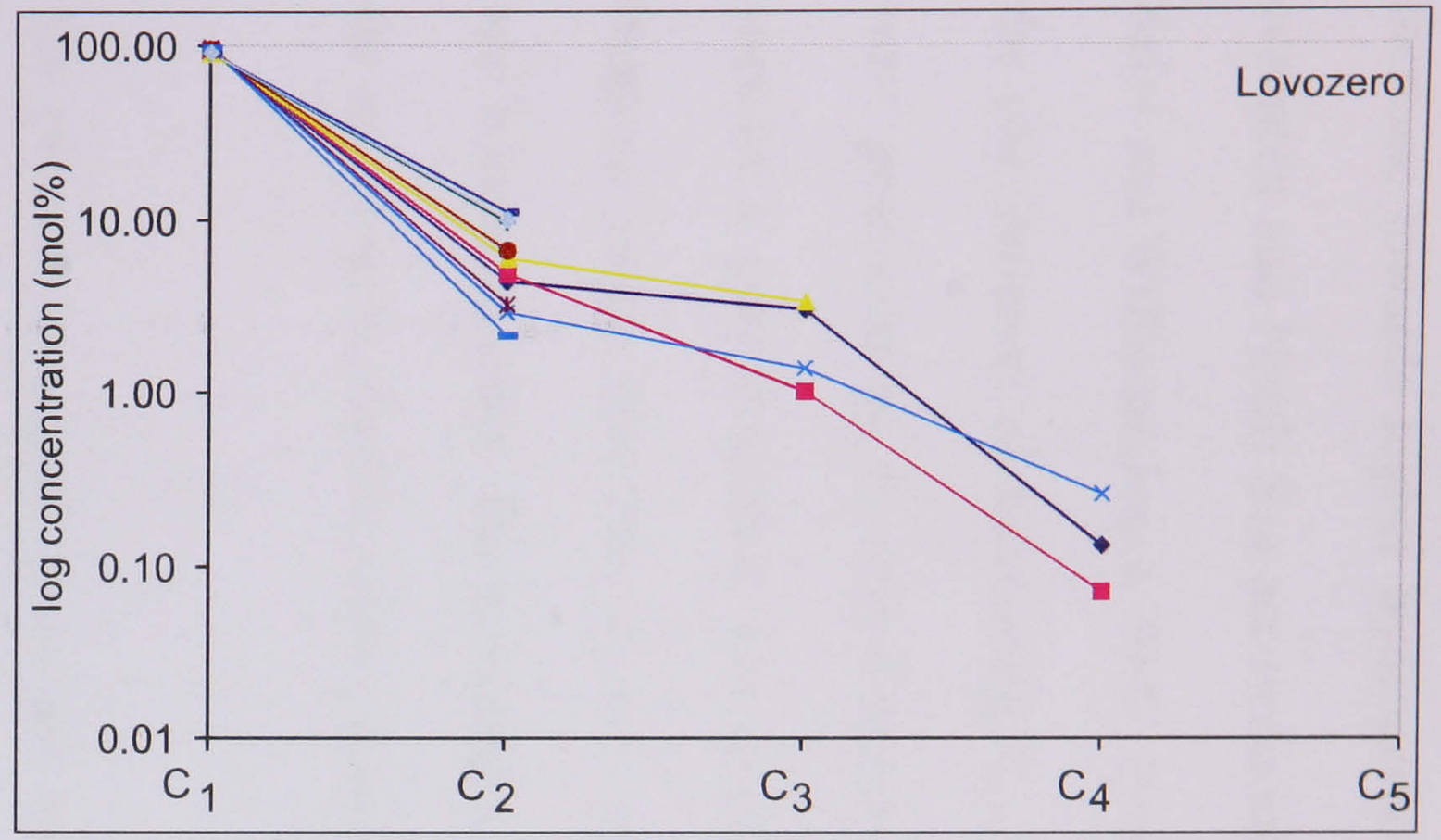

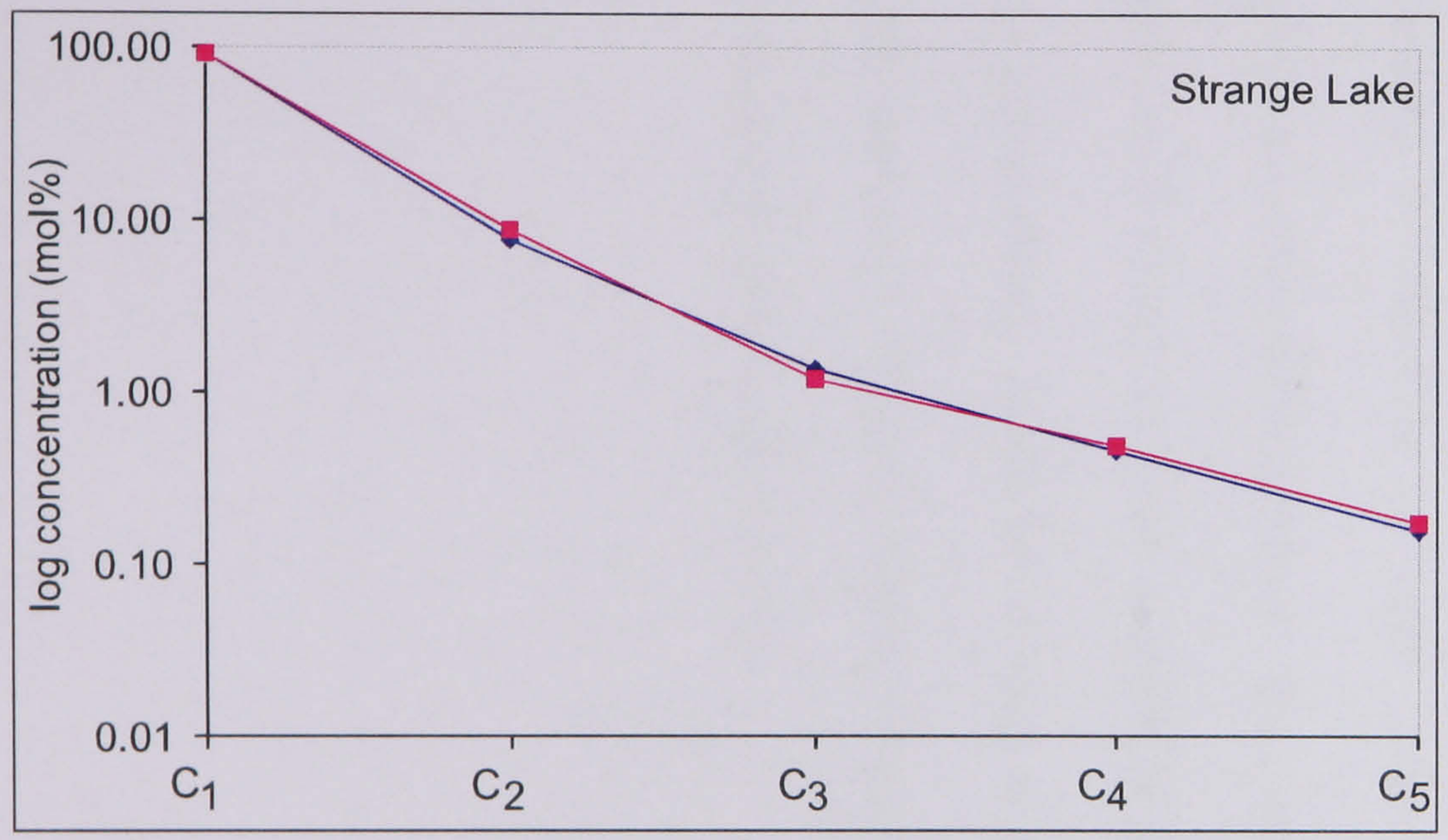

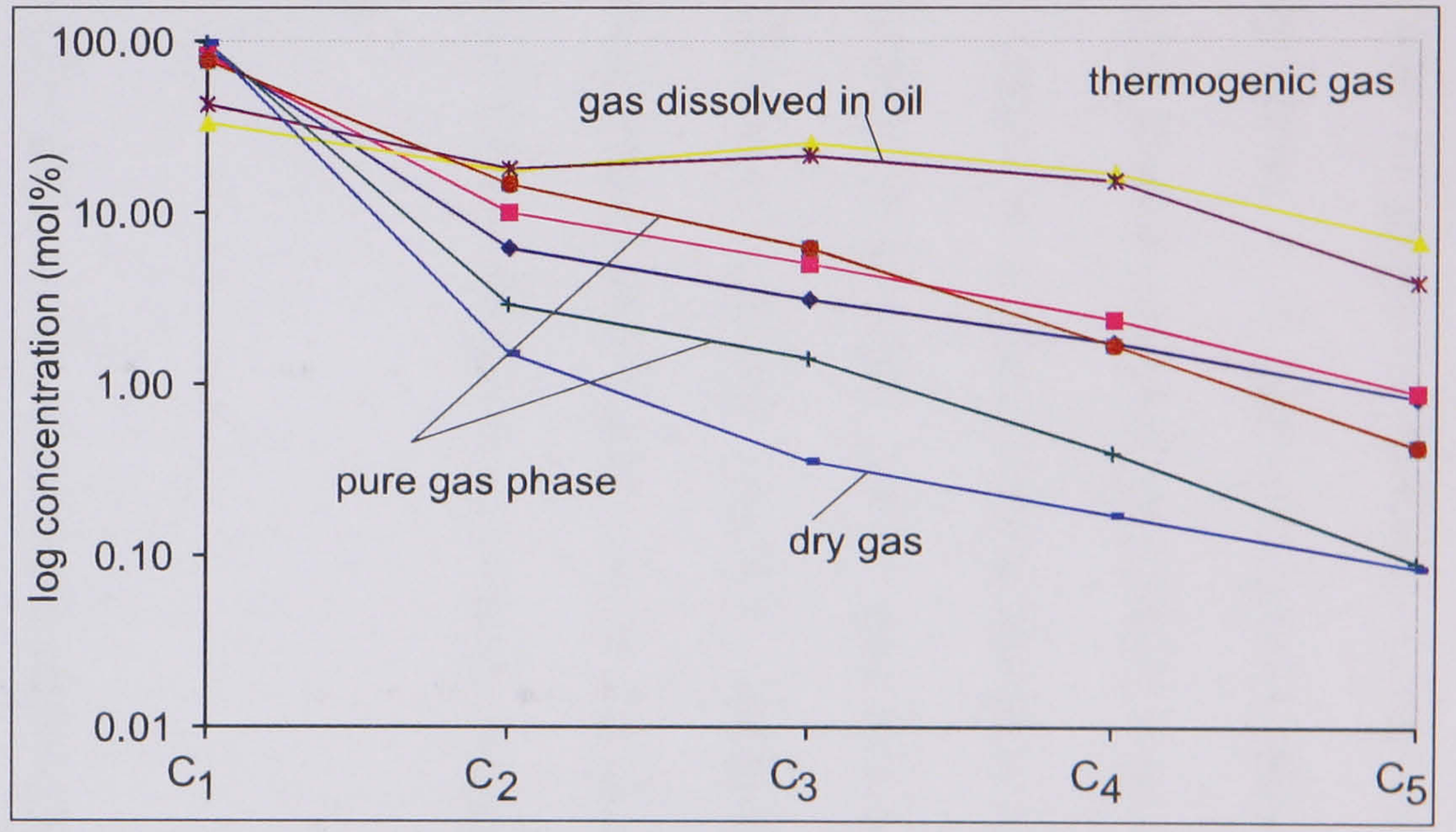

Figure 7.1 continued: Log normalised abundance (in mol%) of methane and higher hydrocarbons in the gas phase of rocks from Strange Lake, Lovozero and Ilimausaq complex. The compositional distribution of thermogenic gas samples of biogenic origin are shown for comparison. Values and references are shown in Table 7.2.

Table 7.6 summarises the ratios of C_{n+1}:C_n for all the data discussed here. The ratios increase towards higher hydrocarbons and in gases of Khibiny complex, Ilímaussaq complex and North Sea are occasionally above 1. In previous works (Szatmari, 1989; Salvi and Williams-Jones, 1997; Potter and Konnerup-Madsen, 2003) it was argued that the phenomenon of increasing C_{n+1}:C_n ratios is a clear indication that hydrocarbons were generated by Fischer-Tropsch reaction (Anderson, 1984) and has been used to support a post-magmatic gas origin. However, **all** gas samples, including these of biogenic origin have low ethane : methane ratios and higher ratios for propane:ethane and butane:propane. The predominance of CH_4 is therefore an unconvincing parameter for an abiogenic hydrocarbon gas origin.

The present investigation reveals no major differences between hydrocarbon ratios of biogenic gas samples and gases extracted from peralkaline rock complexes. The compositional distribution of hydrocarbons is therefore of little value in drawing conclusions about hydrocarbon gas origins. In compositional terms, the hydrocarbons of Khibiny and other peralkaline complexes could therefore have originated from organic material within the host rocks. These hydrocarbons could have been transformed to predominantly thermogenic methane gas and solid organic matter (such as kerogen) under the relatively high P-T conditions during pluton emplacement.

		C_2/C_1	C_3/C_2	C_4/C_3	C_5/C_4
Khibiny	average khibinite	0.039	0.092	0.287	
Khibiny	average rischorrite	0.038	0.246	0.233	
Khibiny	average trachytoid foyaite	0.022	0.177	0.159	
Khibiny	average massive foyaite	0.029	0.490	0.206	
Khibiny	average alkaline syenite	0.101	0.703	0.000	
Khibiny	average ijolite	0.038	0.084	0.307	
Khibiny	average lujavrite	0.033	0.053	0.198	
Khibiny	data Exxon	0.030	0.059	1.184	0.437
range		**0.022 to 0.101**	**0.053 to 0.703**	**0 to 1.184**	**0.437**
Lovozero		0.047	0.676	0.043	
Lovozero	syenite	0.052	0.206	0.070	
Lovozero	urtite	0.065	0.557		
Lovozero	foyaite	0.030	0.467	0.186	
Lovozero	eudialite lujavrite	0.033			
Lovozero	loparite juvite	0.070			
Lovozero	lujavrite	0.106			
Lovozero	lujavrite	0.124			
Lovozero	foyaite	0.021			
Lovozero	urtite	0.108			
range		**0.030 to 0.124**	**0.206 to 0.676**	**0.043 to 0.186**	
Ilimausaq	augite syenite	0.030	0.094	0.347	
Ilimausaq	naujaite	0.123	0.176	0.249	
Ilimausaq	sodalite foyaite	0.104	0.182	0.110	
Ilimausaq	arfvedsonite lujavite	0.129	0.063	0.163	
Ilimausaq	olivine gabbro	0.010	1.286		
Ilimausaq	average in sodalite and neph.	0.117	0.151	0.462	0.250
Ilimausaq	average in arfvedsonite	0.094	0.129	0.500	0.100
range		**0.030 to 0.123**	**0.063 to 1.286**	**0.110 to 0.500**	**0.250 to 1.000**
Strange Lake	fresh pegmatite	0.084	0.180	0.337	0.343
Strange Lake	altered pegmatite	0.098	0.137	0.408	0.350
range		**0.084 to 0.098**	**0.137 to 0.180**	**0.337 to 0.408**	**0.343 to 0.350**
Angola	thermogenic gas	0.070	0.502	0.553	0.470
Angola	thermogenic gas	0.123	0.494	0.482	0.359
Angola	thermogenic gas	0.512	1.492	0.653	0.391
North Sea	thermogenic gas	0.428	1.197	0.715	0.253
North Sea	thermogenic gas	0.189	0.418	0.278	0.247
North Sea	thermogenic gas	0.030	0.490	0.286	0.225
North America	dry gas	0.015	0.236	0.500	0.471
range		**0.015 to 0.512**	**0.236 to 1.492**	**0.278 to 0.715**	**0.253 to 0.471**

Table 7.6: The carbon number ratios calculated from bulk gas analysis (in mol%) from Khibiny, Lovozero, Ilimausaq, Strange Lake complex and biogenic samples from Angola, North Sea and North America.Values and references are shown in Table 7.2.

7.4.3 The spatial distribution of gases within the Khibiny complex

There have been few studies of bulk gas distribution throughout the Khibiny complex. Ikorsky (1977) sampled short, inward-directed traverses and found high gas concentrations in the outer part of the pluton and especially in areas of strong albitisation. Other studies reveal highest total gas contents immediately above or below apatite-nepheline ore zones (Ikorsky *et al.*, 1992). The presence of high post-magmatic fluid fluxes within the Central Arch, a petrologically diverse zone that hosts the REE-enriched apatite–nepheline ore deposits located between outer khibinite and inner foyaites of the Khibiny complex, has been reported by Nivin *et al.* (2001, 2005).

The reasons for the variable gas concentrations within the Khibiny pluton are still debatable. The controlling factors are assumed to be petrology (see Chapter 4) and distance to migration pathways and place of generation (Nivin *et al.*, 2001; Ikorski, 1991).

In this present study, bulk gas contents were found to vary in different areas of the complex over several orders of magnitudes, between c. 100 cm^3/kg and 0.01 cm^3/kg.

To investigate the relationship between petrology and gas content, the modal mineral composition of the three most abundant, optically-distinguishable mineral phases (nepheline, alkali feldspar and the sum of mafic minerals) in all hand-specimens were estimated and plotted versus the total gas content (Fig. 7.2a-c). There is a clear positive correlation between total gas content and nepheline content. However, there appears to be no relationship between gas content and the content of mafic minerals or of feldspar. Microscopic observations and laser Raman studies are in agreement with these findings (Chapter 6). Therefore, the presence of suitable host minerals, namely nephelines,

results in high fluid inclusion populations and hence the storage of high concentrations of hydrocarbons.

A close textural relationship between altered mafic mineral assemblages and fluid inclusion accumulation on a microscopic scale was used as evidence for post-magmatic fluid generation via an F-T reaction (e.g. Potter, 2000). However, this link could not be confirmed regionally during the present study. The lack of a significant correlation between gas content and the modal content of mafic minerals (Fig. 7.2c) is supported by textural observations determined during the course of this study (Chapter 4), where no correlation of fluid inclusion populations and altered mineral assemblages has been observed.

The present study shows that the regional distribution of hydrocarbon gases in the Khibiny complex is spatially controlled, with the highest gas contents occurring in the outer, marginal rocks, decreasing inwards to very low level in the core of the complex (Fig. 7.2d). It is likely that this trend is somewhat enhanced by inward-decreasing modal proportions of nepheline, which is the most suitable host for hydrocarbon-bearing fluid inclusions. The innermost rock type alkaline syenite, for example, is relatively poor in nepheline and therefore may simply not be able to host large methane-filled fluid inclusion populations. Another influence on the spatial gas distribution might be a variation in permeability permitting either the access of H_2O required for potential *in situ* methane generation or methane migration itself. If the methane is not produced *in situ*, varying distance from the methane source could influence the gas distribution within the Khibiny complex.

The spatial gas distribution shown here is broadly in agreement with the data of Ikorsky (1977). However, Nivin *et al.* (2005) reported highest hydrocarbon concentrations within the Central Arch. The authors argued that the high hydrocarbon concentration in this

area is caused by long-lived fluid migration facilitated by stress release during cooling and uplift of the Khibiny complex. The overall decrease in gas content towards the core might therefore be overprinted by late-stage gas fluxes through the Central Arch and further disturbed by lateral variations in rock porosity and permeability.

However, the overall spatial distribution of hydrocarbons suggests that there was an, at least limited, influence from the Khibiny host rocks. It is likely that carbonate and graphitic schists that enclose the Khibiny pluton (see Chapter 4) contain primary organic material, some of which could have been incorporated into the pluton, either during convective fluid flow during emplacement or during subsequent percolation of meteoric waters along fracture systems. This suggestion is consistent with the decreasing trend of $\delta^{13}C$ values toward the margin of the Khibiny complex (Chapter 8).

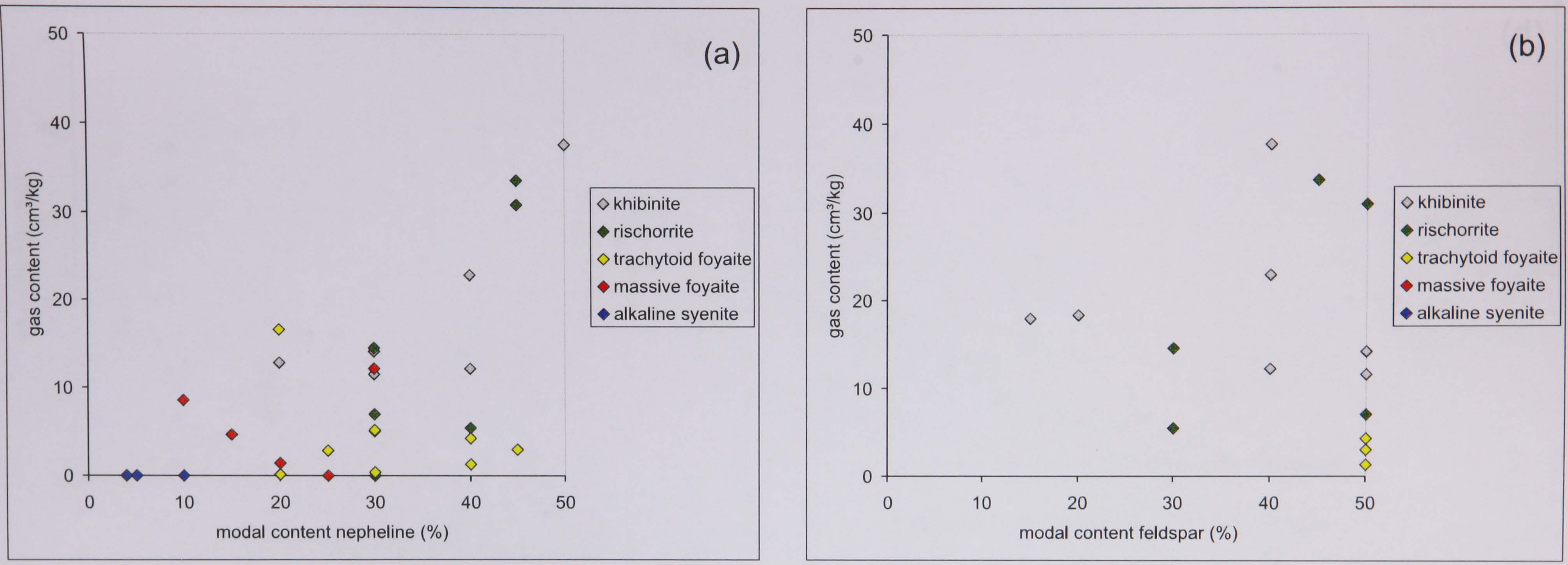

Figure 7.2: Plot of bulk gas content versus (a) modal content of nepheline and (b) modal content of feldspar in the analysed rock samples of the Khibiny pluton.

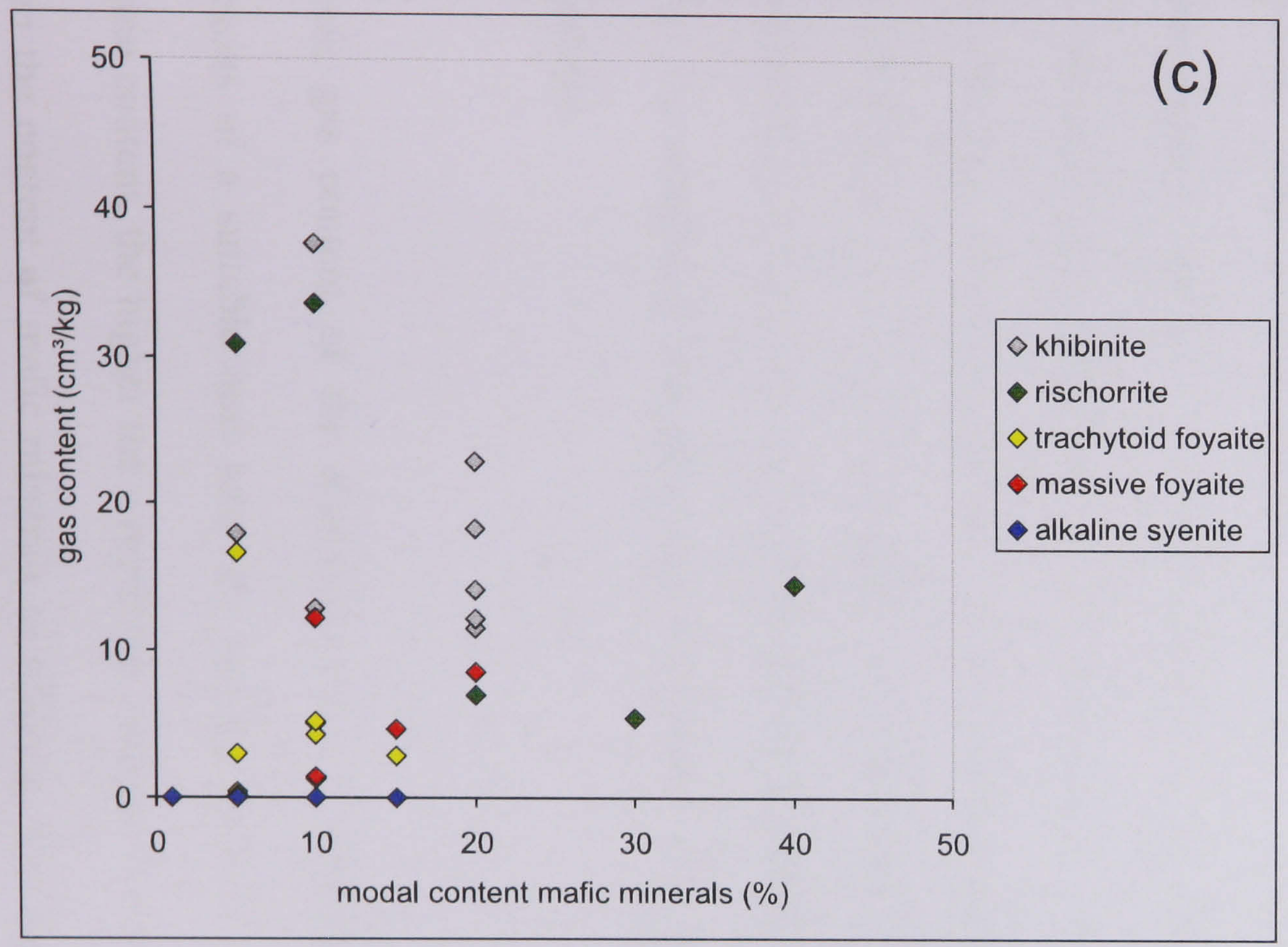

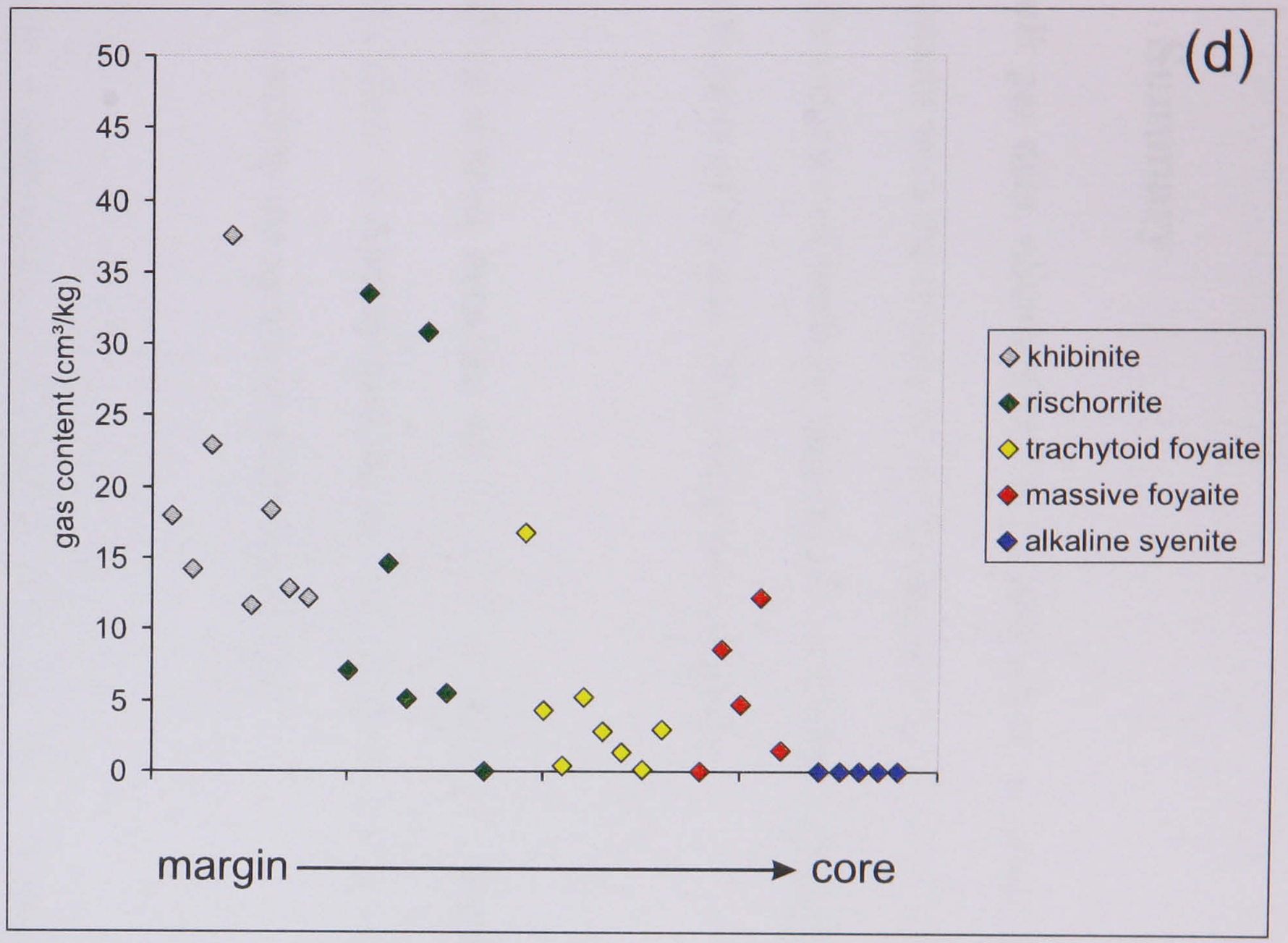

Figure 7.2 continued: Plot of bulk gas content versus (c) modal content of mafic minerals and (d) versus sampling location from the margin of the complex twoards th core.

7.5 Summary

New bulk gas data, obtained by two independent methods, are presented here. They are in agreement with the results of the fluid inclusion study. The gas is characterised by the strong dominance of methane and smaller content of higher hydrocarbons up to pentane. Small amounts of N_2 and CO_2 occur occasionally.

A good agreement between the results of the gas chromatograph data of the Kola Science Centre in Apatity and the GC-MS data from the laboratory of Exxon Mobil in Houston confirm the accuracy of both methods.

The gas compositions generally exhibit the so-called Anderson-Schulz-Flory distribution. They show a log-linear decrease in hydrocarbon concentrations with increasing carbon number, previously thought to be indicative of an abiogenic gas origin. However, the compositions of biogenically-derived gas show comparable patterns. In fact, the similarity of the gas derived from the Khibiny pluton and petroleum-related gas might suggest a comparable thermogenic origin. The compositional distribution of C_1-C_5 components, therefore, cannot be used as a reliable tool for distinguishing biogenic and abiogenic gas origins at moderate to high temperatures.

The bulk gas content of the Khibiny rocks is dependent on the occurrence and proportions of a suitable host mineral, namely nepheline. Generally, the higher the nepheline content, the higher the overall gas content. No comparable correlation exists between the content of mafic minerals or feldspar. The lack of a regional association

between mafic mineral content and gas content does not support a post-magmatic gas generation via Fischer-Tropsch synthesis.

The spatial gas distribution in the Khibiny pluton, with increasing gas concentration towards the marginal area of the pluton, implies an addition of hydrocarbon gases from a surrounding source. This is in agreement with the results of the isotope study presented in Chapter 8. Therefore, the inward migration of biogenically-derived hydrocarbons, generated from organic material contained in the country rocks, is likely.

8 The carbon and hydrogen isotopic composition of the fluids of the Khibiny pluton

8.1 Introduction

Isotopic data can be used to identify the origin and genesis of hydrocarbon gases. Carbon-bearing molecules such as CH_4 are among the most abundant fluids in a variety of geological settings and stable carbon isotope ratios are commonly used to determine the source of such fluids, their formation and reaction pathways and as a geothermometer (Schoell, 1980; Galimov, 1988; Horita, 2001). Furthermore, the combination of hydrogen isotope ratios (δD) and carbon isotope ratios ($\delta^{13}C$) of methane-rich fluids is a powerful method of identifying a variety of source-regions for C-H-O fluids.

There are a wide variety of potential methane sources. Methane can be produced by bacteria under anaerobic conditions in wet environments and in ruminant stomachs and termite guts, but may also originate from fossil carbon sources including biomass burning, coal mining, industrial exhaust, mantle and volcanic emissions (Brèas *et al.*, 2001). The carbon isotope signatures of specific sources are distinctive (Table 8.1.). Methane derived from animal sources shows the most depleted carbon isotopic signature with values between -31 ‰ and -93 ‰ and hydrogen isotope compositions of methane down to -332 ‰ (Brèas *et al.*, 2001). Fossil sources result in carbon and hydrogen isotope compositions of methane of – 2 ‰ to –79 ‰ and -137 ‰ to -250 ‰, respectively. Most fossil methane deposits are attributed to a biogenic origin. Methane

methane source	$\delta^{13}C$	δD	reference
		plant and animal sources	
swamps	-73 to -31	-310	Ciceron and Oremland, 1988 ; Levin et al., 1993
cattle and sheep	-76 to -61		Rust, 1981
rice paddies	-65.4	-332	Levin et al., 1993
termites	-93 to -65		Sugimoto et al., 1998
		fossil sources	
hydrothemal gas (Japan)	-44.2 to -6.4		Ono et al., 1993
thermogenic natural gas	-55 to -25	-250 to -150	Schoell, 1980
biogenic methane	-79 to -60		Rice and Claypool, 1981
coal associated gas	-70 to -15		Deines, 1986
East Pacific Rise	-18 to -15	-126 to -102	Welhan and Craig, 1983
shungite in Karelia	-44.4 to -17.4		Melezhik et al., 2004
Zambales Ophiolite	-7.5 to -6.1	-137 to -118	Abrajano et al., 1990
bulk mantle carbon	-7 to -5	-80 to -50	Kyser, 1986
majority of diamond	-8 to -2		Cartigny, 2005
Ilimaussaq	-9 to -2	-145 to -132	Konnerup-Madsen, 2001

Table 8.1: Some typical carbon and hydrogen isotope values for methane from different natural and fossil sources (from Brèas *et al.*, 2001).

in igneous rocks, as studied here, can originate from two principal sources: the host rock and the magma itself. Host rock related methane is normally generated from organic material mostly contained in sedimentary rocks. However, the possibility that methane may be abiogenic in origin is a relatively recent concept, although specific reaction mechanisms and isotopic characteristics are poorly constrained (Horita and Berndt, 1999; Horita, 2001). The methane can be incorporated into the igneous rock body either as primordial mantle CH_4 or generated from late- or post-magmatic re-equilibrium of mantle-derived CO_2 and H_2O/H_2-bearing fluids.

The isotopic compositions are expressed in classic delta notation (defined as $\delta^{13}C = [(^{13}C / ^{12}C_{sample}) / (^{13}C / ^{12}C_{PDB}) - 1] \times 1000$ for carbon and given in "permill", denoted by ‰ (1 part in 1,000, equally to 1 g / 1 liter).

8.2 A review of previous isotope data published from the Khibiny pluton

To date, reliable isotope data from hydrocarbon gases of the Khibiny alkaline rocks are sparse. Previously published data from hydrocarbon-bearing fluids in the Khibiny pluton (Table 8.2) include $\delta^{13}C_{bulk}$ data and $\delta^{13}C$ data for CH_4 and higher hydrocarbons from free gases (Galimov and Petersilie, 1967; Galimov, 1973; Khitarov *et al.*, 1979; Voitov, 1992). A small set of corresponding δD_{CH4} and $\delta^{13}C_{CH4}$ data is available from Yerokhin (1978) and Voitev (1992). The most recent $\delta^{13}C_{bulk}$ data were published by Potter (2000). $\delta^{13}C_{CO2}$ were published by Galimov and Petersilie (1967) and Potter (2000).

The first results of $\delta^{13}C$ analyses of gas in "mineral pores" were those of E.M. Galimov (Galimov and Petersilie, 1967; Galimov, 1973). The carbon within the sample was

burned in a high vacuum system at 1000°C and converted to CO_2 in an oxygen current over CuO. The isotopic compositions of carbon were examined using a MI-1305 mass spectrometer (Petersilie and Sorensen, 1970). Values for $\delta^{13}C_{bulk}$ and $\delta^{13}C_{methane}$ in a variety of rock types fell in a range from -19.3 ‰ to -3.2 ‰ (Galimov and Petersilie, 1967; Galimov, 1973). $\delta^{13}C$ data from higher hydrocarbons ranged from -26 ‰ to -3.2 ‰ and showed an increasing trend towards the higher homologues, indicative of generation via polymerisation from methane (Galimov, 1973). $\delta^{13}C_{CO2}$ values of -8.5 ‰ and +10.6 ‰, were published by Galimov and Petersilie (1967). Petersilie and Sørensen (1970) noted that carbon isotope values in the Khibiny gases were generally similar to those of diamonds and carbonatites and therefore, characteristic of a magmatic origin.

Voitov *et al.* (1990) and Voitov (1992) investigated free flowing gas ("gas jets") from the Rasvumchorr, Yuksporr and Kukisvumchorr mines in Khibiny pluton and published $\delta^{13}C_{CH4}$ data and some $\delta^{13}C$ data for ethane and propane. Unfortunately, no information on sampling and analysis techniques was given in their papers. The isotopic compositions of methane reported by the authors were in the range of -11.2 ‰ to -6.5 ‰. Voitov (1992) argued that thermodynamic calculations demonstrate an inorganic, high-temperature generation in aqueous fluid during dewatering at 400 to 500°C and 0.5 to 1 kbar (50 to 100 MPa) and suggested that the Fischer-Tropsch reaction, operating in several magma chambers, was a possible driver of hydrocarbon generation. This process was assumed to be accompanied by carbon isotope fractionation and therefore, $\delta^{13}C_{CH4}$ variations were due to different degrees of isotopic depletion of the initial gas. Voitov explained inhomogeneities in the gas compositions and isotopic ratios by ongoing formation of gases in several sites at depths of 25 to 30 km and incomplete mixing of released gases at 10-12 km depth. "Seismic and acoustic emissions" within the massif cause an upward migration toward the surface and

eventual release to the atmosphere. Compared to CH_4, the $\delta^{13}C$ values of higher homologues were as low as -23.9 ‰. This may be due to fractionation during their generation via polymerisation (Voitov, 1992).

Potter (2000) published two $\delta^{13}C_{bulk}$ values and one $\delta^{13}C_{CO2}$ value of gas samples from the Khibiny pluton. The main hydrocarbon-bearing minerals apatite, nepheline and calcite were separated from hand-crushed rock samples. About 100-150 µg of the separated minerals were processed in a high vacuum line at temperatures up to 700°C. The released hydrocarbon gases were immediately transformed to CO_2 by exposure to excess oxygen, produced by heating a CuO coil, transferred to a sample finger and trapped in liquid nitrogen. The gas was analysed in a Prism II mass spectrometer. CO_2-dominant fluids in carbonatites have been released in a similar way, but no additional oxygen supply from CuO was necessary for oxidation. The $\delta^{13}C_{bulk}$ values for the different heating steps range from 25.33 ‰ to -3.28 ‰ and $\delta^{13}C_{CO2}$ from -7.26 ‰ to -3.84 ‰.

Based on microthermometric fluid inclusion observations, Potter (2000) proposed that the majority of methane was released at 400°C by decrepitation. She concluded the carbon origin to be abiogenic but not mantle derived. Higher isotopic values were explained by mixing with primary magmatic CO_2.

Publisher	$\delta^{13}C_{bulkC}$	$\delta^{13}C_{CH4}$	$\delta^{13}C_{C2H6}$	$\delta^{13}C_{C3H8}$	$\delta^{13}C_{CO2}$	δD_{CH4}	minerals or rocks analysed/ location	gas type
		-3.2					khibinite	OG
		-12.8					urtite	OG
		-8.4					ijolite	OG
		-14.6			-8.5		fsp from pegmatite	OG
Galimov and Petersilie, 1967		-8.4			+10.6		eud from pegmatite	OG
		-13.2					trachitoid khibinite	OG
		-11.8					ijolite-urtite	FG
		-19.3					ijolite-urtite	FG
		-18.2					ijolite-urtite	FG
		-16.3					ijolite-urtite	FG
		-19.1					ijolite-urtite	FG
	-7.9						ne in pegmatite in trachytoid khibinite	OG
	-8.1						ne in pegmatite in trachytoid khibinite	OG
	-4.6						eud in pegmatite in middle-grained ne syenite	OG
	-4.3						ne in pegmatite in middle-grained ne syenite	OG
	-6.1						aenig in pegmatite in middle-grained ne syenite	OG
	-11.4						ne with aeg in pegmatite in middle grained ne syenite	OG
Galimov, 1973	-8.1						eud in pegmatite in middle grained ne syenite	OG
	-5.3						ne in pegmatite in titanite foyaite	OG
	-9.2						ne in pegmatite in rischorrite	OG
	-6.2						ne in pegmatite in ijolite-urtite	OG
		-12.8	-24.5	-26			urtite	OG
		-3.2	-9.1	25.7			khibinite	OG
		-7.9	-14.2				eudialyte	OG
Yerokhin, 1978		-6.5				-82		
		-6.5				-66		

Table 8.2: All published carbon and hydrogen isotope data for fluids of the Khibiny pluton (OG-occluded gas, FG-free gas).

Publisher	$\delta^{13}C_{bulkC}$	$\delta^{13}C_{CH4}$	$\delta^{13}C_{C2H6}$	$\delta^{13}C_{C3H8}$	$\delta^{13}C_{CO2}$	δD_{CH4}	minerals or rocks analysed/ location	gas type
Khitarov et al. 1979		-10.6	-23.9				Rasvumchorr mine, hole 7, 1967	FG
		-6.5	-11.7				Rasvumchorr mine, hole 7, 1975	FG
Voitev et al., 1990		-16.5 to -7.7					Rasvumchorr mine	FG
			-12.1				Rasvumchorr mine	FG
			-24				Rasvumchorr mine	FG
		-11.2	-15.6				Rasvumchorr mine	FG
Voitov, 1992						-72	Rasvumchorr mine, hole 7, February 1975, D in CH4	FG
						-56	Rasvumchorr mine, hole 7, March 1975, D in CH4	FG
						-144	Rasvumchorr mine, hole 7, February 1975; D in C2H6	FG
						-173	Rasvumchorr mine, hole 7, March 1975; D in C2H6	FG
		-8.7					Rasvumchorr mine, hole 360, August 1986	FG
		-11.2	-15.6				Rasvumchorr mine, hole 360, August 1986	FG
Potter, 2000	-11.44						urtite, sample 1253-153	OG
	-13.17						urtite, sample 1253-153	OG
	-8.3						urtite, sample 1253-153	OG
	-3.28						urtite, sample 1253-153	OG
	-25.33						urtite, sample 145-P-85	OG
	-17.82						urtite, sample 145-P-85	OG
	-12.34						urtite, sample 145-P-85	OG
				-7.26			carbonatite, sample Kh28	OG
				-5.58			carbonatite, sample Kh28	OG
				-3.84			carbonatite, sample Kh28	OG

Table 8.2 continued: All published carbon and hydrogen isotope data for fluids of the Khibiny pluton (OG-occluded gas, FG-free gas).

8.3 Methodology

8.3.1 Sample preparation

The rock samples studied here were crushed and dry-sieved to separate grain sizes of 2-2.8 mm and 2.8-4 mm. Both fractions were used for isotope analyses. To avoid contamination due to handling and organic surface contaminants, the samples were placed in an ultrasonic bath and washed in a mild NaOCl (3 %) solution for about 30 min. This was followed by several wash cycles with doubly-distilled water. The samples were then dried overnight at 105°C.

Isotope data were obtained at the stable isotope laboratory at the University of Lausanne. Two methods were used to release the fluids contained in fluid inclusions.

3. *Thermal decrepitation* released hydrocarbons and water. The following four fractions were separated for analyses: $\delta^{13}C_{CH4}$, δD_{CH4}, $\delta^{13}C_{CO2}$ and δD_{H2O}.
4. *Crushing* released CO_2 and hydrocarbon gases. They were separated using gas chromatography.

Both methods are detailed in the following section and their advantage and disadvantages will be discussed.

8.3.2 Thermal decrepitation

The fluids hosted in fluid inclusions and other cavities were released thermally into a vacuum system (Fig. 8.1) using a method similar to that described in Kesler *et al.*

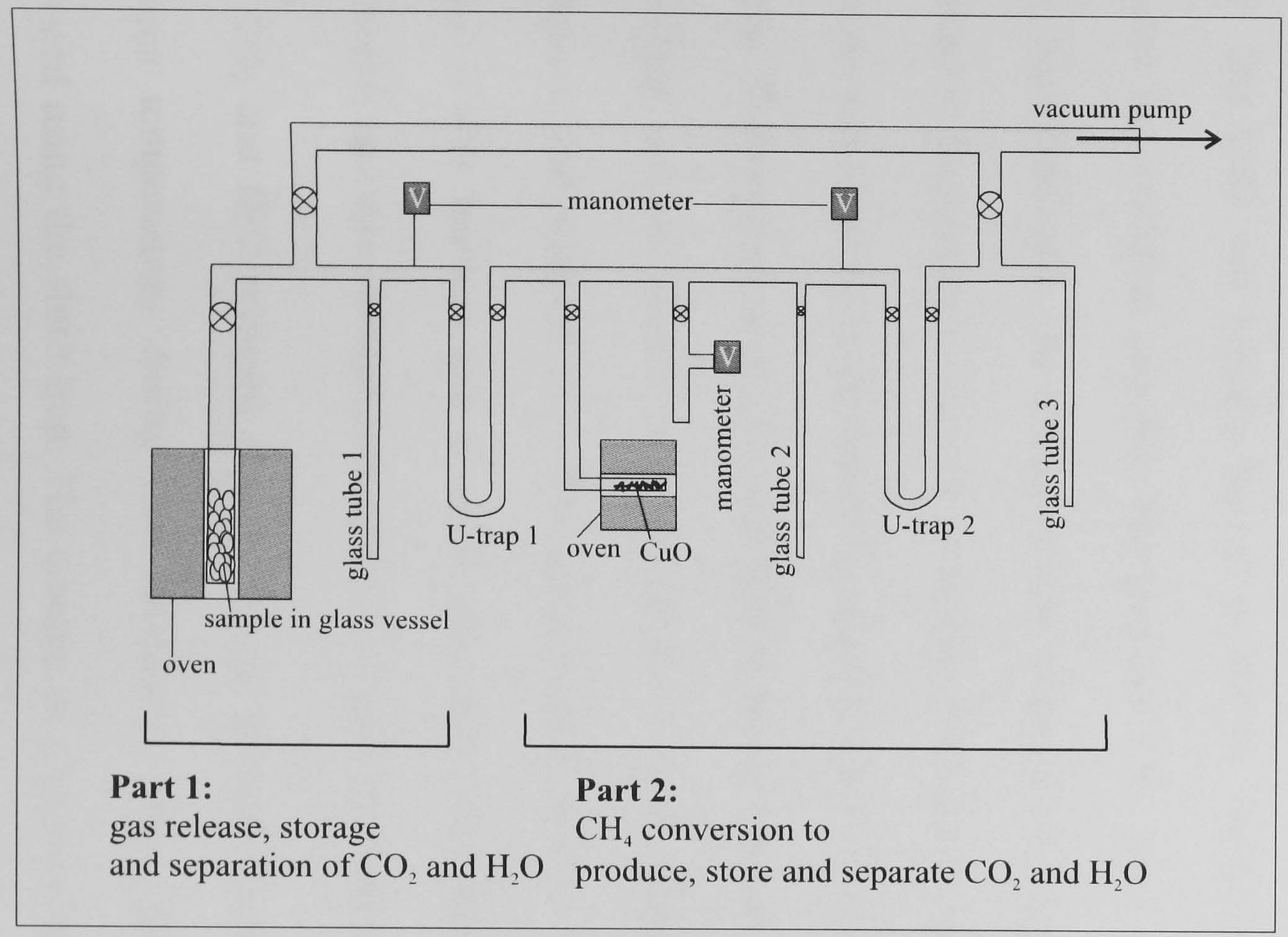

Figure 8.1: Schematic diagram of the vacuum line used for gas extraction from inclusions by thermal decrepitation. The sample is heated in several steps and the gas released into part 1 of the vacuum line. Condensable gas (CO_2 and H_2O) is trapped in the U-trap 1 using liquid nitrogen. Non-condensable gas (CH_4) remains in the line. When gas extraction is finished, CH_4 is transferred over the heated CuO and transformed to CO_2 and H_2O which will be trapped in U-trap 2. Replacing the liquid nitrogen trap with a slush trap releases CO_2 which is transferred to the manometer tube (freezing it with liquid nitrogen) where the volume is measured using the manometer. Then it is transferred into glass tube 2 which is sealed. H_2O is then released into glass tube 3. A similar procedure applies to CO_2 and H_2O trapped in U-trap 1. First, CO_2 is transferred to the manometer tube to reveal the volume before it is transferred into a (new) glass tube 2 and sealed. The water, held subsequently in the slush trap, is now transferred into glass tube 1 and sealed too. In this way four fractions were separated: CO_2 and H_2O from the fluid inclusions and CO_2 and H_2O as the product of CH_4 oxidation.

(1997). Approximately 4 g of sample material with grain sizes between 2 and 2.8 mm was used. Mafic components were removed in advance, to avoid contamination with crystal lattice-bound water from amphibole, biotite or other hydrous phases. The sample was loaded into a silica glass vessel, attached to a vacuum line and degassed at 100°C until no further pressure rise was recorded. The gases were released via thermal decrepitation in three heating steps. At 500°C, 700°C and 900°C the temperature was held constant for 10 min. Gas release started at about 400°C as indicated by a rapid increase of pressure in the closed vacuum line. During this process, released gases were moved through a U-trap, cooled with liquid nitrogen. Here, all condensable gases (e.g. CO_2, higher hydrocarbons and H_2O) were collected. All non-condensable gases (mainly CH_4), were held free in the vacuum line. After complete decrepitation the non-condensable CH_4 was transferred over CuO, which caused its oxidation to CO_2 and H_2O. The CuO was initially heated to 450°C, subsequently increased to 750°C, to enhance the oxidation process. The resultant CO_2 and H_2O were trapped in a U-trap using liquid nitrogen. The oxidation was complete when the pressure in the vacuum line returned to background values or no further pressure changes occurred. Any remaining pressure was assumed to be caused by small amounts of nitrogen and pumped out of the system. The separation of CO_2 and H_2O in both traps was done cryogenically, using a slush trap (ethanol cooled to about -90°C by adding liquid nitrogen). This kept H_2O condensed and released CO_2. The amount of CO_2 was measured with a manometer before it was isolated into a small glass tube and sealed. The H_2O was released afterwards and also isolated and sealed in a small glass tube for analysis.

The CO_2 and H_2O released directly during thermal decrepitation were kept at liquid nitrogen temperatures during CH_4 oxidation. After that, they were cryogenically separated using the slush trap. The amount of CO_2 was measured manometrically and

isolated and sealed into a glass tube. Finally, H_2O was transferred and sealed into a glass tube.

In this way the following four components were separated: CO_2 and H_2O directly from the fluid as well as CO_2 and H_2O, the oxidation product of CH_4 from the fluid. Carbon isotopes were analysed using a ThermoFinnigan gas chromatography/mass spectrometer. δD were analysed on the TC-EA at 1350°C via reduction of water with graphite. Based on repetitive analyses of international standards, the standard deviation is < 5% (pers. comm. T. Vennemann).

8.3.3 Crushing of rock samples

In this method, the gas was released by off-line samples crushing in a high vacuum system (Fig. 8.2), using the "pepper-mill"- technique of Simon (2001). The mill and interior of the extraction system was made of stainless steal and the attached connections to the vacuum pump and the gas storage vessel were made of glass. The system was cleaned with a solution of ultrapure, distilled dichloromethane and subsequently dried at 110°C before usage. Depending on the expected gas release, sample aliquots of 6 to 9 g with grain sizes between 2.8 and 4 mm were placed into the peppermill apparatus and the system closed and evacuated to a stable vacuum. At the same time, the "pepper-mill" was heated slightly to reduce possible surface contamination such as water adsorption on the sample and apparatus. The sample was crushed by hand for about 5 minutes until all rock pieces were pulverized. To avoid effects of fractionation (lighter isotopes "move" faster) during gas release and expansion, the system was held open for 5 minutes to reach equilibrium. The gas sample was then separated from the pepper mill and stored in a vacuum tight glass vessel.

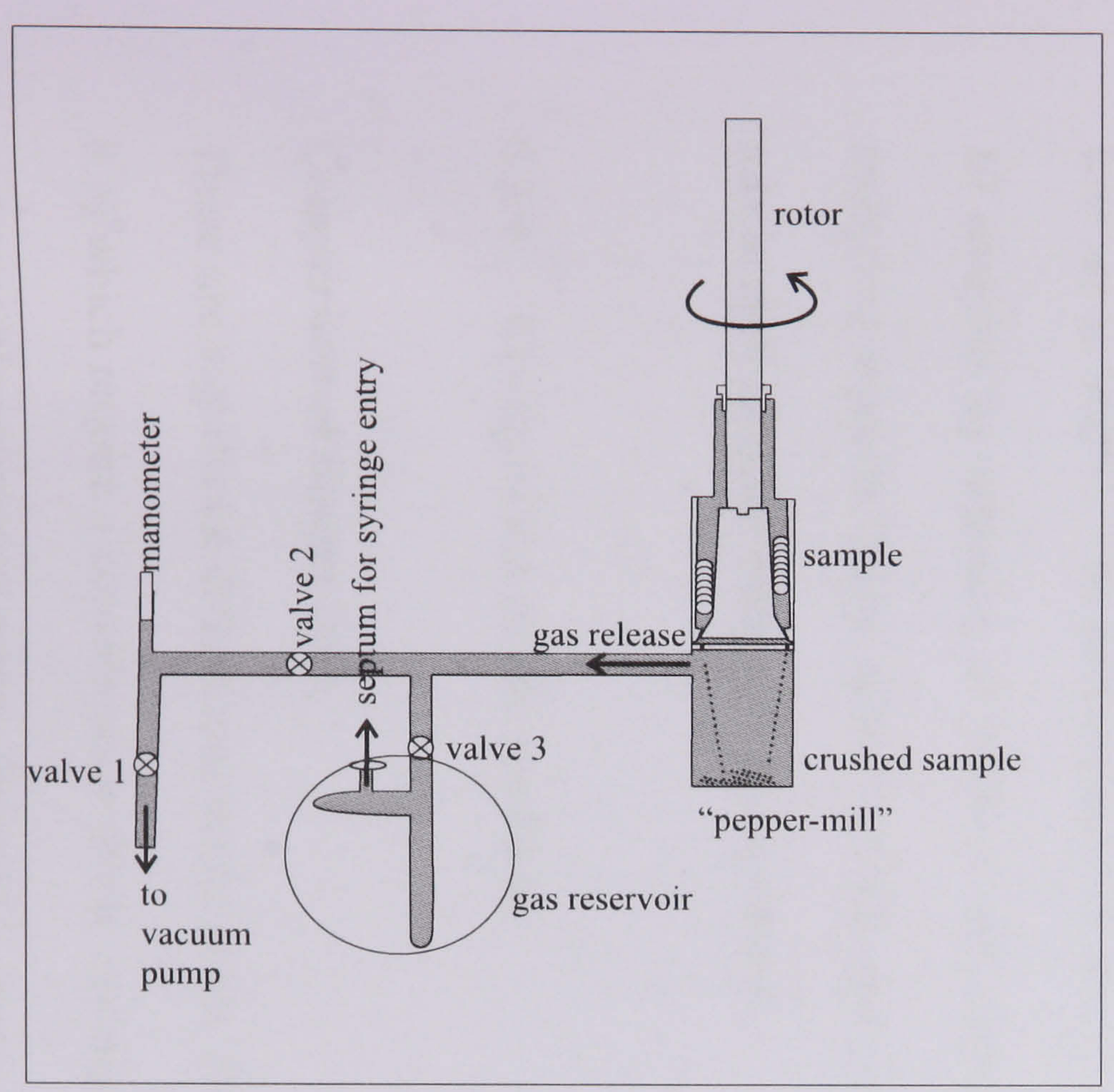

Figure 8.2a: Simplified model of the off-line crushing apparatus. The sample was loaded into the "pepper-mill" and the system evacuated with all valves open. During grinding, valve 2 was closed and the gas released into the system. After 5 min for equilibration valve 3 was closed and the sample stored in the gas reservoir vessel. Sampling was performed with a syringe via a rubber septum. The released gas volume, stored in the reservoir, was sufficient for up to three repeated analyses.

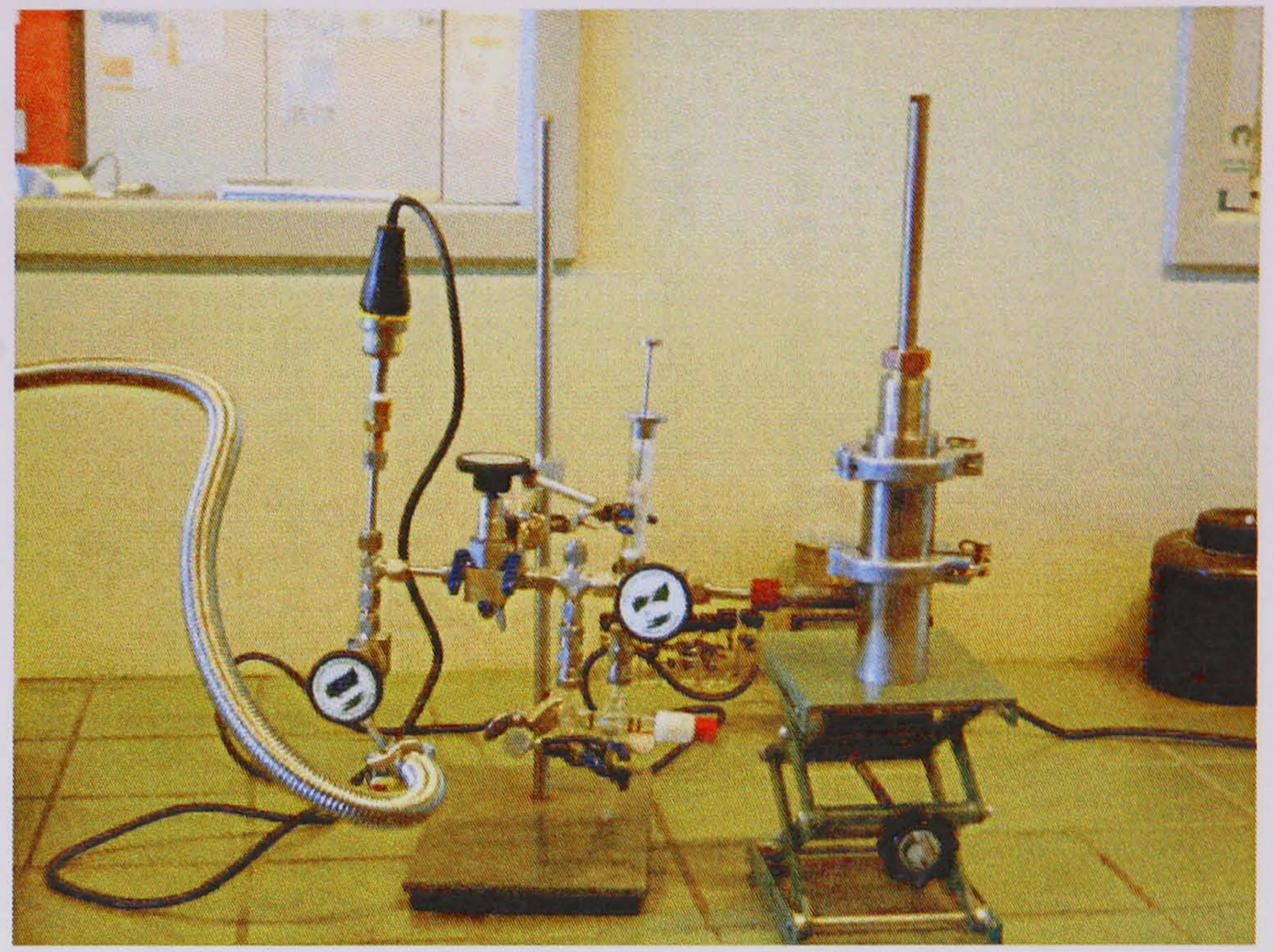

Figure 8.2b: The off-line crushing setup. For descriptions see text on schematic figure a.

Sampling was performed using a gas-tight syringe introduced via a rubber septum into the gas reservoir vessel, sampling 2.5 to 5 ml gas per analysis. Three analyses per crushed sample were performed. The carbon isotope compositions of CO_2 and saturated hydrocarbons were measured using a Hewlett-Packard 6890 gas chromatograph (GC) coupled via a combustion-interface III (C) to a Thermoquest/Finnigan MAT Delta S isotope ratio mass spectrometer (IRMS) (pers. comm. J. Spangenberg, Freedman *et al.*, 1988; Hayes *et al.*, 1990). The GC was operated with a Carboxen^{TM} 1006 PLOT capillary column (30 m x 0.53 mm internal diameter) for the analysis of CH_4 and CO_2 isotope ratios and with a Paraplot Q-HT column for higher hydrocarbons. Helium was used as carrier gas with a linear flow velocity of 3 ml/s. After an initial period of 5 minutes at 35°C, the column was heated to 100°C at 20°C/min followed by an isothermal period of 20 min, and later heated to 220°C at 20°C/min and held there for 5 minutes. The samples were introduced at 230°C. The CuO/NiO/Pt combustion reactor was set at 960°C. The performance of the GC/C/IRMS system was evaluated every 10 analyses by injection of methane and carbon dioxide of known $\delta^{13}C$ values. The analytical reproducibility, tested by daily replicate analysis of a laboratory standard gas mix is ±0.5 ‰ (pers. comm. J. Spangenberg).

8.3.4 Comparison of the methods

Comparison of isotope data

There are significant differences between the data obtained by the two methods (Table 8.3) which require a consideration of the advantages and disadvantages of both methods and possible sources of errors. Generally, gases released through rock crushing provide higher values of $\delta^{13}C_{CH4}$ and lower values of $\delta^{13}C_{CO2}$ than the thermally released

rock type	Sample	$\delta^{13}C_{CH4}$	$\delta^{13}C_{C2H6}$	$\delta^{13}C_{C3H8}$	$\delta^{13}C_{C4H10}$	$\delta^{13}C_{C5H12}$	$\delta^{13}C_{CO2}$	δD
thermal decrepitation								
khibinite	Kh-03-01	-20.7						-155
khibinite	Kh-03-03	-21.3						-168
khibinite	Kh-03-03	-21.2						
khibinite	Kh-03-03	-21.2						-167
khibinite	Kh-03-04	-20.8					0.1	-152.4
rischorrite	Kh-03-10	-16.1						-110.1
rischorrite	Kh-03-42	-17.7					1.8	-167.3
rischorrite	Kh-03-44	-17.9					-3.5	-164.7
massive foyaite	Kh-03-54	-22.6						-178
	mean	**-19.9**					**-0.5**	**-157.9**
	range	**-22.6 to -16.1**					**-3.5 to +1.8**	**-178 to -110.1**
crushing								
khibinite	Kh-03-03	-22.4						-15.5
khibinite	Kh-03-03							-14.9
khibinite	Kh-03-04		-18.7	-18.0	-18.7			
rischorrite	Kh-03-10	-12.6						-16.8
rischorrite	Kh-03-42	-14.4	-17.1	-17.3	-17.5			-15.4
rischorrite	Kh-03-44		-18.9	-19.2	-19.7			
rischorrite	Kh-03-46	-13.3	-19.2	-18.9	-19.4			-13.9
trachytoid foyaite	Kh-03-35	-7.4						-13.7
trachytoid foyaite	Kh-03-37	-8.0	-17.5	-19.6				-13.6
massive foyaite	Kh-03-54	-5.4	-14.3	-13.0	-13.2	-14.0		-13.7
ijolite	Kh-03-68	-10.8						-15.2
	mean	**-11.9**	**-17.6**	**-17.7**	**-17.7**	**-14.0**		**-14.7**
	range	**-22.4 to -5.2**	**-19.2 to 14.3**	**-19.6 to 13**	**-19.7 to -13.2**	**-14.0**		**-16.8 to -13.6**

Table 8.3: Isotopic data obtained for this study by thermal decrepitation and crushing of the rock sample.

equivalents. This consistent pattern suggests a systematic error, either mechanical or theoretical.

The most likely sources of this error are the high temperatures used during thermal decrepitation. The investigated samples frequently contain cancrinite, which is a potential carrier of CO_3 in its framework. It serves as an additional CO_2 source at high temperatures. Heating also causes the breakdown of carbon-bearing minerals such as zeolites, and other organic material such as graphite and bitumen contained in the sample material. The produced gases would mix with CO_2 and CH_4 derived from fluid inclusions and affect their isotopic compositions.

Other sources of errors for both methods could be: (a) contamination with organic material from sample handling and, after gas release; (b) isotopic fractionation; or (c) adsorption of gas onto particle surfaces or apparatus.

Comparison of gas compositions and volumes

The CH_4 and CO_2 volumes obtained by crushing are not the same as those obtained by thermal decrepitation. In attempt to resolve this dichotomy, the bulk gas volumes determined at the Apatity Science Centre (Chapter 7), using online-milling-gas-chromatography, were used for comparison (Table 8.4).

Thermal decrepitation yields the highest gas volumes of between 0.41 to 5.49 mmol CH_4/g sample. Values of between 0.01 and 1.71 mmol CH_4/g sample were derived from crushing. Much lower volumes were derived from bulk gas analyses at the Kola Science Centre, with values ranging between 0.0002 to 0.0044 mmol CH_4/g sample.

The low values resulting from on-line-milling-GC used in the Kola Science Centre are most likely due to the very small sample grain size of 0.25 to 0.63 mm. There is probably an effect of considerable gas loss during the preparation process, as during pre-crushing many of the FIPs (the main locality of fluid inclusions) are opened and the

	bulk gas analyses		crushing		thermal decrepitation	
Sample	ml/kg CH_4	mmol CH_4/g	mmol CO_2/g	mmol CH_4/g	mmol CO_2/g	mmol CH_4/g
Kh-03-01	17.1	0.0008			4.49	1.03
Kh-03-03	22.5	0.0010	0.53	0.23	2.91	1.12
Kh-03-03	22.5	0.0010			2.39	0.85
Kh-03-03	22.5	0.0010			2.00	0.56
Kh-03-04	36.2	0.0016	0.05	1.71	3.89	2.33
Kh-03-10	32.4	0.0014	0.03	0.40	14.15	1.42
Kh-03-42	30.4	0.0014	0.46	0.29	13.81	1.24
Kh-03-44	98.5	0.0044			15.56	5.49
Kh-03-46	16.1	0.0007	0.02	0.64	11.68	1.68
Kh-03-54	11.9	0.0005	0.02	0.10	1.65	0.67
Kh-03-68	20.6	0.0009	0.26	0.72	3.52	0.78
range	**4.22 to 98.5**	**0.0002 to 0.0044**	**0.01 to 0.79**	**0.1 to 1.71**	**0.70 to 15.56**	**0.41 to 5.49**
mean	**31.36**	**0.0014**	**0.19**	**0.58**	**7.16**	**1.61**
amount	1 g		7 g		4 g	
grain size	0.25-0.63 mm		2.8-4 mm		2-2.8 mm	

Table 8.4: Comparison of the CH_4 volume obtained by different methods. Bulk gas analyses were performed at the Kola Science Centre in Apatity (Russia) using a ball mill for crushing and gas release. Gas volumes were obtained by peak-area calculation on the coupled GC (see Chapter 7). For isotope analyses at the University Lausanne, the gas volume, released by crushing with "pepper-mill"-technique and by thermal decrepitation, were obtained manometrically.
Note, bulk gas data are converted from ml/kg to mmol/g for better comparability to isotope data (e.g. sample Kh-03-1: 17.1 ml/kg = 0.017 l/kg = 0.000763 mol/kg = 0.000763 mmol/g ~ 0.0008 mmol/g.

gas gets lost. This is because, as crystals preferentially split along the FIPs, large grain size should yield large gas volumes. Grain sizes used for thermal decrepitation and crushing were 2 to 2.8 mm and 2.8 to 4 mm, respectively. Therefore, the latter should contain most intact (closed) FIPs and yield the highest gas volume. However, the released gas volume is highest in thermally decrepitated samples and it is likely, that thermal decomposition of solid carbonic matter or breakdown of carbon-bearing phases caused an additional gas volume. This is in agreement with the above assumption, that the isotope ratios may be influenced by other phases than that contained in fluid inclusions.

The CO_2 volumes, released by thermal decrepitation, were very high. With values up to 15.6 mmol/ g sample it is often the dominant gas species (Table 8.4). This is an unexpected result, as CO_2 was not detected during bulk gas analyses (Chapter 7) and laser Raman spectroscopy (Chapter 6). The high CO_2 levels in gases released for isotope analyses must therefore be an artefact of the method. It can be produced either by decomposition of CH_4 or the combustion of other carbonic matter such as graphite, bitumen or by thermal breakdown of CO_2-bearing phases such as calcite or cancrinite. This suggestion is supported by the detection of about 0.1 % native carbon in the rock samples of the Khibiny pluton (Chapter 3). A 5 g sample, as used for isotope analysis, therefore contains about 5 mg carbon. Depending on the availability of oxygen and on the completeness of carbon degradation up to 9.3 cm^3 CO_2 can be produced via combustion. In comparison, a 5 g sample that contains on average 30 cm^3 CH_4 from fluid inclusions per kg rock (based on bulk gas analyses) would be expected to yield 0.2 cm^3 CH_4. Together, this would result in a CO_2:CH_4 ratio of 93:2. However, the CO_2:CH_4 ratios obtained during this study are much lower, in a range of 2:1 to 10:1 for thermal decrepitation and between 2:1 and 1:34 for crushing (Tab. 8.4). Therefore, it is

likely that the volume of CO_2 is a function of the incomplete degradation of carbonic matter.

The higher yields of CH_4 compared to CO_2 during crushing suggests that most of the gases were released from fluid inclusions and that only a small proportion of gases were the result of degradation of solid carbonic matter.

The absence of CO_2 in gas released from milling at the Kola Science Centre might be due to the low sample amount combined with intense contact of sample powder and gas that causes adsorption of CO_2 to the particle surface.

Concluding remarks on comparison of extraction methods

Based on the above observations, gas extraction by crushing produced the most reliable data for this study because:

1. Large amounts of sample material made the result most representative.
2. The large grain size assured that the FIPs, as the storage place of most fluid inclusions, were kept largely intact.
3. The design of the crushing apparatus avoided extensive contact between released gases and sample-powder limiting CO2 adsorption.
4. The operation at low temperatures reduced contaminations due to thermal decomposition or combustion of solid carbonic matter contained in the rock sample.

8.4 Results

As discussed above, the $\delta^{13}C$ values obtained in this study vary depending on the method used (Tab.8.3). The $\delta^{13}C$ values of CH_4 and CO_2 for gases obtained by thermal decrepitation are in a range of -22.6 ‰ to -16.1 ‰ and -3.5 ‰ to +1.8 ‰, respectively. In contrast, the $\delta^{13}C$ values obtained by crushing are higher for CH_4, ranging between

–22.4 ‰ to -5.4 ‰ and lower for CO_2 between -16.8 ‰ to -13.6 ‰. The $\delta^{13}C$ values of higher hydrocarbons range between -19.7 ‰ to -13 ‰ and show a tendency to decrease with increasing carbon number. The δD values, obtained using thermal decrepitation, are between -209 ‰ and -110.1 ‰.

The following discussion is largely based on the $\delta^{13}C$ data obtained by off-line crushing-GC-MS. Only δD data from thermal decrepitation were used in the discussion. All other values are presented here for completeness only (Table 8.3) but due to their unreliability they are not used to interpret the origin and generation of CH_4.

8.5 Discussion

The carbon isotope values of CH_4 in the Khibiny pluton range from -22.4 ‰ to -5.4 ‰ with a mean of 11.9 ‰. The range of data obtained in this study can be attributed to different factors. Apart from analytical errors, different gas sources and generation mechanisms, fractionation and contamination affect the isotopic signature of the fluid.

8.5.1 The origin of methane based on isotopic mass balance calculations

Post-magmatic generation of CH_4 via F-T reaction

As previously discussed (Chapter 3), abiogenic CH_4 can be formed post-magmatically from mantle CO_2 via a Fischer-Tropsch (F-T) reaction. Significant amounts of CO_2 were measured during isotope analyses. In the previous section it was concluded that this is most likely an artefact of the analytical method. It is, however, also possible that the CO_2 represents primary magmatic CO_2 which survived the breakdown to CH_4 during a F-T reaction.

A mass balance calculation between detected CO_2 and CH_4 can be used to determine a hypothetical primordial carbon isotope value as well as to demonstrate different degrees of fractionation depending on the completeness of the supposed F-T reaction.

The hypothesis to be tested is that primordial CO_2 reacts either completely to CH_4 or incompletely to a CO_2-CH_4 mixture. The starting point is a 100 % CO_2 fluid. During the (incomplete) F-T reaction the fluid composition can be described as m CO_2 + (100 % - m) CH_4, whereby the proportion of CO_2 constantly decreases and that of CH_4 equally increases.

The following calculation can be used to model the extent of the reaction:

$$F_{primordialCO2} = m_{CO2} \times F_{CO2} + m_{CH4} \times F_{CH4}$$

where "F" indicates the calculated ^{13}C atom fraction in the following phases: (a) primordial CO_2; (b) unconsumed CO_2; and (c) produced CH_4 (as shown as indices in the formula).The measured molecular mass fraction is denoted by "m".

The calculation results in values for the hypothetical primordial CO_2 isotopic composition ranging from -17.6 ‰ to -7.6‰ (Table 8.5). For the mantle, however, a $\delta^{13}C$ value of about –5‰ has been identified as a major isotopic composition signature (Deines, 2002). The deviation from the mantle carbon signature and the wide variety of calculated $\delta^{13}C$ values for the primordial CO_2 starting material indicates that the isotope ratios for the present CO_2 and CH_4 in the fluid cannot be explained by fractionation processes due to different degree of CO_2 reduction in the course of a F-T reaction.

Lancet and Anders (1970) showed that during the early stage of a F-T reaction the $\delta^{13}C$ values of CO_2 and CH_4 are fractionated by up to 100 ‰. With progressing F-T synthesis the CH_4 becomes isotopically heavier and approaches the isotopic composition of the starting CO_2. At the same time, the volume and isotopic composition of CO_2 decreases. In the gases of the Khibiny pluton, however, the isotopic pairs do not follow such a

Sample		$\delta^{13}C_{CH4}$ (F_{CH4})	mmol CH_4 / g	$\delta^{13}C_{CO2}$ (F_{CO2})	mmol CO_2 / g	m_{CH4}	m_{CO2}	$F_{prim.\ CO2}$
khibinite	Kh-03-03	-22.4	0.226	-15.5	0.528	0.299	0.701	-17.566
rischorrite	Kh-03-10	-12.6	0.397	-16.8	0.027	0.936	0.064	-12.849
rischorrite	Kh-03-42	-14.4	0.287	-15.4	0.462	0.384	0.616	-15.006
rischorrite	Kh-03-46	-13.3	0.637	-13.9	0.025	0.963	0.037	-13.306
massive foyaite	Kh-03-54	-10.8	0.099	-15.2	0.016	0.857	0.143	-11.439
ijolite	Kh-03-68	-5.4	0.716	-13.7	0.258	0.735	0.265	-7.600

Table 8.5: Samples used for mass balance calculations to obtain the composition of the hypothetical primordial CO_2 in a FT-reaction. The resulting values of the assumed homogeneous mantle CO_2 source vary widely.

trend (Fig. 8.3). Therefore, it is likely that the CO_2 extracted here is the result of degradation of carbonic matter during analysis and is not primordial CO_2 and was not in equilibrium with CH_4 during a F-T reaction. This is in agreement with the absence of CO_2 in bulk gas aliquots and in fluid inclusions.

Mixing of magmatic CH_4 with biogenic host rock fluid

Several characteristics of the fluid support the hypothesis of a magmatic origin for CH_4. The spatial distribution of methane concentrations (Chapter 7) and $\delta^{13}C$ isotope values, however, indicates a possible interaction with biogenic host rock fluid. Methane concentrations are lowest in the inner parts of the Khibiny pluton and increase outward towards the margin (Chapter 7). Similarly, $\delta^{13}C$ values decrease from the central part of the complex towards the outer part of the complex (Fig. 8.4). Foyaite from the core of the pluton contain methane with a $\delta^{13}C$ value of -5.4 ‰.The marginal khibinite has a $\delta^{13}C_{CH4}$ value of -22.4 ‰. This might be explained by mixing of magmatically derived CH_4 with biogenic methane from the host rock. As discussed in Chapter 4, the possible source of the host rock methane might be a shungite deposit similar to that found in Karelia (Melezhik *et al.*, 1999).

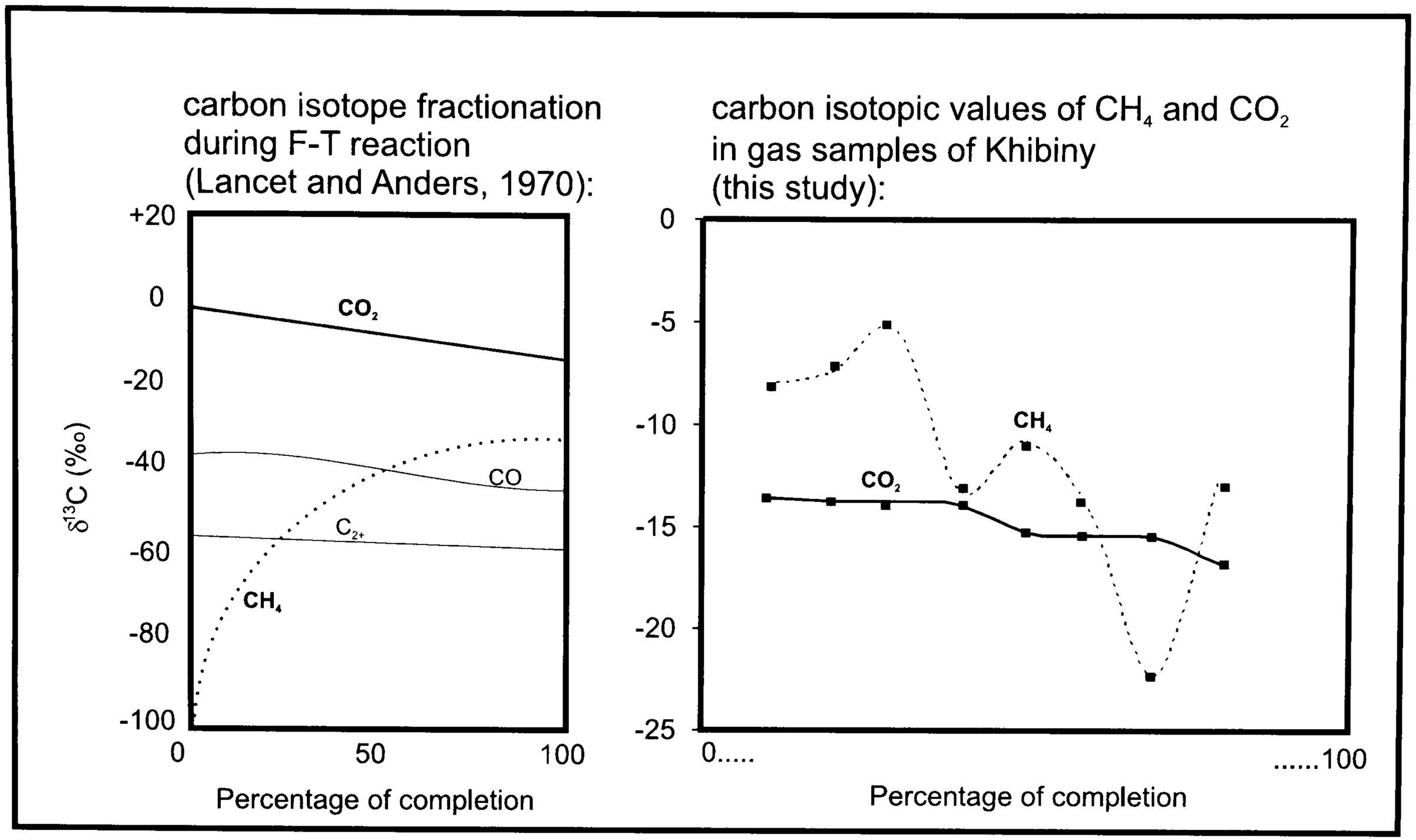

Figure 8.3: Carbon isotope fractionation in the F-T reaction at 400°K based on experimental studies by Lancet and Anders (1970) in comparison with isotopic data for gas from the Khibiny pluton. The experimental study shows that a large isotope fractionation occurs in the early stage of the reaction. With progressing reaction, the carbon isotope values of methane become heavier. The isotope data obtained for fluids from the Khibiny pluton reveal that the values of $\delta^{13}C_{CH4}$ do not show a consistent trend when plotted against decreasing $\delta^{13}C_{CO2}$. In addition, $\delta^{13}C_{CH4}$ values are often heavier than those of $\delta^{13}C_{CO2}$. This is not comparable with the Lancet and Anders model and means that CO_2 and CH_4 isotopic composition cannot be related through an incomplete F-T reaction.

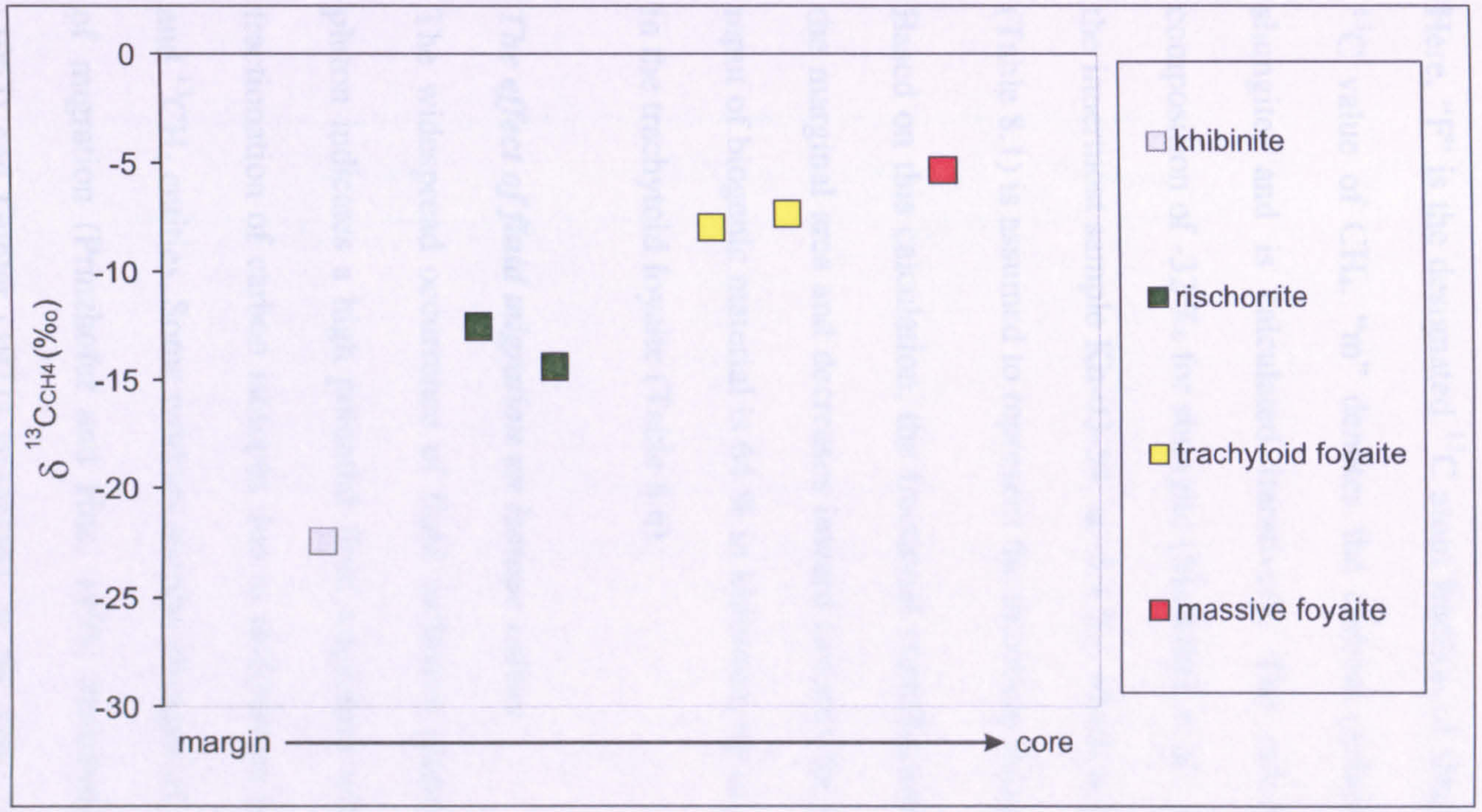

Figure 8.4: Variation in $\delta^{13}C_{CH4}$ signatures from the margin of the complex (khibinite) inward towards the core (foyaites).

Mass balance calculation can be used to determine the possible ratio of biogenic and mantle components from the analytical data. The equation governing the isotope ratio of the assumed mantle and shungite fraction can be expressed as:

$$F_{shu}m_{shu} + F_{mantle}m_{mantle} = F_{meassured}.$$

Here, "F" is the designated ^{13}C atom fraction of shungite and mantle and the measured ^{13}C value of CH_4. "m" denotes the carbon molecular mass fraction of mantle and shungite, and is calculated iteratively. The calculation utilizes the average $\delta^{13}C$ composition of -32 ‰ for shungite (Melezhik *et al.*, 2004). The measured $\delta^{13}C$ value of the innermost sample Kh-03-54, at -5.4 ‰, which is close to that of bulk mantle carbon (Table 8.1) is assumed to represent the uncontaminated mantle signature.

Based on this calculation, the fractional contribution of biogenic material is highest in the marginal area and decreases inward towards the core of the Khibiny complex. The input of biogenic material is 64 % in khibinite, up to 30 % in rischorrite and up to 10 % in the trachytoid foyaite (Table 8.6).

The effect of fluid migration on isotope values

The widespread occurrence of fluid inclusion planes and microcracks in the Khibiny pluton indicates a high potential fluid migration within the complex. This may cause fractionation of carbon isotopes due to differences in molecular mobility of the $^{12}CH_4$ and $^{13}CH_4$ entities. Some workers ascribe changes of up to 5 ‰ in $\delta^{13}C$ values to effects of migration (Prinzhofer and Huc, 1995; Prinzhofer and Pernaton, 1997). Galimov (1967) and Gunter (1971) suggested on the base of experimental data that methane could be enriched in either ^{12}C or ^{13}C to varying degrees because of their mass differences. The extent and direction of this fractionation depends upon the mechanism of migration and the properties of the medium through which the gas is moving. The diffused gas is consistently depleted in the heavier ^{13}C and the diffusion-related isotope

Sample		$\delta^{13}C_{CH4}$	m_{mantle}	$m_{shungite}$
khibinite	Kh-03-03	-22.4	0.36	0.64
rischorrite	Kh-03-10	-12.6	0.73	0.27
rischorrite	Kh-03-46	-13.3	0.7	0.30
rischorrite	Kh-03-42	-14.4	0.7	0.30
trachytiod foyaite	Kh-03-35	-7.4	0.92	0.08
trachytiod foyaite	Kh-03-37	-8.0	0.9	0.10
massive foyaite	Kh-03-54	-5.4	1	0.00

Table 8.6: Results of an iterative mass balance calculation of mixing between a biogenic source (shungite with a carbon isotope signature of -32 ‰) and a mantle source (equivalent to sample Kh-03-54 with -5.4 ‰ assumed to be uncontaminated by host rock fluid). The calculated molar fractions of mantle- and shungite-carbon are shown in the last two columns. The contribution of biogenic carbon is highest in the outer part of the pluton and decreases inward.

effect under experimental conditions is, according to Zhang and Krooss (2001), up to -3.15 ‰. Fuex (1980) indicated that fractionation of methane is also possible due to the different water-solubility of $^{12}CH_4$ and $^{13}CH_4$.

As fluid migration has occurred in the Khibiny pluton in the past and continues in the present day (see Chapter 9), the varying isotope values found in this study might be partly attributed to mass fractionation of $^{12}CH_4$ and $^{13}CH_4$. The extent of this effect, however, is not known for fluids of the Khibiny pluton.

8.5.2 The δD versus $\delta^{13}C$ signature of methane from the Khibiny pluton

The stable isotope compositions of hydrogen and carbon are the most reliable properties to use in determining the origin of methane (Schoell, 1988; Whiticar, 1990). They were applied to methane from various geological settings. In Figure 8.5, biogenic methane (Schoell, 1983; Whiticar, 1999) and abiogenic methane from a variety of geological settings are plotted on a δD versus $\delta^{13}C$ diagram. Abiogenic methane shown here includes geothermal methane from the East Pacific Rise (Welhan and Craig, 1983), methane in fluid inclusions from alkaline igneous rocks in Greenland (Konnerup-Madsen, 1988) and the Kola Peninsula (Nivin *et al.*, 1995) and methane from the Zambales Ophiolite, Philippines (Abrajano *et al.*, 1988). New δD_{CH4} and $\delta^{13}C_{CH4}$ data reported here and existing isotope data of methane from the Khibiny pluton (Yerokhin, 1978; Voitov, 1992) are also plotted.

The δD_{CH4} values presented from the Khibiny pluton vary between -178 ‰ and -110.1 ‰. The δD_{CH4} mean of -157.9 ‰ is close to those of methane from the Lovozero (Nivin *et al.*, 1995) and Ilímaussaq complexes (Konnerup-Madsen, 1988). A large-scale

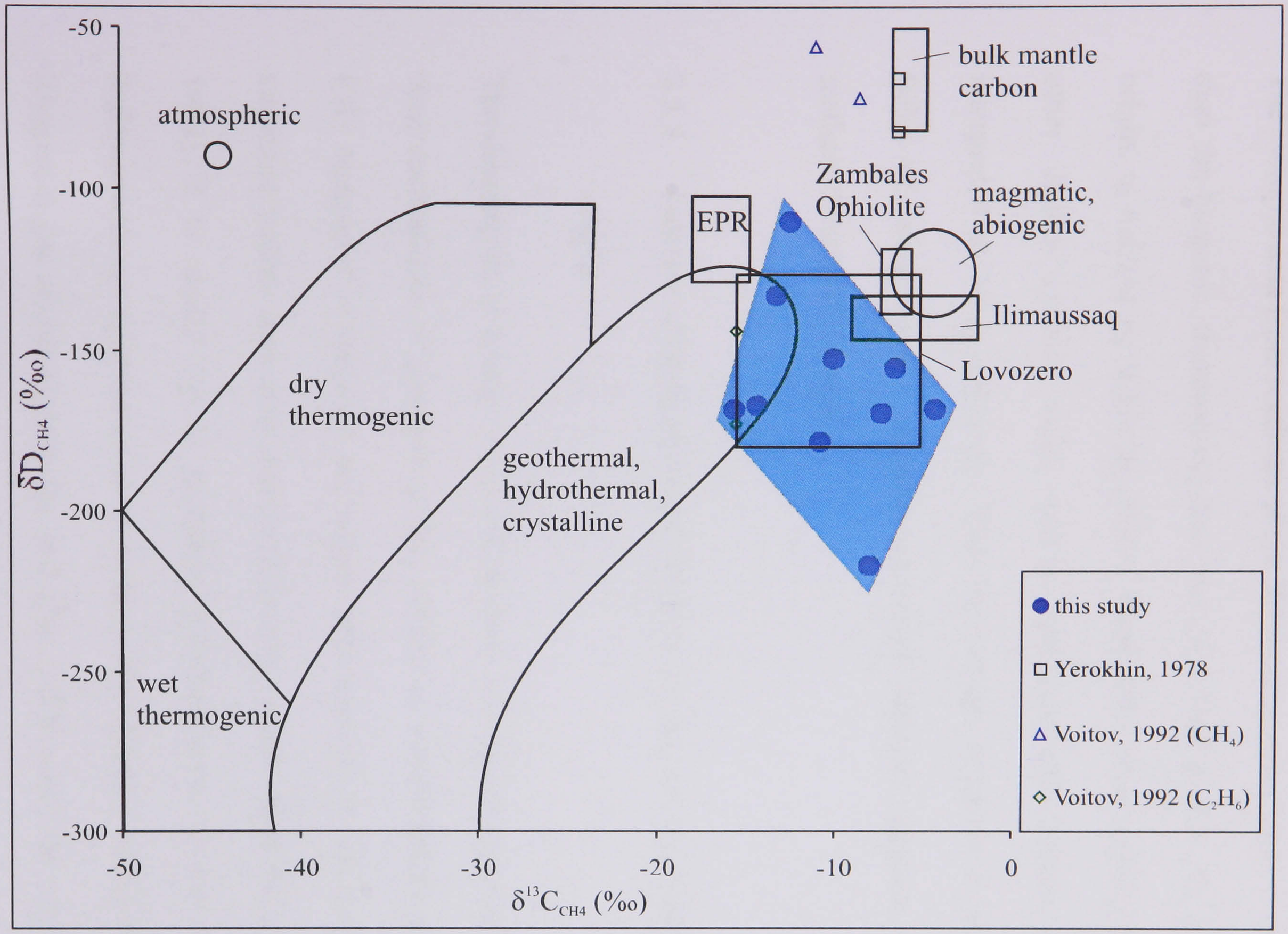

Figure 8.5: δD-δ^{13}C plot showing isotopic signatures for hydrocarbons from various igneous settings that were reported to be abiogenic in origin. Data are taken from Wehlan and Craig (1983) for EPR (East Pacific Rise), Abrajano *et al.* (1990) for methane found in the Zambales Ophiolite, Konnerup-Madsen (2001) for Ilímaussaq values, Nivin *et al.* (1995) for Lovozero values, Whiticar (1999) for the magmatic abiogenic field. Also shown are a number of well-established isotope signatures, namely that of atmospheric methane (Schoell, 1988), of magmatic abiogenic methane, wet and dry thermogenic and geothermal, hydrothermal, crystalline fields (Whiticar, 1999) and of bulk mantle (Kyser, 1986).The blue shaded area and filled circles indicate results of this study. Open marks show isotope data of earlier studies of the Khibiny pluton.

depletion of deuterium in methane, which has been interpreted as isotopic evidence of abiogenic methanogenesis ($CO_2 + H_2O \rightarrow CH_4 + 2\ O_2$) in rocks of the Canadian shield (Sherwood-Lollar *et al.*,1993a,b), is not observed in samples of this study.

The isotopic data from methane of the Khibiny complex show a heavier δC_{CH4} signature than the biogenic, thermogenic data and plot close to that of the magmatic, abiogenic origin, as defined by Whiticar (1999). They differ only slightly from the signatures of other alkaline igneous rocks, such as Lovozero and Ilímaussaq, where methane is interpreted as being abiogenic. That the isotope signature is positioned between the fields of abiogenic and biogenic generated methane suggests a possible mixing of methane from both sources.

8.5.3 Isotope distribution of hydrocarbons as an indicator for abiogenic origin

The distribution of isotope values of methane and higher hydrocarbons are indicative of their mechanisms of generation. The pattern of systematically higher $\delta^{13}C$ values for CH_4 compared to those of the higher hydrocarbons in the same fluid samples is a universal feature that characterises high-temperature abiogenic hydrocarbons (Voitov, 1992). It is caused by an inorganic polymerisation process whereby the heavier hydrocarbons are synthesised from methane (Des Marais, 1985). Samples from a natural (biogenic) gas source (Prinzhofer and Huc, 1995) show the opposite trend, with $\delta^{13}C$ values increasing toward the higher C numbers. This is because of their nature of generation by decomposition of organic material, whereby higher HC develop toward lower homologues with a preferential reaction of the bonds with ^{12}C.

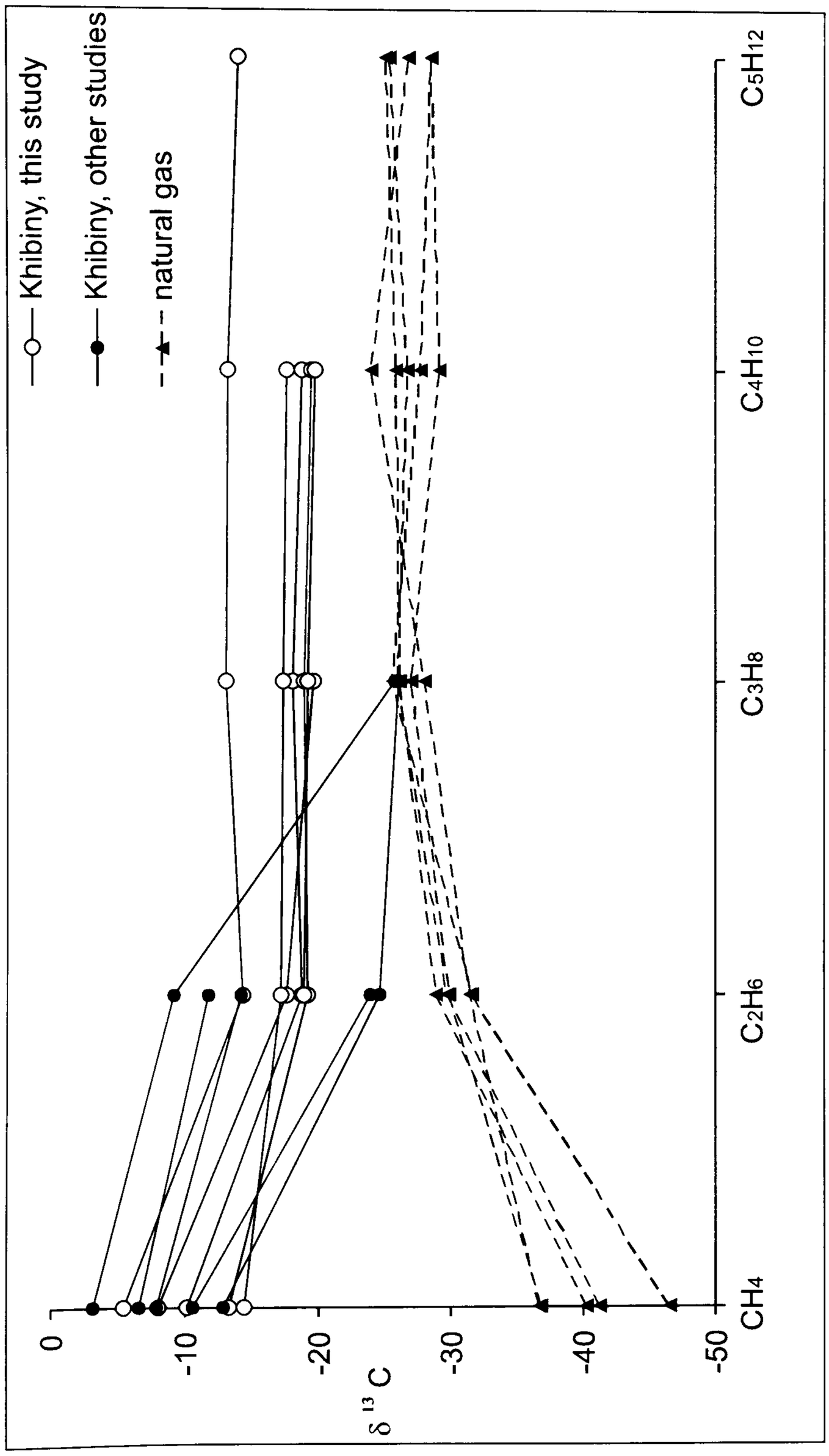

Figure 8.6: Isotope distribution of methane and higher hydrocarbons of gas extracted from the Khibiny pluton (this study; Galimov, 1978; Voitov, 1992) compared with data from natural gas samples (Prinzhofer and Huc, 1995).

The analysed fluids show a significant decrease of $\delta^{13}C$ values from methane to ethane (Fig 8.6). The $\delta^{13}C$ values of higher hydrocarbons (ethane to pentane) are relatively similar with no decreasing tendency. The distribution is, however, significantly different from that of biogenic gas samples and is therefore regarded as being largely abiogenic. The mixing with biogenic methane, suggested in the above sections, might affect the isotope data of higher hydrocarbons and cause the flat-lined distribution.

8.6 Summary

Two different extraction techniques – thermal decrepitation and crushing - have been used to obtain the isotopic signature of gases in the Khibiny pluton. Thermal decrepitation yields unreasonably high CO_2 values, inconsistent with findings of bulk gas and fluid inclusion analyses. The CO_2 is therefore attributed to degradation of carbonic material during sample heating or to release of CO2 from the cancrinite framework, and the data must be viewed as unsound. Of the crushing techniques the most reliable are those that crush large amounts of large grained material.

The $\delta^{13}C_{CH4}$ values of between -22.4 ‰ and -5.4 ‰ indicate an abiogenic origin of the methane gas in Khibiny. However, large-scale migration of hydrocarbon gas within the complex is likely to cause fractionation and result in varying isotope values within the Khibiny complex.

A decrease in $\delta^{13}C$ values from methane to the higher homologues of C supports an abiogenic origin for the hydrocarbon gases found in Khibiny. However, the hypothesis that CH_4 is product of the post-magmatic F-T reaction and CO_2 the unconsumed residue could not be proved by mass balance calculation between CO_2 and CH_4. The detected CO_2 is therefore, as stated above, an artefact of the method.

$\delta^{13}C_{CH4}$ values become lighter toward the pluton margin indicating a potential influence of biogenic CH_4 from the host rock mixing with magmatically derived CH_4. A mass balance calculation suggests that biogenic CH_4 contributes up to 64 % of the total methane in the Khibiny pluton.

The δD_{CH4} values range from -178 ‰ to -110.1 ‰. On a δD versus $\delta^{13}C$ plot, the isotopic data of fluids from the Khibiny pluton are close to that reported from other igneous geological settings and fall between methane signatures of biogenic origin and that of magmatic abiogenic methane.

The latter two results support the hypothesis of mixing of methane from a biogenic source in the host rock with abiogenic, magmatically derived gas.

9 Crack characteristic, density and orientation in the Khibiny pluton and the implication for fluid movement and storage

9.1 Introduction

Previous chapters document that the Khibiny pluton contains large amounts of hydrocarbon gas. The gas is hosted as either occluded gas or free gas and has experienced different stages of fluid migration. Occluded gas mainly occurs in secondary fluid inclusions within healed microfractures. It also occurs in primary fluid inclusions. Free gas is stored along open microcracks. Both types of gas are compositionally similar (Nivin *et al.*, 2001) and are therefore considered as having the same origin. Large volumes of free-flowing methane have been recorded as being released when rocks are fractured as a result of drilling during underground mining (Nivin *et al.*, 2001). This suggests the ease with which sealed microfractures and fluid inclusion planes are opened up and connected. It also indicates that the pluton may be a potential hydrocarbon source to the atmosphere as modern day reactivation of fault systems, by either natural or anthropogenic processes, causes the release of significant amounts of gas.

9.2 Aims and Objectives

Fluid movement and accumulation in geological environments is essentially dependent on permeability and porosity of the rock suite. In igneous rocks, these parameters are

largely defined by crack abundance and interconnectivity. Therefore, the research program reported here aimed to carry out an evaluation of fluid inclusion planes (FIPs) and open microcracks (MCs) in the Khibiny pluton as representatives of palaeo- and present-day fluid pathways, respectively.

Crack appearance, distribution, length, width, orientation and interconnectivity on a microscopic scale were investigated in order to quantify rates and mechanisms of transport, entrapment and degassing of hydrocarbons in the Khibiny pluton. The crack characteristics were processed in a relatively simple statistical model to determine rock porosity and permeability. The calculated porosity values were used to estimate the gas volume of the Khibiny complex.The crack orientation data were analysed to reveal if and how microstructures may contribute to unravelling the rocks stress history.

9.3 Definitions

9.3.1 Microcracks

A microcrack is defined by Simmons and Richter (1976) as an opening that occurs in a rock and has one or two dimensions smaller than the third. Generally, cracks in rocks are produced when the local stress exceeds the local strength (Simmons and Richter 1976) whereby the stress is mechanically or thermally induced. Microcracks are considered to represent the most important small scale fluid vector of a rock (Lespinasse and Cathelineau, 1995).

Cracks are subdivided into the following major groups:

1. grain boundary cracks coinciding with grain boundaries
2. intragranular cracks, which are located totally within a crystal grain

3. intergranular cracks, extending over more than one mineral grain

4. cleavage cracks, which follow cleavage planes in minerals.

There is a close relationship between the characteristics of a microcrack and the process of its formation.

9.3.2 Fluid inclusion planes

When microcracks close, fluid inclusions can easily be trapped within them. The resulting planar arrays within minerals are called fluid inclusion planes. As their generation post-dates mineral growth, the fluid inclusions trapped in these planes are, according to Roedders classification (1984), secondary in origin; i.e. they result from redistribution of fluids during dynamic recrystallisation (Hollister, 1990). Experimental results have shown that microfractures evolve into FIPs by two mechanisms (Smith and Evans, 1984):

1. Crack healing, which occurs in many geological environments and results in the formation of secondary fluid inclusions. It involves the local transport of mineral material as it reforms a fractured lattice or grain boundary.
2. Crack sealing involves material transport from some distance via the pore fluid. Subsequent precipitation on the fracture surface eventually seals the crack.

Brantley *et al.*, 1990 showed in laboratory experiments that microcracks have a wide range of lifetime. Healing rates are basically dependent on time, temperature, fluid pressure, chemistry and crack dimensions (Smith and Evans, 1984; Brantley *et al.*, 1990). Healing occurs via diffusional material transport and is driven by the reduction of surface energy. The healing process takes place over a wide range of P-T conditions and is thermally activated. It is very effective at temperatures of 400 to 600°C and pressures of about 200 MPa. The microcrack lifetime is considerably shortened with

increasing depth even when hydrostatic and lithostatic pressures are equal (Brantley *et al.*, 1990).

9.3.3 Porosity and permeability in igneous rocks

Porosity defines the open pore space in a rock and determines the capacity to accumulate and store material. Natural geological systems are characterized by various types of porosity: pores, vacuoles, joints between mineral grains, grain boundaries, microcracks and fractures.

Plutonic rocks can develop primary and secondary porosity that contribute to transport and storage of fluids in the subsurface (Petford, 2003). The primary structures are formed due to internal stresses related to cooling and crystallisation of the magma (cooling joints). Secondary porosity results from weathering and hydrothermal alteration, tectonic stresses and mineral dissolution by percolating groundwater.

Permeability is the capacity of porous rock to allow movement of a fluid through it. It is the key parameter in any model of fluid flow and transport in rocks (Lonergan *et al.*, 1999). As the matrix porosity in igneous rocks is poorly developed (Brace, 1984), the permeability is directly controlled by brittle discontinuities such as fractures and cracks. The maintenance of high permeability requires that the fractures remain open to fluid transport. However, permeability rates changes with time in a natural situation. They are governed by the competition of crack reducing and crack producing processes. Fracture reducing processes include healing, sealing and cementation, whilst enhancing processes include joint production, brittle failure, weathering and hydrofracturing.

To date, there have been relatively few studies of porosity and permeability in granitoid rocks. Brace (1980, 1984) obtained permeability data by *in situ* measurements of

crystalline rocks. The values of permeability measured in drill holes are in the range of 10^{-18} m² to 10^{-13} m² (1 µD to 100 mD). Petford (2003) published a compilation of the general range of values for porosity and permeability. He showed that porosity ranges from 0.01 % to 1 % for plutonic rocks but that it can increase up to 17 % due to hydrothermal alteration and weathering. The permeability of plutonic rocks ranges between 10^{-21} m² and 10^{-8} m² (1 nD to 10 kD). Sausse *et al.* (2001) calculated porosity and crack permeability in the Brézouard granite (Vosges, France) using a statistical model based on Gueguen and Dienes (1989). The porosity ranged from 4.5 % to 4.75 % and permeability from 0.18 mD to 0.215 mD (equals $1.8*10^{-16}$ m² to $2.15*10^{-16}$ m²). Using a similar model, Lespinasse *et al.* (2005) presented a case study from a granitic core sample from the Nizhnekansky granitoid massif (southern part of the Yenisei Mountain Ridge, Russia). They revealed porosity and permeability data between 1.05 % to 5.5 % and 1.35 mD to 5.47 mD ($1.35*10^{-15}$ m² to $5.47*10^{-15}$ m²), respectively.

9.4 Methods

9.4.1 Sampling and sample preparation

The sampling program, carried out for this study, was concentrated along an ENE-WSW major fault zone (Fig. 4.3). Oriented samples were taken from different rock suites along traverses that crosscut the fault. At least two samples of each rock type (khibinite, rischorrite, albitised foyaite, massive foyaite and alkaline syenite) were chosen for the study of microcracks and FIPs designed to constrain their distribution and orientation. To do so, vertical and horizontal thin sections were prepared (Fig. 9.1). For each section areas of about 1 cm² were analysed. The chosen areas represent the average rock composition in terms of modal mineral proportions. They therefore contain

a high proportion of nepheline and feldspar and only minor mafic minerals (see Chapter 4).

9.4.2 Acquisition of crack parameters

Crack analyses were performed at the University of Nancy, France. By using *ANALYSIS software*, coupled to a microscope, a mosaic consisting of up to nine images of an area of interest in the oriented thin section was recorded (Fig. 9.2a). A low magnification (x2 lens and an ocular of x10) was used to cover the largest possible area but still be able to distinguish between open cracks and FIPs and to record the entire crack lengths.

Each mosaic was then processed using the *AnIma program* (Desindes *et al.*, 2003; Lespinasse *et al.*, 2005). Here, orientation and length of FIPs and open cracks were obtained. The program enables the digitisation of microstructures to produce a map of the intersection between the planar features (e.g. cracks) and the thin section plane (Fig 9.2b). From these lines the two extremities were determined as relative XY coordinates, to automatically calculate length and azimuth. This data set, together with information of type of microstructure, can be instantaneously used in an *Excel file*. In addition, the average widths of the cracks were visually estimated. This procedure was applied to record FIPs and MCs in the representative multi mineral area for porosity and permeability estimations.

Crack orientation data were obtained by mapping three separate nepheline minerals per sample. This was done to avoid any errors resulting from cleavage planes in feldspars or mafic minerals that may overlay the true crack orientation or result in a second main orientation.

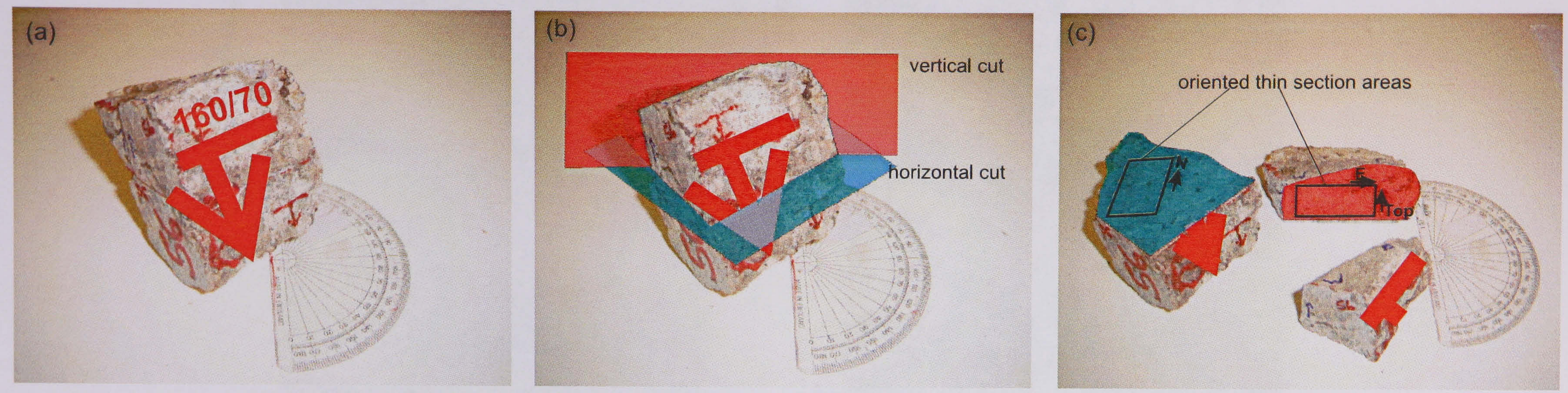

Figure 9.1: Sketch showing the preparation for horizontal and vertival oriented thin sections: (a) oriented hand specimen, (b) cutting planes in hand specimen, (c) marked and oriented thin section planes.

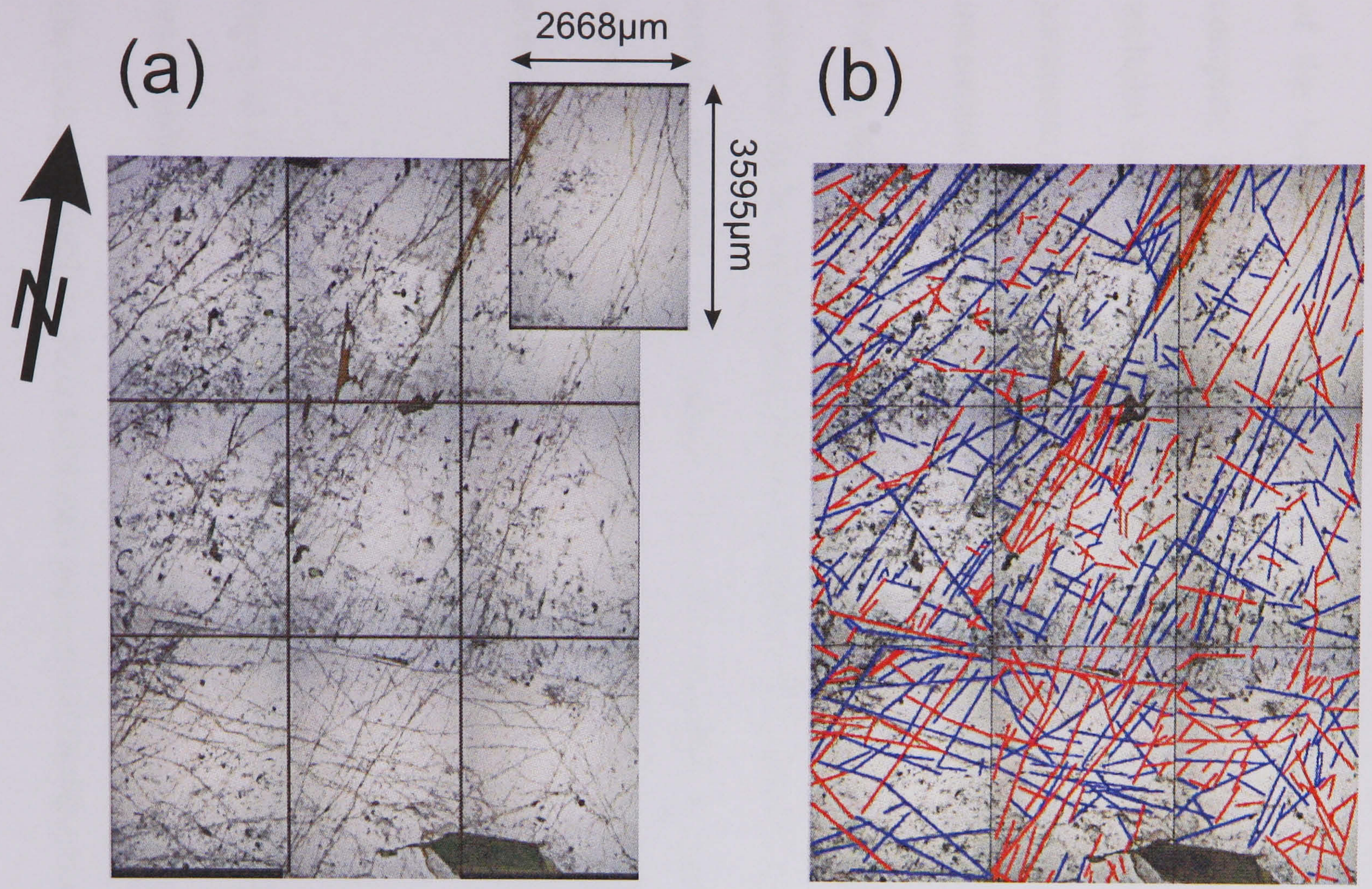

Figure 9.2: Micro structural mapping of a 1cm³ area of a thin section using *AnIma*. (a) shows the mosaic of nine images combined for crack mapping. (b) shows the mapped mosaic. Here, red lines indicate open microcracks and blue lines mark FIPs.

9.4.3 Quantification of porosity and permeability

Besides laboratory tests and drill-hole experiments, crack porosity and permeability can be calculated using geometrical or statistical methods. Here, a modified version of the statistical model developed by Gueguen and Dienes (1989) and used by Sausse *et al.* (2001) and Lespinasse *et al.* (2005) is employed to calculate porosity and permeability of the investigated rocks from the Khibiny pluton. The determination requires a complete description of the three dimensional crack geometry and network. This includes orientation, width, extension, crack density and interconnectivity data. These parameters must be seen as estimates, as they evolve with time during fluid-rock interaction (Sausse *et al.*, 2001).

For the statistical calculation the cracks are described as discs and their diameter is assumed to be represented by the length of the intersection of crack and thin section surface recorded with *AnIma*. It is also thought that all FIPs or microcracks are connected, justified by the high crack density. Based on these assumptions the crack porosity can be quantified through the relationship:

$$\Phi = \frac{L \times \pi \times e}{S}$$

Here, Φ is the porosity, L the cumulative length of the investigated crack family, e the mean width of the cracks and S the studied surface.

The rock permeability K_f is estimated using the following equation:

$$K_f = \frac{\varepsilon \times \pi \times N_f \times c^2 \times e^3}{12}$$

ε is the roughness of the crack planes and assumed to divide to permeability by 2, hence is 0.5 (Lespinasse *et al.*, 2005). The radius c is calculated as

$$c = \frac{\pi}{4Z_f} \quad \text{with} \quad Z_f = \frac{1}{N}\Sigma\frac{1}{L_f}$$

N_f is the volumic density and is calculated as

$$N_f = \frac{2N_{af}Z_f}{\pi \sin\phi}$$

with the surface density

$$N_{Af} = \frac{N}{S}$$

For a better understanding the calculation of modern porosity and permeability of sample Kh-03-1h (using data of MCs) is shown here. The following parameters are known:

- Surface S = 12.64 x 106 µm²,
- Cumulative crack length L = 0.12 x 106 µm,
- Number of cracks N = 191,
- Width e = 2 µm.

Using this data, the porosity Φ is calculated with:

$$\Phi = \frac{0.12\times10^6\,\mu m\times\pi\times2\mu m}{12.64\times10^6\,\mu m^2} = 0.06 = 6\%$$

The permeability K_f is calculated as follows:

$$Z_f = \frac{1}{191}\sum\frac{1}{0.12\times10^6\,\mu m} = 2.56\times10^{-3}\,\mu m^{-1}$$

$$C = \frac{\pi}{4\times2.56\times10^{-3}\,\mu m} = 306.8\mu m^{-1}$$

$$C^2 = 94.13\times10^3\mu m^{-2}$$

$$N_{af} = \frac{191}{12.64 \times 10^{6} \mu m^{2}} = 1.51 \times 10^{-5} \mu m^{-2}$$

$$N_{f} = \frac{2 \times 1.51 \times 10^{-5} \mu m^{-2} \times 2.56 \times 10^{-3} \mu m^{-1}}{\pi} = 2.46 \times 10^{-8} \mu m^{-3}$$

$$K_{f} = \frac{0.5 \mu m^{-1} \times \pi \times 2.46 \times 10^{-8} \mu m^{-3} \times 94.13 \times 10^{3} \mu m^{2} \times 8 \mu m^{3}}{12} = 0.002428 \mu m^{2} = 2.428 \times 1$$

K_f can also be expressed in Darcy, whereby 0.987 µm² correspond to 1 Darcy, and hence:

$$K_{f} = 2.428 \times 10^{-15} m^{2} = 2.452 mD$$

9.4.4 Determination of crack orientation

Data sets of corresponding horizontal and vertical thin sections were obtained in order to reveal the 3-dimensional crack orientation in terms of strike and dip. Rose diagrams were produced for each data set to determine the main crack orientation. The crack orientation derived from the vertical and horizontal sections were then plotted on a lower hemisphere stereo net to derive a true dip and strike value for the major crack sets (Fig. 9.3).This method is valid for data sets with only one dominant crack orientation per observed surface. Therefore, the most pronounced vertical and horizontal crack orientation per sample were combined to achieve the main crack direction.

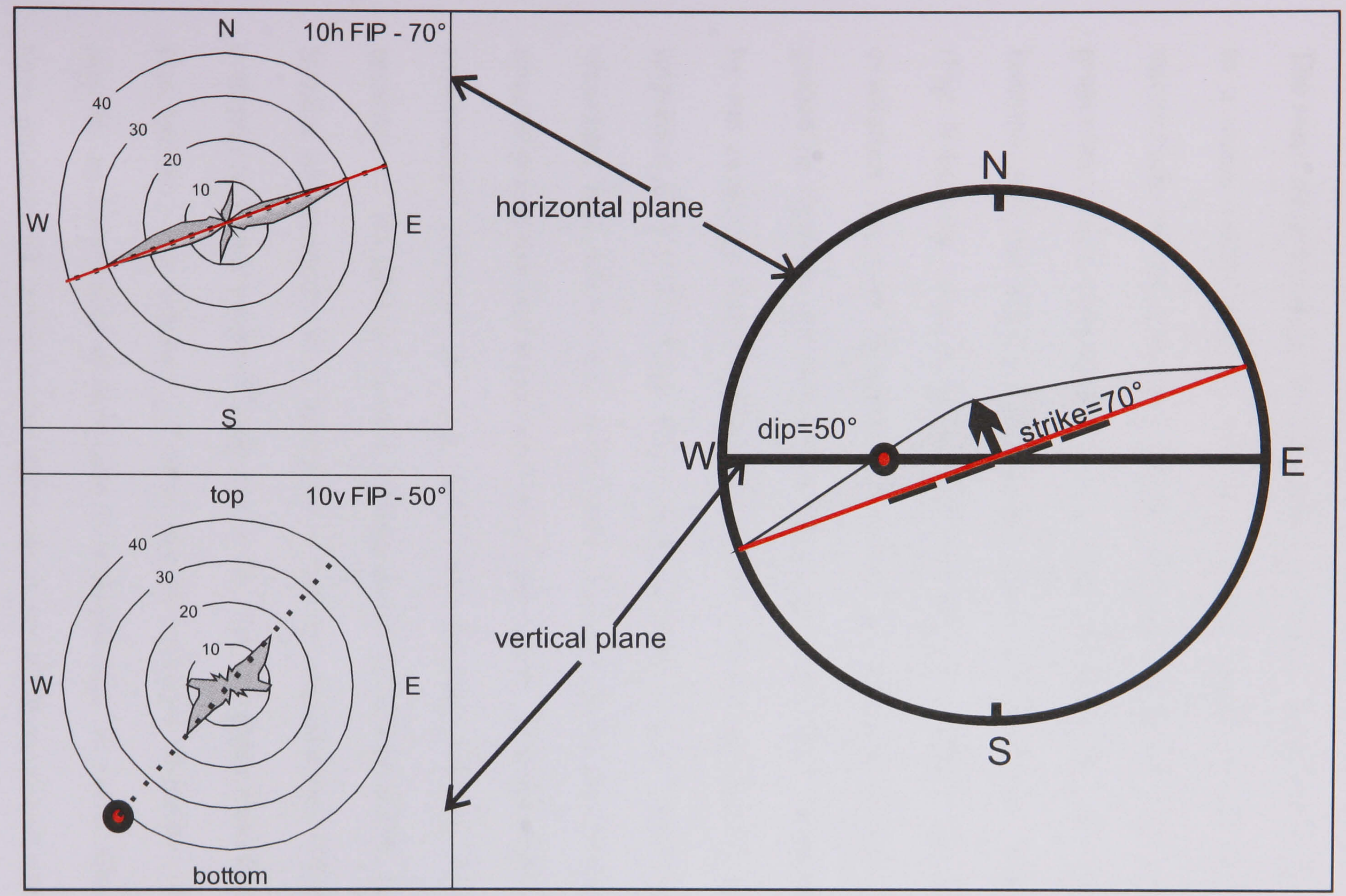

Figure 9.3: Lower hemisphere stereographic projection of cracks measured on a vertical and horizontal surface of the same sample (Kh-03-10). For the horizontal section (10h) 31 FIPs are mapped with a dominant orientation of 70°. The vertical section (10v) shows a westward pitch of 50°. These two main directions were then combined for a great circle projection as shown on the right. The resulting strike and dip of the FIP population are 070° and about 70°WNW, respectively.

9.5 Results and discussion

9.5.1 Characteristics of MCs and FIPs

The main minerals in rocks of the Khibiny pluton are nepheline and alkali feldspar and to a minor extent aegirine and arfvedsonite. These are the minerals in which the microcracks and fluid inclusion planes were investigated. Due to their different physical properties, crack characteristics vary with mineral type. Nepheline behaves as an isotropic material and its poor cleavage allows cracks to form readily in any direction (Fig. 9.4a). By contrast, alkali feldspar exhibits perthitic structures, developed by exsolution. Far more pronounced however are structural features in feldspar crystals guided by cleavage planes and microfractures (Fig. 9.4b). These structures are caused by ion exchange reaction between a Na-rich fluid and alkaline feldspar. During the migration of Na-rich fluids along cleavages and cracks Na-rich feldspar rims along cleavages and microcracks developed. The structures are mostly accompanied by mineral precipitation and fluid inclusion entrapment. This observation is consistent with experimental findings showing that K-rich feldspar converts to Na-feldspar in the presence of Na-rich solutions at temperatures of 250 to 400°C (e.g. Orville, 1963). Similar observations were described in Brown and Parsons (1994) and seem to be common in a wide range of fluid-rich rocks. The entrapped fluid inclusions are small in size, but are very abundant and often lead to a general cloudiness of the feldspars. This may be an overlooked contribution to rock porosity. In mafic minerals FIPs are rare. Very pronounced, however, are open cracks and cleavage planes that may serve as fluid pathways. A continuous transition of MCs or FIPs in nepheline into cleavage planes of arfvedsonite is often observed (Fig. 9.4c).

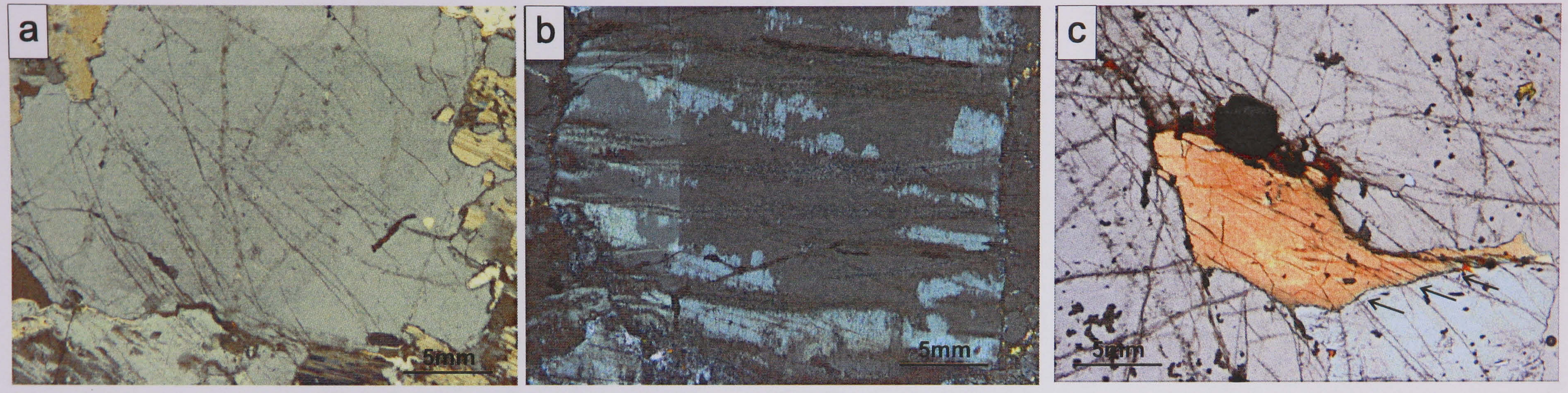

Figure 9.4: Photomicrographs showing typical crack occurrence. (a) shows randomly oriented FIPs in nepheline. Most FIPs are intragranular, only few cross-cut the mineral boundary. (b) illustrates how fluid inclusion planes developed in alkali feldspar. Migrating fluids lead to alteration along MCs and to precipitation of micro minerals and fluid inclusions. (c) shows an amphibole with cleavage planes surrounded by nepheline with randomly orientated FIPs and MCs. Note, FIPs lead into cleavage planes of amphiboles (arrows).

Both, MCs and FIPs show the same general types of outline: planar, curvi-planar or sinusoidal. The similarity is not surprising, as FIPs are interpreted to be former microcracks. Three main groups, similar for microcracks and FIPs, can be distinguished:

1. The most pronounced planes are intergranular cracks, that cross-cut several mineral grains with average widths between 2 µm and 5 µm. Some larger fractures, up to 20 µm width, filled by secondary minerals, were observed (Fig 9.5a).

2. The most abundant group of cracks are about 2 µm wide (Fig 9.4.a and 9.5b). They are often intragranular, propagating from grain boundaries and terminate within the mineral. Others are more dominant and cross-cut multiple grain boundaries. Both these groups can branch out into several planes.

3. Often small planes are observed that nucleate on existing fractures and propagate perpendicular to them (Fig 9.5c). They are mostly very small in width (c. 1 µm) and length (about 50 µm).

In rocks of the Khibiny pluton FIPs mostly consist of the same material as the surrounding minerals, which are mainly nepheline or feldspar. Only in large cracks, of about 100 to 2000 µm width, does the filling consists of materials other than that of the surrounding mineral. Often the filling is of calcite and natrolite. Therefore, for the majority of FIPs crack healing is the likely process of development whereas large cracks close by crack seal mechanism.

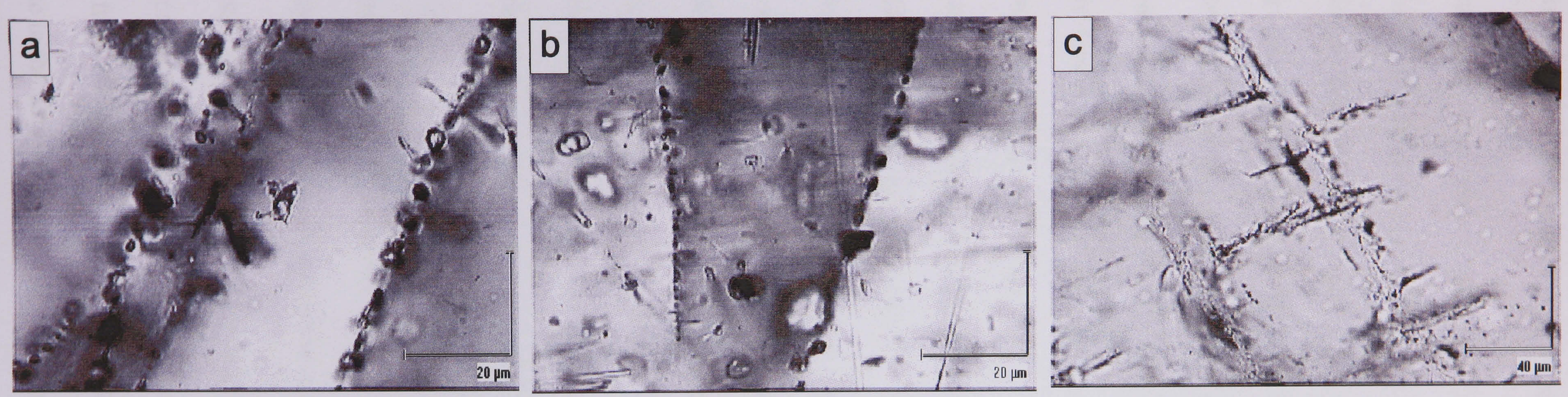

Figure 9.5: Photomicrographs of FIPs. (a) and (b) show the typical appearance of well developed inter- and intra-granular FIPs. (c) shows typical fractures, which propagate away from inter- and intra-granular fractures.

9.5.2 Porosity and permeability data and their implication

At a microscopic scale, microcracks and FIPs record porosity and permeability in plutonic rocks (Roedder, 1984; Lespinasse and Cathelineau, 1990) and hence, can be used to estimate the intensity of past and present fluid migration. The results presented here are based on the analysis of nearly 10,000 FIPs and MCs in 12 samples (Table 9.1). The porosity and permeability were calculated, based on the statistical model described above, separately for FIPs and microcracks. In this way it was possible to estimate fossil and modern fluid migration based on the assumption that sealed FIPs represent ancient fluid pathways and open cracks modern ones. The calculated average of palaeo porosity is 5.56 % and that of modern porosity is 4.80 %. The values vary from 1.65 % to 17.43 % and 1.14 % to 12.41 %, respectively. For the calculation of average porosity and permeability values, the data recorded for sample Kh-03-8 and Kh-03-56 were excluded, as they are exceptionally high. It is likely that superficial chemical and physical alteration increased the crack density. Both FIPs and MCs are heterogeneously distributed, with some rocks containing more FIPs than MCs and some less. That means that porosity and permeability of the rocks in the Khibiny pluton and hence fluid accumulation and migration rates changed in time and space (Fig. 9.6).

It is theoretically possible to estimate the gas content of a rock sample solely on porosity data. Combining palaeo and modern porosity values, the average gas volume in the Khibiny rock volume can be estimated as follows.

The rock volume of the Khibiny Mountains down to a depth of 10 km below surface equals approximately 10,000 km^3. Based on the average palaeo porosity of 5.56 % (obtained from FIP mapping, Tab. 9.1) a potential storage space for methane of 556 km^3 is available in the Khibiny pluton. However, only about 5 % of the FIPs are now filled

sample	FIP	N	sum 1/L	Kf (µm²)	Kf (mD)	Porosity (%)	MC	N	sum 1/L	Kf (µm²)	Kf (mD)	Porosity (%)
1h		180	0.37	0.0028	2.88	7.36		191	0.49	0.0024	2.45	6.04
1v		184	0.39	0.0028	2.86	6.52		152	0.37	0.0020	2.06	4.98
4h		192	0.73	0.0016	1.66	5.77		485	0.27	0.0028	2.83	9.47
5h		114	0.38	0.0011	1.13	4.02		51	0.20	0.0004	0.44	1.14
8h		*297*	*0.78*	*0.0037*	*3.72*	*8.78*		*551*	*1.98*	*0.0050*	*5.05*	*12.41*
8v		*327*	*0.86*	*0.0040*	*4.10*	*12.20*		*341*	*1.13*	*0.0033*	*3.39*	*9.09*
10h		235	0.51	0.0035	3.57	7.16		187	0.54	0.0021	2.13	5.06
10v		223	0.68	0.0024	2.41	5.47		142	0.50	0.0013	1.33	2.61
35h		277	0.85	0.0029	2.97	8.17		229	0.73	0.0023	2.37	5.47
35v		108	0.23	0.0016	1.67	3.79		248	0.66	0.0030	3.07	7.30
41h		256	0.97	0.0022	2.23	4.67		307	1.04	0.0029	2.98	7.05
41v		340	1.33	0.0028	2.86	5.96		139	0.51	0.0012	1.25	3.14
45h		209	1.41	0.0010	1.02	2.02		169	1.04	0.0009	0.90	2.23
45v		142	0.41	0.0016	1.62	3.25		159	0.43	0.0019	1.94	5.58
52h		259	0.61	0.0036	3.62	7.46		196	0.58	0.0022	2.18	4.72
52v		280	0.85	0.0030	3.04	6.86		132	0.42	0.0013	1.37	3.02
54h		55	0.11	0.0009	0.91	1.65		98	0.19	0.0016	1.66	3.70
56h		*291*	*0.65*	*0.0042*	*4.29*	*10.05*		*216*	*0.62*	*0.0024*	*2.48*	*5.27*
56v		*580*	*1.48*	*0.0074*	*7.49*	*17.43*		*157*	*0.44*	*0.0018*	*1.85*	*4.17*
60h		211	0.41	0.0035	3.58	8.89		233	0.78	0.0023	2.29	5.36
average with outlyer:					**2.88**	**6.87**					**2.20**	**5.39**
average without outlyer:					***2.38***	***5.56***					***1.95***	***4.80***

Table 9.1: Results of porosity and permeability calculations of FIPs and MCs. The grey-shaded values are "outliers" and are not included in volume calculations. It is assumed that they are high due to secondary alteration. Indices h and v denote horizontal and vertical oriented sections. N is the number of cracks per analysed area, L the crack length, Kf the permeability in µm² and mD. The porosity is given in %.

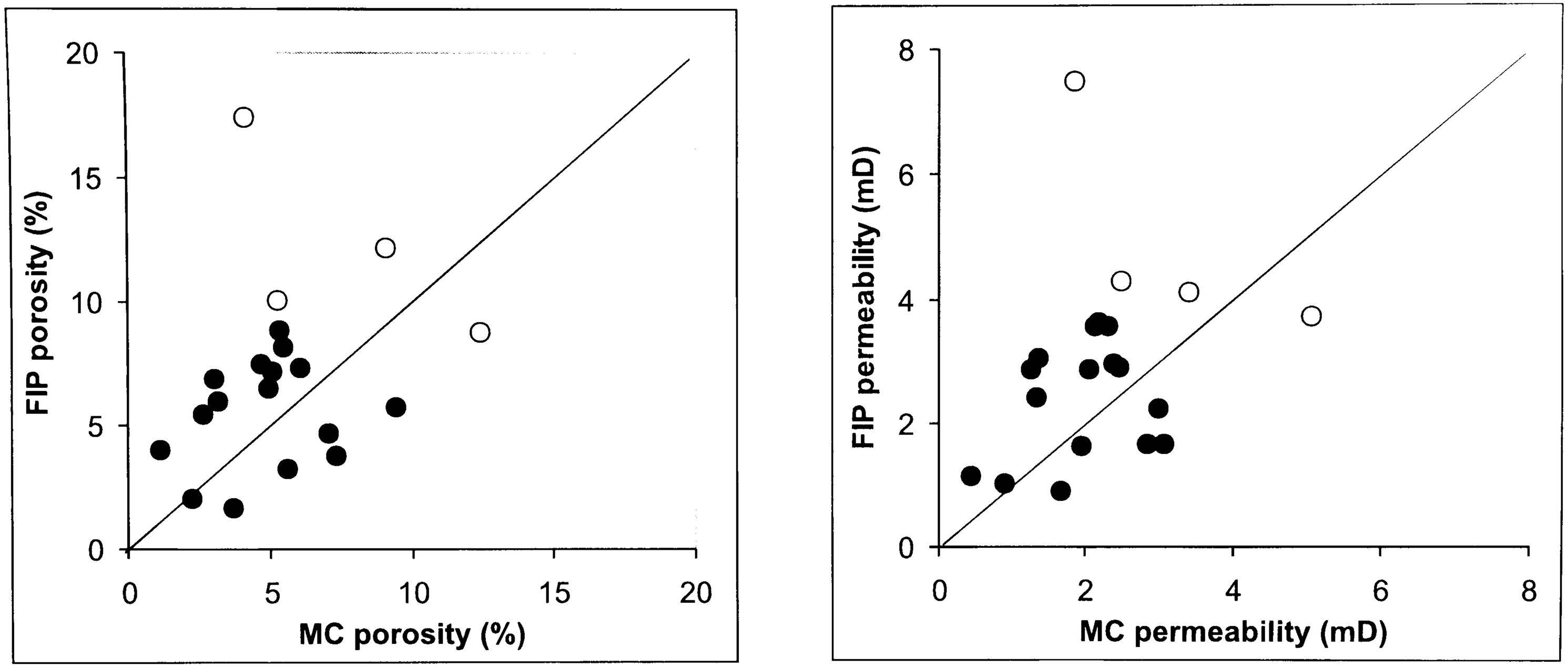

Figure 9.6: Comparison of palaeo and modern porosity and permeability represented by fluid inclusion planes and microcracks, respectively. The open circles indicate"outliers", not used for further calculations.

with fluid inclusions and the remaining 95% constitutes the crack filling cement. Therefore, the methane volume stored in FIPs is at most 27.8 km³ (=5 % of 556 km³). Fluid inclusion studies show that the methane, which is the predominant fluid trapped in the inclusions, has densities between 0.1 and 0.01 g/cm³. As the methane density under standard-temperature-pressure (STP) condition is 0.00067 g/cm³, opening of the inclusions would cause a considerable expansion of the methane gas volume. A discharge of all the gas stored in FIPs (estimated at 27.8 km³) would generate an equivalent gas volume of between 4150 and 415 km³ methane at STP conditions. In a one kg rock sample (with a density of 2.7 g/cm³, hence a volume of about 370 cm³) a potential pore volume of about 1 cm³ is available (Fig. 9.7). If that is filled with methane of a density between 0.1 and 0.01 g/cm³ a methane gas discharge between 154 and 15.4 cm³, respectively is expected from secondary fluid inclusions in FIPs. Additionally, free gas, stored in open cracks, contributes to methane gas discharge. Assuming STP conditions for the storage of this gas, a volume of 17.8 cm³ methane has to be added per kg rock. In the sum, the range of methane gas stored per kg rock is then between 15.4 cm³ (minimum value = all fluid inclusion with density of 0.01 g/cm³ and no additional free gas in microcracks) and 172 cm³ (maximum value = all fluid inclusion trapped with density of 0.1 g/cm³ and all microcracks filled with methane) per kg rock. That is broadly in agreement with the data of Petersilie (1962) who estimated the average methane content to be 28.5 cm³/kg rock. In conclusion, the Khibiny pluton, down to a depth of 10 km below surface stores a methane-dominant gas volume of between 416 km³ and 7649 km³ (illustrated in Fig. 9.7).

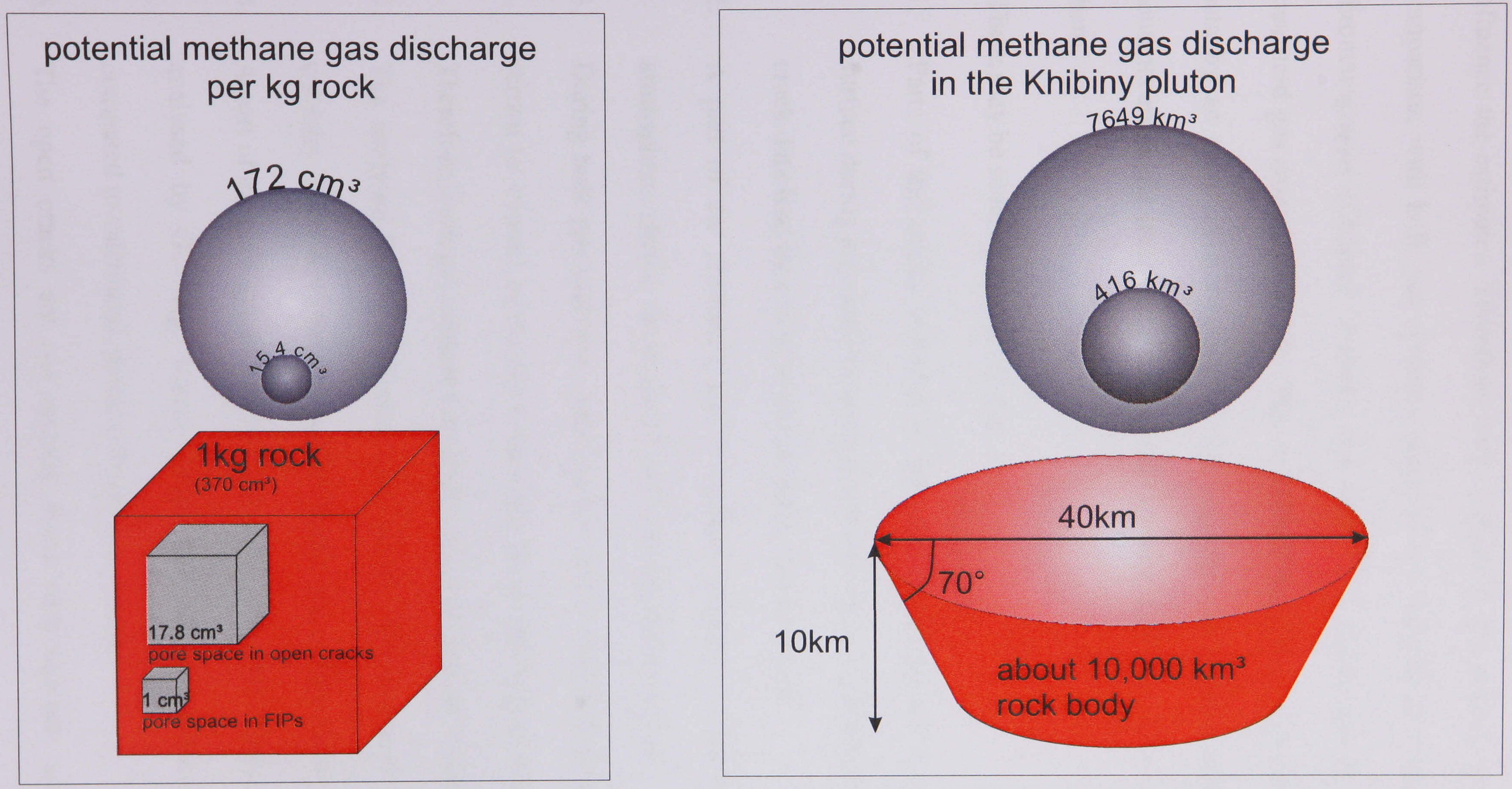

Figure 9.7: Schematic illustration of the amount of methane stored in the Khibiny pluton. (a) shows the potential pore space in fluid inclusion planes and microcracks in 1 kg rock and the resulting minimum and maximum methane gas discharge. (b) illustrates the theoretical minimum and maximum gas discharge possible from the Khibiny pluton down to 10 km. Pluton diameter and dip of margin angle taken from Arzamastsev et al. (2000).

Using porosity data the gas content of the individual samples can be estimated. Many parameters, such as fluid density in inclusions and the degree of filling of open cracks, influence the estimates. Therefore, only a range of gas content can be specified. The comparison with bulk gas contents obtained by conventional rock crushing and gas chromatography (Chapter 7) shows that calculated values tend to be higher than the measured gas content (Fig. 9.8). The calculated maximum values exceed the measured data by an order of a magnitude. Although the calculated minimum values of gas contents are in the same range as the bulk gas data there is no direct correlation between them.

There may be several reasons for this:

1. Parts of the cracks included in the porosity-calculation were developed at the surface during physical or chemical weathering. The porosity calculation based on crack data lead then to an overestimation of gas content.
2. A part of the contained gas in surface samples is already released into the atmosphere. Hence, the analysed bulk gas volume is too low.
3. During bulk gas analyses, some gas loss may occur during the pre-crush process (down to <1mm) especially from weak locations such as microcracks and FIPs. Therefore, bulk gas content may undervalues the real gas content.
4. The analysed bulk gas content can also be underestimated when the gases are coevally adsorbed to the fine particle dust in the crushing chamber.
5. A part of the pore space is taken up by fluids other than hydrocarbons which is not analysed by GC (e.g. water). Then, the bulk gas contents would be lower compared to calculated, porosity-based gas volume.
6. The open cracks are not entirely filled with methane gas. This lead to an overestimation of calculated gas volume.

7. The gas density is varies, which lead to both, over- and under-estimation of calculated gas volumes in the rock samples.

8. The degree of filling of the FIPs is lower than the assumed 5 %. In that case, calculated values exceed analysed bulk gas values.

Sample Kh-03-10 contains high volumes of methane although its calculated porosity is relatively low. The sample is also characterised by strong zeolite weathering and it is thus likely that gas is stored within the zeolite. It shows that not all gas has to be stored in the visible form of fluid inclusions but that the occurrence of zeolite minerals, as a fluid accumulator, increases the gas content in the rocks of the Khibiny pluton.

The calculated permeability values range between 0.91 mD and 4.29 mD for palaeo permeability (using FIP data) between 0.44 mD and 5.05 mD for modern permeability (using MC data). These values are consistent with the present-day gas release pattern (Nivin, 2001) that suggests high permeability enhanced by interconnected open cracks. The results are in agreement with values for crystalline rocks defined by Brace (1984) ranging between μD and D (Fig. 9.9).

Porosity and permeability data in all samples correlate positively (Fig. 9.10). This indicates that cracks represent both pore space and fluid pathway. Unlike sedimentary rocks, where intergranular pore spaces contribute largely to porosity but not necessarily to permeability, in igneous rocks, such as these of the Khibiny pluton, the predominant part of available pore spaces consists of cracks. Therefore, with increasing crack density permeability and porosity increase similarly.

sample	bulk gas content	minimum (cm³/kg)	maximum (cm³/kg)
1h	17.93	20.33	225.70
1v		18.03	198.72
4h	37.60	15.96	194.68
5h	11.63	11.11	115.30
10h	33.58	19.80	216.70
10v		15.12	160.88
35h	4.31	22.58	246.12
35v		10.48	131.81
41h	2.98	12.91	155.18
41v		16.48	176.44
45h	0.05	5.58	64.01
45v		8.99	110.62
52h	8.61	20.63	223.80
52v		18.95	200.73
54h	12.26	4.55	59.19
60h	0.02	24.56	265.49
mean	12.90	15.37	171.45

Table 9.2: Bulk gas data (cm³/kg) obtained by conventional online-crushing-GC at the Kola Science Centre in Apatity (Chapter 7) in comparison with data of gas volumes calculated on the basis of porosity data.

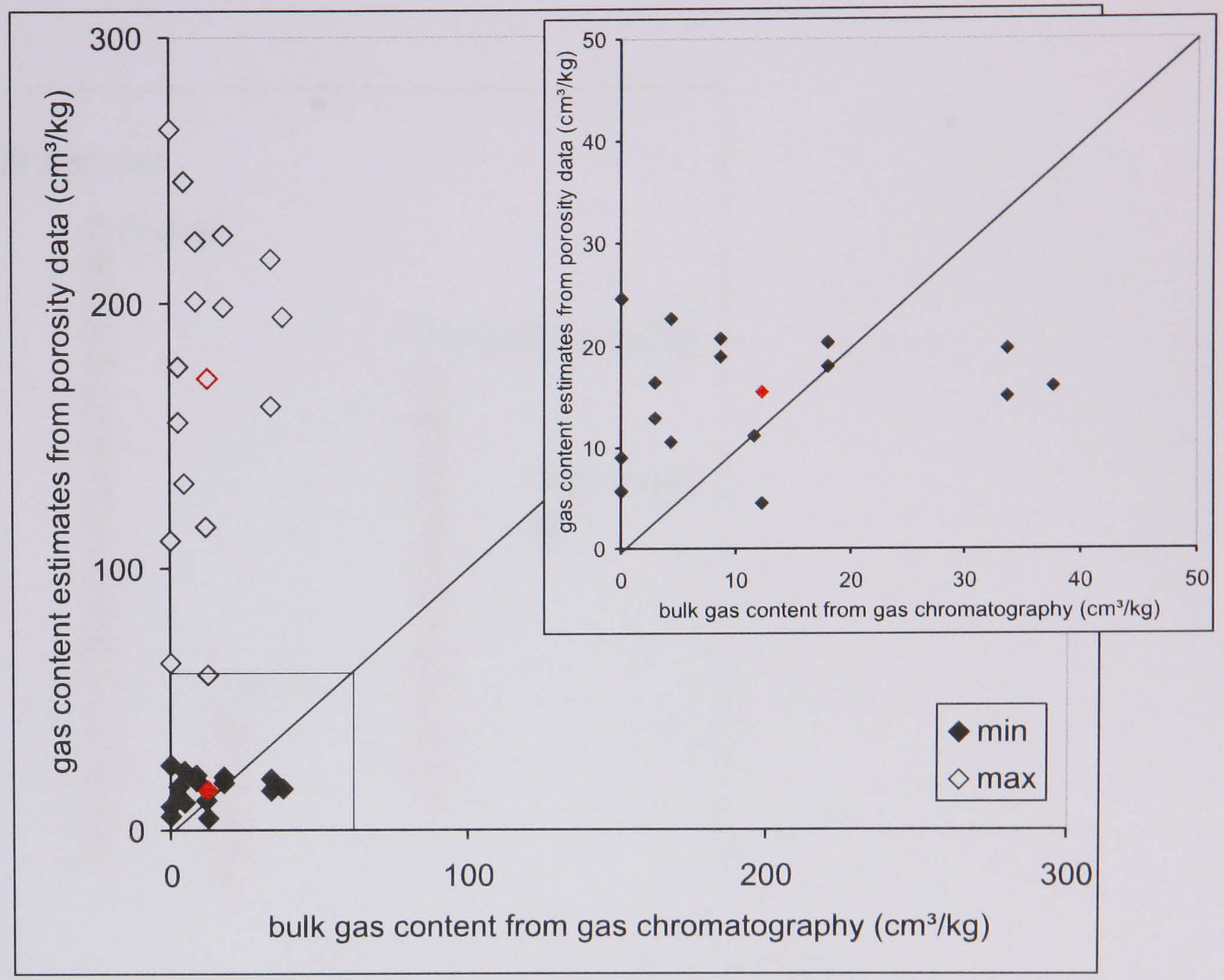

Figure 9.8: Plot of gas volumes calculated from porosity estimates versus data obtained by conventional rock crushing and gas chromatography. Open diamonds indicate the comparison between bulk gas data and calculated maximum values and closed diamonds mark the comparison of bulk gas volume and calculated minimum values. The red signs are the average values.
The small chart focuses on the comparison between bulk gas content and calculated minimum estimates, where both methods produce similar results.

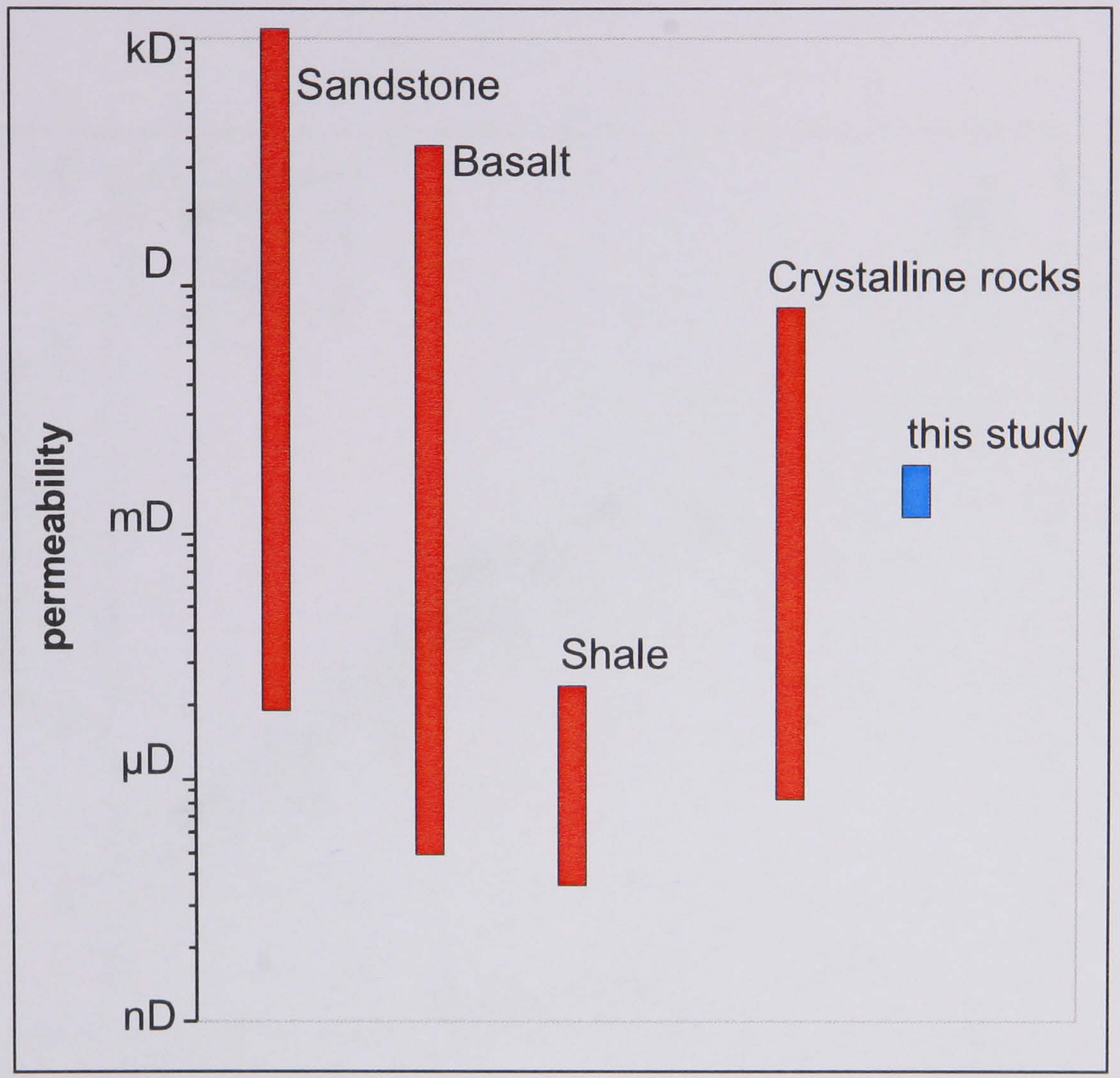

Figure 9.9: Plot of permeability data of different rock types (Brace, 1984) in comparison to data from this study.

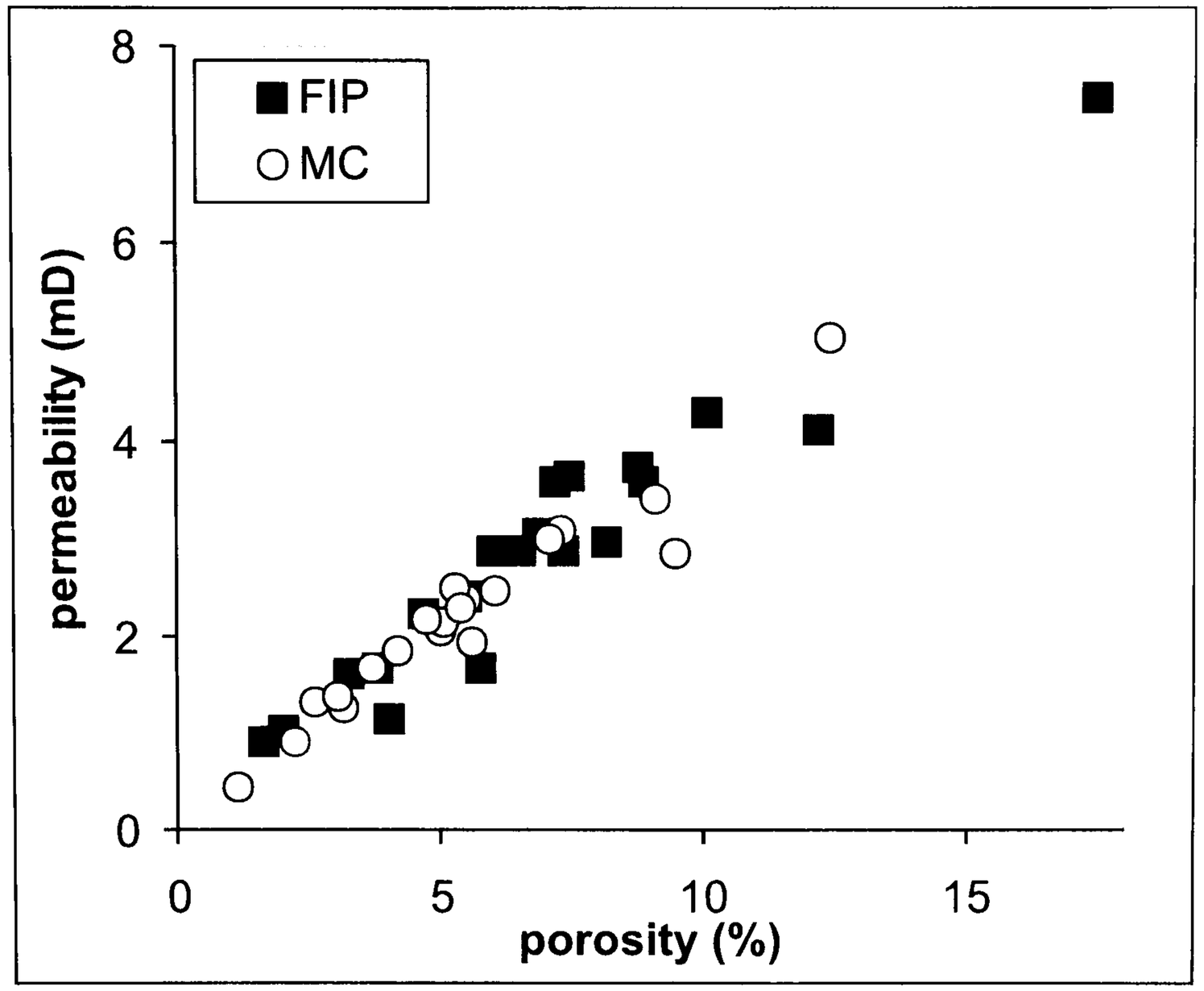

Figure 9.10: Plot of porosity data versus permeability. It shows a positive correlation as cracks provide both pore space and fluid migration pathways.

9.5.3 Differences with rock type

Physical rock properties depend on rock type. However, because of the relatively similar modal composition, grain size and weathering state, the Khibiny rocks investigated in this study are similar in terms of porosity and permeability (Fig 9.11). Highest permeability and porosity values were recorded from the outer khibinite rock sequence and from the innermost samples of alkaline syenite. The enhanced permeability and porosity is caused by high crack abundance. This is, in the case of the outermost rock suite of khibinite, assumed to be due to a strong temperature gradient between pluton and host rock during emplacement, which caused the development of cooling joints. The innermost alkaline syenite contains a high amount of feldspar, strongly affected by weathering which increases crack density. Figure 9.11 shows that porosity does not correlate with gas content, as already discussed above (Table 9.2 and Fig. 9.8). The gas content in the outermost khibinite samples is high, whereas it is low in the innermost alkaline syenites. A high porosity and permeability, which is in igneous rocks caused by high crack abundance, may support a high gas flux but is not necessarily indicative for storage of large amounts of fluids.

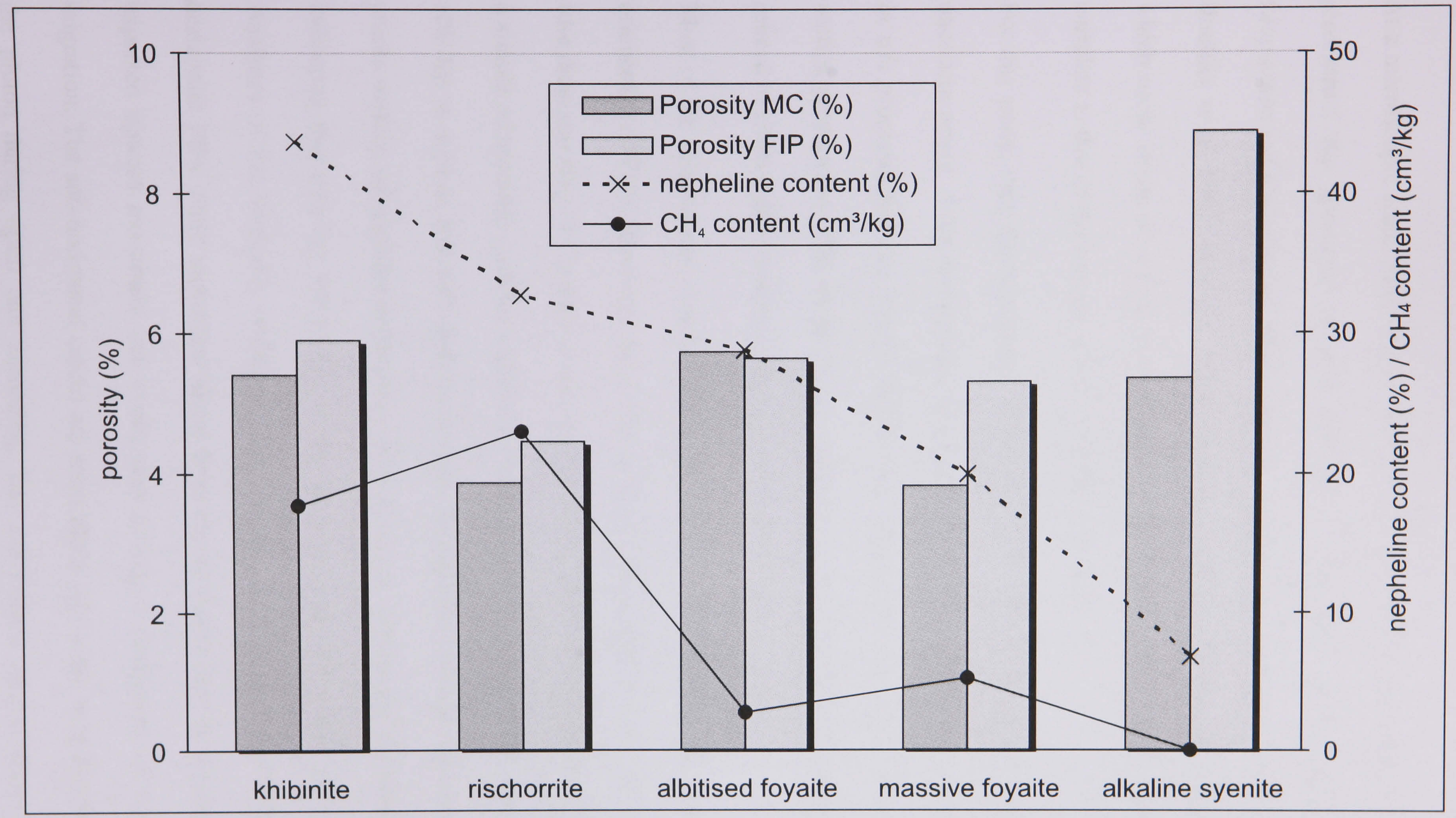

Figure 9.11: Plot of porosity versus rock type and gas content showing that rock type and nepheline content have no major influence on rock porosity.

9.5.4 Orientation of FIPs

At a microscopic scale, microcracks and FIPs can provide reliable structural markers to reconstruct the geometry of past and present-day stress fields (Roedder, 1984; Lespinasse and Cathelineau, 1990). Several authors (e.g. Lespinasse and Pecher, 1986; Boullier *et al*, 1997; Boullier, 1999) demonstrated that FIPs are mode I microcracks which occur in the $\sigma1$-$\sigma2$ plane (orthogonal to $\sigma3$) and therefore, their orientation may correlate to that of the stresses at the time of their creation.

For this study, only the orientation of FIPs was investigated, because of the somewhat uncertain origin of the microcracks. Microcracks are not unambiguously the product of *in situ* processes but can also be induced by superficial weathering, sampling or thin section preparation. FIPs, however, are certainly a product of an early cracking system, related to either a deformation event or to cooling joints.

Most of the investigated samples show a preferential orientation rather than a random orientation of FIPs. However, this seems to be very local phenomenon. As shown in the rose diagrams (Fig. 9.12) there is no uniform crack pattern throughout the complex or in a simple relationship (parallel alignment) to the major fault (Fig. 9.13). The FIPs strike NW-SE as well as SW-NE. Only four of the horizontally oriented thin sections show cracks striking sub-parallel to the major fault. However, the dip and dip directions differ indicating that they are not related to the tectonic event that caused the major fault. Analyses of the vertically orientated thin sections show both, sub-vertical and sub-horizontal FIPs. Fluid movement along these cracks might thus be dominated by the expected upward movement but would also include a component of sub-horizontal migration. The sub-horizontal cracks are most likely associated with decompression of the pluton during uplift and unroofing. The sub-vertical cracks relate probably to

cooling and contraction of the rocks. The influence of tectonic events could not be verified.

FIPs and microcracks have a generally similar range of orientations. This can be due to several reasons or a combination of them.

1. The microcracks developed at the same time as the FIPs but failed to seal and to contain fluid inclusions.
2. Modern stresses partly re-open old fracture systems (FIPs) and created "new" open microcracks.
3. A constant stress field caused the formation of microcracks with similar orientation as the early FIP-system at a later stage. This "later stage" comprises a regime of lower temperature and pressure which causes the inability to effectively close cracks.

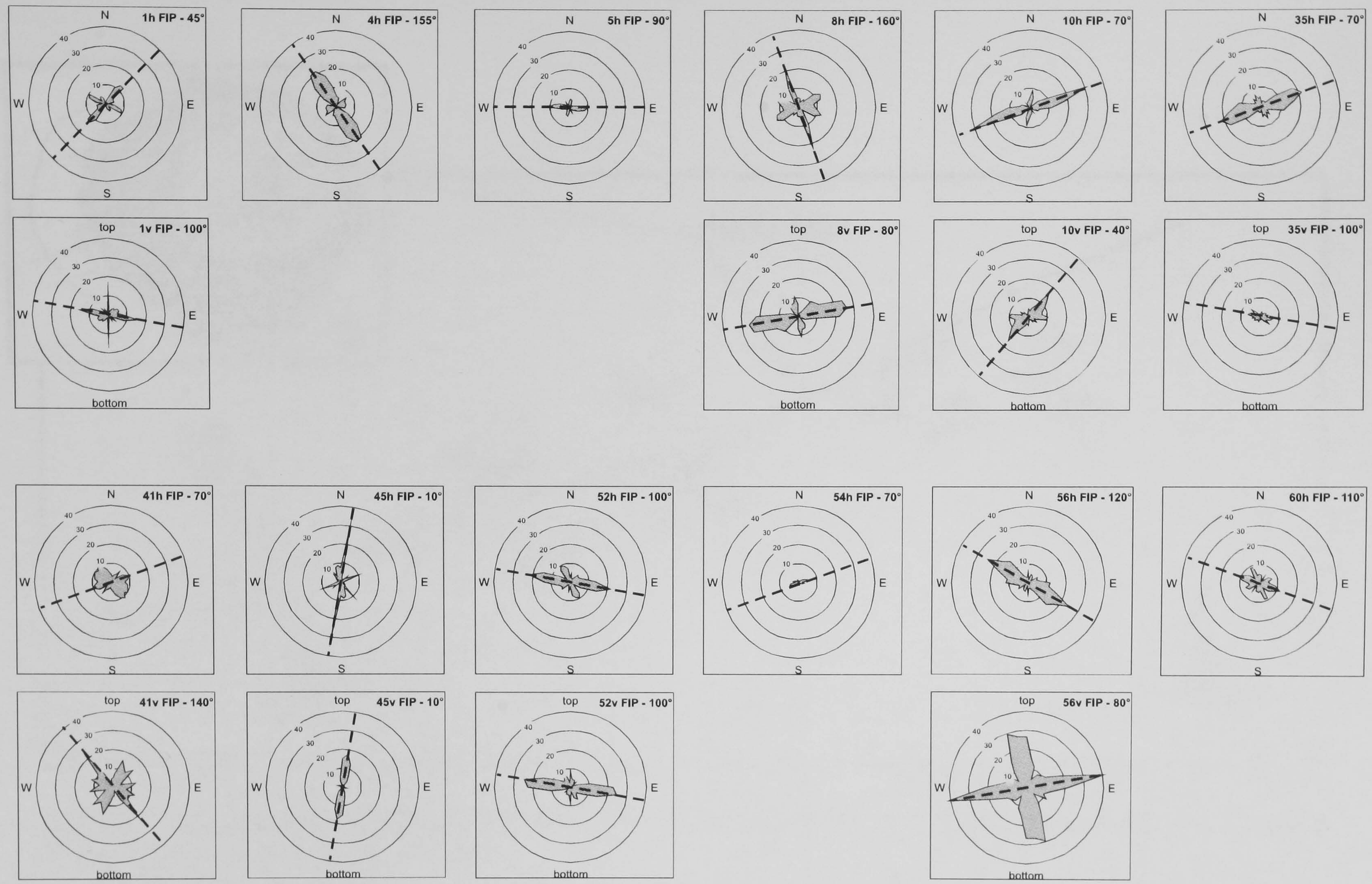

Figure 9.12: Plot of rose diagrams showing orientations of FIPs in horizontal and vertical samples (labelled with "h" and "v" respectively). Dashed lines mark the preferred orientation of the FIPs in a sample.

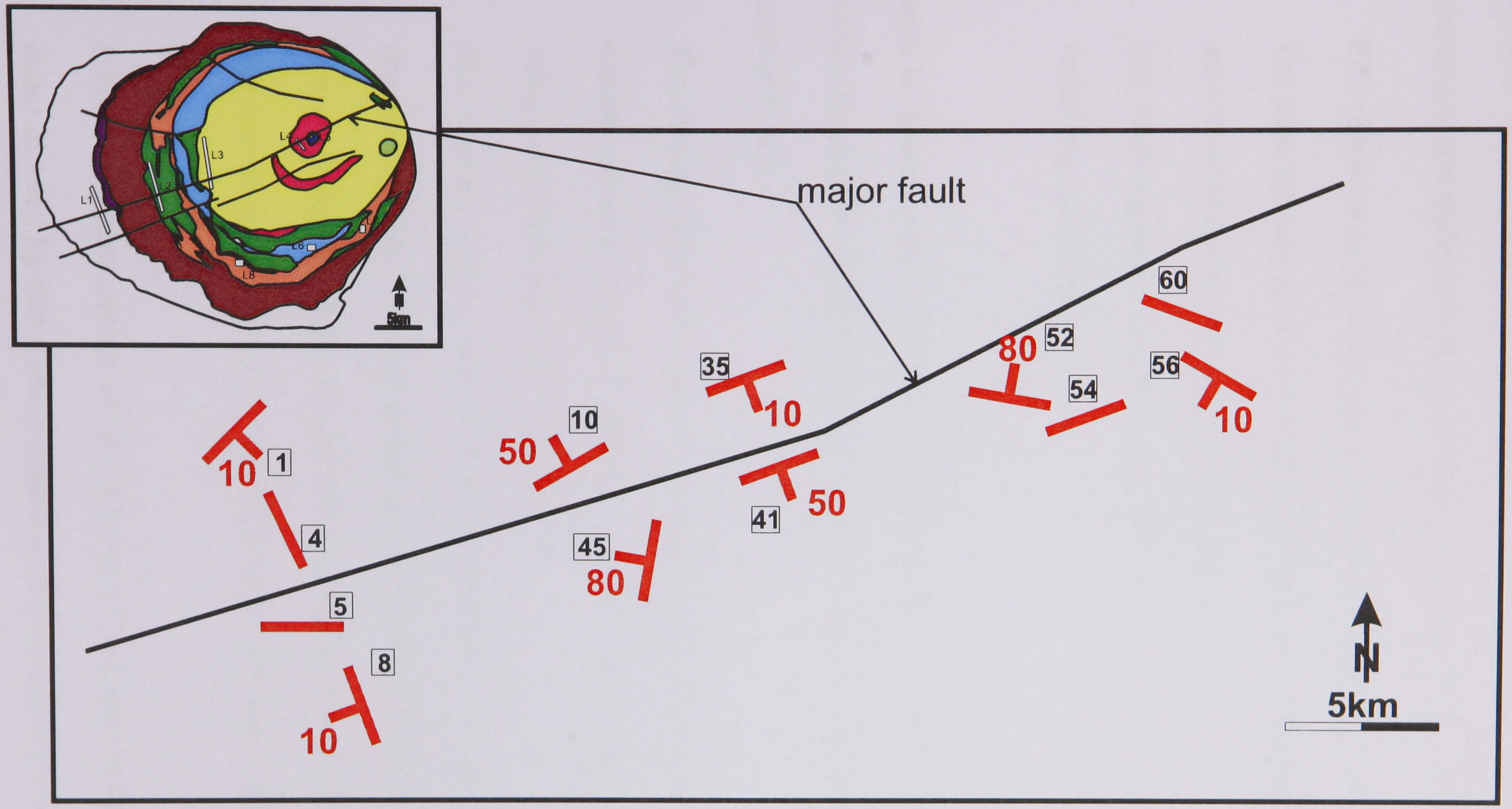

Figure 9.13: Schematic sketch of strike and dip of FIPs in the analysed samples (sample number in squares) related toh the major fault that cross-cut the complex.

9.6 Conclusions

The study of microcrack (MC) and fluid inclusion plane (FIP) characteristics and occurrence in the Khibiny pluton provides information on their distribution.

- FIPs represent palaeo fluid pathways and MCs modern ones.
- The high abundance of both MCs and FIPs indicate a high past and present fluid movement due to largely interconnected cracks.
- The inhomogeneous distribution of MCs and FIPs shows a spatial and temporal variability in fluid flow.

Cracks in igneous rocks serve both, main fluid pathway and storage space. They can therefore be used to calculate porosity and permeability employing a relatively simple statistical model.

- The average palaeo rock porosity, based on FIP observations, is 5.56 % and the modern porosity, based on MC abundance, is on average 4.80 %. The porosity values range between 1.14 % and 17.43 %.
- The average palaeo and modern permeability is 2.38 mD and 1.95 mD, respectively. The data range between 0.44 mD and 7.49 mD.
- Porosity and permeability are positively correlated to each other. This is due to the fact that cracks in igneous rocks serve both accumulation space and the migration pathway.
- Porosity and permeability are independent of rock type in the Khibiny pluton but rather dictated by stress and weathering. The marginal khibinite is slightly more porous. This might be due to the fact that a stronger temperature gradient at the

margin caused a higher density of cooling cracks. The high porosity in the core-near alkaline syenites is related to alkali feldspar alteration.

The calculated porosity values were used to estimate the methane content within the Khibiny pluton.

- The average fluid density in the fluid inclusions was assumed to be in the range from 0.1 to 0.01 g/cm³. For free gas, atmospheric density was assumed. Additionally a fluid inclusion abundance of 5 % in FIPs was assumed. The volume of methane was then calculated to range between 15.4 cm³ and 172 cm³ per kg rock. This is broadly in agreement with the average methane content of 28.5 cm³ per kg rock stated in an early publication by Petersilie (1962).
- The direct comparison of methane content, determined by the above described method versus methane content obtained by bulk gas analyses shows some differences. Mostly, porosity-based estimates are higher than the analysed bulk gas content. This is either due to an overestimation of the porosity-based calculation or due to low yield during bulk gas analyses.
- High porosity and permeability does not correlate directly to high gas content in the Khibiny pluton. This is especially apparent in the alkaline syenites where lowest gas content has been found despite high porosity.

The crack orientations were investigated in three isotropic nepheline minerals per sample to assure that no cleavage planes or other mineral structures alter the results.

- The orientation of MCs and FIPs is similar indicating either the same crack origin or a repetitive opening and closing of cracks. It may also be a sign for a stable stress field throughout time.

- The orientation of FIPs throughout the complex appears to be random. No preferred orientation in relation to the nearby major fault was observed. Therefore, it is likely that microcracks are mainly the result of cooling, uplifting and unroofing of the pluton.

10 A reassessment of models for hydrocarbon generation in the Khibiny nepheline syenite complex, Kola Peninsula, Russia

B. Beeskow, P.J. Treloar, A.H. Rankin, T.W. Vennemann and J. Spangenberg

This chapter focuses on an evaluation of the proposed mechanisms of hydrocarbon generation in alkaline rocks. The work was initially presented at the PERALK workshop 2005 in Tübingen and was published in a special issue of Lithos (Vol. 91, Issue1-4, page 1-18, Peralkaline Rocks - A special issue dedicated to Henning Sørensen).

T.W. Vennemann and J. Spangenberg provided valuable assistance during laboratory isotope analysis at Lausanne. They introduced the author to methods and techniques of stable carbon and hydrogen isotope analysis and data interpretation. The questions addressed during that laboratory analysis had been identified during earlier discussion with P.J. Treloar and A.H. Rankin; the latter's main contribution to the paper was in discussing and interpreting fluid inclusion data. Most of the ideas presented were refined during discussion with P.J. Treloar. B. Beeskow and P.J. Treloar wrote the paper.

This paper was published in the same issue of Lithos as one by Ryabchikov & Kogarko (2006), which also deals with the evolution of CH_4 in the Khibiny paper. They propose a further refinement on the Fischer-Tropsch reaction in which the H_2 that reacted with CO_2 to form CH_4 was not produced by dehydration reactions as suggested by Potter *et*

al. (2004). Instead, it was a primary component originally dissolved in the melt that reacted with CO_2 as it exsolved from the crystallising melt. This paper was published too late for a detailed critique to be included in this thesis. However, the evidence for a magmatic CH_4 origin provided here by melt inclusion observations remains persuasive.

Available online at www.sciencedirect.com
ScienceDirect
Lithos 91 (2006) 1–18
LITHOS
www.elsevier.com/locate/lithos

A reassessment of models for hydrocarbon generation in the Khibiny nepheline syenite complex, Kola Peninsula, Russia

B. Beeskow [a,*], P.J. Treloar [a], A.H. Rankin [a], T.W. Vennemann [b], J. Spangenberg [b]

[a] *Centre for Earth and Environmental Science Research, School of Earth Sciences and Geography, Kingston University, Penrhyn Road, Kingston upon Thames, Surrey KT1 2EE, UK*
[b] *Institute of Mineralogy and Geochemistry, University of Lausanne, BFSH-2, CH-1015, Lausanne, Switzerland*

Received 26 July 2005; accepted 13 March 2006
Available online 30 May 2006

Abstract

Although hydrocarbon-bearing fluids have been known from the alkaline igneous rocks of the Khibiny intrusion for many years, their origin remains enigmatic. A recently proposed model of post-magmatic hydrocarbon (HC) generation through Fischer-Tropsch (FT) type reactions suggests the hydration of Fe-bearing phases and release of H_2 which reacts with magmatically derived CO_2 to form CH_4 and higher HCs. However, new petrographic, microthermometric, laser Raman, bulk gas and isotope data are presented and discussed in the context of previously published work in order to reassess models of HC generation. The gas phase is dominated by CH_4 with only minor proportions of higher hydrocarbons. No remnants of the proposed primary CO_2-rich fluid are found in the complex. The majority of the fluid inclusions are of secondary nature and trapped in healed microfractures. This indicates a high fluid flux after magma crystallisation. Entrapment conditions for fluid inclusions are 450–550 °C at 2.8–4.5 kbar. These temperatures are too high for hydrocarbon gas generation through the FT reaction. Chemical analyses of rims of Fe-rich phases suggest that they are not the result of alteration but instead represent changes in magma composition during crystallisation. Furthermore, there is no clear relationship between the presence of Fe-rich minerals and the abundance of fluid inclusion planes (FIPs) as reported elsewhere. $\delta^{13}C$ values for methane range from −22.4‰ to −5.4‰, confirming a largely abiogenic origin for the gas. The presence of primary CH_4-dominated fluid inclusions and melt inclusions, which contain a methane-rich gas phase, indicates a magmatic origin of the HCs. An increase in methane content, together with a decrease in $\delta^{13}C$ isotope values towards the intrusion margin suggests that magmatically derived abiogenic hydrocarbons may have mixed with biogenic hydrocarbons derived from the surrounding country rocks.

Keywords: Hydrocarbons; Fischer-Tropsch synthesis; Alkaline igneous complex; Abiogenic; Khibiny

1. Introduction

The discovery of significant volumes (about 28.5 cm^3/kg) of hydrocarbon (HC) gas in the Khibiny alkaline complex in the late 1950s (Petersilie, 1960; Petersilie et al., 1961; Petersilie, 1962; Petersilie and Sørensen, 1970) generated much interest in the possibility of natural gas resources being stored in igneous rocks. As magmatic fluids are commonly CO_2- and H_2O-rich, the reduced composition of the gas phase led to a plethora of models for their origin or genesis (see review of Potter and Konnerup-Madsen, 2003). In principle, hydrocarbon gases in igneous rocks can have

* Corresponding author.
E-mail address: B.Beeskow@kingston.ac.uk (B. Beeskow).

0024-4937/$ - see front matter © 2006 Elsevier B.V. All rights reserved.
doi:10.1016/j.lithos.2006.03.006

either a biogenic or an abiogenic origin. Biogenic hydrocarbons in alkaline and other igneous rocks may simply be derived from an organic source in the surrounding country rocks (Whiticar, 1999). The organic matter would be thermally metamorphosed during pluton emplacement and incorporated as thermogenic methane into the magma system. Alternatively, it could have been flushed into the pluton by convective flow of meteoric fluids at a late stage of magmatism (Schutter, 2003), or even later. Three main hypotheses have been proposed to account for the formation of abiogenic hydrocarbons:

(1) Methane and higher hydrocarbons present in the mantle could be incorporated into magmas during mantle melting (Petersilie et al., 1961; Gold, 1979; Sugisaki and Mimura, 1994). These hydrocarbons may have been preserved in the mantle since the early accretion of the Earth or may have formed by reduction of CO and CO_2 under mantle conditions.
(2) Hydrocarbons in igneous rocks could be the result of late magmatic respeciation of a primary CO_2–H_2O-bearing fluid (Konnerup-Madsen et al., 1985).
(3) Post-magmatic mineral-fluid reactions involving the Fischer-Tropsch (FT) synthesis can cause the production of methane and higher hydrocarbons through reduction of magmatic CO_2 during reaction with H_2 produced by hydration of Fe-rich phases at 350 to 400 °C and 0.5 to 2 kbar pressure (Salvi and Williams-Jones, 1997; Potter et al., 2004). FT reactions have also been cited as driving mechanism for hydrocarbon generation at mid ocean ridges where H_2 production results from serpentinisation (e.g. Charlou et al., 1998).

A number of recent papers have highlighted the role of the FT reaction in generating methane and higher hydrocarbons in alkaline igneous rocks (e.g. Salvi and Williams-Jones, 1997; Potter et al., 2004). This model is an elegant one and explains many features of the rock-fluid system in alkaline igneous rocks. However, a number of ambiguities remains that need to be resolved. In this paper, fluid inclusion, petrographic and gas composition data from different rock types of the Khibiny intrusion are presented along with previously published data (e.g. Petersilie, 1962; Galimov, 1973; Voitov, 1992; Potter, 2000; Potter and Konnerup-Madsen, 2003). We highlight data which suggest that the FT reaction may not be as important as previously suggested and reassess existing models in the context of our new data. Earlier studies on the Khibiny pluton (e.g. Galimov, 1973; Voitov, 1992; Nivin et al., 2005) tended to concentrate on atypical parts of the complex, including the apatite ores and pegmatites of the Central Arch region and the carbonatite body in the eastern part of the complex. Here we concentrate on common rock types that make up most of the Khibiny complex.

2. Geology and occurrence of hydrocarbons at Khibiny

The Khibiny pluton was emplaced during the Devonian (Kramm and Sindern, 2004) synchronously with subsidence of the NE–SW trending Khibiny-Kontozero-Graben. It is the largest agpaitic, nepheline syenite body in the Kola Alkaline Province with an exposed area of about 1330 km^2. It has a ring-shaped structure (Fig. 1) that comprises several phases of emplacement (Kogarko, 1995) and is divided into two, approximately equal, parts by a ring like structure known as the Central Arch. In general, Khibiny consists of a variety of nepheline syenites (khibinite, rischorrite, lujavrite and foyaite), foidolites (ijolite and urtite) and minor alkali syenite plus a small carbonatite stock. Their unusual names are mostly historical and related to arbitrary textural criteria and moderate chemical variations. Khibiny is famous for hosting the World's largest apatite deposits, which are apatite-nepheline-ores concentrated around the central ring and also famous for its diverse minor and accessory minerals, which include eudialyte, titanite and astrophyllite (Yakovenchuk et al., 1999).

Hydrocarbons are present in Khibiny as bitumen, as free gases and as occluded gases in fluid inclusions (Nivin et al., 2005 and references therein). The presence of bitumen in pore spaces and mineral inclusions within nepheline was first reported by Petersilie (1962). Sokolov and Chukanov (in press) describe solid organic substances as a common component of the peralkaline rocks and related pegmatites in Khibiny. The occurrence of free gas leads to continued seepage of methane into mine workings (Nivin et al., 2001). It is trapped in sealed fracture systems and can be released spontaneously by erosion or drilling. Nivin (2002) recorded gas discharge rates of up to 5 l/min from single 2 m long and 40 mm diameter shot-holes.

Most studies of hydrocarbons in the Khibiny pluton have been carried out on fluid inclusions as they present the best-preserved data source. They are mainly trapped as secondary inclusions along healed microcracks and are consistently described as being methane-dominated (e.g. Kogarko et al., 1987; Potter and Konnerup-Madsen, 2003). A more detailed description of these inclusions is given below.

3. Methods

For this study, 60 samples of different rock types from surface outcrops throughout the pluton were collected and located by GPS. In earlier studies (e.g. Potter et al., 1998) archived material was used of which the exact sampling locations were unknown.

Polished thin sections were prepared for petrological and microprobe analysis. Major element compositions were determined using Oxford Instruments ISIS EDS

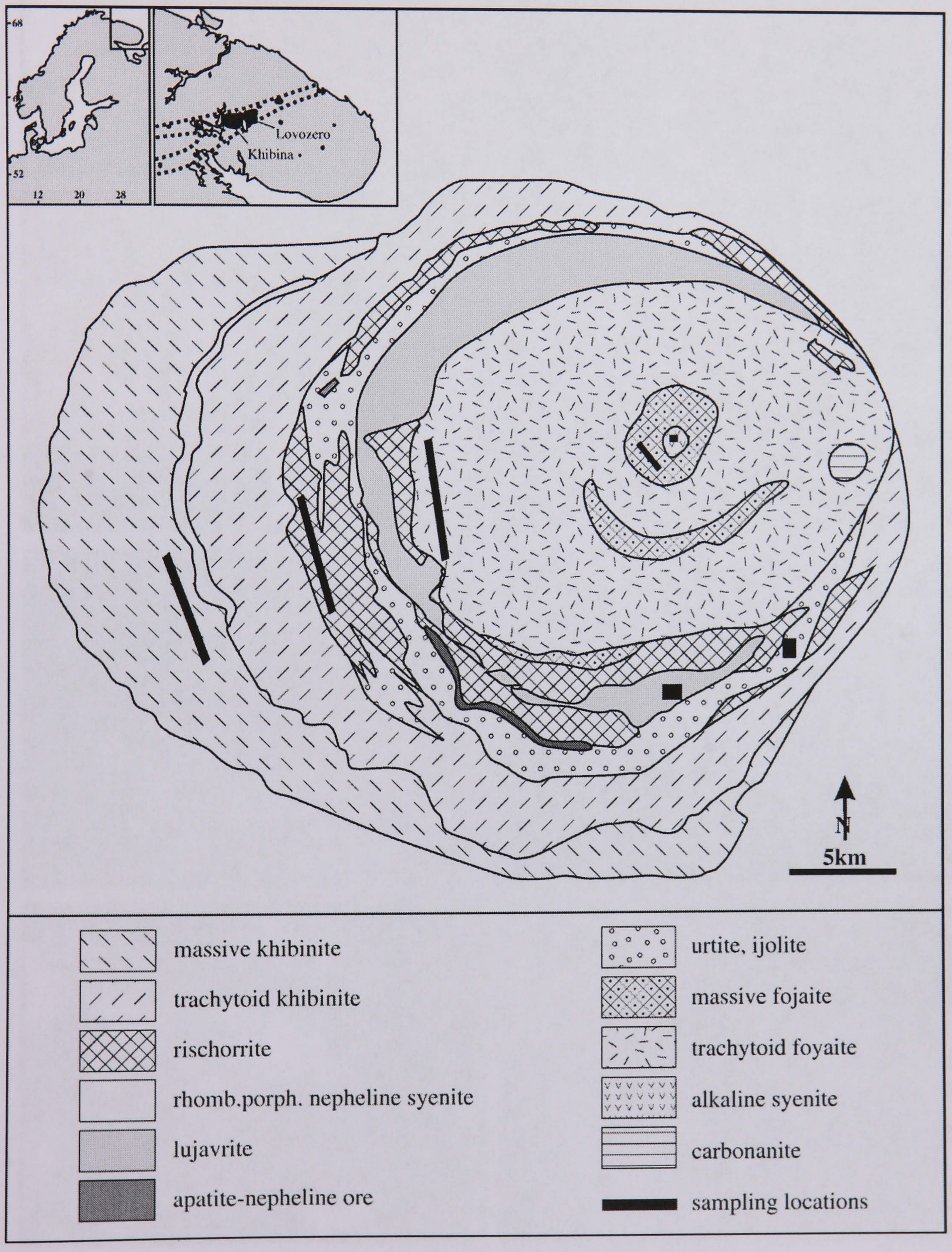

Fig. 1. Simplified geological map of the Khibiny pluton. Samples described here were mostly collected along traverses (bold black lines) or at separate sampling locations (black squares).

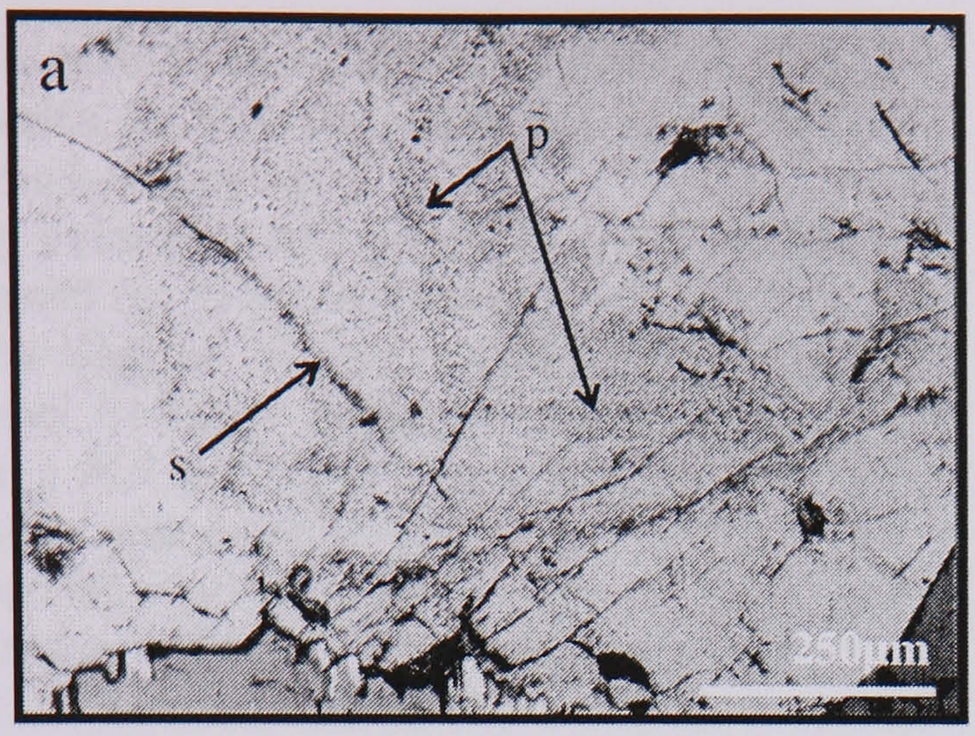
a
p
s
250 µm

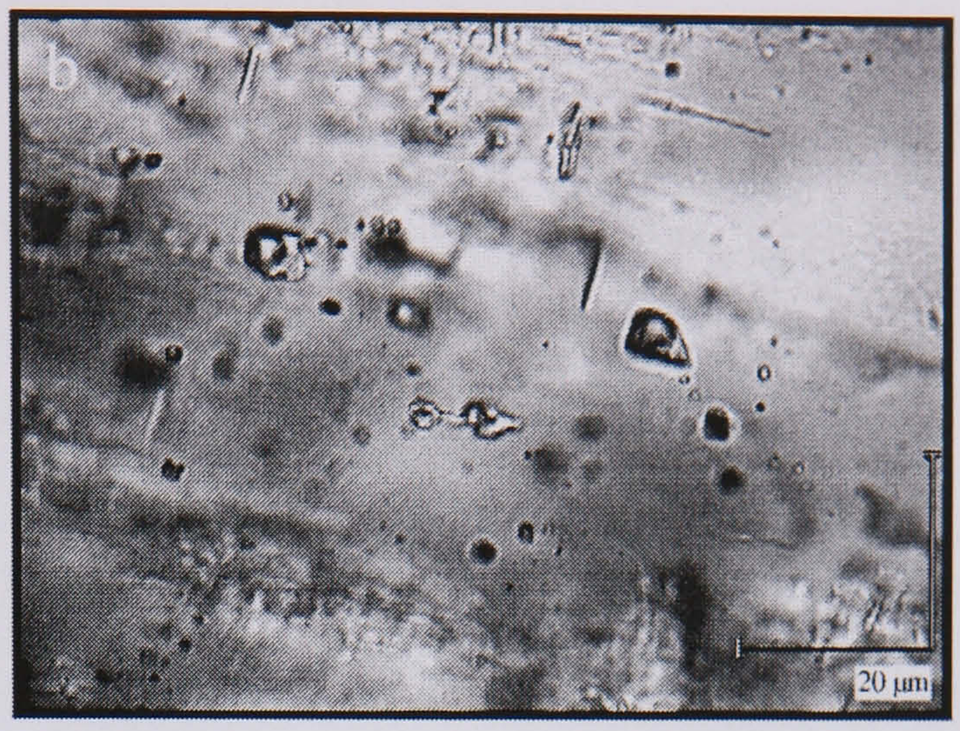
b
20 µm

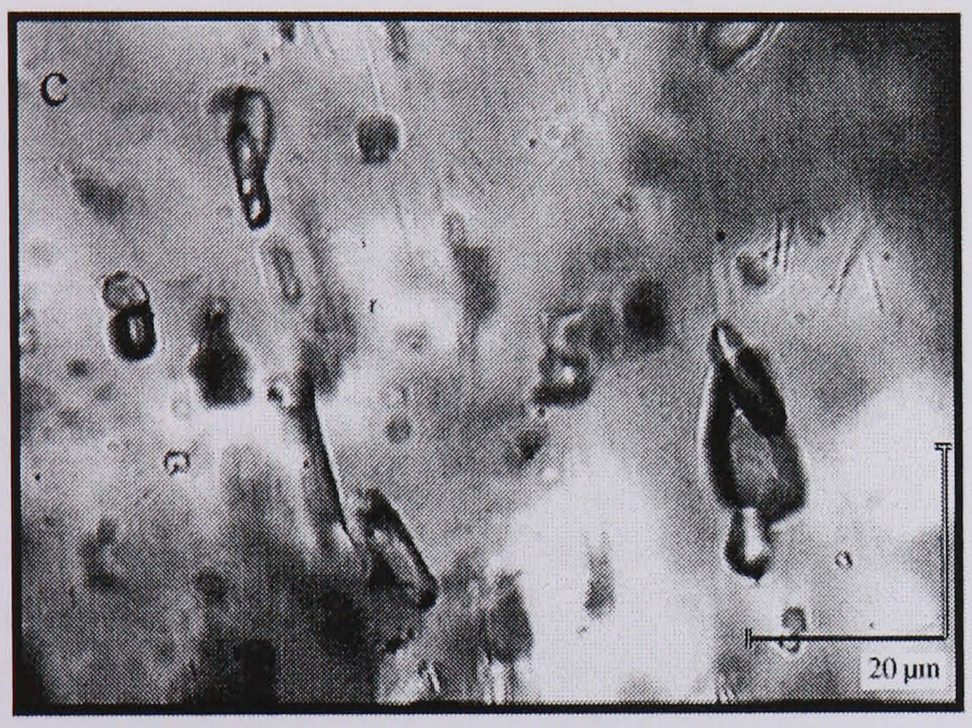
c
20 µm

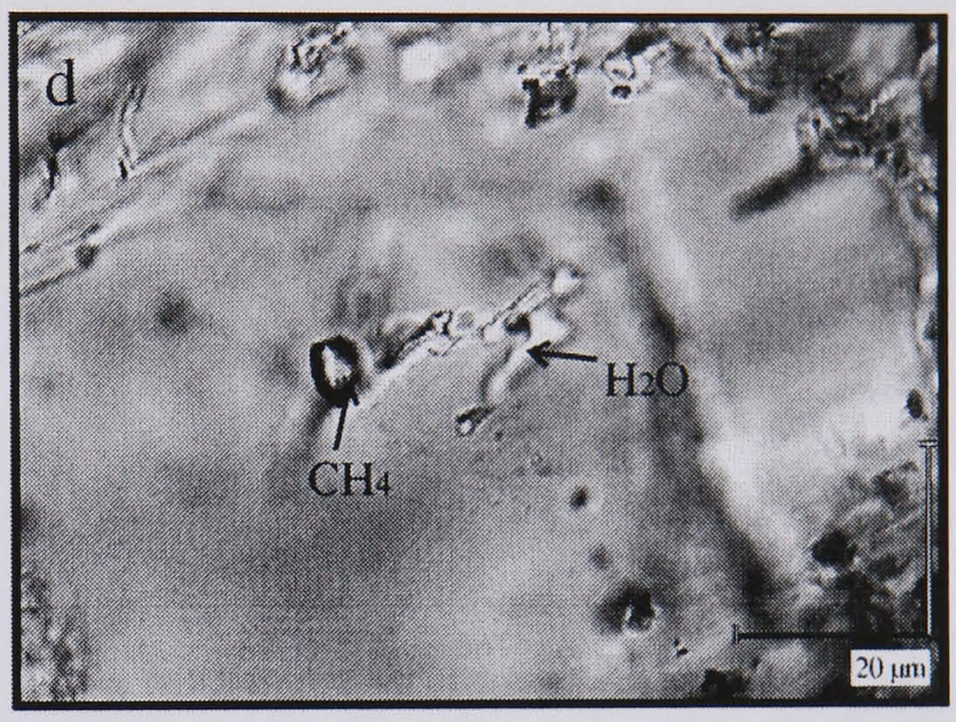
d
H2O
CH4
20 µm

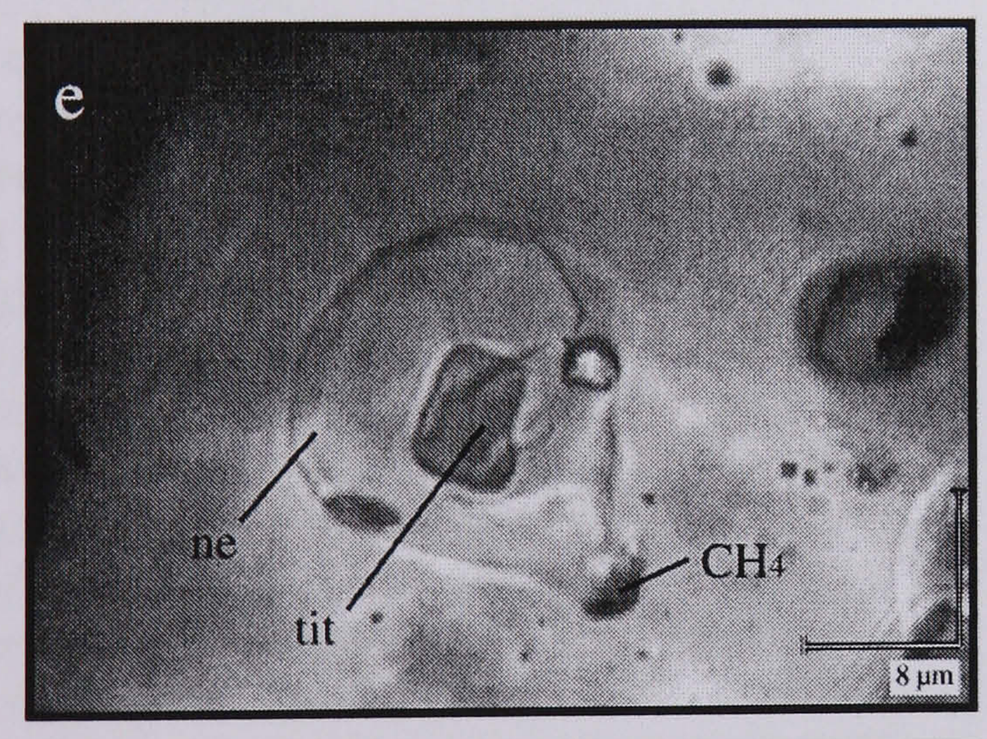
e
ne
tit
CH4
8 µm

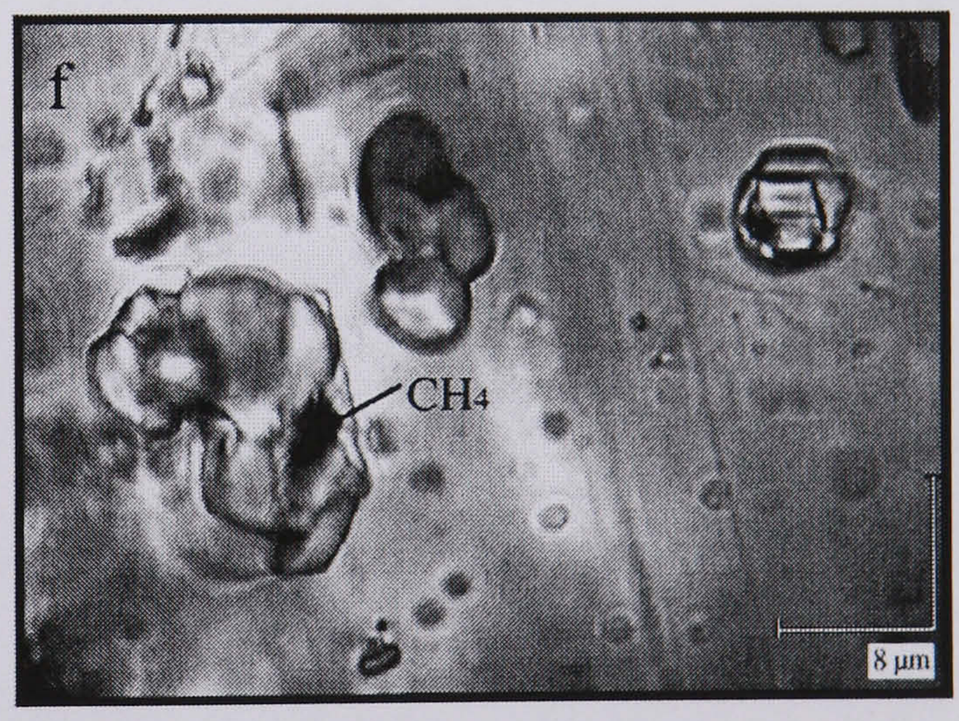
f
CH4
8 µm

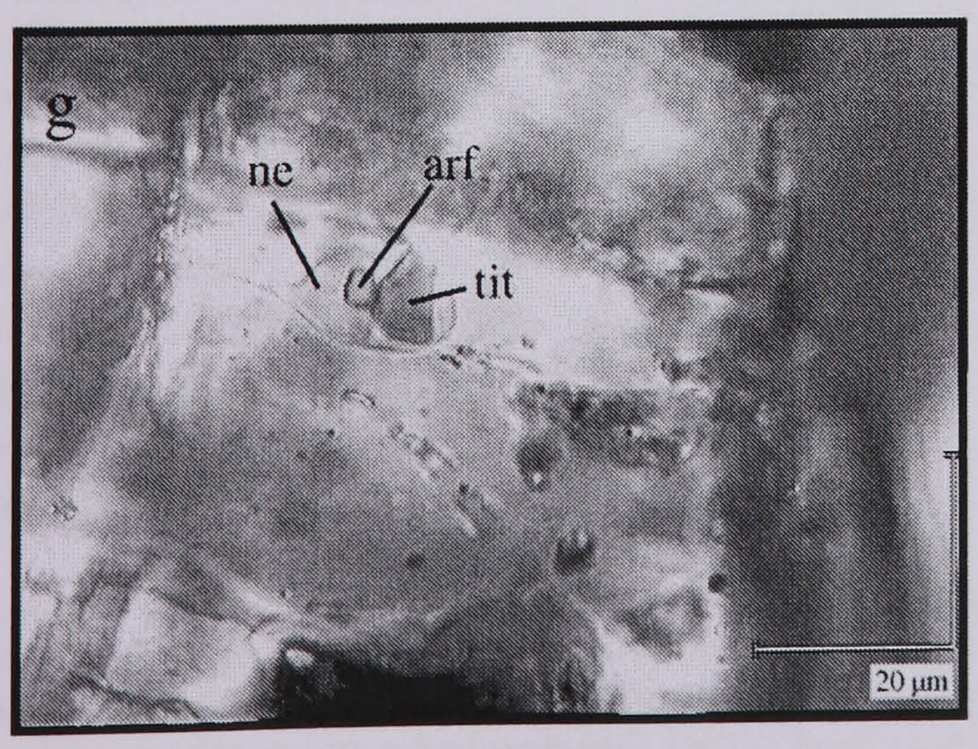
g
ne
arf
tit
20 µm

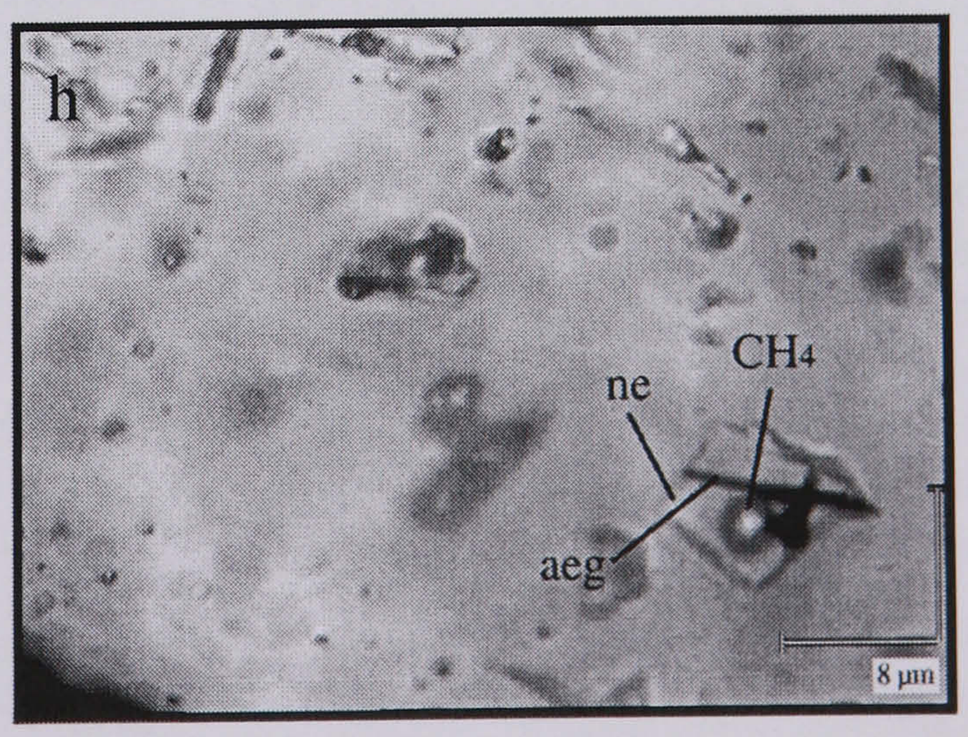
h
CH4
ne
aeg
8 µm

mounted on a JEOL 6310 SEM at Kingston University, and a Cameca SX50 WDS microprobe at the Natural History Museum, London.

Doubly polished wafers of 100–150 μm thickness were prepared for microthermometric and laser Raman microprobe analysis of fluid inclusions. A confocal, multichannel Renishaw laser Raman microprobe RM 1000 with a 514 nm Argon laser and a thermoelectrically cooled CCD detector system was used to determine the composition of the fluid inclusions. The system was attached to an Olympus microscope with lens magnification of ×100 and analytical spot size of 1–3 μm^2. To correct instrumental drift, silicon and diamond standards were used for regular calibration. The peak positions obtained were reproducible within a range of ±1 cm^{-1}. Fluid inclusion microthermometric analyses were carried out using a Linkam THMS 600 low-temperature heating–freezing-stage attached to an Olympus microscope. Measurements were carried out between −196 and 600 °C following the procedure described in Shepherd et al. (1985). The stage was regularly calibrated using the triple point of methane (−182.5 °C) in natural fluid inclusions (Beeskow et al., 2005) and the melting point of CO_2 (−56.6 °C) in synthetic fluid inclusions. The reproducibility was within ±0.2 °C.

Gas chromatographic analyses of the hydrocarbons were carried out at the Kola Science Centre, Apatity, Russia based on the method described by Ikorsky (1999). 1 g of handpicked sample material with the grain size range 0.63–0.25 mm was analysed. Prior to analysis, the samples were flushed with helium and crushed on-line in a vibrating ball mill. The helium carrier gas was passed through the mill again after sample crushing and the gas mixture (extracted gas and helium) was sent to the gas chromatograph column for separation and measurements. The composition was calculated by chromatogram peak area estimation.

Isotope data were obtained at the stable isotope laboratory at the University of Lausanne. To release the methane contained in fluid inclusions, the samples were crushed off-line in a vacuum system by hand, using the "pepper-mill" technique of Simon (2001). The mill and interior of the extraction system was previously cleaned with a solution of ultrapure, distilled dichloromethane and subsequently dried at 110 °C. Gas sampling was performed using a gas-tight syringe and the carbon isotope composition of the saturated hydrocarbons was measured using a Hewlett-Packard 6890 gas chromatograph coupled to a Thermoquest/Finnigan MAT Delta S isotope ratio mass spectrometer via a combustion interface III under a continuous helium flow (Freedman et al., 1988; Hayes et al., 1990). The GC was operated with a Carboxen™ 1006 PLOT capillary column (30 m × 0.53 mm internal diameter) for the analysis of CH_4 and CO_2 and a Paraplot Q-HT column for the analysis of higher hydrocarbons, plus helium as carrier gas (linear flow velocity 3 ml/s). After an initial period of 5 min at 35 °C, the column was heated to 100 °C at 20 °C/min followed by an isothermal period of 20 min, and later heated to 220 °C at 20 °C/min and held there for 5 min. The samples were injected at 230 °C. The CuO/NiO/Pt combustion reactor was set at 960 °C. The performance of the GC/C/IRMS system, including the GC and combustion furnace, was evaluated every 10 analyses by injection of methane and carbon dioxide of known $\delta^{13}C$ values. The analytical reproducibility, tested by daily replicate analysis of a laboratory standard gas mix is ±0.5‰.

4. Analytical data

4.1. Petrology and distribution of fluid inclusions in relationship to mineral assemblage and rock type

A major aim of the present study is to test the potential relationships between fluid inclusion population and altered Fe-rich phase assemblages. The main reaction textures associated with the Fe-bearing phases are: fine-grained lorenzenite and aegirine aggregates around aenigmatite; intergrowths of K-rich feldspar and nepheline around biotite; and titanite rimming ilmenite. None of the samples studied here shows evidence for development of fluid inclusion populations along with these mineral textures. There is no evidence of narrow reaction rims of biotite or/and aegirine around magnetite or of reaction rims between magnetite, titanomagnetite and nepheline (c.f. Potter, 2000).

Alkali feldspar shows a perthitic structure, developed by exsolution processes that leave Na- and K-dominated zones. Far more pronounced, however, are zones of albitisation that follow cleavage planes and microfractures in alkali feldspar. These zones are caused by an ion exchange reaction between a Na-rich fluid and alkali feldspar

Fig. 2. Typical appearance of fluid inclusions. (a) Primary fluid inclusions (p) marking growth planes of a nepheline crystal which are cross-cut by secondary fluid inclusion planes (s); (b) isolated cluster of primary mono- and two-phase inclusions; (c) primary fluid inclusions attached to aegirine micro-crysts; (d) necked-down inclusion showing the separation of a water-rich and methane-rich phase; (e–h) melt inclusions in rischorrite. The crystalline components titanite (tit), arfvedsonite (arf), aegirine (aeg), nepheline (ne) and gaseous methane are identified by laser Raman spectroscopy and labelled. All other phases are unknown. Note, the inclusions are hosted in nepheline, therefore the detected nepheline phase within the inclusion might result from scattering of the host mineral.

Table 1
Bulk gas data from the extracted gas of the Khibiny intrusion

Rock type	Sample	CH_4	C_2H_4	C_2H_6	C_3H_6	C_3H_8	i-C_4H_{10}	α-C_4H_8	*n*-C_4H_{10}	Σβ-C_4H_8
		cm^3/kg	cm^3/kg	cm^3/kg	cm^3/kg	cm^3/kg	cm^3/kg	cm^3/kg	cm^3/kg	cm^3/kg
Khibinite	Kh-03-1	17.10	–	0.730	–	0.075	0.0060	–	0.0150	0.0010
Khibinite	Kh-03-2	13.80	–	0.340	–	0.024	0.0020	–	0.0049	0.0003
Khibinite	Kh-03-3	22.50	–	0.400	0.004	0.035	0.0033	–	0.0069	0.0008
Khibinite	Kh-03-4	36.20	–	1.200	0.007	0.150	0.0120	0.0002	0.0280	0.0017
Khibinite	Kh-03-5	10.90	–	0.650	0.001	0.060	0.0043	–	0.0130	0.0008
Khibinite	Kh-03-6	17.70	–	0.570	0.002	0.056	0.0042	–	0.0088	0.0006
Khibinite	Kh-03-7	12.10	–	0.730	–	0.042	0.0024	–	0.0100	0.0005
Khibinite	Kh-03-8	11.70	–	0.460	0.001	0.038	0.0031	–	0.0087	0.0004
Rischorrite	Kh-03-9	5.97	–	0.950	0.002	0.110	0.0084	–	0.0250	0.0019
Rischorrite	Kh-03-10	32.40	–	1.070	0.005	0.079	0.0063	–	0.0170	0.0014
Rischorrite	Kh-03-11	11.30	–	0.190	0.001	0.012	0.0007	–	0.0026	–
Rischorrite	Kh-03-13	13.90	–	0.580	0.001	0.064	0.0060	–	0.0150	0.0008
Rischorrite	Kh-03-14	4.98	–	0.100	0.001	0.005	0.0003	0.0002	0.0012	–
Rischorrite	Kh-03-42	30.40	–	0.420	0.001	0.026	0.0016	–	0.0050	0.0004
Rischorrite	Kh-03-43	5.40	–	0.100	0.000	0.006	0.0004	–	0.0010	–
Rischorrite	Kh-03-44	98.50	–	3.300	–	0.280	0.0290	0.0015	0.0780	0.0054
Rischorrite	Kh-03-45	0.04	–	0.002	0.001	0.000	–	–	–	–
Rischorrite	Kh-03-48	11.50	–	0.350	0.002	0.024	0.0014	–	0.0042	0.0003
Rischorrite	Kh-03-49	1.10	–	0.018	0.002	0.001	0.0000	0.0003	0.0003	–
Rischorrite	Kh-03-50	0.04	–	0.001	0.001	0.000	–	–	–	–
Trachytoid foyaite	Kh-03-46	16.10	–	0.570	0.002	0.035	0.0025	b.d.	0.0095	0.0004
Trachytoid foyaite	Kh-03-35	4.22	–	0.081	0.002	0.006	0.0005	0.0002	0.0014	–
Trachytoid foyaite	Kh-03-36	0.34	–	0.006	0.001	0.001	0.0000	–	–	–
Trachytoid foyaite	Kh-03-37	5.10	–	0.120	0.004	0.007	0.0003	0.0001	0.0010	–
Trachytoid foyaite	Kh-03-38	2.77	–	0.057	–	0.003	0.0002	–	0.0004	–
Trachytoid foyaite	Kh-03-39	1.30	–	0.026	0.000	0.002	0.0001	–	0.0002	–

Trachytoid foyaite	Kh-03-40	0.12	–	0.001	0.001	0.000	–	–	–	–
Trachytoid foyaite	Kh-03-41	2.87	–	0.093	0.003	0.008	0.0004	0.0002	0.0012	0.0001
Massive foyaite	Kh-03-51	0.01	0	0.001	0.001	0.000	–	–	–	–
Massive foyaite	Kh-03-52	8.46	–	0.140	0.002	0.008	0.0004	0.0005	0.0019	0.0001
Massive foyaite	Kh-03-53	4.60	–	0.083	0.001	0.004	0.0002	0.0002	0.0007	0.0001
Massive foyaite	Kh-03-54	11.90	–	0.330	0.002	0.025	0.0016	0.0001	0.0042	0.0001
Massive foyaite	Kh-03-55	1.44	–	0.017	0.002	0.002	0.0002	0.0002	0.0005	–
Alkaline syenite	Kh-03-56	0.02	–	0.001	0.001	–	–	–	–	–
Alkaline syenite	Kh-03-57	0.01	–	–	–	–	–	–	–	–
Alkaline syenite	Kh-03-58	0.02	0.0004	0.002	0.001	0.000	–	–	–	–
Alkaline syenite	Kh-03-59	0.01	0.0004	0.002	0.002	0.001	–	–	–	–
Alkaline syenite	Kh-03-60	0.02	0.0003	0.002	0.001	0.000	–	–	–	–
Ijolite	Kh-03-61	21.20	–	0.860	–	0.066	0.0059	0.0002	0.0110	0.0007
Ijolite	Kh-03-62	5.99	–	0.360	–	0.023	0.0028	0.0001	0.0054	0.0003
Ijolite	Kh-03-63	38.20	–	1.480	–	0.230	0.0260	0.0001	0.0480	0.0046
Ijolite	Kh-03-64	29.90	–	1.380	–	0.180	0.0230	–	0.0400	0.0040
Ijolite	Kh-03-65	50.10	–	1.640	–	0.120	0.0150	0.0008	0.0370	0.0025
Ijolite	Kh-03-66	43.80	–	2.030	–	0.180	0.0260	0.0009	0.0450	0.0053
Ijolite	Kh-03-67	40.20	–	1.960	–	0.180	0.0230	0.0002	0.0420	0.0035
Ijolite	Kh-03-68	20.60	–	0.810	–	0.079	0.0071	–	0.0140	0.0007
Ijolite	Kh-03-69	13.30	–	0.450	–	0.043	0.0037	–	0.0110	0.0004
Ijolite	Kh-03-70	0.03	–	0.000	–	–	–	–	–	–
Ijolite	Kh-03-71	4.18	–	0.160	0.001	0.016	0.0014	0.0002	0.0030	0.0002
Ijolite	Kh-03-72	2.20	–	0.075	–	0.006	0.0003	–	0.0007	–
Ijolite	Kh-03-73	1.85	–	0.060	0.001	0.003	0.0002	–	0.0004	–
Ijolite	Kh-03-74	4.46	–	0.150	0.001	0.010	0.0007	0.0003	0.0030	0.0001
lujavrite	Kh-03-17	0.94	–	0.040	–	0.002	0.0001	–	0.0003	–
lujavrite	Kh-03-18	1.05	–	0.043	0.001	0.003	0.0002	–	0.0004	–
lujavrite	Kh-03-19	2.59	–	0.120	–	0.007	0.0003	–	0.0010	–
lujavrite	Kh-03-20	3.58	–	0.130	–	0.006	0.0003	–	0.0011	–
lujavrite	Kh-03-21	2.83	–	0.046	–	0.001	–	–	0.0002	–
lujavrite	Kh-03-22	9.85	–	0.160	–	0.007	0.0004	–	0.0015	–

along cleavages or cracks (Orville, 1963; Brown and Parsons, 1994). This type of alteration is ubiquitous in the Central Arch (Nivin et al., 2005).

4.2. Fluid and melt inclusion study

The majority of fluid inclusions are hosted in nepheline, feldspar and eudialyte. Primary inclusions occur in arrays parallel to growth zones in nepheline and have diameters of up to 5 μm (Fig. 2a). Larger primary inclusions, between 10 and 20 μm in diameter, are found in separate clusters, mainly in nepheline (Fig. 2b). These are mono-phase CH_4-rich and two-phase CH_4–H_2O-rich fluid inclusions. A third group of primary fluid inclusions is attached to small aegirine needles (Fig. 2c). They are mono-phase, CH_4-dominated inclusions with a diameter of 5–15 μm.

The majority of fluid inclusions in the Khibiny rocks are secondary. They were trapped after the rock body cooled and indicate a high level of post-magmatic fluid movement. They are mainly present in fluid inclusion planes (FIPs) and are most common in nepheline crystals but also occur along cleavage planes in feldspar. The FIPs represent healed microcracks and predominantly start and terminate at grain boundaries. Small FIPs start and terminate within mineral grains. Longer FIPs cross-cut several mineral grains and are often aligned sub-parallel to each other. Fluid inclusions in the FIPs vary in size between 5 and 20 μm with a well rounded, elongate or even tabular shape. The majority (c. 90%) of inclusions are mono-phase and methane-dominated. About 10% of the population are two-phase fluid inclusions and consist of a methane-rich gas bubble and brine. There is evidence for necking down with methane and water phase separated into disconnected mono-phase inclusions (Fig. 2d) or two-phase inclusions with different degrees of filling. The water-rich phase was probably commonly consumed during secondary mineral growth, leaving the pure methane phase behind.

Multi-solid inclusions are present in some of the samples studied (Fig. 2e–h). They contain variable proportions of arfvedsonite, titanite, aegirine and nepheline as determined by laser Raman spectroscopy together with unidentified, Raman-inactive phases. We interpret these to be silicate melt inclusions. Some of them contain methane-dominated gas bubbles. Observations of homogenisation temperature were not possible due to a strong degradation, cracking and darkening of the nepheline host at temperatures above 500 °C.

4.3. Laser Raman spectroscopy and microthermometry

Primary and secondary fluid inclusions are compositionally similar in terms of microthermometric and laser Raman data. The majority of the mono-phase fluid inclusions analysed by laser Raman spectroscopy show a methane peak at between 2911 and 2915 cm^{-1}. Low concentrations of ethane and propane have been identified with peak positions of 2954 and 2890 cm^{-1}, respectively. In two-phase inclusions, a broad water peak at c. 3400 cm^{-1} was recorded in the liquid phase, the gas bubbles gave strong methane peaks. No free hydrogen was detected in the fluid inclusions using the laser Raman technique. A broad shoulder, the result of fluorescence produced by the host minerals, was present at higher wavelengths and might have swamped the hydrogen signal.

The inclusions mostly display H1 behaviour as defined by Van den Kerkhof (1988). Homogenisation temperatures of the mono-phase inclusions range from −98 to −62 °C. This variation indicates the presence of impurities such as higher hydrocarbons. Most of the methane-dominated inclusions homogenise to vapour, indicating high molar volumes. The homogenisation temperatures of two-phase H_2O–CH_4 inclusions range from 350 to >500 °C. Measurements at higher temperatures were not possible due to degradation of the host mineral. The approximate temperatures of first ice melting (−70 to −40 °C), hydrohalite melting (−38 to −17 °C) and last ice melting (−17 to −1.5 °C) indicate a wide salinity range. The aqueous inclusions contain brine with 5 to 20 wt.% salt.

4.4. Bulk gas data

Gas analyses were carried out at the Kola Science Centre, Apatity, Russia on samples of different rock types in order to identify the amount and composition of gases stored in the rocks of the Khibiny complex. CH_4 is the dominant species with concentrations of up to 100 cm^3/kg rock. Higher hydrocarbons are recorded up to C_4. Their concentrations decrease exponentially with increasing carbon number (Table 1). The results are consistent with laser Raman data where the majority of fluid inclusions contain CH_4 and small proportions of ethane and propane and are similar to those reported in the literature. Other minor volatiles reported in the literature (e.g. Petersilie et al., 1961; Petersilie and Sørensen, 1970; Kogarko et al., 1987; Potter and Konnerup-Madsen, 2003) are CO_2, CO, H_2 and N_2.

A comparison of bulk gas data with mineralogy reveals no strong relationship between Fe-rich mafic mineral content and gas content (Fig. 3a). However, there is a positive correlation between bulk gas content and nepheline content (Fig. 3b). This is because nepheline is the most suitable host for fluid inclusions.

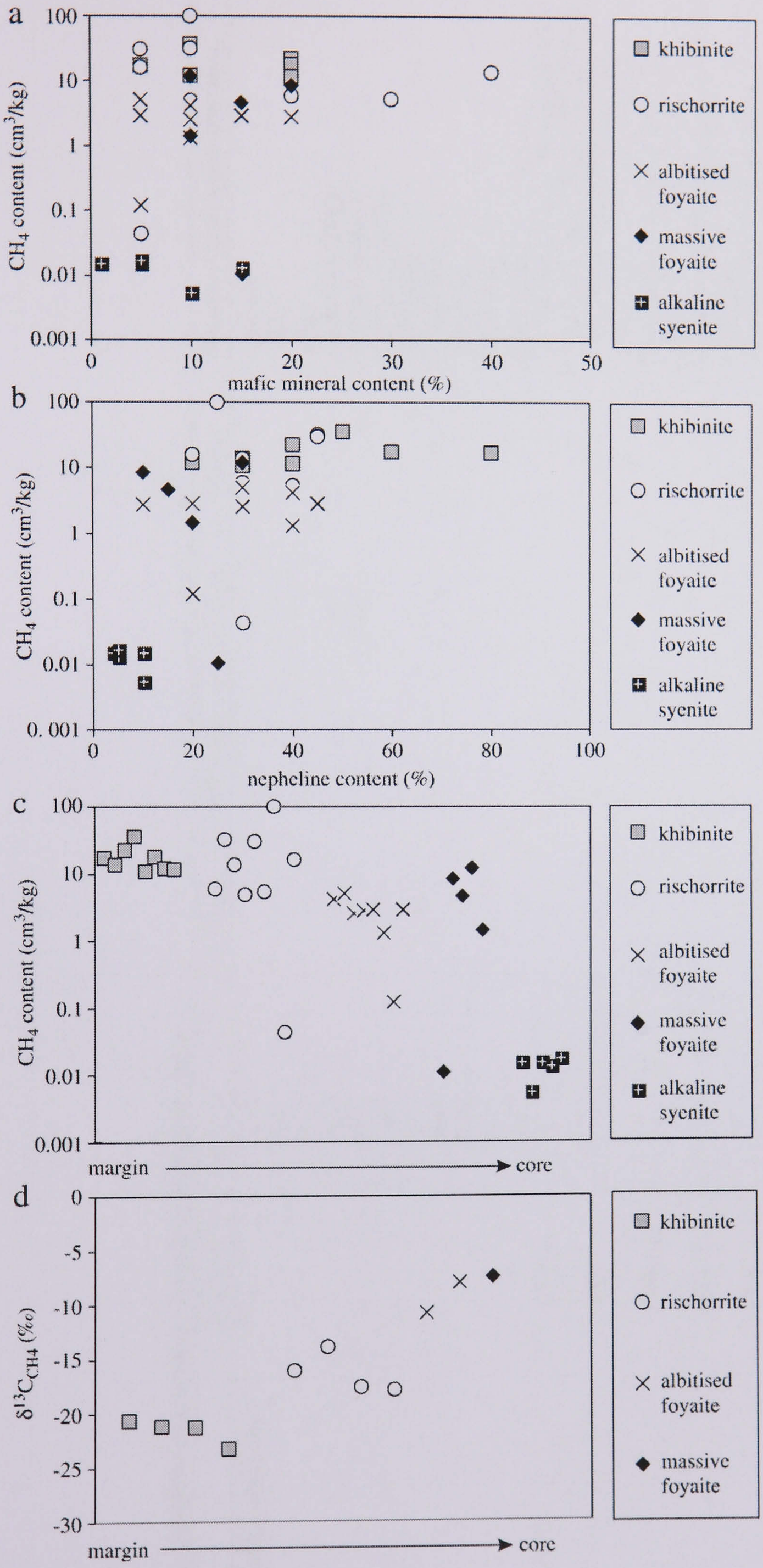

Fig. 3. Methane distribution versus (a) modal distribution of mafic minerals (b) modal distribution of nepheline which is the predominant host mineral for the inclusions and (c) the sampling location from the margin of the complex towards the core. (d) Variation of $\delta^{13}C$ signatures from the margin of the complex (khibinite) towards the core (foyaites).

Table 2
A summary of published isotope data for the gases of the Khibiny pluton

Publisher	$\delta^{13}C_{bulk\ C}$	$\delta^{13}C_{CH4}$	$\delta^{13}C_{C2H6}$	$\delta^{13}C_{C3H8}$	$\delta^{13}C_{CO2}$	δD_{CH4}	Minerals or rocks analysed/location
Galimov and Petersilie (1967)		−3.2					Khibinite
		−12.8					Urtite
		−8.4					Ijolite
		−14.6			−8.5		Fsp from pegmatite
		−8.4			+10.6		Eud from pegmatite
		−13.2					Trachitoid khibinite
		−11.8					Ijolite-urtite
		−19.3					Ijolite-urtite
		−18.2					Ijolite-urtite
		−16.3					Ijolite-urtite
		−19.1					Ijolite-urtite
Galimov (1973)	−7.9						Ne in pegmatite in trachytoid khibinite
	−8.1						Ne in pegmatite in trachytoid khibinite
	−4.6						Eud in pegmatite in middle-grained ne syenite
	−4.3						Ne in pegmatite in middle-grained ne syenite
	−6.1						Aenig in pegmatite in middle-grained ne syenite
	−11.4						Ne with aeg in pegmatite in middle grained ne syenite
	−8.1						Eud in pegmatite in middle grained ne syenite
	−5.3						Ne in pegmatite in titanite foyaite
	−9.2						Ne in pegmatite in rischorrite
	−6.2						Ne in pegmatite in ijolite-urtite
		−12.8	−24.5	−26			Urtite
		−3.2	−9.1	25.7			Khibinite
		−7.9	−14.2				

Yerokhin (1978)		−6.5		−82	Eudialyte
		−6.5		−66	
Khitarov et al. (1979)		−10.6	−23.9		Rasvumchorr mine, hole 7, 1967
		−6.5	−11.7		Rasvumchorr mine, hole 7, 1975
Voitov et al. (1990)		−16.5 to −7.7			Rasvumchorr mine
			−12.1		Rasvumchorr mine
			−24		Rasvumchorr mine
		−11.2	−15.6		Rasvumchorr mine
Voitov (1992)				−72	Rasvumchorr mine, hole 7, February 1975, D in CH_4
				−56	Rasvumchorr mine, hole 7, March 1975, D in CH_4
				−144	Rasvumchorr mine, hole 7, February 1975; D in C_2H_6
				−173	Rasvumchorr mine, hole 7, March 1975; D in C_2H_6
		−8.7			Rasvumchorr mine, hole 360, August 1986
		−11.2	−15.6		Rasvumchorr mine, hole 360, August 1986
Potter (2000)	−11.44				Urtite, sample 1253-153
	−13.17				Urtite, sample 1253-153
	−8.3				Urtite, sample 1253-153
	−3.28				Urtite, sample 1253-153
	−25.33				Urtite, sample 145-P-85
	−17.82				Urtite, sample 145-P-85
	−12.34				Urtite, sample 145-P-85
			−7.26		Carbonatite, sample Kh28
			−5.58		Carbonatite, sample Kh28
			−3.84		Carbonatite, sample Kh28

The results are given in the standard δ-notation, expressed relative to VPDB and VSMOW in permil (‰).

Table 3
Isotope data for the gases of the Khibiny pluton from this study

Rock type	Sample	$\delta^{13}C_{CH_4}$	$\delta^{13}C_{C_2H_6}$	$\delta^{13}C_{C_3H_8}$	$\delta^{13}C_{C_4H_{10}}$	$\delta^{13}C_{C_5H_{12}}$	$\delta^{13}C_{CO_2}$
Khibinite	KH-03-03	−22.4					−15.5
Khibinite	KH-03-03						−14.9
Khibinite	KH-03-04		−18.7	−18.0	−18.7		
Rischorrite	KH-03-10	−12.6					−16.8
Rischorrite	KH-03-42	−14.4	−17.1	−17.3	−17.5		−15.4
Rischorrite	KH-03-44		−18.9	−19.2	−19.7		
Rischorrite	KH-03-46	−13.3	−19.2	−18.9	−19.4		−13.9
Trachytoid foyaite	KH-03-35	−7.4					−13.7
Trachytoid foyaite	KH-03-37	−8.0	−17.5	−19.6			−13.6
Massive foyaite	KH-03-54	−5.4	−14.3	−13.0	−13.2	−14.0	−13.7
Ijolite	KH-03-68	−10.8					−15.2
	Mean	−11.9	−17.6	−17.7	−17.7	−14.0	−14.7
	Range	−22.4 to −5.2	−19.2 to 14.3	−19.6 to 13	−19.7 to −13.2	−14.0	−16.8 to −13.6

The results are given in the standard δ-notation, expressed relative to VPDB in permil (‰).

Therefore, it is likely that the presence of a suitable host mineral for fluid inclusions is more important than the presence of Fe-rich catalyst phases in controlling the bulk gas content in a sample.

The methane content in the samples analysed in this study is highest in the outer, marginal rocks and decreases inwards to very low levels in the core of the complex (Fig. 3c). This is broadly in agreement with the data of Ikorsky (1977) although not with that of Nivin et al. (2005) who report the presence of high post-magmatic fluid fluxes within the Central Arch complex. On the basis of our data, it is likely that a trend of decreasing methane content inward from the margin of the pluton is overprinted by late-stage gas fluxes through the Central Arch. As rock types change towards the core of the intrusion, a number of reasons may explain this observation. These include variations in the modal proportion of those phases most likely to host CH_4 in fluid inclusions; variations in the modal proportions of Fe-rich phases that may catalyse the FT reaction; variations in permeability permitting access of H_2O; or, if the methane is not generated in situ, varying distance from the methane source.

4.5. Isotope data

To date, reliable isotopic data from hydrocarbon gases of the Khibiny alkaline rocks are sparse. Previous data from the hydrocarbon-bearing fluids in Khibiny including $\delta^{13}C_{bulk}$ data, $\delta^{13}C$ and δD data for CH_4 and higher HC from free and occluded gases are summarized in Table 2. Our new data from a preliminary study of different rock types show $\delta^{13}C$ values of −22.4‰ and −5.4‰ for CH_4. In terms of their spatial distribution, an increase in $\delta^{13}C$ values from the outer towards the central part of the

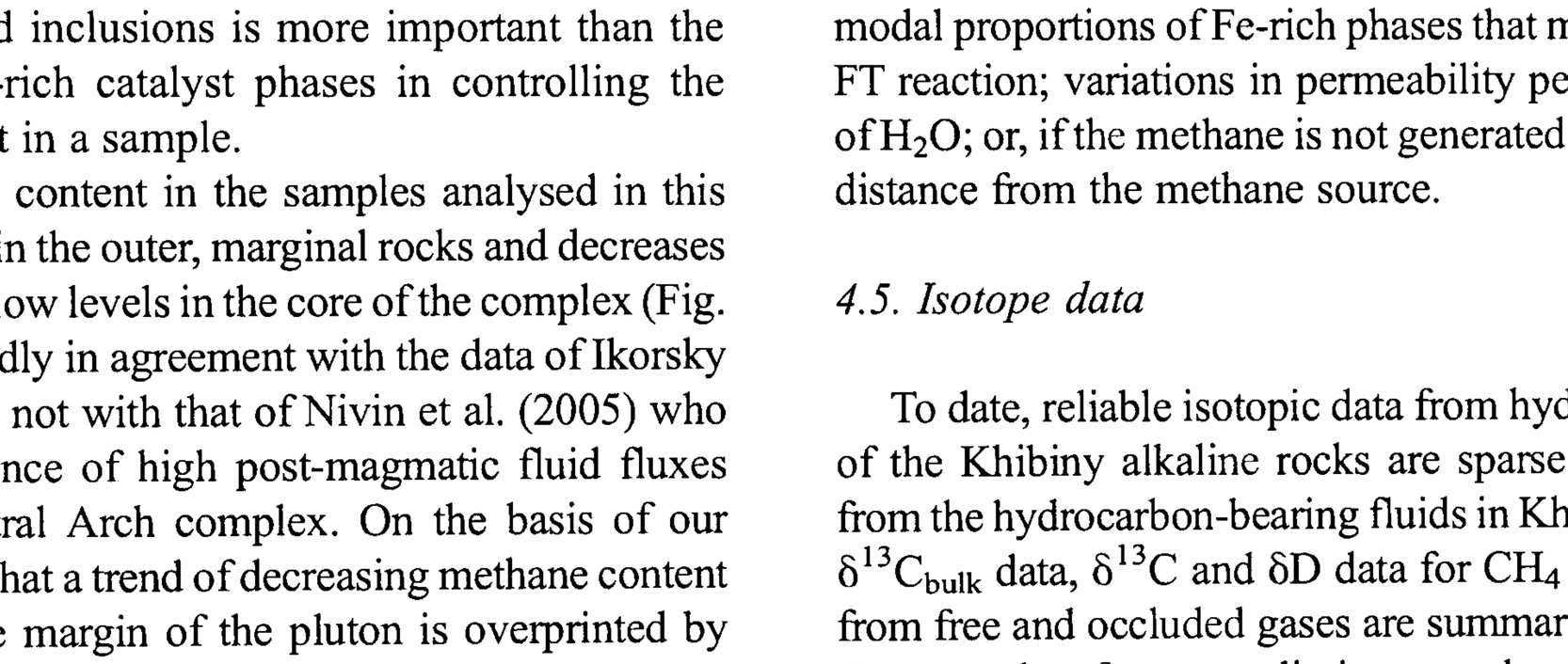

Fig. 4. Log normalised abundance (in mol%) of CH_4 and higher hydrocarbons in the gas phase of the Khibiny complex plotted versus increasing carbon number. For comparison the distribution of a natural gas sample of biogenic origin is shown (from Prinzhofer and Huc, 1995).

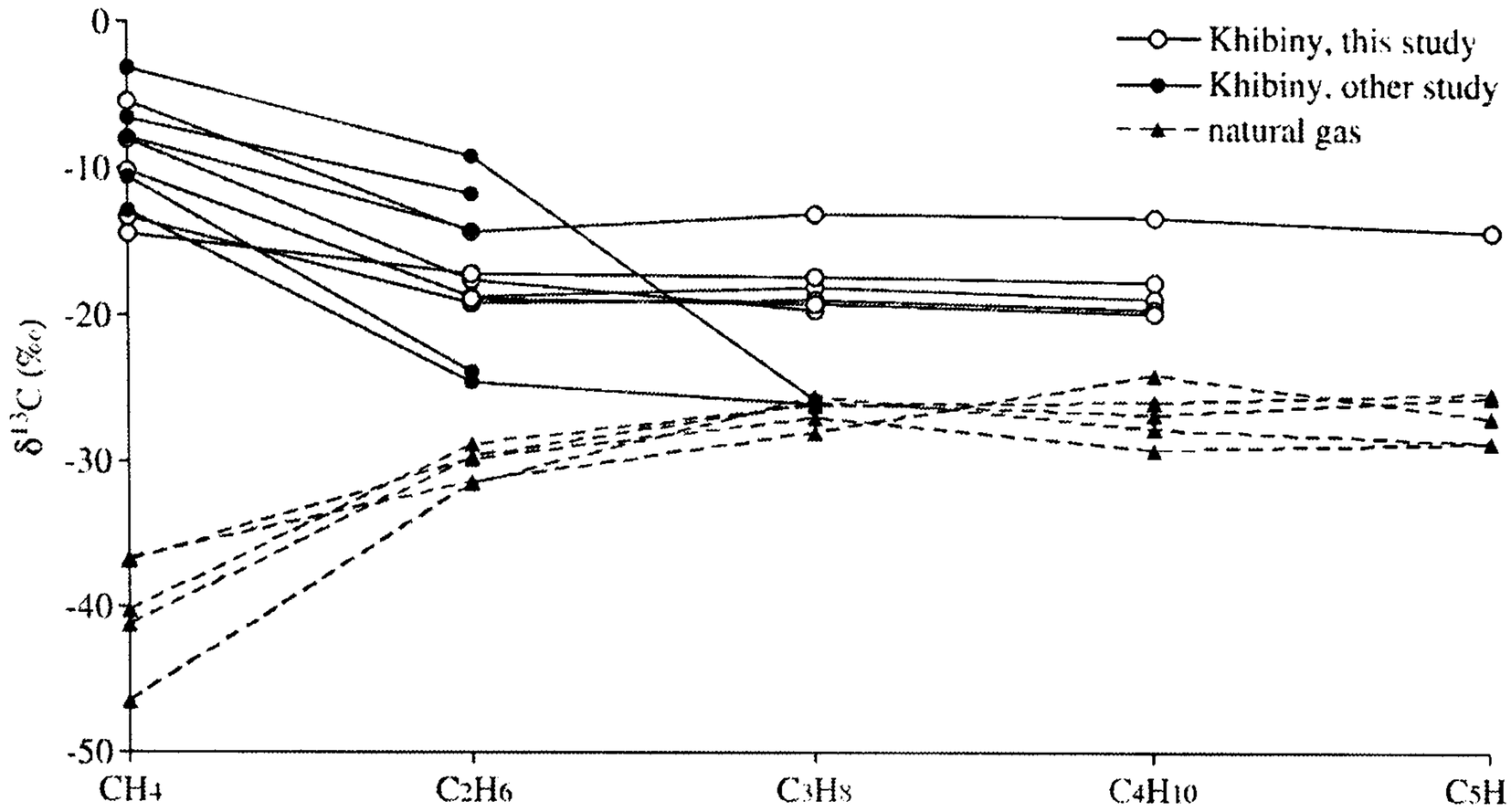

Fig. 5. Isotope distribution of methane and higher hydrocarbons of gas extracted from the Khibiny pluton (Galimov, 1973; Voitov, 1992 and this study) compared with data from natural gas samples (Prinzhofer and Huc, 1995).

complex has been observed (Fig. 3d). Khibinite from the outer part of the complex has a $\delta^{13}C$ value of −22.4‰, whereas foyaite from the core of the pluton contains methane with much less negative values from −8‰ to −5.4‰. The analyses of higher hydrocarbons show a subsequent increase of $\delta^{13}C$ values with increasing carbon number (Table 3 and Fig. 5).

5. Discussion—models for methane generation in alkaline igneous rocks

Several models have been suggested for the accumulation of methane in igneous rocks. These can be grouped into biogenic and abiogenic models. Many workers (e.g. Gold, 1979; Larsen et al., 1992; Krot et al., 1994; Berndt et al., 1996; Salvi and Williams-Jones, 1997; Potter et al., 1998; Konnerup-Madsen, 2001; Markl et al., 2001; Sherwood-Lollar et al., 2002) have stressed the potential likelihood of the abiogenic evolution of methane in igneous rocks, although there remains a debate as to whether this would occur at an early-, late- or post-magmatic stage of the crystallisation history. Here, we re-evaluate various models of methane generation and assess their applicability to the Khibiny pluton.

5.1. Abiogenic origin

Two critical chemical criteria support an abiogenic origin for the HC gases of the Khibiny pluton. Firstly, the carbon number distribution shows a log-linear relationship between the molar amount of the alkane and its carbon number. New bulk gas data presented in this paper confirm the log-linear trend from C_1 to C_4 with concentrations decreasing from 100 to 0.01 mol% (Fig. 4). This trend is close to that predicted by the Schulz-Flory distribution (Anderson, 1984) which is a simple statistical model that is a good indicator of an abiogenic origin of the hydrocarbons, as the higher HCs are formed via polymerisation. In contrast, biogenic alkanes have a shallower slope when plotted on the same diagram. Similar results have been found in other alkaline rock complexes such as Lovozero (Potter et al., 2004), Ilímaussaq (Konnerup-Madsen, 2001) and Strange Lake (Salvi and Williams-Jones, 1997).

Secondly, the $\delta^{13}C$ data set for methane and the higher HC from the Khibiny pluton shows values that decrease from CH_4 towards the higher homologues (Fig. 5). The systematically higher $\delta^{13}C$ values for CH_4 compared to those of the higher hydrocarbons in the same fluid samples are consistent with an inorganic polymerisation process whereby the heavier hydrocarbons are synthesised from methane (Des Marais et al., 1981). This is common in high-temperature abiogenic hydrocarbons (Voitov, 1992) and supports an abiogenic origin for the gases in the Khibiny pluton. Gas samples from a natural (biogenic) gas source would show the opposite trend, with $\delta^{13}C$ values increasing towards the higher C numbers (Prinzhofer and Huc, 1995).

5.1.1. Post-magmatic origin via Fischer-Tropsch synthesis

Hydrocarbons in alkaline rocks including the Khibiny complex could be generated by Fischer-Tropsch synthesis according to the general chemical reaction:

$$nCO_2 + (3n + 1)H_2 \rightarrow C_nH_{2n+2} + 2nH_2O.$$

CH_4 is produced when $n = 1$ and higher hydrocarbons when $n > 1$. The H_2 needed for the reaction is probably

released by hydrothermal alteration of Fe-rich minerals (Salvi and Williams-Jones, 1997; Potter et al., 1998, 2004). However, a number of petrologic features suggest that the importance of the FT reaction in generating CH_4 and higher hydrocarbons in Khibiny may be overstated. Here we highlight a number of criteria suggesting that methane occurrence may not be the result of a simple, closed system behaviour.

5.1.1.1. The entrapment problem. It was suggested by Potter et al. (1998, 2004) that trails of CH_4-bearing fluid inclusions terminate at the margins of hydrated Fe-rich minerals as the result of hydration and associated FT reactions. This termination, or pinning, of FIPs is interpreted as the result of fracturing of the host minerals due to volume expansion of the Fe-phase. However, in the samples studied here, FIPs are a general feature of fractured rocks. They are most pronounced in nepheline and feldspar and no obvious relationship between their abundance and the presence or absence of altered Fe-rich phases has been observed. Hence, there is no strong reason to infer that they were produced during methane production by FT synthesis.

Consequently, microthermometrically derived temperatures and pressures of fluid entrapment do record conditions of fluid migration and secondary trapping, rather than those of methane generation.

5.1.1.2. The alteration problem. A number of hydrothermal reactions (not always balanced) involving the breakdown of phases such as arfvedsonite, nepheline and augite have been cited as linked to FT synthesis (Salvi and Williams-Jones, 1997; Potter and Konnerup-Madsen, 2003; Potter et al., 2004). The precise nature of the reaction chemistry is best determined by reaction textures.

Although arfvedsonite breakdown is commonly cited, we see no textural evidence to suggest that the association of arfvedsonite with aegirine is related to hydration and excessive accumulation of fluid inclusions around the mineral assemblage. We do not find aegirine rims developed around arfvedsonite, nor do we find other evidence of arfvedsonite alteration. The observed increase in Na and Fe and decrease in Mg and Ca from core to rim of arfvedsonite crystals is very typical for igneous fractionation.

Similarly, the augite breakdown reactions cited by other workers involve mineral assemblages which we have rarely found in the Khibiny massif. The reaction may well generate small amounts of methane through an FT reaction. However, the rarity of the complete reaction assemblage means that it is unlikely to have been responsible for the production of large volumes of methane in the complex. Either the reaction has not occurred, or it has gone to completion almost everywhere which is unlikely. The hydration of nepheline to cancrinite (Potter et al., 1998; Potter and Konnerup-Madsen, 2003) is a potential CH_4-producing reaction. Our new, whole rock bulk gas data confirm a positive correlation between cancrinite content and methane concentration. This is most pronounced in the cancrinite-rich rischorrite sample Kh-03-44 which has a methane content of nearly 100 cm^3/kg. However, there is no evidence for a large population of fluid inclusions in these samples. As basic cancrinite may be considered to be a member of the zeolite family (Hassan and Grundy, 1983) it offers a means of gas storage. Therefore, cancrinite can be considered to be a strong adsorbent that incorporates gases such as methane in their crystal structure but is not necessarily linked to CH_4-production.

In many samples methane-rich gas bubbles are attached to a small aegirine needle, mostly within a matrix of nepheline (Fig. 2c). Although this could be the result of an in situ FT reaction on aegirine, a more likely explanation for this texture is the "water glass" phenomenon where gas bubbles in an immiscible H_2O–CH_4 fluid are preferentially attached onto the surface of a small aegirine needle within the late magma/crystal-mush. This would be consistent with the presence of a methane-rich fluid in a crystallising magma and a primary origin for these fluid inclusions.

5.1.1.3. The CO_2 problem. The heterogeneous distribution of methane in the Khibiny complex could be a function of a number of factors. The presence of suitable host minerals, such as nepheline and feldspar, is an obvious control. However, if the FT reaction is the critical driver of methane generation, the distribution of methane in the complex should be related to the availability of Fe-rich minerals needed to catalyse the reaction, the supply of H_2O to drive the hydration reactions and the availability of primary CO_2 in the source rocks. The complex should thus include regions with high CH_4 concentrations, where all the "reactants" needed for FT reactions were present, as well as regions with high CO_2 concentrations where the FT reaction has not taken place, either due to the lack of anhydrous Fe-rich minerals or suitable amounts of late-stage H_2O-rich fluids. However, gas analyses from the Khibiny complex reveal fluids dominated by CH_4 with CO_2 present only in altered samples (Potter and Konnerup-Madsen, 2003) and no inverse relationship between CO_2 and CH_4 content. In fact, no evidence for a primary CO_2-rich magmatic fluid has been found, all identified primary fluid inclusions are CH_4-dominated. Finally, we stress that methane generation through the FT synthesis can only operate in an almost closed system. Too much H_2O

flux will ultimately flush out not just the CO_2 but also all the CH_4 produced. The post-magmatic methane generation from a primary CO_2-rich fluid seems therefore unlikely.

5.1.2. Early-magmatic origin from a mantle source

Methane may form inorganically at mantle conditions of >30 kbar and >1200 K from carbonate species, such as $FeCO_3$ or $MgCO_3$, in the presence of H_2O at oxygen fugacities buffered by iron-bearing phases near the wuestite–magnetite f_{O2} buffer (Scott et al., 2004). Experimental data suggest that such conditions may be widespread in the mantle and that methane at pressures of up to 1 GPa could be the dominant C-bearing fluid phase under reducing conditions in the mantle (Kenney et al., 2002). Ryabchikov et al. (1981) documented very low oxygen fugacities for rocks of mantle origin: olivines from tholeiite basalts and titanium garnets from alkali rocks. Strongly reduced conditions, compared with the crust (QFM), are also believed by Pasteris (1987) to exist in portions of the upper mantle and several studies by, amongst others, Ryabchikov et al. (1981), Eggler and Baker (1982), and Olafsson and Eggler (1983) imply that f_{O2} variations in the mantle would permit different fluid speciation in different regions or materials in the upper mantle. Hydrocarbons traced back to their mantle source have also been found in garnets from the Mir kimberlite pipe (Krot et al., 1994) and Markl et al. (2001) indicated that methane is the stable fluid phase in the low-f_{O2} asthenospheric mantle which appears to be the source of the Ilímaussaq parental melts.

On the basis of $\delta^{13}C$ values of −3.2‰ to −12.8‰, Petersilie (1962) also suggested a magmatic origin for hydrocarbons in the alkaline rocks of the Khibiny pluton. He interpreted the ^{13}C enrichment, similar to that in diamonds, carbonatites and CO_2 of deep-seated origin, as implying a juvenile carbon source (Petersilie and Sørensen, 1970). As an incompatible compound, primary mantle CH_4 could easily be incorporated into mantle derived magmas.

Our observations of silicate melt inclusions which contain methane bubbles (Fig. 2e–h), the attachment of primary methane-rich gas bubbles to aegirine needles (Fig. 2c), and the presence of primary fluid inclusions along growth zones in nepheline (Fig. 2a) support the hypothesis of magmatic CH_4-rich fluid.

5.1.3. Late-magmatic origin via respeciation of a C–O–H fluid

A late-magmatic origin was proposed to explain methane generation in the Ilímaussaq complex by Konnerup-Madsen (2001) and in gabbroic pegmatites within the Skaergaard complex (Larsen et al., 1992). At temperatures <500 °C this involves the respeciation of a carbonic fluid in the C–O–H–graphite system (Huizenga, 2001) under magmatic conditions of QFM to QFM-3, consistent with a volatile-rich, agpaitic magma. These conditions of methane generation are restricted in terms of temperature and chemical composition of the magma. As the Khibiny intrusion contains, apart from the carbonatite, only pure hydrocarbons without any trace of CO_2, it is unlikely that C–O–H-respeciation can be solely responsible for HC production throughout the complex. A further limitation of the model is that, although there is a clear mechanism for CH_4 production through respeciation, the production of the higher hydrocarbons cannot be readily explained. It is therefore unlikely to be a viable mechanism for HC generation in the Khibiny complex.

5.2. Biogenic origin

The host rocks into which the Khibiny complex was emplaced are Archaean granite gneisses and Proterozoic volcanic-sedimentary rocks (Sørensen, 1970; Kogarko, 1995). In the North and South-East the pluton intrudes into Archaean gneisses and in the South and West into the Early Proterozoic Imandra-Varzuga greenstone belt. The greenstone belt comprises an alternating sequence of sedimentary and extrusive volcanic rocks represented by mafic and silicic schists, quartzites, carbonaceous and graphitic schists and metamorphosed limestone and dolomites. Petersilie (1962) described bitumens and low methane contents from some of the schists in the greenstone belt. Mature organic material is present in rocks of the same age in the nearby Lake Onega area (Karelia, NW Russia). Dated at 2 Ga, this constitutes one of the most remarkable accumulations of organic carbon from the Palaeo-Proterozoic. The carbon occurs in the form of shungite, which is a black, non-crystalline, semi-metallic material that contains >98% C (Melezhik et al., 2004). The total carbon reservoir is estimated to exceed 25×10^{10} t. It was accumulated within a volcanic continental rift setting, developed on the rifted eastern margin of the Achaean Baltic shield. It is thus likely that the carbonate and graphitic schists that enclose the Khibiny pluton contain primary organic material some of which could have been incorporated into the pluton either during convective fluid flow during emplacement or during subsequent percolation of meteoric waters along fracture systems. The origin of hydrocarbons could thus be explained by involvement of organic matter from the sedimentary rocks.

Both, the spatial distribution of CH_4 and its isotopic composition (Fig. 2c and d) suggest that there may have been an, at least limited, biogenic influence on HC origin within the Khibiny complex. The CH_4 content increases towards the margin of the complex and $\delta^{13}C$ values decrease toward the margin of the complex. Both these trends are consistent with mixing of methane abiogenically produced within the complex with biogenic methane introduced from the country rocks.

A simple mass balance equation can be used to calculate the relative proportions of the biogenic and mantle components present in the methane gas phase. It uses the analysed isotopic composition of the gas phase itself together with estimates of the isotopic compositions of the two end member components. The equation, governing the isotopic composition of the total carbon in the rock, can be expressed as:

$$F_{\text{shu}} m_{\text{shu}} + F_{\text{mantle}} m_{\text{mantle}} = F_{\text{sample}}$$

where F is the designated $\delta^{13}C$ value of shungite, mantle and the sample and m denotes the molecular mass fraction of C from the two sources. The calculation is based on the overall average $\delta^{13}C$ value of −32‰ of shungite (Melezhik et al., 1999) and the assumption that the measured $\delta^{13}C$ value of the innermost sample Kh-03-54 with −5.4‰ represents the uncontaminated mantle composition. On the basis of these values, the biogenic contribution may be up to 10% in the trachytoid foyaite, up to 30% in the rischorrite and up to 64% in the khibinite.

6. Conclusion—towards a model for CH_4 generation in alkaline rocks

On the basis of the data presented here, together with those elsewhere in the literature, no single simple mechanism is responsible for methane generation within the alkaline rocks of the Khibiny complex. The presence of primary methane-dominated fluid inclusions, melt inclusions containing a methane-rich gas phase, bulk gas data, and the isotopic composition of CH_4 are consistent with an early, abiogenic, magmatic origin. Hence, a reduced carbonic fluid present in the mantle could be a source for the abundant HC gases in the Khibiny complex. However, enhanced CH_4 levels and low $\delta^{13}C$ values suggest that the outer rocks of the complex have a greater biogenic component than those further inwards. This implies the possibility of a marginal biogenic overprint on what is essentially an abiogenic signature.

We find the model of widespread HC generation through a post-magmatic FT type reaction to be untenable. There is little doubt that such a reaction could have operated in some parts of the pluton. Given the correct phase assemblage, the presence of Fe-rich phases, a primary CO_2 fluid, and incipient hydration, then CH_4 and the higher hydrocarbons could have been formed in situ by an FT reaction. However, over the intrusion as a whole an FT type reaction is unlikely to have been important. In particular, there is no evidence for the widespread, strong alteration of mafic mineral assemblages required to produce the H_2 needed to drive the FT reactions, nor is there evidence in the fluid inclusion population for the presence of a primary CO_2-rich magmatic fluid. Primary fluid inclusions are dominated by CH_4. There is no correlation between the presence of Fe-rich phases and high methane contents as predicted for the FT reaction.

In addition, FIPs are widespread throughout the complex and are not related to alteration of Fe-rich assemblages. They are interpreted as fluid pathways and hence, the fluid inclusion entrapment at low P and T corresponds to conditions of HC migration, but not to their generation.

FIPs document a high post-crystallisation permeability that accommodates high fluid flow. It is possible to envisage a situation in which abiogenically derived fluids migrate through the fracture system upwards within the complex and mix with biogenic fluids from the surrounding country rocks that migrate inwards through the same fracture system.

Acknowledgements

Financial support for this study was provided by INTAS grant 01-244. We gratefully acknowledge the discussions with Joanne Potter, Valentin Nivin and Hilary Downes. Serafim Ikorski and Anaida Avedisyan provided not only important gas composition data but also, together with Valentin Nivin, invaluable help during field work. Terry Williams is thanked for his careful help during the work on the Cameca microprobe. BB acknowledges a research studentship from Kingston University in support of the Geodynamics and Crustal Processes Research Group. We are also grateful to F. Wall and I. Veksler for their constructive review on the manuscript and to G. Markl for his helpful editorial comments.

References

Anderson, R.B., 1984. The Fischer-Tropsch Reaction. Academic Press, New York.

Beeskow, B., Rankin, A.H., Murphy, P.J., Treloar, P.J., 2005. Mixed CH_4–CO_2 fluid inclusions in quartz from the South Wales

Coalfield as suitable natural calibration standards for microthermometry and Raman spectroscopy. Chem. Geol. 223, 3–15.
Berndt, M.E., Allen, D.E., Seyfried, W.E., 1996. Reduction of CO_2 during serpentinization of olivine at 300 °C and 500 bar. Geology 24, 351–354.
Brown, W., Parsons, I., 1994. Feldspar in igneous rocks. In: Parsons, I. (Ed.), Feldspars and their Reactions. NATO ASI Series C, vol. 421. Kluwer Academic Publishers, Dordrecht, pp. 449–499.
Charlou, J.L., Fouquet, Y., Bougault, H., Donval, J.P., Etoubleau, J., Jean-Baptiste, P., Dapoigny, A., Appriou, R., Rona, P.A., 1998. Intense CH_4 plumes generated by serpentinization of ultramafic rocks at the intersection of the 15°20′N fracture zone and the Mid-Atlantic Ridge. Geochim. Cosmochim. Acta 62 (13), 2323–2333.
Des Marais, D.J., Donchin, J.H., Nehring, N.l., Truesdell, A.H., 1981. Molecular carbon isotopic evidence for the origin of geothermal hydrocarbons. Nature 292, 826–828.
Eggler, D.H., Baker, D.R., 1982. Reduced volatiles in the system C–O–H: implications to mantle melting, fluid formation, and diamond genesis. In: Akimoto, S., Manghnani, M.H. (Eds.), High-Pressure Research in Geophysics. Advances in Earth and Planetary Sciences, vol. 12. Center for Academic Publications, Tokyo, pp. 237–250.
Freedman, P.A., Gillyon, E.C.P., Jumeau, E.J., 1988. Design and application of a new instrument for GC-isotope ratio MS: American Laboratory, Fairfield, Connecticut, v. June 1988, 114–119.
Galimov, E.M., 1973. Izotopy ugleroda v neftegazovoy geologii (Carbon Isotopes in Petroleum Geology). Nedra, Moscow (in Russian).
Galimov, E.M., Petersilie, I.A., 1967. About carbon isotope composition hydrocarbon gases and CO_2 in alkaline igneous rocks of the Khibiny, Lovozero and Ilímaussaq massifs. Dokl. Akad. Nauk USSR 176, 914–917.
Gold, T., 1979. Terrestrial sources of carbon and earthquake outgassing. J. Petrol. Geol. 1 (3), 3–19.
Hassan, I., Grundy, H.D., 1983. Structure of basic sodalite, $Na_8Al_6Si_6O_{24}(OH)_2.2H_2O$. Acta Crystallogr., C Cryst. Struct. Commun. 39, 3–5.
Hayes, J.M., Freeman, K.H., Popp, N., Hoham, C.H., 1990. Compound-specific isotope analysis, a novel tool for reconstruction of ancient biochemical processes. Org. Geochem. 16, 1115–1128.
Huizenga, J.-M., 2001. Thermodynamic modelling of C–O–H fluids. Lithos 55, 101–114.
Ikorsky, S.V., 1977. About regularities of distribution and time of accumulation of hydrocarbon gases in rocks of the Khibiny alkaline massif. Geokhimiya 11, 1625–1634.
Ikorsky, S.V., 1999. Equipment for analysis of micro included gases extracted from rocks and minerals by crushing. TERRA NOSTRA, Schriften der Alfred–Wegener–Stiftung 99/6, ECROFI XV (European Current Research on Fluid Inclusions), Abstracts and Program. GeoForschungsZentrum Potsdam, Germany, pp. 153–154.
Kenney, J.F., Kutcherov, V.A., Bendeliani, N.A., Alekseev, V.A., 2002. The evolution of multicomponent systems at high pressures: VI. The thermodynamic stability of the hydrogen–carbon system: the genesis of hydrocarbons and the origin of petroleum. Proc. Natl. Acad. Sci. U. S. A. 99, 10976–10981.
Khitarov, N.I., Kravtsov, A.I., Voitov, G.I., Fridman, A.I., Ortenberg, G.A., Pavlov, A.S., 1979. gasui swobodneu wuidelenie Khibinskowo massiwa. Sovetskaya Geol. 2, 62–73 (in Russian).
Kogarko, L.N., 1995. Kola and Karelia. In: Kogarko, L.N., Kononova, V.A., Orlova, M.P., Wooley, A.R. (Eds.), The alkaline Rocks and Carbonatites of the World: Former U.S.S.R. Chapman & Hall, Natural History Museum, London.
Kogarko, L.N., Kosztolanyi, C., Ryabchikov, I.D., 1987. Geochemistry of the reduced fluid in alkali magmas. Geochim. Int. 24-7, 20–27.
Konnerup-Madsen, J., 2001. A review of the composition and evolution of hydrocarbon gases during solidification of the Ilímaussaq alkaline complex, South Greenland. Geol. Greenl. Surv. Bull. 190, 163–170.
Konnerup-Madsen, J., Dubessy, J., Rose-Hansen, J., 1985. Volatiles associated with alkaline igneous rift activity: fluid inclusions in the Ilímaussaq intrusion and the Gardar granitic complexes (South Greenland). Chem. Geol. 37, 79–93.
Kramm, U., Sindern, S., 2004. Timing of Kola ultrabasic, carbonatite and phoscorite–carbonatite magmatism. In: Wall, F., Zaitsev, A. (Eds.), Phoscorites and Carbonatites from Mantle to Mine: the Key Example of the Kola Alkaline Province. Mineralogical Society Book Series, vol. 10, pp. 75–97.
Krot, A.N., Posukhova, T.V., Guseva, Ye.V., Galimov, E.M., Botkunov, A.I., Ramenskaya, M.Ye., Oglobina, A.I., 1994. Origin of garnets containing hydrocarbon inclusions in the Mir Kimberlite Pipe. Geochem. Int. 31 (1), 122–130.
Larsen, R.B., Brooks, C.K., Bird, D.K., 1992. Methane-bearing, aqueous, saline solutions in the Skaergaard intrusion, East Greenland. Contrib. Mineral. Petrol. 112, 428–437.
Markl, G., Marks, M., Schwinn, G., Sommer, H., 2001. Phase equilibrium constraints in intensive crystallization parameters of the Ilímaussaq Complex, South Greenland. J. Petrol. 42 (12), 2231–2257.
Melezhik, V.A., Fallick, A.E., Filippov, M.M., Larsen, O., 1999. Karelian shungite — an indication of 2000 Ma-year-old metamorphosed oil-shale and generation of petroleum: geology, lithology and geochemistry. Earth-Sci. Rev. 47, 1–40.
Melezhik, V.A., Filippov, M.M., Romashikin, A.E., 2004. A giant Palaeoproterozoic deposit of shungite in NW Russia: genesis and practical applications. Pre Geol. Rev. 24, 135–154.
Nivin, V.A., 2002. Gas concentrations in minerals with reference to the problem of the genesis of hydrocarbon gases in rocks of the Khibiny and Lovozero massifs. Geochem. Int. 40, 883–898.
Nivin, V.A., Belov, N.I., Treloar, P.J., Timofeyev, V.V., 2001. Relationships between gas geochemistry and release rates and the geomechanical state of igneous rock massifs. Tectonophysics 336, 233–244.
Nivin, V.A., Treloar, P.J., Konopleva, N.G., Ikorsky, S.V., 2005. A review of the occurrence, form and origin of C-bearing species in the Khibiny Alkaline Igneous Complex, Kola Peninsula, NW-Russia. Lithos 85 (1–4), 93–112.
Olafsson, M., Eggler, D.H., 1983. Phase relations of amphibole, amphibole-carbonate, and phlogopite-carbonate peridotite: petrologic constraints on the asthenosphere. Earth Planet. Sci. Lett. 64, 305–315.
Orville, P.M., 1963. Alkali ion exchange between vapour and feldspar phases. Am. J. Sci. 261, 201–237.
Pasteris, J.D., 1987. Fluid inclusions in mantel xenoliths. In: Nixon, P.H. (Ed.), Mantle Xenoliths. John Wiley & Sons Ltd, Chichester.
Petersilie, I.A., 1960. Hydrocarbon gases and bitumens in intrusive massifs of the central Kola Peninsula. Acad. Sci. U.S.S.R. Izv., Geol. Ser. 1, 27–42.
Petersilie, I.A., 1962. Origin of hydrocarbon gases and disperse bitumens of the Khibiny alkalic massif. Geochem. Int. 1, 15–29.
Petersilie, I.A., Sørensen, H., 1970. Hydrocarbon gases and bituminous substances in rocks from the Ilímaussaq alkaline intrusion, South Greenland. Lithos 3, 59–76.

Petersilie, I.A., Ikorski, S.V., Smirnova, L.I., Romanikhin, A.M., Proskuryakova, E.B., 1961. Application of gas logging to the investigation of natural gases and bitumens in the Khibiny intrusive massif. Geochem. Int. 10, 945–962.

Potter, J., 2000. The characterisation and origin of hydrocarbons in alkaline rocks of the Kola alkaline province. PhD thesis, Kingston University, Kingston upon Thames, UK.

Potter, J., Konnerup-Madsen, J., 2003. A review of the occurrence and origin of abiogenic hydrocarbons in igneous rocks. In: Petford, N., McCaffrey, K.J.W. (Eds.), Hydrocarbons in Crystalline Rocks. Geol. Soc. Lond. Spec. Pub., vol. 214, pp. 151–173.

Potter, J., Rankin, A.H., Treloar, P.J., Nivin, V., Ting, W., Ni, P., 1998. A preliminary study of methane inclusions in alkaline igneous rocks of the Kola igneous province, Russia: implications for the origin of methane in igneous rocks. Eur. J. Mineral. 10, 1167–1180.

Potter, J., Rankin, A.H., Treloar, P.J., 2004. Abiogenic Fischer-Tropsch synthesis of hydrocarbons in alkaline igneous rocks: fluid inclusion, textural and isotopic evidence from the Lovozero complex, N.W. Russia. Lithos 75, 311–330.

Prinzhofer, A.A., Huc, A.Y., 1995. Genetic and post-genetic molecular and isotopic fractionations in natural gases. Chem. Geol. 126, 281–290.

Ryabchikov, I.D., Green, D.H., Wall, W.J., Brey, G.P., 1981. The oxidation state of carbon in the reduced-velocity zone. Geochem. Int. 2, 221–232.

Salvi, S., Williams-Jones, A.E., 1997. Fischer-Tropsch synthesis of hydrocarbons during sub-solidus alteration of the Strange Lake peralkaline granite, Quebec/Labrador, Canada. Geochim. Cosmochim. Acta 61, 83–99.

Schutter, S.R., 2003. Hydrocarbon occurrence and exploration in and around igneous rocks. In: Petford, N., McCaffrey, K.J.W. (Eds.), Hydrocarbons in Crystalline Rocks. Geol. Soc. London, Spec. Pub., vol. 214, pp. 7–33.

Scott, H.P., Hemley, R.J., Mao, H., Herschbach, D.R., Fried, L.E., Howard, W.M., Bastea, S., 2004. Generation of methane in the Earth's mantle: in situ high pressure-temperature measurements of carbonate reduction. PNAS 101-39, 14023–14026.

Shepherd, T.J., Rankin, A.H., Alderton, D.H.M., 1985. A Practical Guide to Fluid Inclusion Studies. Blackie, London.

Sherwood-Lollar, B., Westgate, T.D., Ward, J.A., Slater, G.F., Lacrampe-Couloume, G., 2002. Abiogenic formation of alkanes in the earth's crust as a minor source for global hydrocarbon reservoirs. Nature 416, 522–524.

Simon, K., 2001. Does δD from fluid inclusion in quartz reflect the original hydrothermal fluid? Chem. Geol. 177, 483–495.

Sokolov, S.V., Chukanov, N.V., in press. Solid organic substances in pegmatites and hydrothermalites of the alkaline complexes Khibiny and Lovozero (Kola Peninsula, Russia), unpublished manuscript.

Sørensen, H., 1970. Internal structures and geological settings of the three agpaitic intrusions — Khibiny and Lovozero of the Kola Peninsula and Ilímaussaq, South Greenland. Can. Mineral. 10 (3), 299–334.

Sugisaki, R., Mimura, K., 1994. Mantle hydrocarbons: abiotic or biotic? Geochim. Cosmochim. Acta 58, 2527–2542.

Van den Kerkhof, A.M., 1988. The system CO2–CH_4–N_2 in fluid inclusions: theoretical modelling and geological applications. Ph.D. thesis, Vrije Universiteit Amsterdam, The Netherlands.

Voitov, G.I., 1992. Chemical and carbon-isotope fluctuations in free gases (gas jets) in the Khibiny. Geochem. Int. 14–24.

Voitov, G.I., Adushkin, W.W., Hochberg, M.B., Nosik, L.P., Kutscher, M.I., Nikulina, I.W., Puschkin, M.G., Schogina, L.M., 1990. O chimitschesskoi I isotopnoi nectawjilnostjak gasowuik strui b khibinak. Dokl. Akad. Nauk SSSR 312 (3), 567–571 (in Russian).

Whiticar, M.J., 1999. Carbon and hydrogen isotope systematics of bacterial formation and oxidation of methane. Chem. Geol. 161, 291–314.

Yakovenchuk, V.N., Ivanyuk, G.J., Pahomovsky, Ya.A., Men'shikov, Yu.P., 1999. Minerals of the Khibiny Massif. Zemlya, Moscow, 326 pp. (in Russian).

Yerokhin, V.Y., 1978. Yadernaya geologiya (Nuclear geology). Izd. OTI VNIIYaGG, Moscow, p. 47 (in Russian).

11 Conclusions

11.1 Aim of the study

The discovery of significant volumes of hydrocarbon gas in the Khibiny alkaline complex (Petersilie, 1962) confirmed by many later studies (e.g. Ikorski, 1977; Kogarko *et al.*, 1987; Ikorski *et al.*, 1992; Potter, 2000; Nivin, 2001) has generated much interest in the possibility of natural gas resources being produced and subsequently stored in igneous rocks, especially alkaline ones.

In this study, abundant new data from the Khibiny pluton are presented and discussed in the context of previously published data in order to reassess proposed models of hydrocarbon generation in alkaline igneous rocks. In the course of this work, a variety of conventional and innovative methods and techniques have been combined to constrain some primary characteristics of the hydrocarbon phases present in the Khibiny pluton. Of particular importance has been the use of widely spaced sampling locations to assess the spatial distribution of hydrocarbons in the Khibiny complex. The comprehensive nature of the collected data enables a re-evaluation of the processes influencing hydrocarbon generation, storage and movement in the Khibiny pluton. The new insights developed here might serve as a base for the future investigation of hydrocarbon occurrences in alkaline igneous rock complexes elsewhere in the world.

The main aims of the work can be summarised as:

- constraining the distribution and volume of hydrocarbons stored in the Khibiny pluton
- testing models for hydrocarbon generation
- modelling storage and migration of hydrocarbon gases within the pluton.

11.2 Brief summary of data

There are two main models for hydrocarbon generation in alkaline plutons:

- biogenic evolution largely through incorporation of methane from an organic-rich source in the country rocks and
- abiogenic evolution, which can be mantle-derivation, late-magmatic C-O-H respeciation and post-magmatic Fischer-Tropsch synthesis.

The data obtained for this thesis enable the models for hydrocarbon generation in alkaline igneous rocks to be tested for the Khibiny complex. The results can be summarised as follows.

Petrography

- typical felsic minerals are nepheline and alkali feldspar
- the main mafic minerals are aegirine, arfvedsonite, aenigmatite and titanite
- alteration of mafic minerals is limited and not related to fluid inclusion generation

Fluid inclusion study

- fluid inclusions appear as either primary or secondary fluid inclusions
- c. 90% are methane-dominant and c. 10% water-dominant
- primary inclusions were entrapped near the nepheline syenite solidus, at P-T conditions around 650 MPa and 600°C
- secondary fluid inclusions were entrapped at wide-ranging post-magmatic P-T conditions as miscible or immiscible fluids
- melt inclusions contain a methane-dominant fluid phase, supporting a primary magmatic origin of the fluids

Bulk gas data

- the average bulk gas content is 12.8 cm^3/kg rock
- methane is the dominant gas species
- lower concentrations of the higher hydrocarbons up to pentane were detected
- bulk gas content correlates positively with nepheline content
- the spatial gas distribution shows highest concentrations in the marginal area of the pluton, implying potential addition of hydrocarbons from the host rocks

Solid carbon

- solid carbon content ranges between 0.209 and 0.058 wt% and is highest near the pluton margins
- it is the product of either late- to post-magmatic hydrocarbon respeciation or thermogenic alteration of organic matter derived from the host rocks

Isotope data

- $\delta^{13}C_{CH4}$ values between -22.4 and -5.4 ‰ indicate a likely abiogenic methane origin
- the spatial distribution, with decreasing $\delta^{13}C$ values towards the pluton margin, suggests a potential mixing of biogenic CH_4 derived from the host rocks with abiogenic methane from within the pluton
- mass balance calculations suggest that up to 64 % of the mixed CH_4 may have a biogenic origin

The role of microcracks and fluid inclusion planes

- high abundance of fluid inclusion planes and microcracks indicates high fluid mobility in both the past and the present
- microcracks serve as the main fluid pathways and storage spaces in igneous rocks and can be used to calculate porosity and permeability

- average palaeo and modern porosities are 5.56 % and 4.80 %, respectively
- average palaeo and modern permeabilities are 2.38 mD and 1.95 mD, respectively
- the methane content in the Khibiny pluton, based on porosity values, is estimated to be between 416 km³ and 7649 km³

11.3 Towards a new model for hydrocarbon generation in the Khibiny Mountains

Based on the above summarised data, the following conclusions can be drawn.

A primary abiogenic origin for the hydrocarbons present in the Khibiny pluton is supported by the documented presence of primary methane-dominant fluid inclusions, melt inclusions that contain a methane-rich gas phase and the isotopic composition of CH_4. There is little evidence for either a late- or post-magmatic hydrocarbon generation. There is no clear linkage between hydration reactions and the evolution of fluid inclusion planes nor are relicts of primary CO_2 fluids preserved in the rocks as would be expected had such mechanisms failed to go to completion.

→ A MANTLE-DERIVED, REDUCED CARBONIC FLUID IS THEREFORE LIKELY TO BE THE MAJOR SOURCE FOR HYDROCARBON GASES IN THE KHIBINY COMPLEX.

The spatial distribution data document a high carbon content, high CH_4 levels and low $\delta^{13}C$ values in the outermost parts of the Khibiny complex. This is consistent with a high permeability permitting inward flow of fluids carrying biogenic carbon.

→ A MARGINAL BIOGENIC OVERPRINT CAUSED BY INWARDS MIGRATING FLUIDS FROM THE SURROUNDING COUNTRY ROCKS IS LIKELY.

11.4 The Khibiny pluton in the context of hydrocarbon occurrences in igneous rocks

In many cases the exact origin of hydrocarbons in igneous rocks remains unclear. Methane and higher-order hydrocarbons have been reported from several igneous complexes. A comprehensive list of hydrocarbon occurrences associated with igneous rocks was given by Schutter (2003).

Notable hydrocarbon occurrences explained using abiogenic models include those found in the Ilímaussaq igneous complex (South Greenland), in granite and dolerite intrusions at Siljan (Sweden), in the Zambales Ophiolite (Philippines), in pegmatitic quartz in granite at Strange Lake (Canada), in alkaline igneous intrusions of the Kola igneous province (Russia), in fractures in crystalline rocks of the Canadian shield and at Mid-Ocean Ridges (e.g. Konnerup-Madsen et al., 1979; Abrajano et al., 1988; Jeffrey and Kaplan, 1988; Salvi and Williams-Jones, 1997; Charlou et al., 1998; Potter et al., 1998; Sherwood Lollar et al., 2002;).

In contrast, numerous other hydrocarbon occurrences in igneous rocks have been interpreted as being biogenic in origin. Hydrocarbons in several granite plutons in the British Isles have been attributed to scavenging of thermally decomposed organic material held in overlying sedimentary source rocks (Parnell, 1988). Solid bitumens within a dolerite dyke at Oklo in Gabon (Mossman et al., 2001) were similarly interpreted as the products of oil migration from surrounding sedimentary rocks. Bitumens in basement rocks in Scandinavia, gas-condensate inclusions in the crystalline basement in South Norway and solid bitumens and oil-bearing fluid inclusions in a dolerite sill in the Roper Superbasin in Australia have also been interpreted as being biogenic in origin (Munz et al., 2002; Dutkiewicz, 2004).

Until now, there have been no reported instances of mixed-source hydrocarbons in igneous rocks. These are those in which biogenic fluids, derived from organic-rich host rocks, mix with primary magmatic abiogenic fluids. Although this scenario is a likely one, albeit dependant on geological setting, it is probably largely undescribed due to sampling strategies. To document such a mixing model it is necessary to sample, and analyse, fluids along a traverse from pluton core to rim as has been done during the course of this study.

11.5 Economic potential and ecological significance

Estimates on gas volume made here, based largely on porosity data, range from 416 km^3 to 7649 km^3. What is known from degassing processes in working mines (Nivin et al. 2001) suggests that opening of fracture systems indeed leads to significant gas escape. However, the hydrocarbon reservoir of the Khibiny pluton cannot be regarded today as an economically viable resource. Primarily this is because there are no currently known appropriate techniques for gas extraction and collection from the pluton. Secondly, there remains real uncertainty as to how much methane is present in the complex and the extent to which it is held in connected, or potentially connected, microcrack systems. Therefore it is necessary to enhance both extraction techniques and fracture modelling.

From an environmental stand-point the knowledge of gas content and gas mobility potential is relevant for two reasons. Firstly, a detailed understanding on influencing parameters for hydrocarbon occurrence and distributions is important with respect to safety during underground mining. This knowledge might also be a useful tool during prospective risk assessments to minimize possible explosive failure caused by methane over-pressure. Secondly, degassing of hydrocarbons through the roof of the Khibiny

complex contribute to greenhouse gases. However, this contribution is rather small. The average bulk gas content in one kg rock of the Khibiny pluton is 12.8 cm^3. To put this in to perspective a simple comparison may help: one sheep produces daily approximately 20 litre (20,000 cm^3) methane (Lockyer and Champion, 2001). There are more than a billion sheep kept in the world (http://www.sheep101.info/farm.html) and other ruminants, including cows, similarly produce large daily methane outputs. These volumes must dwarf that released by upward migration through the pluton roof and thus the methane currently stored within the Khibiny pluton cannot be regarded as environmentally significant.

11.6 Recommendation for further work

1. The prime aim of this study was to test the hypothesis of hydrocarbons origin in the Khibiny complex. The textural, fluid inclusion and isotopic data presented here indicate that the methane present in the alkaline rocks at Khibiny are the result of mixing variable degrees of mantle-derived methane and organic methane introduced into the pluton from the host rocks. This new model needs to be rigorously tested. To do this, future work should aim to analyse material from a wide range of rock types collected from across the pluton. Further studies should include bulk-rock analysis, the examination of free gas and gas trapped in fluid inclusions as well as a rigorous isotopic study. The aim would be to develop a spatial map of hydrocarbon distribution and characteristics. As part of this work the distribution and isotope chemistry of biomarkers in bitumens contained within the pluton should be investigated. This work should enable modelling of mixing signatures across the pluton.

2. As this study shows, the respective ratios of the various higher hydrocarbons cannot alone provide a clear indicator of gas origin – biogenic or abiogenic. In

order to verify the origin of the gas, or its mechanism of generation, a comprehensive isotope study is recommended. The present study provides a limited, yet valuable, carbon and hydrogen database. Future work should include the derivation not only of more carbon and hydrogen isotopic data but also of helium isotope data. Helium isotope signatures in particular would help define the extent to which the gas is of mantle origin.

3. Gas extraction from igneous rocks is still very problematic. This affects both the quality of the bulk gas data and also the isotope data derived from the extracted gas. The methods of gas extraction tested here (crushing and thermal gas release) provide different quantitative data. The grain size of the prepared samples may also affect the analytical data. A comprehensive study of gas extraction techniques is required in order to verify if and how temperature affects the composition of the extracted gas as well as to determine how much gas gets lost during sample preparation or by adsorption to fine-grained particle surfaces during milling.

4. A GIS-based, internet-accessible data-base should be compiled for gas distribution data of the Khibiny pluton. Simple access to all scientists working in the Khibiny pluton would save money and time and help resolve problems where different scientific, technological and engineering disciplines interact.

References

Abrajano, T.A., Sturchio, N.C., Bohlke, J.K., Lyon. G.L., Poreda, R.J., Stevens, C.M., 1988. Methane-hydrogen gas seeps, Zambales Ophiolite, Philippines: deep or shallow origin? Chem. Geol. 71, 211-222.

Abrajano, T.A., Sturchio, N.C., Kennedy, B.M., Lyon. G.L., Muehlenbachs, K., Bohlke, J.K., 1990. Geochemistry of reduced gas related to serpentinisation of the Zambales Ophiolite, Philippines. Appl. Geol. 5, 625-630.

Alderton, D.H.M., Oxtoby, N., Brice, H., Grassineau, N. and Bevins, R.E. 2004. The Link Between Fluids and Rank Variation in the South Wales Coalfield: Evidence from Fluid Inclusions and Stable Isotopes, Geofluids 4, Blackwell Publishing Ltd., pp. 221–236.

Andersen, T. and Burke, E.A., 1996. Methane inclusions in shocked quartz from the Gardnos breccia, South Norway. Eur. J. Min. 8, 927-936.

Anderson, R.B., 1984. The Fischer-Tropsch synthesis. Academic Press, New York, pp. 301.

Arzamastsev, A.A., Glaznev, V.N., Raevsky, A.B., Arzamastseva, L.V., 2000. Morphology and internal structure of the Kola Alkaline intrusion, NE Fennoscandian Shield: 3D density modelling and geological implications. Journal of Asian Earth Sciences 18: 213-228.

Bakker R.J. and Jansen, J.B.H., 1994. A mechanism for preferential H_2O leakage from fluid inclusions in quartz, based on TEM observations, Contrib. Mineral. Petrol. 116, 7–16.

Bakker, R.J., 1999. Adaption of the Bowers & Helgeson (1983) equation of state to the H_2O-CO_2-CH_4-N_2-NaCl-system. Chem Geol. 154, 225-236.

Bakker, R.J., 2003. Package FLUIDS 1. Computer programs for analysis of fluid inclusion data and for modelling bulk fluid properties. Chem. Geol. 194, 3-23.

Balaganskaya, Ye., G., Pripachkin, V.A., 1994. Petrological and geochemical features of breccias at the Khibiny apatite-nepheline deposits. Geochem. Int. 31(3), 123-142.

Beeskow, B., Rankin, A.H., Murphy, P.J. and Treloar, P.J., 2005. Mixed CH_4–CO_2 fluid inclusions in quartz from the South Wales Coalfield as suitable natural calibration standards for microthermometry and Raman spectroscopy. Chem. Geol. 223, 3–15.

Berndt, M.E., Allen, D.E. and Seyfried, W.E., 1996. Reduction of CO_2 during serpentinization of olivine at 300°C and 500 bar. Geology 24, 351-354.

Bodnar, R. J. and Vityk, M.O., 1994. Interpretation of microthermoetric data for H_2O-NaCl fluid inclusions. In: De Vivo, B. and Frezzotti, M.L. (Eds.), 1994. Fluid inclusions in minerals: methods and applications. Short course of the working group "Inclusions in minerals", Siena, 117-130.

Boullier, A-M., Firdaous, K. and Boudier, F., 1997. Fluid circulation related to deformation in the Zabargad gneisses (Red Sea rift). Tectonophysics 279, 281-302.

Bowers, T.S. and Helgeson, H.C., 1983. Calculation of the thermodynamic and geochemical consequences of nonideal mixing in the system H_2O-CO_2-NaCl on phase relations in geologic systems: Equation of state for H_2O-CO_2-NaCl fluids at high pressures temperatures. Geochim. Cosmochim. Acta, 47, 1247-1275.

Boullier, A-M., 1999. Fluid inclusions: tectonic indicators. Journal of Structural Geology 21, 1229-1235.

Brace, W.F., 1980. Permeability of crystalline and argillaceous rocks. Int. J. Rock Mech. Min. Sci., 17, 241-251.

Brace, W.F., 1984. Permeability of crystalline rocks: new in situ measurements. Journal of geophysical research 89-B6, 4327-4330.

Brantley, S.L., Evans, B., Hickman, S.H., Crerar, D.A., 1990. Healing of microcracks in quartz: implications for fluid flow. Geology 18, 136-139.

Brèas, O., Guillou, C., Reniero, F., Wada, E., 2001. The global methane cycle: isotopes and mixing ratios, sources and sinks. In: Krumbiegel, P. (Ed.). Isotopes in environmental and health studies, Vol. 37 (4), 257-380.

Brown, W. and Parsons, I., 1994. Feldspar in igneous rocks. In: Parsons, I. (Ed). Feldspars and their reactions. 449-499.NATO ASI Series, C 421, Kluwer Academic Publishers, Dordrecht, 449–499.

Burke, E.A.J., 2001. Raman microspectometry of fluid inclusions. Lithos 55, 139–158.

Burruss, R.C., 1992. Phase behaviour in petroleum-water (brine) systems applied to fluid inclusion studies (abstract) PACROFI IV, Lake Arrowhead, CA, Vol 4, 116-118.

Cartigny, P., 2005. Stable isotopes and the origin of diamond. Elements 1, 79-84.

Castano, J.R., 1988. Geochemical studies, Gravberg-1 Well, Sweden; integration of well site and external laboratory analyses. In: Boden, A. and Eriksson, K.G. (Eds.). Deep Drilling in Crystalline Bedrock, Vol 1, Springer-Verlag, New York, 122-133.

Cesare. B., 1995. Graphite precipitation in C-O-H fluid inclusions: closed system compositional and density changes, and thermobarometric implications. Contrib. Mineral. Petrol. 122, 25-33.

Chalmers, J.M. and Griffiths, P.R., 2002. Handbook of vibrational spectroscopy. Applications in Industry, Materials and the Physical Science Vol. 4, John Wiley and Sons Ltd., Chichester, 2594–2598.

Charlou, J.L., Fouquet, Y., Bougault, H., Donval, J.P., Etoubleau, J., Jean-Baptiste, P., Dapoigny, A., Appriou R. and Rona, P.A., 1998. Intense CH_4 plumes generated by serpentinization of ultramafic rocks at the intersection of the 15°20′N fracture zone and the Mid-Atlantic Ridge, Geochim. Cosmochim. Acta 62 (13), 2323–2333.

Chen, Z., Yan, H., Li, J., Zhang, G., Zhang and Liu, B., 1999. Relationship between Tertiary volcanic rocks and hydrocarbons in the Liaohe Basin, People's Republic of China. AAPG Bulletin 83, 1004-1014.

Chou, I.-M., Pasteris J.D., and Seitz, J.C., 1990. High-density volatiles in the system C–O–H–N for the calibration of a laser Raman microprobe, Geochim. Cosmochim. Acta 54, 535–543.

Cicerone, R.J. and Oremland, R.S., 1988. Biogeochemical aspects of atmospheric methane. Global Biogeochem. Cycles 2 (4), 299-327.

Correns, C.W., 1953. Flüssigkeitseinschlüsse mit Gasblasen als geologische Thermometer: Geol. Rundschau 42, 19-34.

Correns, C.W., 1954. Mineral emit Fluessigkeitseinschlüssen. Aufschluss 5 (3), 46-47.

Darling, W.G., 1998. Hydrothermal hydrocarbon gases: 2, Application in the East African Rift system. Applied Geochemistry 13 (7), 825-840.

Deer, W.A., Howie, R.A. and Zussman, J., 1992. An introduction to the rock forming minerals. 2nd ed. Pearson Prentice Hall, Harlow, pp. 696.

Deicha, G., 1950. Resultate einer neuen Forschungs-Methode an flüssigen Einschlüssen: Schweizer. Min. Pet. Mitteilungen 30, 495-496.

Deines, P., 1986. The isotopic composition of reduced organic carbon. In: Fritz, P and Fontes, J.-C. (Eds.). Handbook of environmental isotope geochemistry. 2B, 329-393.

Deines,P., 2002. The carbon isotope geochemistry of mantle xenoliths. Earth Scince Reviews, 58 (3-4), 247-278.

Des Marais, D. J., Donchin, J. H., Nehring, N.l. and Truesdell, A.H., 1981. Molecular carbon isotopic evidence for the origin of geothermal hydrocarbons. Nature 292, 826-828.

Des Marais, D.J., 1985. Carbon exchange between the mantle and crust and its effect upon the atmosphere: today compared to Archaean time. In: Sundquist E.T. and Broecker, W.S. (Eds.). The Carbon Cycle and Atmospheric CO_2: Natural Variations Archaean to Present. American Geophysical Union, Washington, DC, 602-611.

Desindes, L., Fratczak, P., Lespinasse, M. and Leroy, J., 2003. AnIma: an image analysis program for discontinuities mapping. Acta Mineralogica-Petrographica, Abstract Series 2, Szeged. 48-49.

Droop, G.T.R., 1987. A general equation for estimating Fe^{3+} concentrations in ferromagnesian silicates and oxides from microprobe analyses, using stoechiometric criteria. Min. Mag. 51, 431.435.

Dubessy, J., Poty B. and Ramboz, C., 1989. Advances in C–O–H–N–S fluid geochemistry based on micro-Raman spectrometric analysis of fluid inclusions, Eur. J. Mineral. 1, 517–534.

Dubessy, J., 1994. Single component systems: phase diagrams and their application to fluid inclusions. In: De Vivo, B. and Frezzotti, M.L. (Eds.). Fluid inclusions in minerals: methods and applications. Short course of the working group "Inclusions in minerals", Siena, 95-116.

Dudkin, O.B. and Mitrofanov, F.P., 1994. Features of the Kola Alkali Province. Geochim. Int. 31(3), 1-11.

Dudkin O.B., 2001 On the alkaline plutones ore bearing problem. In: Geology of Mineral Resources of the Kola Region Proceedings of the MSTU, Vol. 3 (2), 299-306 (in Russian).

Dutkiewicz, A., Volk, H., Ridley J. and George S. C., 2004. Geochemistry of oil in fluid inclusions in a middle Proterozoic igneous intrusion: implications for the source of hydrocarbons in crystalline rocks. Org. Geochem. 35(8), 937-957.

Edgar, A.D. and Parker, A.M., 1974. Comparison of melting relationships of some plutonic and volcanic peralkaline undersaturated rocks, Lithos 7, 263-273.

Eggler, D. H., and D. R. Baker, 1982. Reduced volatiles in the system C-O-H: implications to mantle melting, fluid formation, and diamond genesis. In: Akimoto S. and Manghnani, M. H. (Eds.). High-Pressure Research in Geophysics. Advances in Earth and Planetary Sciences 12, Tokyo, 237-250.

Ermakov, N.P., 1944. Determination of temperatures of formation of hydrothermal minerals by studying liquid inclusions. Acad. Sci. URSS Compte rendu 45 (5), 202-204.

Ermakov, N.P., 1966. Use of gas-liquid inclusions in prospecting and exploration for postmagmatic ore deposits and blind ore bodies. Int. Geology Rev. 9-7, 947-956.

Freedman, P.A., Gillyon, E.C.P. and Jumeau, E.J., 1988. Design and application of a new instrument for GC-isotope ratio MS: American Laboratory, Fairfield, Connecticut, 114–119.

Frenkel, M.Y. and Khapayev, V.V., 1990. A convective cumulation model of crystallization differentiation of the melt and formation of the apatite deposits in the Khibiny ijolite-urtite intrusion. Geochem. Int. 27(4), 101-112.

Früh-Green, G.L., Connolly, J.A.D. and Plas, A., 2004. Serpentinization of oceanic peridotites: implications for geochemical cycles and biological activity. In: The Subseafloor Biosphere at Mid-Ocean Ridges, Geophys. Monograph Series 144. Am. Geophys. Union.

Fu, B., Zheng, Y.-F. and Touret, J.L.R., 2002. Petrological, isotopic and fluid inclusion studies of eclogites from Sujiahe, NW Dabie Shan (China). Chem. Geol. 187 (1-2), 107-128.

Fuex, A.N., 1980. Experimental evidence against an appreciable isotopic fractionation of methane during migration. In: Douglas, A.G. and Maxwell, J.R. (Eds). Advances in organic geochemistry, Pergamon, Oxford, 725-732.

Galakhov, A.V., 1975. The petrology of the Khibiny alkaline massif. Izdatelstvo Akademii Nauk SSSR, Kola Branch, Leningrad, pp. 256.

Galimov, E.M. and Petersilie, I.A., 1967. Isotopic composition of carbon and hyfrocarbon gases and CO_2 held in alkalic igneous rocks of the Khibiny, Lovozero and Ilímaussaq plutons. Dokladi Akademii Nauk SSSR 176, 914-917.

Galimov, E.M., 1967. A ^{13}C isotope enrichment effect in methane carbon in the course of its filtration through rocks. Geochem. Int. 4, 1180-1181.

Galimov, E.M., 1973. Izotopy ugleroda v neftegazovoy geologii (Carbon Isotopes in Petroleum Geology), Nedra, Moscow (in Russian).

Galimov, E.M., 1988. Sources and mechanisms of formation of gaseous hydrocarbons in sedimentary rocks. Chem. Geol. 71, 77-95.

Gerlach, T.M., 1980. Chemical characteristics of the volcanic gases from Nyiragongo Lava Lake and the generation of CH_4-rich fluid inclusions. Journal of Volcanic and Geothermal Research 8, 177-189.

Glasby, G.P., 2006. Abiogenic origin of hydrocarbons: An historical overview. Resource Geology 56, 83-96.

Gold, T., 1979. Terrestrial sources of carbon and earthquake outgassing, J. Petrol. Geol. 1 (3), 3–19.

Goldstein R. and Reynolds, T.J., 1994. Systematics of fluid inclusions in diagenetic minerals. SEPM Short Course 31, pp 199.

Guedes, A., Noronha, F., Carmelo Pieto, A., 2005. Characterisation of dispersed organic matter from lower Palaeozoic metasedimentary rocks by organic petrography, X-ray diffraction and micro-Raman spectroscopy analyses. Int. Jour. of Coal Geology 62, 237-249.

Gueguen, Y. and Dienes, J., 1989. Transport properties of rocks from statistics and percolation. Math. Geol. 21-1, 1-13.

Gunter, B.D., 1971. Isotope fractionation during gas chromatographic separations. Jour. Chromat. Sci. 9, 191-194.

Hall, D.L., Bodnar, R.J., and Craig, J.R., 1991. Experimental diffusion of hydrogen into synthetic fluid inclusions in quartz. Metamorphic Geology 13, 345–355.

Hall, D.L. and Sterner, S.M., 1993. Preferential water loss from synthetic fluid inclusions. Contrib. Mineral. Petrol. 114, 489–500.

Hanor, J.S., 1980. Dissolved methane in sedimentary brines: potential effect on the PVT properties of fluid inclusions. Economic Geology 75, 603-609.

Hassan, I. and Grundy, H.D., 1983. Structure of basic sodalite, $Na_8Al_6Si_6O_{24}(OH)_2.2H_2O$, Acta Crystallogr., C Cryst. Struct. Commun. 39, 3–5.

Hayes, J.M., Freeman, K.H., Popp, N. and Hoham, C.H., 1990. Compound-specific isotope analysis, a novel tool for reconstruction of ancient biochemical processes, Org. Geochem. 16, 1115–1128.

Hollister, L.S., 1990. Enrichment of CO_2 in fluid inclusions in quartz by removal of H_2O during crystal-plastic deformation. J. Struct. Geol. 12, 895-901.

Holloway, J.R., 1984. Graphite-CH_4-H_2O-CO_2 equilibria at low grade metamorphic conditions, Geology 12, 455-458.

Holm. N.G. and Charlou, J.L., 2001. Initial indications of abiotic formation of hydrocarbons in the Rainbow ultramafic hydrothermal system, Mid-Atlantic Ridge. Earth and Planetary Science Letter 191, 1-8.

Horita, J. and Berndt, M.E., 1999. Abiogenic methane formation and isotopic fractionation under hydrothermal conditions. Science 285: 1055-1057.

Horita, J., 2001. Carbon isotope exchange in the system CO_2-CH_4 at elevated temperatures. Geochim. Cosmochim. Acta 65 (12), 1907-1919.

Huizenga, J-M., 2001. Thermodynamic modelling of C-O-H fluids. Lithos 55, 101-114.

Hunt, J.M., 1995. Petroleum Geochemistry and Geology. W.H. Freeman and Company, New York, pp. 743.

Hurai, V., Kihle, J., Kotulová, J., Marko, F. and Swierczewska, A., 2002. Origin of methane in quartz crystals from the Tertiary accretionary wedge and fore-arc basin of the western Carpathians. Appl. Geochem. 17, 1259–1271.

Ikorsky S.V., 1965. Gas-liquid and gas inclusions in nepheline from alkaline rocks in the Khibiny massif. In: Mineralogical Thermometry and Barometry. Nauka, Moscow, 233- 237 (in Russian).

Ikorsky, S.V., 1977. About regularities of distribution and time of accumulation of hydrocarbon gases in rocks of the Khibiny alkaline massif. Geokhimiya 11, 1625-1634.

Ikorski, S.V., 1991. Hydrocarbon gases in alkali intrusions. Geochem. Int. 28(6), 17-23.

Ikorsky, S.V., Nivin, V.A. and Pripatschkin, V.A., 1992. Geochimiya gasov, endogenui obrasovanii. Russ. Acad. Nauk, Sankt Petersburg., Petrology 4, 209-220 (in Russian).

Ikorsky, S.V., 1999. Equipment for analysis of micro included gases extracted from rocks and minerals by crushing, TERRA NOSTRA, Schriften der Alfred–Wegener–Stiftung 99/6, ECROFI XV (European Current Research on Fluid Inclusions), Abstracts and Program, GeoForschungsZentrum Potsdam, Germany, 153–154.

Jawhari, T., Roid, A. and Casado, J., 1995. Raman spectroscopic characterization of some commercially available carbon black materials Carbon 33 (11), 1561-1565.

Jeffrey, A.W.A. and Kaplan, I.R., 1988. Hydrocarbons and inorganic gases in the Gravenberg-1 well, Siljan Ring, Sweden. Chem. Geol. 71. 237-255.

Jenden P. D., Hilton D. R., Kaplan I. R. and Craig H., 1993. Abiogenic hydrocarbons and mantle helium in oil and gas fields. In: Howell, D.G. (Ed.). The Futureof Energy Gases - USGS Professional Paper 1570, United States Geological Survey, 57–82.

Jun, Y. 2004. A review of kinetics for Fischer-Tropsch synthesis. CJI Vol. 6-4, http://www.chemistrymag.org/cji/2004/064027re.htm.

Kamenev, E.A., 1987. Exploration, prospecting and appraisal of apatite deposits of the Khibiny type. Leningrad, Nedra, pp. 189.

Kelley,D.S., 1996. Methane-rich fluids in the oceanic crust. J. Geophys. Res. 101, 2943-2962.

Kenney, J.F., Kutcherov, V.A., Bendeliani, N.A. and Alekseev, V.A., 2002. The evolution of multicomponent systems at high pressures: VI. The thermodynamic

stability of the hydrogen–carbon system: the genesis of hydrocarbons and the origin of petroleum, Proc. Natl. Acad. Sci. U. S. A. 99 , 10976–10981.

Kerrich, R., 1976. Some effects of tectonic recrystallisation on fluid inclusions in vein quartz, Contrib. Mineral. Petrol. 59, 195–202.

Kesler, S.E., Vennemann, T.W., Frederickson, C., Breithaupt, A., Vazquez, R. and Furman, F.C., 1997. Hydrogen and oxygen isotope evidence for origin of MVT-forming brines, southern Appalachians. Geochim. Cosmochim. Acta 61 (7), 1513-1523.

Khapayev, V.V. and Kogarko, L.N., 1987. Composition of rock-forming minerals in the Khibiny apatite-bearing intrusion and the origin of the apatite deposits. Geochem. Int. 24 (12), 21-32.

Khitarov, N.I., Kravtsov, A.I., Voitov, G.I., Fridman, A.I., Ortenberg, G.A. and Pavlov, A.S., 1979. Gasui swobodneu wuidelenie Khibinskowo massiwa. Sovetskaya Geologiya 2, 62-73 (in Russian).

Kisch, H.H. and Van den Kerkhof, A.M., 1991. CH_4-rich inclusions from quartz veins in the Valley-and-Ridge province and the anthracite fields of the Pennsylvania Appalachians, Am. Mineral. 76 (1991), 230–240.

Kleinrahm, R. and Wagner, W., 1986. Measurement and correlation of the equilibrium liquid and vapour densities and the vapour pressure along the coexistence curve of methane, J. Chem. Thermodyn. 18, 739–760.

Kogarko, L.N. and Romanchev, B.P., 1982. Phase equilibria in alkaline melts. Internat. Geology Rev. 25(5), 534-546.

Kogarko, L.N., Kosztolanyi, C. and Ryabchikov, I.D., 1987. Geochemistry of the reduced fluid in alkali magmas. Geochim. Int. 24 (7), 20-27.

Kogarko, L.N., 1995. Kola and Karelia. In: Kogarko, L.N., Kononova, V.A., Orlova, M.P., Wooley, A.R. (Eds.). The alkaline Rocks and Carbonatites of the World: Former U.S.S.R. Chapman & Hall, Natural History Museum, London, 10-45.

Konnerup-Madsen, J, Larsen, E. and Rose-Hansen, J., 1979. Hydrocarbon-rich fluid inclusions in minerals from the alkaline Ilímaussaq intrusion, South Greenland. Bulletin de Mineralogie 102, 642-653.

Konnerup-Madsen, J. and Rose-Hansen, J., 1982. Volatiles associated with alkaline igneous rift activity: Fluid inclusions in the Ilímaussaq intrusion and the Gardar granitic complexes (South Greenland). Chem. Geol. 37, 79-93.

Konnerup-Madsen, J., Dubessy, J. and Rose-Hansen, J., 1985. Volatiles associated with alkaline igneous rift activity: fluid inclusions in the Ilímaussaq intrusion and the Gardar granitic complexes (South Greenland), Chem. Geol. 37, 79–93.

Konnerup-Madsen, J., Kreulen, R., Rose-Hansen, J., 1988. Stable isotope characteristics of hydrocarbon gases in the alkaline Ilímaussaq complex, south Greenland. Bull. Mineral. 106, 642-653.

Konnerup-Madsen, J., 2001. A review of the composition and evolution of hydrocarbon gases during solidification of the Ilímaussaq alkaline complex, South Greenland, Geol. Greenl. Surv. Bull. 190, 163–170.

Korobeinikov, A.N., Laajoki, K. and Gehör, S., 2000. Nepheline-bearing alkali feldspar syenite (pulaskite) in the Khibiny pluton, Kola Peninsula, NW Russia: petrological investigation. Journal of Asian Science 18, 205-212.

Kramm U., Kogarko, L.N., Kononova, V.A., Vartiainen, H., 1993. The Kola Alkaline Province, CIS/Finland: Precise Rb-Sr ages define 380-360 Ma range of all magmatism. Lithos 30, 33-44.

Kramm, U. and Kogarko, L.N., 1994. Nd and Sr osotope signatures of the Khibina and Lovozero agpaitic centres, Kola Alkaline Province, Russia. Lithos 32, 225-242.

Kramm, U. and Sindern, S., 2004. Timing of Kola ultrabasic, carbonatite and phoscorite–carbonatite magmatism. In: F. Wall and A. Zaitsev (Eds). Phoscorites and Carbonatites from Mantle to Mine: the Key Example of the Kola Alkaline Province. Mineralogical Society Book Series 10, 75–97.

Krot, A.N., Posukhova, T.V., Guseva, Ye.V., Galimov, E.M., Botkunov, A.I., Ramenskaya M.Ye. and Oglobina, A.I., 1994. Origin of garnets containing hydrocarbon inclusions in the Mir Kimberlite Pipe, Geochem. Int. 31(1), 122–130.

Krumrei, T.V. and Markl, G., 2005. Fluid inclusions in sodalite from the peralkaline Ilímaussaq complex, South Greenland: an indicator of fluid composition changes. In: Peralkaline rocks: Sources, economic potential and evolution from alkaline melts. Abstract vol., 59-60.

Kudryavtsev, N.A., 1951. Against the organic hypothesis of the origin of petroleum. Petroleum Economy 9, 17-29.

Kyser, T.K., 1986. Stable isotope variations in the mantle. In: Valley, J.W., Taylor, H.P., O'Neil, J.R. (Eds.). Stable isotopes in high temperature geological processes. Reviews in Mineralogy 16, 141-164.

Laier, T., 1988. Hydrocarbon gases in the crystalline rocks of the Gravberg-1 well, Swedish deep gas project. Marine and Petroleum Geology 5, 370-377.

Lancet, H.S., Anders, E., 1970. Carbon isotope fractionation in the Fischer-Tropsch synthesis of methane. Science 170, 980-982.

Larsen, L.M. and Sørensen, H., 1987. The Ilímaussaq intrusion – progressive crystallization and formation of layering in an agpaitic magma. In: Fitton, J.C. and

Upton, G.J. (Eds.). Alkaline Igneous Rocks. Geol Soc. Soc. Publ. 30, Blackwell Sci. Publ., Oxford, pp. 473.

Larsen, R.B., Brooks, C.K. and Bird, D.K., 1992. Methane-bearing, aqueous, saline solutions in the Skaergaard intrusion, East Greenland, Contrib. Mineral. Petrol. 112, 428–437.

Le Maitre, R. W., 2002. Igneous Rocks: a Classification and Glossary of Terms: Recommendations of the International Union of Geological Sciences Subcommission on the Systematics of Igneous Rocks. Cambridge University Press.

Leake, B.E., 1978. Nomenclature of amphiboles. Amer. Min. 63, 1023-1052.

Lemmlein, G., 1929. Sekundäre Flüssigkeitseinschlüsse in Mineralien. Zeitschr. Kristallographie 71, 237-256.

Lespade, P., Marchand, R., Couzi,.M. and Cruegte, F. 1984. Caracterisation de materiaux carbones par microspectrometrie Raman. Carbon 22 (4-5), 375-385.

Lespinasse, M. and Pecher, A., 1986. Microfracturing and regional stress field: a study of the preferred orientations of fluid inclusions planes in a granite from the Massif Central, France. J. Struct. Geool. 8 (2), 169-180.

Lespinasse, M. and Cathelineau, M., 1995. Palaeostress magnitudes determination by using fault slip and fluid inclusion plane data. Journal of geophys. Res. 100 (B3), 3895-3904.

Lespinasse, M., Desindes, L., Fratczak, P. and Petrov, V., 2005. Microfissural mapping of natural cracks in rocks: implication for fluid transfer quantification in the crust. Chem. Geol. 223 (1-3), 170-178.

Levin, I., Bergamoachi, P., Dörr, H., Trapp., T., 1993. Stable isotope signature of methane from major sources in Germany. Chemosphere 26, 161-177.

Lippmann, J., Stute, M., Torgersen, T., Moser, D. P., Hall, J. A., Lin, L., Borcsik, M., Bellamy R. E. S., and Onstott T. C., 2003. Dating ultra-deep mine waters with noble gases and ^{36}Cl, Witwatersrand Basin, South Africa. Geochim. Cosmochim. Acta 6723. 14597-4619.

Lockyer, D. R. and Champion, R. A., 2001. Methane production by sheep in relation to temporal changes in grazing behaviour. Agriculture, Ecosystems and Environment 86 (3), 237-246.

Lonergan, L., Wilkinson, J.J. and McCaffrey, K.J.W., 1999. Fractures, fluid flow and mineralization: an introduction. In: McCaffrey, K.J.W. Lonergan, L., Wilkinson, J.J. (Eds.). Fractures, fluid flow and mineralization. Geological society, London, Special publications 155, 1-6.

Lowenstern, J.B., 1995. Applications of silicate-melt inclusions to the study of magmatic volatiles, in magmas, fluids and ore deposits. In: J.F.H. Thompson (Ed.). Min. Assoc. Canada Short Course 23, 71-99.

Luo, J., Zhang, C. and Qu, Z., 1999. Volcanic reservoir rocks: a case study of the Cretaceous Fenghuadian Suite, Huanghua Basin, eastern China. Journal of Petroleum Geology 22, 397-415.

Markl, G., Marks, M., Schwinn, G. and Sommer, H., 2001. Phase equilibrium constraints in intensive crystallization parameters of the Ilímaussaq Complex, South Greenland. J. Petrol. 42 (12), 2231-2257.

Marks, M. and Markl, G., 2003. Ilímausaq „en miniature“: closed-system fractionation in an agpaitic dyke rock from the Gardar Province, South Greenland (contribution to the mineralogy of Ilímausaq no. 117). Mineralogical Magazine 67 (5), 893-919.

Markl, G., 2005. Which parameters govern the evolution of agpaites? In: Peralkaline rocks: Sources, economic potential and evolution from alkaline melts. Abstract vol., 67-68.

McCollom, T.M., Ritter, G. and Simoneit, B.R.T., 1999. Lipid synthesis under hydrothermal conditions by Fischer-Tropsch-type reactions. Origin Life Evol. Biosphere 29, 153-166.

McCollom, T.M. and Seewald, J.S., 2001. A reassessment of the potential for reduction of dissolved CO_2 to hydrocarbons during serpentinization of olivine. Geochim. Cosmochim. Acta 65, 3769-3778.

Melezhik, V.A., Fallick, A.E., Filippov, M.M. and Larsen, O., 1999. Karelian shungite — an indication of 2000 Ma-year-old metamorphosed oil-shale and generation of petroleum: geology, lithology and geochemistry, Earth-Sci. Rev. 47, 1–40.

Melezhik, V.A., Filippov, M.M., Romashikin, A.E., 2004. A giant Palaeoproterozoic deposit of shungite in NW Russia: genesis and practical applications. Ore Geology Reviews 24, 135-154.

Morgan, G.B., I-Ming, C., Pasteris, C., Olsen, S.N., 1993. Re-equilibration of CO_2 fluid inclusions at controlled hydrogen fugacities. H. Metamorph. Geol. 11, 155-164.

Mossman, D.J., Gauthier-Lafaye, F. and Jackson, S., 2001. Carbonaceous substances associated with the palaeoproterozoic natural fission reactors of Oklo, Gabon: paragenesis, thermal maturation and carbon isotopic and trace element compositions. Precambrian Research 106, 135–148.

Mullis, J., 1987. Fluid inclusion studies in very low grade metamorphism. In: M. Frey (Ed.). Low Temperature Metamorphism. Blackie, Glasgow, 162–199.

Munz, I.A., Yardley, B.W.D. and Gleeson, S.A., 2002. Petroleum infiltration of high-grade basement, South Norway: pressure–temperature–time–composition (P–T–t–X) constraints. Geofluids 2, 41–53.

Nelson, R., 2003. Surface Chemistry. In: Dispersing Powders in Liquids, Part 3. Licensed to ERPT, http://www.erpt.org/032Q/Nelsc-00.htm.

Nivin, V.A., Devirts, A.L., Lagutina, Ye.P., 1995. The origin of the gas phase in the Lovozero Massif based on hydrogen-isotope data. Geochem. Int. 32 (8), 65-71.

Nivin V.A., Belov N. I., Treloar P.J. Timofeyev V.V. 2001. Relationships between gas geochemistry and release rates and the geomechanical state of igneous rock massifs. Tectonophysics 336 (1-4), 233-244.

Nivin, V.A., 2002. Gas concentrations in minerals with reference to the problem of the genesis of hydrocarbon gases in rocks of the Khibiny and Lovozero massifs. Geochem. Int. 40, 883-898.

Nivin, V.A., Treloar, P.J., Konopleva, N.G. and Ikorsky, S.V., 2005. A review of the occurrence, form and origin of C-bearing species in the Khibiny Alkaline Igneous Complex, Kola Peninsula, NW-Russia. Lithos 85 (1-4), 93-112.

Oaks, C.S., Bodnar, R.J. and Simonson, J.M., 1990. The system NaCl-$CaCl_2$-H_2O: I. The ice liquidus at 1 atm total pressure. Geochim. Cosmochim. Acta 54, 603-610.

Olafsson, M., and D. H. Eggler, 1983. Phase relations of amphibole, amphibole-carbonate, and phlogopite-carbonate peridotite: petrologic constraints on the asthenosphere, Earth and Plan. Sci. Lett., 64, 305-315.

Olds, R.H., 1953. Critical behaviour of hydrocarbons. In: Farkas, A. (Ed.). Physical Chemistry of hydrocarbons 3. Academic Press, London, 131-153.

Ono, A., Sano, Y., Wakita, H., Giggenbach, W.F., 1993. Carbon isotopes of methane and carbon dioxide in hydrothermal gases of Japan. Geochem. J. 27, 287-295.

Orville, P.M., 1963. Alkali ion exchange between vapour and feldspar phases. American Journal of Science 261, 201-237.

Parnell, J., 1988. Migration of biogenic hydrocarbons into granites: a review of hydrocarbons in British plutons. Marine and Petroleum Geology 5, 385–396.

Pasteris, J.D., 1987. Fluid inclusions in mantel xenoliths. In: P.H. Nixon (Ed.). Mantle Xenoliths. John Wiley & Sons Ltd, Chichester, 691-707.

Pasteris, J.D, Wopenka, B. and Seitz, J.C., 1988. Practical aspects of quantitative laser Raman microprobe spectroscopy for the study of fluid inclusions, Geochim. Cosmochim. Acta 52, 979–988.

Pasteris, J. D., and Wopenka, B., 1991. Raman spectra of graphite as indicators of degree of metamorphism. Canadian Mineralogist 29, 1–9.

Peng, D-Y. and Robinson, D.B., 1976. A New Two-constant Equation of State, Ind. Eng. Chem. Fundam. 15, 59-64.

Petersilie, I.A., 1960. Hydrocarbon gases and bitumens in intrusive massifs of the central Kola Peninsula. Acad. Sci. U.S.S.R. Izv., Geol. Ser. 1, 42-27.

Petersilie, I.A., Ikorski, S.V., Smirnova, L.I., Romanikhin, A.M. and Proskuryakova, E.B., 1961. Application of gas logging to the investigation of natural gases and bitumens in the Khibiny intrusive massif. Geochem. Int. 10, 945-962.

Petersilie, I.A., 1962. Origin of hydrocarbon gases and disperse bitumens of the Khibina alkalic massif. Geochem. Int. 1, 14-29.

Petersilie, I.A., 1964. The gas constitutent and trace bitumens of igneous and metamorphic rocks of the Kola Peninsula. Int. GeoI. C. 22, Abstr. Vol, 9-10.

Petersilie, I.A. and Sørensen, H., 1970. Hydrocarbon gases and bituminous substances in rocks from the Ilímaussaq alkaline intrusion, South Greenland. Lithos 3, 59-76.

Petford, N., 2003. Controls on primary porosity and permeability development in igneous rocks. In: Petford, N. and McCaffrey, K.J.W. (Eds.). Hydrocarbons in crystalline rocks. Geol. Soc. London, Spec. Pub. 214, 93-107.

Pichler, H., Schulz, H. and Elstner, M., 1967. Gesetzmäßigkeiten bei der Synthese von Kohlenwasserstoffen aus Kohlenoxid und Wasserstoff. Brennst. Chem. 48 (78), 32-41.

Piotrowski, J.H. and Edgar, A.D., 1970. Melting relations of undersaturated alkaline rocks from South Greenland. Medd. Grønland, Damn. 181/9, 1-62.

Pironon, J., 2005. Petroleum fluid inclusions. Short course notes. ECROFI X.V.III. Siena.

Placzek, G., 1934. Die Rayleigh und Raman Streuung. In: E. Marx, Editor, Handbuch der Radiologie, Akademische Verlagsgesellschaft, 209–219.

Porvir'ev, V.B.,1974. Inorganic origin of petroleum, AAPG, 58 81 9, 3-33.

Potter, J., Rankin, A.H., Treloar, P.J., Nivin, V., Ting, W. and Ni, P., 1998. A preliminary study of methane inclusions in alkaline igneous rocks of the Kola igneous province, Russia: implications for the origin of methane in igneous rocks. Eur. J. Mineral. 10, 1167-1180.

Potter, J., 2000. The characterisation and origin of hydrocarbons in the alkaline igneous complexes in the Kola Alkaline Province, PhD thesis, Kingston University, Kingston upon Thames, UK, pp. 296.

Potter, J. and Konnerup-Madsen, J., 2003. A review of the occurrence and origin of abiogenic hydrocarbons in igneous rocks. In: N. Petford and K.J.W. McCaffrey (Eds.). Hydrocarbons in Crystalline Rocks. Geol. Soc. Lond. Spec. Pub. 214, 151–173.

Potter, J., Rankin, A.H. and Treloar, P.J., 2004. Abiogenic Fischer-Tropsch synthesis of hydrocarbons in alkaline igneous rocks: fluid inclusion, textural and isotopic evidence from the Lovozero complex, N.W. Russia. Lithos 75, 311-330.

Prinzhofer, A.A. and Huc, A.Y., 1995. Genetic and post-genetic molecular and isotopic fractionations in natural gases. Chem. Geol. 126, 281-290.

Prinzhofer, A. and Pernaton, E., 1997. Isotopically light methane in natural gas: bacterial imprint or diffusive fractionation? Chem. Geol. 142, 193-200.

Pripachkin, V.A., Pavlova, M.A., Galakhova, T.N., Volokhova, T.S. and Malashikina, V.T., 1985. Bitumens of the Khibina carbonatites. Dokl. Akad. Nauk SSSR 281, 1424-1426 (in Russian).

Rice, D.D. and Claypool, G., 1981. Generation, accumulation and resource potential of biogenic gas. Bull. Am. Assoc. Pet. Geol. 65, 5-25.

Roedder, E., 1972. Composition of fluid inclusions, Chapter JJ. In: Fleisher, M. (Ed.). Data of Geochemistry, sixth edition. Geological survey professional paper 440-JJ.

Rosasco, G.J. and Roedder, E., 1975. Laser exited Raman spectroscopy. Science 190, 557-560.

Roedder, E. and Bodnar, R.J., 1980. Geologic pressure determinations from fluid inclusion studies. Ann. Rev. Earth Planet. Sci 8, 263-301.

Roedder, E., 1984. Fluid inclusions. Reviews in Mineralogy 12. Mineralogical Society of America. pp. 644.

Rosasco, G.J. and Roedder, E., 1979. Application of a new Raman microprobe spectrometer to non-destructive analysis of sulphate and other ions in individual phases in fluid inclusions in minerals. Geochim. Cosmochim. Acta 43, 1907-1915.

Rosso, K.M. and Bodnar, R.J., 1995. Microthermometric and Raman spectroscopic detection limits of CO_2 in fluid inclusions and the spectroscopic characterization of CO_2, Geochim. Cosmochim. Acta 59(19), 3961–3975.

Rust, F.E., 1981. Ruminant methane $\delta^{13}C$ values: Relation to atmospheric methane. Science 211, 1044-1046.

Ryabchikov, I.D., Green, D.H., Wall, W.J., Brey, G.P., 1981. The oxidation state of carbon in the reduced-velocity zone. Geochem. Int. 2, 221-232.

Ryabchikov, I.D. and Kogarko, L.N., 2006. Magnetite compositions and oxygen fugacities of the Khibina magmatic system. Lithos 91, 35-45.

Salvi, S. and Williams-Jones, A.E., 1996. The role of hydrothermal processes in concentrating high-field strength elements in the Strange Lake peralkaline complex, northeastern Canada. Geochim. Cosmochim. Acta 60 (11), 1917-1932.

Salvi, S. and Williams-Jones, A.E., 1997. Fischer-Tropsch synthesis of hydrocarbons during sub-solidus alteration of the Strange Lake peralkaline granite, Quebec/Labrador, Canada. Geochim. Cosmochim. Acta 61, 83-99.

Salvi, S. and Williams-Jones, A.E., 2006. Alteration, HFSE mineralisation and hydrocarbon formation in peralkaline igneous systems: Insights from the Strange Lake Pluton, Canada. Lithos 91 (1-4), 19-34.

Santosh, M. Tsunogae, T. Iki, T. Vansutre, S. and Hari, K.R., 2006. Petrology, fluid inclusions and metamorphic history of Bhopalpatnam granulites, central India. Journal of Asian Earth Sciences 28 (1), 81-98.

Sausse, J, Jacquot, E., Fritz, E., Leroy, J. and Lespinasse, M., 2001. Evolution of crack permeability during fluid-rock interaction. Example of the Breyouard granite (Vosges, France). Tectonophysics 336, 199-214.

Scheglov, A.D., Mokaleva, V.N., Markovsky, B.A., Orlova, M.P., Smolkin, V.F., 1993. Sketch map showing the distribution of successions of magmatic complexes in riftogenic systems of the Baltic Shield. Scale 1:5,000,000, Appendix 1 of monography "Magmatism and metallogeny of riftogenic systems in the east part of the Baltic Shield". Committee of Russian Federation of geology and use of mineral resources. All-Russian Geological Research Institute A.P. Karpinski.

Schoell, M., 1980. The hydrogen and carbon isotopic composition of methane from natural gases of various origins. Geochim. Cosmochim. Acta 44 (5), 649-661.

Schoell, M., 1983. Genetic Characterisation of Natureal gases. AAPG Bulletin 67 (12), 2225-2238.

Schoell M. 1988. Multiple origins of CH_4 in the earth. Chemical Geology 71(1-3), 1-10.

Schutter, S.R., 2003. Hydrocarbon occurrence and exploration in and around igneous rocks. In: N. Petford and K.J.W. McCaffrey (Eds.). Hydrocarbons in Crystalline Rocks. Geol. Soc. London, Spec. Pub. 214, 7–33.

Schwinn, G., 1999. Kristallisationsgeschichte und Fluidentwicklung in agpaitischen Gesteinen der Ilímaussaq Intrusion, Südgrönland. Masters thesis, University of Freiburg, pp. 159.

Scott, H.P., Hemley, R.J., Mao, H., Herschbach, D.R., Fried, L.E., Howard, W.M., Bastea, S., 2004. Generation of methane in the Earth's mantle: In situ high pressure-temperature measurements of carbonate reduction. PNAS 101-39, 14023-14026.

Seitz, J.C., Pasteris J.D., and Wopenka, B., 1987. Characterization of CO_2–CH_4–H_2O fluid inclusions by microthermometry and laser Raman microprobe spectroscopy: inferences for clathrate and fluid equilibria, Geochim. Cosmochim. Acta 51, 1651–1664.

Seitz, J.C., Pasteris, J.D. and Chou, I.-M., 1996. Raman spectroscopic characterization of gas mixtures: II. Quantitative composition and pressure determination of the CO_2–CH_4 system, Am. J. Sci. 296, 577–600.

Shablinsky, G.N., 1963. Seismic investigation of abyssal structures of the alkaline massifs of the Kola Peninsula. Zap. Leningrad Gorn. 16-2 (in Russian).

Shepherd, T.J., Rankin, A.H. and Alderton, D.H.M., 1985. A practical guide to fluid inclusion studies. Blackie, London, pp. 239.

Sherwood-Lollar, B., Frape, S.L., Fritz, P., Macko, S.A., Welhan, W.A., Blomqvist, R., Lahermo, P.W., 1993a. Evidence for bacterially generated hydrocarbon gas in Canadian Shield and Fennoscandian Shield rocks. Geochim. Cosmochim. Acta 57, 5073-5085.

Sherwood-Lollar, B., Frape, S.L., Weise, S.M., Fritz, P., Macko, S.A., Welhan, W.A., 1993b. Abiogenic methanogenesis in crystalline rocks. Geochim. Cosmochim. Acta 57, 5087-5097.

Sherwood-Lollar B., Westgate, T.D., Ward, J.A., Slater, G.F. and Lacrampe-Couloume, G., 2002. Abiogenic formation of alkanes in the earth's crust as a minor source for global hydrocarbon reservoirs. Nature 416, 522-524.

Sherwood Lollar, B., Lacrampe-Couloume, G., Slater, G.F., Ward, J., Moser, D.P., Gihring, T.M., Lin, L.-H., Onstott, T.C., 2006. Unravelling abiogenic and biogenic sources of methane in theEarth's deep subsurface. Chem. Geol. 226, 328–339.

Simmons, G. and Richter, D., 1976. Microcracks in rocks. In: Strens, R.G.J. (Ed.) The physics and chemistry of minerals and rocks. Wiley, New York, 105-137.

Simon, K., 2001. Does δD from fluid inclusion in quartz reflect the original hydrothermal fluid? Chem. Geol. 177, 483-495.

Smith, D.L. and Evans, B., 1984. Diffusional crack healing in quartz. Journal of Geophysical Research 89, B6, 4125-4135.

Smith, J.E., Derdman, J.G. and Morris, D.A., 1971. Migration, accumulation and retention of petroleum in the earth. Proceedings of eighth World Petroleum Congress, Moscow. London: Applied Science Publishers, 13-26.

Smith, M.P., 1996. Fluid inclusion volatile well logs of the Gravberg 1 Well, Siljan Ring, Sweden. In Brown, P.E. and Hagemann, S.G. (Eds.) Sixth biennial Pan-American conference on research on fluid inclusions. Program and abstracts, pp. 122.

Sobolev, A.V., Kostyuk, V.P. 1975: Magmatic crystallisation as based on the study of melt inclusions. "Nauka", Novosibirsk, 184-232 (in Russian).

Sobolev, A.V., 1996. Melt inclusions in minerals as a source of principle petrological information. Petrology 4, 228–239.

Sokolov, S.V., Chukanov, N.V., in press. Solid organic substances in pegmatites and hydrothermalites of the alkaline complexes Khibiny and Lovozero (Kola Peninsula, Russia), unpublished manuscript.

Sommer, H., 1999. Kristallisationsgeschichte und Fluidentwicklung in Lujavriten der Ilímaussaq Intrusion in Grönland. Masters thesis, University of Freiburg, pp. 111.

Sorby, H.C., 1858. On the microscopic structure if crystals, indicating the origin of minerals and rocks. Geol. Soc. London, Quarterly Journal 14, 453-500.

Sørensen, H., 1965. On the magmatic evolution of the alkaline province of South Greenland. Rapp. Greenlands Geol. Unders. 7, 1-19.

Sørensen, H., 1970. Internal structures and geological setting of the three agpaitic intrusions – Khibina and Lovozero of the Kola Peninsula and Ilímaussaq, South Greenland. Can. Mineral., 10 (3), 299-344.

Sørensen, H., 1997. The agpaitic rocks; an overview. Min. Mag 61, 485-498.

Sterner, S.M., Hall, D.L., Keppler, H., 1995. Compositional re-equilibration of fluid inclusions in quartz. Contrib. Mineral. Petrol. 119, 1-15.

Sugimoto, A., Inoue, T., Kirtibutr, N. and Abe, E., 1998. Methane oxidation by termite mounds estimated by the carbon isotopic composition of methane. Global Biogeochem. Cycles 12 (4), 595.

Sugisaki, R. and Mimura, K., 1994. Mantle hydrocarbons: abiotic or biotic? Geochim. Cosmochim. Acta 58, 2527-2542.

Szatmari, P., 1989. Petroleum formation by Fischer-Tropsch synthesis in plate tectonics. AAPG Bulletin, 73 (8), 989-998.

Tagiri, M. and Ob, T, 1986. Hydrothermal syntheses of graphite from bituminous coal at 0.5-kbar water vapour pressure and 300-600°C. J. Japan. Assoc. Mineral. Petrol. Econ. Geol. 81, 260-271.

Thiery, R., Van den Kerkhof, A.M. and Dubessy, J., 1994. VX properties of CH_4–CO_2 and CO_2–N_2 fluid inclusions modelling for $T < 31$ °C and $P < 400$ bar, Eur. J. Mineral. 6, 753–771.

Thomas, A.V., Pasteris, J.D., Bray, C.J. and Spooner, E.T.C., 1990. H_2O–CH_4–NaCl–CO_2 inclusions from the footwall contact of the Tanco granitic pegmatite: estimates of internal pressure and composition from microthermometry, laser Raman spectroscopy, and gas chromatography, Geochim. Cosmochim. Acta 54, 559–573.

Touret, J. L. R., 2001. Fluids in metamorphic rocks. Lithos 55 (1-4), 1-25.

Van den Kerkhof, A.M., 1988. The system CO_2–CH_4–N_2 in fluid inclusions: theoretical modelling and geological applications. Ph.D. thesis, Vrije Universiteit Amsterdam, The Netherlands, pp. 206.

Van den Kerkhof, A.M. and Kisch, H.J., 1993. CH_4-rich inclusions from quartz veins in the Valley-and-Ridge province and the anthracite fields of the Pennsylvania Appalachians — reply, Am. Mineral. 8, 220–224.

Vessia, Ø., 2005. Biofuels from lignocellulosic material - In the Norwegian context 2010 – Technology, Potential and Costs. Report. Norwegian University of Science and Technology,Faculty of information technology, mathematics and electrical engineering. Trondheim. http://www.zero.no/transport/bio/vessia_version3-20-12-05.pdf.

Voitov, G.I., Adushkin, W.W., Hochberg, M.B., Nosik, L.P., Kutscher, M.I., Nikulina, I.W., Puschkin M.G. and Schogina, L.M., 1990. O chimitschesskoi I isotopnoi nectawjilnostjak gasowuik strui b khibinak, Dokl. Akad. Nauk SSSR 312 (3), 567–571 (in Russian).

Voitov, G.I., 1992. Chemical and carbon-isotope fluctuations in free gases (gas jets) in the Khibiny, Geochem. Int., 14–24.

Welhan, J.A. and Craig, H., 1983. Methane, hydrogen and helium in hydrothermal fluids at 21°N, East Pacific Rise. In: Rona, P.A., Boström, K., Laubier, L., Smith Jnr, K.L. (Eds.). Hydrothermal processes at seafloor spreading centres. Plenum, New York, 391-409.

Welhan, J.A. and Lupton, J.E., 1987. Light hydrocarbon gases in Guaymas Basin hydrothermal fluids: thermogenic versus abiogenic origin. AAPG Bulletin 71, 215-223.

Whiticar, M.J., 1990. A geochemical perspective of natural gas and atmospheric methane. Org. Geochem. 16, 531-547.

Whiticar, M. 1996. Isotope tracking of microbial methane formation and oxidation. Mitt. Internat. Verein. Limnol. 25: 39–54.

Whiticar, M.J., 1999. Carbon and hydrogen isotope systematics of bacterial formation and oxidation of methane. Chem. Geol. 161, 291-314.

Yakovenchuk, V.N., Ivanyuk, G.J., Pahomovsky, Ya.A. and Men'shikov, Yu.P., 1999. Minerals of the Khibiny Massif, Zemlya, Moscow, pp. 326 (in Russian).

Yerokhin, V.Y., 1978. Yadernaya geologiya (Nuclear geology). Izd. OTI VNIIYaGG, Moscow, 47 (in Russian).

Yoshida, T., Nishizawa, K., Tabat, M., Abe, H., Kodama, T., Tsuji, M., Tamaura, Y., 2000. Methanisation of CO_2 with H_2-reduced magnetite. Journal of Material Sci. 28. 1220-1226.

Zaitsev, A.N., Bell, K., Wall, F., Le Bas, M.J., 1997. Alkaline rare-earth element carbonates from carbonatites of the Khibiny massif: mineralogy and genesis. Trans. (Dokl.) Russ. Acad. Sci. Earth Sci. Sect. 355, 786-790.

Zakrzhevskaya A.G., 1972. Classification of inclusions of mineral forming medium in magmatic rocks of the Khibiny apatite deposits. In: Ore forming medium on inclusions in minerals. Nauka, Moscow, 192-198 (in Russian).

Zhang, T. and Krooss, B.M., 2001. Experimental investigation on the carbon isotope fractionation of methane during gas migration by diffusion through sedimentary rocks at elevated temperature and pressure. Geochim. Cosmochim. Acta 65 (16), 2723-2742.

Zhang, Y.G. and Frantz, J.D., 1992. Hydrothermal reactions involving equilibrium between minerals and mixed volatiles. 2. Investigations of fluid properties in the CO_2-CH_4-H_2O system using synthetic fluid inclusions. Chem. Geol. 100, 51-72.

Ziegenbein, D. and Johannes, W., 1980. Graphite in C-O-H fluids: an unsuitable compound to buffer fluid composition at temperatures up to 700°C. N. Jb. Mineral. Mh. 7, 289-305.

Zirkel, F. 1873. die mikroskopische Beschaffenheit der Mineralien und Gesteine. W. Engelmann, Leipzig, pp. 502.

Zolotov, M.Y. and Shock, E.L., 1999. Abiotic synthesis of polycyclic aromatic hydrocarbons on Mars. J. Geophys. Res. 104, 14033-14049.

Appendices

A 1.0: List of abbreviations

A 4.1a: Sampling list

A 4.1b: Satellite image of sampling locations

A 4.2: Electron microprobe results of selected minerals

A 4.3: Laser Raman spectra of main minerals

A 6.1a: Microthermometric results of methane-dominant inclusions

A 6.1b: Microthermometric results of water-dominant inclusions

List of abbreviations mentioned in the text

AA	antarcticite
ab	albite
aeg	aegirine
aenig	aenigmatite
alk fs	alkali feldspar
amph	amphibole
ap	apatite
arf	arfvedsonite
ASF	Anderson-Schulz-Flory
astr	astrophyllite
BSE	back scattered electron
bt	biotite
canc	cancrinite
EDS	energy disperse system
EoS	Equation of State
EPR	East Pacific Rise
eud	eudialyte
FG	free gas
FIP	fluid inclusion plane

Appendix A1.0: Alphabetical list of abbreviations

F-T	Fischer-Tropsch
GC	gas chromatography
HC	hydrocarbon
HH	hydrohalite
hhc	higher hydrocarbon
lor	lorenzenite
mag	magmatite
MC	microcracks
ne	nepheline
OG	occluded gas
P-T	pressure-temperature
PVTX	pressure volume temperature composition
STP	standard temperature pressure
T_{diss}	temperature of daughter mineral dissolution
TG	thermograph
T_h	homogenisation temperature
tit	titanite
tit-mag	titano-magnetite
xpl	crossed polarised light
zeo	zeolite

Appendix A1.0: Alphabetical list of abbreviations

#	rock type	GPS location		dip direction / dip
Kh-03-1	**khibinite**	67 ° 42 ′ 19.2 ″ N	33 ° 22 ′ 53.6 ″ E	260 / 10
Kh-03-2	**khibinite**	67 ° 42 ′ 22.6 ″ N	33 ° 22 ′ 52.1 ″ E	270 / 30
Kh-03-3	**khibinite**	67 ° 42 ′ 25.8 ″ N	33 ° 22 ′ 50.1 ″ E	325 / 30
Kh-03-4	**khibinite**	67 ° 42 ′ 50.0 ″ N	33 ° 22 ′ 42.1 ″ E	250 / 30
Kh-03-5	**khibinite**	67 ° 41 ′ 14.6 ″ N	33 ° 23 ′ 33.7 ″ E	140 / 75
Kh-03-6	**khibinite**	67 ° 41 ′ 11.6 ″ N	33 ° 23 ′ 53.8 ″ E	230 / 80
Kh-03-7	**khibinite**	67 ° 40 ′ 58.7 ″ N	33 ° 23 ′ 54.2 ″ E	320 / 85
Kh-03-8	**khibinite**	67 ° 40 ′ 45.1 ″ N	33 ° 23 ′ 55.5 ″ E	190 / 85
Kh-03-9	**rischorrite**	67 ° 45 ′ 6.7 ″ N	33 ° 35 ′ 10.3 ″ E	98 / 85
Kh-03-10	**rischorrite**	67 ° 44 ′ 32.1 ″ N	33 ° 35 ′ 16.1 ″ E	30 / 40
Kh-03-11	**rischorrite**	67 ° 44 ′ 17.8 ″ N	33 ° 35 ′ 35.0 ″ E	340 / 80
Kh-03-13	**rischorrite**	67 ° 43 ′ 39.2 ″ N	33 ° 35 ′ 38.3 ″ E	110 / 60
Kh-03-14	**rischorrite**	67 ° 43 ′ 22.3 ″ N	33 ° 35 ′ 36.0 ″ E	340 / 80
Kh-03-42	**rischorrite**	67 ° 42 ′ 40.9 ″ N	33 ° 36 ′ 5.1 ″ E	230 / 30
Kh-03-43	**rischorrite**	67 ° 42 ′ 18.4 ″ N	33 ° 36 ′ 27.0 ″ E	140 / 50
Kh-03-44	**rischorrite**	67 ° 42 ′ 18.4 ″ N	33 ° 36 ′ 27.0 ″ E	340 / 90
Kh-03-45	**rischorrite**	67 ° 42 ′ 14.6 ″ N	33 ° 36 ′ 27.2 ″ E	135 / 70
Kh-03-46	**rischorrite**	67 ° 41 ′ 57.1 ″ N	33 ° 36 ′ 39.9 ″ E	0 / 80
Kh-03-48	**rischorrite**	67 ° 41 ′ 40.7 ″ N	33 ° 36 ′ 54.5 ″ E	260 / 85
Kh-03-49	**rischorrite**	67 ° 41 ′ 26.7 ″ N	33 ° 37 ′ 11.3 ″ E	230 / 85
Kh-03-50	**rischorrite**	67 ° 41 ′ 2.5 ″ N	33 ° 37 ′ 43.7 ″ E	180 / 80
Kh-03-35	**trachytoid foyaite**	67 ° 44 ′ 7.9 ″ N	33 ° 45 ′ 46.1 ″ E	340 / 85
Kh-03-36	**trachytoid foyaite**	67 ° 44 ′ 2.0 ″ N	33 ° 46 ′ 0.3 ″ E	145 / 85
Kh-03-37	**trachytoid foyaite**	67 ° 43 ′ 56.8 ″ N	33 ° 46 ′ 11.4 ″ E	230 / 55
Kh-03-38	**trachytoid foyaite**	67 ° 43 ′ 53.4 ″ N	33 ° 46 ′ 15.1 ″ E	245 / 50
Kh-03-39	**trachytoid foyaite**	67 ° 43 ′ 48.7 ″ N	33 ° 46 ′ 16.1 ″ E	250 / 45
Kh-03-40	**trachytoid foyaite**	67 ° 43 ′ 35.2 ″ N	33 ° 46 ′ 11.4 ″ E	60 / 80
Kh-03-41	**trachytoid foyaite**	67 ° 43 ′ 23.8 ″ N	33 ° 46 ′ 32.1 ″ E	250 / 50
Kh-03-51	**massive foyaite**	67 ° 45 ′ 14.1 ″ N	33 ° 57 ′ 6.6 ″ E	280 / 25
Kh-03-52	**massive foyaite**	67 ° 45 ′ 12.7 ″ N	33 ° 56 ′ 20.5 ″ E	150 / 50
Kh-03-53	**massive foyaite**	67 ° 45 ′ 15.6 ″ N	33 ° 56 ′ 16.2 ″ E	330 / 70
Kh-03-54	**massive foyaite**	67 ° 45 ′ 23.8 ″ N	33 ° 56 ′ 21.6 ″ E	40 / 30
Kh-03-55	**massive foyaite**	67 ° 45 ′ 30.9 ″ N	33 ° 56 ′ 32.3 ″ E	350 / 35

Appendix A4.1a: Sampling list including sampling location and orientation of hand specimen.

#	rock type	GPS location		dip direction / dip
Kh-03-56	**alkaline syenite**	67 ° 47 ′ 39.2 ″N	34 ° 3 ′ 25.6 ″E	150 / 80
Kh-03-57	**alkaline syenite**	67 ° 47 ′ 37.4 ″N	34 ° 3 ′ 31.7 ″E	160 / 75
Kh-03-58	**alkaline syenite**	67 ° 47 ′ 35.7 ″N	34 ° 3 ′ 45.8 ″E	190 / 70
Kh-03-59	**alkaline syenite**	67 ° 47 ′ 33.1 ″N	34 ° 3 ′ 6.6 ″E	140 / 70
Kh-03-60	**alkaline syenite**	67 ° 47 ′ 31.8 ″N	34 ° 3 ′ 16.7 ″E	140 / 75
Kh-03-61	**ijolite**	67 ° 40 ′ 21.3 ″N	34 ° 8 ′ 31.9 ″E	120 / 45
Kh-03-62	**ijolite**	67 ° 40 ′ 21.3 ″N	34 ° 8 ′ 31.9 ″E	130 / 80
Kh-03-63	**ijolite**	67 ° 40 ′ 21.3 ″N	34 ° 8 ′ 31.9 ″E	200 / 40
Kh-03-64	**ijolite**	67 ° 40 ′ 21.3 ″N	34 ° 8 ′ 31.9 ″E	290 / 45
Kh-03-65	**ijolite**	67 ° 40 ′ 21.3 ″N	34 ° 8 ′ 31.9 ″E	320 / 45
Kh-03-66	**ijolite**	67 ° 40 ′ 21.3 ″N	34 ° 8 ′ 31.9 ″E	260 / 85
Kh-03-67	**ijolite**	67 ° 40 ′ 21.3 ″N	34 ° 8 ′ 31.9 ″E	240 / 65
Kh-03-68	**ijolite**	67 ° 40 ′ 21.3 ″N	34 ° 8 ′ 31.9 ″E	90 / 50
Kh-03-69	**ijolite**	67 ° 40 ′ 19.7 ″N	34 ° 8 ′ 41.4 ″E	90 / 45
Kh-03-70	**ijolite**	67 ° 40 ′ 19.7 ″N	34 ° 8 ′ 41.4 ″E	90 / 45
Kh-03-71	**ijolite**	67 ° 40 ′ 21.1 ″N	34 ° 8 ′ 2.5 ″E	130 / 60
Kh-03-72	**ijolite**	67 ° 40 ′ 21.1 ″N	34 ° 8 ′ 2.5 ″E	170 / 80
Kh-03-73	**ijolite**	67 ° 40 ′ 21.1 ″N	34 ° 8 ′ 2.5 ″E	30 / 80
Kh-03-74	**ijolite**	67 ° 35 ′ 48.0 ″N	34 ° 8 ′ 9.3 ″E	280 / 85
Kh-03-17	**lujavrite**	67 ° 39 ′ 21.6 ″N	33 ° 56 ′ 5.5 ″E	30 / 70
Kh-03-18	**lujavrite**	67 ° 40 ′ 29.6 ″N	33 ° 55 ′ 32.2 ″E	110 / 30
Kh-03-19	**lujavrite**	67 ° 40 ′ 21.2 ″N	33 ° 56 ′ 11.6 ″E	80 / 25
Kh-03-20	**lujavrite**	67 ° 40 ′ 31.0 ″N	33 ° 55 ′ 48.8 ″E	45 / 90
Kh-03-21	**lujavrite**	67 ° 40 ′ 31.0 ″N	33 ° 55 ′ 48.8 ″E	165 / 90
Kh-03-22	**lujavrite**	67 ° 40 ′ 31.0 ″N	33 ° 55 ′ 48.8 ″E	210 / 20

Appendix A4.1a: Sampling list including sampling location and orientation of hand specimen.

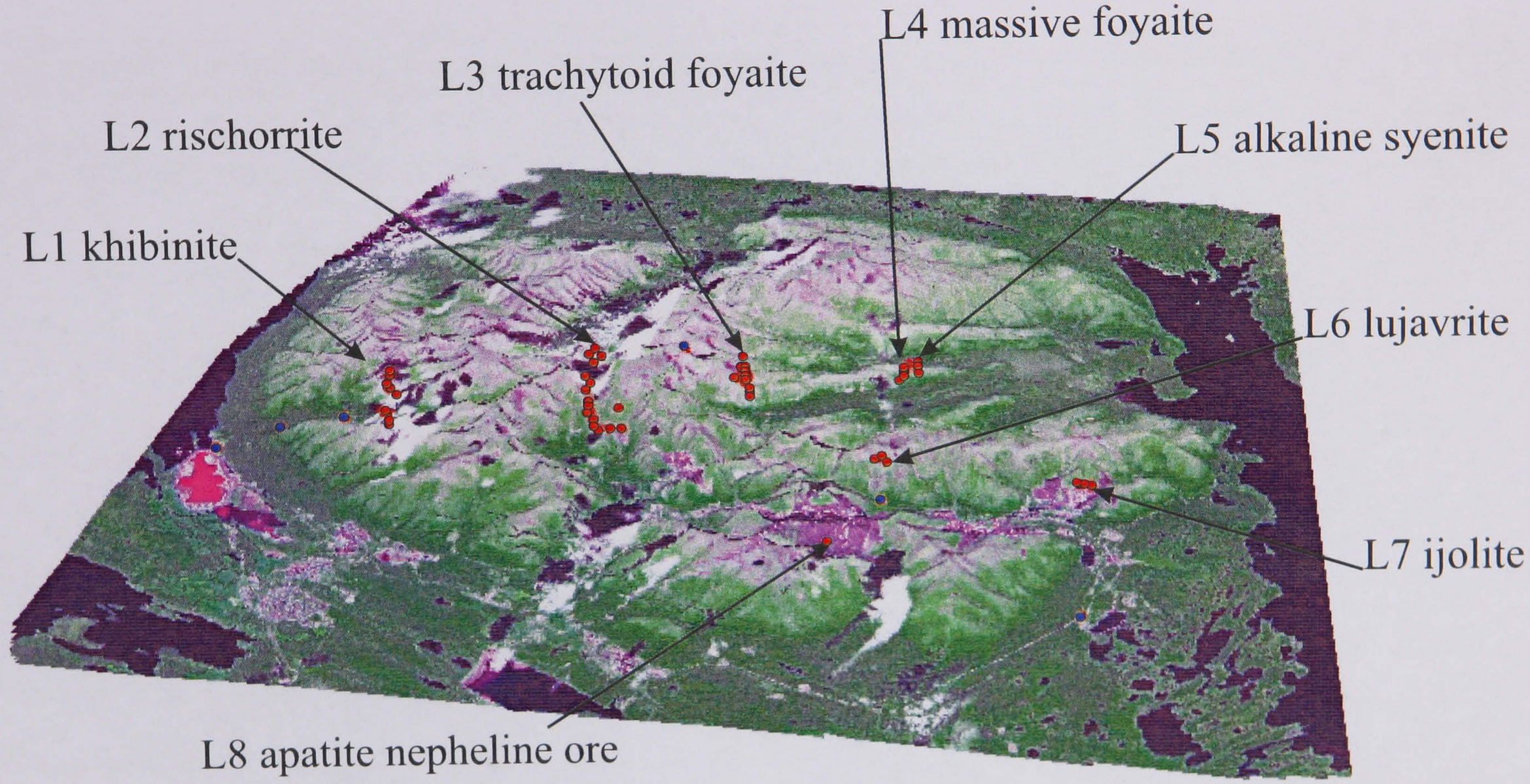

Appendix 4.1b: Satellite image of the Khibiny pluton and sampling locations based on GPS data (see Appendix A4.1a for values).

mineral	amphibole	amphibole	amphibole	amphibole	amphibole	amphibole	amphibole	amphibole	amphibole	amphibole	amphibole	amphibole	amphibole	amphibole	amphibole	amphibole	amphibole
rock type	khibinite	khibinite	khibinite	khibinite	khibinite	khibinite	khibinite	rischorrite	rischorrite	rischorrite	rischorrite	rischorrite	rischorrite	rischorrite	rischorrite	trachytoid foyaite	trachytoid foyaite
#	Kh-03-2	Kh-03-6	Kh-03-6	Kh-03-6	Kh-03-6	Kh-03-6	Kh-03-6	Kh-03-14	Kh-03-14	Kh-03-14	Kh-03-14	Kh-03-14	Kh-03-14	Kh-03-14	Kh-03-14	Kh-03-38	Kh-03-38
SiO_2	50.30	51.75	51.63	50.26	50.40	51.48	51.08	54.04	52.10	37.82	40.78	40.09	41.56	40.87	40.41	47.60	49.62
TiO_2	2.09	2.44	2.44	2.89	3.21	2.16	2.38	1.52	2.26	4.33	9.74	9.57	9.82	9.88	10.07	2.16	2.38
Al_2O_3	3.08	1.03	1.02	4.07	3.84	2.61	3.42	0.49	1.17	9.45	0.64	1.07	0.47	1.34	0.96	4.40	2.79
Fe_2O_3	14.17	19.90	21.60	12.44	18.33	16.98	16.55	24.99	17.69	20.01	31.04	30.39	31.40	31.13	31.74	17.75	17.42
FeO	0.69	8.03	6.12	0.54	3.51	4.13	1.53	0.92	-	8.98	4.67	5.95	4.65	5.56	4.45	8.14	8.46
MnO	-	0.45	0.45	0.84	1.27	1.75	1.24	0.75	0.91	0.67	2.37	2.08	2.21	2.06	2.61	1.75	2.51
MgO	13.30	0.94	0.91	14.50	8.35	8.85	11.20	2.43	11.36	6.87	2.19	2.14	1.73	2.35	1.46	6.35	5.57
CaO	6.76	2.05	2.06	8.58	2.80	3.62	5.76	8.60	5.19	b.d.	0.22	0.44	1.73	0.53	0.27	3.97	1.18
Na_2O	5.79	11.87	11.45	5.35	7.82	7.56	6.42	8.85	5.24	0.61	7.46	7.41	7.45	7.48	7.49	7.26	8.44
K_2O	1.58	-	-	1.47	1.68	1.83	1.57	-	3.49	9.25	-	-	-	-	-	1.72	2.25
TOTAL	97.76	98.46	97.68	100.94	101.21	100.97	101.15	102.59	99.34	97.99	99.11	99.13	101.02	101.20	99.46	101.09	100.63
Si	7.440	7.928	7.985	7.193	7.390	7.556	7.413	8.008	7.733	6.084	6.639	6.532	6.651	6.514	6.585	7.130	7.453
Ti	0.232	0.281	0.284	0.311	0.354	0.238	0.260	0.169	0.252	0.524	1.192	1.173	1.182	1.184	1.234	0.243	0.269
Al	0.537	0.186	0.186	0.687	0.664	0.452	0.585	0.086	0.205	1.792	0.123	0.206	0.089	0.252	0.184	0.777	0.494
Fe^{III}	1.753	2.550	2.793	1.489	2.248	2.084	2.009	3.097	2.196	2.692	4.226	4.140	4.202	4.149	4.325	2.223	2.189
Fe^{II}	0.077	0.921	0.709	0.058	0.385	0.454	0.166	0.102	-	1.081	0.569	0.726	0.557	0.664	0.543	0.913	0.952
Mn	-	0.058	0.059	0.102	0.158	0.218	0.152	0.094	0.114	0.091	0.327	0.287	0.300	0.278	0.360	0.222	0.319
Mg	2.932	0.215	0.210	3.093	1.825	1.936	2.422	0.537	2.513	1.647	0.531	0.520	0.413	0.558	0.355	1.418	1.247
Ca	1.071	0.337	0.341	1.316	0.440	0.569	0.896	1.366	0.825	b.d.	0.038	0.077	0.297	0.091	0.047	0.637	0.190
Na	1.660	3.525	3.433	1.484	2.223	2.151	1.806	2.542	1.508	0.190	2.354	2.340	2.311	2.311	2.366	2.108	2.457
K	0.298	-	-	0.268	0.314	0.343	0.291	-	0.661	1.898	-	-	-	-	-	0.329	0.431
Σ cation	16.000	16.000	16.000	16.000	16.000	16.000	16.000	16.000	16.000	16.000	16.000	16.000	16.000	16.000	16.000	16.000	16.000
O	23.000	23.000	23.000	23.000	23.000	23.000	23.000	23.000	23.000	23.000	23.000	23.000	23.000	23.000	23.000	23.000	23.000

A4.2: Electron microprobe data of selected minerals of the Khibiny pluton ("-" - not detected, FeII/FeIII calculation according Treloar (unpublished))

mineral	amphibole	amphibole	amphibole	amphibole	amphibole	amphibole	amphibole	amphibole	amphibole	amphibole	amphibole	amphibole	amphibole	amphibole	amphibole	amphibole
rock type	trachytoid foyaite	trachytoid foyaite	trachytoid foyaite	trachytoid foyaite	trachytoid foyaite	massive foyaite	massive foyaite	massive foyaite	massive foyaite	massive foyaite	massive foyaite	massive foyaite	massive foyaite	massive foyaite	massive foyaite	alkali syenite
#	Kh-03-39	Kh-03-39	Kh-03-39	Kh-03-39	Kh-03-39	Kh-03-53	Kh-03-53	Kh-03-53	Kh-03-53	Kh-03-53	Kh-03-53	Kh-03-53	Kh-03-53	Kh-03-53	Kh-03-53	Kh-03-58
SiO_2	50.64	47.36	49.12	52.24	50.80	52.21	47.22	46.99	47.69	52.64	47.61	47.61	47.93	52.50	52.28	45.49
TiO_2	1.58	2.34	1.88	1.42	1.69	0.99	1.88	1.96	1.96	1.00	1.94	1.94	1.61	1.00	1.01	1.98
Al_2O_3	1.93	3.82	2.55	1.28	1.87	1.10	3.60	3.41	3.22	1.00	3.16	3.16	3.09	1.13	1.04	4.26
Fe_2O_3	18.12	19.12	19.51	23.02	18.89	23.81	21.42	22.46	20.12	24.97	21.36	21.36	20.52	24.57	23.06	17.94
FeO	6.89	6.96	5.92	5.39	4.92	3.79	7.78	6.42	9.30	2.74	7.61	7.61	8.19	2.81	4.49	9.56
MnO	2.59	2.54	2.62	0.86	2.64	1.19	2.98	2.81	3.12	1.09	2.94	2.94	3.29	1.16	1.16	2.73
MgO	5.65	4.94	5.36	0.80	6.20	1.19	3.73	3.59	3.91	1.33	3.73	3.73	3.88	1.38	1.04	4.38
CaO	0.93	2.12	1.89	3.39	1.10	6.90	2.67	2.91	2.25	7.06	2.64	2.64	2.41	7.34	6.68	2.79
Na_2O	8.46	7.62	7.88	10.72	8.14	9.29	7.13	6.94	7.45	9.09	7.25	7.25	7.42	9.03	9.60	7.44
K_2O	2.12	1.87	1.74	-	2.02	-	2.01	1.87	2.23	-	2.04	2.04	1.99	-	-	1.61
TOTAL	98.90	98.69	98.47	99.11	98.28	100.47	100.41	99.36	101.24	100.92	100.28	100.28	100.34	100.91	100.36	98.18
Si	7.707	7.303	7.556	8.004	7.758	7.942	7.269	7.316	7.273	7.976	7.333	7.333	7.363	7.952	7.950	7.103
Ti	0.181	0.271	0.217	0.164	0.194	0.113	0.218	0.229	0.225	0.114	0.225	0.225	0.186	0.114	0.116	0.233
Al	0.346	0.694	0.462	0.231	0.337	0.197	0.653	0.626	0.579	0.179	0.574	0.574	0.560	0.202	0.186	0.784
Fe^{III}	2.306	2.466	2.509	2.949	2.413	3.029	2.757	2.925	2.566	3.164	2.751	2.751	2.637	3.112	2.932	2.343
Fe^{II}	0.785	0.803	0.682	0.618	0.563	0.431	0.896	0.749	1.062	0.311	0.877	0.877	0.942	0.318	0.512	1.117
Mn	0.334	0.332	0.341	0.112	0.342	0.153	0.389	0.371	0.403	0.140	0.384	0.384	0.428	0.149	0.149	0.361
Mg	1.282	1.135	1.229	0.183	1.411	0.270	0.856	0.833	0.889	0.300	0.856	0.856	0.888	0.311	0.236	1.019
Ca	0.152	0.350	0.312	0.557	0.180	1.125	0.440	0.485	0.368	1.146	0.436	0.436	0.397	1.191	1.088	0.467
Na	2.496	2.278	2.350	3.184	2.410	2.739	2.127	2.095	2.202	2.670	2.164	2.164	2.209	2.651	2.830	2.252
K	0.412	0.368	0.341	-	0.394	-	0.395	0.371	0.434	-	0.401	0.401	0.390	-	-	0.321
Σ cation	16.000	16.000	16.000	16.000	16.000	16.000	16.000	16.000	16.000	16.000	16.000	16.000	16.000	16.000	16.000	16.000
O	23.000	23.000	23.000	23.000	23.000	23.000	23.000	23.000	23.000	23.000	23.000	23.000	23.000	23.000	23.000	23.000

A4.2: Electron microprobe data of selected minerals of the Khibiny pluton ("-" - not detected, FeII/FeIII calculation according Treloar (unpublished))

mineral	amphibole	amphibole	amphibole	amphibole	amphibole
rock type	alkali syenite	alkali syenite	alkali syenite	alkali syenite	alkali syenite
#	Kh-03-58	Kh-03-58	Kh-03-58	Kh-03-58	Kh-03-58
SiO_2	45.00	44.92	35.04	50.78	51.23
TiO_2	2.10	1.97	3.85	0.76	0.73
Al_2O_3	4.56	4.16	9.71	1.07	1.14
Fe_2O_3	19.14	18.65	16.25	22.24	22.00
FeO	8.82	9.19	15.19	4.71	4.91
MnO	2.31	2.57	2.75	0.95	0.95
MgO	4.41	4.16	5.63	1.54	1.50
CaO	2.85	2.53	-	7.08	7.09
Na_2O	7.20	7.25	0.62	9.01	9.21
K_2O	1.50	1.66	9.20	-	-
TOTAL	97.89	97.06	98.24	98.13	98.75
Si	7.057	7.113	5.720	7.897	7.906
Ti	0.248	0.235	0.473	0.089	0.085
Al	0.843	0.777	1.869	0.196	0.207
Fe^{III}	2.511	2.470	2.218	2.892	2.839
Fe^{II}	1.036	1.089	1.857	0.548	0.567
Mn	0.307	0.345	0.380	0.125	0.124
Mg	1.031	0.982	1.370	0.357	0.345
Ca	0.479	0.429	-	1.180	1.172
Na	2.189	2.225	0.196	2.716	2.755
K	0.300	0.335	1.916	-	-
Σ cation	16.000	16.000	16.000	16.000	16.000
O	23.000	23.000	23.000	23.000	23.000

A4.2: Electron microprobe data of selected minerals of the Khibiny pluton ("-" - not detected, FeII/FeIII calculation according Treloar (unpublished))

mineral	feldspar	feldspar	feldspar	feldspar	feldspar	feldspar	feldspar	feldspar	feldspar	feldspar	feldspar	feldspar	feldspar	feldspar	feldspar	feldspar	feldspar	feldspar	feldspar	feldspar
rock type	khibinite	khibinite	khibinite	khibinite	khibinite	khibinite	khibinite	khibinite	khibinite	khibinite	khibinite	khibinite	khibinite	khibinite	khibinite	khibinite	khibinite	khibinite	khibinite	khibinite
#	Kh-03-2	Kh-03-2	Kh-03-2	Kh-03-2	Kh-03-2	Kh-03-2	Kh-03-2	Kh-03-2	Kh-03-2	Kh-03-2	Kh-03-2	Kh-03-2	Kh-03-2	Kh-03-2	Kh-03-2	Kh-03-2	Kh-03-2	Kh-03-2	Kh-03-1	Kh-03-1
SiO_2	65.82	64.54	68.68	69.50	63.75	63.91	65.82	67.94	63.93	68.55	68.97	63.70	66.15	70.50	65.94	68.11	70.17	66.06	65.45	69.52
TiO_2	0.04	0.05	0.02	-	-	0.06	0.04	0.02	0.08	0.02	-	-	-	-	-	-	-	-	-	-
Al_2O_3	18.71	18.27	19.00	18.94	20.75	17.47	18.71	19.92	18.29	19.54	19.48	18.70	18.76	19.65	19.18	19.25	19.53	18.74	18.79	19.63
Fe_2O_3	0.49	0.46	0.15	0.35	0.24	0.50	0.49	0.41	0.46	0.24	0.29	0.24	-	-	-	-	-	-	-	-
Na_2O	5.70	1.61	11.93	11.97	11.94	0.98	5.70	10.45	1.46	12.09	12.12	1.24	1.43	11.99	0.85	11.46	11.39	1.13	0.27	11.26
K_2O	11.29	14.52	0.24	0.10	0.72	15.63	11.29	0.14	14.89	0.43	0.14	15.50	15.63	-	16.41	0.13	0.18	15.04	16.90	0.20
BaO	0.19	0.21	0.03	0.04	0.03	0.26	0.19	0.06	0.43	0.04	0.04	0.65	-	-	-	-	-	-	-	-
TOTAL	102.44	99.77	100.13	101.10	97.53	98.93	102.44	99.51	99.76	101.04	101.11	100.06	101.97	102.14	102.38	98.95	101.27	100.97	101.41	100.61
Si	2.958	2.989	3.005	3.013	2.890	3.003	2.958	2.989	2.976	2.981	2.991	2.963	2.980	3.010	2.972	3.003	3.018	2.997	3.010	2.989
Ti	0.002	0.003	0.001	-	-	0.003	0.002	0.001	0.004	0.001	-	-	-	-	-	-	-	-	-	-
Al	0.991	0.997	0.980	0.968	1.109	0.967	0.991	1.033	1.003	1.001	0.996	1.025	0.996	0.989	1.019	1.000	0.990	1.002	1.002	1.011
Fe^{III}	0.017	0.016	0.005	0.011	0.008	0.018	0.017	0.014	0.016	0.008	0.009	0.008	-	-	-	-	-	0.017	-	-
Na	0.496	0.145	1.012	1.006	1.050	0.089	0.496	0.891	0.132	1.019	1.019	0.112	0.125	0.993	0.074	0.980	0.950	0.099	0.945	0.024
K	0.647	0.858	0.013	0.006	0.042	0.937	0.647	0.008	0.884	0.024	0.008	0.919	0.898	-	0.943	0.007	0.010	0.870	0.011	0.985
Ba	0.007	0.008	0.001	0.001	0.001	0.010	0.007	0.002	0.016	0.001	0.001	0.024	-	-	-	-	-	-	-	-
Σ cation	5.122	5.016	5.018	5.011	5.103	5.029	5.121	4.949	5.036	5.042	5.026	5.053	5.019	4.992	5.028	4.990	4.967	4.987	4.967	5.009
O	8.000	8.000	8.000	8.000	8.000	8.000	8.000	8.000	8.000	8.000	8.000	8.000	8.000	8.000	8.000	8.000	8.000	8.000	8.000	8.000

A4.2: Electron microprobe data of selected minerals of the Khibiny pluton ("-" - not detected)

mineral	feldspar	feldspar	feldspar	feldspar	feldspar	feldspar	feldspar	feldspar	feldspar	feldspar	feldspar	feldspar	feldspar	feldspar	feldspar	feldspar	feldspar	feldspar
rock type	khibinite	khibinite	khibinite	khibinite	rischorrite	rischorrite	rischorrite	rischorrite	rischorrite	rischorrite	trachytoid foyaite	trachytoid foyaite	massive foyaite	massive foyaite	massive foyaite	massive foyaite	massive foyaite	massive foyaite
#	Kh-03-1	Kh-03-1	Kh-03-1	Kh-03-1	Kh-03-9	Kh-03-9	Kh-03-9	Kh-03-9	Kh-03-9	Kh-03-9	Kh-03-35	Kh-03-35	Kh-03-53	Kh-03-53	Kh-03-53	Kh-03-53	Kh-03-53	Kh-03-53
SiO_2	68.46	65.56	70.55	70.05	63.08	63.74	64.48	63.81	63.92	63.72	69.36	62.55	65.41	65.58	69.25	64.58	65.23	69.20
TiO_2	-	-	-	-	-	0.02	0.02	0.03	0.04	0.05	-	-	-	-	-	-	-	-
Al_2O_3	19.29	18.75	20.06	19.93	17.33	17.65	18.01	17.82	17.92	17.96	19.39	18.40	18.34	18.58	19.31	18.72	18.42	19.10
Fe_2O_3	-	-	-	-	0.55	0.84	0.42	0.57	0.66	0.67	0.34	0.25	-	-	-	-	-	-
Na_2O	10.14	0.40	11.98	12.06	0.55	0.42	0.46	0.47	0.44	0.45	11.26	0.11	2.21	1.92	10.98	1.59	1.86	11.01
K_2O	2.92	17.01	0.13	-	16.53	16.66	16.74	16.51	16.61	16.58	0.14	16.06	14.00	14.36	0.18	14.66	14.61	0.24
BaO	-	-	-	-	-	-	-	-	-	-	0.03	0.90	-	-	-	-	-	-
TOTAL	100.81	101.72	102.72	102.04	98.21	99.35	100.23	99.22	99.61	99.53	100.66	98.63	99.96	100.44	99.72	99.55	100.12	99.55
Si	2.998	2.988	2.998	2.996	2.997	2.992	2.993	2.992	2.988	2.983	3.011	2.967	3.002	2.998	3.021	2.984	2.997	3.025
Ti	-	-	-	-	-	0.001	0.001	0.001	0.002	0.003	-	-	-	-	-	-	-	-
Al	0.995	1.007	1.005	1.005	0.971	0.977	0.985	0.985	0.987	0.991	0.992	1.029	0.992	1.001	0.993	1.019	0.997	0.984
Fe^{III}	-	-	-	-	0.020	0.030	0.015	0.020	0.023	0.023	0.011	0.009	-	-	-	-	-	-
Na	0.861	0.035	0.987	1.000	0.051	0.038	0.041	0.043	0.040	0.040	0.948	0.010	0.197	0.170	0.929	0.142	0.166	0.933
K	0.163	0.989	0.007	-	1.002	0.998	0.991	0.987	0.990	0.990	0.008	0.972	0.820	0.837	0.010	0.864	0.856	0.013
Ba	-	-	-	-	-	-	-	-	-	-	0.001	0.033	-	-	-	-	-	-
Σ cation	5.017	5.020	4.997	5.001	5.046	5.037	5.030	5.029	5.031	5.035	4.973	5.028	5.010	5.006	4.952	5.010	5.016	4.956
O	8.000	8.000	8.000	8.000	8.000	8.000	8.000	8.000	8.000	8.000	8.000	8.000	8.000	8.000	8.000	8.000	8.000	8.000

A4.2: Electron microprobe data of selected minerals of the Khibiny pluton ("-" - not detected)

mineral	feldspar	feldspar	feldspar	feldspar	feldspar	feldspar	feldspar	feldspar	feldspar
rock type	massive foyaite	massive foyaite	massive foyaite	alkali syenite	alkali syenite	alkaline syenite	alkaline syenite	alkaline syenite	alkaline syenite
#	Kh-03-53	Kh-03-53	Kh-03-53	Kh-03-58	Kh-03-58	Kh-03-58	Kh-03-58	Kh-03-58	Kh-03-58
SiO_2	68.54	68.69	69.00	63.31	63.10	61.72	63.73	63.73	64.40
TiO_2	-	-	-	-	-	0.02	0.03	0.03	-
Al_2O_3	19.39	18.97	19.38	17.96	18.05	18.75	17.93	17.93	17.95
Fe_2O_3	-	-	-	-	-	0.48	0.54	0.54	0.30
Na_2O	11.03	10.98	11.18	0.31	1.36	0.88	0.49	0.49	0.35
K_2O	0.17	0.15	0.00	16.64	14.55	15.96	15.77	15.77	16.22
BaO	-	-	-	-	-	0.15	0.44	0.44	0.37
TOTAL	99.13	98.79	99.56	98.22	97.06	98.17	99.22	99.03	99.65
Si	3.010	3.025	3.015	2.992	2.992	2.936	2.992	2.992	3.001
Ti	-	-	-	-	-	0.001	0.001	0.001	-
Al	1.004	0.985	0.998	1.000	1.009	1.051	0.992	0.992	0.986
Fe^{III}	-	-	-	-	-	0.017	0.019	0.019	0.010
Na	0.939	0.937	0.947	0.028	0.125	0.081	0.045	0.045	0.031
K	0.010	0.008	0.000	1.003	0.880	0.969	0.944	0.945	0.964
Ba	-	-	-	-	-	0.005	0.016	0.016	0.014
Σ cation	4.962	4.956	4.960	5.024	5.006	5.068	5.016	5.014	5.010
O	8.000	8.000	8.000	8.000	8.000	8.000	8.000	8.000	8.000

A4.2: Electron microprobe data of selected minerals of the Khibiny pluton ("-" - not detected)

mineral	nepheline	nepheline	nepheline	nepheline	nepheline	nepheline	nepheline	nepheline	nepheline	nepheline	nepheline	nepheline	nepheline	nepheline	nepheline	nepheline	nepheline
rock type	rischorrite	rischorrite	rischorrite	rischorrite	rischorrite	rischorrite	rischorrite	rischorrite	rischorrite	rischorrite	rischorrite	rischorrite	trachytoid foyaite	trachytoid foyaite	trachytoid foyaite	trachytoid foyaite	trachytoid foyaite
#	Kh-03-14	Kh-03-14	Kh-03-14	Kh-03-14	Kh-03-14	Kh-03-14	Kh-03-14	Kh-03-14	Kh-03-14	Kh-03-9	Kh-03-9	Kh-03-9	Kh-03-35	Kh-03-35	Kh-03-36	Kh-03-38	Kh-03-38
SiO_2	41.29	40.63	41.25	41.20	41.06	41.47	43.79	42.22	42.53	44.15	44.97	44.15	45.01	45.01	44.33	45.32	45.37
TiO_2	-	-	-	-	-	-	-	-	-	-	-	-	0.02	0.02	-	-	-
Al_2O_3	32.36	32.78	32.18	31.34	32.81	32.35	30.82	33.72	32.61	32.16	32.56	32.16	31.26	31.26	31.61	32.47	32.53
Fe_2O_3	1.56	1.77	1.58	2.40	1.46	1.89	1.09	2.01	1.77	0.61	0.69	0.61	0.97	0.97	0.86	1.40	1.40
MnO	-	-	-	-	-	-	-	-	-	-	-	-	-	-	-	-	-
MgO	-	-	-	-	-	-	-	-	-	-	-	-	-	-	-	-	-
CaO	-	-	-	-	-	-	-	-	-	-	0.56	-	-	-	-	-	-
Na_2O	15.44	15.23	15.25	15.37	15.50	15.28	14.00	15.71	15.59	15.77	11.90	15.77	16.29	16.29	15.77	16.15	16.07
K_2O	7.15	7.94	7.41	7.38	7.82	7.32	8.09	8.13	7.83	5.55	6.14	5.55	6.23	6.23	5.31	6.09	6.08
TOTAL	97.80	98.35	97.67	97.69	98.65	98.31	97.79	101.79	100.33	98.24	97.11	98.24	99.78	99.78	97.88	101.43	101.45
Si	4.113	4.050	4.119	4.135	4.072	4.116	4.333	4.066	4.142	4.295	4.367	4.295	4.341	4.341	4.327	4.297	4.299
Ti	-	-	-	-	-	-	-	-	-	-	-	-	0.002	0.002	-	-	-
Al	3.799	3.851	3.787	3.707	3.834	3.784	3.594	3.827	3.743	3.687	3.726	3.687	3.553	3.553	3.636	3.628	3.632
Fe^{III}	0.130	0.148	0.132	0.201	0.121	0.157	0.090	0.162	0.144	0.050	0.056	0.050	0.078	0.078	0.070	0.111	0.111
Mn	-	-	-	-	-	-	-	-	-	-	-	-	-	-	-	-	-
Mg	-	-	-	-	-	-	-	-	-	-	-	-	-	-	-	-	-
Ca	-	-	-	-	-	-	-	-	-	-	0.058	-	-	-	-	-	-
Na	2.982	2.943	2.953	2.991	2.980	2.940	2.686	2.933	2.943	2.974	2.240	2.974	3.046	3.046	2.984	2.969	2.952
K	0.909	1.010	0.944	0.945	0.989	0.927	1.021	0.999	0.973	0.689	0.760	0.689	0.766	0.766	0.661	0.737	0.735
Σ cation	11.933	12.001	11.935	11.979	11.996	11.925	11.724	11.987	11.945	11.693	11.239	11.693	11.787	11.787	11.678	11.741	11.729
O	16.000	16.000	16.000	16.000	16.000	16.000	16.000	16.000	16.000	16.000	16.000	16.000	16.000	16.000	16.000	16.000	16.000

A4.2: Electron microprobe data of selected minerals of the Khibiny pluton ("-" - not detected)

mineral	feldspar	feldspar	feldspar	feldspar	feldspar	feldspar	feldspar	feldspar	feldspar	feldspar	feldspar	feldspar	feldspar	feldspar	feldspar	feldspar	feldspar
rock type	khibinite	khibinite	khibinite	khibinite	rischorrite	rischorrite	rischorrite	rischorrite	rischorrite	rischorrite	trachytoid foyaite	trachytoid foyaite	massive foyaite	massive foyaite	massive foyaite	massive foyaite	massive foyaite	massive foyaite
#	Kh-03-1	Kh-03-1	Kh-03-1	Kh-03-1	Kh-03-9	Kh-03-9	Kh-03-9	Kh-03-9	Kh-03-9	Kh-03-9	Kh-03-35	Kh-03-35	Kh-03-53	Kh-03-53	Kh-03-53	Kh-03-53	Kh-03-53	Kh-03-53
SiO_2	68 46	65 56	70 55	70 05	63 08	63 74	64 48	63 81	63 92	63 72	69 36	62 55	65 41	65 58	69 25	64 58	65 23	69 20
TiO_2	-	-	-	-	-	0 02	0 02	0 03	0 04	0 05	-	-	-	-	-	-	-	-
Al_2O_3	19 29	18 75	20 06	19 93	17 33	17 65	18 01	17 82	17 92	17 96	19 39	18 40	18 34	18 58	19 31	18 72	18 42	19 10
Fe_2O_3	-	-	-	-	0 55	0 84	0 42	0 57	0 66	0 67	0 34	0 25	-	-	-	-	-	-
Na_2O	10 14	0 40	11 98	12 06	0 55	0 42	0 46	0 47	0 44	0 45	11 26	0 11	2 21	1 92	10 98	1 59	1 86	11 01
K_2O	2 92	17 01	0 13	-	16 53	16 66	16 74	16 51	16 61	16 58	0 14	16 06	14 00	14 36	0 18	14 66	14 61	0 24
BaO	-	-	-	-	-	-	-	-	-	-	0 03	0 90	-	-	-	-	-	-
TOTAL	100 81	101 72	102 72	102 04	98 21	99 35	100 23	99 22	99 61	99 53	100 66	98 63	99 96	100 44	99 72	99 55	100 12	99 55
Si	2 998	2 988	2 998	2 996	2 997	2 992	2 993	2 992	2 988	2 983	3 011	2 967	3 002	2 998	3 021	2 984	2 997	3 025
Ti	-	-	-	-	-	0 001	0 001	0 001	0 002	0 003	-	-	-	-	-	-	-	-
Al	0 995	1 007	1 005	1 005	0 971	0 977	0 985	0 985	0 987	0 991	0 992	1 029	0 992	1 001	0 993	1 019	0 997	0 984
Fe^{III}	-	-	-	-	0 020	0 030	0 015	0 020	0 023	0 023	0 011	0 009	-	-	-	-	-	-
Na	0 861	0 035	0 987	1 000	0 051	0 038	0 041	0 043	0 040	0 040	0 948	0 010	0 197	0 170	0 929	0 142	0 166	0 933
K	0 163	0 989	0 007	-	1 002	0 998	0 991	0 987	0 990	0 990	0 008	0 972	0 820	0 837	0 010	0 864	0 856	0 013
Ba	-	-	-	-	-	-	-	-	-	-	0 001	0 033	-	-	-	-	-	-
Σ cation	5 017	5 020	4 997	5 001	5 046	5 037	5 030	5 029	5 031	5 035	4 973	5 028	5 010	5 006	4 952	5 010	5 016	4 956
O	8 000	8 000	8 000	8 000	8 000	8 000	8 000	8 000	8 000	8 000	8 000	8 000	8 000	8 000	8 000	8 000	8 000	8 000

A4.2: Electron microprobe data of selected minerals of the Khibiny pluton ("-" - not detected)

mineral	feldspar	feldspar	feldspar	feldspar	feldspar	feldspar	feldspar	feldspar	feldspar
rock type	massive foyaite	massive foyaite	massive foyaite	alkali syenite	alkali syenite	alkaline syenite	alkaline syenite	alkaline syenite	alkaline syenite
#	Kh-03-53	Kh-03-53	Kh-03-53	Kh-03-58	Kh-03-58	Kh-03-58	Kh-03-58	Kh-03-58	Kh-03-58
SiO_2	68.54	68.69	69.00	63.31	63.10	61.72	63.73	63.73	64.40
TiO_2	-	-	-	-	-	0.02	0.03	0.03	-
Al_2O_3	19.39	18.97	19.38	17.96	18.05	18.75	17.93	17.93	17.95
Fe_2O_3	-	-	-	-	-	0.48	0.54	0.54	0.30
Na_2O	11.03	10.98	11.18	0.31	1.36	0.88	0.49	0.49	0.35
K_2O	0.17	0.15	0.00	16.64	14.55	15.96	15.77	15.77	16.22
BaO	-	-	-	-	-	0.15	0.44	0.44	0.37
TOTAL	99.13	98.79	99.56	98.22	97.06	98.17	99.22	99.03	99.65
Si	3.010	3.025	3.015	2.992	2.992	2.936	2.992	2.992	3.001
Ti	-	-	-	-	-	0.001	0.001	0.001	-
Al	1.004	0.985	0.998	1.000	1.009	1.051	0.992	0.992	0.986
Fe^{III}	-	-	-	-	-	0.017	0.019	0.019	0.010
Na	0.939	0.937	0.947	0.028	0.125	0.081	0.045	0.045	0.031
K	0.010	0.008	0.000	1.003	0.880	0.969	0.944	0.945	0.964
Ba	-	-	-	-	-	0.005	0.016	0.016	0.014
Σ cation	4.962	4.956	4.960	5.024	5.006	5.068	5.016	5.014	5.010
O	8.000	8.000	8.000	8.000	8.000	8.000	8.000	8.000	8.000

A4.2: Electron microprobe data of selected minerals of the Khibiny pluton ("-" - not detected)

mineral	nepheline	nepheline	nepheline	nepheline	nepheline	nepheline	nepheline	nepheline	nepheline	nepheline	nepheline	nepheline	nepheline	nepheline	nepheline	nepheline	nepheline	nepheline
rock type	khibinite	khibinite	khibinite	khibinite	khibinite	khibinite	khibinite	khibinite	khibinite	khibinite	khibinite	khibinite	rischorrite	rischorrite	rischorrite	rischorrite	rischorrite	rischorrite
#	Kh-03-2	Kh-03-2	Kh-03-2	Kh-03-2	Kh-03-2	Kh-03-2	Kh-03-2	Kh-03-2	Kh-03-2	Kh-03-2	Kh-03-2	Kh-03-2	Kh-03-9	Kh-03-9	Kh-03-9	Kh-03-9	Kh-03-14	Kh-03-14
SiO_2	45.25	47.02	45.42	45.25	47.24	45.70	43.71	45.46	45.88	43.86	41.92	45.62	42.92	44.01	42.11	43.13	41.79	41.65
TiO_2	0.03	0.02	0.04	0.03	0.02	-	-	-	-	-	-	-	-	0.09	-	0.03	-	-
Al_2O_3	31.17	31.36	31.85	31.17	33.06	30.57	33.01	32.34	31.91	31.02	32.94	31.04	33.66	31.00	32.53	32.67	32.08	32.79
Fe_2O_3	1.39	1.33	0.01	1.39	1.35	1.58	0.57	0.94	1.30	1.50	0.49	1.52	1.13	2.93	2.08	1.90	0.96	0.55
MnO	-	0.04	1.29	0.01	0.02	-	-	-	-	-	-	-	-	0.11	-	-	-	-
MgO	0.06	0.07	0.07	0.06	0.02	-	-	-	-	-	-	-	-	0.37	0.05	0.03	-	-
CaO	-	0.01	-	-	0.06	-	-	-	-	-	-	-	-	0.18	-	0.01	-	-
Na_2O	16.72	16.60	17.09	16.72	16.27	16.14	15.98	16.30	16.25	15.52	15.59	15.91	15.79	14.30	16.47	16.30	15.22	15.46
K_2O	5.77	5.08	5.12	5.77	2.00	4.72	6.31	5.68	5.49	5.33	6.62	5.28	7.80	6.82	7.49	7.33	7.35	7.23
TOTAL	100.39	101.51	100.89	100.40	100.04	98.71	99.58	100.72	100.83	97.23	97.56	99.37	101.30	99.83	100.72	101.40	97.40	97.68
Si	4.340	4.423	4.319	4.340	4.413	4.420	4.219	4.322	4.356	4.325	4.145	4.393	4.123	4.278	4.101	4.152	4.165	4.131
Ti	0.004	0.002	0.004	0.003	0.002	-	-	-	-	-	-	-	-	0.010	-	0.004	-	-
Al	3.523	3.476	3.569	3.523	3.640	3.485	3.755	3.623	3.571	3.605	3.838	3.522	3.810	3.552	3.734	3.707	3.768	3.833
Fe^{III}	0.111	0.104	0.001	0.111	0.105	0.128	0.046	0.075	0.103	0.124	0.041	0.122	0.091	0.238	0.169	0.153	0.080	0.046
Mn	-	0.003	0.104	0.001	0.002	-	-	-	-	-	-	-	-	0.009	-	-	-	-
Mg	0.008	0.009	0.010	0.009	0.003	-	-	-	-	-	-	-	-	0.054	0.007	0.004	-	-
Ca	-	0.001	-	-	0.006	-	-	-	-	-	-	-	-	0.019	-	0.001	-	-
Na	3.109	3.027	3.150	3.108	2.946	3.027	2.990	3.004	2.991	2.967	2.989	2.970	2.940	2.695	3.110	3.041	2.941	2.973
K	0.706	0.610	0.621	0.706	0.238	0.582	0.777	0.689	0.665	0.670	0.835	0.648	0.956	0.846	0.930	0.900	0.934	0.915
Σ cation	11.801	11.655	11.778	11.802	11.355	11.642	11.787	11.713	11.686	11.691	11.848	11.656	11.919	11.702	12.051	11.961	11.889	11.896
O	16.000	16.000	16.000	16.000	16.000	16.000	16.000	16.000	16.000	16.000	16.000	16.000	16.000	16.000	16.000	16.000	16.000	16.000

A4.2: Electron microprobe data of selected minerals of the Khibiny pluton ("-" - not detected)

mineral	nepheline	nepheline	nepheline	nepheline	nepheline	nepheline	nepheline	nepheline	nepheline	nepheline	nepheline	nepheline	nepheline	nepheline	nepheline	nepheline	nepheline
rock type	rischorrite	rischorrite	rischorrite	rischorrite	rischorrite	rischorrite	rischorrite	rischorrite	rischorrite	rischorrite	rischorrite	rischorrite	trachytoid foyaite	trachytoid foyaite	trachytoid foyaite	trachytoid foyaite	trachytoid foyaite
#	Kh-03-14	Kh-03-14	Kh-03-14	Kh-03-14	Kh-03-14	Kh-03-14	Kh-03-14	Kh-03-14	Kh-03-14	Kh-03-9	Kh-03-9	Kh-03-9	Kh-03-35	Kh-03-35	Kh-03-36	Kh-03-38	Kh-03-38
SiO_2	41.29	40.63	41.25	41.20	41.06	41.47	43.79	42.22	42.53	44.15	44.97	44.15	45.01	45.01	44.33	45.32	45.37
TiO_2	-	-	-	-	-	-	-	-	-	-	-	-	0.02	0.02	-	-	-
Al_2O_3	32.36	32.78	32.18	31.34	32.81	32.35	30.82	33.72	32.61	32.16	32.56	32.16	31.26	31.26	31.61	32.47	32.53
Fe_2O_3	1.56	1.77	1.58	2.40	1.46	1.89	1.09	2.01	1.77	0.61	0.69	0.61	0.97	0.97	0.86	1.40	1.40
MnO	-	-	-	-	-	-	-	-	-	-	-	-	-	-	-	-	-
MgO	-	-	-	-	-	-	-	-	-	-	-	-	-	-	-	-	-
CaO	-	-	-	-	-	-	-	-	-	-	0.56	-	-	-	-	-	-
Na_2O	15.44	15.23	15.25	15.37	15.50	15.28	14.00	15.71	15.59	15.77	11.90	15.77	16.29	16.29	15.77	16.15	16.07
K_2O	7.15	7.94	7.41	7.38	7.82	7.32	8.09	8.13	7.83	5.55	6.14	5.55	6.23	6.23	5.31	6.09	6.08
TOTAL	97.80	98.35	97.67	97.69	98.65	98.31	97.79	101.79	100.33	98.24	97.11	98.24	99.78	99.78	97.88	101.43	101.45
Si	4.113	4.050	4.119	4.135	4.072	4.116	4.333	4.066	4.142	4.295	4.367	4.295	4.341	4.341	4.327	4.297	4.299
Ti	-	-	-	-	-	-	-	-	-	-	-	-	0.002	0.002	-	-	-
Al	3.799	3.851	3.787	3.707	3.834	3.784	3.594	3.827	3.743	3.687	3.726	3.687	3.553	3.553	3.636	3.628	3.632
Fe^{III}	0.130	0.148	0.132	0.201	0.121	0.157	0.090	0.162	0.144	0.050	0.056	0.050	0.078	0.078	0.070	0.111	0.111
Mn	-	-	-	-	-	-	-	-	-	-	-	-	-	-	-	-	-
Mg	-	-	-	-	-	-	-	-	-	-	-	-	-	-	-	-	-
Ca	-	-	-	-	-	-	-	-	-	-	0.058	-	-	-	-	-	-
Na	2.982	2.943	2.953	2.991	2.980	2.940	2.686	2.933	2.943	2.974	2.240	2.974	3.046	3.046	2.984	2.969	2.952
K	0.909	1.010	0.944	0.945	0.989	0.927	1.021	0.999	0.973	0.689	0.760	0.689	0.766	0.766	0.661	0.737	0.735
Σ cation	11.933	12.001	11.935	11.979	11.996	11.925	11.724	11.987	11.945	11.693	11.239	11.693	11.787	11.787	11.678	11.741	11.729
O	16.000	16.000	16.000	16.000	16.000	16.000	16.000	16.000	16.000	16.000	16.000	16.000	16.000	16.000	16.000	16.000	16.000

A4.2: Electron microprobe data of selected minerals of the Khibiny pluton ("-" - not detected)

mineral	nepheline	nepheline	nepheline	nepheline	nepheline	nepheline	nepheline	nepheline	nepheline	nepheline	nepheline	nepheline	nepheline	nepheline
rock type	trachytoid foyaite	trachytoid foyaite	trachytoid foyaite	massive foyaite	massive foyaite	massive foyaite	massive foyaite	massive foyaite	massive foyaite	lujavrite	lujavrite	lujavrite	alkaline syenite	alkaline syenite
#	Kh-03-38	Kh-03-38	Kh-03-38	Kh-03-53	Kh-03-53	Kh-03-53	Kh-03-53	Kh-03-53	Kh-03-53	Kh-03-21	Kh-03-21	Kh-03-21	Kh-03-58	Kh-03-58
SiO_2	45.99	46.34	45.60	43.77	44.74	43.95	43.98	43.99	44.21	43.34	44.59	43.29	44.24	44.32
TiO_2	-	-	-	-	-	-	-	-	-	0.01	0.01	0.02	0.02	0.02
Al_2O_3	32.59	32.85	33.48	33.10	32.56	32.41	32.43	32.72	32.44	32.83	32.40	32.13	31.87	31.06
Fe_2O_3	1.31	0.84	0.71	0.48	0.66	0.62	0.68	0.63	0.48	0.36	1.08	0.39	0.70	0.93
MnO	-	-	-	-	-	-	-	-	-	-	0.06	0.01	-	-
MgO	-	-	-	-	-	-	-	-	-	-	-	-	-	-
CaO	-	-	-	-	-	0.15	-	-	-	-	0.02	-	0.01	-
Na_2O	14.15	16.13	16.23	15.36	15.60	15.56	15.36	15.55	15.52	16.89	16.82	17.08	16.60	16.80
K_2O	5.72	5.84	6.16	6.59	6.06	6.08	6.18	6.20	6.27	6.75	6.22	6.68	6.13	5.91
TOTAL	100.01	102.00	102.18	99.30	99.62	98.77	98.63	99.09	98.92	100.18	101.21	99.61	99.57	99.04
Si	4.372	4.341	4.276	4.230	4.297	4.266	4.273	4.256	4.282	4.184	4.253	4.209	4.278	4.313
Ti	-	-	-	-	-	-	-	-	-	0.001	0.001	0.002	0.002	0.002
Al	3.651	3.626	3.700	3.770	3.686	3.708	3.713	3.731	3.702	3.736	3.642	3.681	3.632	3.562
Fe^{III}	0.104	0.066	0.056	0.039	0.053	0.050	0.055	0.051	0.039	0.029	0.086	0.031	0.056	0.076
Mn	-	-	-	-	-	-	-	-	-	-	0.005	0.001	-	-
Mg	-	-	-	-	-	-	-	-	-	-	-	-	-	-
Ca	-	-	-	-	-	0.016	-	-	-	-	0.002	-	0.001	-
Na	2.608	2.929	2.950	2.878	2.905	2.928	2.893	2.917	2.914	3.161	3.110	3.220	3.112	3.169
K	0.694	0.698	0.737	0.812	0.742	0.753	0.766	0.765	0.775	0.832	0.757	0.829	0.756	0.733
Σ cation	11.453	11.660	11.718	11.730	11.684	11.721	11.700	11.720	11.711	11.942	11.857	11.972	11.837	11.855
O	16.000	16.000	16.000	16.000	16.000	16.000	16.000	16.000	16.000	16.000	16.000	16.000	16.000	16.000

A4.2: Electron microprobe data of selected minerals of the Khibiny pluton ("-" - not detected)

mineral	aenig matite	aenig matite	biotite	biotite	biotite	titanite	titanite	titanite	titanite	titanite	ilmenite	loren zenite	loren zenite	astro phyllite	astro phyllite	astro phyllite	astro phyllite	cancrinite	cancrinite
rock type	khibinite	khibinite	alkaline syenite	alkaline syenite	alkaline syenite	khibinite	rischorrite	rischorrite	rischorrite	rischorrite	rischorrite	rischorrite	rischorrite	rischorrite	rischorrite	lujavrite	lujavrite	lujavrite	lujavrite
#	Kh-03-2	Kh-03-2	Kh-03-58	Kh-03-58	Kh-03-58	Kh-03-2	Kh-03-9	Kh-03-9	Kh-03-9	Kh-03-9	Kh-03-9	Kh-03-9	Kh-03-9	Kh-03-9	Kh-03-9	Kh-03-21	Kh-03-21	Kh-03-21	Kh-03-21
SiO_2	39.94	40.67	35.33	35.80	34.91	30.06	30.24	30.42	30.42	30.23	0.01	34.73	36.01	34.51	34.51	35.10	36.08	47.45	47.36
TiO_2	9.72	9.91	3.62	3.48	3.52	39.69	39.88	40.11	40.11	40.07	52.30	45.00	43.80	11.98	11.98	11.20	11.44	-	0.04
Al_2O_3	1.27	0.47	9.98	9.99	9.87	0.13	0.11	0.09	0.09	0.10	0.06	0.09	0.07	1.52	1.52	0.98	0.78	32.29	32.24
Fe_2O_3	5.50	3.20	33.08	32.31	31.60	0.35	0.70	0.68	0.68	0.41	29.86	0.00	0.00	0.00	0.00	27.20	27.55	0.04	0.13
FeO	32.78	33.66	0.00	0.00	0.00	0.00	0.00	0.00	0.00	0.00	0.00	1.28	2.52	27.19	27.19	0.00	0.00	0.00	0.00
MnO	3.42	3.53	2.08	2.43	2.31	0.08	0.05	-	-	0.11	19.98	-	-	7.44	7.44	6.31	6.34	-	-
MgO	0.99	1.17	5.43	5.77	5.44	-	-	-	-	-	-	0.02	-	1.85	1.85	2.03	2.11	-	-
CaO	0.23	0.29	-	-	0.04	25.24	26.77	27.14	27.14	26.57	0.03	0.15	0.12	2.12	2.12	1.52	1.47	1.62	1.70
Na_2O	7.59	7.49	0.31	0.20	0.31	1.54	1.05	0.98	0.98	1.12	0.08	18.32	18.22	1.60	1.60	2.50	2.72	14.63	13.03
K_2O	0.02	-	9.46	9.45	9.03	-	0.04	0.09	0.09	0.03	-	0.03	0.02	6.94	6.94	6.34	6.19	0.02	0.00
TOTAL	101.44	100.39	99.29	99.43	97.03	97.08	98.84	99.51	99.51	98.63	102.33	99.60	100.76	95.15	95.15	93.17	94.68	96.05	94.50
Si	5.696	5.813	5.65	5.69	5.68	0.671	0.668	0.668	0.668	0.667	0.000	2.052	1.984	8.244	8.261	7.679	7.744	7.346	7.402
Ti	1.042	1.065	0.65	0.62	0.65	0.999	0.993	0.993	0.993	0.997	1.121	1.877	1.994	2.151	2.088	1.842	1.846	-	0.004
Al	0.213	0.079	1.88	1.87	1.89	0.003	0.003	0.002	0.002	0.003	0.001	0.005	0.003	0.428	0.434	0.254	0.196	5.892	5.940
Fe^{III}	0.000	0.000	3.98	3.87	3.87	0.006	0.012	0.011	0.011	0.007	0.427	0.000	0.000	0.000	0.000	4.976	4.945	0.005	0.017
Fe^{II}	4.497	4.366	0.00	0.00	0.00	0.000	0.000	0.000	0.000	0.000	0.000	0.120	0.036	5.432	5.485	0.000	0.000	0.000	0.000
Mn	0.413	0.427	0.28	0.33	0.32	0.001	0.001	-	-	0.002	0.321	-	-	1.506	1.459	1.170	1.153	-	-
Mg	0.209	0.249	1.29	1.37	1.32	-	-	-	-	-	-	0.002	-	0.660	0.680	0.660	0.676	-	-
Ca	0.035	0.045	-	-	0.01	0.603	0.633	0.638	0.638	0.628	0.001	0.007	0.009	0.543	0.499	0.357	0.338	0.269	0.285
Na	2.097	2.075	0.09	0.06	0.10	0.067	0.045	0.042	0.042	0.048	0.003	2.012	1.987	2.114	2.144	1.770	1.694	4.390	3.948
K	0.003	-	1.93	1.92	1.87	-	0.001	0.002	0.002	0.001	-	0.001	0.002	0.740	0.914	1.060	1.132	0.004	-
Σ cation	14.206	14.120	15.761	15.728	15.703	2.351	2.356	2.357	2.357	2.353	1.874	6.076	6.015	21.819	21.963	19.767	19.725	17.905	17.597
O	20.000	20.000	22.000	22.000	22.000	4.000	4.000	4.000	4.000	4.000	3.000	9.000	9.000	31.000	31.000	31.000	31.000	24.000	24.000

Appendix A4.2 Electron microprobe **data** for selected minerals of the Khibiny pluton ("-" - not detected, Fe^{II}/Fe^{III} **calculation** according Treloar (unpublished))

mineral	clino pyroxene	clino pyroxene	clino pyroxene	clino pyroxene	clino pyroxene	clino pyroxene	clino pyroxene	clino pyroxene	clino pyroxene	clino pyroxene	clino pyroxene	clino pyroxene	clino pyroxene	clino pyroxene	clino pyroxene	clino pyroxene	clino pyroxene	clino pyroxene	clino pyroxene
rock type	khibinite	khibinite	khibinite	khibinite	khibinite	khibinite	khibinite	khibinite	khibinite	khibinite	rischorrite	albitized foyaite	albitized foyaite	albitized foyaite	albitized foyaite	lujavrite	lujavrite	lujavrite	lujavrite
#	Kh-03-2	Kh-03-2	Kh-03-2	Kh-03-2	Kh-03-2	Kh-03-2	Kh-03-2	Kh-03-2	Kh-03-2	Kh-03-2	Kh-03-14	Kh-03-39	Kh-03-39	Kh-03-39	Kh-03-39	Kh-03-21	Kh-03-21	Kh-03-21	Kh-03-21
SiO_2	51.06	51.20	51.87	51.98	52.31	52.53	53.11	53.17	53.76	53.95	51.71	52.54	52.74	52.83	52.99	52.58	52.81	52.13	52.73
TiO_2	1.89	3.50	4.07	1.50	4.65	1.24	3.91	3.21	3.45	4.40	1.51	1.38	1.71	2.26	2.08	1.90	1.47	1.28	1.28
Al_2O_3	0.84	0.92	1.10	1.02	2.36	1.05	1.21	1.09	0.82	1.19	0.36	1.20	1.13	1.09	0.96	1.11	1.09	1.02	1.12
Fe_2O_3	7.48	6.09	5.11	8.52	6.90	5.68	6.08	6.64	4.12	7.73	6.34	3.82	6.03	4.81	6.02	3.00	2.63	3.01	2.40
FeO	18.93	19.71	21.61	14.27	18.50	18.67	20.73	20.25	24.93	19.53	20.48	25.55	23.44	24.07	24.36	26.79	27.52	27.09	27.95
MnO	0.51	0.37	0.54	1.09	0.53	1.00	0.73	0.61	0.54	0.52	0.73	0.64	0.51	1.04	0.52	0.43	0.35	0.37	0.32
MgO	1.87	1.14	0.76	5.02	1.25	3.71	1.21	1.21	0.94	0.81	2.13	1.41	1.05	0.87	0.89	0.75	0.70	0.65	0.72
CaO	7.50	3.41	2.01	13.65	3.22	9.73	3.59	4.58	1.51	2.34	7.65	4.28	3.87	3.24	3.28	2.80	2.58	2.63	2.10
Na_2O	9.02	11.11	12.10	5.92	11.42	8.23	11.53	11.04	12.75	12.03	9.17	11.13	11.05	11.57	11.41	12.13	12.28	11.99	12.41
K_2O	-	-	-	-	-	-	-	-	-	-	-	-	-	-	-	-	-	-	-
TOTAL	99.10	97.45	99.17	102.97	101.14	101.84	102.10	101.80	102.82	102.50	100.08	101.95	101.53	101.78	102.51	101.48	101.44	100.17	101.03
Si	1.990	2.008	1.997	1.950	1.972	1.979	1.991	2.002	1.998	2.013	1.995	1.980	1.999	1.995	1.993	1.987	1.994	1.997	1.998
Ti	0.055	0.103	0.118	0.042	0.132	0.035	0.110	0.091	0.096	0.123	0.044	0.039	0.049	0.064	0.059	0.054	0.042	0.037	0.037
Al	0.039	0.043	0.050	0.045	0.105	0.047	0.053	0.048	0.036	0.052	0.016	0.053	0.051	0.049	0.043	0.049	0.048	0.046	0.050
Fe^{III}	0.244	0.200	0.165	0.267	0.218	0.179	0.191	0.209	0.128	0.241	0.205	0.121	0.191	0.152	0.189	0.095	0.083	0.096	0.076
Fe^{II}	0.552	0.579	0.623	0.401	0.522	0.527	0.582	0.571	0.694	0.546	0.592	0.721	0.665	0.680	0.686	0.758	0.778	0.777	0.793
Mn	0.017	0.012	0.018	0.035	0.017	0.032	0.023	0.019	0.017	0.016	0.024	0.020	0.016	0.033	0.017	0.014	0.011	0.012	0.010
Mg	0.109	0.067	0.044	0.281	0.070	0.208	0.068	0.068	0.052	0.045	0.122	0.079	0.059	0.049	0.050	0.042	0.040	0.037	0.041
Ca	0.313	0.143	0.083	0.549	0.130	0.393	0.144	0.185	0.060	0.094	0.316	0.173	0.157	0.131	0.132	0.113	0.105	0.108	0.085
Na	0.681	0.845	0.903	0.430	0.835	0.601	0.838	0.806	0.919	0.870	0.686	0.813	0.812	0.847	0.832	0.888	0.899	0.890	0.911
K	-	-	-	-	-	-	-	-	-	-	-	-	-	-	-	-	-	-	-
Σ cation	4.000	4.000	4.000	4.000	4.000	4.000	4.000	4.000	4.000	4.000	4.000	4.000	4.000	4.000	4.000	4.000	4.000	4.000	4.000
O	6.000	6.000	6.000	6.000	6.000	6.000	6.000	6.000	6.000	6.000	6.000	6.000	6.000	6.000	6.000	6.000	6.000	6.000	6.000

A4.2: Electron microprobe data of selected minerals of the Khibiny pluton ("-" - not detected, FeII/FeIII calculation according Treloar (unpublished))

mineral	clino pyroxene	clino pyroxene	clino pyroxene	clino pyroxene	clino pyroxene	clino pyroxene	clino pyroxene
rock type	lujavrite	lujavrite	alkali syenite	alkali syenite	alkali syenite	alkali syenite	alkali syenite
#	Kh-03-21	Kh-03-21	Kh-03-58	Kh-03-58	Kh-03-58	Kh-03-58	Kh-03-58
SiO_2	52.50	52.62	51.35	51.47	50.84	50.64	52.39
TiO_2	2.02	1.53	0.68	0.86	0.80	1.02	1.03
Al_2O_3	1.07	1.14	1.16	1.08	1.18	1.00	1.18
Fe_2O_3	2.52	3.44	5.47	7.59	5.17	5.09	7.78
FeO	27.05	26.69	23.98	21.44	24.68	23.42	21.98
MnO	0.48	0.34	0.52	0.95	0.87	0.48	1.11
MgO	0.73	0.65	1.22	1.32	1.39	1.20	1.07
CaO	3.17	2.52	3.89	5.97	6.15	5.05	6.88
Na_2O	12.13	12.11	10.54	9.44	9.73	10.20	9.48
K_2O	-	-	-	-	-	-	-
TOTAL	101.68	101.03	98.81	100.12	100.80	98.10	102.90
Si	1.980	1.997	2.002	1.994	1.957	1.991	1.981
Ti	0.057	0.044	0.020	0.025	0.023	0.030	0.029
Al	0.048	0.051	0.053	0.049	0.054	0.046	0.053
Fe^{III}	0.080	0.109	0.178	0.246	0.166	0.167	0.246
Fe^{II}	0.764	0.759	0.700	0.622	0.711	0.689	0.622
Mn	0.015	0.011	0.017	0.031	0.028	0.016	0.036
Mg	0.041	0.036	0.071	0.076	0.080	0.070	0.060
Ca	0.128	0.102	0.162	0.248	0.254	0.213	0.279
Na	0.887	0.891	0.796	0.709	0.726	0.777	0.695
K	-	-	-	-	-	-	-
Σ cation	4.000	4.000	4.000	4.000	4.000	4.000	4.000
O	6.000	6.000	6.000	6.000	6.000	6.000	6.000

A4.2: Electron microprobe data of selected minerals of the Khibiny pluton ("-" - not detected, FeII/FeIII calculation according Treloar (unpublished))

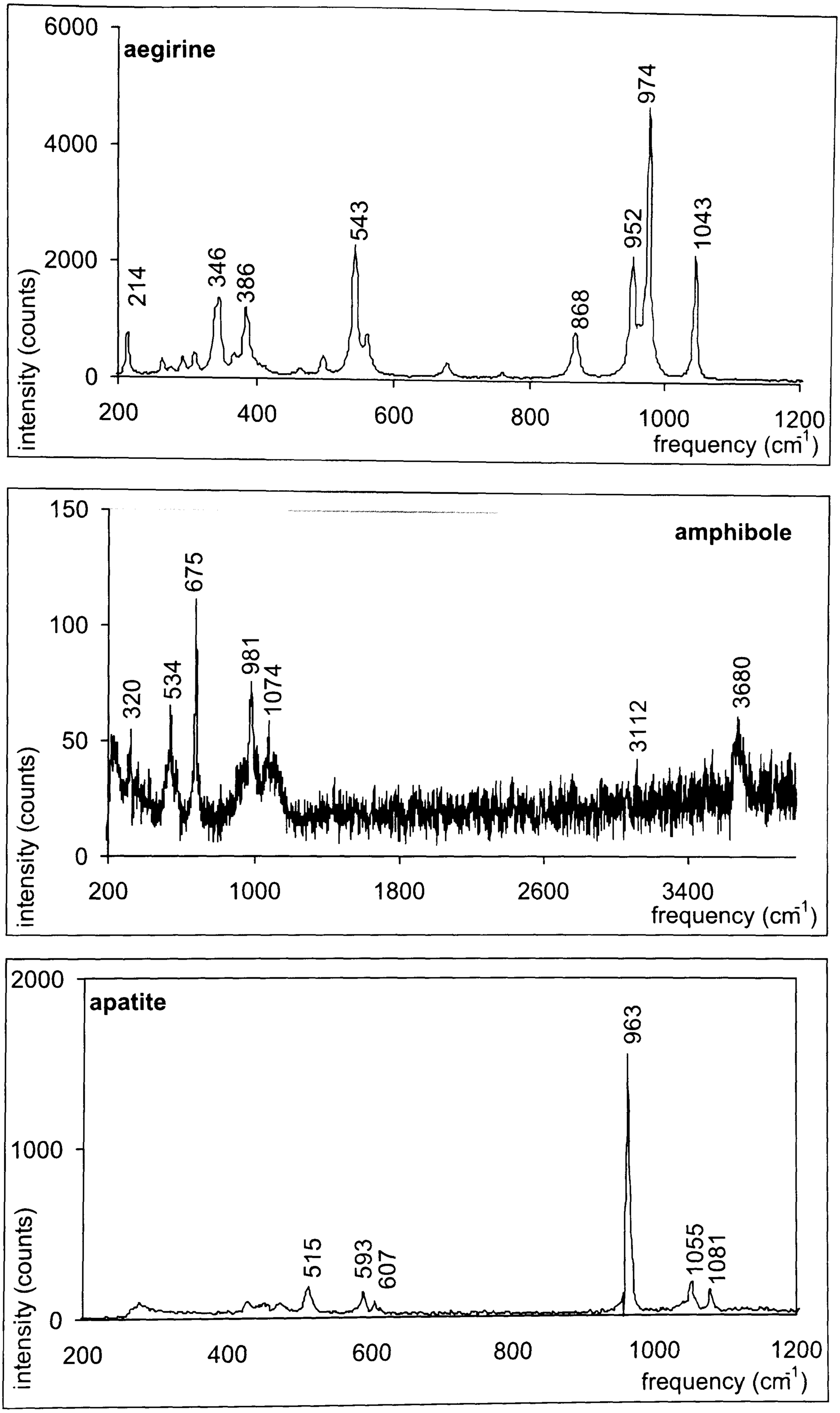

Appendix A4.3: Laser Raman spectra of main minerals of the Khibiny pluton.

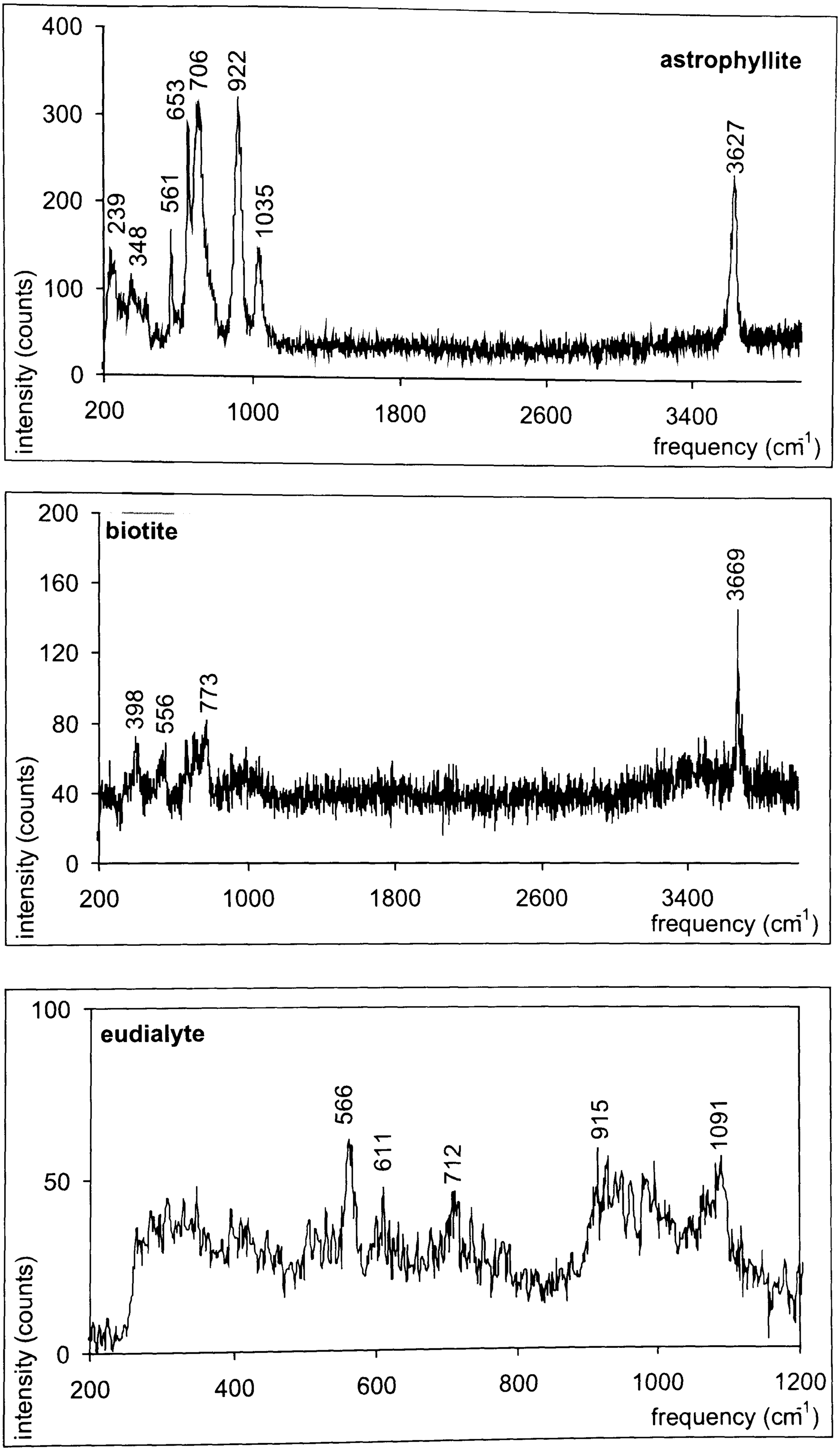

Appendix A4.3: Laser Raman spectra of main minerals of the Khibiny pluton.

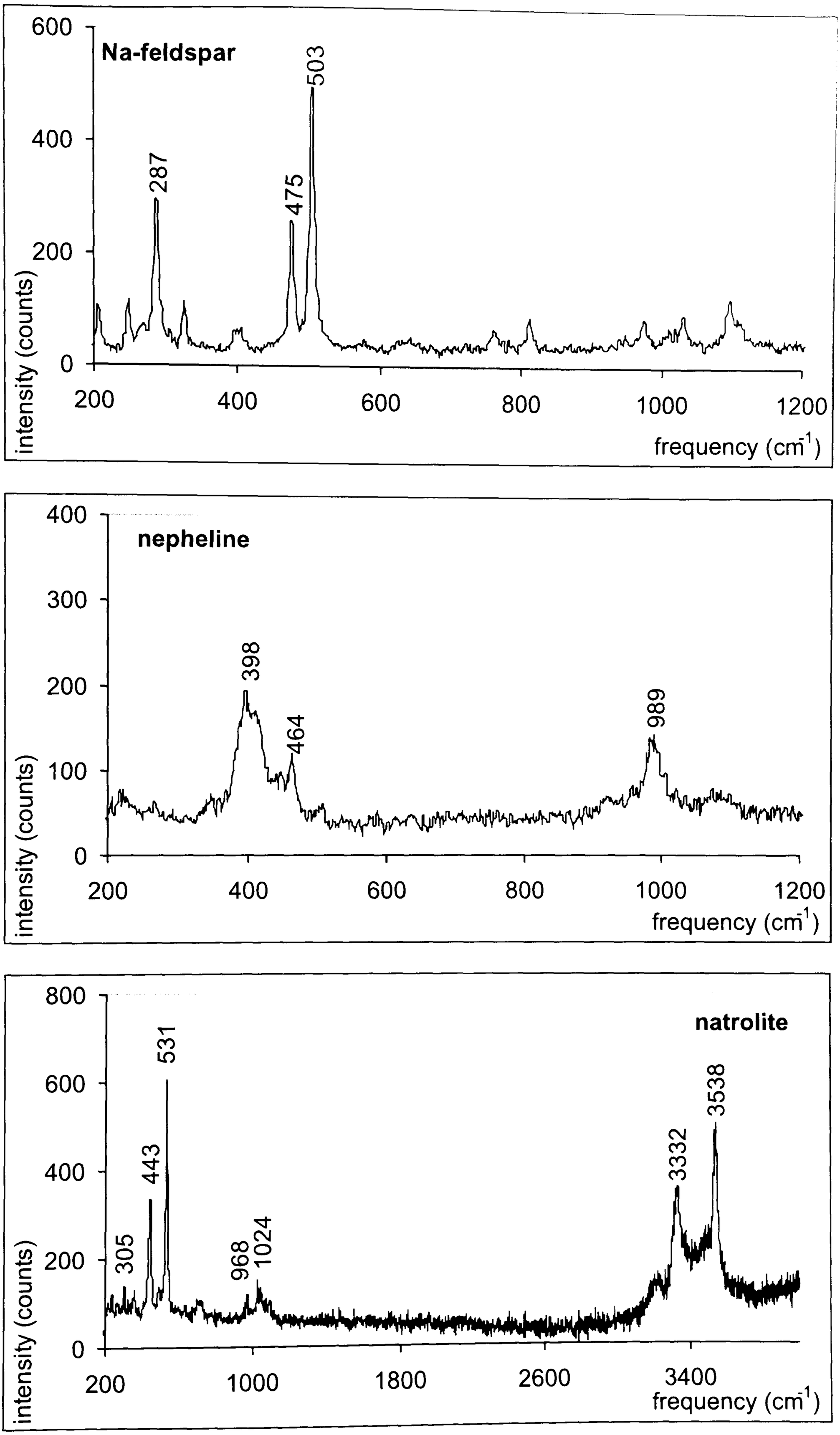

Appendix A4.3: Laser Raman spectra of main minerals of the Khibiny pluton.

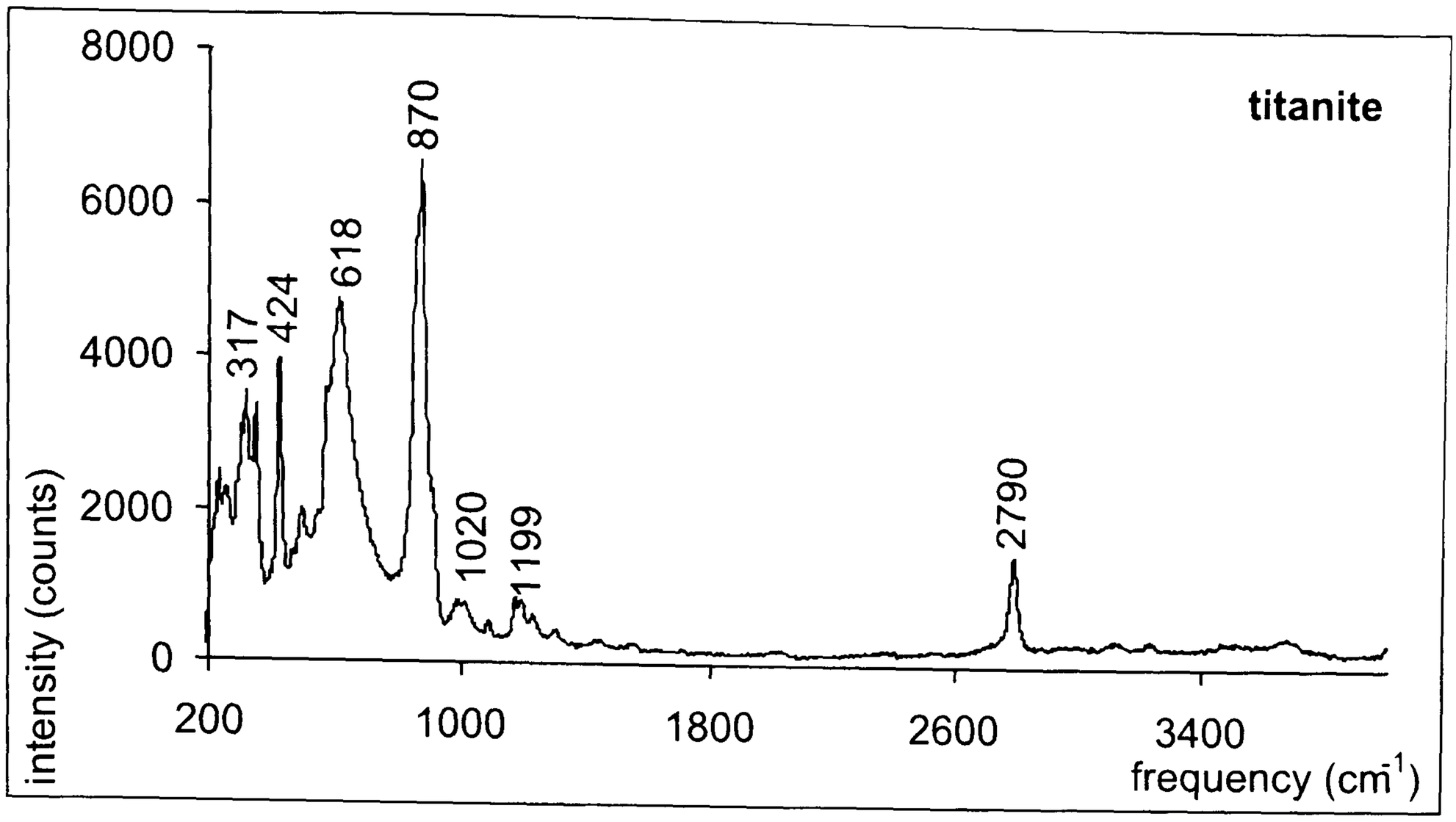

Appendix A4.3: Laser Raman spectra of main minerals of the Khibiny pluton.

#	rock type	sample	host	appears in:	T_h	homo-genise to
1	khibinite	Kh-03-1	nepheline	FIP	-84.9	L
2	khibinite	Kh-03-1	nepheline	clusters	-80.6	V
3	khibinite	Kh-03-1	nepheline	single	-74.8	V
4	khibinite	Kh-03-1	nepheline	clusters	-81.9	V
5	khibinite	Kh-03-1	nepheline	clusters	-82.9	V
6	khibinite	Kh-03-1	nepheline	clusters	-80.4	V
7	khibinite	Kh-03-1	nepheline	clusters	-87.6	V
8	khibinite	Kh-03-1	nepheline	FIP	-79.4	V
9	khibinite	Kh-03-1	nepheline	FIP	-84	V
10	khibinite	Kh-03-1	nepheline	FIP	-80.5	V
11	khibinite	Kh-03-1	nepheline	FIP	-82.5	V
12	khibinite	Kh-03-1	nepheline	FIP	-83.5	V
13	khibinite	Kh-03-1	nepheline	FIP	-81.1	V
14	khibinite	Kh-03-2	nepheline	FIP	84.7	L
15	khibinite	Kh-03-2	nepheline	FIP	-83	L
16	khibinite	Kh-03-2	nepheline	FIP	-77.6	V
17	khibinite	Kh-03-2	nepheline	FIP	-82.1	V
18	khibinite	Kh-03-2	nepheline	FIP	-80.7	V
19	khibinite	Kh-03-2	nepheline	FIP	-87.8	V
20	khibinite	Kh-03-2	nepheline	FIP	-81.1	V
21	khibinite	Kh-03-2	nepheline	clusters	-82	V
22	khibinite	Kh-03-2	nepheline	clusters	-85.3	V
23	khibinite	Kh-03-2	nepheline	clusters	-88.2	V
24	khibinite	Kh-03-3	nepheline	clusters	-81.1	V
25	khibinite	Kh-03-3	nepheline	clusters	-75.6	V
26	khibinite	Kh-03-3	nepheline	single	-82.7	V
27	khibinite	Kh-03-4	nepheline	clusters	-80.2	L
28	khibinite	Kh-03-4	nepheline	clusters	-69.8	L
29	khibinite	Kh-03-4	nepheline	clusters	-77	V
30	khibinite	Kh-03-4	nepheline	clusters	-80.6	V
31	khibinite	Kh-03-4	nepheline	clusters	-84.5	V
32	khibinite	Kh-03-4	nepheline	clusters	-82.1	V
33	khibinite	Kh-03-4	nepheline	clusters	-77.6	V
34	khibinite	Kh-03-4	nepheline	clusters	-77.9	V
35	khibinite	Kh-03-5	nepheline	clusters	-76.3	L
36	khibinite	Kh-03-5	nepheline	clusters	-87.6	V
37	khibinite	Kh-03-5	nepheline	clusters	-81.5	V
38	khibinite	Kh-03-5	nepheline	clusters	-78	V
39	khibinite	Kh-03-5	nepheline	clusters	-83.1	V
40	khibinite	Kh-03-5	nepheline	clusters	80.1	V
41	khibinite	Kh-03-5	nepheline	clusters	-77.6	V
42	khibinite	Kh-03-5	nepheline	FIP	-74.6	V
43	khibinite	Kh-03-5	nepheline	FIP	-82.1	V
44	khibinite	Kh-03-5	nepheline	FIP	-83	V
45	khibinite	Kh-03-5	nepheline	clusters	-83.1	V
46	khibinite	Kh-03-7	nepheline	FIP	-78	L
47	khibinite	Kh-03-7	nepheline	FIP	-81.3	L
48	khibinite	Kh-03-7	nepheline	FIP	-83.5	V
49	khibinite	Kh-03-7	nepheline	FIP	-79.9	V
50	khibinite	Kh-03-7	nepheline	FIP	-82.6	V
51	khibinite	Kh-03-7	nepheline	FIP	-75.1	V
52	khibinite	Kh-03-7	nepheline	FIP	-81.3	V
53	khibinite	Kh-03-7	nepheline	FIP	-82.8	V
54	khibinite	Kh-03-7	nepheline	FIP	-81.1	V

Appendix A6.1a: Microthermometry results of methane-dominant fluid inclusions. Th-homogenisation temperature.

#	rock type	sample	host	appears in:	T_h	homo-genise to
55	khibinite	Kh-03-7	nepheline	FIP	-82.1	V
56	khibinite	Kh-03-7	nepheline	FIP	-81.3	V
57	khibinite	Kh-03-7	nepheline	FIP	-88.2	V
58	khibinite	Kh-03-7	nepheline	FIP	-77	V
59	khibinite	Kh-03-7	nepheline	FIP	77.6	V
60	khibinite	Kh-03-8	nepheline	FIP	-81.2	L
61	khibinite	Kh-03-8	nepheline	FIP	-71.6	L
62	khibinite	Kh-03-8	nepheline	single	-84.6	V
63	khibinite	Kh-03-8	nepheline	FIP	-80.5	V
64	khibinite	Kh-03-8	nepheline	FIP	-81.1	V
65	khibinite	Kh-03-8	nepheline	clusters	-84.5	V
66	khibinite	Kh-03-8	nepheline	clusters	-80.6	V
67	khibinite	Kh-03-8	nepheline	clusters	-74.6	V
68	khibinite	Kh-03-8	nepheline	clusters	-81.5	V
69	rischorrite	Kh-03-10	nepheline	clusters	-81.7	L
70	rischorrite	Kh-03-10	nepheline	clusters	-84	V
71	rischorrite	Kh-03-10	nepheline	clusters	-83	V
72	rischorrite	Kh-03-10	nepheline	clusters	-79	V
73	rischorrite	Kh-03-10	nepheline	clusters	-87.6	V
74	rischorrite	Kh-03-10	nepheline	clusters	-76	V
75	rischorrite	Kh-03-10	nepheline	clusters	-76.4	V
76	rischorrite	Kh-03-10	nepheline	clusters	-87.1	V
77	rischorrite	Kh-03-10	nepheline	clusters	-74	V
78	rischorrite	Kh-03-10	nepheline	clusters	-83.5	V
79	rischorrite	Kh-03-10	nepheline	clusters	-81.4	V
80	rischorrite	Kh-03-10	nepheline	clusters	-81.6	V
81	rischorrite	Kh-03-10	nepheline	clusters	-80.5	V
82	rischorrite	Kh-03-10	nepheline	clusters	-73.7	V
83	rischorrite	Kh-03-10	nepheline	clusters	89.8	V
84	rischorrite	Kh-03-10	nepheline	clusters	-83.1	V
85	rischorrite	Kh-03-10	nepheline	clusters	-87.8	V
86	rischorrite	Kh-03-10	nepheline	single	-81.1	V
87	rischorrite	Kh-03-10	nepheline	clusters	-82.1	V
88	rischorrite	Kh-03-10	nepheline	clusters	-85.3	V
89	rischorrite	Kh-03-10	nepheline	clusters	-88.2	V
90	rischorrite	Kh-03-10	nepheline	clusters	-87.6	V
91	rischorrite	Kh-03-10	nepheline	clusters	-84.9	V
92	rischorrite	Kh-03-10	nepheline	clusters	-79.9	V
93	rischorrite	Kh-03-10	nepheline	clusters	-97.6	V
94	rischorrite	Kh-03-10	nepheline	clusters	-76.5	V
95	rischorrite	Kh-03-10	nepheline	clusters	-79.1	V
96	rischorrite	Kh-03-10	nepheline	clusters	-74	V
97	rischorrite	Kh-03-10	nepheline	clusters	-89.2	V
98	rischorrite	Kh-03-10	nepheline	clusters	-67.6	V
99	rischorrite	Kh-03-10	nepheline	clusters	-88.9	V
100	rischorrite	Kh-03-10	nepheline	clusters	-83.2	V
101	rischorrite	Kh-03-12	nepheline	FIP	-78.1	L
102	rischorrite	Kh-03-12	nepheline	clusters	-84.5	V
103	rischorrite	Kh-03-12	nepheline	clusters	-87.6	V
104	rischorrite	Kh-03-12	nepheline	FIP	-78.9	V
105	rischorrite	Kh-03-12	nepheline	FIP	-84.6	V
106	rischorrite	Kh-03-12	nepheline	FIP	-81	V
107	rischorrite	Kh-03-12	nepheline	FIP	-88.7	V
108	rischorrite	Kh-03-12	nepheline	FIP	-80.7	V

Appendix A6.1a: Microthermometry results of methane-dominant fluid inclusions. Th-homogenisation temperature.

#	rock type	sample	host	appears in:	T_h	homo-genise to
109	rischorrite	Kh-03-12	nepheline	FIP	-78.1	V
110	rischorrite	Kh-03-12	nepheline	FIP	-86	V
111	rischorrite	Kh-03-12	nepheline	FIP	-80.8	V
112	rischorrite	Kh-03-12	nepheline	FIP	-76	V
113	rischorrite	Kh-03-12	nepheline	FIP	-83.5	V
114	rischorrite	Kh-03-12	nepheline	FIP	-85.5	V
115	rischorrite	Kh-03-12	nepheline	FIP	-77.9	V
116	rischorrite	Kh-03-12	nepheline	FIP	-80	V
117	rischorrite	Kh-03-12	nepheline	FIP	-73	V
118	rischorrite	Kh-03-12	nepheline	FIP	-82.2	V
119	rischorrite	Kh-03-12	nepheline	single	-89	V
120	rischorrite	Kh-03-12	nepheline	single	-87.8	V
121	rischorrite	Kh-03-12	nepheline	single	-81.1	V
122	rischorrite	Kh-03-13	nepheline	clusters	-80.6	L
123	rischorrite	Kh-03-13	nepheline	clusters	-83.9	L
124	rischorrite	Kh-03-13	nepheline	clusters	-83.5	V
125	rischorrite	Kh-03-13	nepheline	clusters	-85.3	V
126	rischorrite	Kh-03-13	nepheline	clusters	-85.2	V
127	rischorrite	Kh-03-13	nepheline	clusters	-87.6	V
128	rischorrite	Kh-03-13	nepheline	clusters	-74.3	V
129	rischorrite	Kh-03-13	nepheline	clusters	-73.3	V
130	rischorrite	Kh-03-13	nepheline	clusters	-74.2	V
131	rischorrite	Kh-03-13	nepheline	clusters	-79	V
132	rischorrite	Kh-03-13	nepheline	clusters	-74.3	V
133	rischorrite	Kh-03-13	nepheline	FIP	-79	V
134	rischorrite	Kh-03-13	nepheline	FIP	-74.1	V
135	rischorrite	Kh-03-13	nepheline	FIP	-78.5	V
136	rischorrite	Kh-03-13	nepheline	FIP	-78.8	V
137	rischorrite	Kh-03-13	nepheline	FIP	-87.8	V
138	rischorrite	Kh-03-13	nepheline	FIP	-84	V
139	rischorrite	Kh-03-13	nepheline	FIP	-79	V
140	rischorrite	Kh-03-13	nepheline	FIP	-81.2	V
141	rischorrite	Kh-03-13	nepheline	FIP	-84.5	V
142	rischorrite	Kh-03-13	nepheline	FIP	-82.3	V
143	rischorrite	Kh-03-13	nepheline	FIP	-67.6	V
144	rischorrite	Kh-03-13	nepheline	FIP	-73.5	V
145	rischorrite	Kh-03-13	nepheline	FIP	-78.1	V
146	rischorrite	Kh-03-13	nepheline	FIP	-83	V
147	rischorrite	Kh-03-13	nepheline	FIP	-79	V
148	rischorrite	Kh-03-14	nepheline	clusters	-81.4	L
149	rischorrite	Kh-03-14	alk fsp	clusters	-85.3	L
150	rischorrite	Kh-03-14	alk fsp	clusters	-88.2	L
151	rischorrite	Kh-03-14	alk fsp	clusters	-69.6	L
152	rischorrite	Kh-03-14	alk fsp	clusters	-74	L
153	rischorrite	Kh-03-14	nepheline	clusters	-67.6	V
154	rischorrite	Kh-03-14	nepheline	clusters	-87.4	V
155	rischorrite	Kh-03-14	nepheline	clusters	-83	V
156	rischorrite	Kh-03-14	nepheline	clusters	-79	V
157	rischorrite	Kh-03-14	nepheline	clusters	-80.3	V
158	rischorrite	Kh-03-14	nepheline	clusters	-83.5	V
159	rischorrite	Kh-03-14	nepheline	clusters	-81.8	V
160	rischorrite	Kh-03-14	nepheline	clusters	-69.6	V
161	rischorrite	Kh-03-14	nepheline	clusters	-64.5	V
162	rischorrite	Kh-03-14	nepheline	clusters	-73	V

Appendix A6.1a: Microthermometry results of methane-dominant fluid inclusions. Th-homogenisation temperature.

#	rock type	sample	host	appears in:	T_h	homo-genise to
163	rischorrite	Kh-03-14	nepheline	clusters	-83	V
164	rischorrite	Kh-03-14	nepheline	clusters	-79	V
165	rischorrite	Kh-03-14	nepheline	clusters	-87.8	V
166	rischorrite	Kh-03-14	nepheline	clusters	-81.1	V
167	rischorrite	Kh-03-14	nepheline	clusters	-82	V
168	rischorrite	Kh-03-14	alk fsp	clusters	-79	V
169	rischorrite	Kh-03-14	alk fsp	clusters	-70.6	V
170	rischorrite	Kh-03-14	alk fsp	clusters	-74	V
171	rischorrite	Kh-03-14	alk fsp	clusters	-83	V
172	rischorrite	Kh-03-14	alk fsp	clusters	-84.8	V
173	rischorrite	Kh-03-14	alk fsp	clusters	-80.7	V
174	rischorrite	Kh-03-14	alk fsp	clusters	-68.6	V
175	rischorrite	Kh-03-14	alk fsp	clusters	-76.7	V
176	rischorrite	Kh-03-14	alk fsp	clusters	-78.1	V
177	rischorrite	Kh-03-14	alk fsp	clusters	-77.6	V
178	rischorrite	Kh-03-14	alk fsp	clusters	-78.1	V
179	rischorrite	Kh-03-14	alk fsp	clusters	-75.6	V
180	rischorrite	Kh-03-14	alk fsp	clusters	-83	V
181	rischorrite	Kh-03-14	alk fsp	clusters	-84.8	V
182	rischorrite	Kh-03-14	alk fsp	clusters	-74	V
183	rischorrite	Kh-03-42	nepheline	clusters	-82.1	L
184	rischorrite	Kh-03-42	nepheline	clusters	-87.8	L
185	rischorrite	Kh-03-42	nepheline	clusters	-81.1	L
186	rischorrite	Kh-03-42	nepheline	FIP	-81.7	V
187	rischorrite	Kh-03-42	nepheline	FIP	-71.6	V
188	rischorrite	Kh-03-42	nepheline	FIP	-71.9	V
189	rischorrite	Kh-03-42	nepheline	FIP	-72.9	V
190	rischorrite	Kh-03-42	nepheline	FIP	-83	V
191	rischorrite	Kh-03-42	nepheline	FIP	-79	V
192	rischorrite	Kh-03-42	nepheline	FIP	-87.8	V
193	rischorrite	Kh-03-42	nepheline	FIP	-81.1	V
194	rischorrite	Kh-03-42	nepheline	FIP	-82	V
195	rischorrite	Kh-03-42	nepheline	FIP	-85.3	V
196	rischorrite	Kh-03-42	nepheline	single	-77.6	V
197	rischorrite	Kh-03-42	nepheline	clusters	-83	V
198	rischorrite	Kh-03-42	nepheline	clusters	-80.3	V
199	rischorrite	Kh-03-42	nepheline	clusters	-72.6	V
200	rischorrite	Kh-03-42	nepheline	clusters	-73.4	V
201	rischorrite	Kh-03-42	nepheline	clusters	-76.3	V
202	rischorrite	Kh-03-42	nepheline	clusters	-87.1	V
203	rischorrite	Kh-03-42	nepheline	clusters	-77.8	V
204	rischorrite	Kh-03-42	nepheline	clusters	-83.5	V
205	rischorrite	Kh-03-42	nepheline	clusters	-86.9	V
206	rischorrite	Kh-03-42	nepheline	clusters	-73.6	V
207	rischorrite	Kh-03-42	nepheline	clusters	-74.1	V
208	rischorrite	Kh-03-42	nepheline	clusters	-73.1	V
209	rischorrite	Kh-03-42	nepheline	clusters	-83	V
210	rischorrite	Kh-03-42	nepheline	clusters	-80.7	V
211	rischorrite	Kh-03-42	nepheline	clusters	-87.8	V
212	rischorrite	Kh-03-42	nepheline	single	-81.1	V
213	rischorrite	Kh-03-42	nepheline	clusters	-82	V
214	rischorrite	Kh-03-42	nepheline	clusters	-85.3	V
215	rischorrite	Kh-03-42	nepheline	clusters	-88.2	V
216	rischorrite	Kh-03-42	nepheline	clusters	-79	V

Appendix A6.1a: Microthermometry results of methane-dominant fluid inclusions. Th-homogenisation temperature.

#	rock type	sample	host	appears in:	T_h	homo-genise to
217	rischorrite	Kh-03-42	nepheline	clusters	-78.6	V
218	rischorrite	Kh-03-42	nepheline	clusters	-82.2	V
219	rischorrite	Kh-03-42	nepheline	clusters	-80.9	V
220	rischorrite	Kh-03-42	nepheline	clusters	-81.5	V
221	rischorrite	Kh-03-42	nepheline	clusters	-80.4	V
222	rischorrite	Kh-03-42	nepheline	clusters	-69.6	V
223	rischorrite	Kh-03-42	nepheline	clusters	-71.1	V
224	rischorrite	Kh-03-42	nepheline	clusters	-80.3	V
225	rischorrite	Kh-03-42	nepheline	clusters	-82	V
226	rischorrite	Kh-03-42	nepheline	clusters	-85.3	V
227	rischorrite	Kh-03-42	nepheline	clusters	-88.2	V
228	rischorrite	Kh-03-42	nepheline	clusters	-84.5	V
229	rischorrite	Kh-03-43	nepheline	FIP	-83.5	L
230	rischorrite	Kh-03-43	nepheline	clusters	-67.6	V
231	rischorrite	Kh-03-43	nepheline	FIP	-70.7	V
232	rischorrite	Kh-03-43	nepheline	FIP	-71.2	V
233	rischorrite	Kh-03-43	nepheline	FIP	-83	V
234	rischorrite	Kh-03-43	nepheline	FIP	-80.7	V
235	rischorrite	Kh-03-43	nepheline	FIP	-68.6	V
236	rischorrite	Kh-03-43	nepheline	FIP	-77.8	V
237	rischorrite	Kh-03-43	nepheline	FIP	-75.9	V
238	rischorrite	Kh-03-43	nepheline	FIP	-83	V
239	rischorrite	Kh-03-43	nepheline	FIP	-80.7	V
240	rischorrite	Kh-03-43	nepheline	FIP	-79	V
241	rischorrite	Kh-03-43	nepheline	FIP	-80.3	V
242	rischorrite	Kh-03-43	nepheline	FIP	-71.7	V
243	rischorrite	Kh-03-43	nepheline	FIP	-81.4	V
244	rischorrite	Kh-03-43	nepheline	FIP	-73	V
245	rischorrite	Kh-03-43	nepheline	FIP	-83	V
246	rischorrite	Kh-03-43	nepheline	single	-80.3	V
247	rischorrite	Kh-03-43	nepheline	single	-87.8	V
248	rischorrite	Kh-03-43	nepheline	single	-81.1	V
249	rischorrite	Kh-03-43	nepheline	clusters	-82	V
250	rischorrite	Kh-03-43	nepheline	clusters	-85.3	V
251	rischorrite	Kh-03-43	nepheline	clusters	-88.2	V
252	rischorrite	Kh-03-43	nepheline	clusters	-87.8	V
253	rischorrite	Kh-03-43	nepheline	clusters	-81.1	V
254	rischorrite	Kh-03-43	nepheline	clusters	-82	V
255	rischorrite	Kh-03-44	nepheline	clusters	-85.3	V
256	rischorrite	Kh-03-44	nepheline	clusters	-88.2	V
257	rischorrite	Kh-03-44	nepheline	clusters	-82.1	V
258	rischorrite	Kh-03-44	nepheline	clusters	-73.8	V
259	rischorrite	Kh-03-44	nepheline	clusters	-80.6	V
260	rischorrite	Kh-03-45	nepheline	FIP	-72.6	V
261	rischorrite	Kh-03-45	nepheline	FIP	-77.9	V
262	rischorrite	Kh-03-45	nepheline	FIP	-80.5	V
263	rischorrite	Kh-03-45	nepheline	FIP	-81.9	V
264	rischorrite	Kh-03-45	nepheline	FIP	-77.8	V
265	rischorrite	Kh-03-45	nepheline	FIP	-84	V
266	rischorrite	Kh-03-45	nepheline	FIP	-83.6	V
267	rischorrite	Kh-03-45	nepheline	FIP	-81.2	V
268	rischorrite	Kh-03-45	nepheline	FIP	-84.5	V
269	rischorrite	Kh-03-45	nepheline	FIP	-82.3	V
270	rischorrite	Kh-03-45	nepheline	FIP	-87.6	V

Appendix A6.1a: Microthermometry results of methane-dominant fluid inclusions. Th-homogenisation temperature.

#	rock type	sample	host	appears in:	T_h	homo-genise to
271	rischorrite	Kh-03-45	nepheline	FIP	-98.9	V
272	rischorrite	Kh-03-45	nepheline	FIP	-79.7	V
273	rischorrite	Kh-03-45	nepheline	FIP	-83	V
274	rischorrite	Kh-03-46	alk fsp	clusters	-85.3	L
275	rischorrite	Kh-03-46	alk fsp	clusters	-88.2	L
276	rischorrite	Kh-03-46	alk fsp	clusters	-77.6	L
277	rischorrite	Kh-03-46	alk fsp	clusters	-72.1	L
278	rischorrite	Kh-03-46	nepheline	FIP	-83.2	V
279	rischorrite	Kh-03-46	nepheline	clusters	-87.6	V
280	rischorrite	Kh-03-46	nepheline	clusters	-73.1	V
281	rischorrite	Kh-03-46	nepheline	clusters	-84	V
282	rischorrite	Kh-03-46	nepheline	clusters	-83.2	V
283	rischorrite	Kh-03-46	nepheline	clusters	-80.1	V
284	rischorrite	Kh-03-46	nepheline	clusters	-74.7	V
285	rischorrite	Kh-03-46	nepheline	clusters	-83.5	V
286	rischorrite	Kh-03-46	nepheline	clusters	-79.9	V
287	rischorrite	Kh-03-46	nepheline	clusters	-97.6	V
288	rischorrite	Kh-03-46	nepheline	clusters	-76.1	V
289	rischorrite	Kh-03-46	nepheline	clusters	-83.2	V
290	rischorrite	Kh-03-46	nepheline	clusters	-83	V
291	rischorrite	Kh-03-46	nepheline	clusters	-79.5	V
292	rischorrite	Kh-03-46	nepheline	clusters	-87.8	V
293	rischorrite	Kh-03-46	nepheline	clusters	-81.1	V
294	rischorrite	Kh-03-46	nepheline	clusters	-82	V
295	rischorrite	Kh-03-46	alk fsp	clusters	-78	V
296	rischorrite	Kh-03-46	alk fsp	clusters	-88.6	V
297	rischorrite	Kh-03-46	alk fsp	clusters	-84.4	V
298	rischorrite	Kh-03-46	alk fsp	clusters	-83.1	V
299	rischorrite	Kh-03-46	alk fsp	clusters	-74.8	V
300	rischorrite	Kh-03-46	alk fsp	clusters	-80.8	V
301	rischorrite	Kh-03-46	alk fsp	clusters	-87.6	V
302	rischorrite	Kh-03-46	alk fsp	clusters	-73.3	V
303	rischorrite	Kh-03-46	alk fsp	clusters	-79.1	V
304	rischorrite	Kh-03-46	alk fsp	clusters	-66.6	V
305	rischorrite	Kh-03-46	alk fsp	clusters	-79.9	V
306	rischorrite	Kh-03-46	alk fsp	clusters	-64.3	V
307	rischorrite	Kh-03-46	alk fsp	clusters	-82.3	V
308	rischorrite	Kh-03-46	alk fsp	clusters	-84.8	V
309	rischorrite	Kh-03-46	alk fsp	clusters	-84.1	V
310	rischorrite	Kh-03-50	nepheline	clusters	-74.9	L
311	rischorrite	Kh-03-50	nepheline	clusters	82.2	V
312	rischorrite	Kh-03-50	nepheline	clusters	-87.6	V
313	rischorrite	Kh-03-50	nepheline	clusters	-74.1	V
314	rischorrite	Kh-03-50	nepheline	clusters	-75.9	V
315	rischorrite	Kh-03-50	nepheline	clusters	-80.3	V
316	rischorrite	Kh-03-50	nepheline	clusters	-79.9	V
317	rischorrite	Kh-03-50	nepheline	clusters	-87.8	V
318	rischorrite	Kh-03-50	nepheline	clusters	-81.2	V
319	rischorrite	Kh-03-50	nepheline	clusters	-82.9	V
320	rischorrite	Kh-03-50	nepheline	clusters	-85.3	V
321	albitised foyaite	Kh-03-35	albite	FIP	-88.2	V
322	albitised foyaite	Kh-03-35	albite	FIP	-85.1	V
323	albitised foyaite	Kh-03-35	albite	FIP	-89.8	V
324	albitised foyaite	Kh-03-35	albite	single	-83.1	V

Appendix A6.1a: Microthermometry results of methane-dominant fluid inclusions. Th-homogenisation temperature.

#	rock type	sample	host	appears in:	T_h	homo-genise to
325	albitised foyaite	Kh-03-35	albite	single	-88.9	V
326	albitised foyaite	Kh-03-35	albite	single	-85.6	V
327	albitised foyaite	Kh-03-35	albite	clusters	-81.5	V
328	albitised foyaite	Kh-03-35	albite	clusters	-76.9	V
329	albitised foyaite	Kh-03-35	albite	clusters	-80.2	V
330	albitised foyaite	Kh-03-36	nepheline	FIP	-88.2	V
331	albitised foyaite	Kh-03-36	nepheline	FIP	-81.7	V
332	albitised foyaite	Kh-03-37	nepheline	FIP	-77.8	V
333	albitised foyaite	Kh-03-37	albite	clusters	-74.9	V
334	albitised foyaite	Kh-03-37	albite	single	-85.9	V
335	albitised foyaite	Kh-03-37	albite	clusters	-79.6	V
336	albitised foyaite	Kh-03-37	nepheline	FIP	-84.2	V
337	albitised foyaite	Kh-03-37	nepheline	FIP	-80.5	V
338	albitised foyaite	Kh-03-37	nepheline	FIP	-84.8	V
339	albitised foyaite	Kh-03-37	nepheline	clusters	-79.9	V
340	albitised foyaite	Kh-03-37	nepheline	FIP	-87.9	V
341	albitised foyaite	Kh-03-37	albite	clusters	-84.2	V
342	albitised foyaite	Kh-03-37	nepheline	FIP	-80.5	V
343	albitised foyaite	Kh-03-37	nepheline	FIP	-78.3	V
344	albitised foyaite	Kh-03-37	nepheline	FIP	-74.8	V
345	albitised foyaite	Kh-03-37	nepheline	FIP	-83.8	V
346	albitised foyaite	Kh-03-37	nepheline	FIP	-78.9	V
347	albitised foyaite	Kh-03-37	nepheline	FIP	-74	V
348	albitised foyaite	Kh-03-37	nepheline	FIP	-81.5	V
349	albitised foyaite	Kh-03-37	albite	FIP	-88.3	V
350	albitised foyaite	Kh-03-37	albite	FIP	-74	V
351	albitised foyaite	Kh-03-37	albite	FIP	-83	V
352	albitised foyaite	Kh-03-37	albite	FIP	-79	V
353	albitised foyaite	Kh-03-37	albite	FIP	-82.6	V
354	albitised foyaite	Kh-03-37	albite	FIP	-76.9	V
355	albitised foyaite	Kh-03-37	albite	FIP	-83	V
356	albitised foyaite	Kh-03-37	albite	FIP	-84.8	V
357	albitised foyaite	Kh-03-37	eudialite	single	-78.5	V
358	albitised foyaite	Kh-03-37	eudialite	single	-76	V
359	albitised foyaite	Kh-03-37	eudialite	single	-79.8	V
360	albitised foyaite	Kh-03-37	eudialite	clusters	-66.5	V
361	albitised foyaite	Kh-03-37	eudialite	clusters	-78.9	V
362	albitised foyaite	Kh-03-37	eudialite	clusters	-73	V
363	albitised foyaite	Kh-03-37	nepheline	FIP	-79	V
364	albitised foyaite	Kh-03-37	nepheline	FIP	-87.8	V
365	albitised foyaite	Kh-03-37	nepheline	FIP	-81.1	V
366	albitised foyaite	Kh-03-37	albite	clusters	-82	V
367	albitised foyaite	Kh-03-37	albite	single	-74	V
368	albitised foyaite	Kh-03-39	albite	clusters	-83	V
369	albitised foyaite	Kh-03-39	nepheline	FIP	-79	V
370	albitised foyaite	Kh-03-40	nepheline	FIP	-67.6	V
371	albitised foyaite	Kh-03-40	nepheline	FIP	-74	V
372	albitised foyaite	Kh-03-40	nepheline	clusters	-74	V
373	albitised foyaite	Kh-03-40	nepheline	FIP	-83	V
374	albitised foyaite	Kh-03-40	albite	clusters	-79	V
375	albitised foyaite	Kh-03-40	nepheline	FIP	-74	V
376	albitised foyaite	Kh-03-41	nepheline	FIP	-83.5	V
377	albitised foyaite	Kh-03-41	nepheline	FIP	-79	V
378	albitised foyaite	Kh-03-41	nepheline	FIP	-67.6	V

Appendix A6.1a: Microthermometry results of methane-dominant fluid inclusions. Th-homogenisation temperature.

#	rock type	sample	host	appears in:	T_h	homo-genise to
379	albitised foyaite	Kh-03-41	nepheline	FIP	-74	V
380	albitised foyaite	Kh-03-41	nepheline	clusters	-73	V
381	albitised foyaite	Kh-03-41	nepheline	clusters	-74	V
382	albitised foyaite	Kh-03-41	albite	clusters	-83	V
383	albitised foyaite	Kh-03-41	albite	clusters	-79	V
384	albitised foyaite	Kh-03-41	albite	clusters	-90.4	V
385	albitised foyaite	Kh-03-41	albite	clusters	-89.5	V
386	albitised foyaite	Kh-03-41	albite	clusters	-91	V
387	massive foyaite	Kh-03-51	alk fsp	clusters	-67.6	V
388	massive foyaite	Kh-03-51	alk fsp	clusters	-81.4	V
389	massive foyaite	Kh-03-51	alk fsp	clusters	-80.4	V
390	massive foyaite	Kh-03-51	alk fsp	clusters	-83.2	V
391	massive foyaite	Kh-03-51	alk fsp	clusters	-79.9	V
392	massive foyaite	Kh-03-51	alk fsp	clusters	-79.6	V
393	massive foyaite	Kh-03-51	alk fsp	clusters	-73.1	V
394	massive foyaite	Kh-03-51	alk fsp	clusters	-73.9	V
395	massive foyaite	Kh-03-51	alk fsp	clusters	-82.1	V
396	massive foyaite	Kh-03-51	nepheline	FIP	-78.5	V
397	massive foyaite	Kh-03-51	nepheline	FIP	-81.3	V
398	massive foyaite	Kh-03-51	nepheline	FIP	-82.2	V
399	massive foyaite	Kh-03-51	nepheline	FIP	-81.2	V
400	massive foyaite	Kh-03-51	nepheline	FIP	-79.6	V
401	massive foyaite	Kh-03-51	nepheline	FIP	-73.1	V
402	massive foyaite	Kh-03-51	nepheline	FIP	-73.9	V
403	massive foyaite	Kh-03-51	nepheline	FIP	-80.2	V
404	massive foyaite	Kh-03-51	nepheline	FIP	-78.9	V
405	massive foyaite	Kh-03-51	nepheline	FIP	-63.8	V
406	massive foyaite	Kh-03-51	nepheline	FIP	-81.8	V
407	massive foyaite	Kh-03-51	nepheline	FIP	-80.5	V
408	massive foyaite	Kh-03-51	nepheline	FIP	-84.3	V
409	massive foyaite	Kh-03-51	nepheline	FIP	-82.2	V
410	massive foyaite	Kh-03-51	nepheline	FIP	-82.2	V
411	massive foyaite	Kh-03-51	nepheline	FIP	-74	V
412	massive foyaite	Kh-03-51	nepheline	FIP	-79.2	V
413	massive foyaite	Kh-03-52	nepheline	single	-77.6	V
414	massive foyaite	Kh-03-52	nepheline	single	-74	V
415	massive foyaite	Kh-03-52	eudialite	clusters	-82.6	V
416	massive foyaite	Kh-03-52	eudialite	clusters	-74	V
417	massive foyaite	Kh-03-52	eudialite	clusters	-73.3	V
418	massive foyaite	Kh-03-52	eudialite	clusters	-74.1	V
419	massive foyaite	Kh-03-52	nepheline	FIP	-79.9	V
420	massive foyaite	Kh-03-52	nepheline	FIP	-67.6	V
421	massive foyaite	Kh-03-52	nepheline	FIP	-80.4	V
422	massive foyaite	Kh-03-52	nepheline	FIP	-80.6	V
423	massive foyaite	Kh-03-52	alk fsp	clusters	-74.1	V
424	massive foyaite	Kh-03-52	alk fsp	clusters	-79.9	V
425	massive foyaite	Kh-03-52	alk fsp	clusters	-77.6	V
426	massive foyaite	Kh-03-52	alk fsp	clusters	-74	V
427	massive foyaite	Kh-03-54	nepheline	FIP	-79.7	L
428	massive foyaite	Kh-03-54	nepheline	FIP	-87.6	L
429	massive foyaite	Kh-03-54	nepheline	FIP	-74.5	L
430	massive foyaite	Kh-03-54	alk fsp	clusters	-67.6	V
431	massive foyaite	Kh-03-54	alk fsp	clusters	-74	V
432	massive foyaite	Kh-03-54	alk fsp	clusters	-73	V

Appendix A6.1a: Microthermometry results of methane-dominant fluid inclusions. Th-homogenisation temperature.

#	rock type	sample	host	appears in:	T_h	homo-genise to
433	massive foyaite	Kh-03-54	nepheline	FIP	-83	V
434	massive foyaite	Kh-03-54	nepheline	FIP	-79	V
435	massive foyaite	Kh-03-54	nepheline	FIP	-67.6	V
436	massive foyaite	Kh-03-54	nepheline	clusters	-78.4	V
437	massive foyaite	Kh-03-54	nepheline	clusters	-79.4	V
438	massive foyaite	Kh-03-54	nepheline	clusters	-83.1	V
439	massive foyaite	Kh-03-54	nepheline	clusters	-79.9	V
440	massive foyaite	Kh-03-54	nepheline	FIP	-79.9	V
441	massive foyaite	Kh-03-54	nepheline	FIP	-82.9	V
442	massive foyaite	Kh-03-54	nepheline	FIP	-81.4	V
443	massive foyaite	Kh-03-54	nepheline	FIP	-83.2	V
444	massive foyaite	Kh-03-54	nepheline	FIP	-79.9	V
445	massive foyaite	Kh-03-54	nepheline	FIP	-77.8	V
446	massive foyaite	Kh-03-54	nepheline	FIP	-82.8	V
447	massive foyaite	Kh-03-54	nepheline	FIP	-81.5	V
448	massive foyaite	Kh-03-54	nepheline	FIP	-79.8	V
449	massive foyaite	Kh-03-54	nepheline	FIP	-74.9	V
450	massive foyaite	Kh-03-54	nepheline	FIP	-67.8	V
451	massive foyaite	Kh-03-54	nepheline	FIP	-80.7	V
452	massive foyaite	Kh-03-54	albite	single	-79.3	V
453	massive foyaite	Kh-03-54	albite	single	-87.6	V
454	massive foyaite	Kh-03-54	albite	single	-74.3	V
455	massive foyaite	Kh-03-54	alk fsp	clusters	-77.6	V
456	massive foyaite	Kh-03-54	alk fsp	clusters	-74.5	V
457	massive foyaite	Kh-03-54	alk fsp	clusters	-81.3	V
458	massive foyaite	Kh-03-54	alk fsp	clusters	-80.4	V
459	massive foyaite	Kh-03-54	alk fsp	clusters	-79.2	V
460	massive foyaite	Kh-03-55	nepheline	FIP	-77.7	V
461	massive foyaite	Kh-03-55	nepheline	FIP	-74	V
462	massive foyaite	Kh-03-55	nepheline	FIP	-79.3	V
463	massive foyaite	Kh-03-55	nepheline	clusters	-80.6	V
464	massive foyaite	Kh-03-55	nepheline	clusters	-74.2	V
465	massive foyaite	Kh-03-55	nepheline	clusters	-80.7	V
466	massive foyaite	Kh-03-55	nepheline	clusters	-82	V
467	alkaline syenite	Kh-03-57	alk fsp	clusters	-68.9	L
468	alkaline syenite	Kh-03-57	nepheline	FIP	-75.5	L
469	alkaline syenite	Kh-03-56	alk fsp	FIP	-86.3	V
470	alkaline syenite	Kh-03-56	alk fsp	FIP	-90.1	V
471	alkaline syenite	Kh-03-56	alk fsp	FIP	-91.1	V
472	alkaline syenite	Kh-03-56	alk fsp	FIP	-85	V
473	alkaline syenite	Kh-03-56	alk fsp	FIP	-88.3	V
474	alkaline syenite	Kh-03-56	alk fsp	FIP	-98.7	V
475	alkaline syenite	Kh-03-56	alk fsp	clusters	-92.5	V
476	alkaline syenite	Kh-03-56	alk fsp	clusters	-87.4	V
477	alkaline syenite	Kh-03-56	alk fsp	clusters	-87.2	V
478	alkaline syenite	Kh-03-56	alk fsp	clusters	-89	V
479	alkaline syenite	Kh-03-56	nepheline	clusters	-90.8	V
480	alkaline syenite	Kh-03-56	nepheline	clusters	-75.3	V
481	alkaline syenite	Kh-03-56	nepheline	clusters	-84.3	V
482	alkaline syenite	Kh-03-56	nepheline	clusters	-86.1	V
483	alkaline syenite	Kh-03-56	nepheline	clusters	-75.3	V
484	alkaline syenite	Kh-03-56	nepheline	clusters	-85.1	V
485	alkaline syenite	Kh-03-57	alk fsp	clusters	-80.3	V
486	alkaline syenite	Kh-03-57	alk fsp	clusters	-75.3	V

Appendix A6.1a: Microthermometry results of methane-dominant fluid inclusions. Th-homogenisation temperature.

#	rock type	sample	host	appears in:	T_h	homo-genise to
487	alkaline syenite	Kh-03-57	alk fsp	clusters	-80.3	V
488	alkaline syenite	Kh-03-57	alk fsp	clusters	-68.9	V
489	alkaline syenite	Kh-03-57	alk fsp	FIP	-75.3	V
490	alkaline syenite	Kh-03-57	alk fsp	FIP	-74.3	V
491	alkaline syenite	Kh-03-57	alk fsp	FIP	-92.4	V
492	alkaline syenite	Kh-03-57	alk fsp	FIP	-86.3	V
493	alkaline syenite	Kh-03-57	alk fsp	FIP	-89.6	V
494	alkaline syenite	Kh-03-57	alk fsp	FIP	-78	V
495	alkaline syenite	Kh-03-57	alk fsp	clusters	-93.8	V
496	alkaline syenite	Kh-03-57	alk fsp	clusters	-80.3	V
497	alkaline syenite	Kh-03-57	alk fsp	clusters	-81.1	V
498	alkaline syenite	Kh-03-57	alk fsp	clusters	-90.3	V
499	alkaline syenite	Kh-03-57	nepheline	clusters	-92.1	V
500	alkaline syenite	Kh-03-57	nepheline	FIP	-84.5	V
501	alkaline syenite	Kh-03-57	nepheline	FIP	-86.3	V
502	alkaline syenite	Kh-03-57	nepheline	FIP	-75.5	V
503	alkaline syenite	Kh-03-57	nepheline	FIP	-85.3	V
504	alkaline syenite	Kh-03-57	nepheline	FIP	-80.5	V
505	alkaline syenite	Kh-03-59	alk fsp	clusters	-69.1	V
506	alkaline syenite	Kh-03-59	alk fsp	clusters	-75.5	V
507	alkaline syenite	Kh-03-59	alk fsp	clusters	-80.4	V
508	alkaline syenite	Kh-03-59	alk fsp	clusters	-80.5	V
509	alkaline syenite	Kh-03-59	alk fsp	clusters	-69.1	V
510	ijolite	Kh-03-65	nepheline	single	-75.2	L
511	ijolite	Kh-03-65	nepheline	single	-78.7	L
512	ijolite	Kh-03-67	nepheline	single	-87.5	L
513	ijolite	Kh-03-67	nepheline	single	-89.9	L
514	ijolite	Kh-03-61	nepheline	clusters	-75.5	V
515	ijolite	Kh-03-61	nepheline	clusters	-74	V
516	ijolite	Kh-03-61	nepheline	FIP	-76.3	V
517	ijolite	Kh-03-61	nepheline	FIP	-85.3	V
518	ijolite	Kh-03-61	nepheline	FIP	-87.1	V
519	ijolite	Kh-03-61	nepheline	FIP	-76.3	V
520	ijolite	Kh-03-61	nepheline	FIP	-86.1	V
521	ijolite	Kh-03-62	nepheline	FIP	-81.3	V
522	ijolite	Kh-03-62	nepheline	FIP	-69.9	V
523	ijolite	Kh-03-62	nepheline	clusters	-75.1	V
524	ijolite	Kh-03-62	nepheline	FIP	-80.1	V
525	ijolite	Kh-03-62	nepheline	FIP	-68.7	V
526	ijolite	Kh-03-62	nepheline	FIP	-75.1	V
527	ijolite	Kh-03-62	nepheline	FIP	-68.7	V
528	ijolite	Kh-03-62	nepheline	clusters	-75.1	V
529	ijolite	Kh-03-62	nepheline	clusters	-74.1	V
530	ijolite	Kh-03-65	nepheline	FIP	-98.7	V
531	ijolite	Kh-03-65	nepheline	FIP	-81.2	V
532	ijolite	Kh-03-65	nepheline	FIP	-75.7	V
533	ijolite	Kh-03-65	nepheline	FIP	-78.9	V
534	ijolite	Kh-03-65	nepheline	FIP	-77.6	V
535	ijolite	Kh-03-65	nepheline	FIP	-75.4	V
536	ijolite	Kh-03-65	nepheline	FIP	-83.6	V
537	ijolite	Kh-03-65	nepheline	FIP	79.4	V
538	ijolite	Kh-03-65	nepheline	FIP	-73	V
539	ijolite	Kh-03-66	nepheline	FIP	-62.5	V
540	ijolite	Kh-03-66	nepheline	FIP	-79	V

Appendix A6.1a: Microthermometry results of methane-dominant fluid inclusions. Th-homogenisation temperature.

#	rock type	sample	host	appears in:	T_h	homo-genise to
541	ijolite	Kh-03-66	nepheline	FIP	-67.6	V
542	ijolite	Kh-03-66	nepheline	FIP	-74	V
543	ijolite	Kh-03-66	nepheline	FIP	-67.6	V
544	ijolite	Kh-03-66	nepheline	clusters	-74	V
545	ijolite	Kh-03-66	nepheline	clusters	-73	V
546	lujavrite	Kh-03-18	nepheline	clusters	-80.7	V
547	lujavrite	Kh-03-18	nepheline	single	-83	V
548	lujavrite	Kh-03-18	nepheline	FIP	-79	V
549	lujavrite	Kh-03-18	nepheline	FIP	-77.6	V
550	lujavrite	Kh-03-18	nepheline	FIP	-74	V
551	lujavrite	Kh-03-18	nepheline	FIP	-74.9	V
552	lujavrite	Kh-03-18	nepheline	clusters	-82.3	V
553	lujavrite	Kh-03-18	nepheline	clusters	-79.1	V
554	lujavrite	Kh-03-18	nepheline	clusters	-93.1	V
555	lujavrite	Kh-03-22	nepheline	clusters	-98.2	V
556	lujavrite	Kh-03-22	nepheline	single	-89.9	V
557	lujavrite	Kh-03-22	nepheline	single	-81.5	V
558	lujavrite	Kh-03-22	nepheline	single	-81.1	V
559	lujavrite	Kh-03-22	nepheline	single	-83	V
560	lujavrite	Kh-03-22	nepheline	FIP	-74	V
561	lujavrite	Kh-03-22	nepheline	FIP	-83.1	V
562	lujavrite	Kh-03-22	nepheline	FIP	-79	V
563	lujavrite	Kh-03-22	nepheline	FIP	-83.1	V

Appendix A6.1a: Microthermometry results of methane-dominant fluid inclusions. Th-homogenisation temperature.

#	rock type	sample	host	appears in:	phases at room temp.	vapour phase consists of	fluid homo-genise to	approx. T first ice melting	approx. T HH melting	T last ice melting	T_{diss} daughter min	T_h
1	khibinite	Kh-03-3	nepheline	clusters	L+V	CH4	V	-58	-36	-8.6		427
2	khibinite	Kh-03-3	nepheline	single	L+V	H2O	decr.	-53	-33	-8.6		>500
3	khibinite	Kh-03-4	nepheline	clusters	L+V	H2O	V	-48	-31	-2.1		350
4	khibinite	Kh-03-8	nepheline	clusters	L+V+S	H2O	decr.	-56	-30	-7.9	203	>500
5	khibinite	Kh-03-8	nepheline	clusters	L+V	H2O	V	-49	-30	-7.8		325
6	khibinite	Kh-03-8	nepheline	clusters	L+V	H2O	V	-56	-29	-5.4		350
7	khibinite	Kh-03-8	nepheline	single	L+V	CH4	V	-52	-27	-6.6		452
8	khibinite	Kh-03-4	nepheline	clusters	L+V	CH4	V	-49	-25	-5.3		425
9	khibinite	Kh-03-4	nepheline	clusters	L+V	CH4	V	-52	-25	-9.6		395
10	khibinite	Kh-03-8	nepheline	clusters	L+V	H2O	V	-51	-25	-8.7		355
11	khibinite	Kh-03-4	nepheline	clusters	L+V	H2O	V	-56	-25	-3.3		350
12	khibinite	Kh-03-7	nepheline	FIP	L+V	H2O	V	-52	-24	-8		330
13	khibinite	Kh-03-8	nepheline	clusters	L+V+S	H2O	decr.	-47	-24	-3.2	189	>500
14	khibinite	Kh-03-8	nepheline	single	L+V	H2O	V	-53	-24	-5.6		481
15	khibinite	Kh-03-7	nepheline	FIP	L+V	H2O	V	-56	-24	-4.1		420
16	khibinite	Kh-03-8	nepheline	clusters	L+V	H2O	V	-51	-24	-5.6		467
17	khibinite	Kh-03-3	nepheline	single	L+V	CH4	decr.	-51	-23	-2.2		>500
18	khibinite	Kh-03-8	nepheline	clusters	L+V	H2O	V	-51	-21	-3.1		395
19	khibinite	Kh-03-3	nepheline	clusters	L+V	CH4	decr.	-51	-21	-5.6		>500
20	khibinite	Kh-03-4	nepheline	clusters	L+V	CH4	V	-50	-20	-5.3		255
21	rischorrite	Kh-03-12	nepheline	clusters	L+V	H2O	decr.	-55	-32	-6.6		>500
22	rischorrite	Kh-03-50	nepheline	clusters	L+V	H2O	decr.	-50	-31	-12.3		>500
23	rischorrite	Kh-03-12	nepheline	clusters	L+V	H2O	decr.	-55	-31	-3.4		>500
24	rischorrite	Kh-03-42	nepheline	clusters	L+V	H2O	V	-56	-30	-7.9		367
25	rischorrite	Kh-03-12	nepheline	clusters	L+V	H2O	decr.	-55	-30	-3.5		>500
26	rischorrite	Kh-03-12	nepheline	clusters	L+V	H2O	decr.	-50	-27	-8.6		>500
27	rischorrite	Kh-03-12	nepheline	clusters	L+V	CH4	decr.	-47	-24	-3.2		>500
28	rischorrite	Kh-03-42	nepheline	clusters	L+V	H2O	V	-56	-24	-2.5		374
29	rischorrite	Kh-03-42	nepheline	clusters	L	H2O	V	-51	-23	-8.9		379
30	rischorrite	Kh-03-50	nepheline	clusters	L+V+S	CH4	decr.	-56	-23	-14.5	265	>500
31	rischorrite	Kh-03-42	nepheline	clusters	L+V	CH4	decr.	-48	-22	-9.6		>500
32	rischorrite	Kh-03-42	nepheline	clusters	L+V+S	CH4	V	-41	-21	-3.6	179	383

Appendix A6.1b: Microthermometry results of aqueous fluid inclusions. HH-hydrohalite; T_{diss}-temperature of dissolution; T_h-homogenisation temperature.

#	rock type	sample	host	appears in:	phases at room temp.	vapour phase consists of	fluid homo-genise to	approx. T first ice melting	approx. T HH melting	T last ice melting	T_{diss} daughter min	T_h
33	rischorrite	Kh-03-50	nepheline	clusters	L+V	CH4	decr.	-54	-21	-16.7		>500
34	albitised foyaite	Kh-03-37	albite	clusters	L+V	H2O	V	-56	-29	-2.8		380
35	albitised foyaite	Kh-03-35	albite	clusters	L+V	H2O	decr.	-52	-28	-8.4		>500
36	albitised foyaite	Kh-03-41	eudialite	clusters	L+V	H2O	V	-55	-25	-2		290
37	albitised foyaite	Kh-03-37	albite	clusters	L+V	CH4	V	-54	-22	-10.4		433
38	albitised foyaite	Kh-03-37	albite	clusters	L+V	CH4	decr.	-56	-22	-2		>500
39	albitised foyaite	Kh-03-40	albite	clusters	L+V	CH4	decr.	-51	-22	-3.4		>500
40	albitised foyaite	Kh-03-37	albite	clusters	L+V	CH4	L	-52	-22	-1.7		460
41	albitised foyaite	Kh-03-40	nepheline	clusters	L+V	CH4	decr.	-56	-22	-7.2		>500
42	albitised foyaite	Kh-03-35	albite	clusters	L+V	CH4	decr.	-50	-21	-5.8		>500
43	albitised foyaite	Kh-03-41	albite	clusters	L+V	CH4	decr.	-47	-21	-1.5		>500
44	albitised foyaite	Kh-03-35	albite	clusters	L+V	CH4	decr.	-56	-21	-7.1		>500
45	albitised foyaite	Kh-03-41	nepheline	clusters	L+V	CH4	decr.	-56	-20	-15.7		>500
46	albitised foyaite	Kh-03-37	eudialite	clusters	L+V	CH4	decr.	-55	-20	-6.7		>500
47	massiv foyaite	Kh-03-55	nepheline	clusters	L+V	CH4	V	-56	-37	-3.8		456
48	massiv foyaite	Kh-03-55	nepheline	clusters	L+V	H2O	decr.	-56	-37	-2.8		>500
49	massiv foyaite	Kh-03-51	nepheline	clusters	L+V	CH4	V	-53	-35	-8.5		455
50	massiv foyaite	Kh-03-52	nepheline	clusters	L+V	H2O	V	-53	-35	-3.2		487
51	massiv foyaite	Kh-03-52	albite	clusters	L+V	CH4	decr.	-55	-25	-6.7		>500
52	massiv foyaite	Kh-03-55	nepheline	clusters	L+V	CH4	L	-56	-23	-9.5		390
53	massiv foyaite	Kh-03-55	albite	clusters	L+V	CH4	decr.	-55	-23	-7		>500
54	massiv foyaite	Kh-03-55	nepheline	clusters	L+V	H2O	V	-53	-23	-5.1		421
55	massiv foyaite	Kh-03-51	albite	clusters	L+V	CH4	V	-52	-20	-9.9		387
56	alkaline syenite	Kh-03-57	nepheline	clusters	L+V	CH4	V	-47	-39	-2.3		388
57	alkaline syenite	Kh-03-60	nepheline	clusters	L+V	H2O	L	-56	-28	-5.8		411
58	alkaline syenite	Kh-03-60	nepheline	clusters	L+V	CH4	L	-54	-24	-5.5		389
59	alkaline syenite	Kh-03-56	nepheline	clusters	L+V	CH4	decr.	-54	-22	-6		>500
60	alkaline syenite	Kh-03-56	nepheline	clusters	L+V	CH4	decr.	-54	-22	-5.4		>500
61	alkaline syenite	Kh-03-57	nepheline	clusters	L+V	CH4	decr.	-53	-20	-5.5		>500
62	alkaline syenite	Kh-03-60	nepheline	clusters	L+V	H2O	V	-56	-20	-7.3		399
63	ijolite	Kh-03-65	nepheline	FIP	L+V	H2O	decr.	-50	-35	-4.3		>500
64	ijolite	Kh-03-61	nepheline	clusters	L+V	H2O	V	-52	-34	-12.5		490

Appendix A6.1b: Microthermometry results of aqueous fluid inclusions. HH-hydrohalite; T_{diss}-temperature of dissolution; T_h-homogenisation temperature.

#	rock type	sample	host	appears in:	phases at room temp.	vapour phase consists of	fluid homo-genise to	approx. T first ice melting	approx. T HH melting	T last ice melting	T_{diss} daughter min	T_h
65	ijolite	Kh-03-65	nepheline	clusters	L+V	H2O	decr.	-53	-33	-2.5		>500
66	ijolite	Kh-03-66	nepheline	clusters	L+V	CH4	decr.	-53	-31	-6.5		>550
67	ijolite	Kh-03-65	nepheline	FIP	L+V	CH4	V	-55	-29	-3.3		455
68	ijolite	Kh-03-66	nepheline	single	L+V	H2O	L	-52	-28	-7.7		465
69	ijolite	Kh-03-61	nepheline	clusters	L+V	H2O	decr.	-56	-27	-3.6		>500
70	ijolite	Kh-03-66	nepheline	clusters	L+V	H2O	V	-47	-26	-4.5		375
71	ijolite	Kh-03-62	nepheline	clusters	L+V	CH4	V	-56	-23	-9.5		438
72	ijolite	Kh-03-62	nepheline	clusters	L+V	H2O	V	-56	-23	-8.3		412
73	ijolite	Kh-03-66	nepheline	clusters	L+V	CH4	V	-55	-23	-4.5		387
74	ijolite	Kh-03-65	nepheline	clusters	L+V	CH4	decr.	-47	-23	-7.8		>500
75	ijolite	Kh-03-66	nepheline	clusters	L+V	CH4	L	-47	-21	-1.5		422
76	ijolite	Kh-03-62	nepheline	clusters	L+V	CH4	decr.	-53	-20	-4.5		>500
77	lujavrite	Kh-03-22	nepheline	clusters	L+V	H2O	decr.	-54	-39	-9.5		>500
78	lujavrite	Kh-03-22	nepheline	clusters	L+V	H2O	decr.	-58	-39	-5.8		>500
79	lujavrite	Kh-03-18	nepheline	clusters	L+V	H2O	decr.	-55	-38	-7.7		>500
80	lujavrite	Kh-03-18	nepheline	clusters	L+V	H2O	decr.	-55	-38	-7.7		>500
81	lujavrite	Kh-03-18	nepheline	clusters	L+V	H2O	decr.	-55	-35	-8.5		>500
82	lujavrite	Kh-03-18	nepheline	single	L+V	H2O	V	-56	-24	-8		480
83	lujavrite	Kh-03-22	nepheline	clusters	L+V	H2O	V	-56	-24	-8		480
84	lujavrite	Kh-03-22	nepheline	clusters	L+V	CH4	decr.	-53	-23	-4.9		>500
85	lujavrite	Kh-03-18	nepheline	clusters	L+V	CH4	decr.	-54	-22	-5.5		>500
86	lujavrite	Kh-03-18	nepheline	single	L+V	CH4	decr.	-50	-22	-9		>500
87	lujavrite	Kh-03-22	nepheline	clusters	L+V	CH4	decr.	-40	-21	-6.5		>500
88	lujavrite	Kh-03-18	nepheline	clusters	L+V	CH4	decr.	-51	-21	-6		>500
89	lujavrite	Kh-03-22	nepheline	clusters	L+V	CH4	decr.	-56	-21	-4		>500

Appendix A6.1b: Microthermometry results of aqueous fluid inclusions. HH-hydrohalite; T_{diss}-temperature of dissolution; T_h-homogenisation temperature.